Molecular Design Strategies for Enhancing Triplet Harvesting Efficiency in Organic Emitters and Aggregates via Thermally Activated Delayed Fluorescence (TADF) and Room Temperature Phosphorescence (RTP)

विद्या वाचस्पति की उपाधि की अपेक्षाओं की आंशिक पूर्ति में प्रस्तुत शोध प्रबंध

A thesis submitted in the partial fulfilment of the requirements of the degree of Doctor of Philosophy

द्वारा / By

अभिजीत चटर्जी / Abhijit Chatterjee
पंजीकरण सं. 20172014 / Registration No.: 20172014

शोध प्रबंध पर्यवेक्षक / Thesis Supervisor: प्रो. पार्थ हाजरा/ Prof. Partha Hazra

भारतीय विज्ञान शिक्षा एवं अनुसंधान संस्थान पुणे
INDIAN INSTITUTE OF SCIENCE EDUCATION AND RESEARCH
2024

Dedicated to Baba, Maa, Dada, and Jui, for their unwavering belief in my potential

INDIAN INSTITUTE OF SCIENCE EDUCATION AND RESEARCH PUNE
(An Autonomous Institution, Ministry of Education, Govt. of India) Dr. Homi Bhabha Road, Pashan Pune – 411008

Declaration

I declare that this written submission represents my ideas in my own words and where others' ideas have been included; I have adequately cited and referenced the original sources. I declare that I have acknowledged collaborative work and discussions wherever such work has been included. I also declare that I have adhered to all principles of academic honesty and integrity and have not misrepresented or fabricated or falsified any idea/data/fact/source in my submission. I understand that violation of the above will be cause of disciplinary action by the institute and can also evoke penal action from the sources which have thus not been properly cited or from whom proper permission has not been taken when needed.

The work reported in this Thesis is the original work done by me under the guidance of Prof. Partha Hazra.

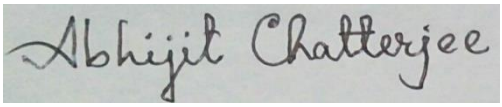

Date: 13th January, 2024 **Mr. Abhijit Chatterjee**

INDIAN INSTITUTE OF SCIENCE EDUCATION AND RESEARCH PUNE
(An Autonomous Institution, Ministry of Education, Govt. of India) Dr. Homi Bhabha Road, Pashan Pune – 411008

Certificate

Certified that the work incorporated in this thesis entitled "***Molecular Design Strategies for Enhancing Triplet Harvesting Efficiency in Organic Emitters and Aggregates via Thermally Activated Delayed Fluorescence (TADF) and Room Temperature Phosphorescence (RTP)***," submitted by ***Mr. Abhijit Chatterjee*** was carried out by the candidate, under my supervision. The work presented here or any part of it has not been included in any other thesis submitted previously for the award of any degree or diploma from any other University or Institution.

Partha Hazra

Date: 13th January, 2024 **Prof. Partha Hazra**

Acknowledgment

First and foremost, I would like to express my sincere appreciation to my supervisor, **Prof. Partha Hazra,** for his exceptional guidance, encouragement, and expertise throughout my doctoral journey. Your insightful feedback and unwavering support have laid the foundation for my academic progress, and I am truly grateful for your mentorship. I would also like to extend my gratitude to the members of my research advisory committee, **Prof. RGB, Prof. Vaidhyanthan, and Prof. Pankaj Mandal**, for their valuable suggestions and critical feedback, which have significantly enriched this work. Your time, effort, and dedication have been crucial in shaping the direction of this research. I am deeply thankful to my collaborators—**Prof. Mayurika Lahiri, Prof. Pankaj Mandal from IISER Pune, Prof. Santhosh Babu Sukumaran from NCL Pune, and Prof. Rajamalli from IISc Bangalore**—whose discussions, suggestions, and technical contributions have been indispensable to the progress of this project. Furthermore, I am grateful to **Dr. Madan D. Ambhore, Dr. Tariq Sheikh, Dr. Habibul Arfin, Dr. Rintu M. Umesh, Ms. Riteeka Tanwar, Ms. Aswini Narayanan, Mr. Ajay Malik, Mr. Ashwath K., and Mr. Santhosh Aedelli** for their continuous support and guidance throughout the research.

My sincere thanks go to the non-teaching staff and technical experts at our department and IISER Pune, especially **Mr. Mayuresh Kulkarni, Dr. Sandeep Kumar Mishra, Mr. Nitin Dalvi, Mr. Mahesh Jadhav, Dr. Abhijit Biswas, Dr. Sandeep Kanade, and Mr. Sanjay Kumar Meena,** for their prompt assistance whenever required.

I am deeply appreciative of **IISER Pune and DST-SERB**, **Government of India**, for their fellowship and research funding, which have been crucial for this work. I would also like to thank the **National Supercomputing Mission, Government of India**, for providing access to high-performance computing resources, facilitating the computational aspects of this research. Additionally, I am thankful to **DST-SERB**, Government of India, and the **Infosys Foundation** for covering the expenses of my participation in the international conference.

To my senior lab mates—**Dr. Sagar, Dr. Bibhisan, Dr. Konoya, Dr. Aslam, and Dr. Joy**—thank you for being a second family during the early days in the lab, a time when life felt at its peak. From troubleshooting experiments to celebrating successes (and occasional failures) with coffee breaks, laughter, and dinner parties, these experiences have been truly rewarding. Special thanks to **Dr. Joy** for teaching me about instrumentation techniques and for being a constant source of collaboration and motivation. I also cherish the post-Covid Saturday night

parties with **Aslam** and **Joy**, where Aslam cooked delicious mutton kosha—unforgettable memories. I am thankful to my juniors—**Mr. Madhusudan, Ms. Sundaravalli, Ms. Anwesha, Dr. Sandhya, Ms. Priyanka, and Mr. Adil**—for their collaboration and for fostering a positive, engaging atmosphere in the lab. I would especially like to thank my colleague and friend, Ms. **Sundaravalli**, for her support, insightful assistance, and stimulating scientific discussions, which contributed to maintaining a healthy and productive lab environment.

Outside the academic sphere, I am fortunate to have shared this journey with an incredible group of friends—**Tamoghna**, **Laha**, **Panda**, **Sayan Saha**, **Pratim**, **Sumit**, and **Rathee Bhai**. The late-night UEFA Champions League and Football World Cup matches, where we cheered for our favorite teams and debated every goal, will remain some of my most cherished memories. Weekend parties, experimenting with new recipes during group cooking sessions, and simply spending time together brought joy and balance to my otherwise hectic schedule. These moments of camaraderie reminded me of the importance of relaxing and cherishing friendships.

I also want to express my deep gratitude to **Lionel Messi**, whose exceptional skill, dedication, and perseverance on the field have been a constant source of inspiration. His performances with **Barcelona** and the **Argentina national team** have not only brought immense joy to millions of fans like myself but have also reinforced the values of hard work, passion, and resilience. I also want to thank **Mohun Bagan**, my cherished football club, for instilling a sense of pride and motivation in me. Football, in all its forms—whether through Messi's brilliance, the legacy of Barcelona and Argentina, or the pride of Mohun Bagan—has provided comfort during challenging moments, teaching me valuable lessons on teamwork, resilience, and dedication.

On a personal level, I am profoundly grateful to my family for their unwavering support. To my parents, **Debiprasad Chatterjee** and **Mili Chatterjee**, my brother **Swarnajit Chatterjee** (**Babu**), my friend **Jit**, and my sister-in-law **Payel Goswami (Piu)**, thank you for your unconditional love, sacrifices, and belief in me. Your encouragement has been a constant source of strength. To my partner, **Jui**, thank you for your patience, understanding, and emotional support during this long journey. You have been a pillar of support, especially during difficult times, and have made me stronger than I ever thought possible.

I am also deeply thankful for the solace I have found in music. The timeless beauty of **ghazals**, the depth of **Hindustani classical music**, and the emotive power of **thumris** have been therapeutic companions during challenging times, offering me peace and introspection. Music has always reminded me of its ability to heal, soothe, and uplift the spirit.

As a **Bengali nationalist**, I take immense pride in the rich culture, heritage, and beauty of my motherland, **Bengal**. I will always be indebted to my motherland. From its picturesque rural landscapes to its vibrant traditions and folk arts, I remain deeply fascinated by the essence of my homeland. The history, the people, and the natural beauty continue to inspire me and strengthen my connection to the land.

Lastly, I would like to thank all my friends and well-wishers for their continued encouragement and kind words. Your presence and support have been vital to navigating this challenging journey. This thesis is a culmination of many shared efforts, and I am genuinely thankful to each and every one of you for being part of this experience.

Abhijit Chatterjee

Synopsis

This thesis focuses on the design and development of multifunctional luminogens with efficient triplet harvesting aiming to enhance their performance in optoelectronic and sensory devices. It addresses many notable challenges like- aggregation-caused quenching (ACQ) in organic solid-state emitters and explores how systematic molecular modifications can overcome ACQ and enable efficient luminescence. Key aspects of the thesis include the molecular design of materials and the impact of structural variations on photophysical behavior, particularly thermally activated delayed fluorescence (TADF) and room temperature phosphorescence (RTP) efficiency. The thesis also investigates the factors influencing TADF efficiency in organic molecular aggregates, contributing to the development of high-performance OLED devices. Additionally, notable contributions have been made by utilizing hyperfluorescence processes to achieve pure and efficient yellow emission. Overall, the thesis contributes to advancing multifunctional luminogens, offering valuable insights for their application in optoelectronics, bioimaging, and related fields.

Chapter 1. Introduction to thermally activated delayed fluorescence (TADF), room temperature phosphorescence (RTP), and other related pathways for efficient solid-state emission: Fundamentals and applications

The principles governing light emission in organic solid-state emitters are significantly influenced by their mode of aggregation. Strong π-π stacking interactions typically result in quenched emission in the solid state, a phenomenon commonly referred to as aggregation-caused quenching (ACQ). In contrast, aggregation-induced emission (AIE) produces the opposite effect, enabling materials to emit light in the solid state. This chapter explores the crucial structure-property relationships and underlying mechanisms of these phenomena. Beyond achieving strong solid-state emission, another critical consideration is the efficiency of these emitters when implemented in real-world OLED applications. In this regard, efficient utilization of both singlet and triplet excitons, termed triplet harvesting, is of paramount importance. Thermally activated delayed fluorescence (TADF), which addresses these efficiency challenges, is a key focus. A comprehensive analysis of TADF mechanisms and the factors influencing them is provided. Additionally, other effective triplet harvesting approaches, such as room-temperature phosphorescence (RTP) and TADF-sensitized hyperfluorescence, are also discussed in detail.

Chapter 2. Emergence of Aggregation Induced Emission (AIE), Room-Temperature Phosphorescence (RTP), and Multistimuli Response from a Single Organic Luminogen by Directed Structural Modification

This research focuses on developing novel multifunctional metal-free organic luminogens with Aggregation Induced Emission (AIE), Room-Temperature Phosphorescence (RTP), and mechanochromic behavior through systematic molecular engineering. Starting with TPANDI (Fig. 1), initially non-emissive due to strong π–π stacking among its planar naphthalene diimide units in aggregated states, modifications to the acceptor core in TPANMI and TPAPMI disrupt π–π stacking, transforming their behavior from Aggregation Caused Quenching (ACQ) to AIE. While TPANMI and TPAPMI exhibit AIE and RTP properties, they lack mechanochromic activity. To achieve simultaneous AIE, RTP, and mechanochromism, structural refinements introduced a cyano-ethylene group and a benzene linker in TPACNPMI (Fig. 1). This modification induced mechanochromic behavior alongside AIE and RTP properties. The study highlights the transformative capability of systematic structural engineering in converting molecules from ACQ to multifunctional luminogens. and was published in the Journal of Physical Chemistry B, J. Phys. Chem. B 2021, 125, 46, 12832–12846.

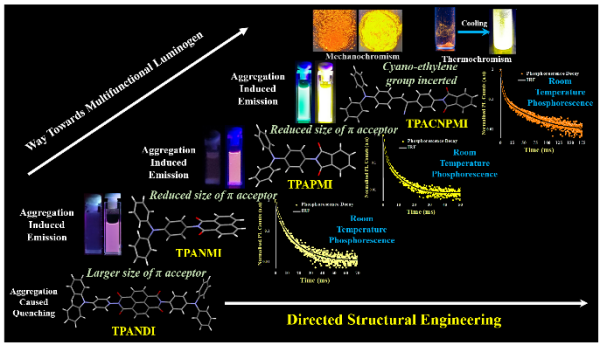

Chapter 3. Engineering TADF, Mechanochromism, and Second Harmonic Up-conversion Properties in Regioisomeric Substitution Space

In this research, the applicant focuses on investigating the trifecta of Thermally Activated Delayed Fluorescence (TADF), Second Harmonic Generation (SHG), and mechanochromic luminescence (MCL) across three regio-isomers based on donor–acceptor structures. Through rigorous experimentation, it sis shown that the TADF properties can be finely adjusted from the ortho to the para isomer. Specifically, the ortho-isomer, DPAOCN, exhibits the slowest reverse intersystem crossing (RISC) rate ($\sim 10^2$–10^4 s^{-1}), whereas the para-isomer, DPAPCN, displays the highest TADF efficiency with an RISC rate approaching $\sim 10^6$ s^{-1}. These variations

in TADF efficiency primarily arise from differences in energy splitting (ΔE_{ST}) values and the extent of spin–orbit coupling (SOC) between the lowest singlet and triplet states. Additionally, the crystal structures of these isomers differ significantly: the ortho-isomer adopts a non-centrosymmetric and chiral $P2_12_12_1$ space group, whereas the other two crystallize in the centrosymmetric $P2_1/C$ space group. Remarkably, the non-centrosymmetric packing of the ortho-isomer leads to exceptional mechanochromic luminescence properties, emitting green, yellow, and orange light, alongside impressive SHG characteristics with a $\chi^{(2)}$ value of 0.19 pmV^{-1} at 1220 nm and a Laser-Induced Damage Threshold (LIDT) of 13.27 GW cm^{-2}. Furthermore, the electroluminescence potential of all three isomers through converted LED (cLED) device fabrication is explored. Moreover, these isomers demonstrate significant two-photon absorption activity in both solution and crystal states and are successfully utilized in two-photon confocal cell imaging. This region-isomeric fine-tuning approach of TADF efficiency adopted by the applicant was considered to be greatly contributing to the TADF community for designing highly efficient TADF emitters and was published in the journal- Chemical Science, Chem. Sci., 2023,14, 13832-13841.

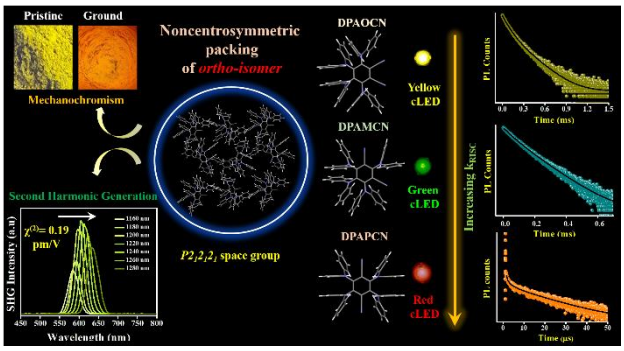

Chapter 4. Navigating the ΔE_{ST} Factor by Excited State Potential Energy Surface Analysis in Aggregation Induced Delayed Fluorescence Emitters

This study presents three donor-acceptor-based luminogens—TN, TA, and TP—exhibiting aggregation-induced delayed fluorescence (AIDF) properties. A combination of solvent-phase analysis and QM/MM-based calculations highlights a significant reduction in ΔE_{ST} values in the aggregated state, which is key to their AIDF behavior. These luminogens, characterized by a strong charge-transfer nature, effectively enhance singlet exciton diffusion length, enabling efficient photocurrent generation. Furthermore, their remarkable two-photon absorption capabilities underscore their potential for applications such as anti-Stokes shifted photoluminescence (ASPL) and two-photon cell imaging. Just accepted in *Chemical Communications* (https://doi.org/10.1039/D4CC05113K).

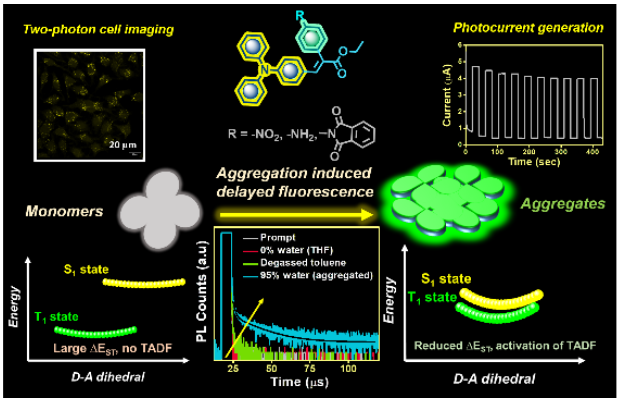

Chapter 5. Donor Unit Engineering and Structural Dynamics for Enhanced TADF Performance in Organic Molecular Aggregates

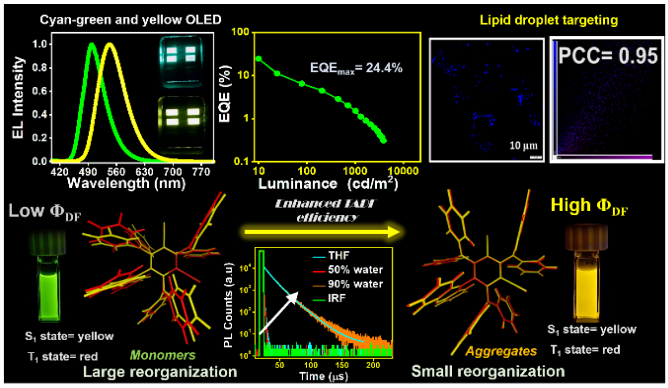

This study delves into the key factors enhancing the thermally activated delayed fluorescence (TADF) efficiencies of molecular aggregates, emphasizing the importance of energy gaps, spin-orbit coupling, and structural reorganization in the excited state. By synthesizing and analyzing a novel series of TADF emitters, it is demonstrated that the donor unit—such as phenoxazine, carbazole, and their derivatives—plays a pivotal role in influencing reverse intersystem crossing (RISC) rates, TADF lifetimes, and emission characteristics. Among these, phenoxazine-based emitters exhibit the highest TADF efficiency with rapid RISC rates (~10^6 cm^{-1}), while carbazole-based emitters show slower rates (~10^3-10^4 cm^{-1}), longer TADF lifetimes, and diverse emission colors. Interestingly, the incorporation of carbazole-based emitters with mechanochromic luminescence (MCL) properties highlights their potential as multifunctional luminogens without compromising TADF performance. The fabrication of OLED devices with external quantum efficiencies exceeding 20% demonstrates the practical utility of these materials in advanced optoelectronic applications. This work provides critical insights into the design of efficient TADF emitters and establishes a foundation for developing high-performance, solution-processable materials for next-generation organic electronic devices, enabling advancements in light-emitting and sensing technologies.

List of Abbreviations

FWHM	Full width at Half Maximum
EDDM	Electron Density Difference Maps
ACQ	Aggregation Caused Quenching
CT	Charge Transfer
LE	Locally Excited
HOMO	Highest Occupied Molecular Orbital
HPS	Hexaphenyl Silole
LUMO	Lowest Unoccupied Molecular Orbital
OLED	Organic Light Emitting Diode
PXRD	Powder X-Ray Diffraction
RIR	Restricted Intramolecular Rotation
RIV	Restricted Intramolecular Vibration
RIM	Restricted Intramolecular Motion
SCXRD	Single Crystal X-Ray Diffraction
TDDFT	Time-Dependent Density Functional Theory
DFT	Density Functional Theory
TCSPC	Time-Correlated Single Photon Count
μM	Micromolar
ns	Nanosecond
UV-Vis	Ultraviolet-Visible
TADF	Thermally Activated Delayed Fluorescence
RTP	Room-temperature Phosphorescence
QM/MM	Quantum mechanics/molecular mechanics
MCL	Mechanochromic Luminescence
RISC	Reverse Inter-system crossing
ISC	Intersystem crossing
SOCME	Spin-orbit coupling matrix element
SHG	Second Harmonic Generation
AIE	Aggregation Induced Emission
RMSD	Root-mean squared deviation

Publications

[First author]

1. **Abhijit Chatterjee**†, Sundaravalli Narayanan†, Sachin Thorat, Ajay J. Malik, Madan D. Ambhore, Aswini Narayanan, Anil Kumar Sihag, Sukumaran Santhosh Babu, Mayurika Lahiri, and Partha Hazra*. "Multifunctional Luminogens with Synergy of Aggregation-Induced Delayed Fluorescence, Two-Photon Absorption, and Photocurrent Generation". ***Chemical Communications***, Vol. 61, No. 7, 1447-1450, Jan. 2025 (†Contributed equally).
2. **Abhijit Chatterjee**, Joy Chatterjee, Subrahmanyam Sappati, Riteeka Tanwar, Madan D. Ambhore, Habibul Arfin, Rintu M. Umesh, Mayurika Lahiri, Pankaj Mandal, and Partha Hazra*. "Engineering TADF, mechanochromism, and second harmonic up-conversion properties in regioisomeric substitution space". ***Chemical Science***, Vol. 14, No. 47, 13832-13841, Nov. 2023.
3. **Abhijit Chatterjee**, Joy Chatterjee, Subrahmanyam Sappati, Tariq Sheikh, Rintu M. Umesh, Madan D. Ambhore, Mayurika Lahiri and Partha Hazra*. "Emergence of Aggregation Induced Emission (AIE), Room-Temperature Phosphorescence (RTP), and Multistimuli Response from a Single Organic Luminogen by Directed Structural Modification". ***The Journal of Physical Chemistry B***, Vol. 125, No. 46, 12832–12846, Nov. 2021.

[Co-author]

4. Javed Shaikh, Anindita Bhowmick†, **Abhijit Chatterjee**†, Debasish Laha, Ramakrishna G. Bhat*. "Palladium-Catalyzed C3-(sp2)-H Alkenylation of Pyrroles: A Direct Access to Novel Organic Thermally Activated Delayed Fluorescence (TADF) Materials". ***The Journal of Organic Chemistry***, Vol. 90, No. 1, 59–74, Jan. 2025 (†Contributed equally).
5. Joy Chatterjee, **Abhijit Chatterjee**, Riteeka Tanwar, Prakash Panwaria, Sajid Saikia, Madan D. Ambhore, Pankaj Mandal,* and Partha Hazra*. "Activation of TADF in Photon Up-converting Crystals of Dinuclear Cu(I)-iodide Complexes by Ligand Engineering". ***The Journal of Physical Chemistry Letters***, Vol. 15, No. 23, 6069–6080, May 2024.
6. Anindita Bhowmick, **Abhijit Chatterjee**, Sidharth S. Pathak and Ramakrishna G. Bhat. "A visible light-driven direct synthesis of industrially relevant glutaric acid diesters from aldehydes". ***Chemical Communications***, Vol. 59, No. 79, 11875-11878, Aug. 2023.
7. Joy Chatterjee, **Abhijit Chatterjee** and Partha Hazra*. "Intrinsic-to-extrinsic emission tuning in luminescent Cu nanoclusters by in-situ ligand engineering". ***Physical Chemistry Chemical Physics***, Vol. 23, No. 45, 25850-25865, Oct. 2021.
8. Joy Chatterjee, Riteeka Tanwar, Anupama S†, **Abhijit Chatterjee**†, Madan D. Ambhore,

Mukul Kabir, Pankaj Mandal*, Partha Hazra*. “Controlling Triplet-Harvesting Pathways and Nonlinear Optical Properties in Cu(I) Iodide-Based Polymers through Ligand Engineering”. ***The Journal of Physical Chemistry Letters,*** Vol. 16, No. 6, 1549–1558, Feb. 2025 (†Contributed equally).

9. Souvik Panda Mahapatra, Saikat Pahan, **Abhijit Chatterjee**, Souvik Roy, DRGKoppalu R. Puneeth Kumar, Hosahudya Gopi*. “Exploring Macroscopic Dipoles of Designed Cyclic Peptide Ordered Assemblies to Harvest Piezoelectric Properties”. ***Angewandte Chemie International Edition***., Vol. 63, No. 38, e202409969, Sep. 2024.

10. Javed Y. Shaikh, Anindita Bhowmick, **Abhijit Chatterjee**, Nitin A. Thombare, Ramakrishna G. Bhat. “Transient Directing Group Enabled C3-(sp2)−H Alkenylation of Five Membered Heterocyclic Aldehydes: An Access to Mechanochromic Luminogen”. ***Advanced Synthesis & Catalysis***, Vol. 365, No. 17, 2922–2928, July 2023.

11. Joy Debnath, Dhananjaya Keshamasetthy, Jacob Combs, Katherine Leon, Daniela Vullo, **Abhijit Chatterjee**, Robert McKenna, Claudiu T. Supuran. “A comparative study of diaryl urea molecules with and without sulfonamide group on Carbonic anhydrase IX and XII inhibition and its consequence on breast cancer cells”. ***Bioorganic Chemistry***, Vol.145, No. 0045-2068, 107192, April 2024.

Table of Contents

2. Emergence of Aggregation Induced Emission (AIE), Room-Temperature Phosphorescence (RTP), and Multistimuli Response from a Single Organic Luminogen by Directed Structural Modification

3. Engineering TADF, Mechanochromism, and Second Harmonic Up-conversion Properties in Regioisomeric Substitution Space

4. Navigating the ΔE_{ST} Factor by Excited State Potential Energy Surface Analysis in Aggregation Induced Delayed Fluorescence Emitters

5. Donor Unit Engineering and Structural Dynamics for Enhanced TADF Performance in Organic Molecular Aggregates

Chapter-1

Introduction to thermally activated delayed fluorescence (TADF), room temperature phosphorescence (RTP), and other related pathways for efficient solid-state emission: Fundamentals and applications

1.1 Introduction to aggregation-induced emission or AIE:

The concept of "aggregate" is commonly defined as a collection or ensemble of elements forming a whole. The Oxford Dictionary characterizes it as "a whole formed by combining several separate elements," while Wikipedia describes it as "a collection of items that are gathered together to form a total quantity." This definition is evident in various contexts, such as concrete in construction, which exemplifies the idea of an aggregate material. In scientific discourse, aggregates often refer to clusters of molecules or particles. This notion becomes particularly relevant in photophysical studies, where aggregation can influence luminescence properties significantly. One notable photophysical phenomenon linked to molecular aggregation is concentration quenching (CQ). As described in the literature, CQ refers to the reduction in emission intensity as the concentration of a luminophore increases. This effect, extensively documented by Birks in studies on aromatic molecules, often arises from the aggregation of luminophores, leading to non-radiative processes that suppress fluorescence (**Figure 1**). For instance, fluorescein exhibits a marked CQ effect; its fluorescence diminishes in mixed solvent systems as aggregation increases, ultimately resulting in complete quenching under specific conditions. This behavior results from π–π stacking interactions that generate non-emissive species like excimers. While CQ presents a significant challenge in applications requiring high emission efficiency, the opposite photophysical event, aggregation-induced emission (AIE),[1–10] has garnered attention for its potential benefits (**Figure 1**). Unlike CQ, AIE describes systems where aggregation enhances luminescence. Molecules exhibiting AIE, often referred to as AIEgens, remain weakly emissive in dilute solutions but emit strongly upon aggregation in anti-solvents or solid states. A classic example is hexaphenylsilole (HPS),[11] which shows negligible fluorescence as a monomer but becomes strongly emissive in poor solvent mixtures due to aggregation (**Figure 1**). The AIE effect has broad implications for developing advanced materials. By leveraging the luminescence properties of aggregates, researchers can design new optoelectronic materials, chemical sensors, and biomedical probes.[4,10,12–15] This approach contrasts with efforts to mitigate CQ, which typically involve modifying molecular structures to prevent aggregation but often lead to trade-offs in performance. In contrast, AIE exploits aggregation as a beneficial phenomenon, paving the way for innovative applications in solid-state luminescent materials (**Figure 1**). Research into AIE continues to uncover insights into the mechanisms governing luminescence in the aggregate state. This has facilitated the development of molecular engineering strategies

centered on restricting intramolecular motions, a key factor in AIE behavior. By understanding and harnessing these mechanisms, AIE research holds the promise of advancing luminescence technologies that were previously constrained by CQ effects.

1.2 Mechanistic Analysis of AIE Phenomena

Understanding the mechanisms that drive aggregation-induced emission (AIE) is crucial for enhancing our knowledge of luminescence processes and for guiding the development of new AIE materials. Several mechanisms have been proposed to explain the phenomenon of Aggregation-Induced Emission (AIE); e.g. the restriction of intramolecular rotation (RIR),[16] J-aggregate formation (JAF), twisted intramolecular charge transfer (TICT),[17] and excited-state intramolecular proton transfer (ESIPT).[18–20] This section synthesizes insights from different studies to provide a comprehensive view of the emission processes in AIE systems, focusing on the structural and morphological factors that influence their luminescent properties.

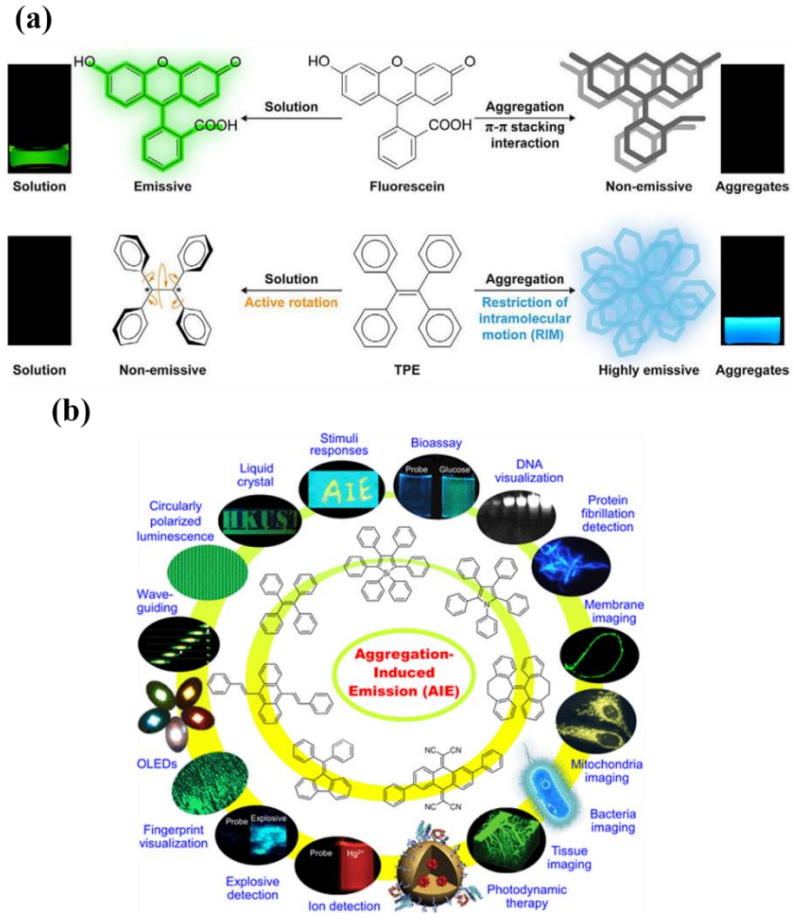

Figure 1: (a) Aggregation caused quenching (ACQ) phenomena of perylene and aggregation induced emission (AIE) phenomena of HPS, (b) technological applications of AIEgens in various fields. Figure (b) has been reproduced with permission from ref. 11 (*Chem. Rev.* **2015**, *115* (21), 11718–11940).

1.2.1 Restriction of Intramolecular Rotation (RIR)

A fundamental principle in physics is that motion, whether molecular or macroscopic, requires energy. At the molecular level, such motions include rotations and vibrations. One of the most well-documented mechanisms for AIE is the restriction of intramolecular rotation (RIR). In

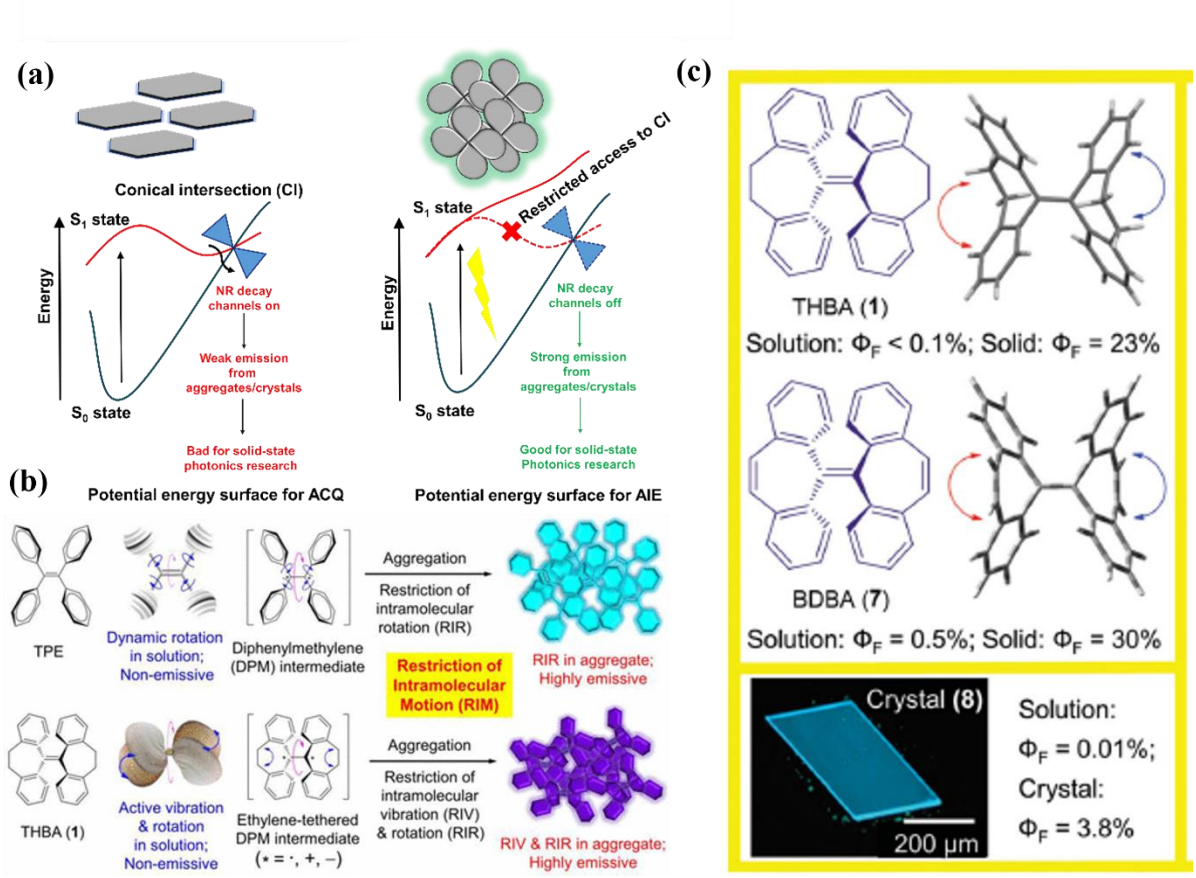

Figure 2: (a) Understanding of AIE phenomenon by a restricted access to conical intersection (RACI) approach, (b) mechanism of AIE in TPE and THBA, (c) restriction of intermolecular vibration (RIV) mechanism for different AIE gens. Figure (b) has been reproduced with permission from ref. 11 (*Chem. Rev.* **2015**, *115* (21), 11718–11940). Figure (c) has been reproduced with permission from ref. 21 (*Adv. Mater.* **2014**, *26* (31), 5429–5479).

molecules such as hexaphenylsilole (HPS) and tetraphenylethene (TPE) (**Figure 2**), AIE arises from the rotational freedom of peripheral phenyl rings around a central core. These rotations act as non-radiative relaxation pathways in dilute solutions, leading to minimal luminescence. However, in aggregated states, physical constraints restrict these intramolecular motions, thereby suppressing non-radiative decay and enabling radiative transitions. This shift results in enhanced fluorescence. Experimental investigations with HPS,[16] for example, have demonstrated that luminescence intensity increases under conditions that hinder rotational

freedom—such as higher solvent viscosity, lower temperatures, and elevated pressure. Similarly, introducing bulky substituents or cross-linking structural units can enhance emission by limiting internal rotations. Theoretical models and simulations further corroborate the RIR mechanism,[22,23] showing that low-frequency intramolecular motions are effectively restricted in aggregated states, supporting the notion that such motion restrictions underlie the AIE behavior in many molecular rotor systems.

1.2.2 Restriction of Intramolecular Vibrations (RIV)

Advancements in the study of Aggregation-Induced Emission (AIE) have led to the discovery of novel AIEgens, whose luminescence mechanisms extend beyond the traditional Restriction of Intramolecular Rotations (RIR) framework. One notable example is tetra(2-hydroxyphenyl) benzobisoxazole (THBA) (**Figure 2**),[24,25] which exhibits AIE behavior despite the absence of rotatable moieties. The phenyl rings of THBA are locked by ethylene bridges, eliminating the possibility of rotational freedom. However, THBA remains non-emissive in solution and highly luminescent upon aggregation (**Figure 2**). This observation suggests that rotational motions alone do not account for its photophysical properties. To explain this phenomenon, the Restriction of Intramolecular Vibrations (RIV) mechanism has been proposed. Vibrational modes, similar to rotational ones, can act as non-radiative decay pathways for exciton energy. Computational studies employing quantum mechanics/molecular mechanics (QM/MM) methods provide compelling evidence for this hypothesis.[26] For isolated THBA, six vibrational modes with significant reorganization energies (>200 cm^{-1}) are identified, cumulatively dissipating 5679 cm^{-1} of excited-state energy. Upon aggregation, the number of such modes decreases to three, with a total energy dissipation of approximately 4016 cm^{-1}. This reduction, combined with diminished vibrational activity, facilitates radiative decay, thereby enhancing luminescence. Other AIEgen systems have corroborated the RIV phenomenon as well. For example, dibenzocyclooctatetraene-based AIEgens exhibit pronounced luminescence in the crystalline state, despite their structural flexibility in solution. In solution, dynamic conformational changes—such as ring inversions of the cyclooctatetraene (COT) core—leads to large non-radiative deactivation.[27] In crystals, however, these motions are restricted by intermolecular steric interactions, promoting aggregate emission. Structural non-planarity in these AIEgens prevents π-π stacking, further reinforcing their luminescence. Another system, composed of a COT core linked to naphthaleneimide groups, illustrates how cooling enhances AIE. The suppression of COT ring vibrations at low temperatures leads to increased emission intensity, highlighting the critical role of RIV in controlling luminescent behavior.

Additionally, non-COT systems such as 1,4-phenyl-di(p-ethenyl-N-methylpyridinium) ditosylate (DMDPS) demonstrate AIE activity via RIV (**Figure 3**). In this system, vibrational motions of its Λ-shaped core are implicated in exciton energy dissipation, which is mitigated in aggregated states.[28] These findings collectively establish the RIV mechanism as a complementary framework to RIR, broadening the understanding of AIE. The restriction of vibrational modes further explains the basic mechanism of AIEgens and opens new avenues for designing materials with customized luminescent properties.

1.2.3 Restriction of Intramolecular Motions (RIM)

The luminescence mechanism of Aggregation-Induced Emission (AIE) has been progressively expanded beyond the individual concepts of Restriction of Intramolecular Rotations (RIR) and

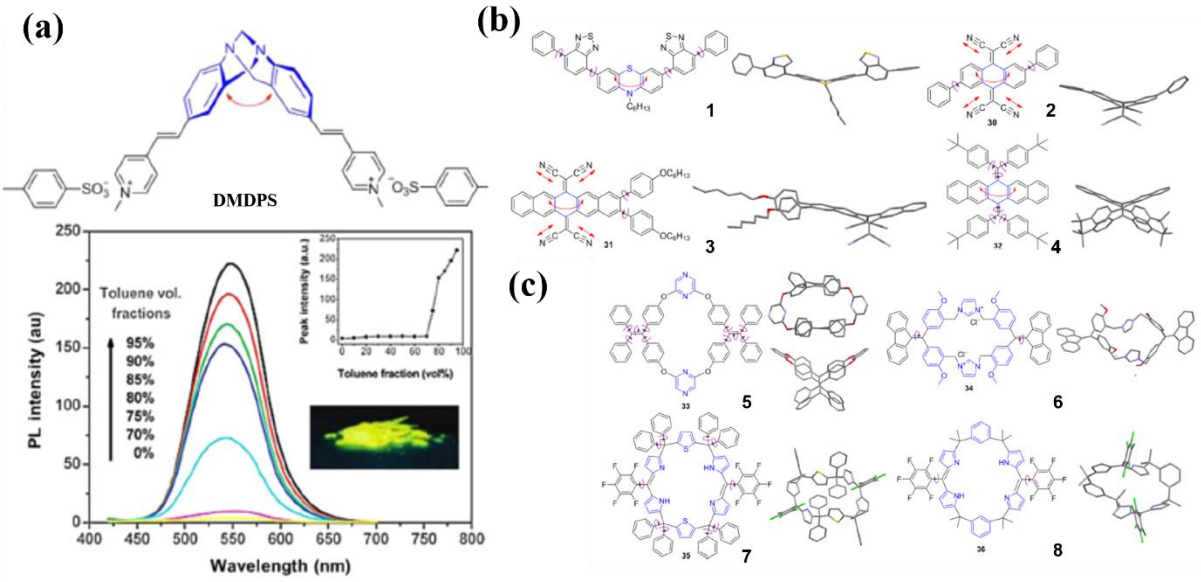

Figure 3: (a) Molecular structure and AIE studies of DMDPS in binary mixtures. The inset shows the comparison of PL intensities and the PL emission in the solid state. (b) luminogens whose AIE nature is ascribed to the restriction of intramolecular motions (RIM). Figures (a), (b) & (c) have been reproduced with permission from ref. 11 (*Chem. Rev.* **2015**, *115* (21), 11718–11940).

Vibrations (RIV) to encompass a broader framework known as the Restriction of Intramolecular Motions (RIM). This unified mechanism posits that both rotational and vibrational motions contribute to non-radiative energy dissipation in isolated molecules, while their suppression in the aggregated state enhances radiative decay, thereby inducing AIE.

Several AIEgens exemplify the RIM mechanism by combining vibrational cores with rotatable peripheral units. Phenothiazine derivative **1**,[29] for instance, adopts a butterfly-like molecular architecture, as revealed by density functional theory (DFT) calculations (**Figure 3**). In this solution, the rotational motions of the benzothiadiazole and phenyl rings, along with the vibrational modes of the phenothiazine core, dissipate excited-state energy non-radiatively. Upon aggregation, these intramolecular motions are restricted, activating luminescence. Similarly, the tetracyanoanthraquinodimethane-based AIEgen **2**[30] shows non-emissive behavior in dilute solutions but exhibits yellow fluorescence in higher water fractions. Its anthraquinodimethane core adopts a boat-like configuration, enabling flapping vibrations and phenyl ring rotations to consume exciton energy (**Figure 3**). Aggregation restricts these motions, with intermolecular C−H···N hydrogen bonds further stabilizing the structure and enhancing emission. When this core is extended to form pentacenequinodimethane (**3**),[31] the AIE effect persists. In solution, flapping motions of the bent core, phenyl rotations, and cyano vibrations dominate, leading to non-radiative decay (**Figure 3**). Aggregation induces nanoaggregate formation, as confirmed by scanning electron microscopy (SEM), which constrains these motions, allowing radiative decay to prevail. Interestingly, hydrocarbon-based AIEgens, such as **4**,[32] lacking cyano groups, still demonstrate AIE behavior. Its significantly bent pentacenequinodimethane framework, combined with the twisted conformation of its phenyl rings, effectively facilitates exciton energy dissipation via vibrational and rotational dynamics, even in monomeric phase (**Figure 3**). In the crystal state, even without hydrogen bonding, structural rigidification via aggregation facilitates bright blue emission. RIM extends beyond small molecules to macrocyclic AIEgens. For instance, oxacalixarene (**5**),[33] containing tetraphenylethylene (TPE) units (**Figure 3**), exhibits gradual luminescence enhancement as the extent of aggregation increases. In solution, phenyl and diphenylmethane rotors dissipate energy through non-radiative decay. However, aggregate formation restricts these motions, turning on emission.

Similarly, imidazolium macrocycle **6**[34] and calixthiaphyrin **7**[35] showcase Aggregation-Enhanced Emission (AEE) through RIM. In solution, the vibrational and rotational motions of their constituent units dominate exciton relaxation pathways. However, as aggregation occurs, these intramolecular motions are suppressed, leading to enhanced fluorescence. Even systems with reduced phenyl content, such as calixbenzophyrin (**8**),[36] demonstrate AEE upon aggregation (**Figure 3**). The RIM mechanism combines the photophysical fundamentals of RIR and RIV, highlighting their synergistic role in AIE. It provides a comprehensive framework for

understanding the non-radiative decay processes in isolated AIEgens and how aggregation redirects exciton relaxation through radiative channels. This unified perspective broadens the scope for designing novel AIE materials with diverse structural features and optimized photophysical properties.

1.3 Thermally Activated Delayed Fluorescence (TADF) and Its Implications for Revolutionizing the Field of OLEDs.

Organic light-emitting diodes (OLEDs) (**Figure 4**) have demonstrated significant utility owing to their highly efficient electroluminescence, lightweight nature, mechanical flexibility, potential for solution processing, and cost-effective manufacturing.[37–46] Devices fabricated through vacuum processing have already entered the market, serving applications in full-color flat-panel displays and solid-state lighting. In OLEDs, light emission occurs through the recombination of charges injected from electrodes, leading to the generation of singlet and triplet excitons in a 25%:75% ratio, assuming equal recombination efficiency and neglecting spin-statistics-altering processes.[44] To enhance OLED efficiency, it is crucial to utilize triplet excitons, typically "dark states" in organic systems. Phosphorescent OLEDs, incorporating heavy metals such as iridium or platinum, achieve near 100% internal quantum efficiency

(IQE) through strong spin-orbit coupling (SOC).[44] However, the reliance on rare and costly elements increases fabrication costs, and challenges like developing stable, deep-blue phosphors remain unresolved (**Figure 4**). While processes like triplet-triplet annihilation (TTA)[47] and exciton-polaron interaction (EPI)[48] offer partial solutions, their bimolecular nature complicates device control. In this regard, thermally activated delayed fluorescence (TADF) leverages unimolecular reverse intersystem crossing (RISC) to harness triplet excitons fully (**Figure 4**).[49–60] Effective TADF design involves reducing the energy gap (ΔE_{ST}) between singlet and triplet states by separating the highest occupied molecular orbital (HOMO) and lowest unoccupied molecular orbital (LUMO). The factors that influence RISC rates are discussed briefly below-

1.3.1 Singlet and triplet excited states:

The foundational molecular design strategy for thermally activated delayed fluorescence (TADF) materials is predicated on minimizing the energy gap (ΔE_{ST}) between the first singlet (S_1) and triplet (T_1) excited states. This principle is based on ensuring that both S_1 and T_1 states arise primarily from a charge-transfer transition between the donor-localized highest occupied molecular orbital (HOMO) and acceptor-localized lowest unoccupied molecular orbital (LUMO). Under this configuration, the electron exchange energy (K_{HL}) approaches zero,

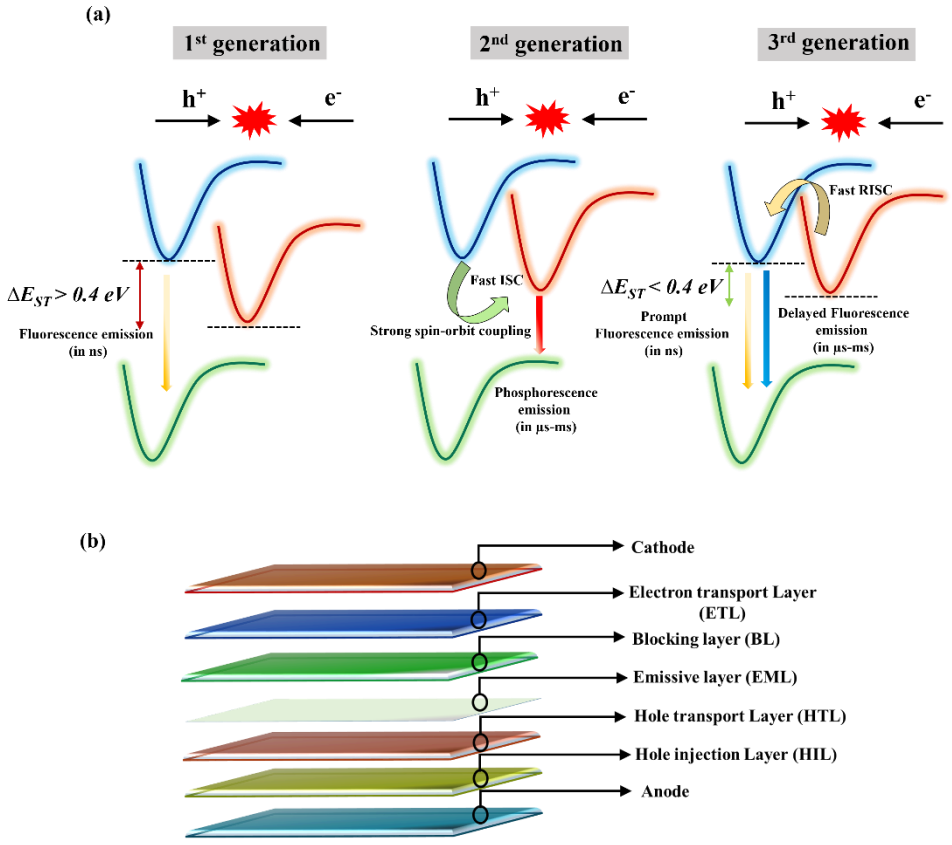

Figure 4: (a) Different generations of OLEDs along with their emission mechanisms (blue=S_1 state, red=T_1 state, and green S_0 state). (b) Different layers of an OLED.

leading to a minimal ΔE_{ST}.[51] The S_1 and T_1 state energies are described by equations incorporating the one-electron energy values of the HOMO and LUMO, Coulomb repulsion energy (J_{HL}), and electron exchange energy (K_{HL})-

$$E_{S_1} = h_H + h_L + J_{HL} + K_{HL} \quad (1)$$

$$E_{T_1} = h_H + h_L + J_{HL} - K_{HL} \quad (2)$$

$$\Delta E_{ST} = 2K_{HL} \quad (3)$$

$$J_{HL} = \iint d\vec{r}_1\, d\vec{r}_2\, H(\vec{r}_1)\, H(\vec{r}_1) \frac{1}{r_{12}}\, L(\vec{r}_2)\, L(\vec{r}_2) \quad (4)$$

$$K_{HL} = \iint d\vec{r}_1\, d\vec{r}_2\, H(\vec{r}_1)\, L(\vec{r}_1) \frac{1}{r_{12}}\, H(\vec{r}_2)\, L(\vec{r}_2) \quad (5)$$

(Here, h_H [h_L] denotes the one-electron energy of the HOMO (H) [LUMO (L)] orbital, while J_{HL} is the Coulomb repulsion energy between electron 1 residing on HOMO and electron 2 residing on LUMO, and K_{HL} denotes the corresponding electron exchange energy. To sum up, the integral K_{HL} between frontier molecular orbitals (FMOs) is required to be as small as possible, indicating that a very small overlap, even close to zero, between the highest occupied

molecular orbital (HOMO) and lowest unoccupied molecular orbital(LUMO) is necessary to induce a strong RISC process). Notably, while K_{HL} stabilizes the T_1 state, it destabilizes the S_1 state, causing the triplet state to exhibit localized excitation (LE) characteristics and the singlet state to adopt a charge-transfer (CT) nature.[51] Advanced computational techniques, such as natural transition orbitals (NTOs), are critical for accurately describing the electronic structure of extended π-conjugated systems with strong CT characteristics. For example, in the TADF emitter PXZ-TRZ, the spatial separation between electron and hole NTOs, facilitated by a nearly orthogonal molecular geometry, yields a very small ΔE_{ST} (~0.06 eV), enhancing reverse intersystem crossing (RISC). Conversely, in ACRFLCN, the T_1 state is more localized due to the substantial overlap of NTOs, resulting in a larger ΔE_{ST} (~0.24 eV). This behavior underscores the influence of molecular structure on the spatial overlap of wave functions and, consequently, the efficiency of TADF mechanisms.[51] Understanding these parameters is crucial for designing TADF emitters with optimized performance for organic light-emitting diode (OLED) applications.

1.3.2 Spin-orbit coupling:

The efficiency of the thermally activated reverse intersystem crossing (RISC) process, which enables the transition from the T_1 to S_1 states, can be analyzed using the Marcus electron-transfer theory. Within its Marcus-Levich-Jortner formulation, the RISC rate depends on the spin-orbit coupling (SOC) matrix element $\langle S_1|\hat{H}_{SO}|T_1\rangle$, the Marcus reorganization energy (λ_m) associated with low-frequency vibrations, and the effective energy ($\hbar\omega_{eff}$) of high-frequency intramolecular vibrational modes.

$$k_{\mathrm{RISC}} = \frac{2\pi}{\hbar}\left|\langle \mathrm{S}_1|\hat{H}_{\mathrm{SO}}|\mathrm{T}_\mathrm{I}\rangle\right|^2 \frac{1}{\sqrt{4\pi\lambda_\mathrm{M}k_\mathrm{B}T}}\sum_{n=0}^{\infty} \mathrm{e}^{-s}\frac{S^n}{n!} \exp\left[-\frac{(\Delta E_{\mathrm{ST}}+\lambda_\mathrm{M}+n\hbar\omega_{\mathrm{eff}})^2}{4\lambda_\mathrm{M}k_\mathrm{B}T}\right] \quad (6)$$

This expression parallels the framework used to model charge transport in organic semiconductors, but with SOC replacing electronic coupling. Importantly, the SOC magnitude is crucial in determining RISC rates. For instance, second-generation OLED emitters such as iridium-tris-phenylpyridine exhibit SOC values of approximately 150 cm^{-1}, whereas purely organic TADF materials typically have much weaker SOC values, often ≤1 cm^{-1}. Despite these lower values, even a modest enhancement in SOC can exponentially increase the RISC rate. In twisted charge-transfer (CT) TADF emitters, the S_1 and T_1 states often exhibit significant CT characteristics, resulting in a small ΔE_{ST} but minimal SOC due to the formal cancellation of

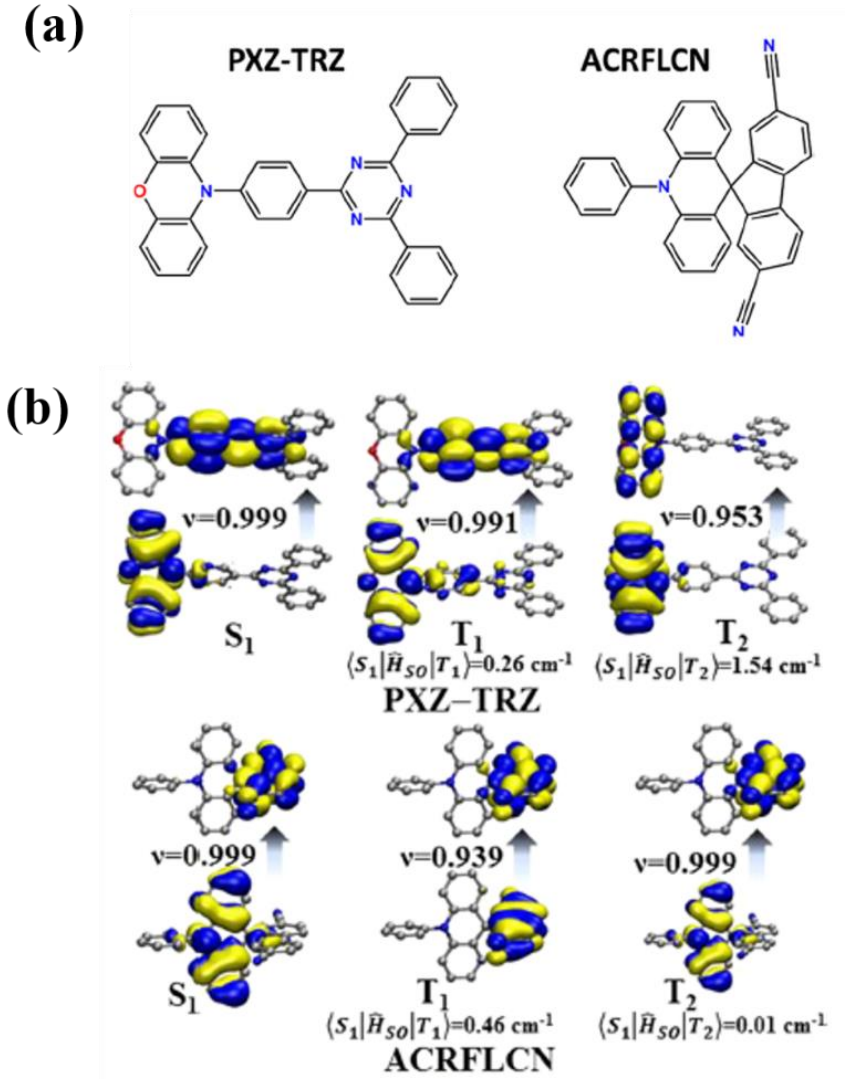

Figure 5: (a) Molecular structures of PXZ-TRZ and ACRFLCN, CT based TADF emitters. (b) Natural transition orbital (NTO) analysis along with spin-orbit coupling values in between S_1, T_1 & T_2 states of PXZ-TRZ & ACRFLCN. Figure (a) has been reproduced with permission from ref. 52 (*Acc. Chem. Res.* **2018**, *51* (9), 2215–2224). Figure (b) has been reproduced with permission from ref. 51 (*J. Am. Chem. Soc.* **2017**, *139* (11), 4042–4051).

spin-orbit coupling between states with identical spatial orbital occupations. This phenomenon arises because the SOC operator requires a change in orbital angular momentum to compensate for changes in spin angular momentum. For example, in the molecule ACRFLCN, the SOC between the predominantly CT S_1 and T_1 states is minimal (~0.01 cm^{-1}). However, when there is a disparity in the electronic character of these states, as in PXZ-TRZ, where T_1 is a local excitation (LE) state and S_1 is a CT state, SOC can increase substantially (up to 1.54 cm^{-1}) (**Figure 5**). Furthermore, the introduction of heavy atoms such as bromine, exploiting the

heavy-atom effect, can enhance SOC between excited states. This enhancement supports both reverse ISC (T_1/T_2 to S_1) and forward ISC (S_1 to T_1/T_2), the latter of which can be detrimental to fluorescence quantum yield if it dominates over radiative decay. Thus, optimizing SOC requires balancing fluorescence and ISC rates to ensure efficient RISC without compromising overall emission efficiency. These findings emphasize the importance of tailoring the excited-state properties and molecular design to maximize TADF performance.[51]

1.3.3 Effects of molecular vibrations:

To understand the combined effects of spin-orbit coupling (SOC) and the singlet-triplet energy gap (ΔE_{ST}) on reverse intersystem crossing (RISC) rates, the $T_1 \rightarrow S_1$ transition has been evaluated using Marcus-Levich-Jortner theory. The RISC rate, modeled using Equation 6, demonstrates that when ΔE_{ST} is below 0.1 eV, the process is significantly rapid, exceeding 10^5 s^{-1} which aligns well with empirical observations of smart thermally activated delayed fluorescence (TADF) emitters such as PXZ-TRZ. This rate meets the temporal requirements for display technologies. However, for ΔE_{ST} values equal to or greater than 0.3 eV, RISC rates decline sharply to below 10^3 s^{-1} indicating limited triplet harvesting efficiency. Interestingly, some molecules, such as DTC-DBT, exhibit efficient TADF behavior despite having $\Delta E_{ST} \geq$ 0.3 eV. This efficiency can be attributed to dynamic effects, particularly molecular vibrations. In DTC-DBT rotational modes involving carbazole groups, with frequencies below 20 cm^{-1}, lead to near-degeneracy of the S_1/S_2 and T_1/T_2 states, enhancing SOC between S_1 & T_2 states ($\langle S_1|\hat{H}_{SO}|T_2\rangle$) and vibronic coupling between T_1 & T_2 states (**Figure 6**).[52] This phenomenon opens a new $T_2 \rightarrow S_1$ conversion channel, enabling efficient RISC in such materials even with higher static ΔE_{ST} values. Quantum dynamics simulations have further supported the importance of vibronic interactions in RISC processes. Studies reveal that vibronic couplings between local excitation (LE) and charge-transfer (CT) triplet states, as in donor-acceptor-donor (D-A-D) systems, significantly increase RISC rates. These findings suggest that RISC efficiency depends not only on the direct S_1-T_1 energy gap but also on intermediate state contributions (e.g., T_2). In this regard, it is important to note that molecular vibrations also modulate SOC dynamically. Out-of-plane deformations enhance interactions between $^1\pi\pi^*$ and $^3\pi\pi^*$ states, favoring intersystem crossing (ISC). For instance, twisting angles in conjugated polymers have been shown to amplify SOC between singlet and triplet states. Additionally, studies on psoralen and other organic systems demonstrate the role of linear vibronic couplings in augmenting SOC, reinforcing the significance of molecular geometry and vibrations in ISC and RISC processes. Beyond traditional RISC, alternative mechanisms have been proposed to

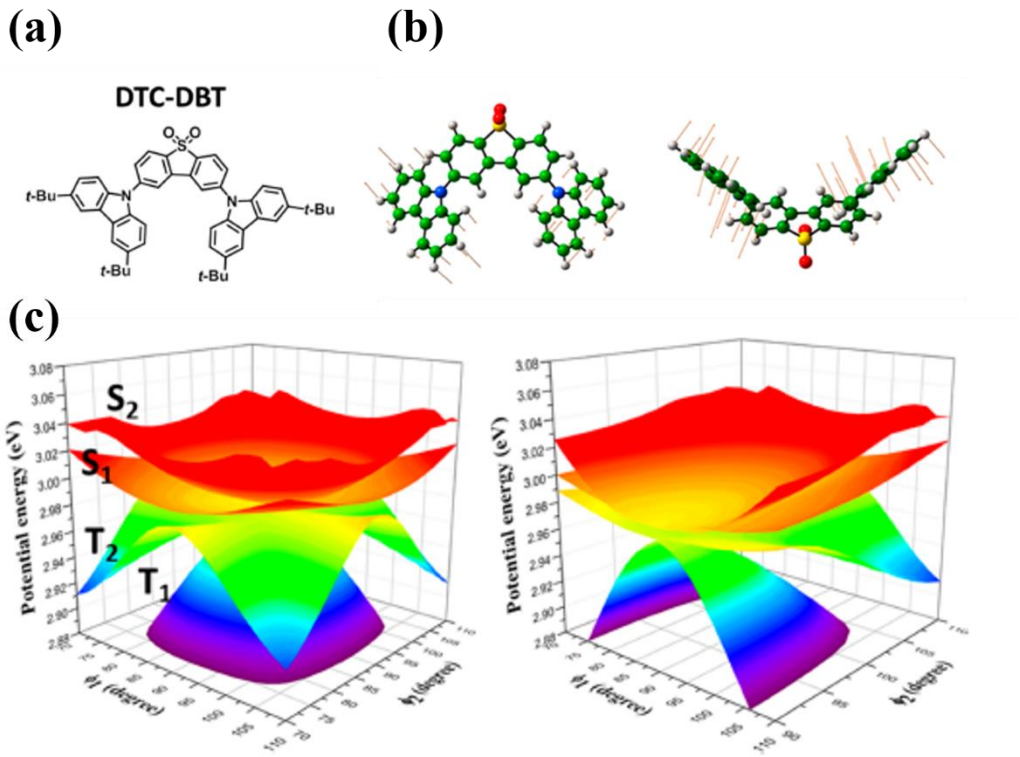

Figure 6: (a) Molecular structure of DTC-DBT. (b) Illustration of the displacement vectors of low-frequency normal modes in DTC-DBT. (c) Potential energy surface (PES) of excited S_1, S_2, T_1 & T_2 states in DTC-DBT. Figures (a), (b) & (c) have been reproduced with permission from ref. 52 (*Acc. Chem. Res.* **2018**, *51* (9), 2215–2224).

explain efficient triplet-to-singlet conversion in organic emitters. For instance, some systems utilize a wide energy separation between T_2 and T_1 to slow $T_2 \rightarrow T_1$ internal conversion, facilitating $T_2 \rightarrow S_2$ transitions. Others exploit interactions between triplet excitons and neighboring charge carriers (polarons) to generate singlet excitons, thereby surpassing the internal quantum efficiency limits of fluorescent organic light-emitting diodes (OLEDs). These findings underscore the necessity of considering vibronic and spin-vibronic couplings for a comprehensive understanding of RISC dynamics. Advanced theoretical frameworks, such as second-order perturbation theory, offer insights into these processes, enabling the design of next-generation OLED materials with optimized triplet-to-singlet conversion efficiencies.[61]

1.3.4 Advancements in Organic TADF Emitters and Impact on OLED Performance:

In organic light-emitting diodes (OLEDs), the most important parameter that defines its credibility is the external quantum efficiency (EQE) value. The EQE[62] is expressed as

$$EQE = \Phi_{PL} \times \gamma \times EUE \times \eta_{OUT} \quad (7)$$

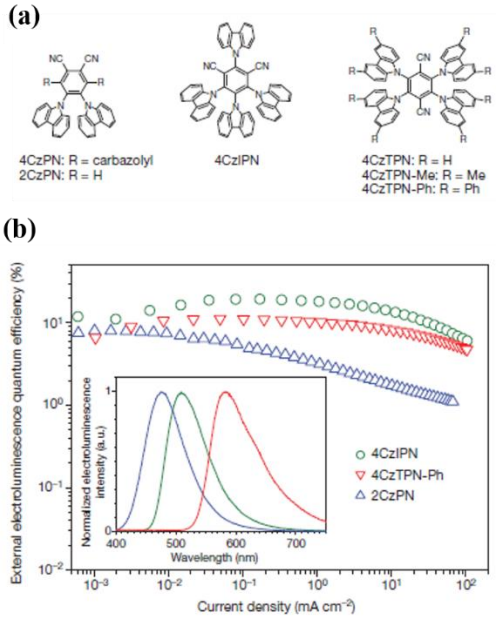

Figure 7: (a) TADF emitters reported by Adachi and co-workers in 2012. (b) EQE vs current density plots of the TADF emitters. Figures (a) & (b) have been reproduced with permission from ref. 63 (*Nature* **2012**, *492* (7428), 234–238).

In this context, Φ_{PL} represents the photoluminescence quantum yield (PLQY), γ denotes the charge balance factor, and EUE refers to the exciton utilization efficiency. Together, these three parameters determine the internal quantum efficiency (IQE). Meanwhile, η_{out} corresponds to the light outcoupling efficiency, typically constrained to 20%–30% in multilayer OLEDs. Consequently, achieving exceptionally high external quantum efficiencies (EQEs) necessitates careful optimization of both IQE and η_{out} simultaneously. In 2012, for the first time, Adachi and coworkers introduced a series of efficient thermally activated delayed fluorescence (TADF) emitters, utilizing benzene substituted with cyano groups as electron-withdrawing groups (EWGs) and highly twisted neighboring carbazole units as electron-donating groups (EDGs).[63] By varying the number of carbazole units and their substitution patterns on the benzene core, the photoluminescence (PL) properties of these TADF molecules were tuned across a range from sky blue (473 nm) to orange (577 nm), achieving photoluminescence quantum yields (PLQYs) between 26.1% and 74.3%. These molecules exhibited distinct nanosecond-scale prompt decay components along with microsecond-scale delayed decay components. The corresponding organic light-emitting diodes (OLEDs) demonstrated remarkable performance, with external quantum efficiencies (EQEs) of 19.3 ± 1.5% for the green emitter 2,4,5,6-tetra(9H-carbazol-9-yl) isophthalonitrile (4CzIPN) 11.2 ± 1.0% for the –

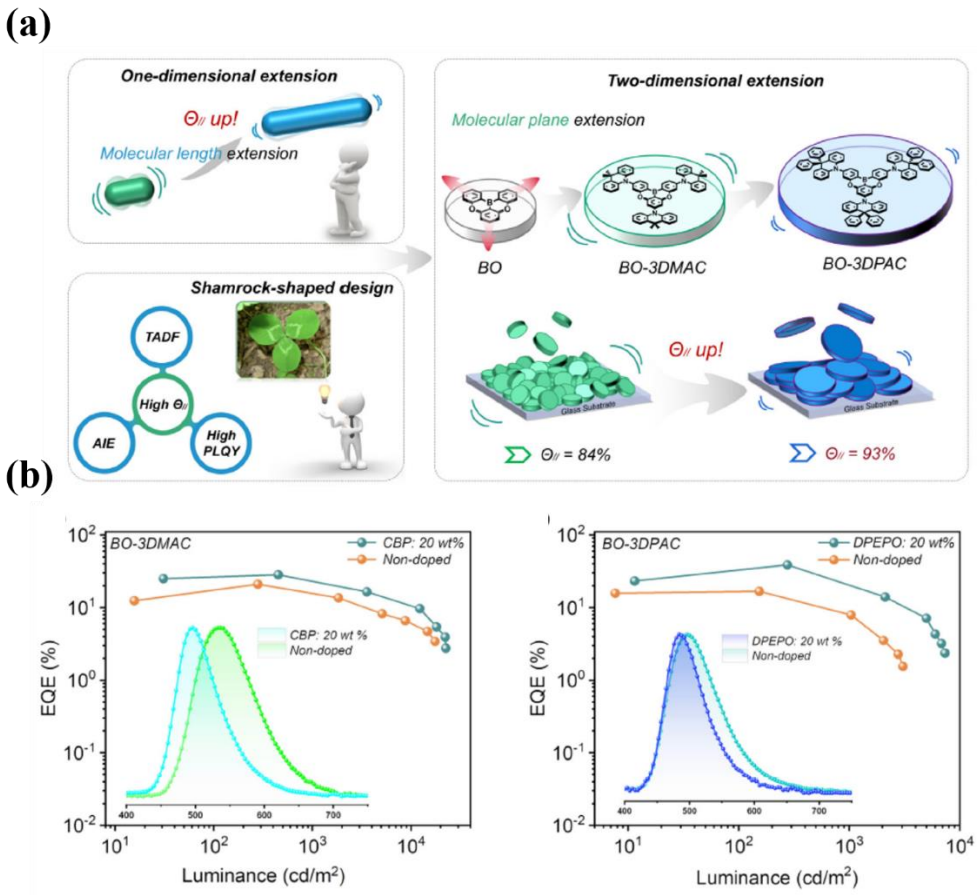

Figure 8: (a) Design strategy of conventional TADF emitters and shamrock-shaped design along with the molecular stryctures of BO-3DMAC & BO-3DPAC. (b) External quantum efficiencies (EQE) vs luminance curves for BO-3DMAC & BO-3DPAC.

orange emitter 2,3,5,6-tetrakis(3,6-diphenyl-9H-carbazol-9-yl) terephthalonitrile (4CzTPN-Ph), and 8.0 ± 1.0% for the sky-blue emitter 4,5-di(9H-carbazol-9-yl) phthalonitrile (2CzPN) (**Figure 7**).[63] This work marked the first successful demonstration of the small-molecule TADF concept in OLEDs, enabling the effective harvesting of all excitons during the electroluminescence process i.e. internal quantum efficiency (IQE), $\eta_{int.}$~100%. In addition to internal quantum efficiency (IQE), the light outcoupling efficiency η_{out} remains a significant challenge in advancing TADF-based OLEDs with higher external quantum efficiencies (EQEs). To address these performance bottlenecks, various strategies have been proposed to enhance η_{out} in the last few years, among which increasing the horizontal dipole ratios Θ// of emitters is a promising and cost-effective approach.[64] Theoretically, optimizing Θ// could improve η_{out} from the typical range of 20–30% to approximately 45% by employing high molecular weight emitters with rod- or dish-like molecular geometries. In this regard, donor-

acceptor (D_3-A) molecules with shamrock-shaped geometries have emerged as an innovative design paradigm. For instance, Adachi et al. developed a shamrock-shaped emitter, mBDPA TOAT, in 2021, achieving a maximum EQE (EQE_{max}) of 17.3% with narrow red emission.[65] Similarly, in 2022, Zysman-Colman and colleagues reported the molecule 3Cz-DiKTa, which exhibited an EQE_{max} of 24.4%.[66] They further improved the design, introducing two new molecules with EQE_{max} values exceeding 30%.[67] Notably, TADF molecules with shamrock-shaped structures often exhibit beneficial properties such as aggregation-induced emission (AIE), reduced efficiency roll-off, and narrow emission bands when appropriate donor and acceptor groups are incorporated (**Figure 8**). Building on this concept, in 2023, Chi and co-workers proposed a design strategy utilizing an oxygen-bridged boron (BO) acceptor core with intrinsic planarity and three substitution sites.[68] The BO unit, serving as the electron acceptor, is characterized by its high rigidity and wide planarity, ensuring suppressed intramolecular motion and elevated Θ//. Their planar structure in multiple directions and increased molecular weight resulted in Θ// values of 70–94%. These rigid and shamrock-shaped donor-acceptor structures endow BO-3DMAC and BO-3DPAC with strong TADF characteristics, achieving photoluminescence quantum yields (PLQYs) of 86.5% and 99.6%, respectively. Sky-blue TADF-OLEDs based on BO-3DMAC and BO-3DPAC were fabricated using a host-guest doping technique, delivering EQE_{max} values of 28.3% and 38.7%, respectively (**Figure 8**).[68] These results highlight the effectiveness of the shamrock-shaped molecular design in achieving high-performance OLEDs.

1.4 Other ways of triplet harvesting using organic emitters:

1.4.1 Hyperfluorescent emitters:

The development of third-generation organic light-emitting diodes (OLEDs) has been significantly advanced by the introduction of thermally activated delayed fluorescence (TADF) emitters. TADF emitters achieve near-unity internal quantum efficiency (IQE), making them highly promising candidates for cost-effective and sustainable OLED applications. However, the inherent broad emission spectra of TADF materials compromise the color purity of the devices, while the prolonged lifetimes of excitons contribute to degradation mechanisms that ultimately reduce external quantum efficiency (EQE) and device stability.[69] In response to these challenges, hyperfluorescent (HF) emitters have emerged as a potential solution, often referred to as the fourth generation of OLEDs. HF systems combine the unique properties of TADF and

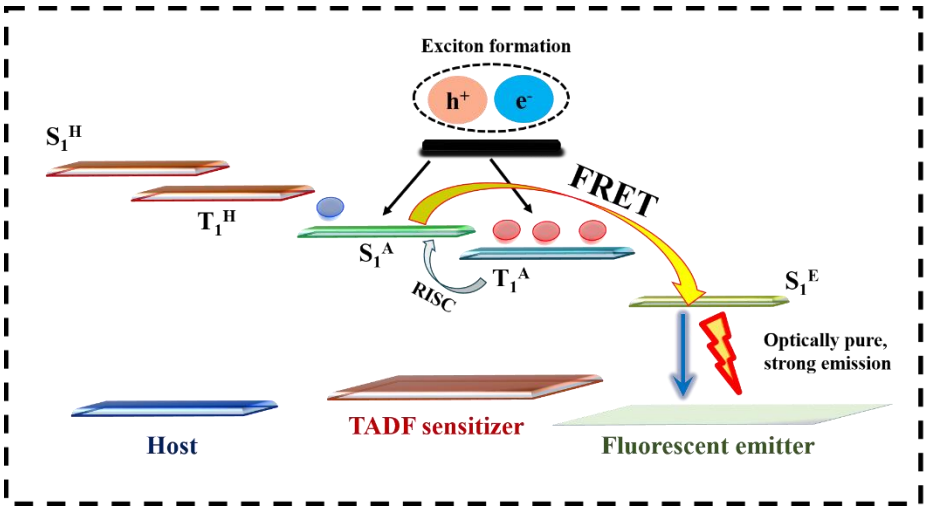

Figure 9: Mechanism of TADF sensitized hyperfluorescence emission from a terminal singlet emitter with narrow-band emission.

fluorescent emitters, creating a synergistic emission mechanism. The key principle involves Förster resonance energy transfer (FRET), where the triplet excitons generated by the TADF donor are transferred to a fluorescent acceptor, resulting in efficient singlet emission (**Figure 9**).[69–77] This hybrid approach achieves significantly higher photon yields—up to four times greater than conventional fluorescent emitters under identical excitation conditions. Moreover, HF emitters exhibit narrow-band and intense emissions, addressing the limitations of TADF materials in terms of color purity and stability. The exploration of HF emitters continues to gain momentum, driven by their potential to deliver OLEDs with superior optical and operational performance. Recent advancements have focused on elucidating the molecular design principles, optimizing the photophysical properties, and integrating HF emitters into device architectures. These developments underscore the transformative potential of HF technology in the evolution of high-performance OLEDs.

1.4.2 Spectral overlap for energy transfer process:

Spectral overlap refers to the extent of coincidence between the absorption spectrum of a fluorescent emitter (acting as the FRET acceptor) and the emission spectrum of a charge transport material, often referred to as the TADF assistant host (acting as the FRET donor). This overlap is a critical parameter influencing energy transfer efficiency in HF-based organic light-emitting diodes (OLEDs). When the emission spectrum of the assistant host, aligns with the absorption spectrum of the final fluorescent dopant, energy transfer is facilitated through the FRET process. This non-radiative process allows the TADF assistant host to transfer energy

to the fluorescent dopant, significantly enhancing the overall efficiency of the system. The efficiency of this energy transfer is determined by the Förster radius (R_f), which represents the distance at which energy transfer efficiency is 50%.[78]

$$R_0^{\ 6} = \frac{9000\Phi_F\kappa^2}{128\pi^5 n^4} J_F \quad (8)$$

Here, η is the refractive index of the medium, Φ_F denotes the prompt quantum yield of the TADF assistant host, k^2 denotes the dipole orientation factor and J_F signifies the overlap integral of the donor's emission spectrum and the acceptor's absorption spectrum and is given by equation no. (9)-

$$J_F = \int F_D(\lambda)\varepsilon_A(\lambda)\lambda^4 d\lambda \quad (9)$$

(where $F_D(\lambda)$ signifies the normalized emission spectrum of the TADF emitter and $\varepsilon_A(\lambda)$ holds for the molar extinction coefficient of the fluorescent emitter, respectively). A higher overlap integral J_F increases the Förster radius and, consequently, the energy transfer efficiency, which is essential for optimizing the performance of hyperfluorescent (HF) OLEDs. Adachi et al. (2014) demonstrated the utility of the FRET mechanism in HF-OLEDs, where TADF assistant hosts efficiently transferred energy to narrowband fluorescent dopants embedded in a host matrix. This approach improved color purity and device stability. The success of this method hinges on the narrow full-width at half-maximum (FWHM) emission of the final dopant and the high radiative decay rate of the TADF assistant host, which enables rapid and complete energy transfer. Additionally, recent studies have proposed complementary strategies that integrate FRET with triplet-to-singlet transitions to maximize exciton utilization. Lindner et al. introduced a rational design combining these mechanisms to achieve external quantum efficiencies (EQEs) up to 27% with narrow FWHM emission.[78] Similarly, Penfold et al. employed quantum chemical and dynamical simulations to investigate HF processes, identifying critical parameters for optimizing FRET rates and enhancing triplet harvesting.[79] To achieve efficient HF systems, precise control over the molecular design and spatial arrangement of TADF sensitizers and fluorescent emitters is necessary. Key considerations include a short excited-state lifetime for TADF sensitizers, high absorption coefficients of final emitters, and strong spectral overlap between donor and acceptor molecules. These factors collectively ensure rapid energy transfer, high color purity, and improved device stability in HF-OLEDs. Consequently, advanced material synthesis, device optimization, and simulation techniques remain pivotal in the pursuit of highly efficient and stable OLED technologies.

1.4.3 Room temperature phosphorescent (RTP) emitters:

Room temperature phosphorescence (RTP), historically dominated by metal-containing compounds excels in RTP due to their strong spin-orbit coupling (SOC), which facilitates intersystem crossing (ISC) and stabilizes long-lived phosphorescent excited states.[80–90] However, the use of purely organic molecules for RTP is increasingly explored. These benefits stem from the absence of heavy metals such as ruthenium, osmium, iridium, rhodium, and platinum, which are conventionally used in organometallic phosphorescent systems. Early studies on organic RTP date back to 1978, when Bilen et al. observed unusual room-temperature afterglow emissions in crystalline solids of organic compounds such as carbazole, dibenzothiophene, and triphenylene. Recent advancements have revitalized interest in organic RTP due to their potential applications, including anti-counterfeiting, temperature sensing, and bioimaging. The occurrence of RTP in organic materials is often more frequent than previously assumed, particularly in the solid state. Advances in understanding aggregation-induced emission (AIE) and crystallization-induced emission (CIE) have revealed the pivotal role of molecular aggregation and crystal packing in enabling RTP.[91] AIE, as discussed in the previous sections demonstrates that molecular aggregation in solids suppresses non-radiative decay pathways such as rotations and vibrations, which dominate in solution. This restriction of intramolecular motion enables efficient radiative decay, yielding fluorescence or phosphorescence.[92] In the context of CIE, crystallization can lock molecular motions and foster specific intermolecular interactions, such as C–H···π, C–H···O, C–H···X (X = halogen atom), and hydrogen bonding. These interactions minimize non-radiative decay and protect triplet excitons from quenching by oxygen. However, the impact of crystal packing extends beyond rigidification, as certain molecular arrangements enable enhanced RTP through intermolecular electronic interactions.[92] Crystallization-induced phosphorescence (CIP) represents a specialized subset of CIE, where crystal packing suppresses molecular vibrations and conformational rearrangements to prolong triplet exciton lifetimes. Such packing can stabilize triplet states, leading to room-temperature ultralong phosphorescence (RTUP).[91,93–101] RTUP exhibits exceptionally long lifetimes (up to seconds), reminiscent of inorganic phosphors, and is facilitated by triplet exciton trapping in specific molecular organizations, such as H-aggregates (**Figure 10**). Recent studies have emphasized the tunability of organic RTP through molecular design and co-crystallization strategies. In two-component co-crystals, for instance, halogen atoms in one molecule act as heavy atoms to enhance SOC, leading to efficient ISC. These findings underscore the intricate relationship between molecular structure, packing, and

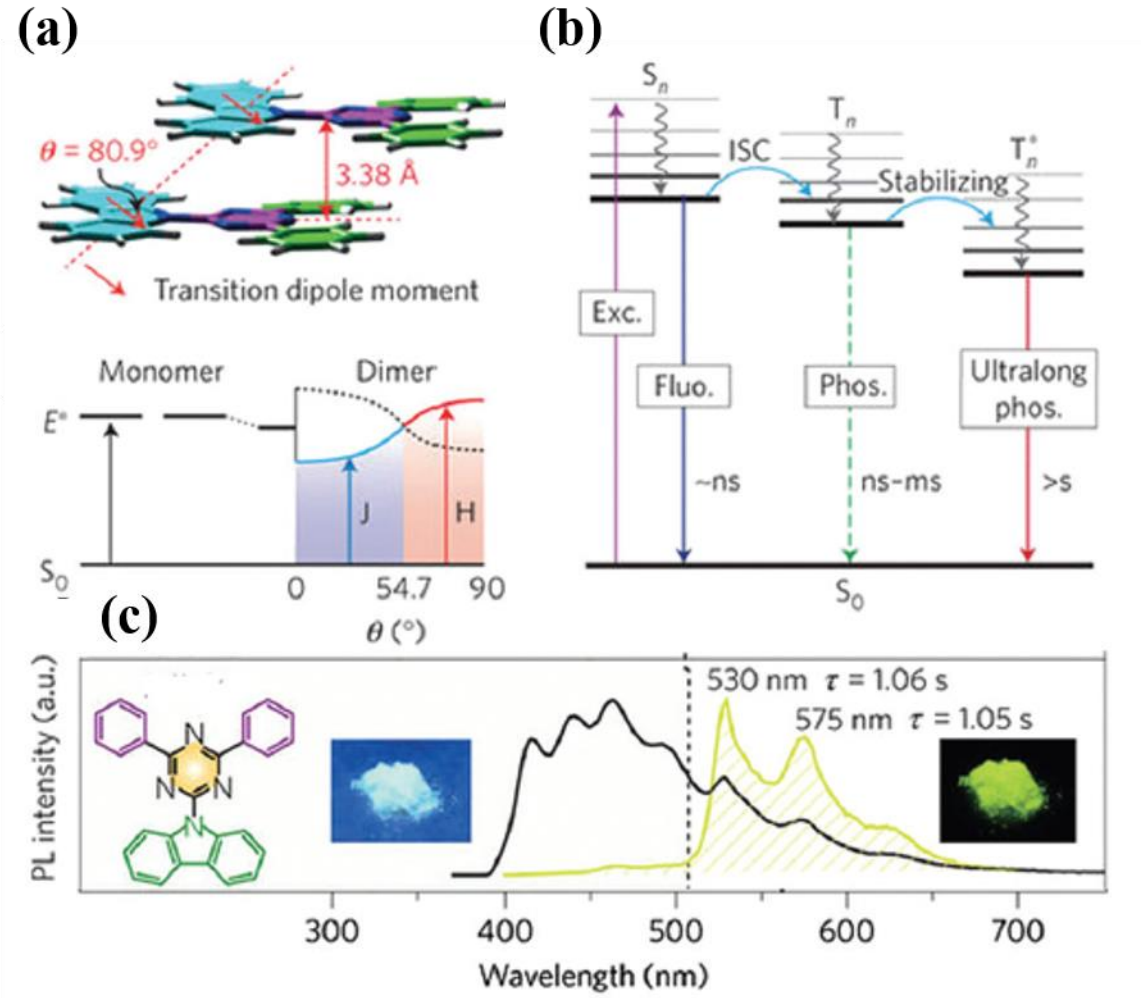

Figure 10: (a) Schematic representation of the formation of H-aggregates by transition dipole moment (TDM) analysis. (b) Schematic representation of ultralong phosphorescence from a stabilized triplet state through H-aggregate formation. (c) Photophysical features of green ultralong phosphorescence through H-aggregate formation. Figures (a), (b), & (c) have been reproduced with permission from ref. 82 (*J. Mater. Chem. C* **2018**, *6* (17), 4603–4626).

emissive properties, paving the way for the design of next-generation RTP materials with tailored properties for diverse applications. Ongoing research aims to refine the understanding of organic RTP mechanisms, leveraging advanced spectroscopic techniques and computational tools like Time-Dependent Density Functional Theory (TDDFT). These approaches are critical for elucidating the interplay between molecular dynamics, packing, and electronic transitions, ultimately guiding the rational development of high-performance organic phosphorescent materials.

1.5 Motivation of the Thesis:

Multifunctional luminogens represent a cornerstone in the advancement of next-generation optoelectronic and sensory devices, offering a plethora of applications ranging from light-emitting diodes to bioimaging and security technologies. This thesis is motivated by the need to design and understand innovative luminescent materials that integrate multiple functionalities such as Aggregation-Induced Emission (AIE), Room-Temperature Phosphorescence (RTP), mechanochromic luminescence (MCL), and Thermally Activated Delayed Fluorescence (TADF). By addressing the challenges of molecular design, structural tuning, and mechanistic insight, this thesis aims to contribute to the broader field of luminescent materials science. The *second chapter* aims at the transformative potential of multifunctional luminogens. Traditional luminogens often suffer from aggregation-caused quenching (ACQ), limiting their efficiency in solid states—a crucial requirement for optoelectronics applications. Systematic molecular engineering, therefore, offers a pathway to overcome ACQ and unlock multifunctionality. The design and synthesis of materials that simultaneously exhibit AIE, RTP, and MCL properties—such as triphenylamine (TPA) derivatives—demonstrate the feasibility of integrating these functionalities through targeted structural modifications. This approach is not only scientifically intriguing but also technologically significant, enabling the realization of "all-in-one" smart emitters for diverse applications. Furthermore, this thesis is driven by the quest to unravel the interplay between molecular structure and photophysical properties (*third chapter*). By leveraging regio-isomeric variations in donor-acceptor systems, it becomes possible to fine-tune properties like TADF efficiency, mechanochromism, and second harmonic generation (SHG). These findings underscore the critical role of structural asymmetry, packing, and molecular dynamics in dictating the photophysical behavior of luminogens. The demonstration of regio-isomeric tuning to achieve high TADF efficiency and mechanochromic behavior exemplifies the potential of rational molecular design in creating advanced luminescent materials. The *fourth* and *fifth chapters* deal with the fundamentals and applications of TADF emitters with enhanced exciton up-conversion in aggregated/solid state. The understanding of the factors boosting the TADF efficiency in the solid state is fundamentally a topic of high importance for solid-state photonics research. In the fourth chapter, we showcase the importance of the S_1-T_1 energy gap in activating solid-state delayed fluorescence by a detailed potential energy surface (PES) analysis. Herein, for the first time, the long-lived singlet excitons have been utilized for photocurrent generation in the micro-ampere (μA) region. In the fifth chapter, we have

showcased, through combined theoretical and experimental studies, that a lower structural reorganization in the aggregated state compared to the gas/solution state is responsible for enhanced delayed fluorescence efficiency in the aggregated/solid state, along with the lowest singlet-triplet energy gap or the spin-orbit coupling value. We have also successfully fabricated. The fabrication of green and orange solution-processable organic light-emitting diode (OLED) devices with a high external quantum efficiency (EQE_{max}> 20%) further emphasizes the practical implications of this research.Moreover, we have used our broad-band AIE-DF emitters and narrow-band yellow fluorescent emitters to achieve optically pure yellow and red emission with high efficiency through the hyperfluorescence process. We have thoroughly assessed the FRET time scale to comment on the energetics of hyperfluorescence, which will be very beneficial for designing high-performance HF devices in the future. In summary, this thesis is motivated by the interdisciplinary challenge of designing and understanding multifunctional luminogens with AIE, RTP, TADF, and MCL properties. Through systematic structural modification, mechanistic exploration, and device integration, this thesis seeks to advance the scientific and technological boundaries of luminescent materials, contributing to their application in optoelectronics, bioimaging, and beyond.

1.6 References:

(1) Wu, T.; Huang, J.; Yan, Y. Self-Assembly of Aggregation-Induced-Emission Molecules. *Chem. Asian J.* **2019**, *14* (6), 730–750. https://doi.org/10.1002/asia.201801884.

(2) Zhao, Z.; Zhang, H.; Lam, J. W. Y.; Tang, B. Z. Aggregation-Induced Emission: New Vistas at the Aggregate Level. *Angew. Chem. Int. Ed. Engl.* **2020**, *59* (25), 9888–9907. https://doi.org/10.1002/anie.201916729.

(3) Bandyopadhyay, S.; Kalangi, S. K.; Singh, V.; Bhosale, R. S. Introduction to Aggregation Induced Emission (AIE) Materials. *Prog. Mol. Biol. Transl. Sci.* **2021**, *184*, 1–9. https://doi.org/10.1016/bs.pmbts.2021.10.001.

(4) Khandare, D. G. Aggregation-Induced Emission Materials for Cell Membrane Imaging. *Prog. Mol. Biol. Transl. Sci.* **2021**, *184*, 81–99. https://doi.org/10.1016/bs.pmbts.2021.06.008.

(5) Hu, R.; Wang, J.; Qin, A.; Tang, B. Z. Aggregation-Induced Emission-Active Biomacromolecules: Progress, Challenges, and Opportunities. *Biomacromolecules*

2022, *23* (6), 2185–2196. https://doi.org/10.1021/acs.biomac.1c01516.

(6) Ge, S.; Wang, E.; Li, J.; Tang, B. Z. Aggregation-Induced Emission Boosting the Study of Polymer Science. *Macromol. Rapid Commun.* **2022**, *43* (16), e2200080. https://doi.org/10.1002/marc.202200080.

(7) Zhou, Y.; Hua, J.; Ding, D.; Tang, Y. Interrogating Amyloid Aggregation with Aggregation-Induced Emission Fluorescence Probes. *Biomaterials* **2022**, *286*, 121605. https://doi.org/10.1016/j.biomaterials.2022.121605.

(8) Liu, Y.; Chen, X.; Liu, X.; Guan, W.; Lu, C. Aggregation-Induced Emission-Active Micelles: Synthesis, Characterization, and Applications. *Chem. Soc. Rev.* **2023**, *52* (4), 1456–1490. https://doi.org/10.1039/d2cs01021f.

(9) Wang, B.; Liu, Y.; Chen, X.; Liu, X.-T.; Liu, Z.; Lu, C. Aggregation-Induced Emission-Active Supramolecular Polymers: From Controlled Preparation to Applications. *Chem. Soc. Rev.* **2024**, *53* (20), 10189–10215. https://doi.org/10.1039/d3cs00017f.

(10) Ghosh, S.; Adhikari, S.; Sarathi Addy, P. Aggregation Induced Emission Based Luminogenic (AIEgenic) Probes for the Biomarker Detection. *Chem. Asian J.* **2024**, e202401096. https://doi.org/10.1002/asia.202401096.

(11) Mei, J.; Leung, N. L. C.; Kwok, R. T. K.; Lam, J. W. Y.; Tang, B. Z. Aggregation-Induced Emission: Together We Shine, United We Soar! *Chem. Rev.* **2015**, *115* (21), 11718–11940. https://doi.org/10.1021/acs.chemrev.5b00263.

(12) Ma, Y.; Yin, W.; Ji, S.; Wang, J.; Lam, J. W. Y.; Kwok, R. T. K.; Huo, Y.; Sun, J.; Tang, B. Z. Red/NIR Emissive Aggregation-Induced Emission-Active Photosensitizers with Strong Donor-Acceptor Strength for Image-Guided Photodynamic Therapy of Cancer. *Luminescence* **2023**, *38* (12), 2086–2094. https://doi.org/10.1002/bio.4599.

(13) Zhan, C.; You, X.; Zhang, G.; Zhang, D. Bio-/Chemosensors and Imaging with Aggregation-Induced Emission Luminogens. *Chem. Rec.* **2016**, *16* (4), 2142–2160. https://doi.org/10.1002/tcr.201600045.

(14) Zhu, F.-Y.; Mei, L.-J.; Tian, R.; Li, C.; Wang, Y.-L.; Xiang, S.-L.; Zhu, M.-Q.; Tang, B. Z. Recent Advances in Super-Resolution Optical Imaging Based on Aggregation-Induced Emission. *Chem. Soc. Rev.* **2024**, *53* (7), 3350–3383. https://doi.org/10.1039/d3cs00698k.

(15) Jia, X.; Shen, D.; Deng, J.; Wang, K.; Wang, X.; Guo, Y.; Sun, L.; Jin, H.; Xia, Q.; Feng, H.; Jing, B.; Sun, J.; Wan, W.; Liu, Y.; Li, M. Isophorone-Based Crystallization-

Induced-Emission Sensors Detect Proteome Aggregation in Live Cells and Tissues with Breast Cancer. *Anal. Chim. Acta* **2024**, *1317*, 342916. https://doi.org/10.1016/j.aca.2024.342916.

(16) Chen, J.; Law, C. C. W.; Lam, J. W. Y.; Dong, Y.; Lo, S. M. F.; Williams, I. D.; Zhu, D.; Tang, B. Z. Synthesis, Light Emission, Nanoaggregation, and Restricted Intramolecular Rotation of 1,1-Substituted 2,3,4,5-Tetraphenylsiloles. *Chem. Mater.* **2003**, *15* (7), 1535–1546. https://doi.org/10.1021/cm021715z.

(17) Hong, Y.; Lam, J. W. Y.; Tang, B. Z. Aggregation-Induced Emission: Phenomenon, Mechanism and Applications. *Chem. Commun. (Camb).* **2009**, No. 29, 4332–4353. https://doi.org/10.1039/b904665h.

(18) Stoerkler, T.; Retailleau, P.; Jacquemin, D.; Ulrich, G.; Massue, J. Heteroaryl-Substituted Bis-Anils: Aggregation-Induced Emission (AIE) Derivatives with Tunable ESIPT Emission Color and PH Sensitivity. *Chemistry* **2023**, *29* (14), e202203766. https://doi.org/10.1002/chem.202203766.

(19) Stoerkler, T.; Ulrich, G.; Laurent, A. D.; Jacquemin, D.; Massue, J. Interplay between Dual-State and Aggregation-Induced Emission with ESIPT Scaffolds Containing Triphenylamine Substituents: Experimental and Theoretical Studies. *J. Org. Chem.* **2023**, *88* (13), 9225–9236. https://doi.org/10.1021/acs.joc.3c00806.

(20) Dwivedi, B. K.; Singh, V. D.; Paitandi, R. P.; Pandey, D. S. Substituent-Directed ESIPT-Coupled Aggregation-Induced Emission in Near-Infrared-Emitting Quinazoline Derivatives. *Chemphyschem* **2018**, *19* (20), 2672–2682. https://doi.org/10.1002/cphc.201800579.

(21) Mei, J.; Hong, Y.; Lam, J. W. Y.; Qin, A.; Tang, Y.; Tang, B. Z. Aggregation-Induced Emission: The Whole Is More Brilliant than the Parts. *Adv. Mater.* **2014**, *26* (31), 5429–5479. https://doi.org/10.1002/adma.201401356.

(22) Yang, J.; Wei, H.; Ou, Q.; Li, Q.; Peng, Q.; Zheng, X. Theoretical Study of the Photocyclization Reaction-Induced Dual Aggregation-Induced Emission Phenomenon. *J. Phys. Chem. A* **2024**, *128* (1), 217–224. https://doi.org/10.1021/acs.jpca.3c07188.

(23) Gong, Q.; Li, Y.; Nie, X.; Liu, F. Theoretical Insights into Aggregation-Induced Emission with the Ionic π Fluorophore: The Importance of Choosing the Dimer QM Model in the ONIOM Study. *J. Phys. Chem. A* **2023**, *127* (34), 7148–7155. https://doi.org/10.1021/acs.jpca.3c02952.

(24) Luo, J.; Song, K.; Gu, F. long; Miao, Q. Switching of Non-Helical Overcrowded Tetrabenzoheptafulvalene Derivatives. *Chem. Sci.* **2011**, *2* (10), 2029–2034. https://doi.org/10.1039/C1SC00340B.

(25) He, Z.; Ke, C.; Tang, B. Z. Journey of Aggregation-Induced Emission Research. *ACS Omega* **2018**, *3* (3), 3267–3277. https://doi.org/10.1021/acsomega.8b00062.

(26) Leung, N. L. C.; Xie, N.; Yuan, W.; Liu, Y.; Wu, Q.; Peng, Q.; Miao, Q.; Lam, J. W. Y.; Tang, B. Z. Restriction of Intramolecular Motions: The General Mechanism behind Aggregation-Induced Emission. *Chemistry* **2014**, *20* (47), 15349–15353. https://doi.org/10.1002/chem.201403811.

(27) Yuan, C.; Saito, S.; Camacho, C.; Kowalczyk, T.; Irle, S.; Yamaguchi, S. Hybridization of a Flexible Cyclooctatetraene Core and Rigid Aceneimide Wings for Multiluminescent Flapping π Systems. *Chemistry* **2014**, *20* (8), 2193–2200. https://doi.org/10.1002/chem.201303955.

(28) Yuan, C.; Xin, Q.; Liu, H.; Wang, L.; Jiang, M.; Tao, X. Λ-Shaped Optoelectronic Materials Based on Tröger's Base. *Sci. China Chem.* **2011**, *54* (4), 587–595. https://doi.org/10.1007/s11426-011-4224-z.

(29) Yao, L.; Zhang, S.; Wang, R.; Li, W.; Shen, F.; Yang, B.; Ma, Y. Highly Efficient Near-Infrared Organic Light-Emitting Diode Based on a Butterfly-Shaped Donor-Acceptor Chromophore with Strong Solid-State Fluorescence and a Large Proportion of Radiative Excitons. *Angew. Chem. Int. Ed. Engl.* **2014**, *53* (8), 2119–2123. https://doi.org/10.1002/anie.201308486.

(30) Liu, J.; Meng, Q.; Zhang, X.; Lu, X.; He, P.; Jiang, L.; Dong, H.; Hu, W. Aggregation-Induced Emission Enhancement Based on 11,11,12,12,-Tetracyano-9,10-Anthraquinodimethane. *Chem. Commun. (Camb).* **2013**, *49* (12), 1199–1201. https://doi.org/10.1039/c2cc38817k.

(31) Sharma nee Kamaldeep, K.; Kaur, S.; Bhalla, V.; Kumar, M.; Gupta, A. Pentacenequinone Derivatives for Preparation of Gold Nanoparticles: Facile Synthesis and Catalytic Application. *J. Mater. Chem. A* **2014**, *2* (22), 8369–8375. https://doi.org/10.1039/C4TA00397G.

(32) Banal, J. L.; White, J. M.; Ghiggino, K. P.; Wong, W. W. H. Concentrating Aggregation-Induced Fluorescence in Planar Waveguides: A Proof-of-Principle. *Sci. Rep.* **2014**, *4*, 4635. https://doi.org/10.1038/srep04635.

(33) Zhang, C.; Wang, Z.; Song, S.; Meng, X.; Zheng, Y.-S.; Yang, X.-L.; Xu, H.-B. Tetraphenylethylene-Based Expanded Oxacalixarene: Synthesis, Structure, and Its Supramolecular Grid Assemblies Directed by Guests in the Solid State. *J. Org. Chem.* **2014**, *79* (6), 2729–2732. https://doi.org/10.1021/jo402884a.

(34) Wang, J.-H.; Feng, H.-T.; Luo, J.; Zheng, Y.-S. Monomer Emission and Aggregate Emission of an Imidazolium Macrocycle Based on Bridged Tetraphenylethylene and Their Quenching by C60. *J. Org. Chem.* **2014**, *79* (12), 5746–5751. https://doi.org/10.1021/jo500884z.

(35) Karthik, G.; Krushna, P. V.; Srinivasan, A.; Chandrashekar, T. K. Calix[2]Thia[4]Phyrin: An Expanded Calixphyrin with Aggregation-Induced Enhanced Emission and Anion Receptor Properties. *J. Org. Chem.* **2013**, *78* (17), 8496–8501. https://doi.org/10.1021/jo401232a.

(36) Salini, P. S.; Thomas, A. P.; Sabarinathan, R.; Ramakrishnan, S.; Sreedevi, K. C. G.; Reddy, M. L. P.; Srinivasan, A. Calix[2]-m-Benzo[4]Phyrin with Aggregation-Induced Enhanced-Emission Characteristics: Application as a HgII Chemosensor. *Chemistry* **2011**, *17* (24), 6598–6601. https://doi.org/10.1002/chem.201100046.

(37) Tankelevičiūtė, E.; Samuel, I. D. W.; Zysman-Colman, E. The Blue Problem: OLED Stability and Degradation Mechanisms. *J. Phys. Chem. Lett.* **2024**, *15* (4), 1034–1047. https://doi.org/10.1021/acs.jpclett.3c03317.

(38) Luo, J.; Rong, X.-F.; Ye, Y.-Y.; Li, W.-Z.; Wang, X.-Q.; Wang, W. Research Progress on Triarylmethyl Radical-Based High-Efficiency OLED. *Molecules* **2022**, *27* (5). https://doi.org/10.3390/molecules27051632.

(39) Kwon, J. H. Editorial: High Color Purity Boron-Based OLED Materials. *Frontiers in chemistry*. Switzerland 2024, p 1441517. https://doi.org/10.3389/fchem.2024.1441517.

(40) Huang, Y.; Hsiang, E.-L.; Deng, M.-Y.; Wu, S.-T. Mini-LED, Micro-LED and OLED Displays: Present Status and Future Perspectives. *Light. Sci. Appl.* **2020**, *9*, 105. https://doi.org/10.1038/s41377-020-0341-9.

(41) Grotjahn, S.; König, B. Common Ground and Divergence: OLED Emitters as Photocatalysts. *Chem. Commun. (Camb).* **2024**, *60* (89), 12951–12963. https://doi.org/10.1039/d4cc04409f.

(42) Kozlov, M. I.; Kuznetsov, K. M.; Goloveshkin, A. S.; Burlakin, A.; Sandzhieva, M.; Makarov, S. V; Ilina, E.; Utochnikova, V. V. Solution-Processed OLED Based on a

Mixed-Ligand Europium Complex. *Mater. (Basel, Switzerland)* **2023**, *16* (3). https://doi.org/10.3390/ma16030959.

(43) Teli, S. R.; Matus, V.; Aguiar, C. L.; Perez-Jimenez, R.; Ghassemlooy, Z.; Zvanovec, S. Curved OLED-Based NLOS Optical Camera Communications Links. *Appl. Opt.* **2023**, *62* (30), 8204–8210. https://doi.org/10.1364/AO.496760.

(44) Banerjee, S.; Singh, P.; Purkayastha, P.; Kumar Ghosh, S. Evolution of Organic Light Emitting Diode (OLED) Materials and Their Impact on Display Technology. *Chem. Asian J.* **2024**, e202401291. https://doi.org/10.1002/asia.202401291.

(45) Sim, J. H.; Kwon, J.; Chae, H.; Kim, S.-B.; Cho, H.; Lee, W.; Kim, S. H.; Byun, C.-W.; Hahn, S.; Park, D. H.; Yoo, S. OLED Catheters for Inner-Body Phototherapy: A Case of Type 2 Diabetes Mellitus Improved via Duodenal Photobiomodulation. *Sci. Adv.* **2023**, *9* (35), eadh8619. https://doi.org/10.1126/sciadv.adh8619.

(46) Turkoglu, G.; Cinar, M. E.; Ozturk, T. Triarylborane-Based Materials for OLED Applications. *Molecules* **2017**, *22* (9). https://doi.org/10.3390/molecules22091522.

(47) Dou, Q.; Jiang, L.; Kai, D.; Owh, C.; Loh, X. J. Bioimaging and Biodetection Assisted with TTA-UC Materials. *Drug Discov. Today* **2017**, *22* (9), 1400–1411. https://doi.org/10.1016/j.drudis.2017.04.003.

(48) Biswas, S.; Zhao, R.; Alowa, F.; Zacharias, M.; Sharifzadeh, S.; Coker, D. F.; Seferos, D. S.; Scholes, G. D. Exciton Polaron Formation and Hot-Carrier Relaxation in Rigid Dion-Jacobson-Type Two-Dimensional Perovskites. *Nat. Mater.* **2024**, *23* (7), 937–943. https://doi.org/10.1038/s41563-024-01895-z.

(49) Xiao, Y.; Wang, H.; Xie, Z.; Shen, M.; Huang, R.; Miao, Y.; Liu, G.; Yu, T.; Huang, W. NIR TADF Emitters and OLEDs: Challenges, Progress, and Perspectives. *Chem. Sci.* **2022**, *13* (31), 8906–8923. https://doi.org/10.1039/d2sc02201j.

(50) Naveen, K. R.; Palanisamy, P.; Chae, M. Y.; Kwon, J. H. Multiresonant TADF Materials: Triggering the Reverse Intersystem Crossing to Alleviate the Efficiency Roll-off in OLEDs. *Chem. Commun. (Camb).* **2023**, *59* (25), 3685–3702. https://doi.org/10.1039/d2cc06802h.

(51) Samanta, P. K.; Kim, D.; Coropceanu, V.; Brédas, J.-L. Up-Conversion Intersystem Crossing Rates in Organic Emitters for Thermally Activated Delayed Fluorescence: Impact of the Nature of Singlet vs Triplet Excited States. *J. Am. Chem. Soc.* **2017**, *139* (11), 4042–4051. https://doi.org/10.1021/jacs.6b12124.

(52) Chen, X.-K.; Kim, D.; Brédas, J.-L. Thermally Activated Delayed Fluorescence (TADF) Path toward Efficient Electroluminescence in Purely Organic Materials: Molecular Level Insight. *Acc. Chem. Res.* **2018**, *51* (9), 2215–2224. https://doi.org/10.1021/acs.accounts.8b00174.

(53) Ferraro, V.; Bizzarri, C.; Bräse, S. Thermally Activated Delayed Fluorescence (TADF) Materials Based on Earth-Abundant Transition Metal Complexes: Synthesis, Design and Applications. *Adv. Sci. (Weinheim, Baden-Wurttemberg, Ger.* **2024**, *11* (34), e2404866. https://doi.org/10.1002/advs.202404866.

(54) Zhang, T.; Xiao, Y.; Wang, H.; Kong, S.; Huang, R.; Ka-Man Au, V.; Yu, T.; Huang, W. Highly Twisted Thermally Activated Delayed Fluorescence (TADF) Molecules and Their Applications in Organic Light-Emitting Diodes (OLEDs). *Angew. Chem. Int. Ed. Engl.* **2023**, *62* (39), e202301896. https://doi.org/10.1002/anie.202301896.

(55) Bryden, M. A.; Zysman-Colman, E. Organic Thermally Activated Delayed Fluorescence (TADF) Compounds Used in Photocatalysis. *Chem. Soc. Rev.* **2021**, *50* (13), 7587–7680. https://doi.org/10.1039/d1cs00198a.

(56) He, Z.; Huang, Z.; Li, T.; Song, J.; Wu, J.; Ma, X. Achieving Tunable Monomeric TADF and Aggregated RTP via Molecular Stacking. *ACS Appl. Mater. Interfaces* **2024**, *16* (40), 54742–54750. https://doi.org/10.1021/acsami.4c14265.

(57) Kim, C. A.; Van Voorhis, T. Maximizing TADF via Conformational Optimization. *J. Phys. Chem. A* **2021**, *125* (35), 7644–7654. https://doi.org/10.1021/acs.jpca.1c05104.

(58) Yersin, H.; Czerwieniec, R.; Shafikov, M. Z.; Suleymanova, A. F. TADF Material Design: Photophysical Background and Case Studies Focusing on Cu(I) and Ag(I) Complexes. *Chemphyschem* **2017**, *18* (24), 3508–3535. https://doi.org/10.1002/cphc.201700872.

(59) Zhao, X.; Zhu, L.; Li, Q.; Yin, H.; Shi, Y. The Interplay between ESIPT and TADF for the 2,2'-Bipyridine-3,3'-Diol: A Theoretical Reconsideration. *Int. J. Mol. Sci.* **2022**, *23* (22). https://doi.org/10.3390/ijms232213969.

(60) Wu, H.; Shi, Y.-Z.; Wang, K.; Yu, J.; Zhang, X.-H. Conformational Isomeric Thermally Activated Delayed Fluorescence (TADF) Emitters: Mechanism, Applications, and Perspectives. *Phys. Chem. Chem. Phys.* **2023**, *25* (4), 2729–2741. https://doi.org/10.1039/d2cp05119b.

(61) Chen, X.-K.; Zhang, S.-F.; Fan, J.-X.; Ren, A.-M. Nature of Highly Efficient Thermally

Activated Delayed Fluorescence in Organic Light-Emitting Diode Emitters: Nonadiabatic Effect between Excited States. *J. Phys. Chem. C* **2015**, *119* (18), 9728–9733. https://doi.org/10.1021/acs.jpcc.5b00276.

(62) Van der Zee, B.; Li, Y.; Wetzelaer, G.-J. A. H.; Blom, P. W. M. Efficiency of Polymer Light-Emitting Diodes: A Perspective. *Adv. Mater.* **2022**, *34* (13), e2108887. https://doi.org/10.1002/adma.202108887.

(63) Uoyama, H.; Goushi, K.; Shizu, K.; Nomura, H.; Adachi, C. Highly Efficient Organic Light-Emitting Diodes from Delayed Fluorescence. *Nature* **2012**, *492* (7428), 234–238. https://doi.org/10.1038/nature11687.

(64) Liang, X.; Tu, Z.-L.; Zheng, Y.-X. Thermally Activated Delayed Fluorescence Materials: Towards Realization of High Efficiency through Strategic Small Molecular Design. *Chemistry* **2019**, *25* (22), 5623–5642. https://doi.org/10.1002/chem.201805952.

(65) Fan, X.-C.; Wang, K.; Shi, Y.-Z.; Chen, J.-X.; Huang, F.; Wang, H.; Hu, Y.-N.; Tsuchiya, Y.; Ou, X.-M.; Yu, J.; Adachi, C.; Zhang, X.-H. Managing Intersegmental Charge-Transfer and Multiple Resonance Alignments of D3-A Typed TADF Emitters for Red OLEDs with Improved Efficiency and Color Purity. *Adv. Opt. Mater.* **2022**, *10* (3), 2101789. https://doi.org/https://doi.org/10.1002/adom.202101789.

(66) Wu, S.; Li, W.; Yoshida, K.; Hall, D.; Madayanad Suresh, S.; Sayner, T.; Gong, J.; Beljonne, D.; Olivier, Y.; Samuel, I. D. W.; Zysman-Colman, E. Excited-State Modulation in Donor-Substituted Multiresonant Thermally Activated Delayed Fluorescence Emitters. *ACS Appl. Mater. Interfaces* **2022**, *14* (19), 22341–22352. https://doi.org/10.1021/acsami.2c02756.

(67) Wu, S.; Kumar Gupta, A.; Yoshida, K.; Gong, J.; Hall, D.; Cordes, D. B.; Slawin, A. M. Z.; Samuel, I. D. W.; Zysman-Colman, E. Highly Efficient Green and Red Narrowband Emissive Organic Light-Emitting Diodes Employing Multi-Resonant Thermally Activated Delayed Fluorescence Emitters. *Angew. Chem. Int. Ed. Engl.* **2022**, *61* (52), e202213697. https://doi.org/10.1002/anie.202213697.

(68) Li, G.; Pu, J.; Yang, Z.; Deng, H.; Liu, Y.; Mao, Z.; Zhao, J.; Su, S.-J.; Chi, Z. High-Efficiency Thermally Activated Delayed Fluorescence Materials via a Shamrock-Shaped Design Strategy to Enable OLEDs with External Quantum Efficiency over 38%. *Aggregate* **2023**, *4* (6), e382. https://doi.org/https://doi.org/10.1002/agt2.382.

(69) Gawale, Y.; Ansari, R.; Naveen, K. R.; Kwon, J. H. Forthcoming Hyperfluorescence

Display Technology: Relevant Factors to Achieve High-Performance Stable Organic Light Emitting Diodes. *Front. Chem.* **2023**, *11*, 1211345. https://doi.org/10.3389/fchem.2023.1211345.

(70) Haase, N.; Danos, A.; Pflumm, C.; Stachelek, P.; Brütting, W.; Monkman, A. P. Are the Rates of Dexter Transfer in TADF Hyperfluorescence Systems Optically Accessible? *Mater. horizons* **2021**, *8* (6), 1805–1815. https://doi.org/10.1039/d0mh01666g.

(71) Wang, J.; Zou, P.; Chen, L.; Bai, Z.; Liu, H.; Chen, W.-C.; Huo, Y.; Tang, B. Z.; Zhao, Z. Promising Interlayer Sensitization Strategy for the Construction of High-Performance Blue Hyperfluorescence OLEDs. *Light. Sci. Appl.* **2024**, *13* (1), 139. https://doi.org/10.1038/s41377-024-01490-6.

(72) Liu, H.; Fu, Y.; Chen, J.; Tang, B. Z.; Zhao, Z. Energy-Efficient Stable Hyperfluorescence Organic Light-Emitting Diodes with Improved Color Purities and Ultrahigh Power Efficiencies Based on Low-Polar Sensitizing Systems. *Adv. Mater.* **2023**, *35* (22), e2212237. https://doi.org/10.1002/adma.202212237.

(73) Zhang, K.; Wang, X.; Chang, Y.; Wu, Y.; Wang, S.; Wang, L. Carbazole-Decorated Organoboron Emitters with Low-Lying HOMO Levels for Solution-Processed Narrowband Blue Hyperfluorescence OLED Devices. *Angew. Chem. Int. Ed. Engl.* **2023**, *62* (47), e202313084. https://doi.org/10.1002/anie.202313084.

(74) Alipour, M.; Izadkhast, T. Toward Highly Efficient Hyperfluorescence-Based Emitters through Excited-States Alignment Using Novel Optimally Tuned Range-Separated Models. *Phys. Chem. Chem. Phys.* **2022**, *24* (38), 23718–23736. https://doi.org/10.1039/d2cp03395j.

(75) Lee, H.; Braveenth, R.; Muruganantham, S.; Jeon, C. Y.; Lee, H. S.; Kwon, J. H. Efficient Pure Blue Hyperfluorescence Devices Utilizing Quadrupolar Donor-Acceptor-Donor Type of Thermally Activated Delayed Fluorescence Sensitizers. *Nat. Commun.* **2023**, *14* (1), 419. https://doi.org/10.1038/s41467-023-35926-1.

(76) Jin, J.; He, Z.; Liu, D.; Mei, Y.; Wang, J.; Wan, H.; Li, J. Donor-Modified Asymmetric N/B/O Multi-Resonance TADF Emitters for High-Performance Deep-Blue OLEDs with the BT.2020 Color Gamut. *Chem. Sci.* **2024**, *15* (43), 18135–18145. https://doi.org/10.1039/d4sc04896b.

(77) Xu, K.; Li, N.; Ye, Z.; Guo, Y.; Wu, Y.; Gui, C.; Yin, X.; Miao, J.; Cao, X.; Yang, C. High-Performance Deep-Blue Electroluminescence from Multi-Resonance TADF

Emitters with a Spirofluorene-Fused Double Boron Framework. *Chem. Sci.* **2024**, *15* (43), 18076–18084. https://doi.org/10.1039/d4sc04835k.

(78) Bartkowski, K.; Zimmermann Crocomo, P.; Kochman, M. A.; Kumar, D.; Kubas, A.; Data, P.; Lindner, M. Tandem Rigidification and π-Extension as a Key Tool for the Development of a Narrow Linewidth Yellow Hyperfluorescent OLED System. *Chem. Sci.* **2022**, *13* (34), 10119–10128. https://doi.org/10.1039/d2sc03342a.

(79) Giret, Y.; Eng, J.; Pope, T.; Penfold, T. A Quantum Dynamics Study of the Hyperfluorescence Mechanism. *J. Mater. Chem. C* **2021**, *9* (4), 1362–1369. https://doi.org/10.1039/D0TC04225K.

(80) Zhang, Y.; Li, H.; Yang, M.; Dai, W.; Shi, J.; Tong, B.; Cai, Z.; Wang, Z.; Dong, Y.; Yu, X. Organic Room-Temperature Phosphorescence Materials for Bioimaging. *Chem. Commun. (Camb).* **2023**, *59* (36), 5329–5342. https://doi.org/10.1039/d3cc00923h.

(81) Zhi, J.; Zhou, Q.; Shi, H.; An, Z.; Huang, W. Organic Room Temperature Phosphorescence Materials for Biomedical Applications. *Chem. Asian J.* **2020**, *15* (7), 947–957. https://doi.org/10.1002/asia.201901658.

(82) Forni, A.; Lucenti, E.; Botta, C.; Cariati, E. Metal Free Room Temperature Phosphorescence from Molecular Self-Interactions in the Solid State. *J. Mater. Chem. C* **2018**, *6* (17), 4603–4626. https://doi.org/10.1039/C8TC01007B.

(83) Gu, F.; Ma, X. Stimuli-Responsive Polymers with Room-Temperature Phosphorescence. *Chemistry* **2022**, *28* (15), e202104131. https://doi.org/10.1002/chem.202104131.

(84) Zhou, J.; Tian, B.; Zhai, Y.; Wang, M.; Liu, S.; Li, J.; Li, S.; James, T. D.; Chen, Z. Photoactivated Room Temperature Phosphorescence from Lignin. *Nat. Commun.* **2024**, *15* (1), 7198. https://doi.org/10.1038/s41467-024-51545-w.

(85) Chang, B.; Chen, J.; Bao, J.; Sun, T.; Cheng, Z. Molecularly Engineered Room-Temperature Phosphorescence for Biomedical Application: From the Visible toward Second Near-Infrared Window. *Chem. Rev.* **2023**, *123* (24), 13966–14037. https://doi.org/10.1021/acs.chemrev.3c00401.

(86) Nandi, R. P.; Kalluvettukuzhy, N. K.; Pagidi, S.; Thilagar, P. Molecular Persistent Room-Temperature Phosphorescence from Tetraarylaminoboranes. *Inorg. Chem.* **2023**, *62* (3), 1122–1134. https://doi.org/10.1021/acs.inorgchem.2c03386.

(87) Patil, Y.; Demangeat, C.; Favereau, L. Recent Advances in Room Temperature

Phosphorescence of Chiral Organic Materials. *Chirality* **2023**, *35* (7), 390–410. https://doi.org/10.1002/chir.23551.

(88) Ma, X.-K.; Liu, Y. Supramolecular Purely Organic Room-Temperature Phosphorescence. *Acc. Chem. Res.* **2021**, *54* (17), 3403–3414. https://doi.org/10.1021/acs.accounts.1c00336.

(89) Hamzehpoor, E.; Ruchlin, C.; Tao, Y.; Liu, C.-H.; Titi, H. M.; Perepichka, D. F. Efficient Room-Temperature Phosphorescence of Covalent Organic Frameworks through Covalent Halogen Doping. *Nat. Chem.* **2023**, *15* (1), 83–90. https://doi.org/10.1038/s41557-022-01070-4.

(90) Li, H.; Ma, H.; Zhang, P.; An, Z.; He, X. Modulating Room-Temperature Phosphorescence of Phenothiazine Dioxide via External Heavy Atoms. *Angew. Chem. Int. Ed. Engl.* **2024**, e202419366. https://doi.org/10.1002/anie.202419366.

(91) Ito, S.; Hosokai, T.; Tanaka, K.; Chujo, Y. Regulating the Photoluminescence of Aluminium Complexes from Non-Luminescence to Room-Temperature Phosphorescence by Tuning the Metal Substituents. *Commun. Chem.* **2024**, *7* (1), 202. https://doi.org/10.1038/s42004-024-01295-z.

(92) Gong, Y.; Chen, G.; Peng, Q.; Yuan, W. Z.; Xie, Y.; Li, S.; Zhang, Y.; Tang, B. Z. Achieving Persistent Room Temperature Phosphorescence and Remarkable Mechanochromism from Pure Organic Luminogens. *Adv. Mater.* **2015**, *27* (40), 6195–6201. https://doi.org/10.1002/adma.201502442.

(93) Yin, Z.; Xie, Z.; Zhang, X.; Xue, Y.; Zhang, D.; Liu, B. Cocrystallization-Induced Red Ultralong Organic Phosphorescence. *Angew. Chem. Int. Ed. Engl.* **2024**, e202417868. https://doi.org/10.1002/anie.202417868.

(94) Li, J.; Duan, R.; Zhu, Y.; Chen, M.; Dai, X.; Duan, G.; Ge, Y. Triarylmethanol Derivatives with Ultralong Organic Room-Temperature Phosphorescence. *Chemistry* **2024**, e202403475. https://doi.org/10.1002/chem.202403475.

(95) Shi, H.; Yao, W.; Ye, W.; Ma, H.; Huang, W.; An, Z. Ultralong Organic Phosphorescence: From Material Design to Applications. *Acc. Chem. Res.* **2022**, *55* (23), 3445–3459. https://doi.org/10.1021/acs.accounts.2c00514.

(96) Jiang, J.; Du, X.; Zhang, K. Achieving Ultralong Room-Temperature Phosphorescence in Covalent Organic Framework System. *J. Phys. Chem. Lett.* **2024**, *15* (6), 1658–1667. https://doi.org/10.1021/acs.jpclett.4c00110.

(97) Cao, P.; Zheng, H.; Wu, P. Multicolor Ultralong Phosphorescence from Perovskite-like Octahedral α-AlF(3). *Nat. Commun.* **2022**, *13* (1), 5712. https://doi.org/10.1038/s41467-022-33540-1.

(98) Li, Q. High-Dissymmetry Circularly Polarized Ultralong Phosphorescence. *Light. Sci. Appl.* **2023**, *12* (1), 243. https://doi.org/10.1038/s41377-023-01288-y.

(99) Zheng, H.; Cao, P.; Wang, Y.; Lu, X.; Wu, P. Ultralong Room-Temperature Phosphorescence from Boric Acid. *Angew. Chem. Int. Ed. Engl.* **2021**, *60* (17), 9500–9506. https://doi.org/10.1002/anie.202101923.

(100) Ma, X.-K.; Zhang, W.; Liu, Z.; Zhang, H.; Zhang, B.; Liu, Y. Supramolecular Pins with Ultralong Efficient Phosphorescence. *Adv. Mater.* **2021**, *33* (14), e2007476. https://doi.org/10.1002/adma.202007476.

(101) Cheng, Z.; Shi, H.; Ma, H.; Bian, L.; Wu, Q.; Gu, L.; Cai, S.; Wang, X.; Xiong, W.-W.; An, Z.; Huang, W. Ultralong Phosphorescence from Organic Ionic Crystals under Ambient Conditions. *Angew. Chem. Int. Ed. Engl.* **2018**, *57* (3), 678–682. https://doi.org/10.1002/anie.201710017.

Chapter -2

Emergence of Aggregation Induced Emission (AIE), Room-Temperature Phosphorescence (RTP), and Multistimuli Response from a Single Organic Luminogen by Directed Structural Modification

2.1 Motivation:

Multi-functional organic luminogens exhibiting simultaneous aggregation-induced emission (AIE), room temperature phosphorescence (RTP), and mechanochromism have recently attracted considerable attention owing to their potential applications in optoelectronics and bio-imaging. However, a comprehensive correlation among these three distinguished properties is yet to be unveiled, which will help to decipher defined methodologies to design future generation multi-functional organic materials. Herein, we have demonstrated a route to obtain a multi-functional organic luminogen, starting from an ACQphore (TPANDI) by simple structural engineering. We have shown that a slight reduction in the length of the planar acceptor moieties can effectively inhibit the undesirable π-π stacking interaction between molecules in the condensed state, and thereby, cause an ACQ to AIE type transformation from TPANDI to TPANMI and TPAPMI. Both TPANMI and TPAPMI exhibit RTP properties (even in ambient conditions) due to presence of a reasonably low singlet-triplet energy gap (ΔE_{ST}). In our study, these two luminogens were found to be mechano-inactive. Interestingly, an insertion of the cyano-ethylene group and benzene linker in between the triphenylamine and phthalimide moieties introduced another luminogen TPACNPMI, that can simultaneously exhibit AIE, RTP and mechanochromic properties.

2.2 Introduction:

Solid State luminescence is a burgeoning field of fundamental and applied research. Especially, organic emitters that exhibit reversibility between distinct luminescence colors or multi-stimuli responsive behavior (e.g. mechanochromism, thermochromism and vapochromism) have gathered considerable attention owing to their potential applications in optoelectronic devices, sensors, probes, security and storage devices.[1–8] However, most of the organic emitters suffer a notorious aggregation caused quenching (ACQ) effect in the solid state, which truncates their scope of various applications as a proficient light emitting candidate.[9] In 2001, Tang and co-workers paved the way towards the avoidance of this undesirable event.[10] A new photophysical term was coined as aggregation induced emission (AIE) and aggregation induced emission enhancement (AIEE) in this context. These two intriguing phenomena can transform non-emissive or weakly emissive aggregates of organic luminogens into highly emissive ensembles in higher content of anti-solvent or in the solid state by inhibiting the π-π co-facial stacking of adjacent aromatic ring.[9] Consequently, it led towards the revelation of a new horizon for

organic luminogens to be utilized in real world applications such as, organic light emitting diodes (OLEDs), light emitting liquid crystals, optical waveguide emitters and in several bio-medical as well as bio-sensing applications.[11–20]

Recently, amalgamation of several photophysical processes with the AIE and mechanochromism has augmented the field of solid-state luminescence, and has emerged as a primary methodology to develop multifunctional "all in one" type future generation luminogens[20,21]. One of the most capable accelerators for the development of this particular field is the triplet state engineering, which involves phenomena, like thermally activated delayed fluorescence (TADF) and room temperature phosphorescence (RTP). In particular, RTP has drawn considerable attention owing to its potential application in the development of highly efficient, environmentally friendly, heavy-metal free and cost-effective luminescent materials for optoelectronic devices as well as for biological applications.[22–24] Generally, phosphorescence occurs via a spin-forbidden process, which involves an intersystem crossing from the lowest singlet (S_1) to the lowest triplet state (T_1) followed by a radiative transition from the T_1 state to the ground S_0 state. The intersystem crossing is facilitated by spin-orbit coupling, which is more prevalent in the case of heavy metal containing moieties. Therefore, for metal-free organic luminogens, spin-forbidden transitions remain inadequate, and non-radiative decay through intermolecular collisions and molecular motion becomes predominant. Researchers came up with several notions to increase the rate of intersystem crossing by promoting spin-orbit coupling in organic emitters and a subsequent increment in the rate of radiative relaxation from T_1 to S_0. Bolton et al. reported a turn-on phosphorescence in the crystal state of 2,5-dihexyloxy-4-bromobenzaldehyde; where, the authors revealed a C-Br·· ·O=C type halogen bonding to be responsible for this type of turn-on phosphorescence in crystals.[25] Later, Shi et al. also demonstrated a Br···Br type halogen bonding in crystal phase which expedites RTP in a series of di-bromo benzene derivatives with alkyl group.[26] Several prodigious works on the development of multifunctional luminogens has also been reported, where RTP and mechanochromic properties coexist in a single organic molecule. For instance, Prof. Tang's group reported three-mono or di-bromo substituted benzophenone derivatives, which exhibited simultaneous RTP and mechanochromic properties.[27] Crystallization of these luminogens induced the phosphorescence emission to occur through structural rigidification, and those crystals were found to exhibit a blue shifted emission upon grinding. Prof. Xue et al. reported a carbazole based luminogen exhibiting persistent RTP with a lifetime of ~540 ms.[28] Moreover, a phosphorescence to fluorescence emission switching was observed upon

mechanical stimulus, which was caused by molecular planarization and enhanced π-π interaction under grinding. Prof. Chi and co-workers reported that the original micro-crystals of both the SHB_2T and SDB_2T (constituted by sulfone as acceptor and di-benzo thiophene as donor) exhibit white light emission with blue-violet fluorescence and yellow phosphorescence along with mechanochromic properties. Here, the microcrystals of SDB_2T showed a red-shift of the fluorescence emission from 392 nm to 414 nm and an enfeebled yellow phosphorescence upon mechanical grinding, thus manifesting a white-to-blue emission tuning.[29]

Despite conducting considerable research works in this field, several structure-property correlations are yet to be unraveled, which is consequential in developing facile and well-defined methodologies in the field of multifunctional organic luminogens. In this regard, the establishment of a comprehensive interrelation among AIE, mechanochromism, and RTP can provide adequate transparency to the structure-property relationships of these luminophores, which will also help to decipher several photophysical processes, and eventually lead to the advancement of multifunctional organic materials. Here in this article, we have designed and synthesized four organic luminogens. Starting from a molecule with ACQ properties, we have demonstrated that a simple structural modification can effectively modulate the packing fashion in the condensed state, and can bring about an ACQ to AIE type transformation. Moreover, the presence of closely spaced singlet and triplet energy states in all these AIE active luminogens, can facilitate the intersystem crossing (ISC) process, and consequently it leads towards room-temperature phosphorescence behavior. Finally, it was observed that an introduction of a cyano-ethylene group along with a benzene linker between the donor and acceptor could bring about easy and distinct mechanochromic behavior in the final molecule. Thus, starting from a molecule with ACQ nature, upon minimal and systematic modification of molecular structure, a multi-functional luminogen with AIE, RTP along with easy and distinct mechanochromic properties was obtained.

2.3 Design strategy:

In order to implement our desired target, we have considered the following points during the design of our organic luminogens: presence of (a) donor-acceptor (D-A) type framework in each luminogen, (b) a twisted and flexible donor moiety, (c) a planar acceptor core, the length of which can be reduced to decrease the extent of the π…π interaction in the subsequent molecules, and thereby to achieve ACQ to AIE type transformation, and (d) multiple sites to facilitate several non-covalent interactions, which can lead to the emergence of RTP as well as

mechanochromic behavior. Most importantly, (e) the donor and acceptor moieties have been chosen in such a way that they contain atoms with non-bonding electrons, which can favor the (n, π^*) transition leading to an increased rate of intersystem crossing between several excited singlet and triplet states, and thereby facilitates RTP process.[30] Assessing the aforementioned aspects, initially, we have designed three luminogens, namely, TPANDI, TPANMI, TPAPMI with triphenylamine as donor and naphthalene diimide, naphthalene monoimide, phthalimide as electron deficient acceptors, respectively (**Scheme 1**). Triphenylamine (TPA), owing to its propeller-shaped structure, can inhibit the undesirable π-π stacking in the aggregated state, which can be useful as an efficient building block for the AIE luminogens. Also, the twisted skeleton and higher degree of flexibility of TPA moiety can expedite the multi-stimuli responsive behavior in TPA-based luminogens.[31,32] On the contrary, all the acceptors are structurally planar and can behave as excellent electron acceptors because of their electron-deficient nature. Moreover, the presence of carbonyl oxygen along with the nitrogen atoms present in the acceptor molecule can promote the production of triplet excitons through (n, π^*) transition. In the fourth luminogen, namely, TPACNPMI, we have inserted an additional cyano-ethylene group along with a benzene linker between the donor TPA and acceptor phthalimide moiety (**Scheme 1**). The presence of carbonyl oxygen and the incorporation of the cyano-ethylene group can make several strong and short contacts with the neighbouring aromatic hydrogen atoms leading to the increase in its degree of responsiveness under mechanical stimulus.

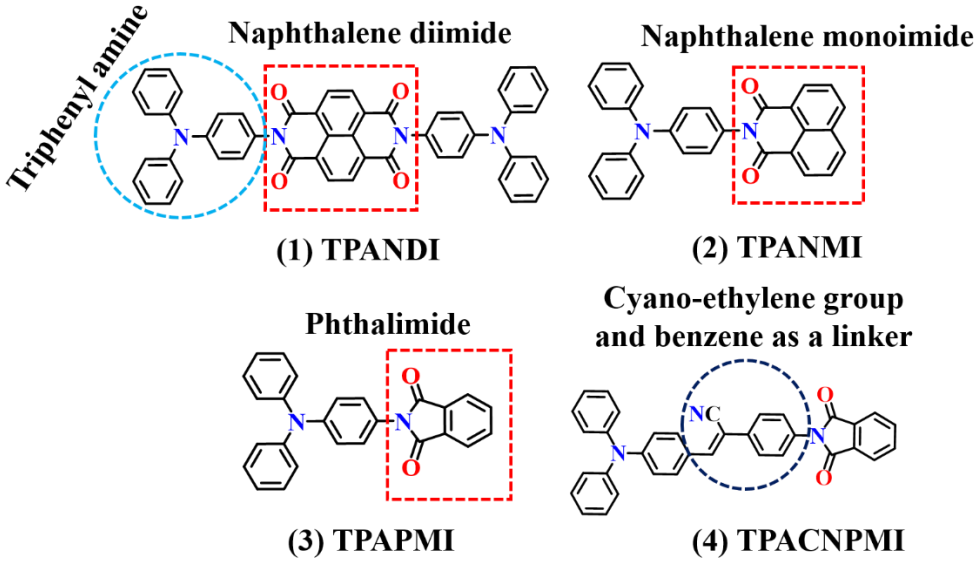

Scheme 1: Structures of the designed organic luminogens.

2.4 Brief synthesis procedure and characterization data:

Herein, we adopted two different synthetic schemes to synthesize our designed luminogens.

(a) The first synthetic route involves nitration of triphenylamine using $NaNO_3$ and glacial acetic acid in chloroform, followed by its reduction from nitro to an amine using $NH_2NH_2.H_2O$ and Pd/C catalyst in ethanol at reflux condition, and finally, the condensation reaction was done with 1,4,5,8-napthalenetetracarboxylic dianhydride, 1,8-naphthalic anhydride, and phthalic anhydride to produce TPANDI, TPANMI, and TPAPMI, respectively (**Scheme S1, details in section A1 of Appendix**).

(b) TPACNPMI was synthesized using a different synthetic route (**Scheme S2**). Initially, mono-formylation of triphenylamine was carried out using $POCl_3$ and DMF, followed by a condensation reaction with 4-nitrophenyl acetonitrile in piperidine/ethanol solution, and then a reduction of the nitro functionality to amine was done using SnCl2 in ethanol solvent. Finally, a condensation reaction was performed with phthalic anhydride in glacial acetic acid at reflux conditions to synthesize the final compound, i.e., TPACNPMI (**details in section A2 in Appendix**).

All the starting materials and final compounds were characterized using ^{1}H, ^{13}C NMR spectroscopy and HRMS studies (**section A3 in Appendix**). Single crystal diffracted molecular structure has been provided as an additional characterization proof (**section A4 in Appendix)**. Good quality single crystals of TPANDI were grown from a 1:1 mixture of DCM and methanol by slow evaporation method within 2-3 days; whereas for all other luminogens, crystals were obtained from the reaction mixture. *Here is the characterization data for all the compounds*:

4-nitro-N,N-diphenylaniline (a)

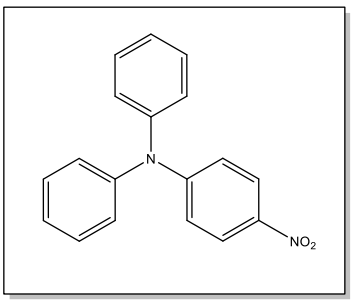

^{1}H NMR (400 MHz, $CDCl_3$): δ 8.10 – 8.02 (m, 2H), 7.43 – 7.36 (m, 4H), 7.28 – 7.19 (m, 6H), 6.97 – 6.92 (m, 2H).

^{13}C NMR (100 MHz, $CDCl_3$): δ 153.56, 145.71, 140.19, 130.01, 129.43, 126.60, 125.82, 125.55, 123.67, 123.30, 118.19.

HRMS (ESI TOF): *m/z* calcd. For $C_{18}H_{15}N_2O_2$ $[M+H]^+$ 291.1133 found 291.1125.

N1,N1-diphenylbenzene-1,4-diamine (b)

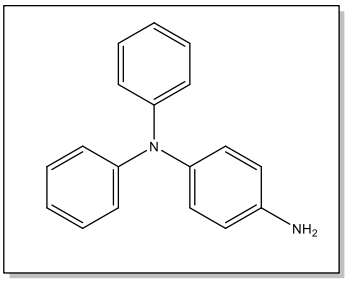

^{1}H NMR (400 MHz, $CDCl_3$): δ 7.27 – 7.17 (m, 4H), 7.12 – 7.02 (m, 4H), 7.01 – 6.89 (m, 4H), 6.68 – 6.62 (m, 2H), 3.42 (bs, 2H, NH_2).

^{13}C NMR (100 MHz, $CDCl_3$): δ 148.37, 142.97, 139.13, 129.33, 129.10, 127.92, 124.29, 122.66, 121.60, 116.37.

HRMS (ESI TOF): *m/z* calcd. For $C_{18}H_{16}N_2$ $[M]^+$ 260.1313 found 260.1316.

4-(diphenylamino)benzaldehyde (c)

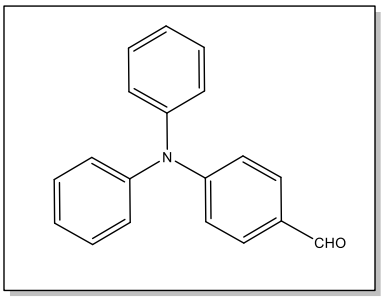

^{1}H NMR (400 MHz, $CDCl_3$): δ 9.81 (s, 1H), 7.76 – 7.62 (m, 2H), 7.34 (dd, *J* = 10.4, 5.4 Hz, 4H), 7.22 – 7.12 (m, 6H), 7.01 (t, *J* = 8.9 Hz, 2H).

^{13}C NMR (100 MHz, $CDCl_3$): δ 190.56, 153.45, 146.23, 131.41, 129.83, 129.29, 129.16, 126.41, 125.21, 124.24, 119.42.

HRMS (ESI TOF): *m/z* calcd. For $C_{19}H_{16}NO$ $[M+H]^+$ 274.1232 found 274.1233.

(*Z*)-3-(4-(diphenylamino)phenyl)-2-(4-nitrophenyl)acrylonitrile (d)

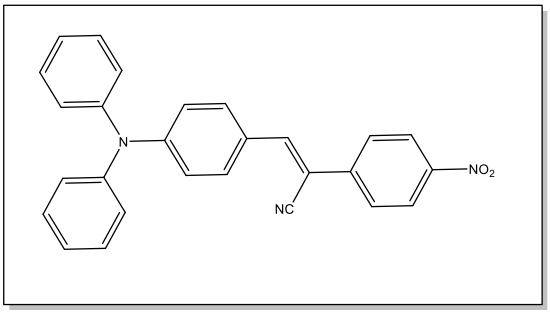

^{1}H NMR (400 MHz, $CDCl_3$): δ 8.26 (t, *J* = 5.6 Hz, 2H), 7.80 (dt, *J* = 11.4, 5.7 Hz, 4H), 7.56 (s, 1H), 7.38 – 7.31 (m, 4H), 7.18 (dd, *J* = 11.9, 5.4 Hz, 6H), 7.04 (d, *J* = 8.9 Hz, 2H).

^{13}C NMR (100 MHz, $CDCl_3$): δ 151.15, 147.32, 146.21, 144.84, 141.53, 131.56, 129.80, 126.20, 125.19, 125.09, 124.40, 120.09, 118.19, 104.70.

HRMS (ESI TOF): *m/z* calcd. For $C_{27}H_{19}N_3O_2$ $[M]^+$ 417.1477 found 417.1472.

(*Z*)-2-(4-aminophenyl)-3-(4-(diphenylamino)phenyl)acrylonitrile (e)

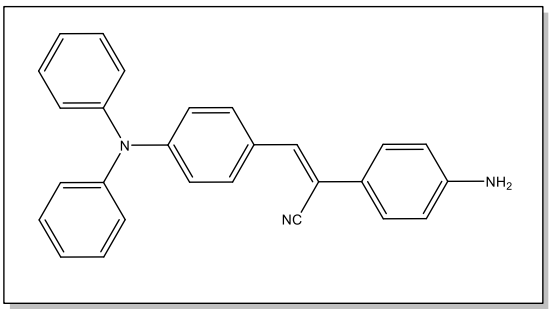

^{1}H NMR (400 MHz, $CDCl_3$): δ 7.72 (d, *J* = 8.7 Hz, 1H), 7.45 (d, *J* = 8.5 Hz, 1H), 7.33 – 7.26 (m, 5H), 7.23 – 7.17 (m, 1H), 7.15 (d, *J* = 7.8 Hz, 2H), 7.07 (dt, *J* = 11.0, 7.7 Hz, 6H), 6.82 (d, *J* = 8.7 Hz, 1H), 6.71 (d, *J* = 8.5 Hz, 1H), 6.62 (t, *J* = 8.1 Hz, 1H), 3.84 (bs, 2H, NH_2).

^{13}C NMR (100 MHz, $CDCl_3$): δ 149.35, 147.11, 146.90, 138.30, 130.24, 129.57, 127.29, 127.02, 125.54, 125.26, 124.14, 121.46, 115.23, 108.24.

HRMS (ESI TOF): *m/z* calcd. For $C_{27}H_{21}N_3$ $[M]^+$ 387.1735 found 387.1736.

2,7-bis(4-(diphenylamino)phenyl)benzo[lmn][3,8]phenanthroline-1,3,6,8(2H,7H)-tetraone (TPANDI) (1)

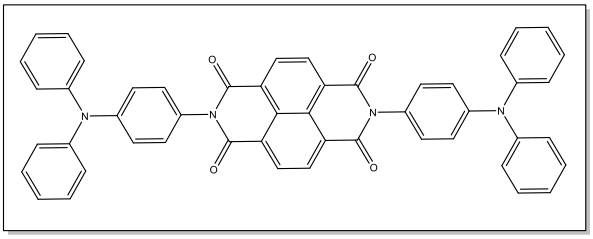

^{1}H NMR (400 MHz, $CDCl_3$): δ 8.85 (s, 4H), 7.31 (t, *J* = 7.4 Hz, 8H), 7.21 (d, *J* = 8.0 Hz, 12H), 7.16 (d, *J* = 8.4 Hz, 4H), 7.08 (t, *J* = 6.9 Hz, 4H).

^{13}C NMR (100 MHz, $CDCl_3$): δ 163.26, 148.53, 147.37, 131.54, 129.53, 129.05, 127.59, 127.22, 127.13, 125.31, 123.74, 122.84.

MALDI (TOF): *m/z* calcd. For $C_{50}H_{32}N_4O_4$ $[M]^+$ 752.2424 found 752.1351.

2-(4-(diphenylamino)phenyl)-1H-benzo[de]isoquinoline-1,3(2H)-dione (TPANMI) (2)

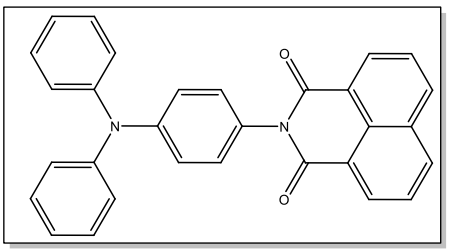

^{1}H NMR (400 MHz, $CDCl_3$): δ 8.68 (dd, *J* = 7.3, 1.0 Hz, 2H), 8.29 (dd, *J* = 8.3, 0.9 Hz, 2H), 7.87 – 7.78 (m, 2H), 7.36 – 7.27 (m, 4H), 7.27 – 7.14 (m, 8H), 7.12 – 7.04 (m, 2H).

^{13}C NMR (100 MHz, $CDCl_3$): δ 164.67, 148.07, 147.62, 134.35, 131.86, 131.73, 129.47, 129.33, 128.99, 128.64, 127.18, 125.09, 123.45, 123.38, 123.03.

HRMS (ESI TOF): *m/z* calcd. For $C_{30}H_{21}N_2O_2$ $[M+H]^+$ 441.1603 found 441.1595.

2-(4-(diphenylamino)phenyl)isoindoline-1,3-dione (TPAPMI) (3)

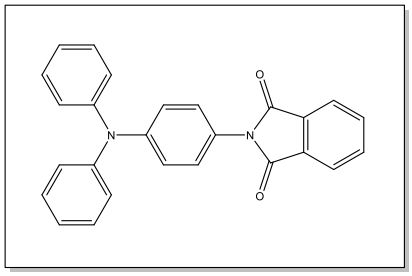

^{1}H NMR (400 MHz, $CDCl_3$): δ 7.97 – 7.91 (m, 2H), 7.81 – 7.74 (m, 2H), 7.30 – 7.23 (m, 6H), 7.17 – 7.10 (m, 6H), 7.08 – 7.01 (m, 2H).

^{13}C NMR (100 MHz, $CDCl_3$): δ 167.63, 147.69, 147.46, 134.42, 131.89, 129.47, 127.37, 125.24, 125.00, 123.77, 123.51, 123.11.

HRMS (ESI TOF): *m/z* calcd. For $C_{26}H_{19}N_2O_2$ $[M+H]^+$ 391.1447 found 391.1446.

(*Z*)-2-(4-(1,3-dioxoisoindolin-2-yl)phenyl)-3-(4-(diphenylamino)phenyl)acrylonitrile (TPACNPMI) (4)

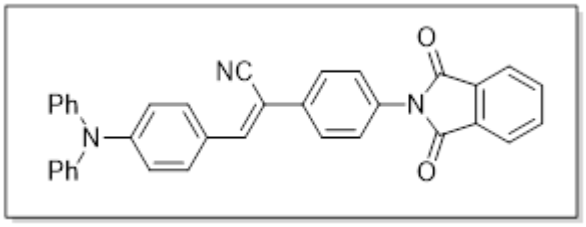

^{1}H NMR (400 MHz, $CDCl_3$): δ 8.01 – 7.94 (m, 2H), 7.85 – 7.75 (m, 6H), 7.58 – 7.52 (m, 2H), 7.47 (s, 1H), 7.37 – 7.28 (m, 4H), 7.21 – 7.10 (m, 6H), 7.09 – 7.03 (m, 2H).

^{13}C NMR (100 MHz, $CDCl_3$): δ 167.17, 167.06, 150.28, 149.82, 146.62, 146.54, 144.50, 142.50, 134.79, 134.68, 131.90, 131.75, 131.67, 131.37, 130.92, 129.71, 129.68, 129.64, 126.88, 126.41, 126.23, 125.86, 125.67, 124.57, 124.51, 123.97, 120.86, 120.39, 118.62, 109.49, 106.70.

HRMS (ESI TOF): *m/z* calcd. For $C_{35}H_{24}N_3O_2$ $[M+H]^+$ 518.1868 found 518.1860.

2.5 Instrumentation:

^{1}H NMR (at 400 MHz) and ^{13}C NMR (at 100 MHz) characterizations of each synthesized compound were performed using JEOL ECS-400 and Bruker Ascend ^{TM} 400 spectrometer

using deuterated chloroform ($CDCl_3$) as solvent (having residual chloroform) and tetramethylsilane (TMS) as the internal standard. Chemical shift (δ) values were measured in ppm downfield from $CDCl_3$ (δ = 7.26 ppm) for ^1H NMR and relative to central $CDCl_3$ resonance (δ = 77.16 ppm) for ^{13}C NMR. High resolution mass spectra (HRMS) for all the compounds were recorded using ESI TOF in Water's SYNAPT G2 mass spectrometer. MALDI-TOF mass spectrum of TPANDI was collected in 4800 plus MALDI-TOF analyzer. Single-crystal diffraction analysis data were collected at 100K with a BRUKER KAPPA APEX II CCD Duo diffractometer (operated at 1500 W power: 50 kV, 30 mA) using graphite monochromatic Mo Kα radiation (λ = 0.71073 Å) and Cu Kα radiation (λ = 1.54178 Å). The structures were solved by direct methods and refined by least-squares against F2 utilizing the software packages SHELXL-97.[33,34] More information on crystal structures can also be obtained from the Cambridge Crystallographic Data Centre under CCDC deposition number. Dynamic Light Scattering (DLS) experiment was performed using Nano ZS-90 apparatus with 633 nm red laser (90^0 angle) from Malvern instruments. Atomic force microscopy (AFM) imaging experiment was carried out using Keysight 5500 AFM instrument (Agilent Technologies) under tapping mode using silicon nitride tip. Field Emission Scanning Microscopy (FESEM) imaging experiment was performed using the ZEISS instrument by drop-casting the THF/water or dioxane/water binary mixture on silicon wafers. Powder XRD experiments were carried out using BRUKER D8 advance X-ray diffractometer with Cu-K_α radiation source. Steady state absorption spectra were recorded on Shimadzu, UV-2600 UV spectrophotometer. Steady state emission spectra of all the AIE experiments, solution based emission measurements and mechanochromic emission study of TPACNPMI were carried out using Fluoromax-4 spectrofluorometer (Horiba Jobin Yvon). All other solid state emission spectra, phosphorescence emission spectra in the 'Room Temperature Phosphorescence (RTP)' section and mechanochromic emission study of the other two luminogens (TPANMI and TPAPMI) were performed using Edinburgh FLS980 instruments. Microsecond flash lamp (of 1.5-2.5 μs band width) was used during phosphorescence decay collection and phosphorescence spectra measurement. 800 nm mode-locked Ti-sapphire laser (Mai-Tai, Spectra Physics) excitation source was focused on the sample for the two-photon absorption experiment. Two-photon cell imaging was performed using multiphoton microscope (Leica, Germany) at 63X oil immersion objective.

2.6 Experimental section:

Fabrication of nano-aggregates and other details in AIE study

Different fractions of distilled water (bad solvent) were added dropwise in a solution of THF/1,4 dioxane containing 30 μm of luminogen under vigorous stirring and was used for performing the AIE experiment. In case of TPANMI and TPAPMI, to avoid scattering originated due to aggregate formation, a 400 nm long pass filter is used during PL spectra recording. Although, no scattering was observed in lower water content, but just to make an appropriate and justified PL intensity comparison, we have used the filter in each fraction of water content. Furthermore, fabricated nano-aggregates were then characterized using DLS, FESEM and AFM studies.

Density Functional Theory (DFT) calculation

Quantum chemical calculations were performed using Gaussian 09 program[35] using 'PARAM Brahma Facility' under the National Supercomputing Mission, Government of India at IISER Pune. Initially geometry optimization of all the luminogens were carried out in gas phase and the nature of the stationary point (minima on the PE surface) was confirmed by frequency analysis[36,37] and the spatial distribution of HOMOs and LUMOs were obtained at the B3LYP/6-311++G (d, p) level. Furthermore, TD-DFT calculations were carried out to get the energy information of several excited singlet and triplet states on equal no. of singlet and triplet states (td (50-50, n-states=15)) by B3LYP functional. Based on the results obtained from TD-DFT calculations, we computed the electron density difference map (EDDM) for first bright transition (lowest energy state with maximum oscillator strength) using Gauss-Sum software[38].

Spin orbit coupling matrix element calculation

Spin orbit coupling matrix between different excited singlet and triplet states were calculated using the zeroth-order regular approximation (ZORA) to the Dirac equation. In this approximation, the SOC operator, $\widehat{H}_{SOC,}$ is described as eq. 1[39]

$$\widehat{H}_{SOC} = \frac{c^2}{(2c^2 - v)^2} \sigma \cdot (\nabla v \times p) \qquad (1)$$

Where c, v, σ and p signify speed of light, Kohn-Sham potential, Pauli spin-matrix vector and linear momentum operator respectively. The first-order perturbation is applied on scalar relativistic orbitals after the self-consistent field (SCF) and TD-DFT calculations to obtain SOC effects. B3LYP functional coupling with 6-311++G (d, p) are used to calculate SOC values. All such calculations are done using PySOC package.[40]

Cell culture and drug treatments

MCF7 cells were obtained from the European Collection of Cell Cultures (ECACC). The cells were maintained in 100 mm dishes (Eppendorf or Corning) and were grown in high-glucose Dulbecco's Modified Eagle Medium (DMEM; Lonza) containing 10% heat-inactivated FBS (Invitrogen) and 100 units/mL penicillin-streptomycin (Invitrogen) and incubated at 37°C humidified 5% CO_2 incubators (Eppendorf or Thermo Scientific).

For multiphoton imaging experiments, 5X 10^4 MCF7 cells were seeded on coverslip and incubated at 37°C with 5% CO_2 for 18hrs. Cells were treated with 10 µM of compound TPACNPMI and incubated for 24 hrs. Post treatment, cells were washed with 1X PBS twice and fixed with 4% paraformaldehyde for 20 minutes in dark. After fixation, cells were again washed with PBS and mounted onto slides. The cells were imaged in multiphoton microscope (Leica, Germany) at 63X oil immersion objective.

For the MTT assay, 0.5 X 10^4 MCF7 cells were seeded in each well of a 96 well plate and incubated at 37°C with 5% CO_2 for 18 hours post seeding. Cells were treated with different concentrations of compound. 24 hrs post treatment, drug containing media was removed and, 0.5 mg/ml thiazolyl blue tetrazolium (MTT) containing DMEM was added to the cells and incubated at 37°C after covering with aluminum foil. 4 hours post MTT addition, MTT-DMEM medium mixture was aspirated from the wells and 100 µl of DMSO was added to dissolve the purple MTT-formazan crystals. The absorbance was recorded at 570nm using the multimode Varioskan Flash plate reader (Thermo Scientific, USA).

2.7 Results and Discussion:

2.7.1 Charge transfer analysis:

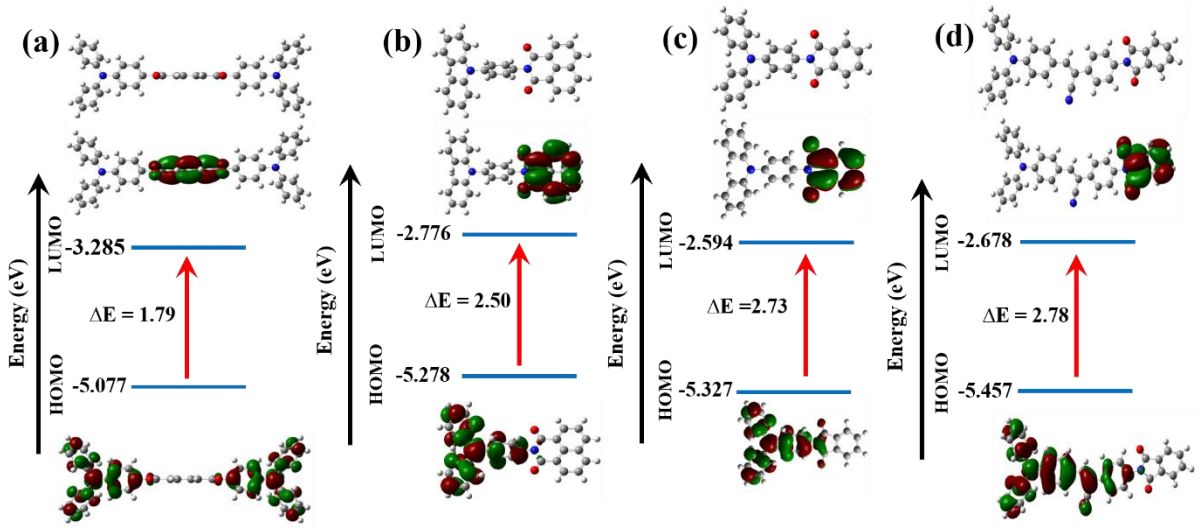

Figure 1: HOMO and LUMO molecular orbitals of (a) TPANDI, (b) TPANMI, (c) TPAPMI, and (d) TPACNPMI with their associated energy values.

To validate the viability of our molecular design, theoretical calculations were conducted using the DFT method at the B3LYP/6-311++G (d, p) level. The DFT-optimized molecular structures of the designed luminogens along with the highest occupied molecular orbitals (HOMOs) and lowest unoccupied molecular orbitals (LUMOs) with corresponding energy levels are shown in **Figure 1**. In all the cases, the HOMOs and LUMOs are spatially separated and reside exclusively on the donor and acceptor (NDI, NMI, PMI) moieties, respectively. Thus, there will be a substantial intramolecular charge transfer (ICT) from the electron rich donor to the electron deficient acceptor part upon photo-excitation. We also calculated the electron density difference map (EDDM) for the first bright transition (transition having considerable oscillator strength, obtained from time-dependent DFT calculation) to visualize the movement of charge during that particular transition. Notably, for charge transfer luminogens, these kinds of EDDM plots are usually accompanied by two different colors. Here, the cyan color signifies the region where the charge is being accumulated, and the yellow color indicates the region from where the electronic charges are being depleted during an electronic transition (**Figure 2**). Interestingly, for the first bright transition, it was observed that the charges are getting depleted from the electron rich TPA part (in TPACNPMI, it extends further till the cyano-ethylene and benzene linker part) and are getting accumulated in the electron-deficient NDI (for TPANDI), NMI (for TPANMI) and PMI (for TPAPMI and TPACNPMI) regions (**Figure 2**), which again validates the charge transfer nature of our luminogens.

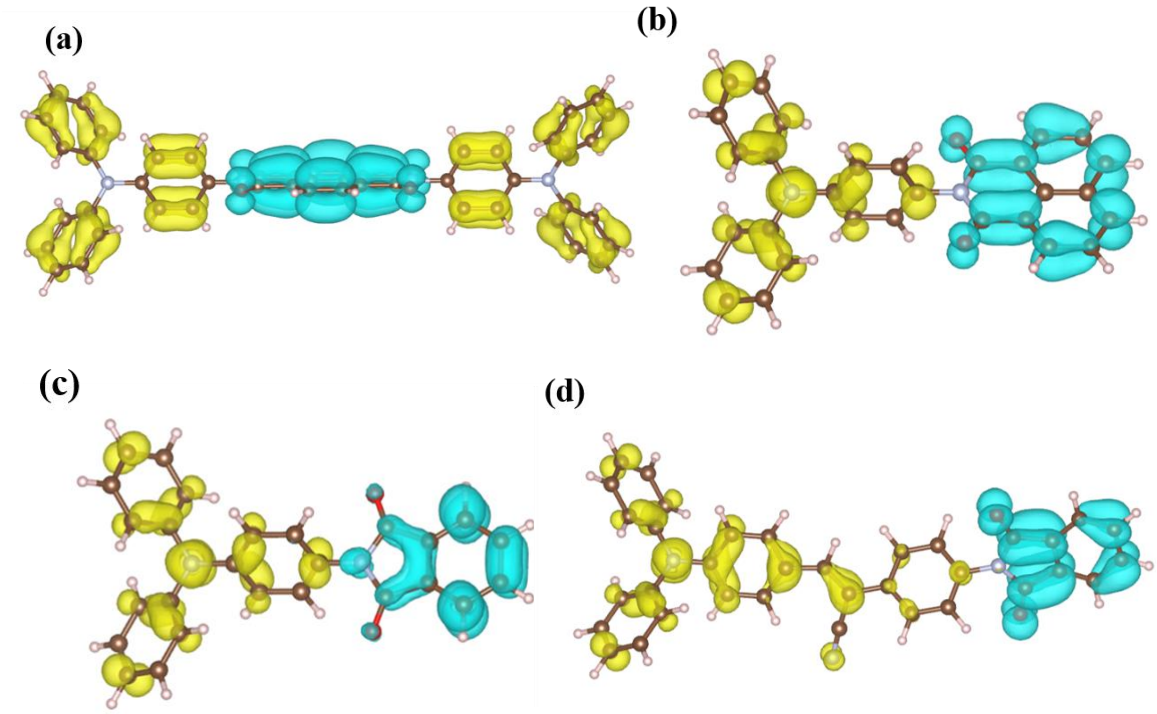

Figure 2: Iso-surfaces of electron density difference map (EDDM) of (a) TPANDI (for transition to S_4 state), (b) TPANMI (for transition to S_2 state), (c) TPAPMI (for transition to S_2 state) and (d) TPACNPMI (for transition to S_2 state). The first bright transition (except TPANMI, in which the transition being considered (S_2) is energetically very close to the first bright transition (S_3)) is considered based on the outcome of TD-DFT calculations.

2.7.2 Optical properties and aggregation-induced emission (AIE) study

In the solution phase, TPANDI, TPANMI, and TPAPMI show absorption bands with vibrational structures in the range of 325-400 nm, 300-370 nm, and 300-370 nm, respectively, which can be attributed to the π-π^* electronic transitions (**Figure A1 in Appendix**). The emission spectra of TPANDI manifest two overlapped emission bands in THF, a band with vibrational feature peaked at ~404 nm and another broad emission band with maxima at > 460 nm, which are attributed to relaxation from the locally excited state (LE) and charge transfer (CT) states, respectively. The recognition of these emission bands has been further justified by collecting the emission spectra in the solvents of different polarities (**Figure A2 in Appendix**). In non-polar solvent like toluene, the intensity of the red-shifted CT band is reasonably weak compared to the emission band generated due to decay from LE state. Intensity of the red shifted band increases with raising the solvent polarity, and gradually achieves highest intensity in THF and acetonitrile. The relative difference between the intensities of LE and CT peaks

gradually diminishes with increasing the solvent polarity. Interestingly, upon further increase in the solvent polarity (in DMSO), the intensity of the red-shifted emission band is significantly reduced (**Figure A2 in Appendix**) due to substantial stabilization of the CT state. TPANDI-like dual emissive features (from LE and CT state) were also observed in case of TPANMI and TPAPMI. For TPANMI, the LE and CT peaks were located at ~ 390 nm and ~ 600 nm, respectively, in 1,4-dioxane (**Figure A2 in Appendix**). Similarly, for TPAPMI, the emission maxima corresponding to LE and CT states were found to be centered at ~ 380 nm and ~ 600 nm, respectively, in the same solvent (**Figure A2 in Appendix**). For both these molecules, the CT band undergoes a gradual downturn in terms of emission intensity accompanied by a significant red-shift with an increase in solvent polarity (from toluene to acetonitrile) (**Figure A2 in Appendix**). Unlike the previous luminogens, TPACNPMI exhibits two well-separated absorption bands, one in the UV region (centered at ~ 295 nm) and another in the visible region (centered at ~ 400 nm) in all organic solvents (**Figure A1 in Appendix**). The absorption band in the UV region can be attributed to the π-π^* electronic transition, and the absorption band in the visible region can be accredited to the CT transition from the donor (TPA) to the acceptor (phthalimide) moiety. Interestingly, the emission spectra of TPACNPMI manifest a single emission peak, which is typically distinct from the emission features of the other three luminogens (**Figure A2 in Appendix**). In non-polar solvents like *n*-hexane, the emission band is composed of vibrational structures, which get broadened with a significant red shift when the polarity of the solvent is increased. Thus, the FWHM of the emission band also increases from 55 nm (in *n*-hexane) to 103 nm (in acetonitrile) (**Figure A2 in Appendix**). Although the relative contributions of LE and CT states in the broad emission band are indeterminate from the solvent-dependent studies, nevertheless the higher FWHM with dissipating vibrational features strongly suggests an increased CT character in the emissive excited state.

Solid state luminescence properties are mostly dictated by the emission behavior of luminogens in the aggregated state. Since the molecules are insoluble in water, increasing the aqueous proportion in a binary solvent system constituted of water/THF or 1,4-dioxane, would result in the formation of nano-aggregates. Hence, the optical properties of all the molecules were studied in organic solvent (THF or 1,4-dioxane)/water binary mixtures (**Figure 3**). In the case of TPANDI, the emission intensities of LE and CT bands get drastically reduced with an increasing aqueous proportion in a dilute solution (30 µM) of THF and the luminogen becomes almost non-emissive at very high water content (**Figure A4 in Appendix**), which clearly depicts TPANDI to be an ACQphore. Surprisingly, the emissive behavior of nano-aggregates

resulting from TPANMI, TPAPMI and TPACNPMI is significantly different compared to that

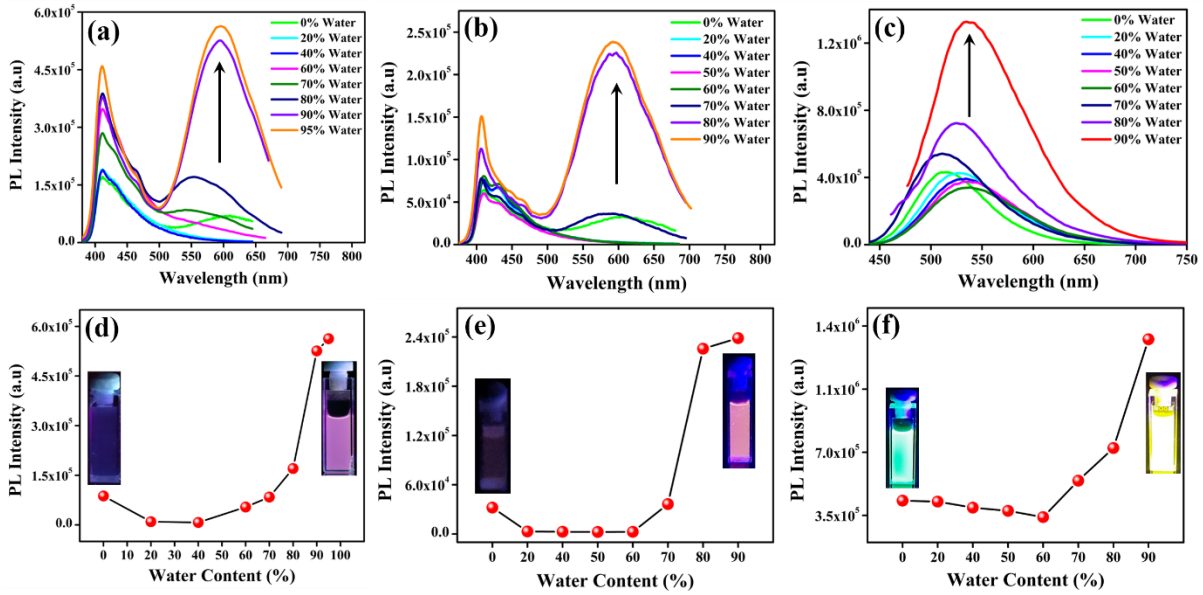

Figure 3: Emission spectra of (a) TPANMI and (b) TPAPMI in dioxane/water binary mixture. Emission spectra of (c) TPACNPMI in THF/water binary mixture. Emission intensity (of red-shifted emission peak) vs. water content (%) plot for (d) TPANMI, (e) TPAPMI, (f) TPACNPMI along with cuvette images (ex 365 nm) at the lowest and highest water content. Emission spectra of TPANMI (a, d) and TPAPMI (b, e) were collected by exciting at 335 nm and 347 nm, respectively. Emission spectra of TPACNPMI (c, f) were collected by exciting at respective absorption maximum (**Figure A5 in Appendix**).

of TPANDI. For both TPANMI and TPAPMI (**Figure 3**), the CT band (at ~ 602 nm for TPANMI and at ~ 604 nm for TPAPMI) gets depleted at lower water contents (fraction of water, f_w = 20% and 40%) in dioxane/water system. However, as the water content is gradually increased further to 60% (for TPANMI) and 70% (for TPAPMI), the particular peak rises up with a moderate blue-shift of ~ 50 nm. The initial depletion in the intensity at lower water content is due to adequate stabilization of the CT state owing to higher polarity of water and represents the solvatochromic behavior of the molecules. The uprise of the blue-shifted CT peak can be attributed to the formation of nano-aggregates induced by the immediate hydrophobic environment formed at relatively higher water content. Interestingly, as the water content was increased further up to ≥90%, intensity of the CT peak was increased ~ 6 fold compared to the intensity obtained in bulk 1,4-dioxane (**Figure 3**). This particular finding can be regarded as a consequence of the aggregation induced emission (AIE) effect. For TPACNPMI, upon increasing the water content initially up to 60%, the emission peak exhibits a continuous red shift from 515 nm to 538 nm, along with a declining intensity, which suggests that the solvatochromic nature of the molecule dominates in lower water contents (**Figure 3**).

However, when the water fraction slightly increases to 70%, a sudden enhancement takes place with a blue-shift of ~ 30 nm. Interestingly, beyond f_w= 70%, the emission is further enhanced with a red-shift up to 535 nm at 90% of water content (**Figure 3**). All these features suggest an aggregation-induced emission (AIE) behavior of TPACNPMI. Furthermore, the formation of nano-aggregates at higher water content for all these AIEgens was confirmed by DLS, AFM, and SEM studies (**Figure 4**, **Figure A6 in Appendix**).

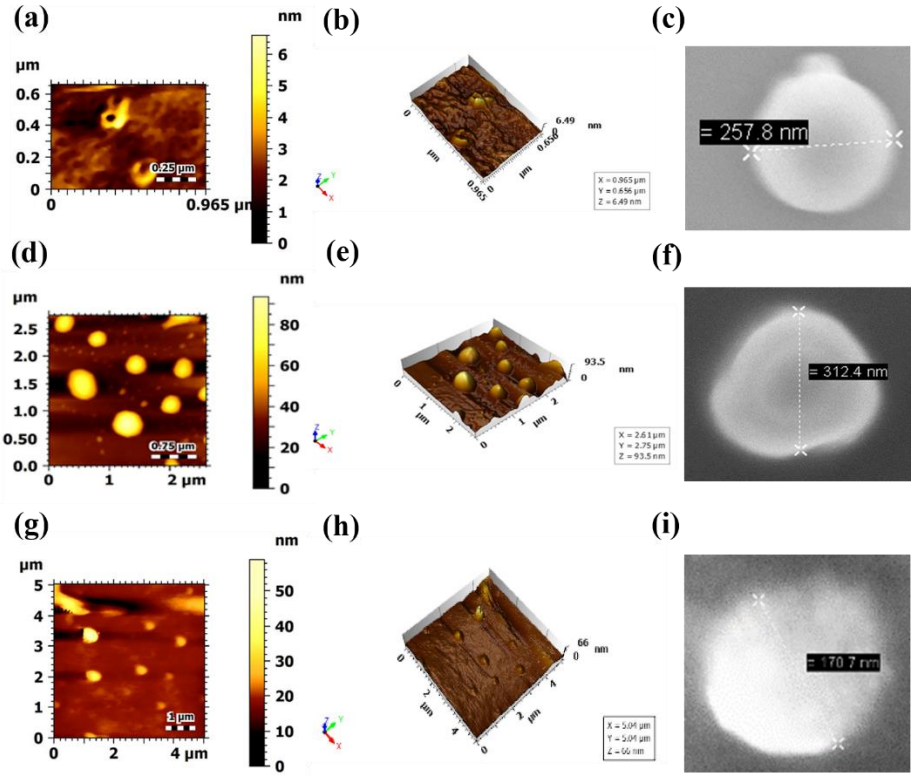

Figure 4: AFM images of aggregates formed by (a) TPANMI, (d) TPAPMI and (g) TPACNPMI. AFM images (3D height) of aggregates formed by (b) TPANMI, (e) TPAPMI and (h) TPACNPMI. FESEM images of aggregates formed by (c) TPANMI, (f) TPAPMI and (i) TPACNPMI.

The disparity in the emissive behavior of TPANDI and the other three luminogens in the aggregated state may emerge from the diverse spatial arrangements of the respective molecules in the solid state. In order to visualize the relative orientation of the molecules in the condensed state, single crystal X-ray diffraction (SCXRD) studies were carried out. Aggregation caused quenching (ACQ) usually occurs due to an effective π···π stacking interaction between adjacent organic monomers. SCXRD analysis of TPANDI crystal illustrates that two neighboring planar NDI core moieties lie above one another (co-facial type) at a very close distance of ~ 3.3Å (**Figure 5a**, **Figure A7 in Appendix**) with a subtle displacement, which falls in the range of

an effective π···π stacking interaction (from 3.3Å- 3.8Å).[41] The presence of two bulky .

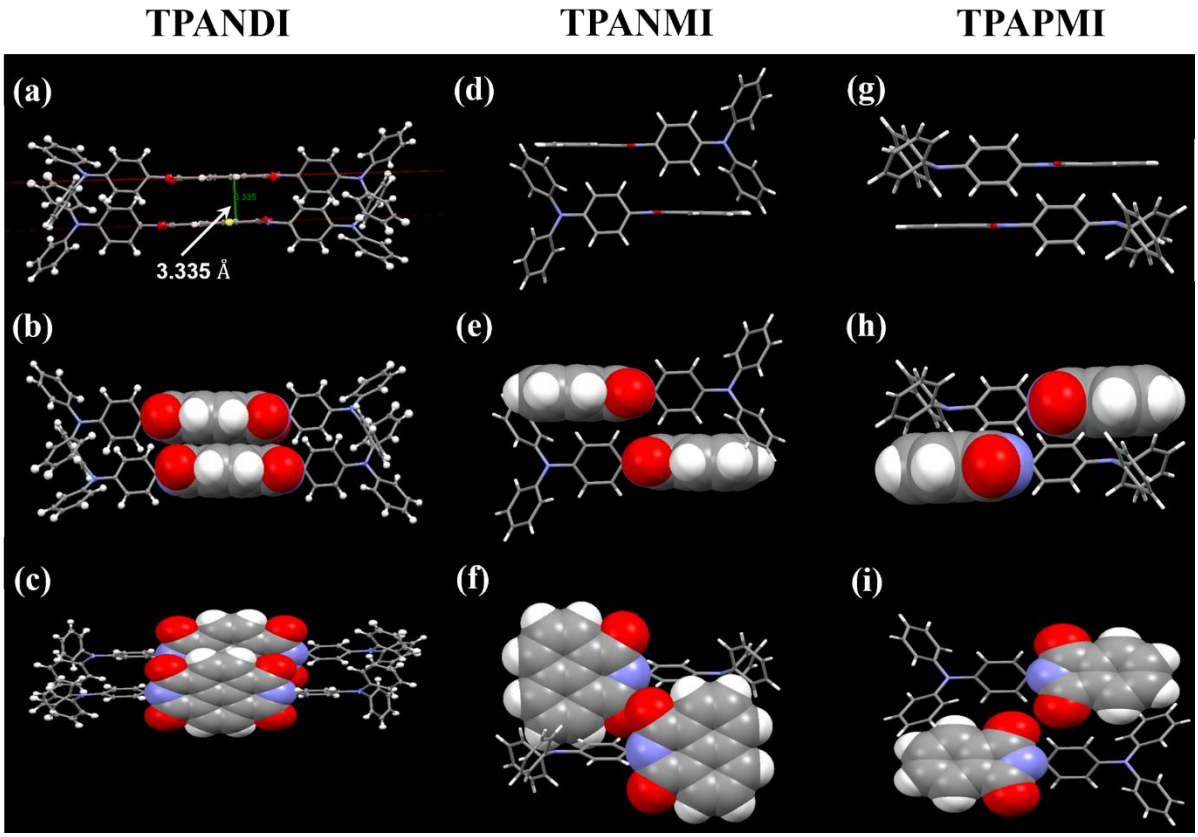

Figure 5: (a) π-π stacking interaction between two acceptor cores in TPANDI. Space-filling model of TPANDI from (b) side-view and (c) top-view. Arrangement of two neighboring molecules of (d) TPANMI and (g) TPAPMI in the crystalline state. Space-filling model of TPANMI from (e) side view, (f) top view. Space filling model of TPAPMI from (h) side view, (i) top view.

triphenylamine moieties at two terminal ends often restricts the co-facial stacking of molecules.[42] Nevertheless, in case of TPANDI, the TPA moiety fails to inhibit the π···π stacking between two NDI moieties due to the higher length of the planar core, which ultimately results in emission quenching in the aggregated state. On the other hand, TPANMI and TPAPMI display an entirely different packing arrangement in the crystalline state. SCXRD analysis shows that, TPANMI molecules are arranged in a brick-layer stacking mode and TPAPMI adopts a herringbone packing mode in the crystalline state (**Figure A7 in Appendix**). The dihedral angle between the phenyl ring of TPA group adjacent to the acceptor moiety appears as one of the crucial factors in this regard. In TPANMI, the phenyl ring is attached to the planar NMI acceptor core with a large dihedral angle of 71.85° (**Figure 15a**); whereas, in case of TPAPMI, the dihedral angle between the phenyl ring and the PMI group is only 43.03°

(**Figure 15b**). Such prominent change in dihedral angle may be attributed to differential sizes

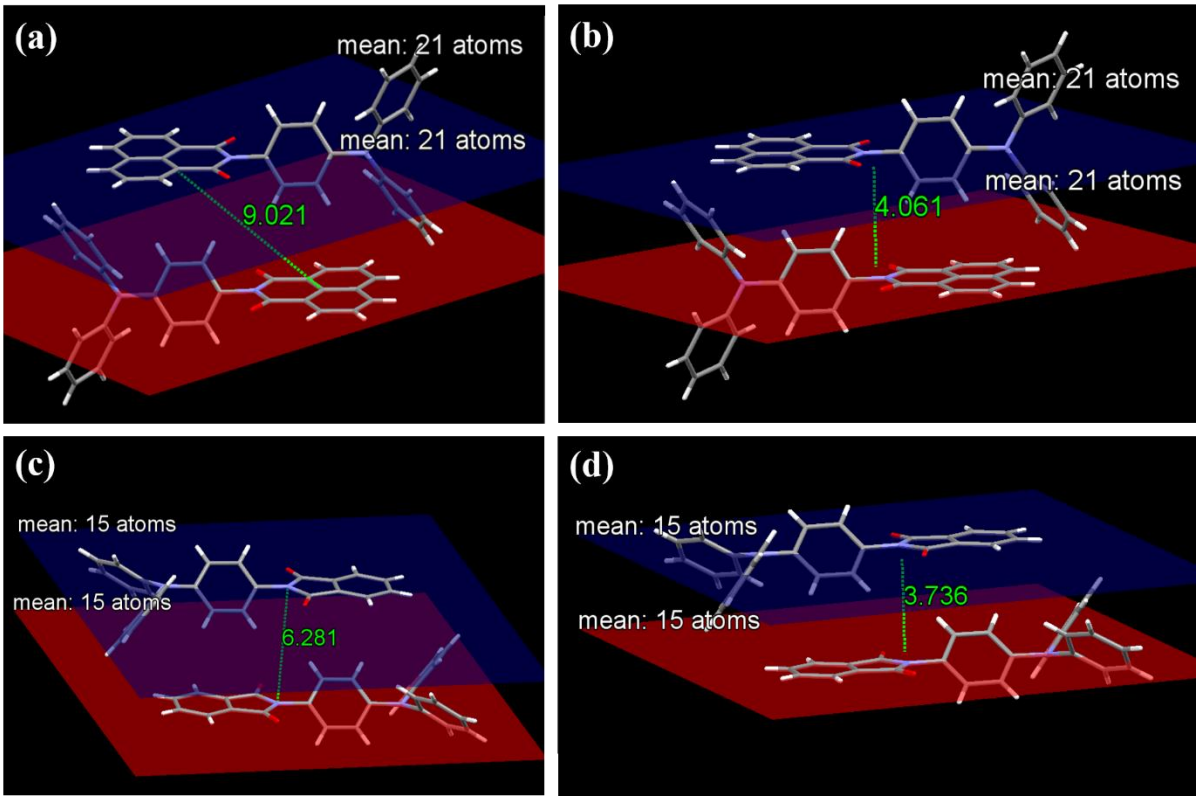

Figure 6: Diagonal distance (in Å) of two planar acceptor moieties in (a) TPANMI and (c) TPAPMI. Perpendicular distance (in Å) of the planes passing through the acceptor moieties of (b) TPANMI and (d) TPAPMI. Images have been processed by Mercury 3.7 software.

of the acceptor moieties. Interestingly, for both the cases, space-filling model illustrates that the planar acceptor moieties are displaced in such a way that the NMI and PMI acceptor cores are lying above the donor-TPA moiety (**Figure 5**), which significantly reduces the π···π overlap between neighboring molecules. Notably, a shortened length of the planar acceptor moieties in TPANMI and TPAPMI, strengthen the impact of bulky triphenylamine. As a result, the diagonal and the perpendicular distance of two planar acceptor moieties were found to be increased (**Figure 6**), which results in the less effective π···π stacking. We believe that the synergistic effects of such shortened planar acceptor moieties and an emergence of profound impact of bulky triphenylamine moiety together dictate their AIE behavior. Moreover, in TPACNPMI, two neighboring luminogens orient themselves in a head-to-tail fashion (**Figure A7 in Appendix**). Here, the terminal phthalimide moiety lies closer to the triphenylamine moiety of the neighboring luminogen in a slipped orientation. In this case, the presence of multiple rotatable single bonds increases the possibilities of several non-radiative decay pathways, which may affect the emission efficiency in bulk solvent; however, in the aggregated state due to restricted intramolecular rotation (RIR) and restricted intramolecular vibration

(RIV) such non-radiative decay pathways may be ceased, leading to the emergence of its AIE properties

2.7.3 Room temperature phosphorescence (RTP) study

Energy gap between the lowest singlet and the lowest triplet state of a donor-acceptor based luminogen is largely dependent on the nature of donor and acceptor moieties forming the molecular framework. A strong electron-rich donor and a strong electron-deficient acceptor can lead to a well-separated highest occupied molecular orbital (HOMO) and lowest unoccupied molecular orbital (LUMO), which eventually can lead to a less ΔE_{ST}.[43] We have already shown that the HOMO resides on the donor moiety (triphenylamine, TPA) and the LUMO lies on the respective acceptor moiety in all the four luminogens, and at the same time they maintain a large twisting angle between donor-acceptor. Such systems often provide a very less singlet-triplet energy gap or ΔE_{ST}, which can increase the rate of intersystem crossing or ISC. Moreover, all these luminogens contain atoms with non-bonding electrons, which are very useful for populating triplet state through intersystem crossing (ISC).[44,45] TPANMI in its crystalline phase (at room temperature), exhibits a broad spectrum with the emission maxima located at ~ 625 nm (**Figure 7**) and a tri-exponential decay feature comprising of ~ 2 ns, ~ 7 ns and ~ 32 ns lifetime components (**Figure A8 in Appendix**) which clearly indicates the excited state decay to be a fluorescence emission. However, a red shifted emission band having maxima at ~750 nm was obtained upon collecting the emission profile at 100 µs lamp triggered delay (**Figure 7**). Interestingly, a tri-exponential emission transient having lifetime components of ~ 1 ms, ~ 4 ms and ~ 12 ms was obtained (**Figure 7**) upon collecting the emission decay at ~750 nm, which suggests the room temperature phosphorescence (RTP) behavior of TPANMI. Similarly, in the case of TPAPMI (at room temperature), the fluorescence decay at ~ 617 nm was found to be tri-exponential in nature, having components of ~ 0.7 ns, ~ 3 ns, and ~ 13 ns (**Figure A8 in Appendix**). When the emission profile was collected at 100 µs lamp triggered delay, the phosphorescence spectrum was generated with an emission maximum centered at ~750 nm. The emission decay profile (collected at 750 nm) manifested tri-exponential behavior with components of ~ 433 µs, ~ 1.5 ms and ~ 7 ms (**Figure 7**). Unlike the previous cases (TPANMI and TPAPMI), the crystals of TPACNPMI exhibit two different emission peaks at ~ 535 nm and ~ 635 nm, respectively (**Figure 7**). The emission transient at ~ 635 nm shows a tri-exponential behavior with components of ~ 1 ns, ~ 5 ns, and ~ 12 ns (**Figure A8 in Appendix**). Whereas, the decay profile corresponding to the emission peak at ~535 nm was found to be relatively shorter in terms of lifetime, having a bi-exponential nature with

components of ~ 0.6 ns and ~ 3.3 ns (**Figure A8 in Appendix**). In this case also, upon collecting the emission at 100 µs lamp triggered delay, a red-shifted phosphorescence spectrum was obtained with emission maximum situated at ~ 715 nm (**Figure 7**). Upon collecting the phosphorescence decay at ~ 715 nm, a tri-exponential decay profile was found with components of ~ 1 ms, ~ 4.5 ms, and ~ 39 ms (**Figure 7**).

To investigate the mechanism of the observed room temperature phosphorescence from the AIE active luminogens, time-dependent density functional theory (TD-DFT) calculations were performed for both the singlet and triplet states. Here, it is pertinent to mention that an effective intersystem crossing is required for the phosphorescence emission channels to be activated, and the energy gap between the lowest singlet and lowest triplet states (ΔE_{ST}) can play a critical role in this regard, as the extent of an efficacious ISC process is inversely proportional to the ΔE_{ST} value. Interestingly, both the TPANMI and TPAPMI possess a reasonably small ΔE_{ST} value of 0.003 eV and 0.056 eV (**Figure 8**), respectively. Although in TPACNPMI, ΔE_{ST} is higher (0.534 eV) compared to other two luminogens, but due to presence of another triplet state T_2 having considerably lower energy gap (0.04 eV) with the S_1 state (**Figure 8**), the intersystem crossing process is also facilitated here. Notably, all the above discussions are

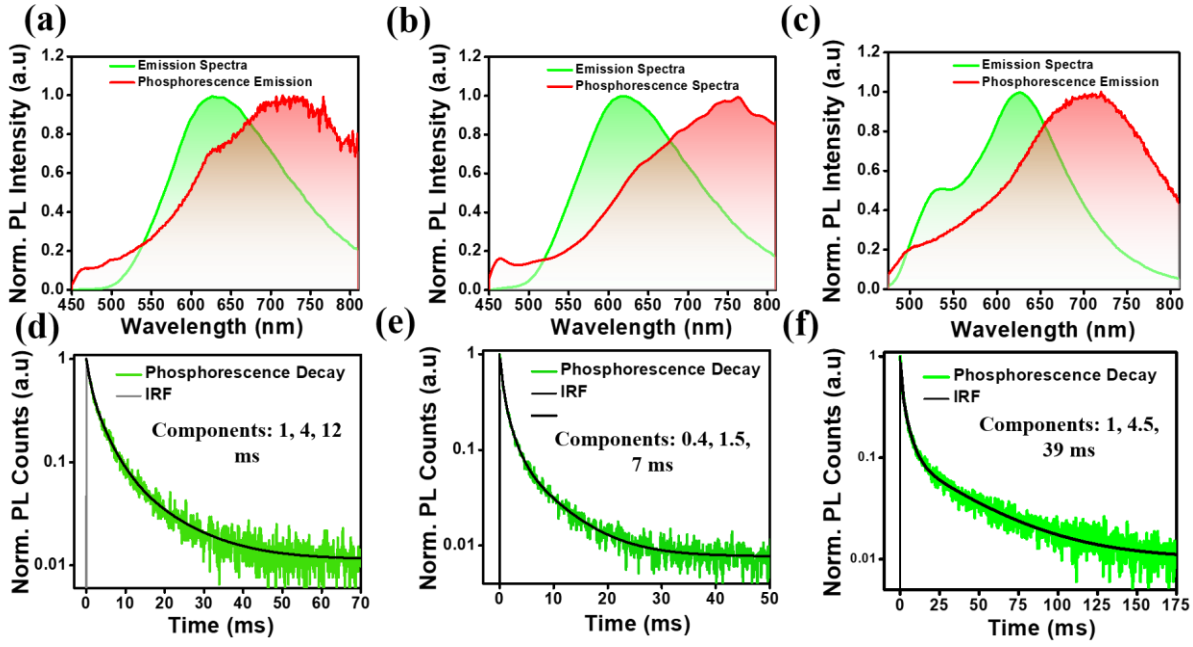

Figure 7: Emission spectra and phosphorescence spectra of (a) TPANMI, (b) TPAPMI and (c) TPACNPMI. Phosphorescence decay profile for (d) TPANMI (collected at 750 nm), (e) TPAPMI (collected at 750 nm) and (f) TPACNPMI (collected at 715 nm) collected using 100 µs lamp triggered delay.

based on the assumption that the ISC process is occurring through the lowest singlet, i.e., the S_1 state, even though it can be excited to higher singlet states. In another possible scenario, the ISC process also can take place via excited singlet states other than S_1. For example, in TPANMI, the S_2-S_1 gap is calculated to be 1.50 eV, and such a high energy gap can lead to a slow IC process, thus, increasing the probability of ISC involving higher excited singlet state, S_2.[46] Although, in this case, the first bright excited singlet state is S_3 (oscillator strength, f = 0.3205) but it possesses a reasonably lower energy gap of 0.03 eV with the S_2 state; therefore, the excitons can quickly relax to the S_2 state through IC. As the S_2-S_1 energy gap is high, the ISC process can even take place via S_2 state (**Figure 9**). Notably, here the S_2 state is energetically very close (within $\pm$0.3 eV) to numerous triplet states (T_5-T_{15}), and some of those states are having a high spin-orbit coupling matrix element (ξ) values (as high as 8.109) with the S_2 state (**Figure 9**), which facilitates the ISC process from the S_2 state. In TPAPMI, the energy gap between S_1 and S_2 is 0.98 eV, and the first bright state is S_2 (oscillator strength, f = 0.2155). As S_2 and S_1 share a large energy gap; thus, the ISC process can even occur from S_2 state to several triplet states (T_3-T_7) having considerable ξ values (**Figure 9**). On the contrary, in TPACNPMI, the S_2-S_1 energy gap is comparatively lower (0.34 eV); which eventually leads to a faster IC, and the ISC process is more likely to take place via the S_1 state.[46] All these theoretical studies suggest favorable and efficient ISC processes for all the three luminogens, and thereby lead to the emergence of efficient phosphorescence emission.

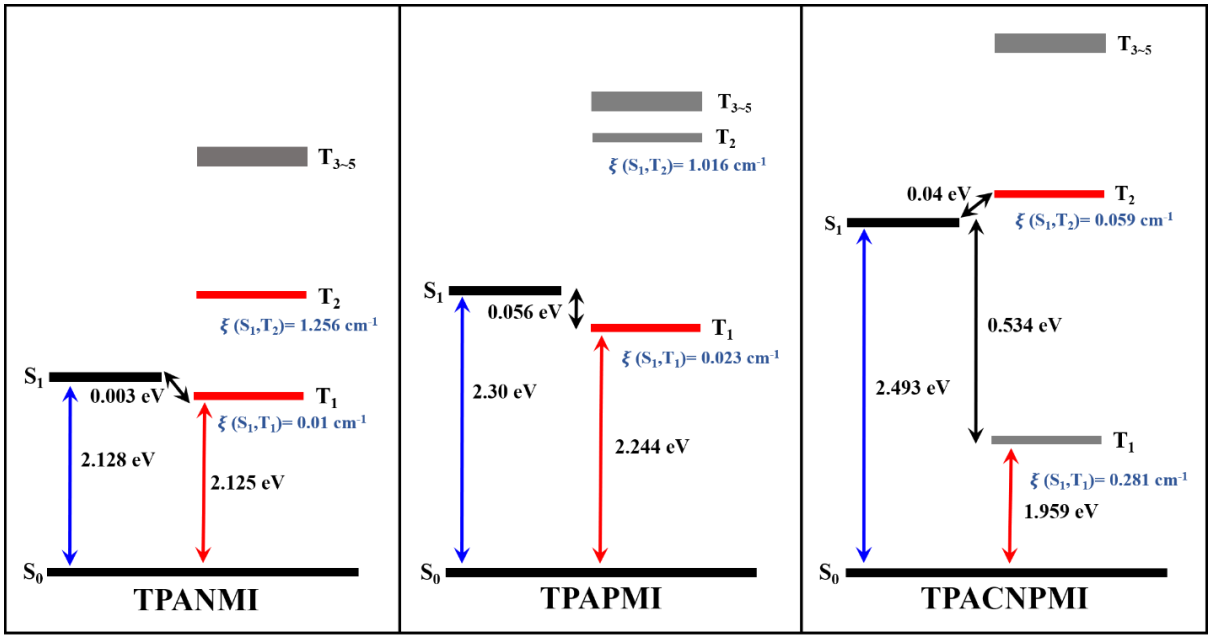

Figure 8: Energy level diagrams of TPANMI, TPAPMI and TPACNPMI for both singlet and triplet states (ξ indicates spin-orbit coupling matrix element).

Short intermolecular contacts provide a constrained environment, which restricts the motion of several bond vibrations with higher energy (C-H stretching may possess energy of ~ 0.37 eV in aromatic molecules), thereby reducing the extent of non-radiative deactivation.[35,47] Thus, non-covalent interactions play an important role to dictate the room temperature phosphorescence (RTP) characteristics of luminogens.

To gain a better insight, crystal structures of TPANMI, TPAPMI and TPACNPMI were analyzed. All these AIE active luminogens have several non-covalent interactions with reasonably short distances in their crystalline phase, such as, C-H···π (2.7-2.8Å), C-H···O (2.69Å) in case of TPANMI, and similarly, C-H···π (2.8Å), C-H···O (2.63Å) in case of TPAPMI (**Figure 10**). Interestingly, due to the incorporation of an additional cyano-ethylene group in TPACNPMI, additional C-H···N (2.68Å) interactions were observed along with C-H···π (2.8Å) and C-H···O (2.65Å) interactions (**Figure 10**). In order to quantitatively evaluate each type of non-covalent interactions, Hirshfeld surface analysis was performed (**Section A4 in Appendix**). The specific contributions of several non-covalent interactions were calculated and summarized in **Figure 11**. It was observed that, van der Waals (H···H) interactions occupy

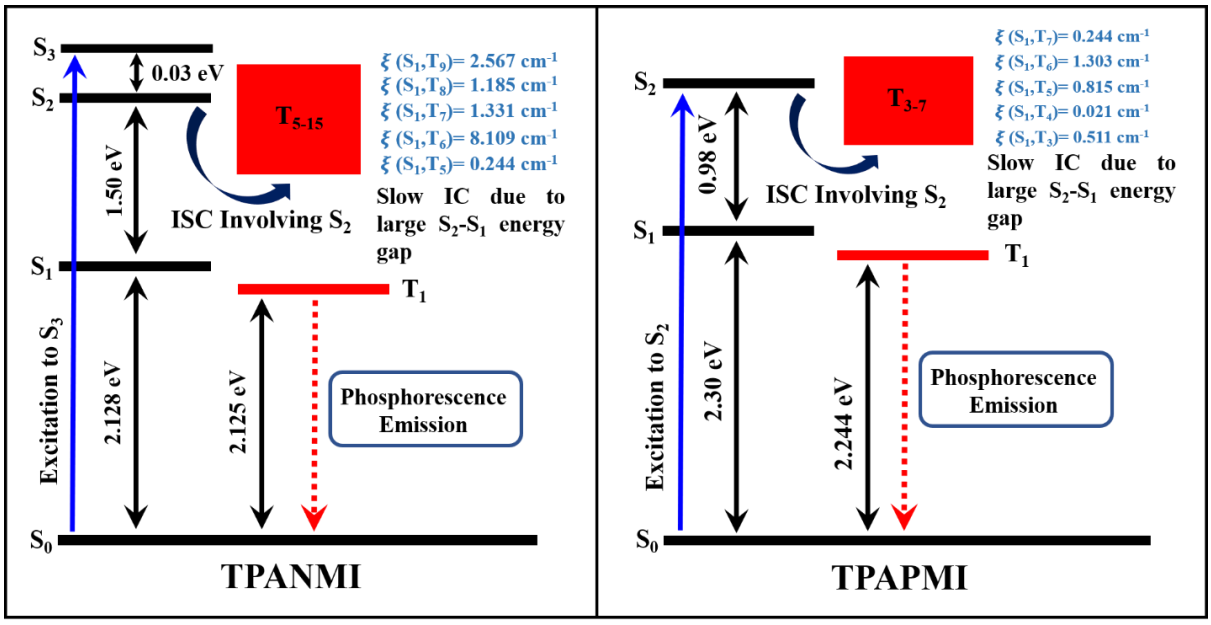

Figure 9: Energy level diagrams of TPANMI and TPAPMI for both the singlet and triplet states in case of a slow internal conversion (IC) rate (ξ indicates spin-orbit coupling matrix element).

a significant portion (**Figure 11, Figure A9 in Appendix**); even though the enthalpy of stabilization of such interactions are reasonably poor (~ 0.4-4 kJ/mol). Significant contributions of C-H···π (~ 10.3 kJ/mol)[48] and C-H···O interactions (usually~ 41-104 kJ/mol)[49] account for

higher enthalpy of stabilization leading to the formation of firmly packed molecular networks. Additionally, the percentage of C-H···N interactions (5.2%) were found to be increased in TPACNPMI due to the presence of additional cyano-ethylene moiety (**Figure 11, Figure A9 in Appendix**). Notably, the contribution of the π···π (C···C) interactions are relatively smaller compared to other interactions in all these three AIE luminogens. However, maximum contributions of π…π interactions (5.6 %) were found in the case of TPANDI (**Figure A10 in Appendix**), which is accountable for its ACQ properties, as we discussed in the earlier section.

2.7.4 Temperature dependent emission properties

AIE luminogens exhibiting emission-switch upon decreasing the temperature have potential scope of applications in the fabrication of low-temperature thermal sensors.[50] Most of the common organic luminogens exhibit enhanced emission at cryogenic temperatures due to suppression in non-radiative decay pathways at lower temperatures; but only a few of them can switch their emission color and can exhibit low-temperature thermochromic properties. In

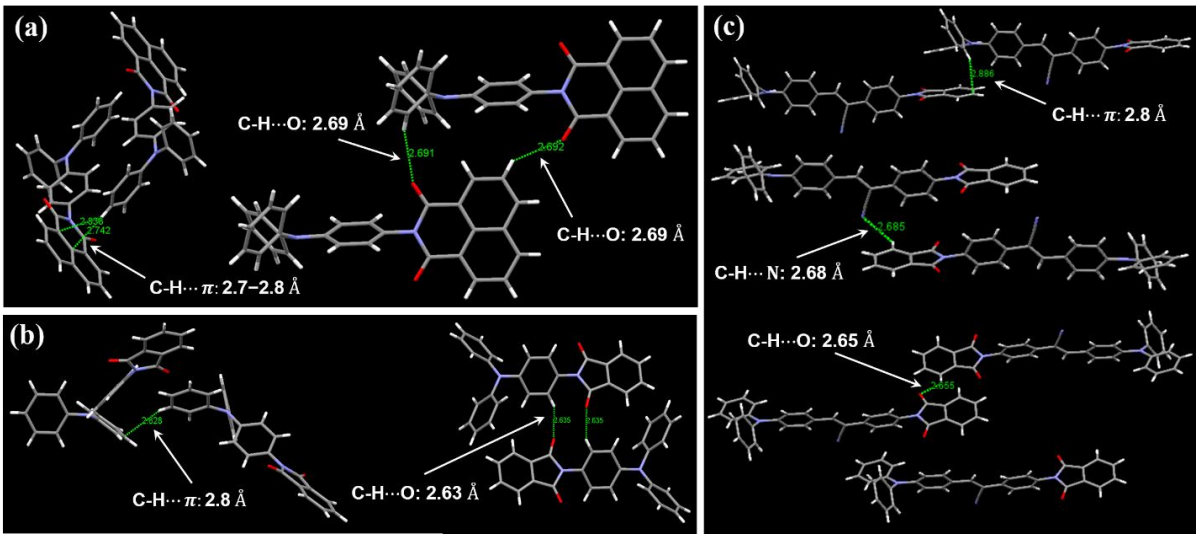

Figure 10: Presence of several short contact non-covalent interactions in the crystals of (a) TPANMI, (b) TPAPMI and (c) TPACNPMI.

order to investigate the cryogenic emissive behavior, low-temperature photoluminescence studies were carried out for all the AIE active luminogens. It was observed that, TPANMI and TPAPMI exhibited a gradually enhanced emission in the crystalline phase, upon lowering the temperature from room temperature (295 K) to 25 K, without any considerable emission switch (**Figure 12**). Surprisingly, a totally opposite scenario appears in the case of TPACNPMI. As already mentioned earlier, at room temperature (295 K), the orange-emissive crystals of

TPACNPMI have two emission peaks at ~ 535 nm and ~ 635 nm. Upon decreasing the

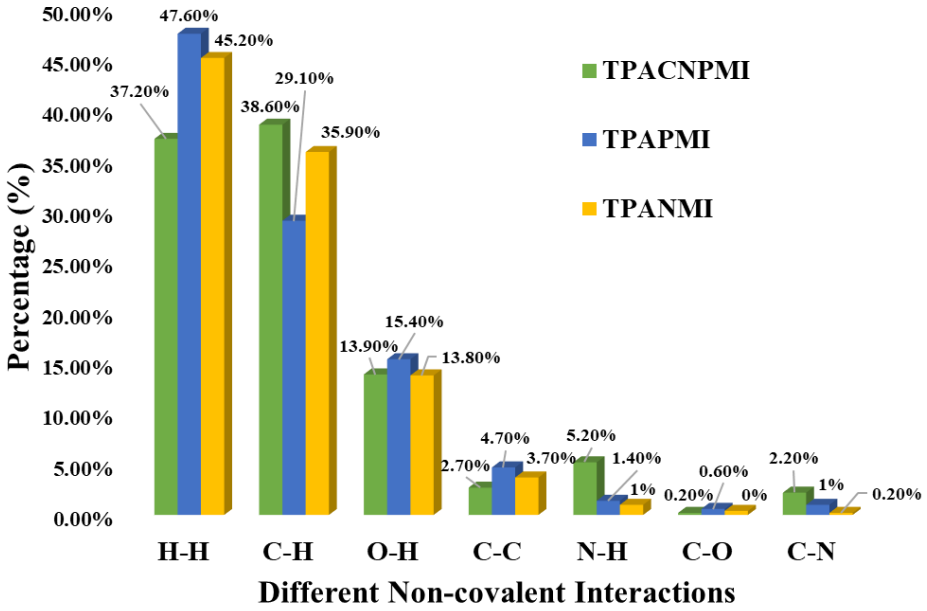

Figure 11: Histogram summarizing the contribution of different non-covalent interactions obtained from 2-D fingerprint plots in Hirshfeld Surface analysis.

temperature, both the peaks became gradually enhanced due to sequential decrease in the number of non-radiative decay channels. However, the extent of increment for the ~ 535 nm peak was higher compared to that of ~ 635 nm peak upon decreasing the temperature (**Figure 12**). As a result, a distinct emission color switching from orange to greenish-yellow was observed at cryogenic temperatures, suggesting the presence of low-temperature thermochromic property in TPACNPMI.

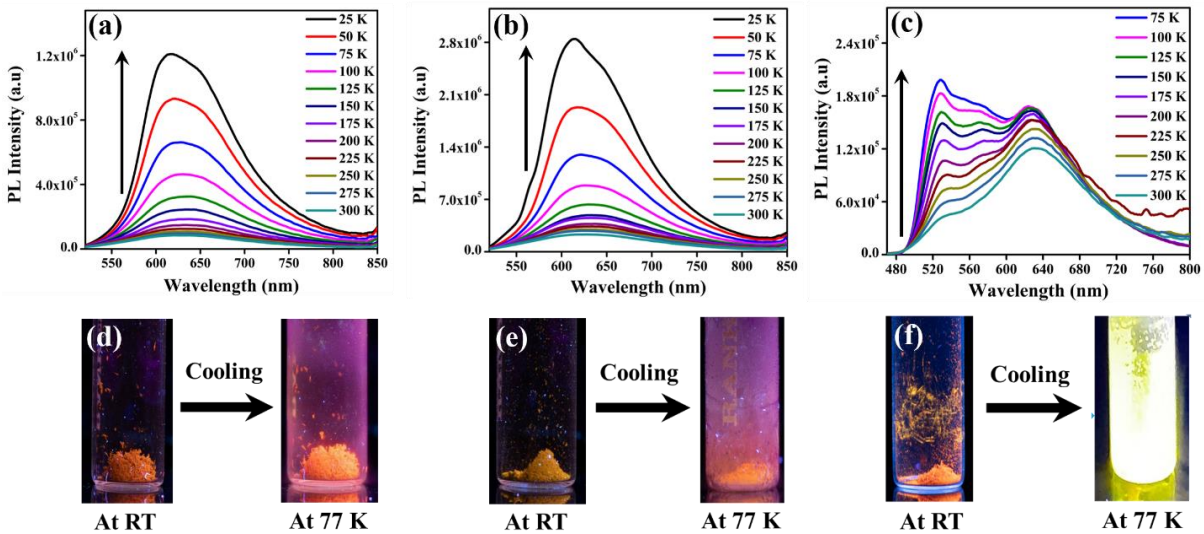

Figure 12: Temperature-dependent photoluminescence spectra of (a) TPANMI, (b) TPAPMI and (c) TPACNPMI. Enhanced emission of (d) TPANMI, (e) TPAPMI in the crystalline phase under UV lamp (365 nm) at room temperature (RT, 295 K) and at 77 K. Emission switch of (f) TPACNPMI in the crystalline state under UV lamp (365 nm) at RT (295 K) and at 77 K.

2.7.5 Mechanochromic study

Solid state emissive properties of TPANMI, TPAPMI and TPACNPMI should largely depend upon their molecular arrangements in crystalline phase owing to flexible nature of the molecules and the presence of several non-covalent interactions. Perturbing a particular arrangement by applying external mechanical stimuli and heat may lead to distinct alteration in photoluminescence properties and excited state processes in the bulk crystal. TPANMI crystals exhibit a broad emission spectrum with an emission maxima lying at ~ 625 nm. Even after vigorous grinding with a mortar and pestle (by maximum manual force) only a slight blue shift along with a ~ 15 nm reduction of FWHM was observed (**Figure 14**). In the case of TPAPMI also, no apparent luminescence color change was observed upon grinding the orange

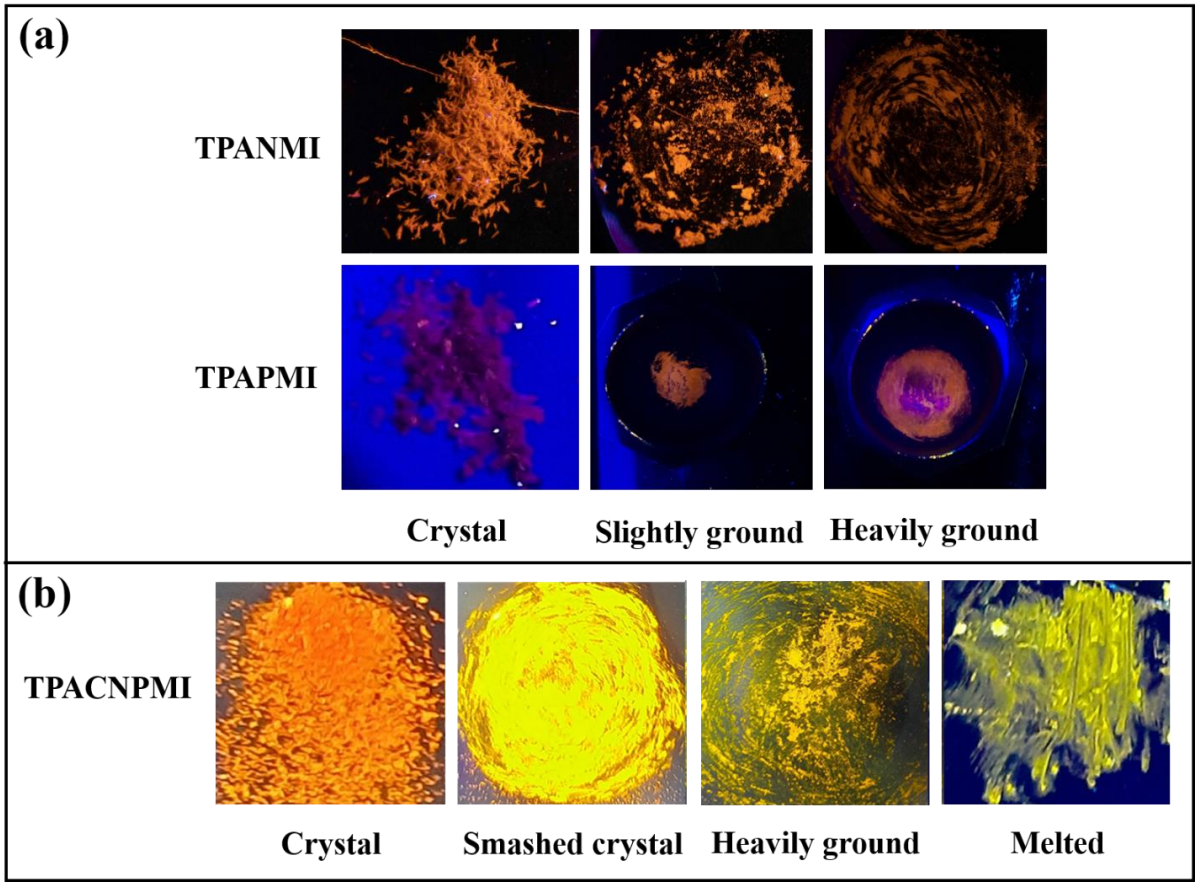

Figure 13: (a) Crystals of TPANMI and TPAPMI under different extents of mechanical stimuli. (b) Crystals of TPACNPMI upon different extents of mechanical stimuli and in the melted condition. All the images have been collected by exciting with a 365 nm UV lamp.

emitting crystals (**Figure 13**), with the emission maxima situated at ~612 nm (**Figure 14**). However, the emissive behavior of TPACNPMI was found to be quite different. The micro-crystals of TPACNPMI exhibits orange emission with an emission maximum locating at ~ 615 nm. Interestingly, upon smashing the crystals by applying a moderate manual force with mortar and pestle, a ~ 45 nm blue shift (**Figure 14**) in the emission maxima was observed with a luminescence color switching from orange to yellowish orange (emission maxima at ~ 570 nm). It further experienced a blue shift of ~ 30 nm upon heavy grinding (**Figure 14**) and exhibited a greenish-yellow emission (maximum at ~ 540 nm) (**Figure 13**). Interestingly, upon melting the compound (TPACNPMI), a green emissive melt was obtained with the emission maxima situated at ~ 527 nm (**Figure 14**), suggesting a meltochromic behavior of the luminogen. As TPACNPMI is responsive towards both pressure and temperature, it can be designated as a representative 'stimuli-responsive' luminogen; whereas, such distinct luminescence color change was absent in other two luminogens, and therefore, they (TPANMI and TPAPMI) can be treated as 'stimuli-inactive' luminogens. Such easy and prompt tri-color emission tuning properties of TPACNPMI with occurrence of orange, yellowish orange and greenish yellow emission are still rare in the family of stimuli-responsive luminogens.

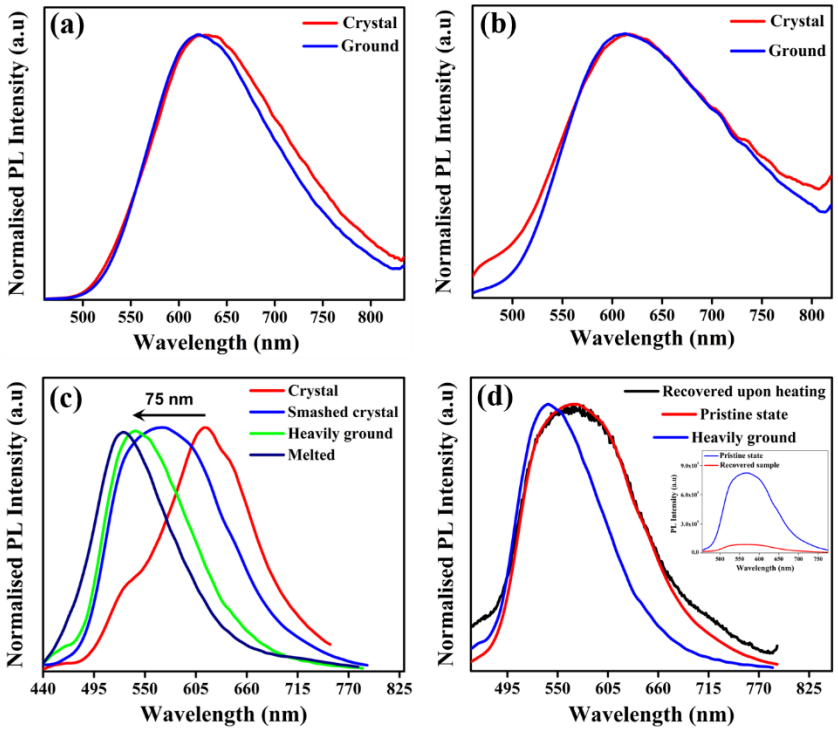

Figure 14: Emission spectra of crystals under different extents of mechanical stimuli in (a) TPANMI (b) TPAPMI. Emission spectra of (c) TPACNPMI crystals under different extents of mechanical stimuli and melting and (d) its reversibility from a heavily ground state to pristine state upon heating.

Majorly, three factors are responsible for a luminogen to exhibit mechanochromic activity, i.e., flexibility, a twisted donor-acceptor based structure and presence of multiple non-covalent interactions.[8] For CT type luminogens in crystalline phase, mechanical grinding may lead to alteration in dihedral angle between the donor and the acceptor moieties due to the presence of sufficient flexibility and twisting characteristics in their molecular skeleton. This alteration in the dihedral angle can eventually lead to a modulation in the extent of orbital overlap between the donor and the acceptor moieties, and may give rise to a considerable shift in emission band. Notably, in all our designed luminogens, presence of propeller shaped triphenylamine provides enough flexibility and twisting.

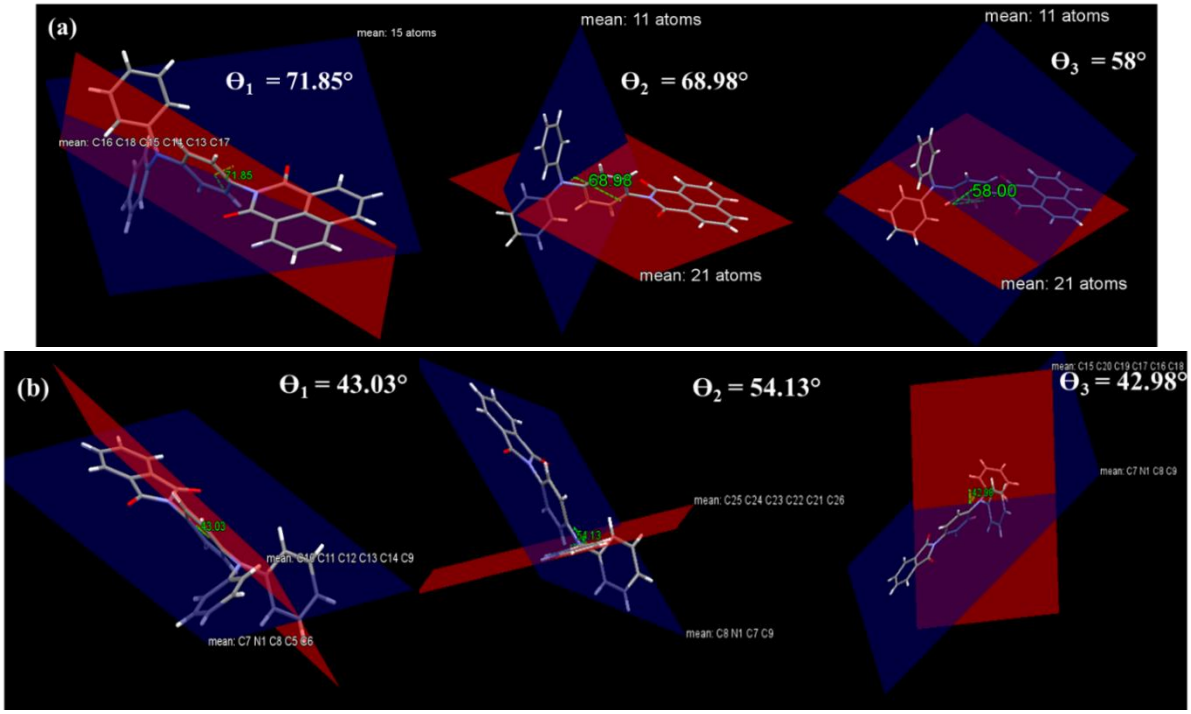

Figure 15: Twisting angles of the phenyl groups of triphenylamine moiety with the planar acceptor core in (a) TPANMI and (b) TPAPMI.

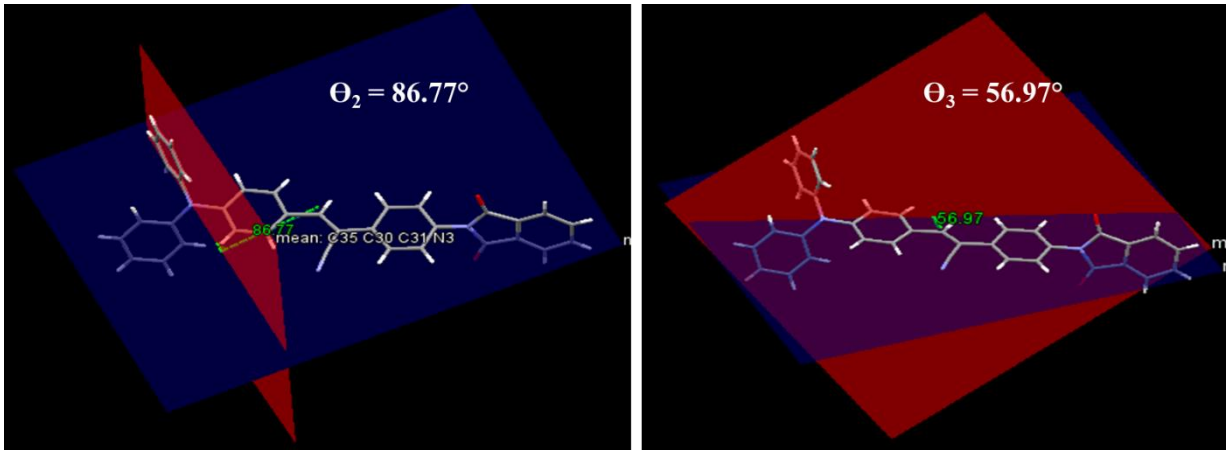

Figure 16: Twisting angles of the terminal phenyl groups of triphenylamine moiety with the nearly planar middle part in TPACNPMI. In each case, two planes have been drawn, one containing the terminal phenyl ring under consideration and the other containing the junctional phenyl group of triphenylamine moiety, the cyano-ethylene group and the benzene linker.

In TPANMI, the three phenyl groups of donor TPA make dihedral angles of 71.85° (Θ_1), 68.98° (Θ_2) and 58° (Θ_3), respectively, with the planar acceptor NMI which shows a twisted nature of the donor moiety (**Figure 15a**). In TPAPMI, similar twisted behavior is observed with a relatively smaller dihedral angles (Θ_1 = 43°, Θ_2 = 54.13° and Θ_3 = 43°) due to a smaller size of phthalimide acceptor core (**Figure 15b**). In TPACNPMI also, the junctional phenyl group of TPA (adjacent to the cyano-ethylene moiety) makes large dihedral angles with the other two terminal phenyl groups (Θ_2 = 86.77° and Θ_3 = 57°) (**Figure 16**). Moreover, the junctional phenyl group of TPA moiety lies almost planar with the plane containing cyano-ethylene group and benzene linker with a quite small angle of 1.9° (**Figure A11 in Appendix**). Notably, this type of planar conformation might lead to an electronic structure having larger overlap between donor and acceptor orbitals generating a more stabilized CT state with red-shifted emission. However, upon mechanical grinding, a blue shifted emission of TPACNPMI is observed, suggesting formation of a more twisted configuration where the extent of overlap between donor-acceptor orbitals is relatively lesser.[51] Moreover, the benzene linker in TPACNPMI provides an additional dihedral angle (69.59°) with the terminal planar phthalimide moiety (**Figure A12 in Appendix**); presence of such additional dihedral angles is responsible for gaining extra flexibility and can be beneficial for deriving mechanochromic properties. Therefore, the incorporation of cyano-ethylene group along with the benzene linker can contribute additional flexibility in the molecular skeleton, and further, the presence of a planar central part opens up the possibilities of forming a twisted conformation under mechanical grinding, which together lead to the observed mechanochromism in TPACNPMI. Another

factor that can bring about mechanochromic activity in a luminogen is the presence of several non-covalent interactions. Generally, a greater contribution of C-H···π interaction along with a meagre π···π interaction (a higher ratio of C-H···π to π···π interaction) are highly desirable due to a higher enthalpy of stabilization of C-H···π interaction (~ 10.3 kJ/mol).[8] Higher extent of π···π interaction can lead to a higher chance of planarity and exciton-phonon coupling in the bulk crystal,[52] which often give rise to a quenched emission with a less emission contrast, and these are detrimental for observing mechanochromism. Notably, among all these luminogens, TPACNPMI crystal has a maximum contribution of C-H···π interaction (38.60%) and a minimum contribution of π···π interaction (only 2.70%) (**Figure 11**), giving rise to a maximum ratio of C-H···π interaction to π···π interaction, i.e., 14.29, which in case of TPANMI and TPAPMI are 9.70 and 6.19, respectively. Furthermore, in TPACNPMI, an additional C-N···H interaction contribution of 5.20% is obtained due to the presence of cyano-ethylene moiety (**Figure 11**). All these factors are combinedly believed to be responsible for the observed mechano-active behavior of TPACNPMI.

The foremost importance of any mechanochromic luminogen is its ability of reversing back to its original pristine state. Intriguingly, under the naked eye it was observed that the heavily ground powder of TPACNPMI (with greenish yellow emission emerging at ~ 540 nm) transformed to the initial pristine state (with yellowish orange emission located at ~ 570 nm) under thermal annealing with a diminished emission intensity (**Figure 14d**). After recovery, the measured emission spectra exactly match the emission profile of the pristine powder, which further validates our claim.

PXRD experiment was also carried out to get insight into the details of the observed mechanochromic behavior. Crystals of TPACNPMI exhibit sharp and intense reflection peaks suggesting a well-ordered microcrystalline structure (**Figure A13 in Appendix**). With slight grinding of those crystals, a decrease in the intensity of those peaks along with the disappearance of some reflection peaks was observed (**Figure A11 in Appendix**). Notably, further heavy grinding leads to the emergence of a diffused or broad halo band (with the reduced intensity of reflection peaks) (**Figure A11 in Appendix**), which suggests a modulation of crystallinity in TPACNPMI and its transformation to an amorphous state. Similarly, in TPANMI and TPAPMI, the crystals exhibited sharp and intense reflection peaks indicative of the crystallinity of those compounds; but upon mechanical grinding, the diffraction peaks attenuate or even disappear with the appearance of a broad halo (**Figure A11 in Appendix**), indicating towards a amorphous nature of the ground powder. Although, TPANMI and

TPAPMI did not exhibit a distinct emission shift upon mechanical grinding, which indicates such phase transition leads to the formation of a state, which is energetically very similar to that of the crystalline state and is responsible for its mechano-inactive behavior.

2.8 Applications:

2.8.1 Photoluminescence thermometer:

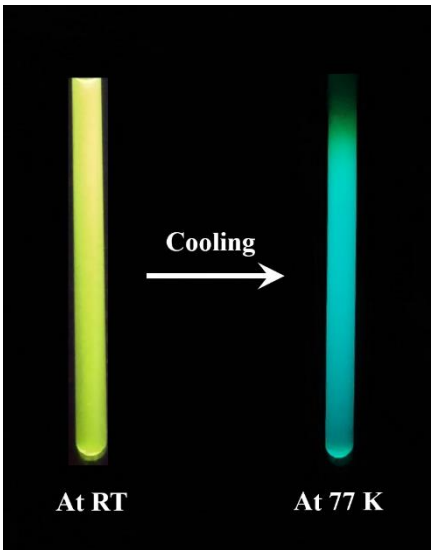

Figure 17: Distinct emission switch of TPACNPMI in glass-freezing mixture (methanol : ethanol = 4 : 1) upon cooling from room temperature (295 K) to cryogenic temperature (77 K).

Conventional thermometers cannot be used in marine research, underground research, tunnels, automobile and aircraft industries.[53,54] Thus, photoluminescence-based thermometers have recently drawn considerable attention due to their prompt response and good spatial resolution.[53,55] Among all of our designed luminogens, TPACNPMI seems to be a promising candidate for luminescence-based thermometer, as it exhibits a well-distinct emission switching from greenish yellow to cyan-green emission upon cooling the solution containing TPACNPMI in glass forming alcoholic mixture (methanol and ethanol are taken in 4:1 ratio) from 295 K to 77 K (**Figure 17**). However, the other two luminogens (TPANMI and TPAPMI) are not useful in this regard, as they are non-emissive both in RT (295 K) and at 77 K due to higher stabilization of the CT state in such a polar medium.

2.8.2 Two-photon cell imaging:

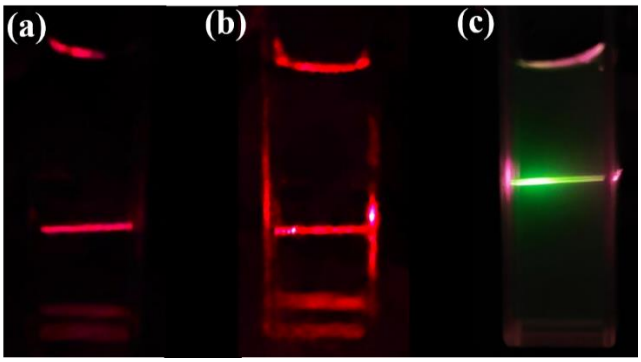

Figure 18: (a) A laser beam of 800 nm focused on a solution of TPANMI in 5% DMSO/water (10 μM) and no fluorescence was observed. (b) A laser beam of 800 nm focused on a solution of TPAPMI in 5% DMSO/water (10 μM) and no fluorescence was observed. (c) A laser beam of 800 nm focused on a solution of TPACNNMI in 5% DMSO/water (10 μM) and a clear green fluorescence was observed.

Two-photon cell imaging has emerged as a powerful tool and has unmatched advantages over the conventional one-photon imaging due to minimal photo-damaging, capability of deep tissue penetration and excellent resolution.[56–58] In this context, aggregation induced emissive organic luminogens (AIEgens) have emerged as an excellent class of compounds for two-photon bio-imaging owing to their high emissivity in the aggregated state and minimum photo-bleaching effect.[59] Among all of our AIE active luminogens, intriguingly, TPACNPMI exhibits two-photon absorption properties (two photon absorption cross-section was found to be ~ 510 GM at 845 nm excitation wavelength, see **section A7 in Appendix** for details) (**Figure 18**). Thus, we have performed two-photon imaging experiments using TPACNPMI. From the two-photon image, it is evident that our luminogen is well capable of lighting up cells, largely the cytoplasm part (**Figure 19**). In order to look into the cytotoxic behavior of our luminogen, MTT viability assay of MCF7 cells was carried out. No significant decrease in viability was observed in samples incubated with up to 15 μM TPACNPMI (**Figure A14 in Appendix**), which indicates that TPACNPMI does not exhibit toxic effect towards the cell upto that concentration.

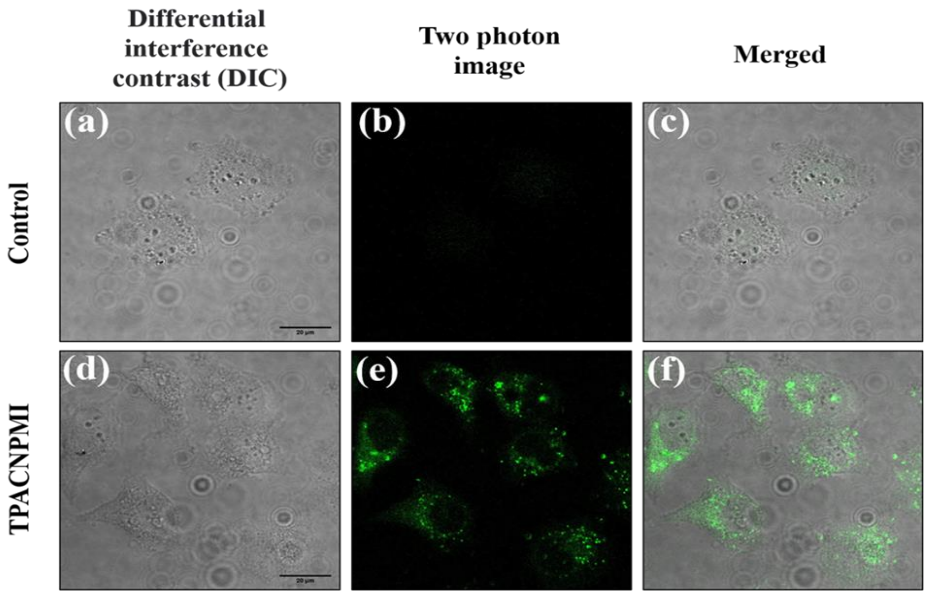

Figure 19: Two-photon microscopy image (excitation wavelength = 800 nm, collection window is from 550 nm to 620 nm) of MCF-7 cells: top row- without the treatment of dye and bottom row -with treatment of 10 µM TPACNPMI. (a and d) differential interference contrast (DIC) images, (b) cells without dye treatment, (e) cells treated with dye (TPACNPMI) and (c and f) DIC image merged with dye image.

2.9 Conclusion:

In summary, this research article focuses on designing novel multi-functional luminogens exhibiting simultaneous AIE, RTP and mechanochromic behavior by systematic molecular engineering. This journey starts from an ACQ phore, TPANDI. The longer and larger acceptor core in TPANDI makes it non-emissive in the aggregated state due to an effective π-π stacking interaction in between planar naphthalene diimide moieties. Interestingly, a simple structural change in acceptor core from naphthalene diimide to naphthalene monoimide and phthalimide can effectively inhibit the π-π stacking interaction in the condensed state, and can bring about ACQ to AIE type transformation in TPANMI and TPAPMI. Moreover, the presence of closely spaced singlet and triplet states in all these AIE active luminogens can facilitate the intersystem crossing (ISC) process, and consequently bring about room-temperature phosphorescence phenomenon. Although these two luminogens exhibit simultaneous AIE and RTP properties, they are mechanically inactive, and therefore, it requires further structural engineering to obtain simultaneous AIE, RTP and mechanochromism. Finally, it has been demonstrated that an introduction of a cyano-ethylene group along with a benzene linker in between the donor triphenylamine and acceptor phthalimide moieties can bring about easy and distinct

mechanochromic behavior (along with AIE and RTP properties) in the final molecule i.e. TPACNPMI. Thus, starting from a molecule with ACQ nature, upon minimal and systematic modification of molecular structure, a multi-functional luminogen with AIE, RTP along with easy and distinct mechanochromic properties were obtained.

2.10 Appendix

Section A1) Detailed synthetic procedure of (1) TPANDI, (2) TPANMI and (3) TPAPMI:

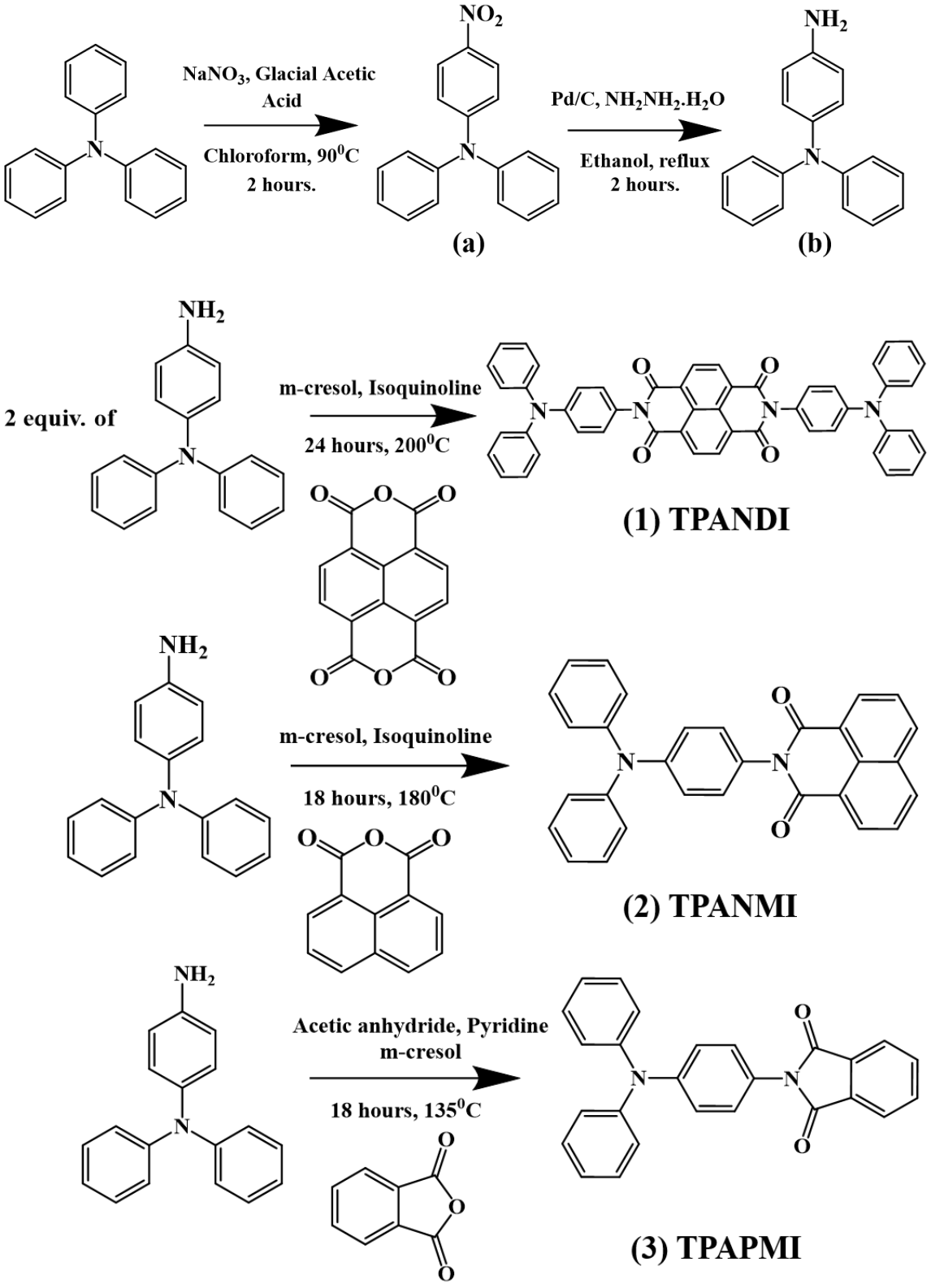

Scheme S1: Synthetic route for the synthesis of (1) TPANDI, (2) TPANMI and (3) TPAPMI.

The synthetic route of TPANDI, TPANMI and TPAPMI along with all the intermediate steps are outlined in Scheme S1. The final products are obtained in three steps, which are discussed here.

Synthesis of (a) $TPANO_2$: $TPANO_2$ and $TPANH_2$ were synthesized according to the reported procedure.[60] Commercially available triphenylamine (~500 mg, ~2 mmol) was taken in a reflux equipment. A mixture of glacial acetic acid (18 ml) and chloroform (6 ml) was added to the RB flask and stirred well. Finally, $NaNO_3$ (171.6 mg, 2.02 mmol) was added to the reaction mixture and stirred at 90^0 C for 2 hours. After 2 hours, the reaction was over and it was verified by TLC. Then the RB flask was cooled to room temperature. The reaction mixture was diluted with 50 ml of water and the organic layer was extracted with 50 ml of dichloromethane (DCM). The organic layer was further washed with 5% aqueous $NaHCO_3$ (to remove the unreacted acid), brine solution (~50 ml) and collected with filtration through anhydrous Na_2SO_4 to remove water. Solvent was removed from the organic layer under reduced pressure and a crude oily compound was obtained. Finally, the compound was obtained as orange crystals from a 1:1 ethanol & water mixture and characterized by ^1H NMR, ^{13}C NMR, HRMS mass spectrometry.

Synthesis of (b) $TPANH_2$: In a reflux equipment, (a) $TPANO_2$ (~600 mg, ~2 mmol) was dissolved in 20 ml anhydrous ethanol. After that, 10% Pd/C (~29.7 mg) was added to the reaction mixture as a catalyst. The reaction mixture was heated to reflux temperature and stirred for 15 minutes. After that, hydrazine monohydrate (12.4 ml) was added dropwise to the hot solution. Finally, it was refluxed for 2 more hours. The progress of the reaction was clearly visible by the change of the colour of reaction mixture from yellow to colourless. After 2 hours, the hot reaction mixture was filtered over celite pad washing several times with DCM. The

filtrate was collected and dried over anhydrous Na_2SO_4 to remove moisture. It was finally concentrated under reduced pressure and nice light pink crystals were obtained from a mixture of ethanol and water and characterized by ^{1}H NMR, ^{13}C NMR, HRMS mass spectrometry.

Synthesis of (1) TPANDI: TPANDI was synthesized according to a reported procedure.[61] In a 50 ml round-bottom flask fitted with an argon inlet, a Dean-Stark trap, and a reflux condenser, naphthalenetetracarboxylic dianhydride (NTDA) (~268 mg, ~1mmol), (b) $TPANH_2$ (~520 mg, 2mmol) and 2 ml of isoquinoline were dissolved in ~18 ml of m-cresol. The reaction was refluxed to 200^0C for 24 hours. Some amount of m-cresol was distilled off during the course of the reaction. After 24 hours, the RB flask was cooled to 100^0C. The reaction mixture then poured into methanol and kept undisturbed for 10-15 mins. Purple precipitate was observed inside the mixture. The precipitate was collected by filtration and washed several times with methanol. Unreacted NTDA was removed by washing the precipitation several times with 10% NaOH. Finally, it was dried under high vacuum for at least one hour. Purple coloured compound was obtained and characterised by ^{1}H NMR, ^{13}C NMR and MALDI-TOF mass spectrometry.

Synthesis of (2) TPANMI: TPANMI was synthesized according to a reported procedure.[61] 0.26 gm (1mmol) (b) TPA-NH_2 along with 0.21 gm (1.06 mmol) of 1,8-naphthalic anhydride were dissolved in 20 ml of m-cresol in a 50 ml RB flask. The mixture was vigorously stirred for 15 minutes and after that a few drops of isoquinoline were added. The reaction mixture was then stirred for 18 hours at 180°C. After 18 hours, the solution was allowed to cool for 10-15 minutes at room temperature and then poured slowly with stirring into 150 ml of methanol in a conical flask. The conical was kept untouched for next one hour and reddish orange crystals were obtained as the desired product. The crystals were then dried well under high vacuum and characterized by ^{1}H NMR, ^{13}C NMR, HRMS and single crystal X-ray diffraction.

Synthesis of (3) TPAPMI: 0.26 gm (1mmol) (b) TPA-NH_2 along with 0.15 gm (1 mmol) of phthalic anhydride were dissolved in 20 ml of m-cresol in a 50 ml RB flask. The mixture was vigorously stirred for 15 minutes and after that 2 ml of acetic anhydride and 1 ml of pyridine were added to the mixture. The reaction mixture was then stirred at 135°C for 18 hours. After that the solution was allowed to cool for another 15 minutes at room temperature and then poured slowly into 150 ml of methanol in a conical flask. The conical was kept aside for next 2-3 days and yellowish crystals were obtained as the desired product. The crystals then dried well under high vacuum and were characterized by ^{1}H NMR, ^{13}C NMR, HRMS and single crystal X-ray diffraction.

Section A2) Detailed synthetic procedure of (4) TPACNPMI:

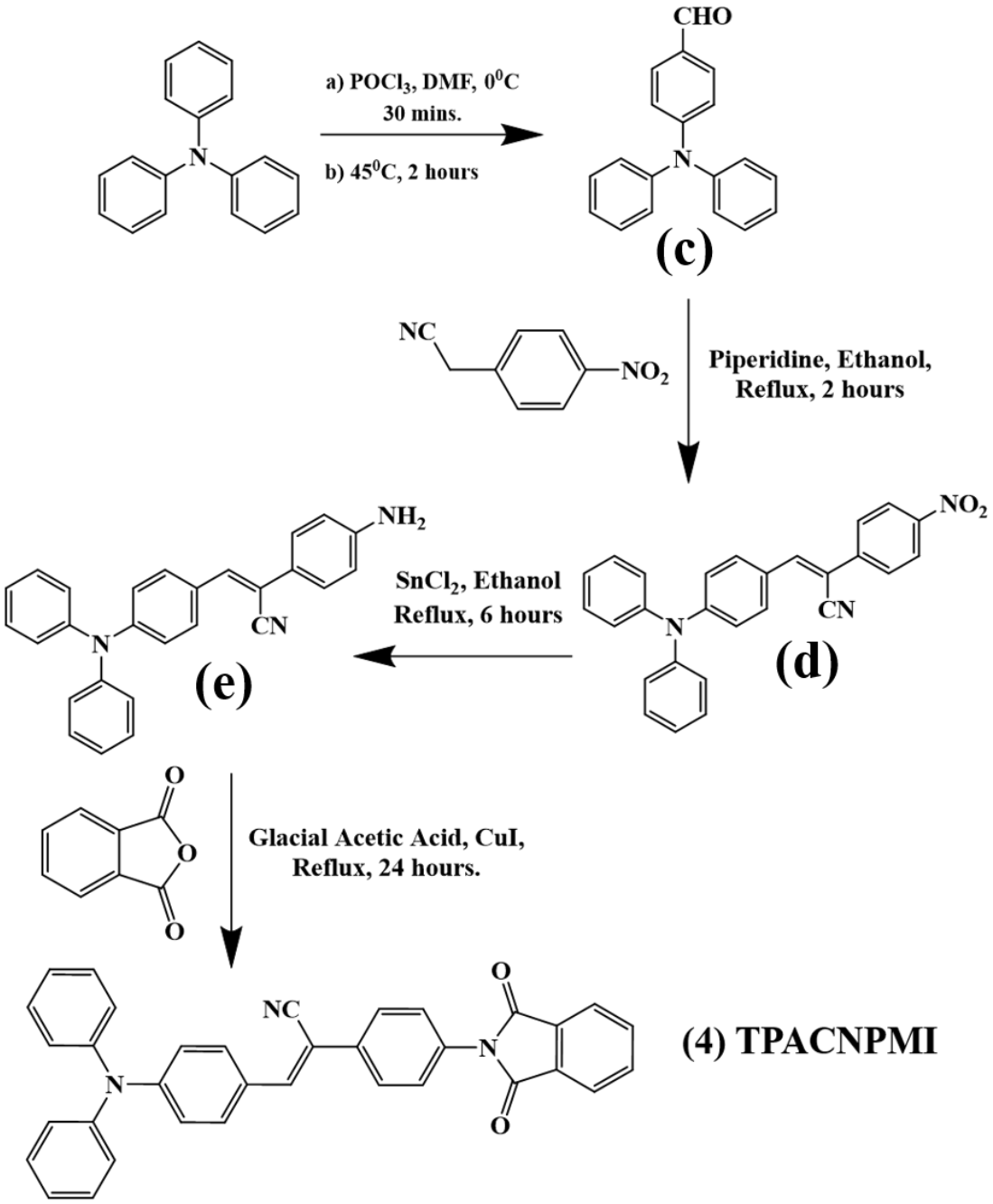

Scheme S2: Synthetic route for the synthesis of (4) TPACNPMI.

The synthetic route of TPACNPMI along with all the intermediate steps are outlined in Scheme S2. The final product is obtained in four steps, which are discussed here. We followed reported procedures for the synthesis of (c) TPACHO, (d) TPACNNO$_2$ and (e) TPACNNH$_2$.[62]

Synthesis of (c) TPACHO: In a one-necked flask, triphenylamine (4 gm, 16 mmol, 1 equiv.) was dissolved in dry DMF (17.8 ml) and the solution was cooled at 0°C with continuous stirring under argon atmosphere. After that, phosphoryl chloride (7.6 ml, 82 mmol, 5.13 equiv.) was slowly added to the reaction mixture and stirred for another 30 minutes at 0°C. The reaction mixture was then allowed to cool to room temperature and stirred for 1 hour, then for another 2 hours at 45°C under argon atmosphere. After completing this, the reaction mixture was poured into ice water and neutralized by slow addition of aq. NaOH solution. The residue was then dried and recrystallized with alcohol to give the desired compound and characterized by ^{1}H NMR, ^{13}C NMR, HRMS mass spectrometry. The compound was used in the next step without further purification.

Synthesis of (d) TPACNNO$_2$: In a 100 ml RB flask, TPACHO (0.273 gm, 1 mmol), 4-nitrophenylacetonitrile (0.194 gm, 1.2 mmol) were dissolved in 30 ml ethanol with refluxing. After that 1 ml of piperidine was added to the reaction mixture with appearance of red colour. The reaction was then continued for another 2 hours. The solution was then filtered and washed several times with ethanol. Finally, red coloured compound was obtained and characterized by ^{1}H NMR, ^{13}C NMR, HRMS mass spectrometry.

Synthesis of (e) TPACNNH$_2$: In a 100 ml RB flask, 0.147 gm of TPACNNO$_2$ (0.35 mmol) and stannous chloride (0.393 gm, 1.75 mmol) were dissolved in 30 ml of ethanol. Then, the reaction mixture was refluxed for 6 hours. After that a newly formed green fluorescent spot was observed on TLC plate without any existence of starting nitro product. The solution was then cooled and its pH was adjusted to 8.0 with saturated sodium bicarbonate. The product was extracted with DCM and purified further by SiO_2 flash column chromatography (pet ether and ethyl acetate solvent system). Finally, characterization was done using ^{1}H NMR, ^{13}C NMR and HRMS mass spectrometry studies.

Synthesis of (4) TPACNPMI: In a 50 ml RB flask, 774.98 mg (2 mmol) of the starting amine i.e. (e) TPACNNH$_2$ and 296.04 mg (2 mmol) of phthalic anhydride were dissolved in 20 ml of glacial acetic acid. The mixture was refluxed for 15 minutes, after that 40 mg of CuI was added and the reaction mixture was refluxed for another 24 hours. The completion of the reaction was confirmed by TLC, which also indicates a total conversion of the starting amine functionality. The solution was then cooled and divided into two parts- one half portion was kept aside for crystallisation and saturated aqueous NaHCO$_3$ solution was added drop wise to the other half for neutralisation. After the neutralisation being completed, the organic layer was collected with ethyl acetate and washed further with water and brine solution and collected with filtration through anhydrous Na$_2$SO$_4$ to remove excess water. The compound was further purified by SiO$_2$ flash column chromatography (pet ether and ethyl acetate solvent system), dried under high vacuum and characterized by ^{1}H NMR, ^{13}C NMR and HRMS mass spectrometry studies. Nice orange crystals were obtained from the other part (kept for crystallisation); collected, dried in high vacuum characterized by ^{1}H NMR, ^{13}C NMR and HRMS mass spectrometry and single crystal X-ray diffraction studies.

Section A3: Characterization Figures

^{1}H NMR data of **(1) TPANDI**

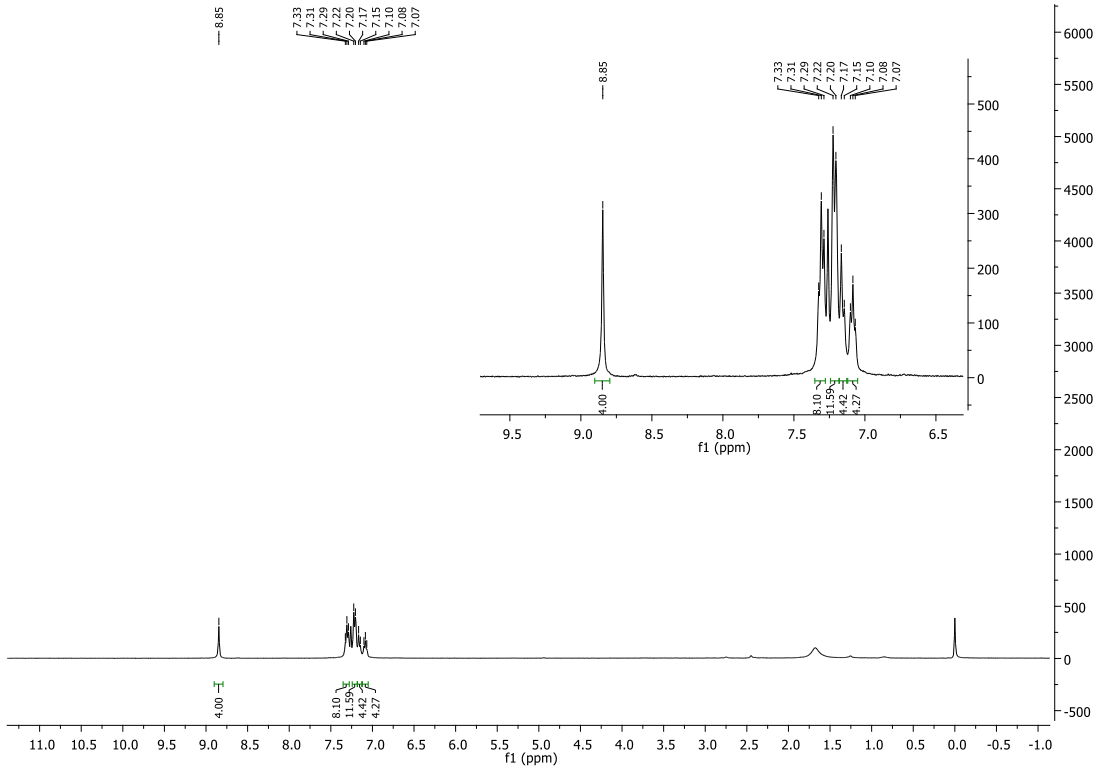

^{13}C NMR data of **(1) TPANDI**

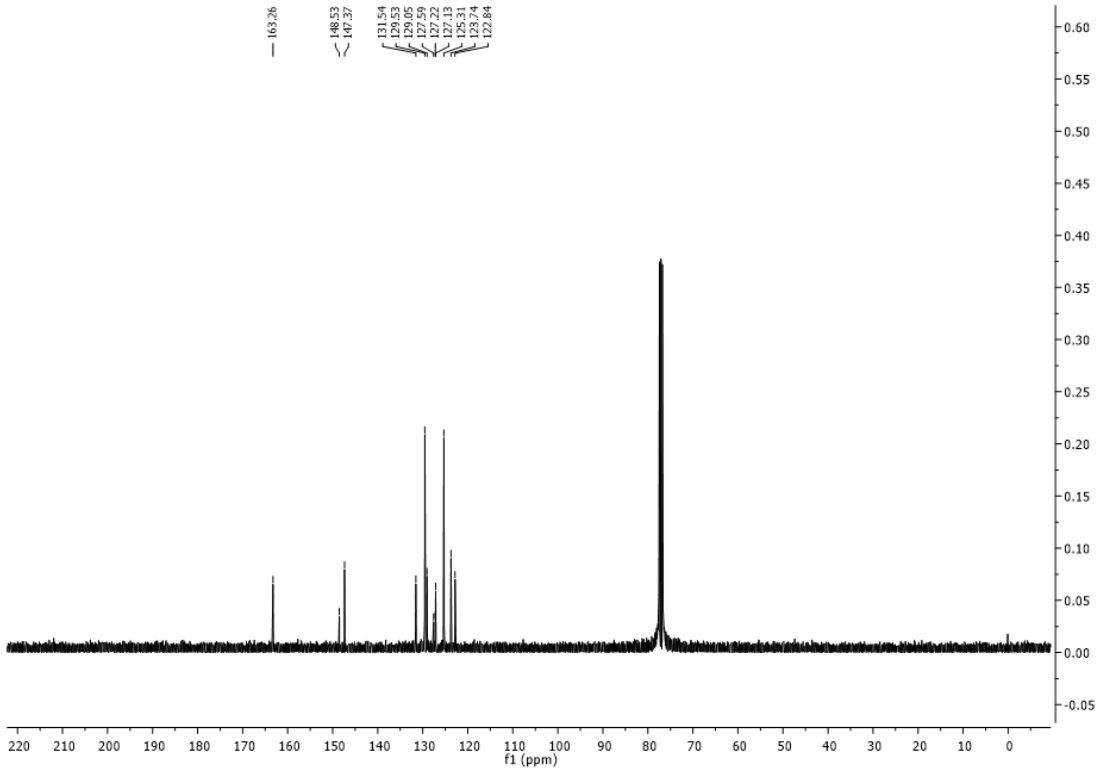

MALDI (TOF) data of **(1) TPANDI**

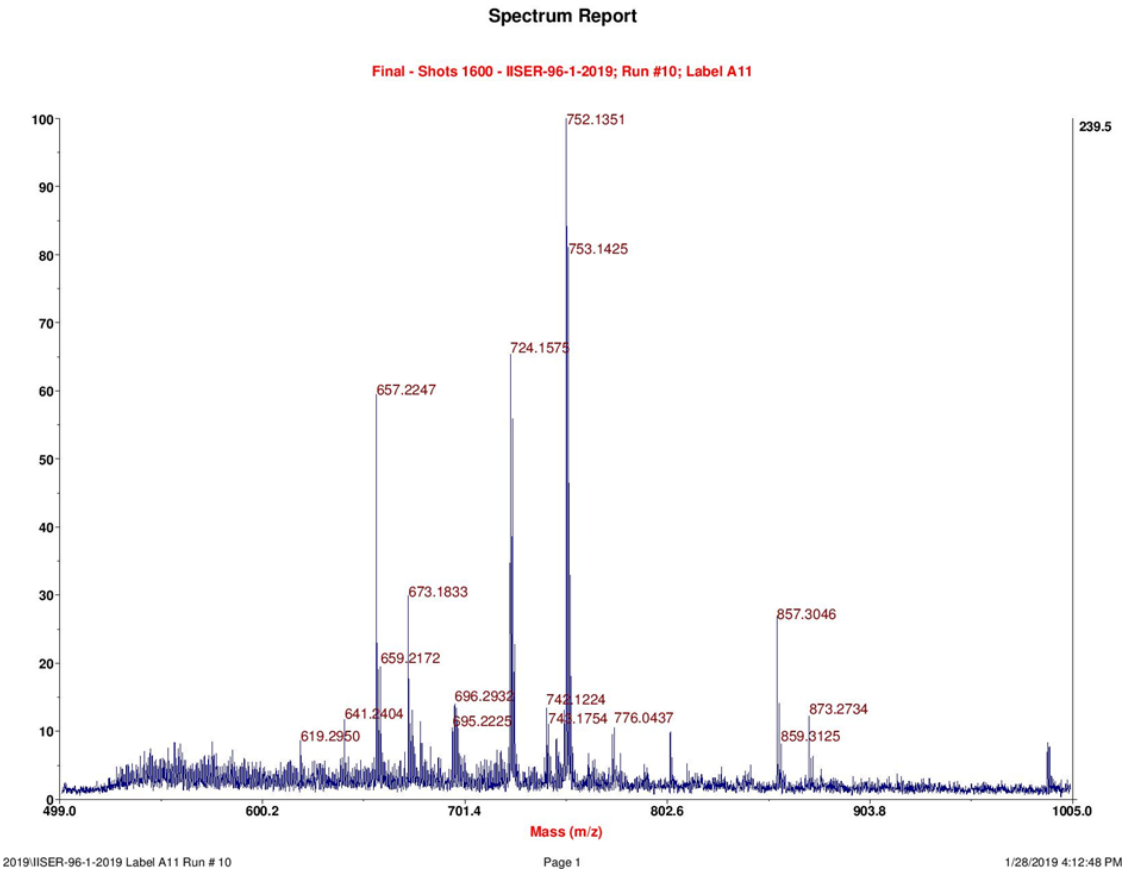

^{1}H NMR data of **(2) TPANMI**

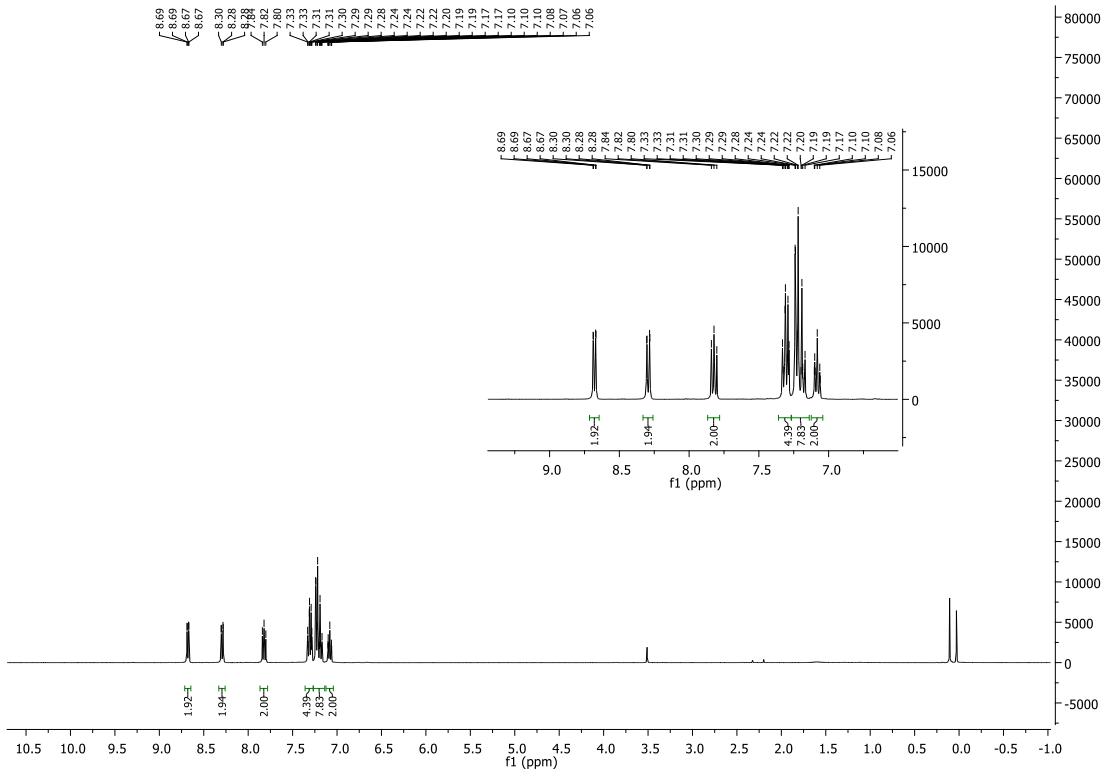

^{13}C NMR data of (2) **TPANMI**

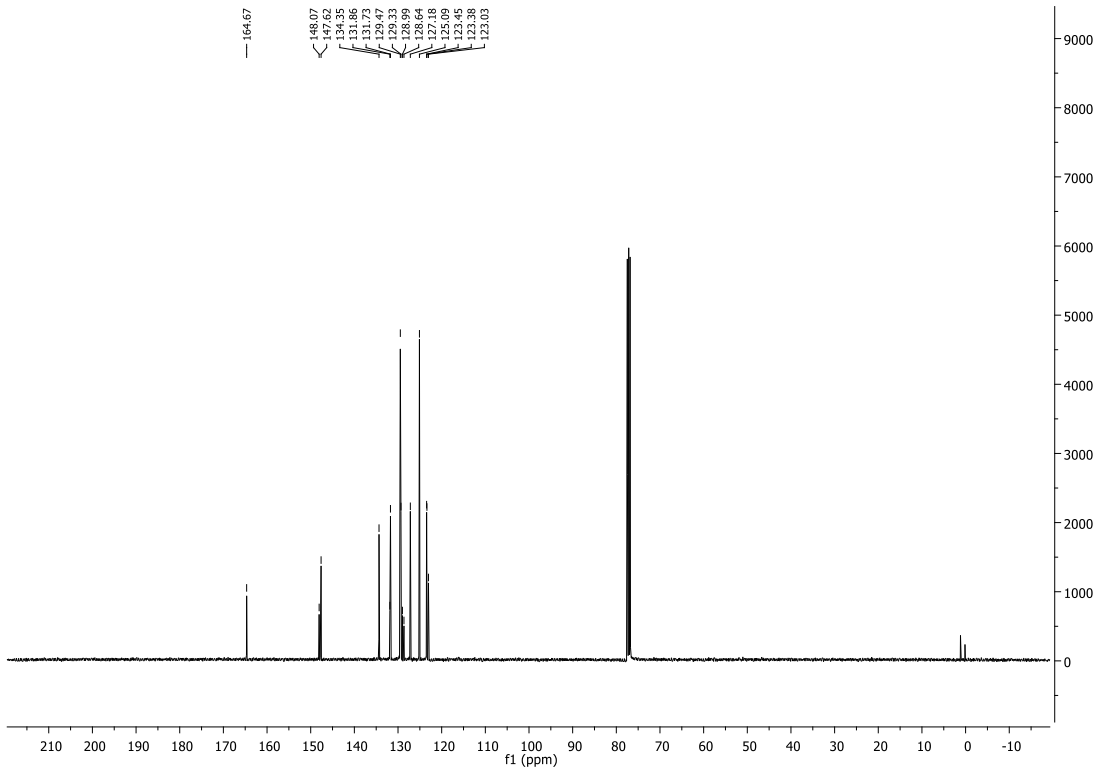

HRMS data of (2) **TPANMI**

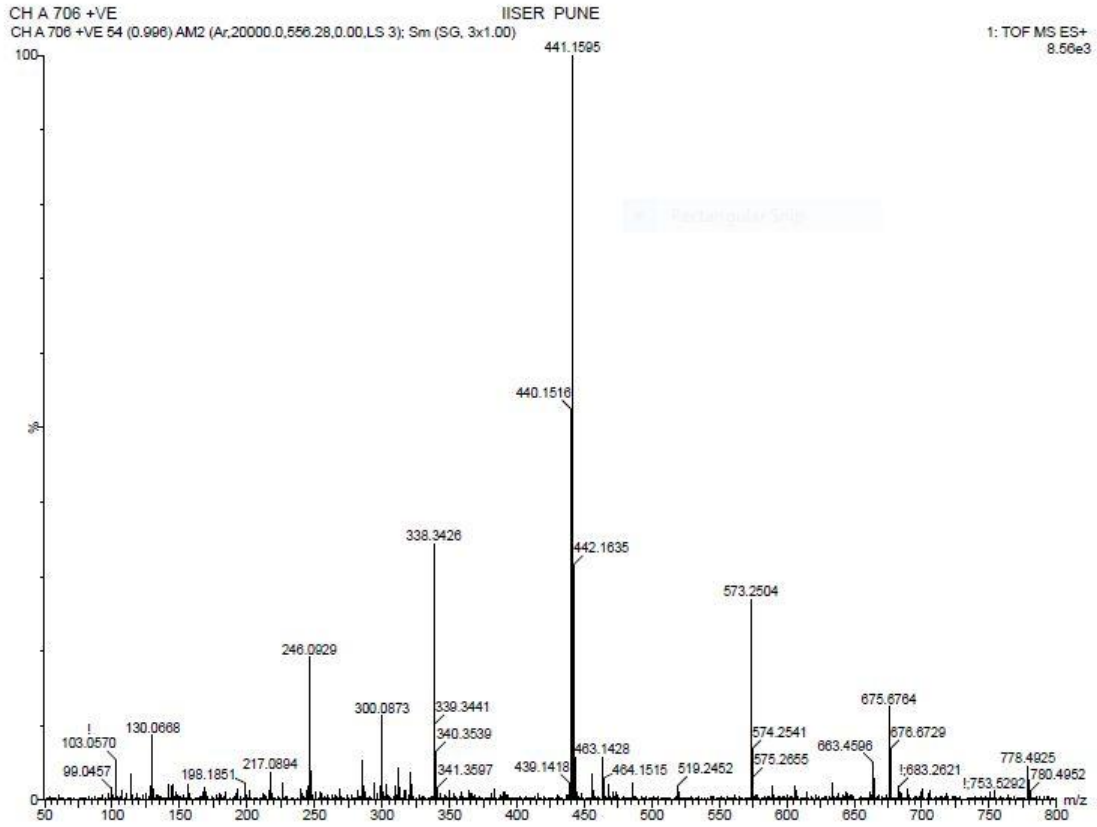

^{1}H NMR data of (3) **TPAPMI**

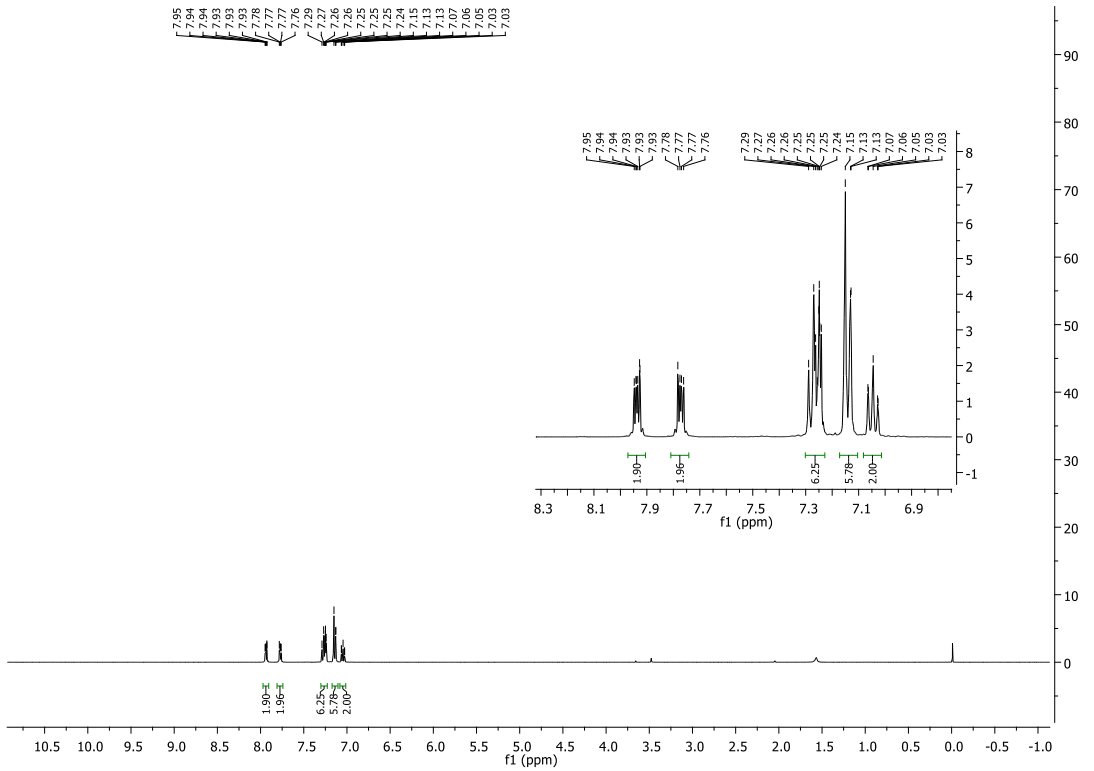

^{13}C NMR data of (3) **TPAPMI**

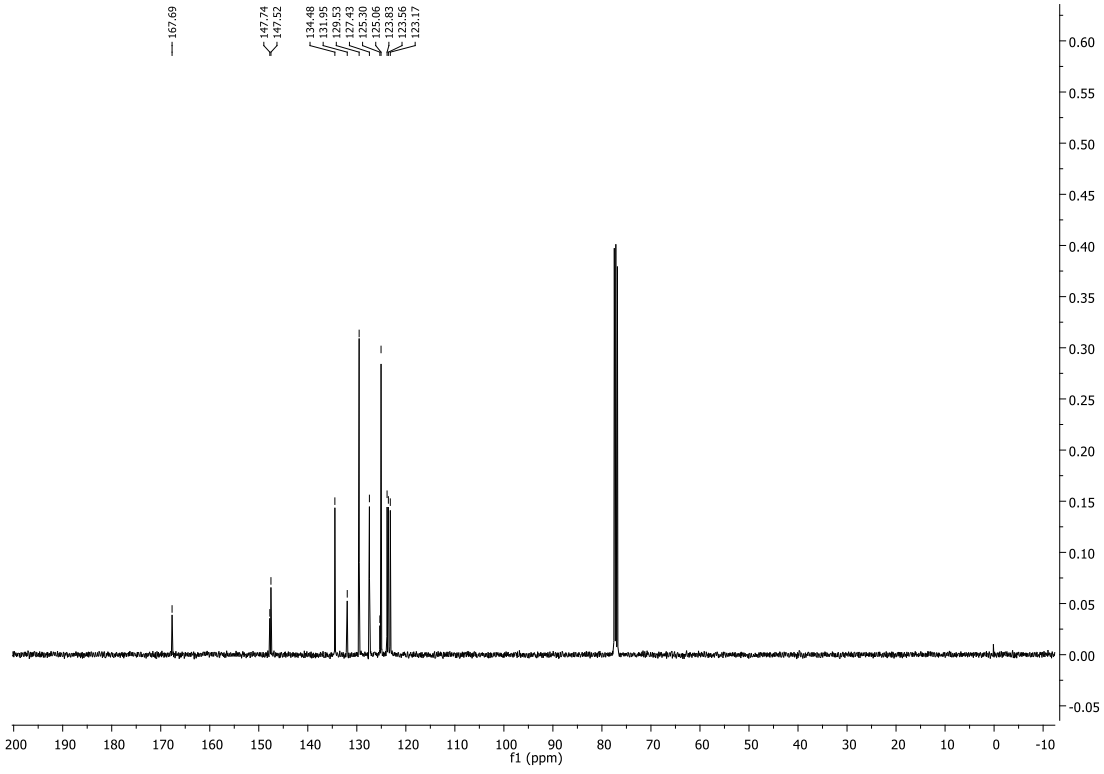

HRMS data of (3) **TPAPMI**

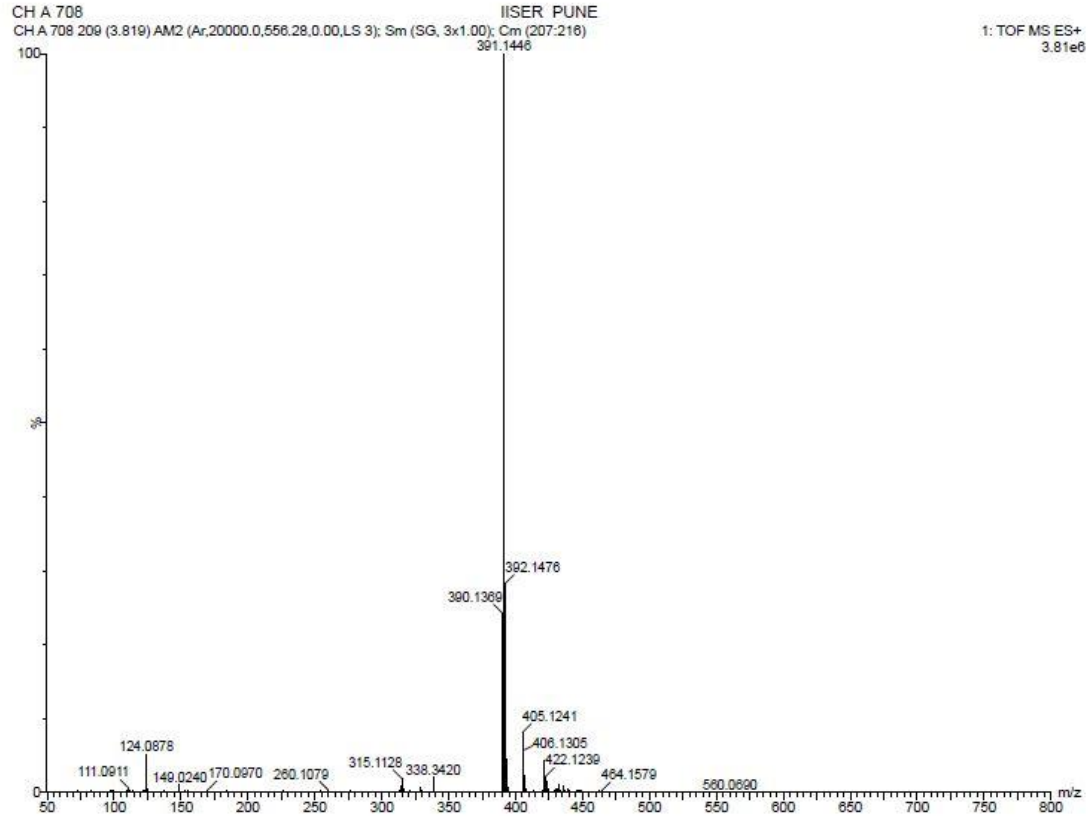

^{1}H NMR data of (4) **TPACNPMI**

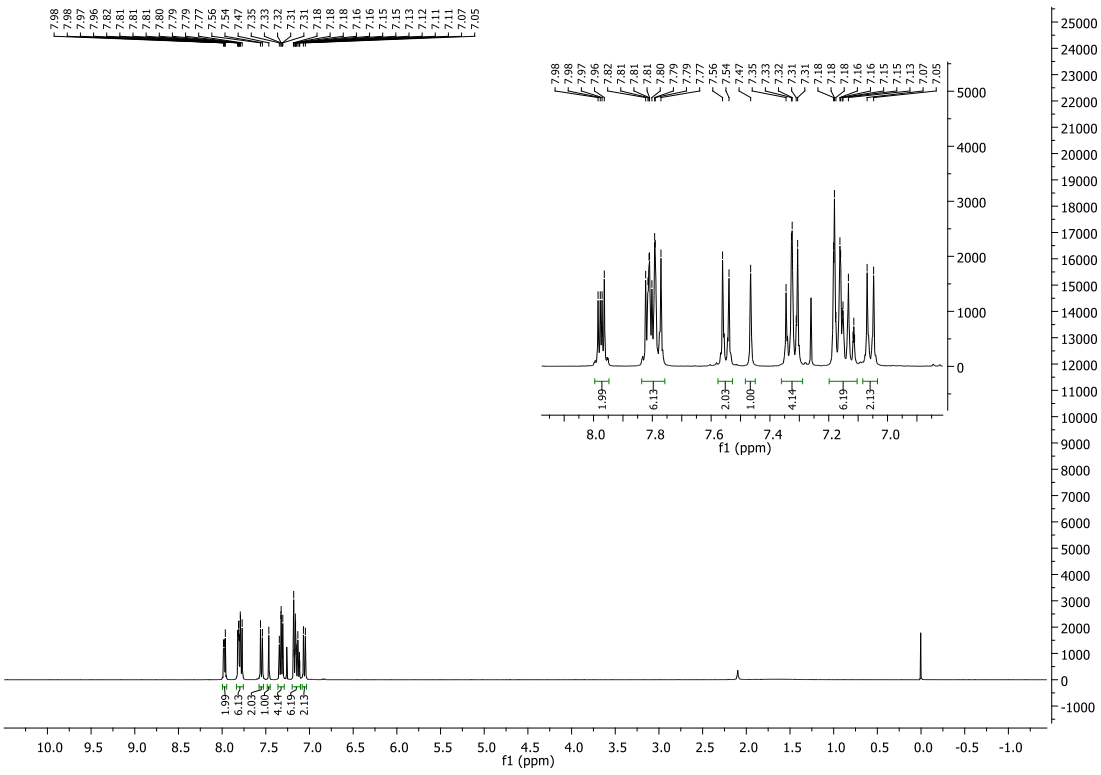

^{13}C NMR data of (4) **TPACNPMI**

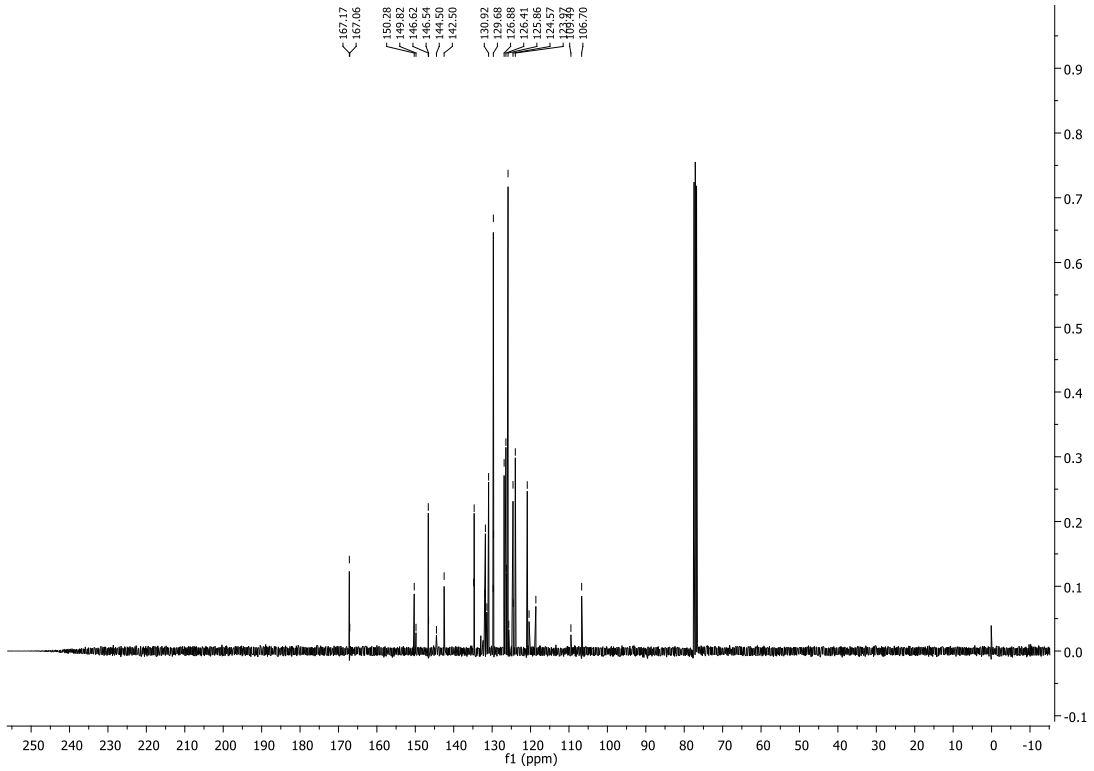

HRMS data of (4) **TPACNPMI**

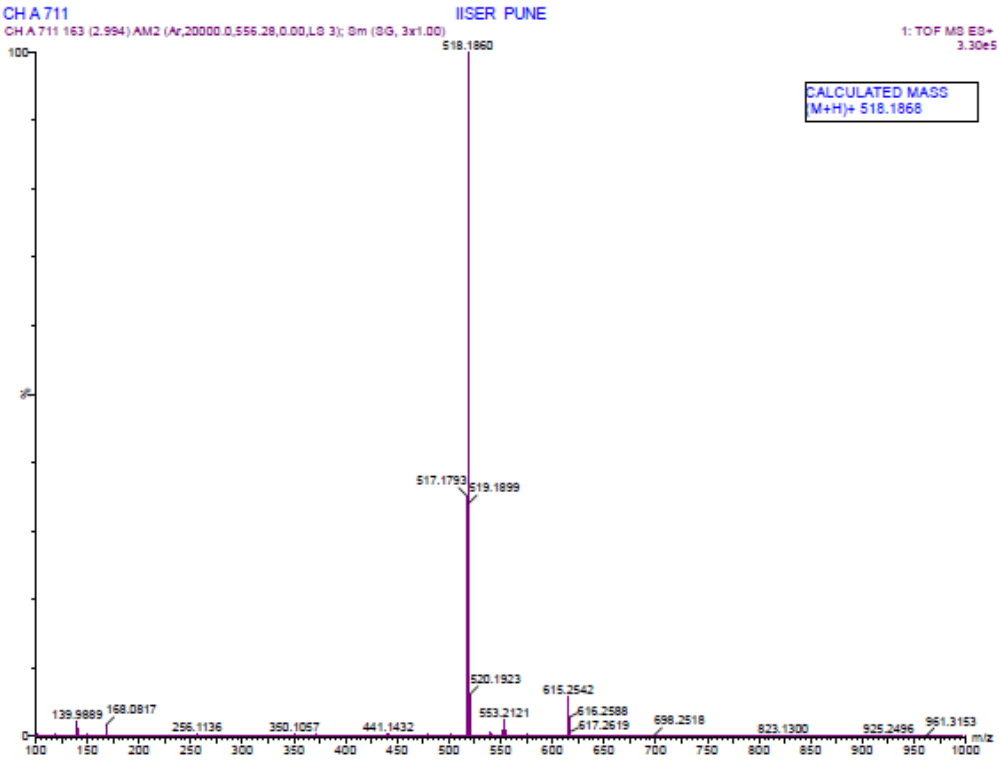

^{1}H NMR data of (a) **TPANO$_2$**

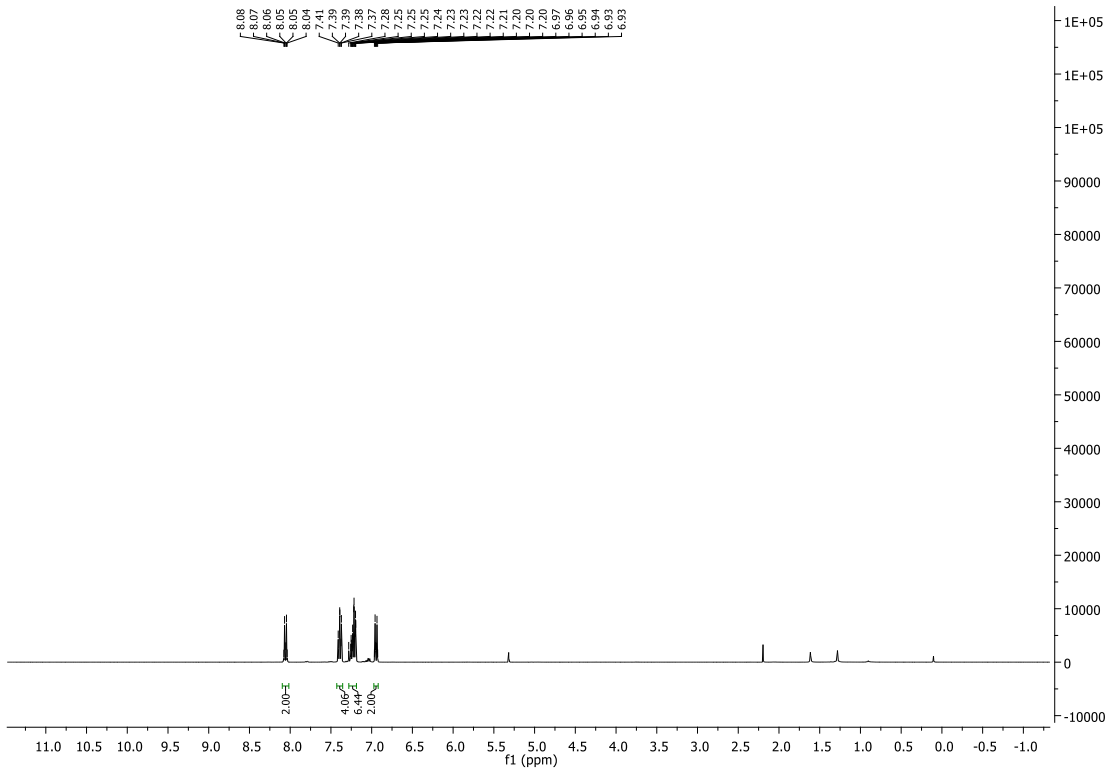

^{13}C NMR data of (a) **TPANO$_2$**

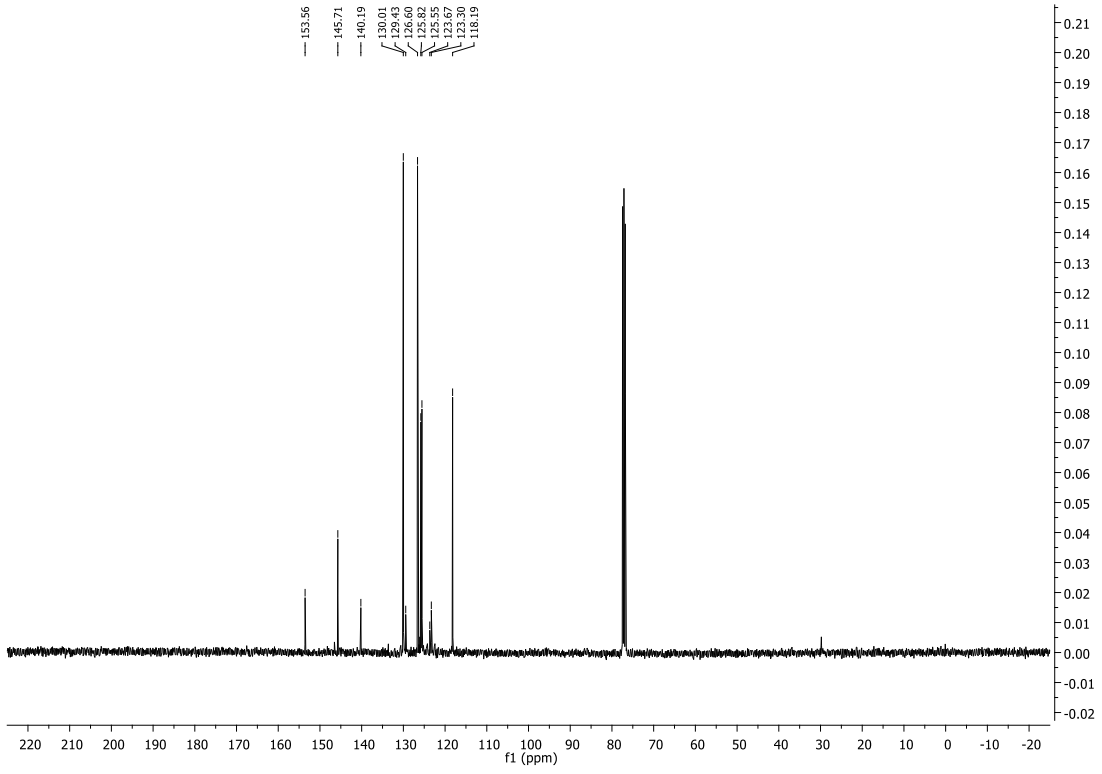

HRMS data of (a) **TPANO$_2$**

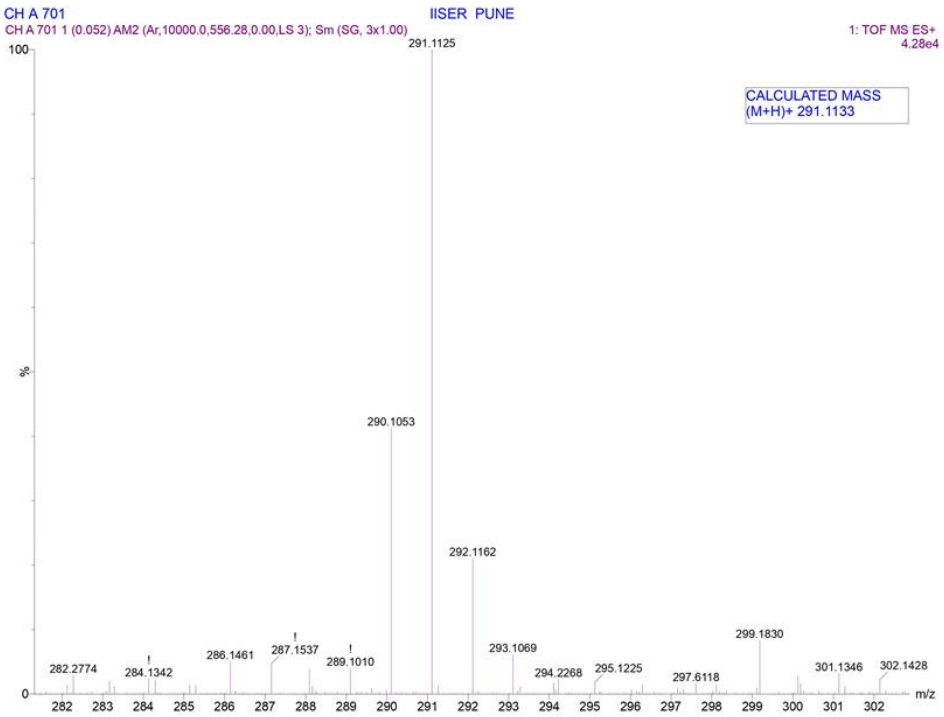

^{1}H NMR data of (b) **TPANH$_2$**

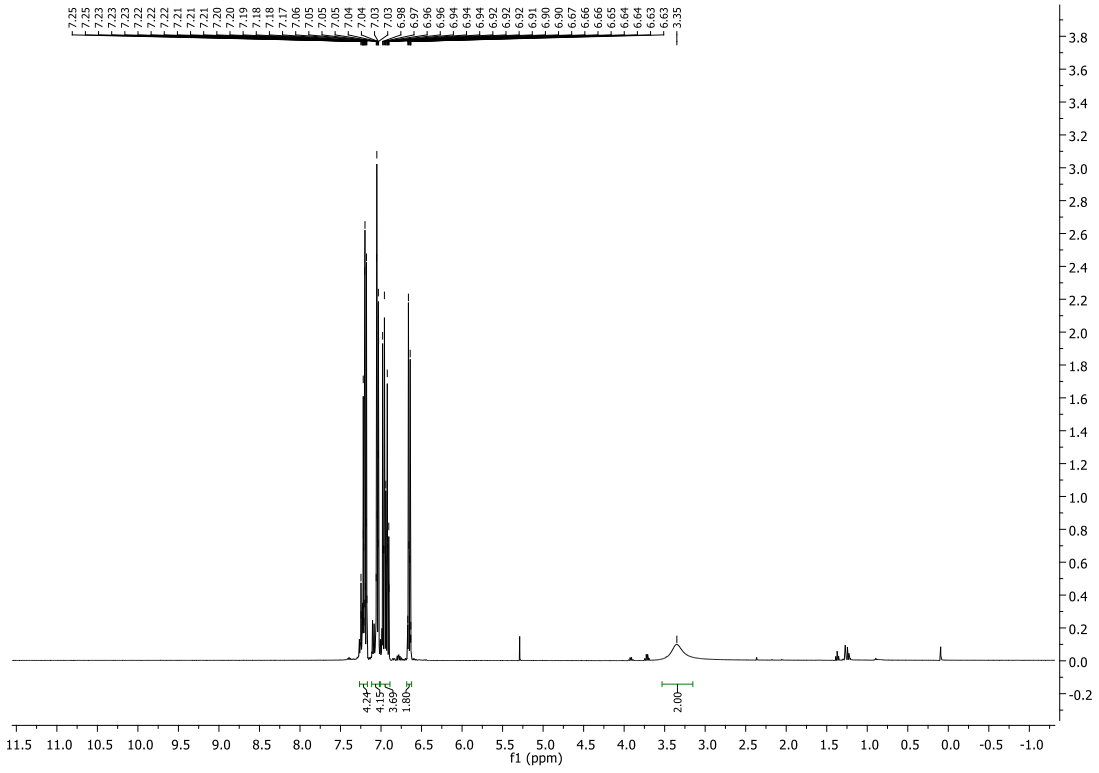

^{13}C NMR data of (b) **TPANH$_2$**

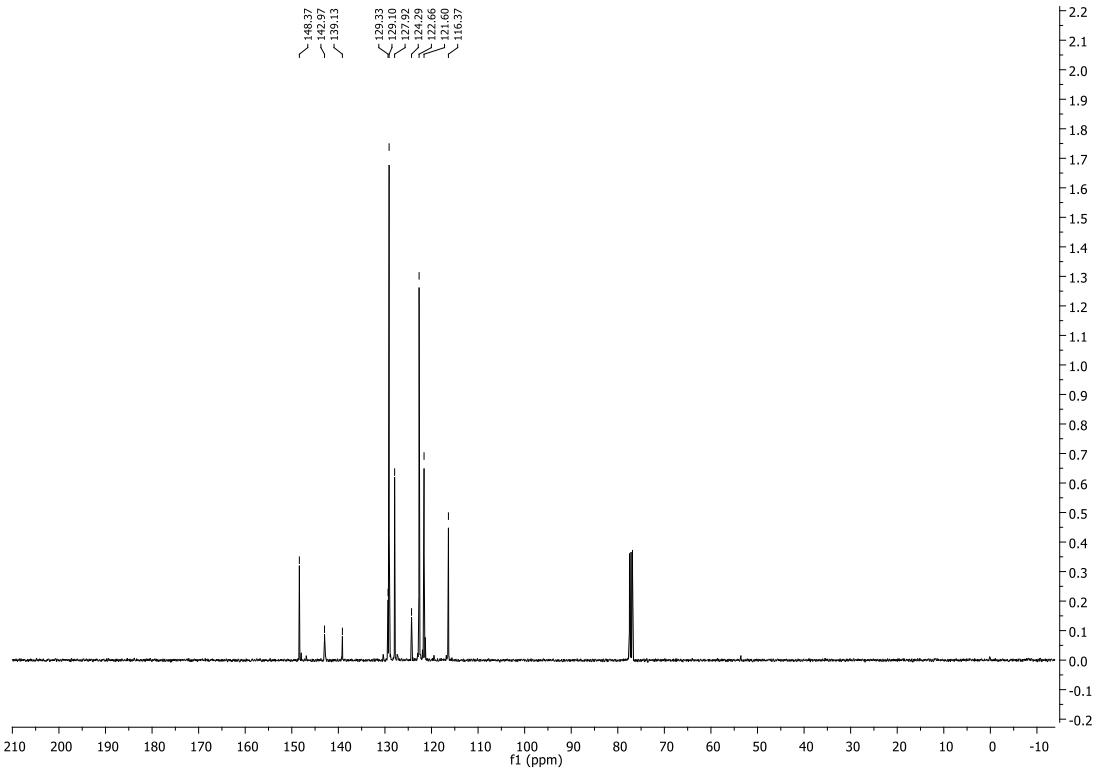

HRMS data of (b) **TPANH$_2$**

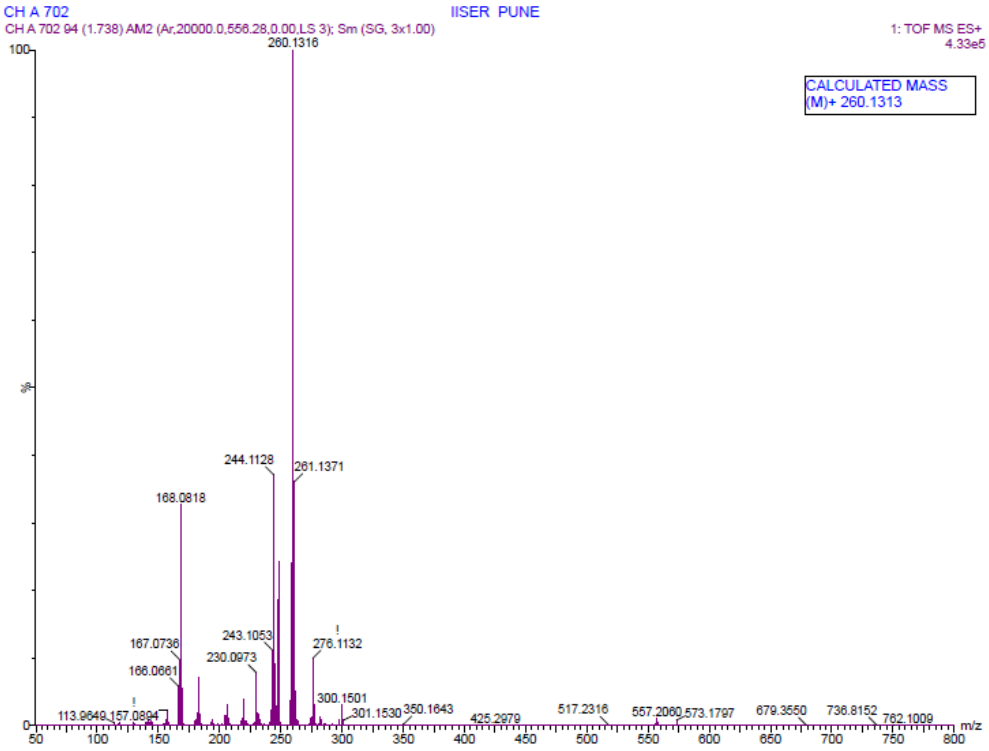

^{1}H NMR data of (c) **TPACHO**

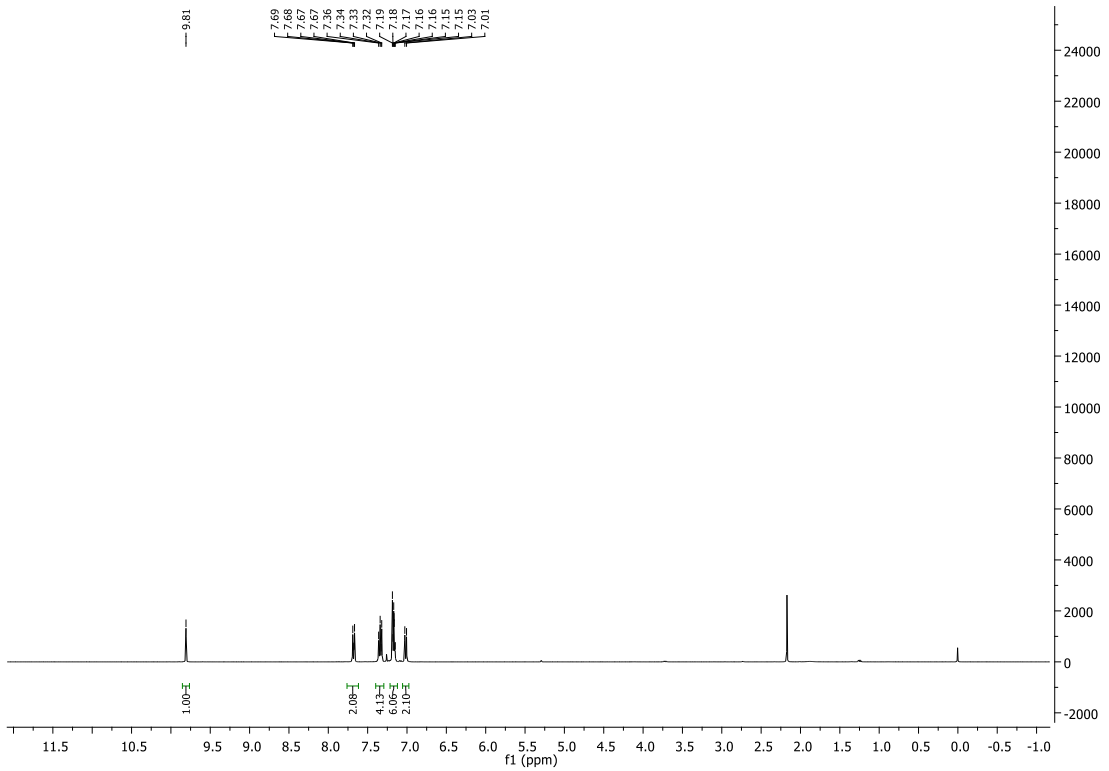

^{13}C NMR data of (c) **TPACHO**

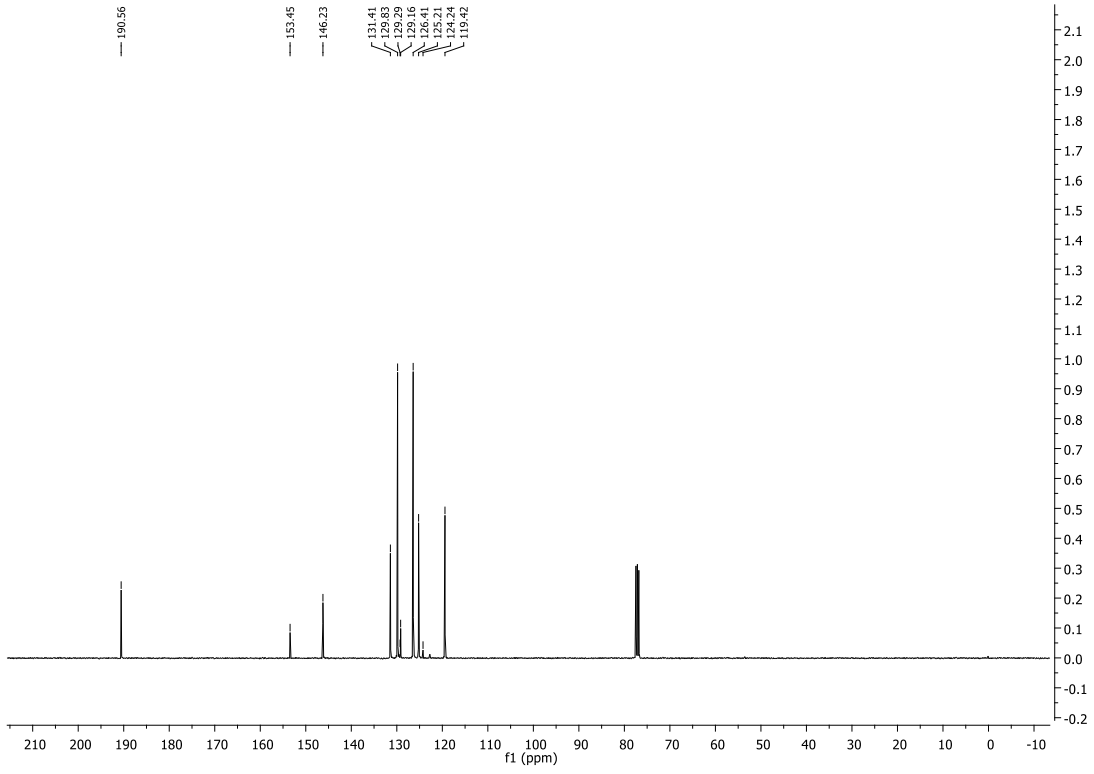

HRMS data of (c) **TPACHO**

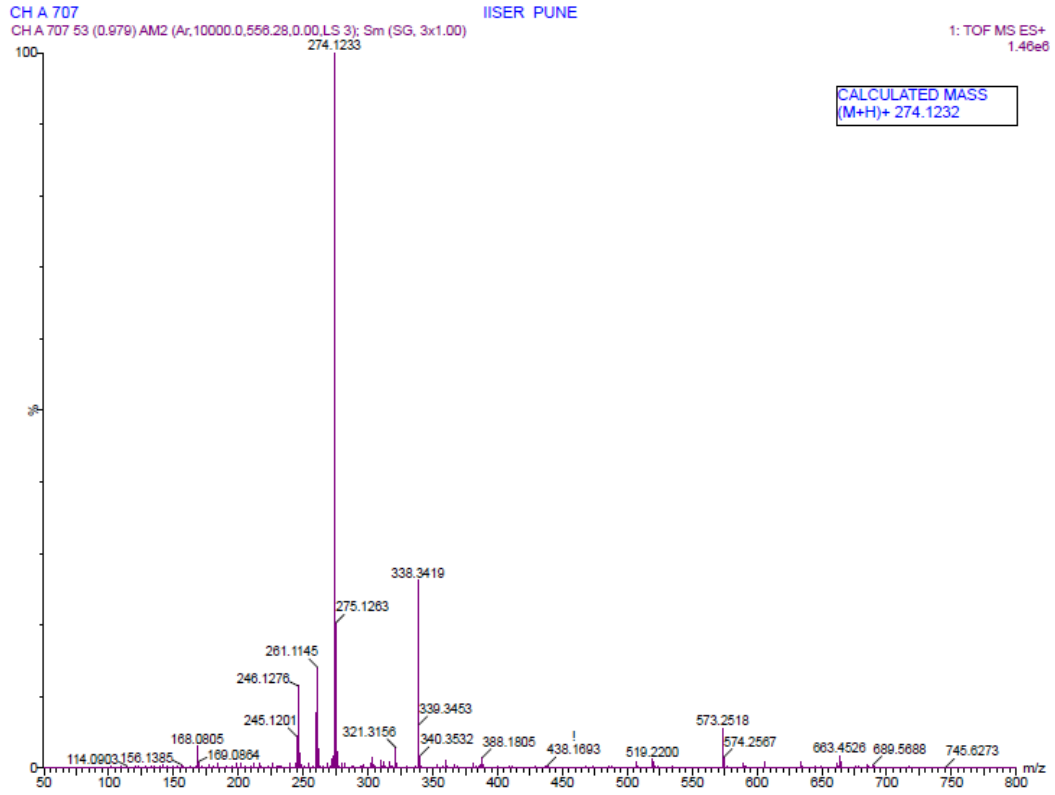

^{1}H NMR data of (d) **TPACNNO$_2$**

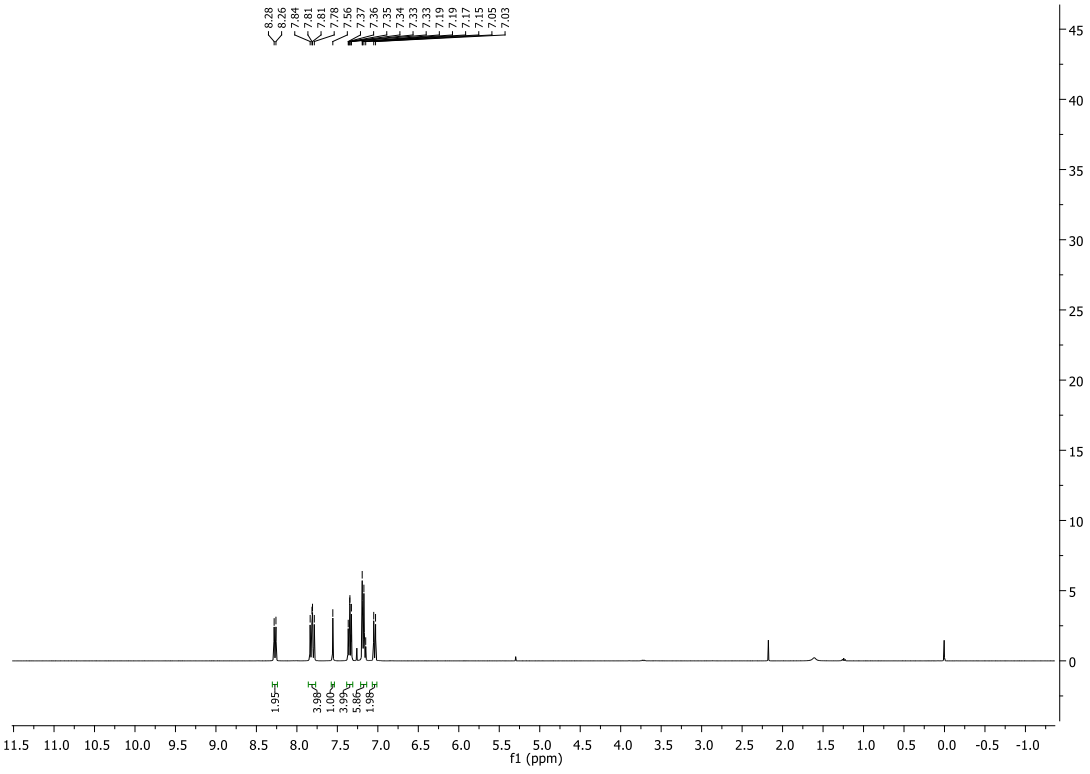

^{13}C NMR data of (d) **TPACNNO$_2$**

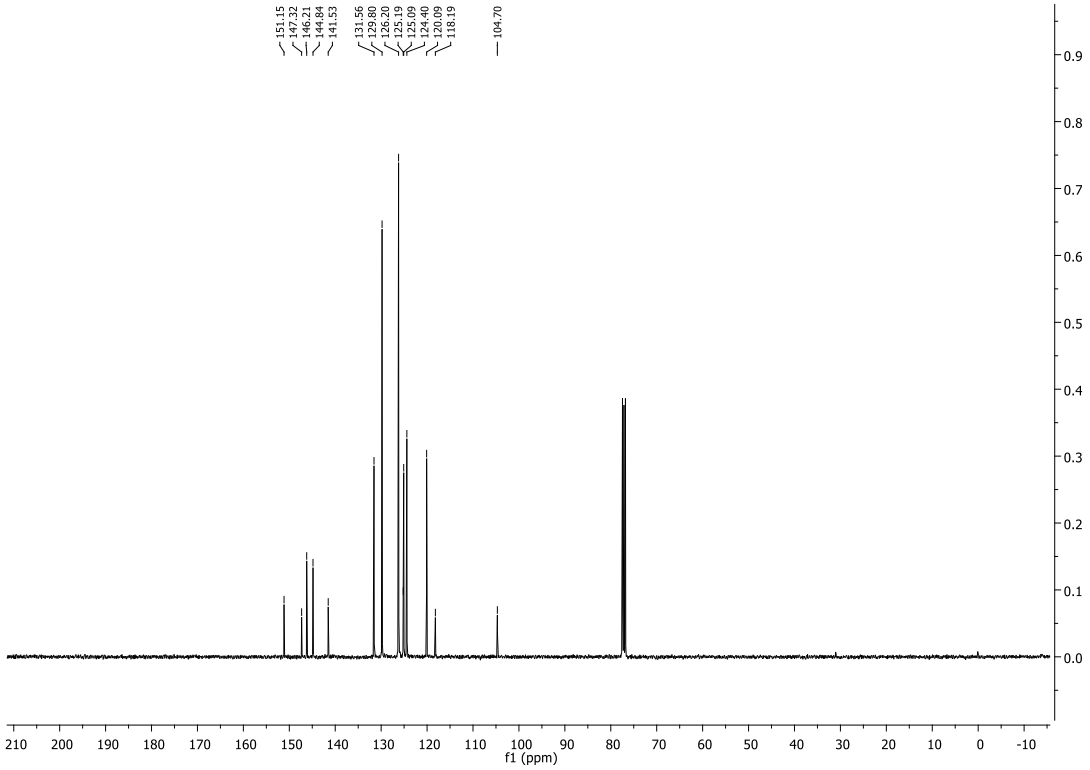

HRMS data of (d) **TPACNNO$_2$**

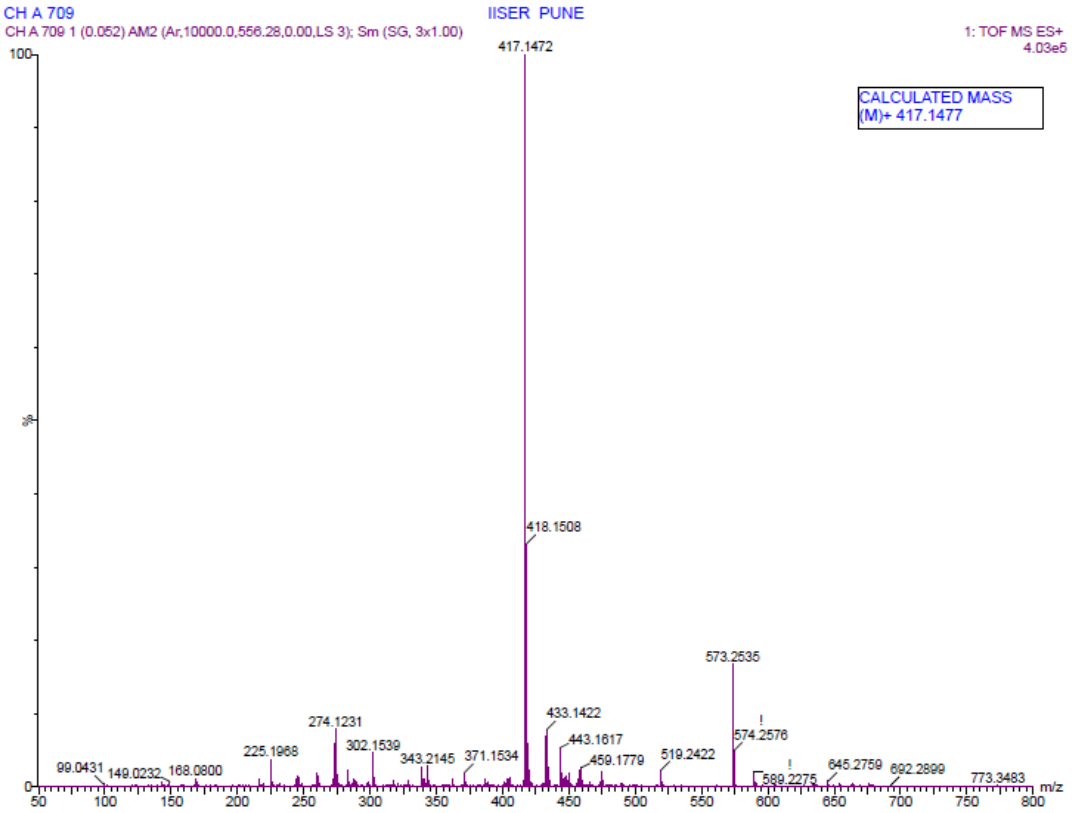

^{1}H NMR data of (e) **TPACNNH$_2$**

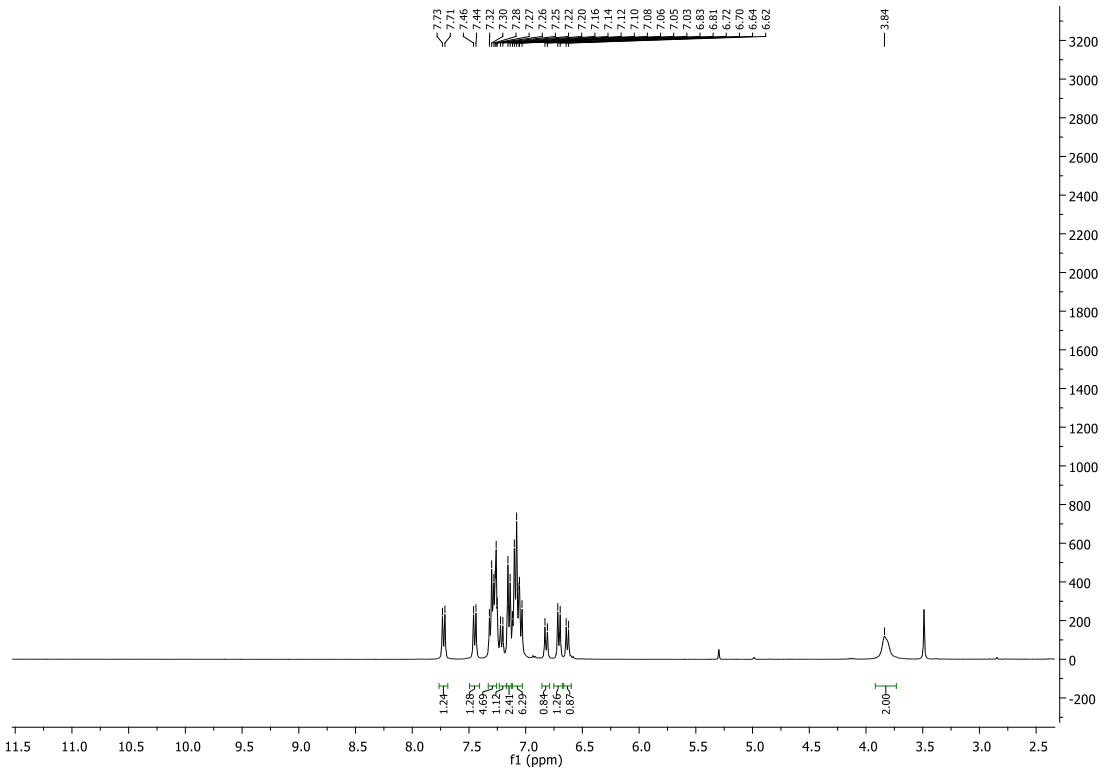

^{13}C NMR data of (e) **TPACNNH$_2$**

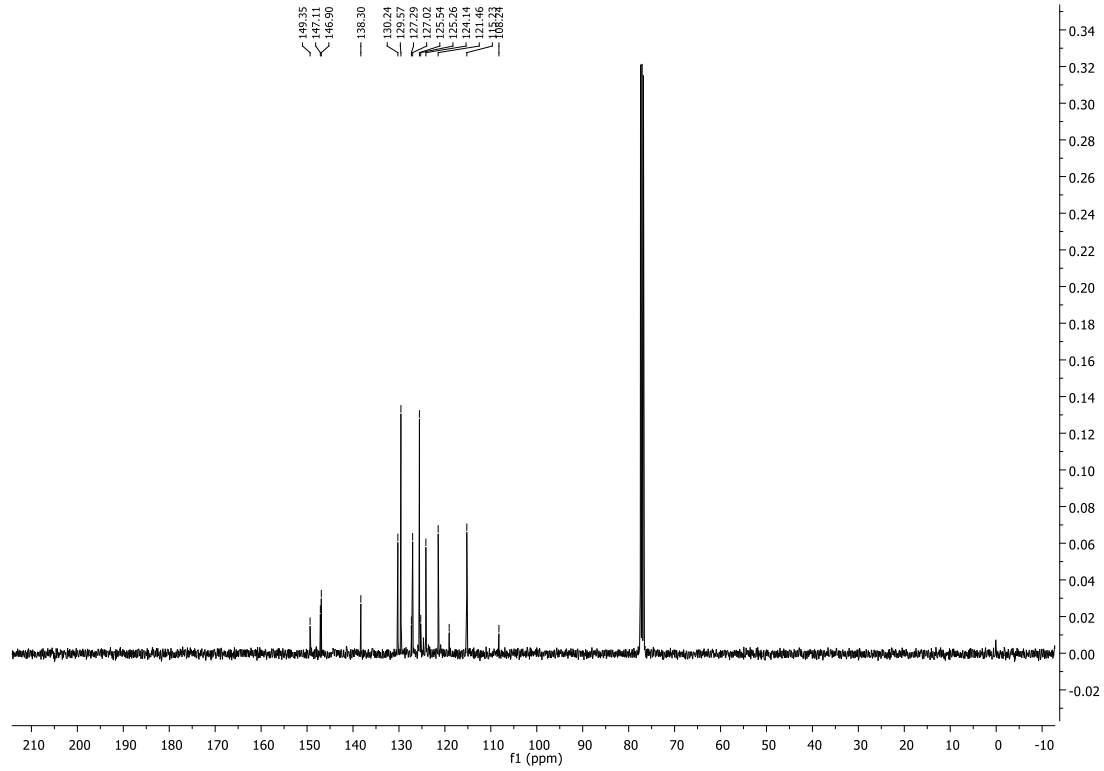

HRMS data of (e) **TPACNNH$_2$**

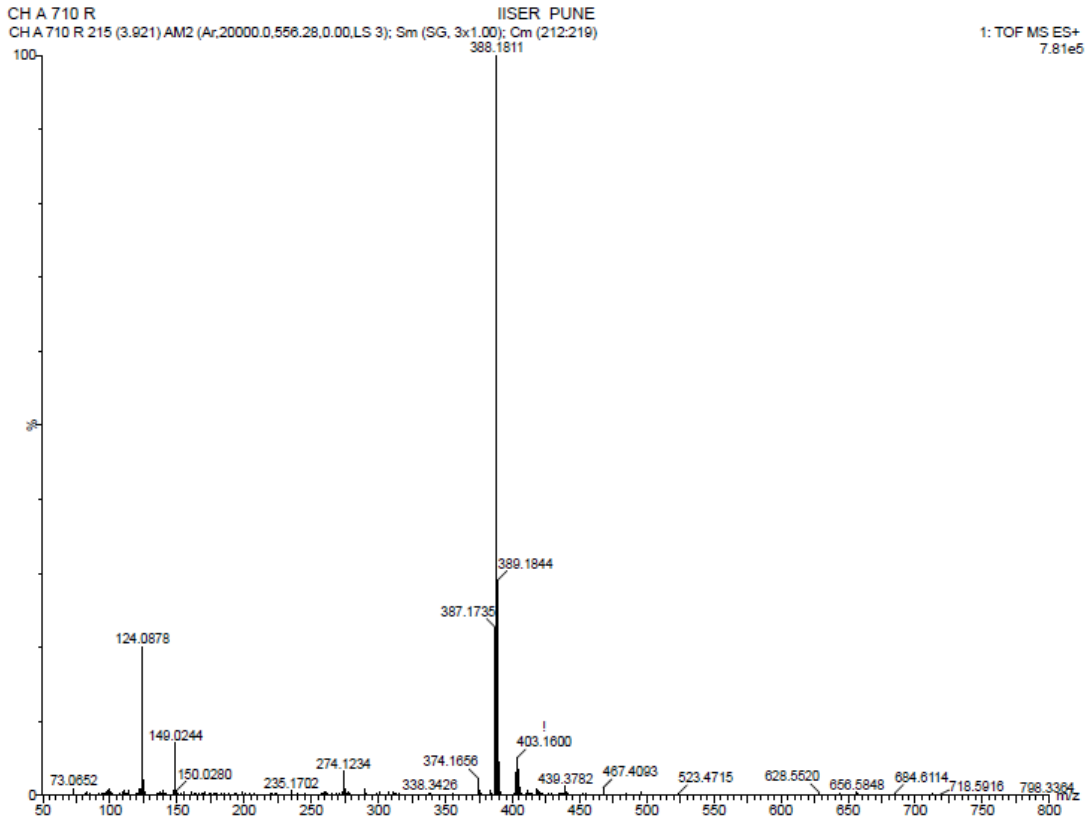

Section A4: Crystallographic Data

TPANDI:

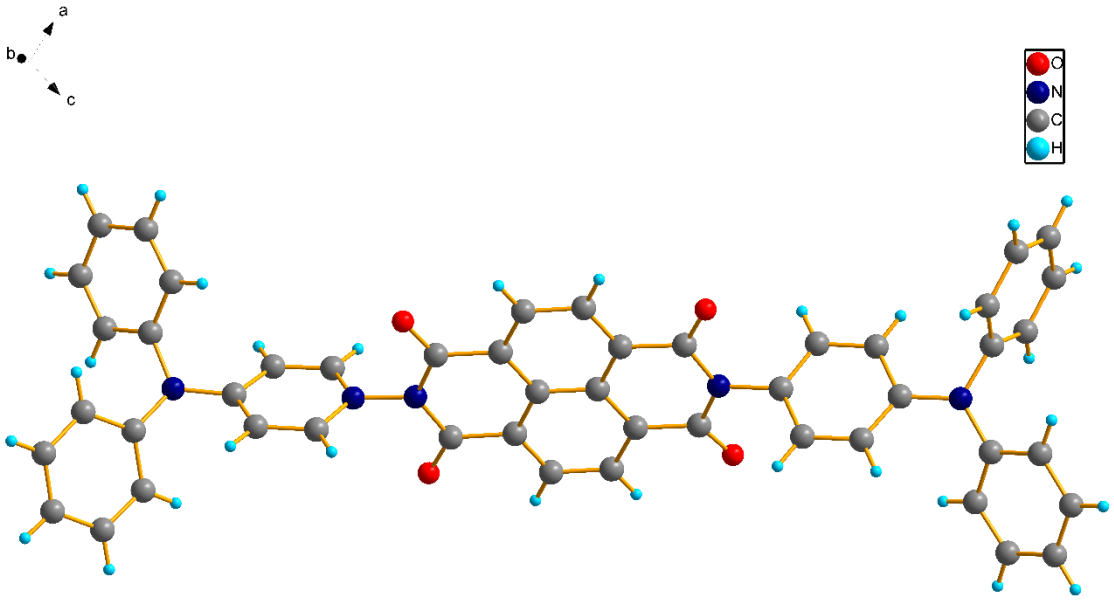

Crystal data and structure refinement for TPANDI.

Identification code	TPANDI
CCDC	2106243
Empirical formula	$C_{60}H_{60}N_{60}O_{60}Cl_{360}$
Formula weight	2547.21
Temperature/K	100(2)
Crystal system	monoclinic
Space group	Pc
a/Å	18.3596(14)
b/Å	14.4215(12)
c/Å	23.4992(17)
α/°	90

β/°	105.753(4)
γ/°	90
Volume/Å^3	5988.3(8)
Z	2
ρ_{calc}g/cm^3	1.413
μ/mm^{-1}	1.919
F(000)	2642.0
Radiation	CuKα (λ = 1.54178)2Θ range for data collection/° 5 to 157.064
Index ranges	-23 ≤ h ≤ 23, -18 ≤ k ≤ 17, -29 ≤ l ≤ 24
Reflections collected	59802
Independent reflections 0.1170,	25788 [R_{int} = R_{sigma}=0.1215]
Data/restraints/parameters	25788/2/1664
Goodness-of-fit on F^2	0.912
Final R indexes [I>=2σ (I)] 0.0867, wR_2 = 0.2233	R_1 =
Final R indexes [all data] 0.1354, wR_2 = 0.2659	R_1 =
Largest diff. peak/hole / e Å^{-3} 0.79/-0.79	0.79/-
Flack parameter	0.478(16)

TPANMI:

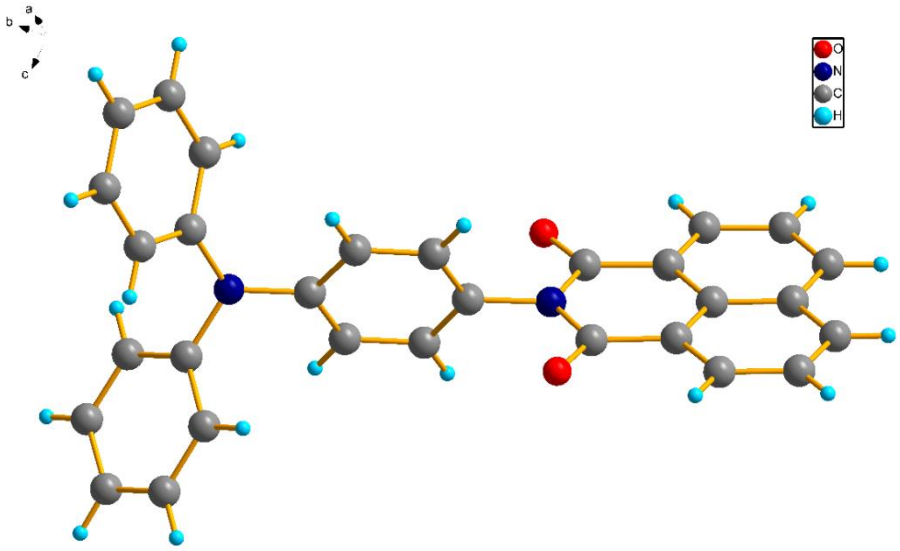

Crystal data and structure refinement for TPANMI.

Identification code	TPANMI
CCDC	2106244
Empirical formula	$C_{30}H_{20}N_2O_2$
Formula weight	440.48
Temperature/K	100(2)
Crystal system	monoclinic
Space group	$P2_1/c$
a/Å	13.17(4)
b/Å	9.67(2)
c/Å	17.61(4)
α/°	90
β/°	104.68(8)
γ/°	90
Volume/Å^3	2169(10)

Z	4
ρ_{calc}g/cm^3	1.348
μ/mm^{-1}	0.085
F(000)	920.0
Radiation	MoKα (λ = 0.71073)2Θ range for data collection/° 3.198 to 49.996
Index ranges	$-15 \leq h \leq 15$, $-11 \leq k \leq 11$, $-20 \leq l \leq 20$
Reflections collected	24067
Independent reflections	3830 [R_{int} = 0.24, R_{sigma} = 0.2427]
Data/restraints/parameters	3830/0/307
Goodness-of-fit on F^2	1.069
Final R indexes [I>=2σ (I)]	R_1 = 0.0799, wR_2 = 0.1372
Final R indexes [all data]	R_1 = 0.2409, wR_2 = 0.1885
Largest diff. peak/hole / e Å^{-3}	0.31/-0.34

TPAPMI:

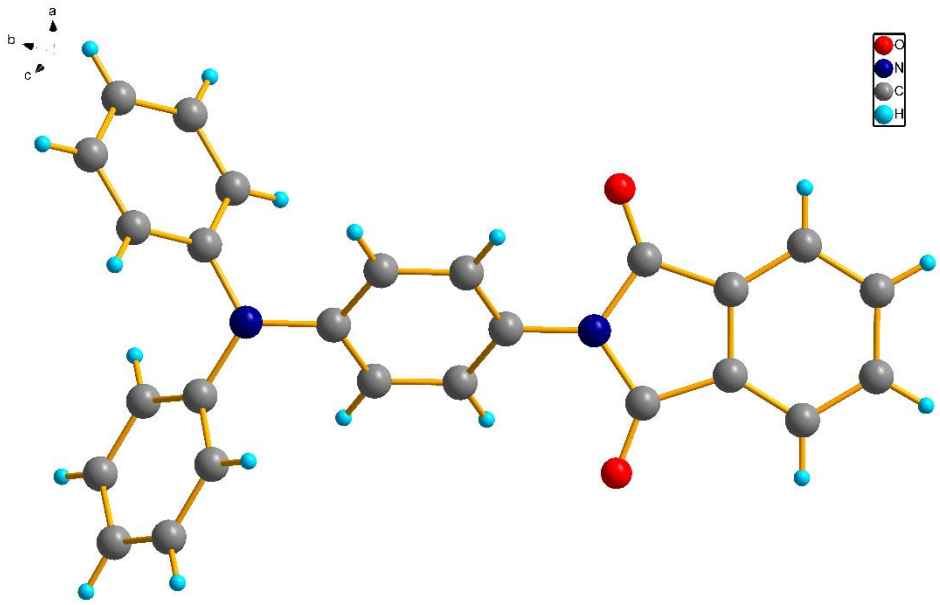

Crystal data and structure refinement for TPAPMI

Identification code	TPAPMI
CCDC	2106245
Empirical formula	$C_{26}H_{18}N_2O_2$
Formula weight	390.42
Temperature/K	100(2)
Crystal system	monoclinic
Space group	$P2_1/c$
a/Å	12.5507(6)
b/Å	9.3347(4)
c/Å	16.6937(8)
α/°	90
β/°	94.800(2)
γ/°	90
Volume/Å^3	1948.92(16)

Z	4
ρ_{calc}g/cm^3	1.331
μ/mm^{-1}	0.678
F(000)	816.0
Radiation	CuKα (λ = 1.54178)2Θ range for data collection/° 7.068 to 130.102
Index ranges	-14 ≤ h ≤ 14, -10 ≤ k ≤ 10, -19 ≤ l ≤ 19
Reflections collected	16486
Independent reflections	3329 [R_{int} = 0.0720, R_{sigma} = 0.0510]
Data/restraints/parameters	3329/0/272
Goodness-of-fit on F^2	1.039
Final R indexes [I>=2σ (I)]	R_1 = 0.0415, wR_2 = 0.1018
Final R indexes [all data]	R_1 = 0.0537, wR_2 = 0.1080
Largest diff. peak/hole / e Å^{-3}	0.22/-0.18

TPACNPMI:

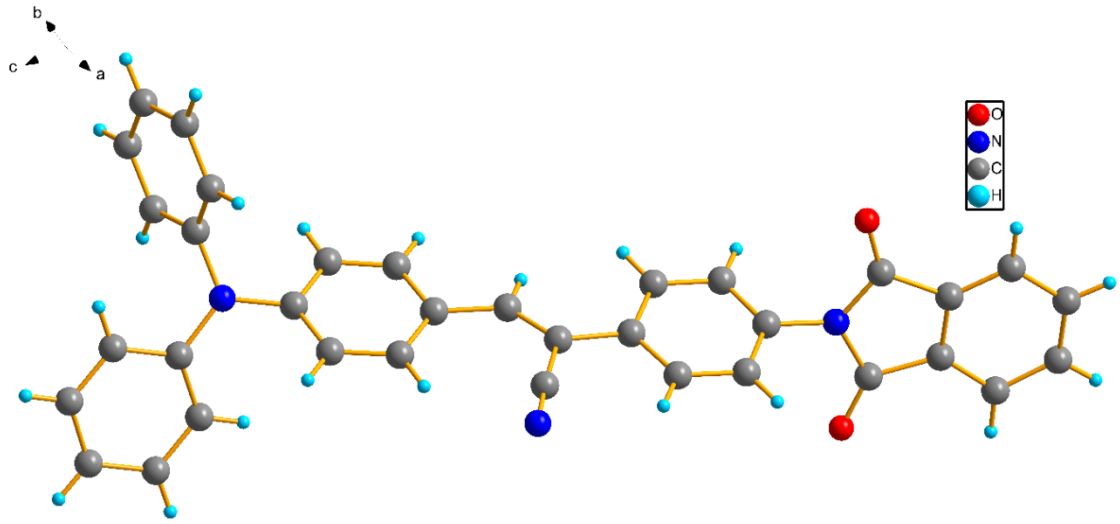

Crystal data and structure refinement for TPACNPMI

Identification code	TPACNPMI
CCDC	2106242
Empirical formula	$C_{35}H_{23}N_3O_2$
Formula weight	517.56
Temperature/K	100(2)
Crystal system	triclinic
Space group	P-1
a/Å	9.488(5)
b/Å	11.739(7)
c/Å	12.478(7)
α/°	90.134(16)
β/°	111.372(15)

γ/°	98.711(14)
Volume/Å^3	1276.8(13)
Z	2
ρ_{calc}g/cm^3	1.346
μ/mm^{-1}	0.085
F(000)	540.0
Radiation	MoKα (λ = 0.71073)2Θ range for data collection/° 3.512 to 49.996
Index ranges	-11 ≤ h ≤ 11, -12 ≤ k ≤ 13, -14 ≤ l ≤ 13
Reflections collected	14765
Independent reflections	4506 [R_{int} = 0.24, R_{sigma} = 0.3794]
Data/restraints/parameters	4506/0/361
Goodness-of-fit on F^2	0.809
Final R indexes [I>=2σ (I)]	R_1 = 0.0738, wR_2 = 0.1026
Final R indexes [all data]	R_1 = 0.2529, wR_2 = 0.1543
Largest diff. peak/hole / e Å^{-3}	0.30/-0.38

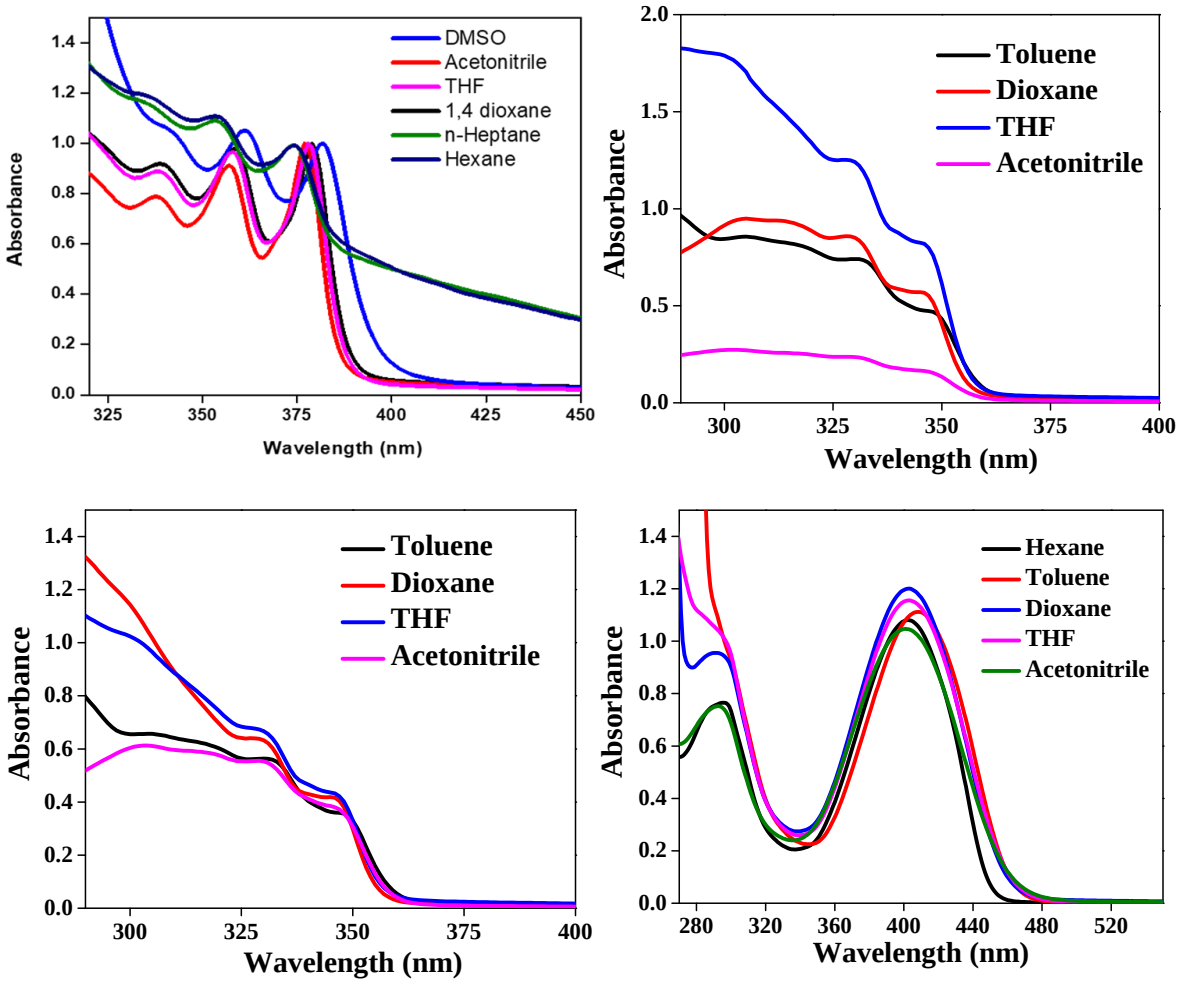

Figure A1: Absorption spectra of TPANDI (top row left column), TPANMI (top row right column), TPAPMI (bottom row left column), and TPACNPMI (bottom row right column) in different solvents using 30 µm of luminogen concentration in each case.

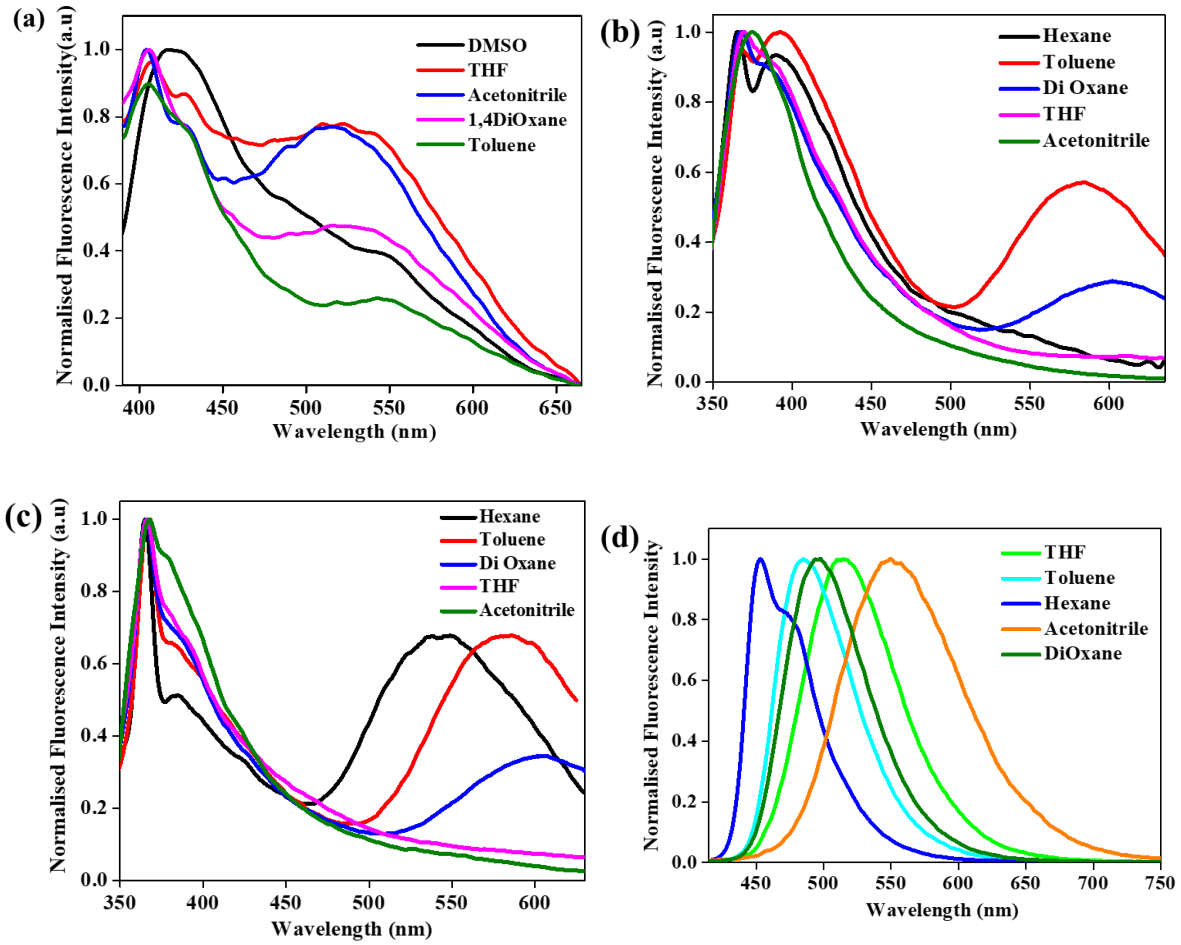

Figure A2: Emission spectra of TPANDI (330 nm excitation) (a), TPANMI (330 nm excitation) (b), TPAPMI (330 nm excitation) (c), and TPACNPMI (402 nm excitation) (d) in different solvents using 30 µm of luminogen concentration in each case.

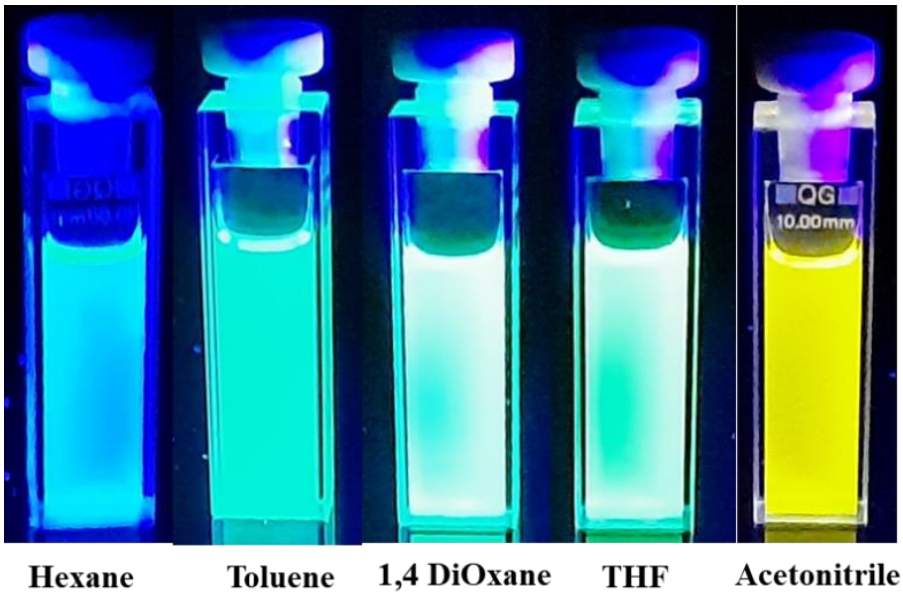

Figure A3: Cuvette images of a 30 µm solution of TPACNPMI in solvents of different polarities upon exposure to a high power 365 nm UV lamp.

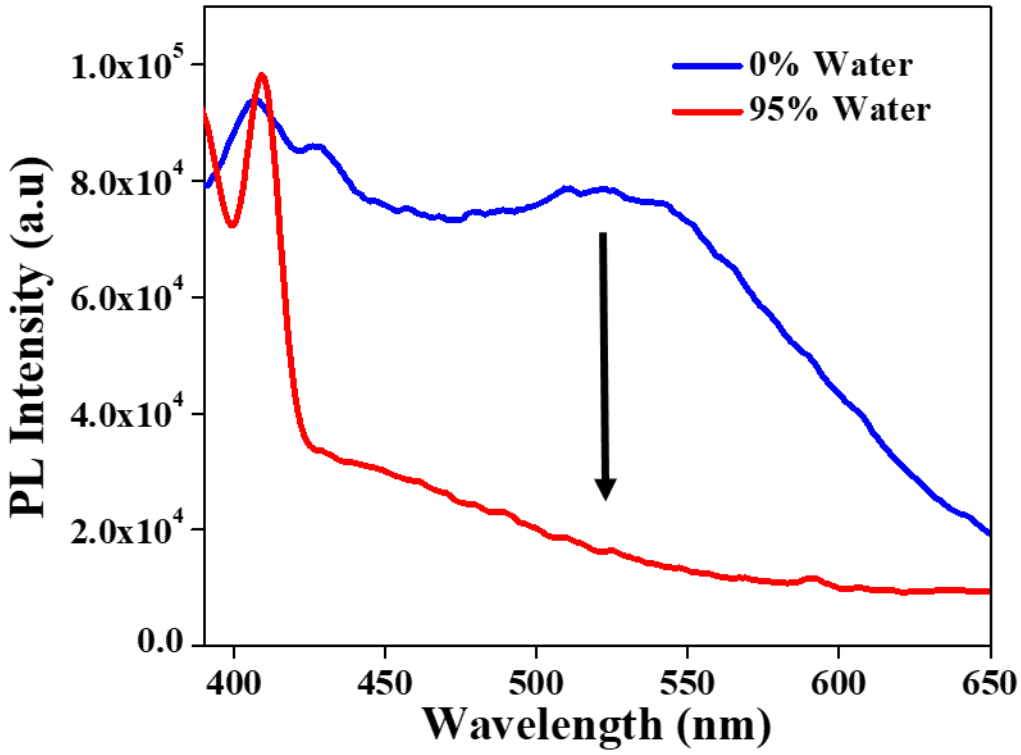

Figure A4: Aggregation Caused Quenching (ACQ) phenomenon of TPANDI (30 µm) in THF-water binary mixture upon excitation at 340 nm. water binary mixture upon excitation at 340 nm.

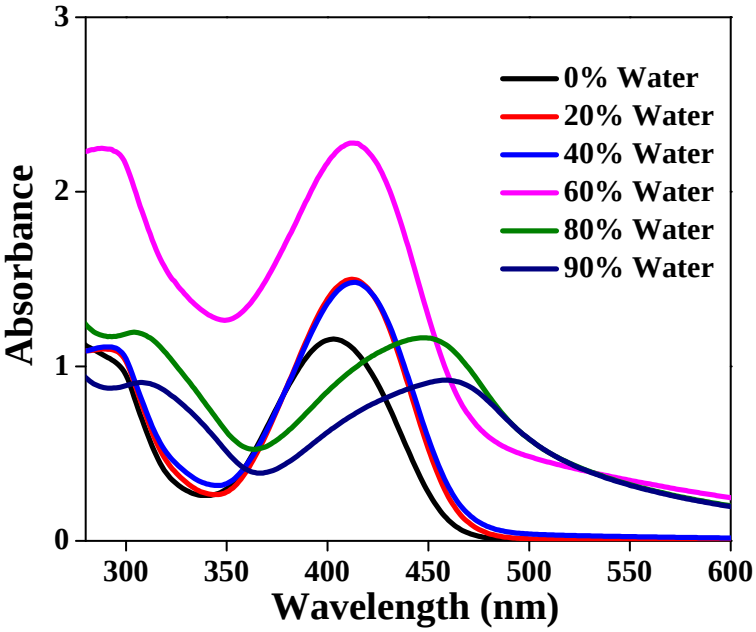

Figure A5: Absorption spectra of TPACNPMI (30µm concentration) in different fractions of water. It clearly shows a considerable shift in absorption spectra in different fractions of water volume.

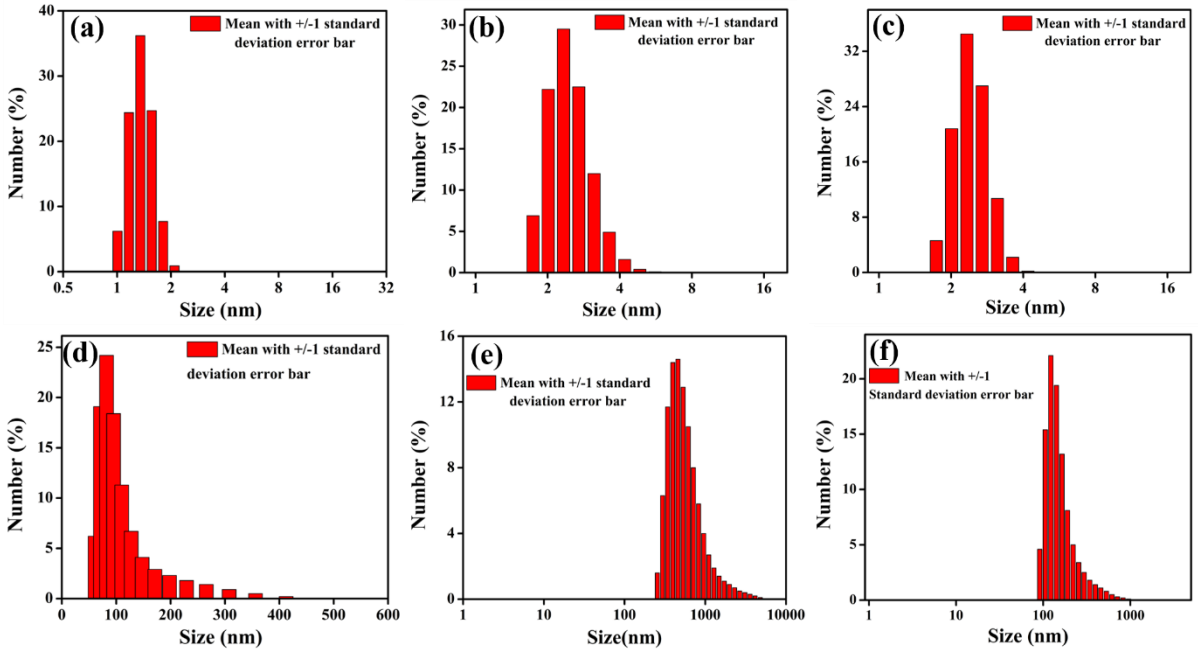

Figure A6: DLS studies at 0% water content of (a) TPANMI, (b) TPAPMI and (c) TPACNPMI and at higher water content of (d) TPANMI (95% water) (e) TPAPMI (90% water) and (f) TPACNPMI (90% water).

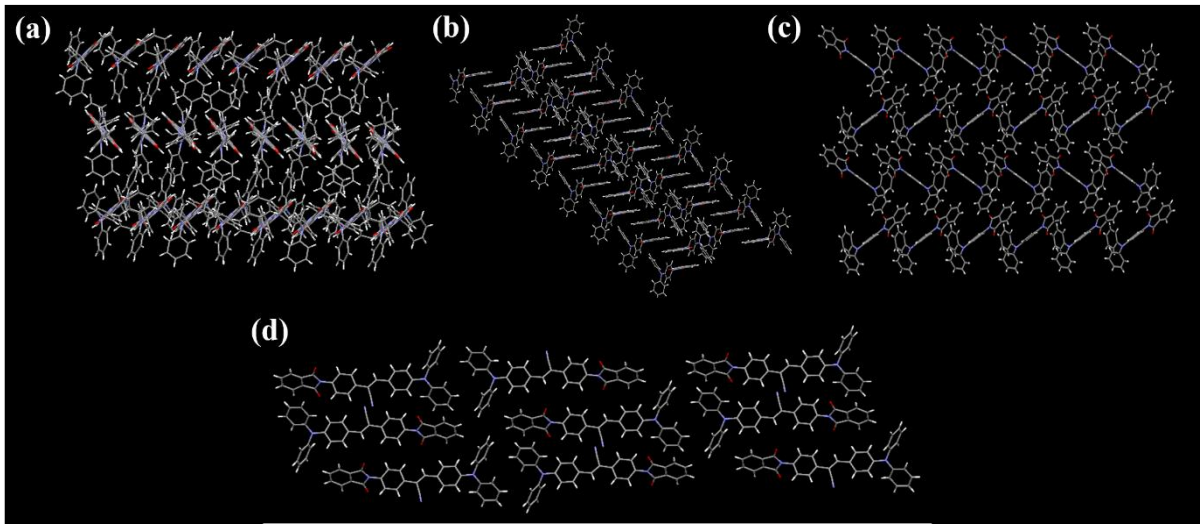

Figure A7: Crystal packing of (a) TPANDI, (b) TPANMI, (c) TPAPMI and (d) TPACNPMI.

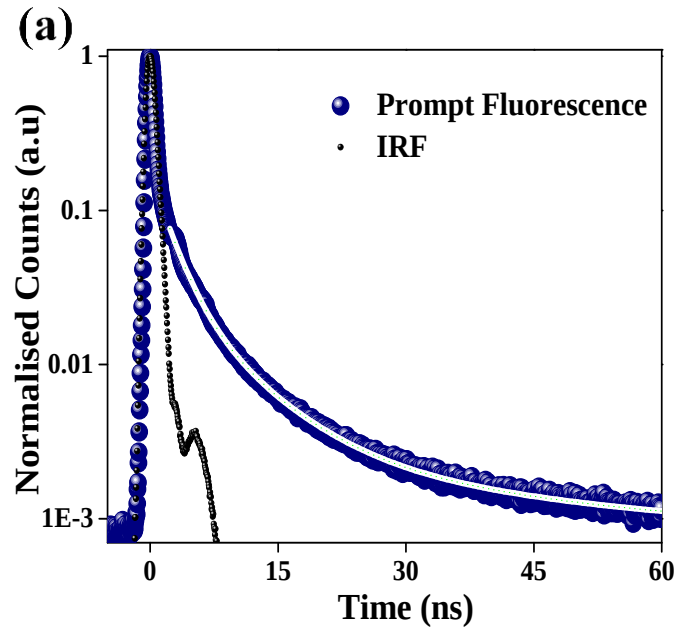
(a)
Prompt Fluorescence
IRF
Normalised Counts (a.u)
1
0.1
0.01
1E-3
0
15
30
45
60
Time (ns)

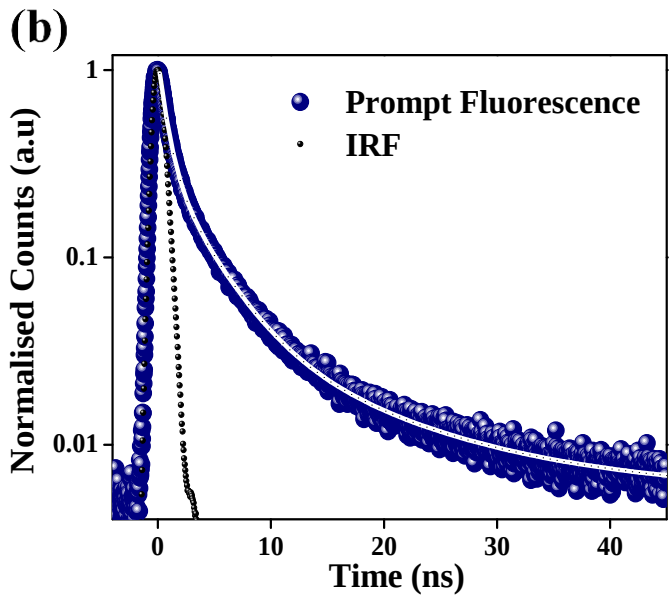
(b)
Prompt Fluorescence
IRF
Normalised Counts (a.u)
1
0.1
0.01
0
10
20
30
40
Time (ns)

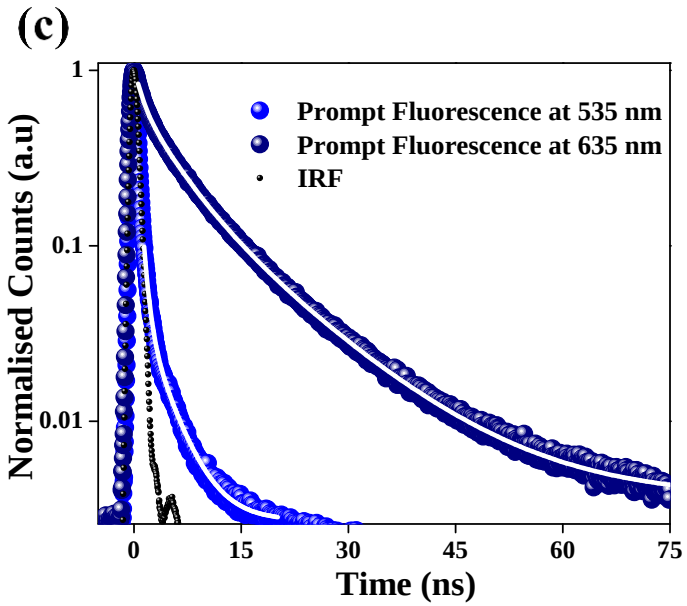

Figure A8: Prompt fluorescence decay of (a) TPANMI crystals collected at 625 nm, (b) TPAPMI microcrystals at 617 nm (b) and TPACNPMI microcrystals at both 535 nm and 635 nm.

Section A4: Hirshfeld Surface Analysis

The best possible way to depict solid state intermolecular interaction is the Hirshfeld surface analysis. The concept of Hirshfeld surface originated from an attempt to give an idea of space occupied by a molecule in a crystal for the purpose of partitioning the crystal electron density into molecular fragments.[63-65] d_e and d_i are the two interactions to be mapped on the Hirshfeld surface; where d_e is the distance of an atom external to the generated Hirshfeld surface and d_i is the distance of an atom internal to the Hirshfeld surface. These two values together generate a 2-D fingerprint plot where different colors indicate the frequency of occurrence of interaction. In this regard, the normalized contact distance based on d_e, d_i and the van der Waals radii of the atom enables the identification of the region of importance to intermolecular interactions.[63-65] The d_{norm} values are mapped onto the Hirshfeld surface by a red-white-blue color scheme, where red color indicates closer contact and negative d_{norm} value, the blue region suggests longer contact and positive d_{norm} value, and the white color indicates the distance of contact exactly equal to the van der Waals separation and a d_{norm} value equals to zero.[63-66] Here in this

work, Hirshfeld surface of all the designed luminogens are generated using Crystal Explorer 3.1 software with iso-value of 0.5.[66]

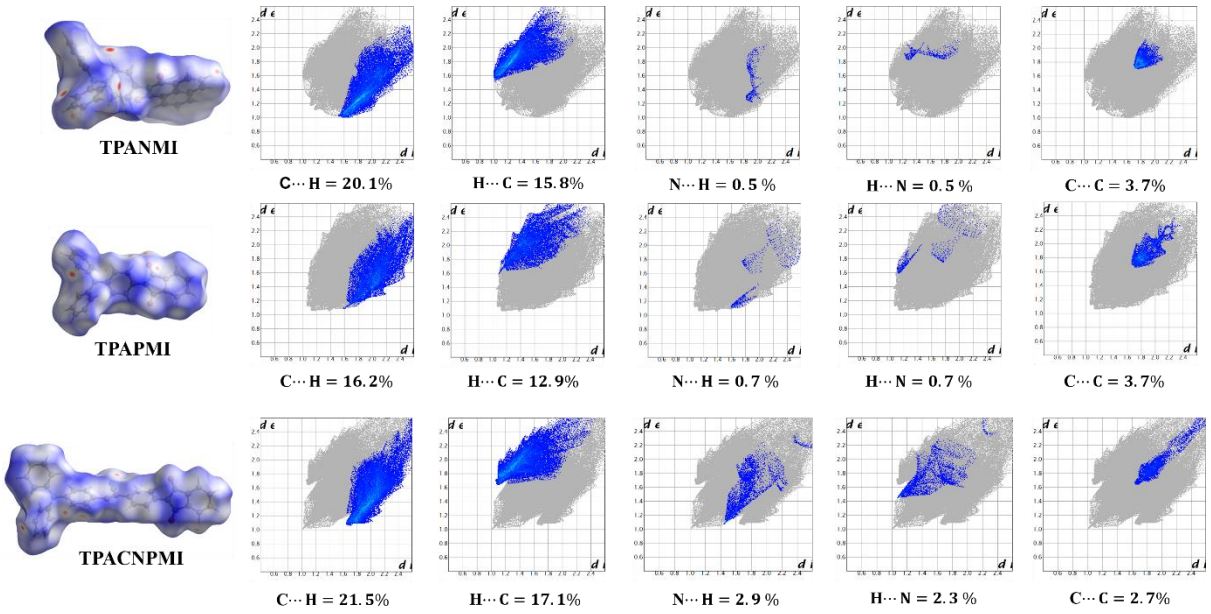

Figure A9: Normalized distance (d_{norm}) mapped over Hirshfeld surface of each luminogen (top row- TPANMI, middle row- TPAPMI, bottom row- TPACNPMI) along with generated finger print plots obtained from d_{norm} to decipher percentage of each type of non-covalent interaction. The grey part in the finger print plot indicates total interactions.

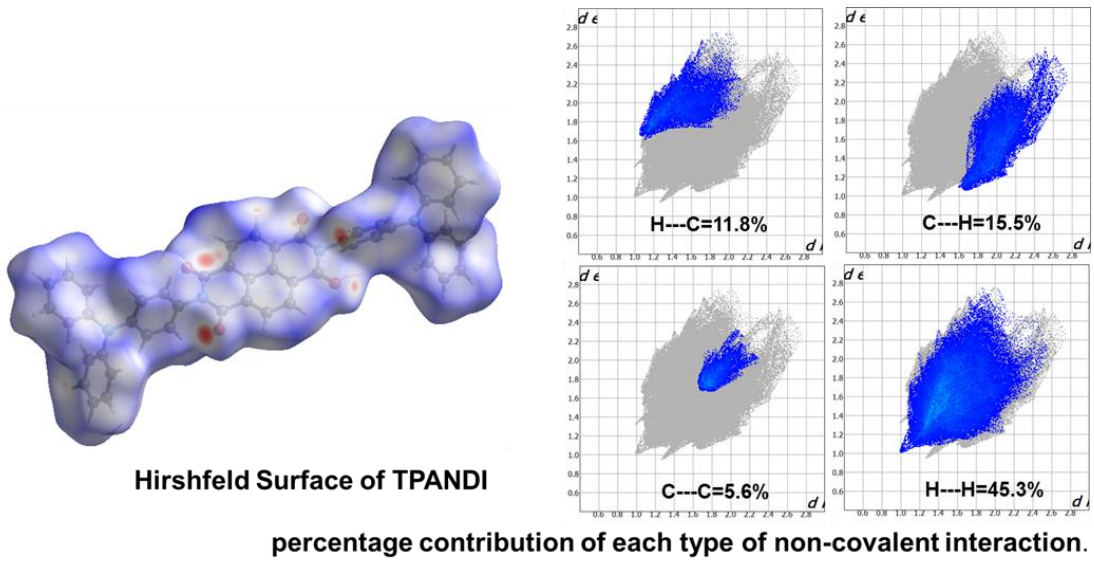

Figure A10: Normalized distance (d_{norm}) mapped over Hirshfeld surface of TPANDI along with generated finger print plots obtained from d_{norm} to decipher percentage of each type of non-covalent interaction. The grey part in the finger print plot indicates total interactions.

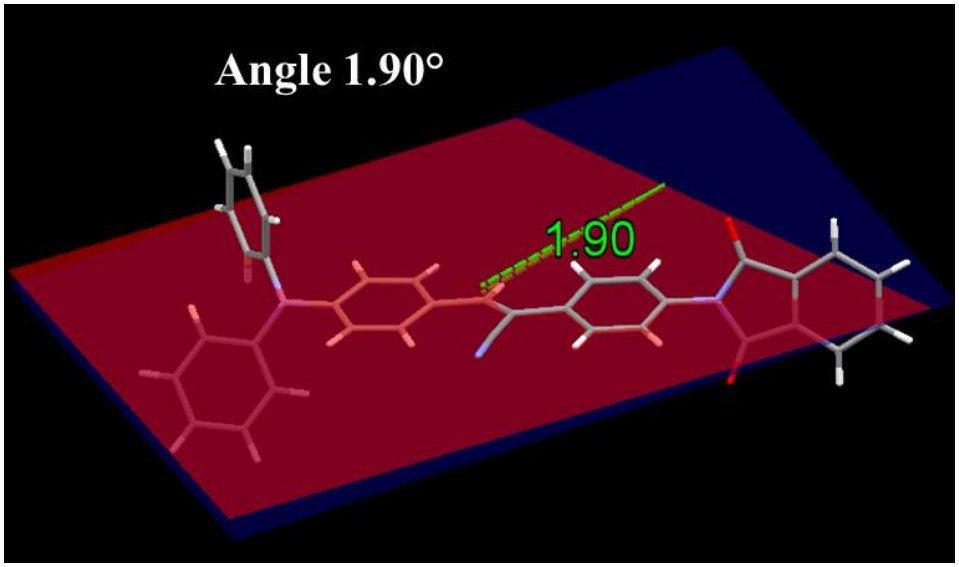

Figure A11: Two planes going through the phenyl ring of triphenylamine moiety and another one bearing the cyano-ethylene group and benzene linker makes a very small angle of 1.90^0.

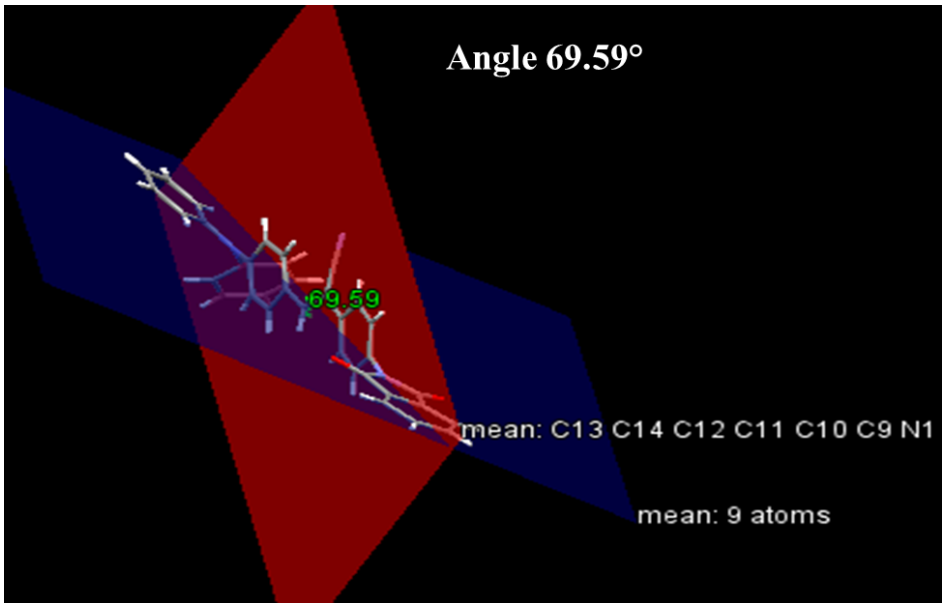

Figure A12: Twisting angle between the planar middle core and the planar phthalimide acceptor moiety.

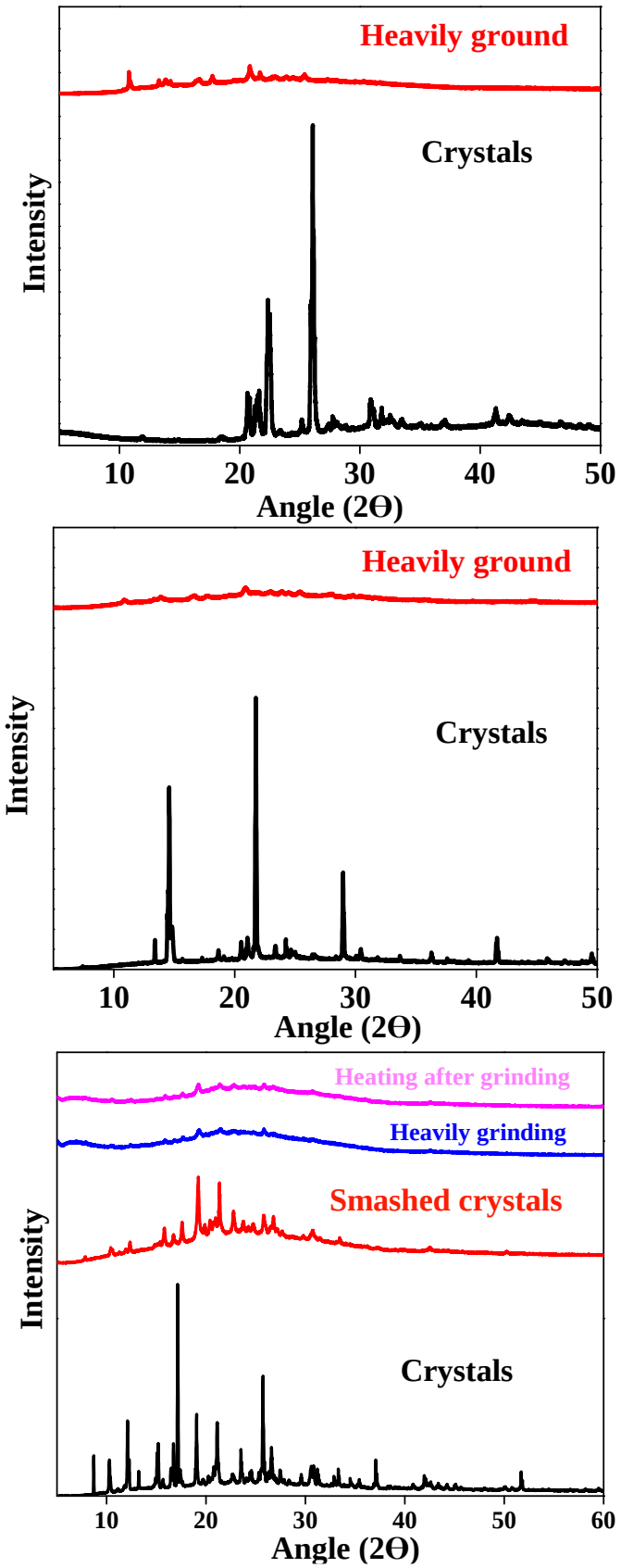

Figure A13: PXRD data of TPANMI (top), TPAPMI (middle) and TPACNPMI (bottom).

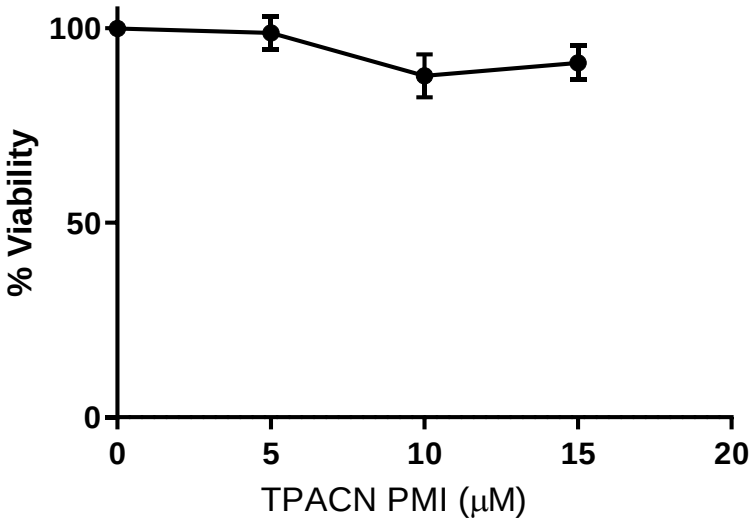

Figure A14: MTT viability assay of MCF7 in presence of different concentration of dye (TPACNPMI).

Section A6: Solution state thermally activated delayed fluorescence (TADF)

Solution state photophysical properties of AIE active luminogens can vary a lot from its solid state photophysics, and some time it can be highly interesting too. Whether, the nature of emission in solution state also involves triplet excitons, we measured the steady-state emission spectra for all the AIE active luminogens in aerated and degassed toluene. Interestingly, the emission intensity in degassed toluene got enhanced for all the AIE active luminogens, suggesting an involvement of triplet excitons in the emission process as these triplet excitons are often very much sensitive towards oxygen and humidity. Upon collecting the emission of the purged toluene solution at a delay time of several microsecond (to effectively remove the emission contribution from prompt fluorescence), it was observed that in all three cases, the delayed emission is taking place from the same state as that of prompt fluorescence (S_1 state), which proves that in solution state these AIE active luminogens are able to exhibit TADF (thermally activated delayed fluorescence) properties.

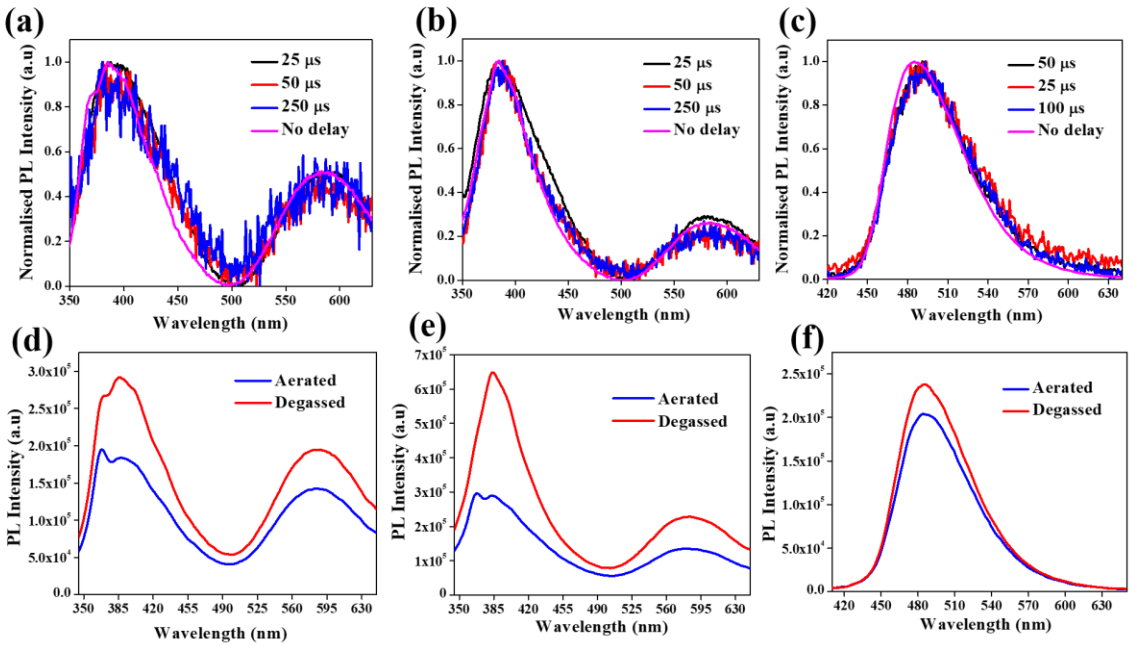

Figure A15: PL spectra of (a) TPANMI, (b) TPAPMI and (c) TPACNPMI in degassed toluene at different time-delay. Steady-state spectra of (d) TPANMI, (e) TPAPMI and (f) TPACNPMI in both aerated and degassed condition. Excitation wavelength in case of TPANMI and TPAPMI was 330 nm and 400 nm for TPACNPMI.

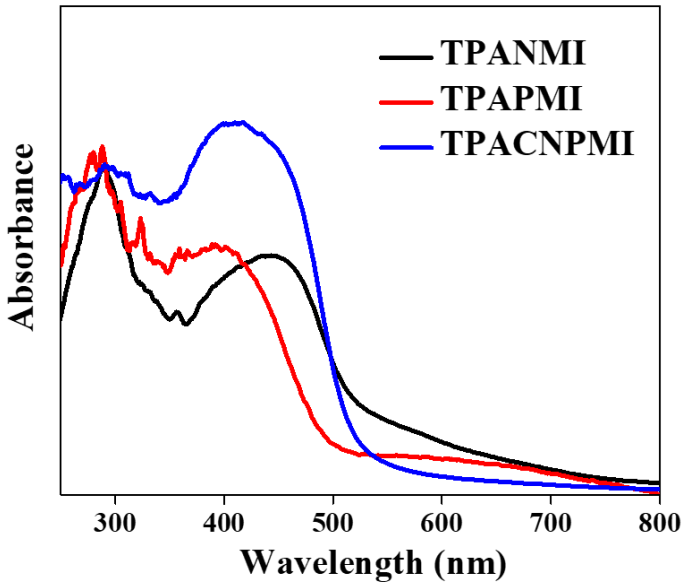

Figure A16: DRS-UV-Vis absorption spectra of TPANMI, TPAPMI and TPACNPMI in crystalline state.

Section A7: Two photon absorption properties of TPACNPMI

We have measured the two-photon absorption cross section of the two-photon active AIEgen, TPACNPMI (100 μM sample in 5% DMSO-water) using a multiphoton microscope (Leica, Germany) with tuneable fs-laser excitation source (Figure A17). For the collection of two-photon excited emission spectrum (TPEF) the sample was excited at 845 nm and the emission was collected with a 10 nm step-size. The excitation spectrum was collected by keeping the emission window constant (520-620 nm) upon changing the excitation from 710 nm-1300 nm with 20 nm difference.

Several techniques can be used to measure two-photon absorption cross-section of two-photon active luminogens such as- Z-scan, TPEF technique etc. We have used the later method here with rhodamine 6G in methanol as the reference compound and the excitation wavelength was chosen as 845 nm. At first, the TPEF cross-section was calculated using equation (1)[67].

$$\sigma_e = \sigma_{e,r} \frac{C_r}{C} \frac{n_r}{n} \frac{F}{F_r} \qquad (1)$$

In this equation, r stands for the reference compound, n for refractive index, c for concentration and F for integral fluorescence intensity. Further the TPA cross section can be obtained from the TPEF cross-section using equation (2)[67].

$$\sigma = \sigma_e / \phi' \qquad (2)$$

In this equation, ϕ' stands for two photon excited fluorescence quantum yield. Since, it is very difficult to obtain ϕ' directly, we have assumed that $\phi' = \phi$ (where ϕ is the single photon excited fluorescence quantum yield of the sample). The fluorescence quantum yield of the sample (100 µM of TPACNPMI in 5% DMSO-water) was found to be 5.78% (measured using an integrated sphere). Following this way, the two-photon cross-section of the sample was found to be ~ 510 GM (excitation at 845 nm).

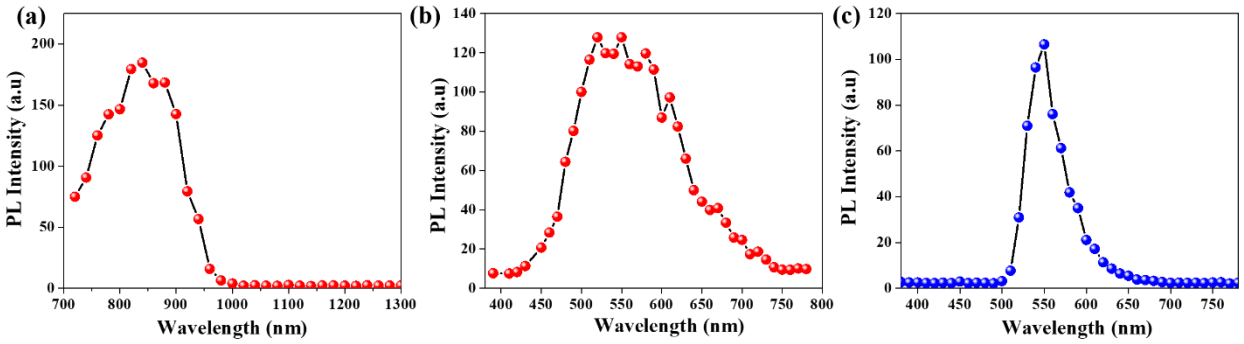

Figure A17: (a) Two photon excited fluorescence excitation spectrum of 100 µM TPACNPMI in 5% DMSO-water mixture. (b) two photon excited fluorescence emission (TPEF) spectrum of 100 µM TPACNPMI in 5% DMSO-water mixture (sample). (b) two photon excited fluorescence emission (TPEF) spectrum of 20 µM rhodamine 6G in methanol.

2.11 References:

(1) Balch, A. L. Dynamic Crystals: Visually Detected Mechanochemical Changes in the Luminescence of Gold and Other Transition-Metal Complexes. *Angew. Chem., Int. Ed.* **2009**, *48* (15), 2641–2644.

(2) Yoon, S.-J.; Chung, J. W.; Gierschner, J.; Kim, K. S.; Choi, M.-G.; Kim, D.; Park, S. Y. Multistimuli Two-Color Luminescence Switching via Different Slip-Stacking of Highly Fluorescent Molecular Sheets. *J. Am. Chem. Soc.* **2010**, *132* (39), 13675–13683.

(3) Zhang, G.; Lu, J.; Sabat, M.; Fraser, C. L. Polymorphism and Reversible Mechanochromic Luminescence for Solid-State Difluoroboron Avobenzone. *J. Am. Chem. Soc.* **2010**, *132* (7), 2160–2162.

(4) Yagai, S.; Okamura, S.; Nakano, Y.; Yamauchi, M.; Kishikawa, K.; Karatsu, T.; Kitamura, A.; Ueno, A.; Kuzuhara, D.; Yamada, H.; et al. Design Amphiphilic Dipolar π-Systems for Stimuli-Responsive Luminescent Materials Using Metastable States. *Nat. Commun.* **2014**, *5* (1), 4013.

(5) Sun, H.; Liu, S.; Lin, W.; Zhang, K. Y.; Lv, W.; Huang, X.; Huo, F.; Yang, H.; Jenkins, G.; Zhao, Q.; et al. Smart Responsive Phosphorescent Materials for Data Recording and Security Protection. *Nat. Commun.* **2014**, *5* (1), 3601.

(6) Li, Z.; Toivola, R.; Ding, F.; Yang, J.; Lai, P.-N.; Howie, T.; Georgeson, G.; Jang, S.-H.; Li, X.; Flinn, B. D.; et al. Highly Sensitive Built-In Strain Sensors for Polymer Composites: Fluorescence Turn-On Response through Mechanochemical Activation. *Adv. Mater.* **2016**, *28* (31), 6592–6597.

(7) Lavrenova, A.; Balkenende, D. W. R.; Sagara, Y.; Schrettl, S.; Simon, Y. C.; Weder, C. Mechano- and Thermoresponsive Photoluminescent Supramolecular Polymer. *J. Am. Chem. Soc.* **2017**, *139* (12), 4302–4305.

(8) Roy, B.; Reddy, M. C.; Hazra, P. Developing the Structure–Property Relationship to Design Solid State Multi-Stimuli Responsive Materials and Their Potential Applications in Different Fields. *Chem. Sci.* **2018**, *9* (14), 3592–3606.

(9) Mei, J.; Leung, N. L. C.; Kwok, R. T. K.; Lam, J. W. Y.; Tang, B. Z. Aggregation-Induced Emission: Together We Shine, United We Soar! *Chem. Rev.* **2015**, *115* (21), 11718–11940.

(10) Luo, J.; Xie, Z.; Lam, J. W. Y.; Cheng, L.; Chen, H.; Qiu, C.; Kwok, H. S.; Zhan, X.; Liu, Y.; Zhu, D.; et al. Aggregation-Induced Emission of 1-Methyl-1,2,3,4,5-Pentaphenylsilole. *Chem. Commun.* **2001**, No. 18, 1740–1741.

(11) Li, D.; Yu, J.; Xu, R. Mesoporous Silica Functionalized with an AIE Luminogen for Drug Delivery. *Chem. Commun.* **2011**, *47* (39), 11077–11079.

(12) Qin, W.; Ding, D.; Liu, J.; Yuan, W. Z.; Hu, Y.; Liu, B.; Tang, B. Z. Biocompatible Nanoparticles with Aggregation-Induced Emission Characteristics as Far-Red/Near-Infrared

Fluorescent Bioprobes for In Vitro and In Vivo Imaging Applications. *Adv. Funct. Mater.* **2012**, *22* (4), 771–779.

(13) Zhao, N.; Li, M.; Yan, Y.; Lam, J. W. Y.; Zhang, Y. L.; Zhao, Y. S.; Wong, K. S.; Tang, B. Z. A Tetraphenylethene-Substituted Pyridinium Salt with Multiple Functionalities: Synthesis, Stimuli-Responsive Emission, Optical Waveguide and Specific Mitochondrion Imaging. *J. Mater. Chem. C* **2013**, *1* (31), 4640–4646.

(14) Hu, R.; Leung, N. L. C.; Tang, B. Z. AIE Macromolecules: Syntheses, Structures and Functionalities. *Chem. Soc. Rev.* **2014**, *43* (13), 4494–4562.

(15) Wang, Z.; Yan, L.; Zhang, L.; Chen, Y.; Li, H.; Zhang, J.; Zhang, Y.; Li, X.; Xu, B.; Fu, X.; et al. Ultra Bright Red AIE Dots for Cytoplasm and Nuclear Imaging. *Polym. Chem.* **2014**, *5* (24), 7013–7020.

(16) Wang, H.; Liu, G. Advances in Luminescent Materials with Aggregation-Induced Emission (AIE) Properties for Biomedical Applications. *J. Mater. Chem. B* **2018**, *6* (24), 4029–4042.

(17) Feng, G.; Liu, B. Aggregation-Induced Emission (AIE) Dots: Emerging Theranostic Nanolights. *Acc. Chem. Res.* **2018**, *51* (6), 1404–1414.

(18) Guo, L.-X.; Xing, Y.-B.; Wang, M.; Sun, Y.; Zhang, X.-Q.; Lin, B.-P.; Yang, H. Luminescent Liquid Crystals Bearing an Aggregation-Induced Emission Active Tetraphenylthiophene Fluorophore. *J. Mater. Chem. C* **2019**, *7* (16), 4828–4837.

(19) Roy, R.; Sajeev, N. R.; Sharma, V.; Koner, A. L. Aggregation Induced Emission Switching Based Ultrasensitive Ratiometric Detection of Biogenic Diamines Using a Perylenediimide-Based Smart Fluoroprobe. *ACS Appl. Mater. Interfaces* **2019**, *11* (50), 47207–47217.

(20) De, J.; M. M., A. H.; Yadav, R. A. K.; Gupta, S. P.; Bala, I.; Chawla, P.; Kesavan, K. K.; Jou, J.-H.; Pal, S. K. AIE-Active Mechanoluminescent Discotic Liquid Crystals for Applications in OLEDs and Bio-Imaging. *Chem. Commun.* **2020**, *56* (91), 14279–14282.

(21) Han, T.; Gu, X.; Lam, J. W. Y.; Leung, A. C. S.; Kwok, R. T. K.; Han, T.; Tong, B.; Shi, J.; Dong, Y.; Tang, B. Z. Diaminomaleonitrile-Based Schiff Bases: Aggregation-Enhanced Emission, Red Fluorescence, Mechanochromism and Bioimaging Applications. *J. Mater. Chem. C* **2016**, *4* (44), 10430–10434.

(22) Kabe, R.; Notsuka, N.; Yoshida, K.; Adachi, C. Afterglow Organic Light-Emitting Diode. *Adv. Mater.* **2016**, *28* (4), 655–660.

(23) Zhen, X.; Tao, Y.; An, Z.; Chen, P.; Xu, C.; Chen, R.; Huang, W.; Pu, K. Ultralong Phosphorescence of Water-Soluble Organic Nanoparticles for In Vivo Afterglow Imaging. *Adv. Mater.* **2017**, *29* (33), 1606665.

(24) Hayduk, M.; Riebe, S.; Voskuhl, J. Phosphorescence Through Hindered Motion of Pure Organic Emitters. *Chem. – A Eur. J.* **2018**, *24* (47), 12221–12230.

(25) Bolton, O.; Lee, K.; Kim, H.-J.; Lin, K. Y.; Kim, J. Activating Efficient Phosphorescence from Purely Organic Materials by Crystal Design. *Nat. Chem.* **2011**, *3* (3), 205–210.

(26) Shi, H.; An, Z.; Li, P.-Z.; Yin, J.; Xing, G.; He, T.; Chen, H.; Wang, J.; Sun, H.; Huang, W.; et al. Enhancing Organic Phosphorescence by Manipulating Heavy-Atom Interaction. *Cryst. Growth Des.* **2016**, *16* (2), 808–813.

(27) Gong, Y.; Chen, G.; Peng, Q.; Yuan, W. Z.; Xie, Y.; Li, S.; Zhang, Y.; Tang, B. Z. Achieving Persistent Room Temperature Phosphorescence and Remarkable Mechanochromism from Pure Organic Luminogens. *Adv. Mater.* **2015**, *27* (40), 6195–6201.

(28) Xue, P.; Sun, J.; Chen, P.; Wang, P.; Yao, B.; Gong, P.; Zhang, Z.; Lu, R. Luminescence Switching of a Persistent Room-Temperature Phosphorescent Pure Organic Molecule in Response to External Stimuli. *Chem. Commun.* **2015**, *51* (52), 10381–10384.

(29) Xu, B.; Wu, H.; Chen, J.; Yang, Z.; Yang, Z.; Wu, Y.-C.; Zhang, Y.; Jin, C.; Lu, P.-Y.; Chi, Z.; et al. White-Light Emission from a Single Heavy Atom-Free Molecule with Room Temperature Phosphorescence, Mechanochromism and Thermochromism. *Chem. Sci.* **2017**, *8* (3), 1909–1914.

(30) Zhao, J.; Wu, W.; Sun, J.; Guo, S. Triplet Photosensitizers: From Molecular Design to Applications. *Chem. Soc. Rev.* **2013**, *42* (12), 5323–5351.

(31) Chang, Z.-F.; Jing, L.-M.; Liu, Y.-Y.; Liu, J.-J.; Ye, Y.-C.; Zhao, Y. S.; Yuan, S.-C.; Wang, J.-L. Constructing Small Molecular AIE Luminophores through a 2,2-(2,2-Diphenylethene-1,1-Diyl)Dithiophene Core and Peripheral Triphenylamine with Applications in Piezofluorochromism, Optical Waveguides, and Explosive Detection. *J. Mater. Chem. C* **2016**, *4* (36), 8407–8415.

(32) Zhan, Y.; Yang, P.; Li, G.; Zhang, Y.; Bao, Y. Reversible Piezofluorochromism of a Triphenylamine-Based Benzothiazole Derivative with a Strong Fluorescence Response to Volatile Acid Vapors. *New J. Chem.* **2017**, *41* (1), 263–270.

(33) Sheldrick, G. M. A Short History of {\it SHELX}. *Acta Crystallogr. Sect. A* **2008**, *64* (1), 112–122.

(34) Sheldrick, G. M. Crystal structure refinement with SHELXL. *Acta Crystallogr., Sect. A: Found. Adv.* **2015**, 71, 3−8.

(35) Frisch, M. J.; Trucks, G. W.; Schlegel, H. B.; Scuseria, G. E.; Robb, M. A.; Cheeseman, J. R.; Scalmani, G.; Barone, V.; Mennucci, B.; Petersson, G. A.; et al. Gaussian 09, Revision C.01; Gaussian Inc.: Wallingford, CT, **2009**.

(36) Becke, A. D. Density-Functional Exchange-Energy Approximation with Correct Asymptotic Behavior. *Phys. Rev. A* **1988**, *38* (6), 3098–3100.

(37) Lee, C.; Yang, W.; Parr, R. G. Development of the Colle-Salvetti Correlation-Energy Formula into a Functional of the Electron Density. *Phys. Rev. B* **1988**, *37* (2), 785–789.

(38) Time-dependent Density Functional Theory, Lecture Notes of Physics; Marques, M. A. L., Ullrich, C.

(39) Isukapalli, S. V. K.; Lekshmi, R. S.; Samanta, P. K.; Vennapusa, S. R. Formation of Excited Triplet States in Naphthalene Diimide and Perylene Diimide Derivatives: A Detailed Theoretical Study. *J. Chem. Phys.* **2020**, *153* (12), 124301.

(40) Gao, X.; Bai, S.; Fazzi, D.; Niehaus, T.; Barbatti, M.; Thiel, W. Evaluation of Spin-Orbit Couplings with Linear-Response Time-Dependent Density Functional Methods. *J. Chem. Theory Comput.* **2017**, *13* (2), 515–524.

(41) Janiak, C. A Critical Account on π–π Stacking in Metal Complexes with Aromatic Nitrogen-Containing Ligands. *J. Chem. Soc. Dalt. Trans.* **2000**, No. 21, 3885–3896.

(42) Li, C.; Yang, W.; Zhou, W.; Zhang, M.; Xue, R.; Li, M.; Cheng, Z. Branching Effect for Aggregation-Induced Emission in Fluorophores Containing Imine and Triphenylamine Structures. *New J. Chem.* **2016**, *40* (10), 8837–8845.

(43) Samanta, P. K.; Kim, D.; Coropceanu, V.; Brédas, J.-L. Up-Conversion Intersystem Crossing Rates in Organic Emitters for Thermally Activated Delayed Fluorescence: Impact of the Nature of Singlet vs Triplet Excited States. *J. Am. Chem. Soc.* **2017**, *139* (11), 4042–4051.

(44) Sasikumar, D.; John, A. T.; Sunny, J.; Hariharan, M. Access to the Triplet Excited States of Organic Chromophores. *Chem. Soc. Rev.* **2020**, *49* (17), 6122–6140.

(45) Koninti, R. K.; Miyata, K.; Saigo, M.; Onda, K. Achieving Thermally Activated Delayed Fluorescence from Benzophenone by Host–Guest Complexation. *J. Phys. Chem. C* **2021**, *125* (31), 17392–17399.

(46) Isukapalli, S. V. K.; Lekshmi, R. S.; Samanta, P. K.; Vennapusa, S. R. Formation of Excited Triplet States in Naphthalene Diimide and Perylene Diimide Derivatives: A Detailed Theoretical Study. *J. Chem. Phys.* **2020**, *153* (12), 124301.

(47) Zhang, L.; Li, M.; Hu, T.-P.; Wang, Y.-F.; Shen, Y.-F.; Yi, Y.-P.; Lu, H.-Y.; Gao, Q.-Y.; Chen, C.-F. Phthalimide-Based "D–N–A" Emitters with Thermally Activated Delayed Fluorescence and Isomer-Dependent Room-Temperature Phosphorescence Properties. *Chem. Commun.* **2019**, *55* (81), 12172–12175.

(48) Xie, Z.; Yang, B.; Li, F.; Cheng, G.; Liu, L.; Yang, G.; Xu, H.; Ye, L.; Hanif, M.; Liu, S.; et al. Cross Dipole Stacking in the Crystal of Distyrylbenzene Derivative: The Approach toward High Solid-State Luminescence Efficiency. *J. Am. Chem. Soc.* **2005**, *127* (41), 14152–14153.

(49) Itoh, Y.; Nakashima, Y.; Tsukamoto, S.; Kurohara, T.; Suzuki, M.; Sakae, Y.; Oda, M.; Okamoto, Y.; Suzuki, T. N+-C-H···O Hydrogen Bonds in Protein-Ligand Complexes. *Sci. Rep.* **2019**, *9* (1), 767.

(50) Wang, T.; Hu, Z.; Nie, X.; Huang, L.; Hui, M.; Sun, X.; Zhang, G. Thermochromic Aggregation-Induced Dual Phosphorescence via Temperature-Dependent Sp3-Linked Donor-Acceptor Electronic Coupling. *Nat. Commun.* **2021**, *12* (1), 1364.

(51) Imoto, H.; Fujii, R.; Naka, K. 3,4-Diaminomaleimide Dyes – Simple Luminophores with Efficient Orange-Red Emission in the Solid State. *European J. Org. Chem.* **2018**, *2018* (6), 837–843.

(52) Dreuw, A.; Plötner, J.; Lorenz, L.; Wachtveitl, J.; Djanhan, J. E.; Brüning, J.; Metz, T.; Bolte, M.; Schmidt, M. U. Molecular Mechanism of the Solid-State Fluorescence Behavior of

the Organic Pigment Yellow 101 and Its Derivatives. *Angew. Chem., Int. Ed.* **2005**, *44* (47), 7783–7786.

(53) Tang, S.-X.; Wang, N.; Xu, X.-D.; Feng, S. A Ratiometric Fluorescent Thermometer Based on Amphiphilic Alkynylpyrene Derivatives. *New J. Chem.* **2019**, *43* (17), 6461–6464.

(54) Feng, J.; Tian, K.; Hu, D.; Wang, S.; Li, S.; Zeng, Y.; Li, Y.; Yang, G. A Triarylboron-Based Fluorescent Thermometer: Sensitive Over a Wide Temperature Range. *Angew. Chem., Int. Ed.* **2011**, *50* (35), 8072–8076.

(55) Hariharan, P. S.; Venkataramanan, N. S.; Moon, D.; Anthony, S. P. Self-Reversible Mechanochromism and Thermochromism of a Triphenylamine-Based Molecule: Tunable Fluorescence and Nanofabrication Studies. *J. Phys. Chem. C* **2015**, *119* (17), 9460–9469.

(56) Lu, Q.; Wu, C.-J.; Liu, Z.; Niu, G.; Yu, X. Fluorescent AIE-Active Materials for Two-Photon Bioimaging Applications. *Frontiers in Chemistry* **2020**, 8, 1205.

(57) Bednarska, J.; Zaleśny, R.; Arul Murugan, N.; Bartkowiak, W.; Ågren, H.; Odelius, M. Elucidating the Mechanism of Zn2+ Sensing by a Bipyridine Probe Based on Two-Photon Absorption. *J. Phys. Chem. B* **2016**, *120* (34), 9067–9075.

(58) Şimşek, Y.; Brown, A. Two-Photon Absorption Properties of Gold Fluorescent Protein: A Combined Molecular Dynamics and Quantum Chemistry Study. *J. Phys. Chem. B* **2018**, *122* (22), 5738–5748.

(59) Zheng, Z.; Zhang, T.; Liu, H.; Chen, Y.; Kwok, R. T. K.; Ma, C.; Zhang, P.; Sung, H. H. Y.; Williams, I. D.; Lam, J. W. Y.; et al. Bright Near-Infrared Aggregation-Induced Emission Luminogens with Strong Two-Photon Absorption, Excellent Organelle Specificity, and Efficient Photodynamic Therapy Potential. *ACS Nano* **2018**, *12* (8), 8145–8159.

(60) Yuan Chiu, K.; Xiang Su, T.; Hong Li, J.; Lin, T.-H.; Liou, G.-S.; Cheng, S.-H. Novel Trends of Electrochemical Oxidation of Amino-Substituted Triphenylamine Derivatives. *J. Electroanal. Chem.* **2005**, *575* (1), 95–101.

(61) Hsiao, S.-H.; Chen, Y.-Z. Electroactive and Ambipolar Electrochromic Polyimides from Arylene Diimides with Triphenylamine N-Substituents. *Dye. Pigment.* **2017**, *144*, 173–183.

(62) Zhao, B.; Yang, B.; Hu, X.; Liu, B. Two Colorimetric and Ratiometric Fluorescence Probes for Hydrogen Sulfide Based on AIE Strategy of α–Cyanostilbenes. *Spectrochim. Acta*

Part A Mol. Biomol. Spectrosc. **2018**, *199*, 117–122.

(63) Martin, A. D.; Britton, J.; Easun, T. L.; Blake, A. J.; Lewis, W.; Schröder, M. Hirshfeld Surface Investigation of Structure-Directing Interactions within Dipicolinic Acid Derivatives. *Cryst. Growth Des.* **2015**, *15* (4), 1697–1706.

(64) Martin, A. D.; Hartlieb, K. J.; Sobolev, A. N.; Raston, C. L. Hirshfeld Surface Analysis of Substituted Phenols. *Cryst. Growth Des.* **2010**, *10* (12), 5302–5306.

(65) McKinnon, J. J.; Jayatilaka, D.; Spackman, M. A. Towards Quantitative Analysis of Intermolecular Interactions with Hirshfeld Surfaces. *Chem. Commun.* **2007**, No. 37, 3814–3816.

(66) Spackman, P. R.; Turner, M. J.; McKinnon, J. J.; Wolff, S. K.; Grimwood, D. J.; Jayatilaka, D.; Spackman, M. A. CrystalExplorer: A Program for Hirshfeld Surface Analysis, Visualization and Quantitative Analysis of Molecular Crystals. *J. Appl. Crystallogr.* **2021**, *54* (3), 1006–1011.

(67) Cao, D.; Liu, Z.; Li, G.; Liu, G.; Zhang, G. Synthesis and Blue-Violet Two-Photon Excited Fluorescence of a New Organoboron Compound. *J. Mol. Struct.* **2008**, *874* (1), 46–50.

Chapter -3

Engineering TADF, Mechanochromism, and Second Harmonic Up-conversion Properties in Regioisomeric Substitution Space

3.1 Motivation:

This chapter explores the distinct TADF efficiency of three donor-acceptor based regio-isomers: DPAOCN (ortho-isomer), DPAMCN (meta-isomer), and DPAPCN (para-isomer). DPAPCN exhibits maximum TADF efficiency in both solution and solid-state with an impressive reverse inter-system crossing (RISC) rate of ~ 10^6 s^{-1}; the underlying cause being the minimum singlet-triplet splitting energy or ΔE_{ST} (< 0.1 eV) and maximum SOC (spin-orbit coupling) value of ~ 1.3 cm^{-1} between the S_1 & T_1 states. The ortho-isomer, on the other hand, has the slowest RISC rate due to its highest singlet-triplet splitting energy and lowest SOC value. Apart from TADF, differences in crystal packing of the regio-isomers can result in intriguing bulk phase properties like- mechanochromic luminescence (MCL) and non-linear optical properties like- second harmonic generation (SHG). DPAOCN, with its non-centrosymmetric $P2_12_12_1$ space group and substantial crystal void volume, enchants with reversible tri-color mechanochromic luminescent behavior, while the meta and para isomers, due to their centrosymmetric packing and diminished crystal void volume, remain inert to mechanical pressure. Expanding the horizon of possibilities, the non-centrosymmetric nature of ortho-isomer further renders it an excellent SHG material, with the $\chi^{(2)}$ value of 0.19 pm/V at 1220 nm and laser-induced damage threshold (LIDT) value of 13.27 GW/cm^2. Additionally, converted LEDs (c-LEDs) are fabricated to explore the electroluminescence potential of the regio-isomers for practical OLED applications. Further, the two-photon activity of all three isomers finds application in two-photon confocal cell imaging. Overall, exploration of TADF, SHG, and mechanochromic luminescent properties has been conducted among the regio-isomers. The para-isomer has been identified as the most efficient TADF emitter, whereas, the ortho-isomer is the one endowed with all the aforementioned attributes.

3.2 Introduction:

Multifunctional organic luminescent materials with delayed fluorescence and phosphorescence have revolutionized the field of optoelectronics by providing a flexible platform for applications in organic light-emitting diodes (OLED), bio-imaging, sensing, and photocatalysis.[1–8] Over the last decade, plenty of attempts have been made towards improving TADF efficiencies, minimizing the efficiency roll-off, and expanding the scope of these prodigious emitters to be utilized in bright OLED displays. Several effective strategies have been implemented, such as enhancing intramolecular charge transfer (ICT),[9–11] increasing

molecular rigidity,[12,13] incorporating through-space charge transfer (TSCT),[14,15] and so on. All these strategies involve significant structural modifications that encompass major perturbations in the molecular architecture for tuning TADF properties. Nevertheless, there remains a lack of generalized strategies for well-directed customization of the molecular skeleton of the emitters, which can moderately enhance the TADF efficiency while keeping all other associated properties unperturbed. Moreover, it is of utmost importance to incorporate such changes through minimal structural modulation, so that productivity and cost-effectiveness can be maintained. Additionally, it is crucial to avoid the introduction of large functional groups and changing the overall molecular skeleton, as this can sometimes lead to conclusions that do not correspond to the actual design strategy. In this aspect, regio-isomerism can be an important step forward as it can lead to a dramatic impact on the energy levels (both singlets and triplets) of a chromophoric entity. The introduction of the regio-isomers to improve the TADF functionalities is still under development and is restricted to a few structural frameworks.[16,17] Moreover, simultaneous tuning of TADF efficiencies along with color changes over a wider range remains elusive to date. Our work aims to explore this methodology by focusing on three regio-isomers (ortho, meta, and para) based on diphenylamine donors (**Scheme 1**) that provide sequential control of emission. characteristics and TADF efficiencies. Additionally, the cost-effective structural changes in three isomers can competently tune the singlet-triplet energy gap, thereby improving the thermal up-conversion efficiency. The results in solution, doped film, and powdered states show an increasing rate of reverse-intersystem crossing (RISC) from ortho to para isomers which is consistent with experimentally calculated ΔE_{ST} values along with a wide range of emission color tunability from green to red. The RISC rates can even go up to ~10^6 s^{-1} in the para-isomer compared to only ~10^2-10^4 s-1 of the ortho-isomer. The electroluminescence potential of all three isomers has been further explored through the fabrication of converted LEDs (c-LEDs) with three different emission colors. Moreover, these three different regio-isomers inherently induce perturbations in the symmetry elements at the molecular level, which modulates the crystal packing arrangement and induces anisotropy in the polarizability of the condensed bulk phase, and results in the revelation of important bulk properties like- mechanochromic luminescence (MCL), non-linear optical (NLO) properties like – second harmonic generation (SHG), and so on.[18–20] The insertion of molecular asymmetry in the ortho-isomer led to a non-centrosymmetric $P2_12_12_1$ crystal space group, resulting in excellent reversible tri-color mechanachromic luminescent characteristics and making it a superb SHG material with a $\chi^{(2)}$ value of 0.19 pm/V at 1220 nm and laser-induced

damage threshold (LIDT) value of 13.27 GW/cm^2. Notably, the stimuli-responsive emission property of ortho-isomer makes it an ideal mechanochromic luminescent TADF molecule (MCL-TADF). This class of smart luminogens combines mechanochromism and TADF, offering exciting prospects in sensing, displays, and lighting technology. Furthermore, due to the charge transfer nature of all three isomers, they are active for two-photon absorption, which has been further exploited for two-photon excited confocal cell imaging without compromising cellular viability. Altogether, this work explores the multi-faceted nature of three donor-acceptor regioisomers with a major focus on TADF, SHG, and mechanochromic luminescent properties. Based on the molecular level understanding and bulk phase properties, the para-isomer is identified as the most efficient TADF emitter with the largest RISC rate, whereas, the ortho-isomer is judiciously extracted as the one to manifest simultaneous TADF, mechanochromic luminescence, and SHG properties.

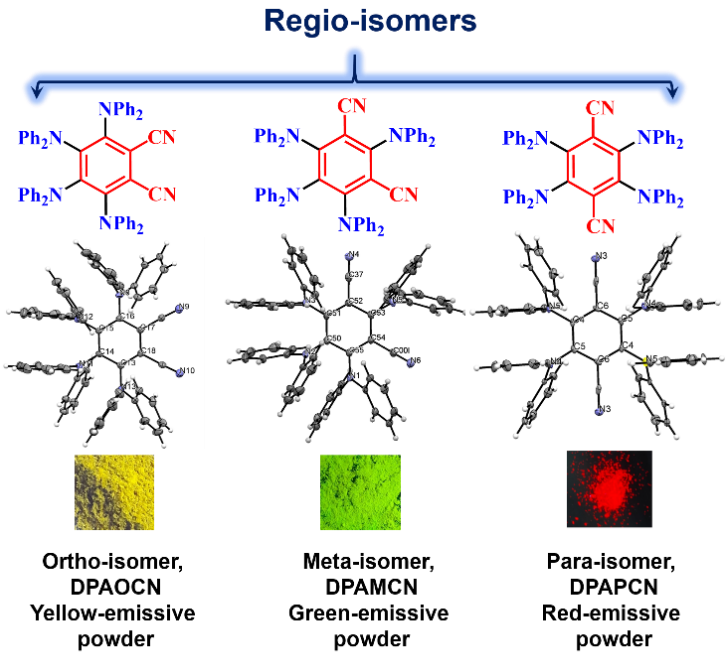

Scheme 1. Molecular structures of all three regio-isomers.

3.3 Brief synthetic procedure and characterization data:

All the final products have been synthesized by a nucleophilic substitution reaction in dry polar aprotic solvent using NaH as a base in a single-step reaction. Varying time-condition is used unless the starting material in each case gets consumed. The final products in all three cases have been purified by a SiO_2 column chromatography, using a DCM-Hexane solvent system. The products are thoroughly characterized using ^{1}H, ^{13}C, HRMS spectroscopic techniques, and

finally by single crystal X-ray diffraction data. Details are outlined in **Section A1 of Appendix**. The characterization data of all three molecules are stated below-

(a) For DPAOCN:

^{1}H NMR (400 MHz, CHLOROFORM-D): δ 7.19 (dd, *J* = 8.4, 7.5 Hz, 8H), 6.97 (dd, *J* = 10.6, 4.1 Hz, 4H), 6.85 (dd, *J* = 8.3, 7.5 Hz, 8H), 6.77 (dd, *J* = 8.5, 0.9 Hz, 8H), 6.69 (t, *J* = 7.3 Hz, 4H), 6.43 (dd, *J* = 8.5, 0.8 Hz, 8H).

^{13}C NMR (100 MHz, CHLOROFORM-D): δ 150.43, 148.02, 144.92, 143.90, 128.96, 127.71, 123.86, 123.55, 122.41, 122.30, 116.96, 113.57.

HRMS (ESI TOF): *m/z* calcd. For $C_{56}H_{41}N_6$ $[M+H]^+$ 797.3393 found 797.3394.

(b) For DPAMCN:

^{1}H NMR (400 MHz, CHLOROFORM-D): δ 7.32-7.22 (m, 4H), 7.13 – 7.06 (m, 12H), 7.02 (t, *J* = 7.4 Hz, 2H), 6.96-6.84 (m, 8H), 6.70 (d, *J* = 7.7 Hz, 10H), 6.56 (d, *J* = 7.8 Hz, 4H).

^{13}C NMR (100 MHz, CHLOROFORM-D): δ 154.32, 151.91, 145.66, 144.80, 143.28, 140.4, 129.51, 128.73, 127.69, 124.31, 124.08, 123.06, 122.76, 122.72, 121.20, 113.28, 113.14.

HRMS (ESI TOF): *m/z* calcd. For $C_{56}H_{41}N_6$ $[M+H]^+$ 797.3393 found 797.3385.

(c) For DPAPCN:

^{1}H NMR (400 MHz, CHLOROFORM-D): δ 7.15 – 7.08 (m, 16H), 6.88 (t, *J* = 7.4 Hz, 8H), 6.82 – 6.76 (m, 16H).

^{13}C NMR (100 MHz, CHLOROFORM-D): δ 146.05, 144.87, 128.89, 123.70, 122.67, 122.13, 113.34.

HRMS (ESI TOF): *m/z* calcd. For $C_{56}H_{41}N_6$ $[M+H]^+$ 797.3393 found 797.3322.

3.4 Instrumentation:

^{1}H NMR (at 400 MHz) and ^{13}C NMR (at 100 MHz) data characterizations of all the synthesized compounds are performed using JEOL ECS-400 and Bruker Ascend TM 400 spectrometer using deuterated chloroform ($CDCl_3$) as solvent (having residual chloroform) and tetramethylsilane (TMS) as the internal standard. Chemical shift (δ) values are measured in

ppm downfield from CDCl3 (δ = 7.26 ppm) for 1H NMR and relative to central $CDCl_3$ resonance (δ = 77.16 ppm) for ^{13}C NMR. High-resolution mass spectra (HRMS) for all the compounds are recorded using ESI TOF in Water's SYNAPT G2 mass spectrometer. Single-crystal diffraction analysis data were collected at 100K with a BRUKER KAPPA APEX II CCD Duo diffractometer (operated at 1500 W power: 50 kV, 30 mA) using graphite monochromatic Mo Kα radiation (λ = 0.71073 Å). The structures were solved by direct methods and refined by least-squares against F2 utilizing the software package SHELXL-97.[21-22] More information on crystal structures can also be obtained from the Cambridge Crystallographic Data Centre under the CCDC deposition number. Powder XRD experiments are carried out using BRUKAR D8 advanced X-ray diffractometer with a Cu-Kα radiation source. Steady-state solution-based absorption spectra are recorded on Shimadzu, UV-2600 UV spectrophotometer. Steady-state emission spectra and time-gated emission spectra of all the samples in solution and solid state are carried out using Fluoromax-4C spectrofluorimeter and Fluorolog-3 phosphorimeter (HORIBA), respectively. TGA experiments were carried out using PerkinElmer STA 6000 instrument. Solid state UV-VIS absorption spectrum was collected using Shimadzu UV-3600i plus spectrophotometer. Time-resolved PL decay profiles have been recorded either using a diode-laser source (for a total time window <50 μs) or a microsecond flash lamp source (of 1.5-2.5 μs bandwidth and in cases where the total time window > 50 μs) in Edinburgh FLS980 instruments. 800 nm mode-locked Ti-sapphire laser (Mai-Tai, Spectra-Physics) excitation source was focused on the sample for the two-photon absorption experiment. Two-photon cell imaging and two-photon excitation-emission spectra collection are performed using a multiphoton microscope (Leica, Germany) at 63X & 10X oil immersion objectives, respectively. For femtosecond fluorescence up-conversion measurements the samples are excited at 375 nm and 400 nm using the second harmonic of a mode-locked Ti-sapphire laser (Mai Tai, Spectra-Physics). The fundamental beams (760 nm or 800 nm) are frequency doubled in a nonlinear crystal of β-barium borate (BBO). Samples are loaded in a 1 mm thick rotating sample chamber. Fluorescence emitted from the sample is upconverted in another nonlinear crystal (BBO) using a gate pulse (760 nm or 800 nm) of the fundamental beam and passed through a variable delay line before up-conversion. The sum frequency of the fluorescence and gate pulse is detected as a function of the time delay between excitation and gate pulses. The angle between the polarization of the pump and gate pulses is maintained at the magic angle to eliminate effects from rotational diffusion. The upconverted signal is dispersed in a monochromator and detected using photon-counting electronics. A

cross-correlation function obtained using the raman scattering from ethanol provided a full width at half-maximum (FWHM) of ~300 fs. Estimated uncertainties in the up-conversion measurements are ~15−20%. The average excitation power is varied but was around 8 ± 0.5 mW, and an average collection time of 2.5 s is used. No degradation of the sample is observed as the traces overlapped after each repetition, and the optical absorption measurements do not show any change before and after the measurements. The fluorescence decays are deconvoluted using a Gaussian-shaped excitation pulse by Igor Pro 6.0 analysis software. During analysis of upconverted decay profiles, the long component lifetime obtained from TCSPC is kept fixed.

3.5 Materials:

For synthesis purpose, all the important starting materials like tetrafluorophthalonitrile, tetrafluoroisophthalonitrile and tetrafluoroterephthalonitrile etc. are purchased from sigma-aldrich and were used without any further purification. For spectroscopic studies in solution, spectroscopic grade solvents were purchased from Spectrochem. Pvt. Ltd. India. For solid-state emission studies crystals or powdered samples were held in between two quartz slides purchased from TED PELLA INC.

3.6 Experimental section:

Fabrication of emitter-doped PMMA films:

Quantitative amounts of PMMA are dissolved in spectroscopic grade chloroform by heating at 50°C for 10 minutes and followed by sonication for another 5 minutes. Thereafter, a quantitative amount of emitters has been added to the PMMA solution and 0.2 ml of the resulting solution is used for spin-coating on a quartz plate at 2000 rpm for 30 seconds. The quartz plate was then kept in high vacuum for another 20 minutes prior to photophysical studies.

Density Functional Theory (DFT) calculation:

Quantum chemical calculations are performed using the Gaussian 09 program[23] using a high-performance cluster facility provided by IISER Pune. Initially, geometry optimization of all the luminogens is carried out in the gas phase and the nature of the stationary point (minima on the PE surface) is confirmed by frequency analysis[24-25] at the CAM-B3LYP/6-311++G (d, p) level. Furthermore, TD-DFT calculations are carried out to visualize the spatial distribution of HOMOs and LUMOs as well as to get the energy information of several excited singlet and

triplet states on equal no. of singlet and triplet states (td (50-50, n-states=10)) by CAM-B3LYP functional using TD-SCF method. Additionally, excited S_1 state geometry optimization is successfully performed at the B3LYP/6-31G (d, p) level after obtaining a frequency-analysed ground state optimized structure at the B3LYP/6-31G (d, p) level.

Spin-orbit coupling matrix element calculation

The spin-orbit coupling matrix between different excited singlet and triplet states was calculated using the zeroth-order regular approximation (ZORA) to the Dirac equation. In this approximation, the SOC operator, $\widehat{H}_{SOC,}$ is described as[26]

$$\widehat{H}_{SOC} = \frac{c^2}{(2c^2 - v)^2}\sigma \cdot (\nabla v \times p)$$

Where c, v, σ, and p signify the speed of light, Kohn-Sham potential, Pauli spin-matrix vector, and linear momentum operator respectively. The first-order perturbation is applied on scalar relativistic orbitals after the self-consistent field (SCF) and TD-DFT calculations to obtain SOC effects. CAM-B3LYP functional coupling with slater-type all-electron TZP basis is used to calculate SOC values. All such calculations are done using the PYSOC program.[27]

Fractional quantum yield calculation for film and powdered state

For fractional quantum yield calculation in solid state (film and pristine powdered state), the intensity of the emission at 0 delays has been measured (PF+DF), followed by a delayed emission (with delay time = 20 times of the average lifetime of prompt fluorescence or τ_{PF}) intensity measurement (only DF). The difference gives the quantitative estimate of the prompt fluorescence contribution.

Cell culture and drug treatments

MCF7 cells are obtained from the European Collection of Cell Cultures (ECACC). The cells are maintained in 100 mm dishes (Eppendorf or Corning) and are grown in high-glucose Dulbecco's Modified Eagle Medium (DMEM; Lonza) containing 10% heat-inactivated FBS (Invitrogen) and 100 units /mL penicillin-streptomycin (Invitrogen) and incubated at 37°C humidified 5% CO_2 incubators (Eppendorf or Thermo Scientific).

For multiphoton imaging experiments, 5X 10^4 MCF7 (ECACC) cells are seeded on a coverslip and incubated at 37°C with 5% CO_2 for 18hrs. Cells are treated with 10 µM of compound (DPAOCN, DPAMCN, and DPAPCN) and incubated for 24 hrs. Post-treatment, cells are washed with 1X PBS twice and fixed with 4% paraformaldehyde for 20 minutes in dark. After fixation, cells are again washed with PBS and mounted onto slides. The cells are imaged in a multiphoton microscope (Leica, Germany) at 63X oil immersion objective. For the MTT assay, 0.5 X 10^4 MCF7 cells are seeded in each well of a 96-well plate and incubated at 37°C with 5% CO_2 for 18 hours post-seeding. Cells are treated with different concentrations of the compound. 24 hrs post-treatment, drug-containing media is removed and, 0.5 mg/ml thiazolyl blue tetrazolium (MTT) containing DMEM is added to the cells and incubated at 37°C after covering with aluminum foil. 4 hours post MTT addition, the MTT-DMEM medium mixture is aspirated from the wells and 100 µl of DMSO is added to dissolve the purple MTT-formazan crystals. The absorbance is recorded at 570nm using the multimode Varioskan Flash plate reader (Thermo Scientific, USA).

3.7 Result and discussion:

3.7.1 Charge-transfer emission and TADF properties in solution state

All the compounds show two successive broad absorption bands in toluene. The bands were named as high energy (HE) bands and low energy (LE) bands. The HE bands are located within 320-420 nm, 310-430 nm, and 320-400 nm for DPAOCN, DPAMCN, and DPAPCN,

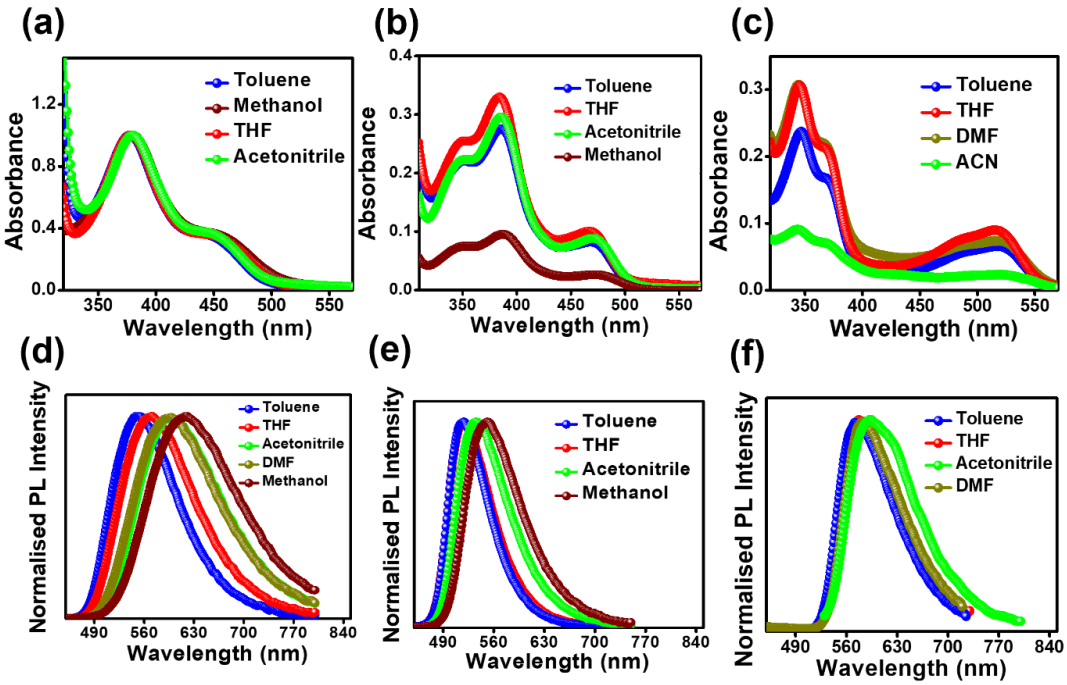

Figure 1: Absorption and emission spectra of (a) & (d) DPAOCN, (b) & (e) DPAMCN, and (c) & (f) DPAPCN in solvents of different polarity (10 µM concentration).

respectively. The LE bands are located in the range of 430-490 nm, 440-500 nm, and 440-550 nm for DPAOCN, DPAMCN, and DPAPCN, respectively (**Figure 1**). The emergence of the HE band can be attributed to the molecular π-π* transition and the LE band to the charge transfer (CT) transition from the peripheral diphenyl donor moieties to the core acceptor moiety. Well-separated HOMO and LUMO molecular orbitals obtained from density functional theory (DFT) calculations at CAM-B3LYP/6-311++G (d, p) level (**Figure A1 in Appendix**) and polarity-dependent emission spectra (**Figure 1**) confirm our conjecture about the charge transfer natures of our probes. Notably, the extent of red shift in the emission maxima is most pronounced in DPAOCN, which exhibits a substantial ~45 nm red shift while altering the solvent from toluene to acetonitrile. On the other hand, DPAMCN and DPAPCN display a smaller redshift of 22 nm and 20 nm, respectively, suggesting the highest dipole moment of DPAOCN in the excited state. The computed dipole moments obtained from the optimized S_1 state geometries (**Figure A3 in Appendix**) confirm the trend further, with the largest S_1 state dipole moment in DPAOCN (7.88 D), followed by DPAMCN (5.90 D) and the least in DPAPCN (0.002 D). Furthermore, the investigation of emission lifetime across varying solvent polarities provides a comprehensive elucidation of the excited states. In DPAOCN, the lifetime of the mono-exponential decay profile increases from 3.57 ns to 5.35 ns when the

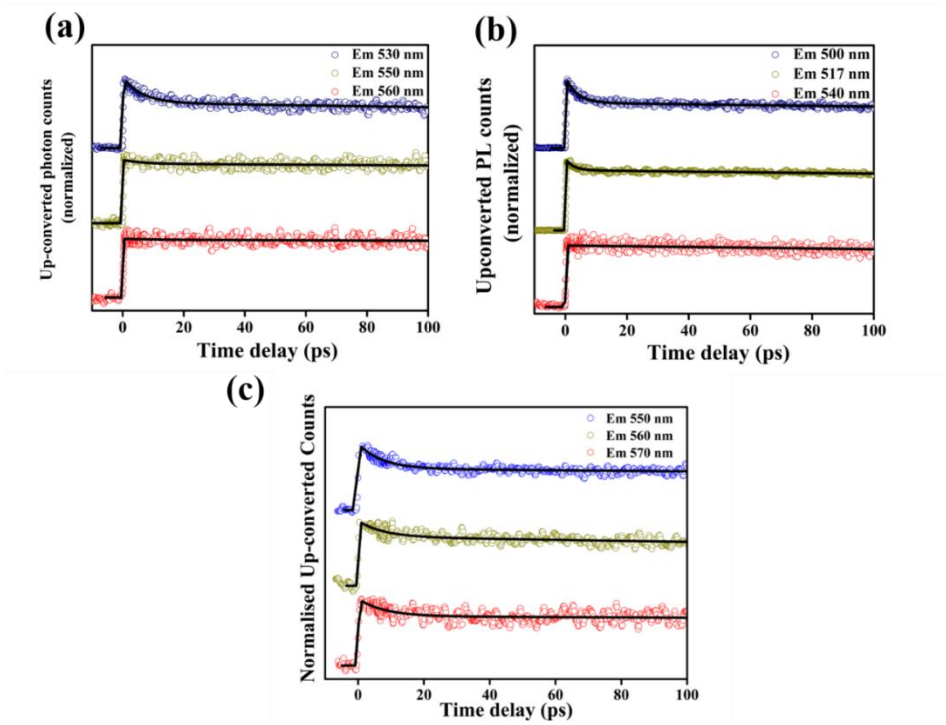

Figure 2: Fluorescence up-conversion decay profiles of (a) DPAOCN, (b) DPAMCN, and (c) DPAPCN in toluene (concentration 30 µm).

solvent was changed from toluene to THF. However, the lifetime decreases to 1.25 ns in a highly polar solvent like methanol, indicating a total charge separation and increased non-radiative decay in highly polar solvents (**Figure A4 & Table A1 in Appendix**). In contrast, DPAMCN and DPAPCN, owing to their lower excited state dipole moments, lead to an incomplete charge separation process (**Figure A4 & Table A2, A3 in Appendix**). As a result, the fluorescence lifetime shift in variable solvent polarity is less pronounced than that observed in DPAOCN. Next, the fluorescence up-conversion technique was employed to investigate the ultra-fast dynamical processes in excited states. In case of DPAOCN in toluene, the decay kinetics (excitation 400 nm, collection wavelength 530 nm) exhibits a bi-exponential behavior, with a short decay component of approximately 6 ps, having a contribution of 37% ± 0.8% along with a very long radiative decay (with a lifetime of ~3.5 ns). Interestingly, when the collection wavelength is progressively increased to 550 nm and subsequently to 560 nm, the contribution of the 6 ps decay transient decreases to 7% ± 1.14% (at 550 nm), and becomes negligible at 560 nm (**Figure 2 & Table A4 in Appendix**). Similar observations are obtained for DPAMCN and DPAPCN, however, with different magnitudes of short and long decay components (**Figure 2 & Table A4 in Appendix**). These findings inferred that the rapid decay component in all three isomers can be attributed to the conformational relaxation process following photoexcitation and subsequent formation of the charge transfer state.

In order to confirm the TADF process, photo-physical studies were carried out in degassed toluene. All three luminogens in degassed toluene experience an enhanced PL intensity compared to their aerated form (**Figure 3 a,b,c**). Additionally, time-gated emission spectra in degassed toluene were found to be perfectly overlapped with the steady-state emission spectra for all three isomers (**Figure 3 d, e, f**), suggesting the presence of delayed fluorescence from the singlet state. Fractional quantum yields of both prompt fluorescence and delayed fluorescence (Φ_{PF} & Φ_{DF}) are measured from the degassing experiment and delayed fluorescence contribution is found to be highest in the para-isomer (**Table 1**). The delayed fluorescence lifetimes, in degassed toluene are found to be longest in the ortho-isomer and shortest in the para-isomer (1.01 ms for DPAOCN, 695 µs for DPAMCN, and 4.13 µs for DPAPCN) (**Figure A5 in Appendix**). Interestingly, red-shifted phosphorescence emission bands are observed upon decreasing the temperature to 77 K in DPAOCN and DPAMCN.

However, the red shift in DPAPCN is modest, indicating energetically close S_1 and T_1 states

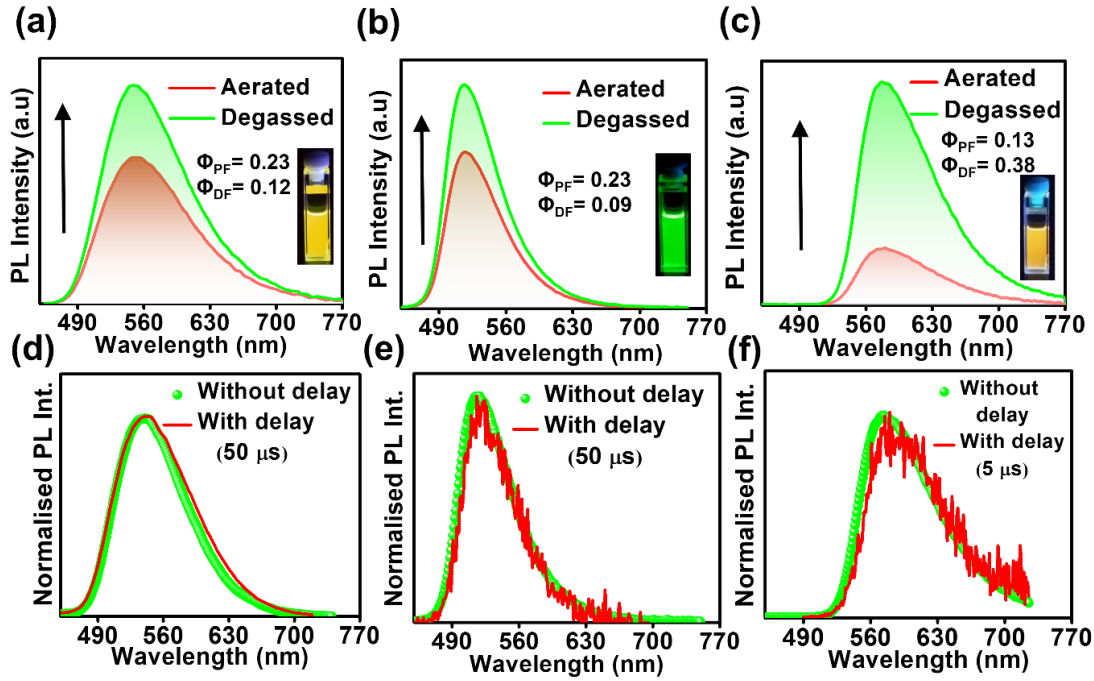

Figure 3: Emission spectra in aerated and degassed toluene of (a) DPAOCN, (b) DPAMCN, and (c) DPAPCN (for 30 µm of luminogen concentration). Steady-state and time-gated emission spectra in degassed toluene of (d) DPAOCN, (e) DPAMCN, and (f) DPAPCN. 2 ms sample windows were used for DPAOCN and DPAMCN, whereas, for DPAPCN, a 1 ms sample window was used for gated spectra measurement.

(**Figure A6 in Appendix**). From the onset of TADF and phosphorescence emission bands, the calculated ΔE_{ST} values are found to be highest in DPAOCN (0.27 eV) and lowest in DPAPCN (0.05 eV) (Table 1). We calculate the reverse inter-system crossing (RISC) rates for each luminogen in toluene and unsurprisingly, maximum k_{RISC} rate is found in DPAPCN (~ 10^6 s^{-1}), while the rate is minimum in DPAOCN (~10^2 s^{-1}) (**Table 1**) obeying the energy barrier law. The variation of ΔE_{ST} in all three regio-isomers is consistent with the trends obtained from the TDDFT calculations i.e. maximum in the case of DPAOCN and minimum in DPAPCN (**Figure A7 in Appendix**). As the rate of reverse intersystem crossing process (k_{RISC}) is crucially dependent upon the nature of the two states involved, it is important to reveal the nature of the S_1 and T_1 states. RISC rate is more pronounced in molecules where the S_1 state is found to be more of a charge transfer (CT) character and the T_1 state is more of a locally excited (LE) character or vice versa due to enhanced spin-orbit coupling between such states, which is in accordance with the El-Sayed rule.[28]

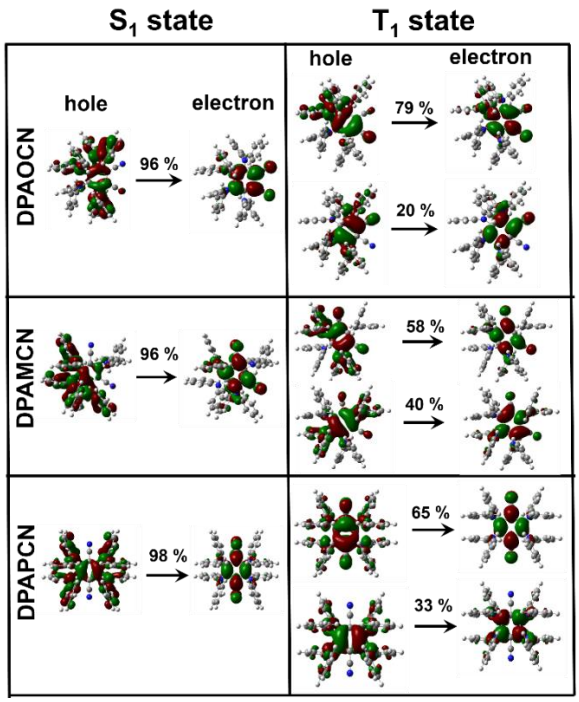

Figure 4: Natural transition orbital (NTO) analysis for S_1 and T_1 states of all three isomers. Hole and electron pairs of S_1 & T_1 states of DPAOCN, DPAMCN & DPAPCN.

Natural transition orbital (NTO) calculations show that, in all three cases, the hole and electron orbitals of the S_1 state are spatially well separated suggesting a predominant CT behavior of the S_1 state which is well-corroborated with the experimental results. For the T_1 state, however, all three molecules exhibit a predominant locally excited (LE) nature due to spatially superimposed hole and electron pairs in both significant NTO pairs (**Figure 4**). This is also supported by our experimental findings where the T_1 state emission at 77 K undergoes a negligible shift upon changing the solvent polarity from toluene to a polar glass-freezing alcoholic mixture (4:1 = methanol: ethanol) or DMSO, confirming the predominant LE nature (**Figure A8 in Appendix**). Such a behavioral change of the associated S_1 and T_1 states is reflected in moderate to high spin-orbit coupling values of the two states. Although, among the three, DPAPCN exhibits the maximum spin-orbit coupling value of 1.32 cm^{-1}, which may be responsible for its much accelerated RISC rate (**Figure A7 in Appendix**).

3.7.2 TADF properties in solid state

Table 1: *Photophysical data of all three regio-isomers in different states. All the quantum yields have been measured using an integrated sphere.* ϕ_{PF} *and* ϕ_{DF} *signify fractional quantum yield of prompt fluorescence and delayed fluorescence, respectively.*

Compound	ϕ_{PF}	ϕ_{DF}	E_{S1} [eV]	E_{T1} [eV]	ΔE_{ST} [eV]	k_r[a] (S_1-S_0) (s^{-1})	k_{ISC}[b] (S_1-T_1) (s^{-1})	k_{RISC}[c] (T_1-S_1) (s^{-1})
DPAOCN								
Solution[d]	0.23	0.12	2.60	2.33	0.27	6.4×10^7	2.1×10^8	6.7×10^2
Film	0.21	0.43	2.46	2.29	0.17	4.7×10^7	1.8×10^8	2.0×10^4
Powder	0.02	0.22	2.46	2.24	0.22	9.1×10^6	4.5×10^8	3.0×10^4
DPAMCN								
Solution [d]	0.23	0.09	2.58	2.38	0.20	1.3×10^8	4.5×10^8	7.3×10^2
Film	0.04	0.65	2.45	2.35	0.10	3.2×10^7	8.0×10^8	1.6×10^5
Powder	0.02	0.12	2.47	2.26	0.21	1.8×10^7	9.0×10^8	1.8×10^5
DPAPCN								
Solution[d]	0.13	0.38	2.32	2.27	0.05	7.5×10^7	5.0×10^8	8.1×10^5
Film	0.03	0.93	2.25	2.19	0.06	1.6×10^7	5.4×10^8	2.9×10^6
Powder	0.02	0.26	2.14	2.05	0.09	2.4×10^7	1.2×10^9	7.8×10^6

[a] k_r (S_1-S_0) = ϕ_{PF}/τ_{PF}, [b] k_{ISC} (S_1-T_1)= (1-ϕ_{PF}) /τ_{PF}, [c] k_{RISC} (T_1-S_1)= ϕ_{DF} / ($k_{ISC}.\tau_{PF}.\tau_{DF}.\phi_{PF}$).

[d] Measured using 30 µm of sample concentration in aerated and degassed conditions.

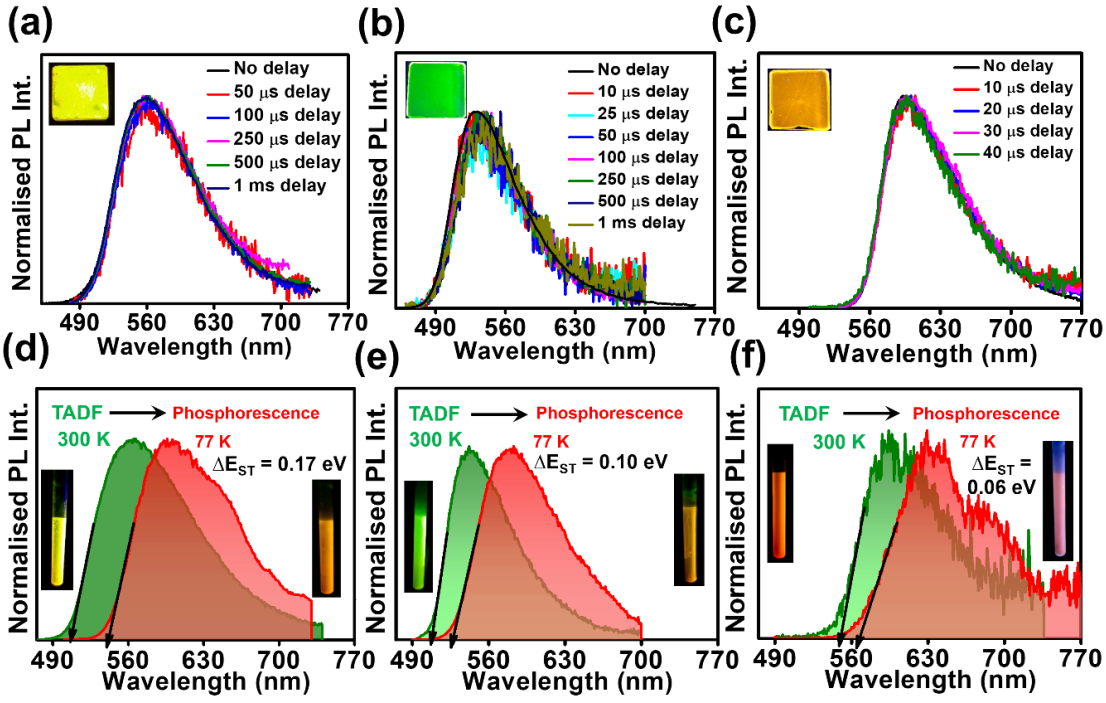

Figure 5: Time-gated emission spectra of 10 wt% emitter-doped PMMA films of (a)

DPAOCN, (b) DPAMCN, and (c) DPAPCN. Time-gated emission spectra of 10 wt % emitter doped PMMA films at RT (298 K) and 77 K for (d) DPAOCN, (e) DPAMCN, and (f) DPAPCN. Time delays for room temperature spectra measurement are kept at 50 µs (for DPAOCN & DPAMCN) and 10 µs (for DPAPCN). For the collection of spectra at 77 K, a 0.25 ms delay has been used for DPAOCN & DPAMCN, and a 0.1 ms delay has been used for DPAPCN. Sample windows for all the room temperature spectra measurements have been kept at 2 ms and low-temperature spectra measurements have been kept at 10 ms.

Studying the photo-physical properties of emitter-doped host matrix films is crucial for evaluating their suitability in OLED devices and reducing concentration quenching effects. In our study, we use PMMA as a host matrix due to its high triplet state energy (~3.1 eV), which effectively halts energy transfer from emitters to the host moiety. Time-gated emission spectra of 10 wt% emitter-doped PMMA films align well with the steady-state emission profile, indicating the dominance of the TADF process in all three molecules (**Figure 5 a,b,c**). Here also, the delayed fluorescence lifetime is found to be longest in DPAOCN (0.130 ms), followed by DPAMCN (0.104 ms), and shortest in DPAPCN (11.05 µs) (**Figure A9 in Appendix**). Subsequently, DPAPCN has the maximum rate of reverse inter-system crossing (2.9×10^6 s^{-1})

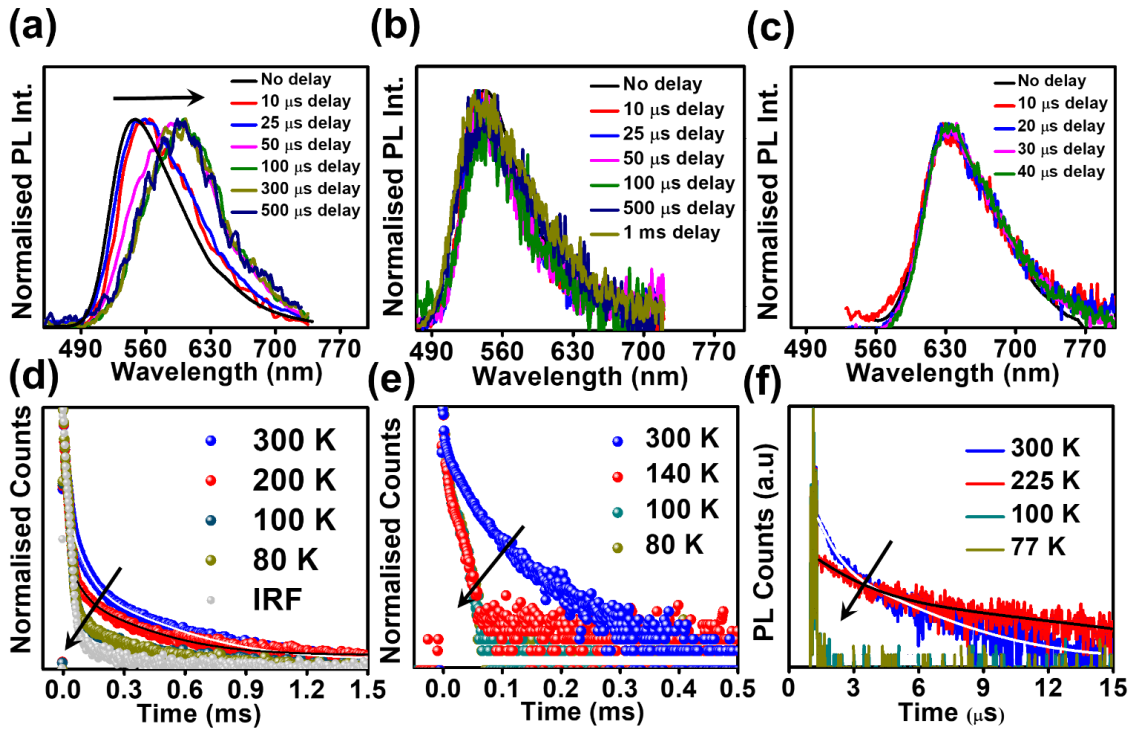

Figure 6: (a) & (d) Time-gated emission spectra (with varying time delay) and temperature-dependent emission of DPAOCN powder (collected at 550 nm). (b) & (e) Time-gated emission spectra (with varying time delay) and temperature-dependent emission of DPAMCN powder.

(c) & (f) Time-gated emission spectra (with varying time delay) and temperature-dependent emission of DPAPCN powder. Sample windows in all cases are kept at 2 ms.

and DPAOCN exhibits the lowest rate (2×10^4 s^{-1}) (**Table 1**). The variation of k_{RISC} is also consistent with the ΔE_{ST} of the molecules which is the highest in DPAOCN (0.17 eV) and the lowest in DPAPCN (0.06 eV) (**Figure 5d,e,f**). In powder form, both DPAMCN and DPAPCN exhibit an almost complete overlap of steady-state and time-gated emission spectra at different delays indicating a prevailed TADF process (**Figure 6 b, c**). The TADF lifetimes of DPAMCN and DPAPCN powder in vacuum are found to be 33 µs and 1.68 µs, respectively. Moreover, temperature-dependent TRPL studies show a gradual decline in delayed emission lifetime with decreasing temperature for both compounds, thus confirming the thermally assisted delayed fluorescence process (**Figure 6 e, f**). At 77K, TADF emission intensities of both the luminogens are suppressed, and phosphorescence bands emerged for both DPAMCN and DPAPCN. From the onset of TADF and phosphorescence emission, the experimentally obtained ΔE_{ST} is determined to be 0.21 eV (DPAMCN) and 0.09 eV (for DPAPCN) (**Figure A11 in Appendix**). Interestingly, for DPAOCN, the gated emission spectra collected at shorter time delays (10 µs and 25 µs) show the dominance of emission from the singlet state (~550 nm) as it matches well with the steady state emission profile, but at a time delay of 50 µs, a red shift in the emission maxima (~600 nm) is observed, accompanied by a small hump at ~550 nm. With further increased time delay, the small hump at ~550 nm disappears, and the emission maxima reside at ~600 nm (**Figure 6a**). Temperature-dependent lifetime measurements at the two major peaks (550 nm and 600 nm) reveal that the anticipated TADF peak (550 nm) exhibits a decrease in delayed emission lifetime with a decrease in temperature, while the 600 nm peak shows an increased emission lifetime, and manifests an ultra-long emission at cryogenic temperatures, indicating phosphorescent emission (**Figure 6d, Figure A12 in Appendix**). The calculated ΔE_{ST} value for DPAOCN is 0.22 eV. Additionally reverse intersystem crossing (RISC) rates are calculated for all three cases. DPAOCN exhibits the slowest RISC rate (3×10^4 s^{-1}), while DPAPCN demonstrates the most efficient RISC (7.89×10^6 s^{-1}), consistent with their ΔE_{ST} values (**Table 1**). The emergence of room-temperature phosphorescent emission in DPAOCN is likely attributed to the combination of lower and inefficient RISC rate and a considerably higher SOCME value between T_1 and S_0 states than the other two regio-isomers (1.68 cm^{-1} compared to 0.71 cm^{-1} and 0 of DPAMCN and DPAPCN, respectively) (**Figure A7 in Appendix**). In addition to that, a rigid environment in the powdered state may also facilitate its RTP behavior.

3.7.3 Mechanochromic luminescent (MCL) properties

Crystal symmetry plays a vital role in determining the photo-physical properties of luminescent materials. The responsiveness of organic luminogens to external stimuli relies heavily on the presence of a center of inversion in their crystal arrangement. However, increased molecular flexibility and short-range non-covalent interactions in the crystalline phase alone do not

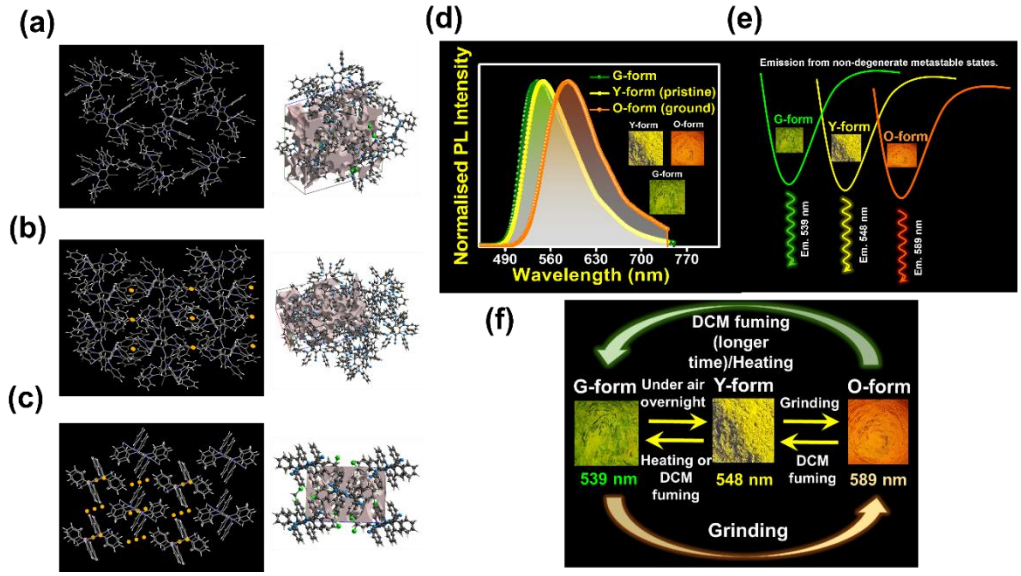

Figure 7: (a) Non-centrosymmetric crystal packing and crystal voids inside a unit cell of DPAOCN. (b) Centrosymmetric crystal packing along with the center of inversion (i) symmetry elements (shown as yellow dots) and crystal voids inside a unit cell of DPAMCN. (c) Centrosymmetric crystal packing along with the center of inversion (i) symmetry elements (shown as yellow dots) and crystal voids inside a unit cell of DPAPCN. (d) DPAOCN pristine powder undergoing a red shift upon mechanical grinding (ex. 370 nm). (e) & (f) scheme of tri-color emission & multi-stimuli responsive behavior of DPAOCN under several external stimuli (photos collected using a 365 nm UV lamp).

guarantee stimuli responsiveness. This is particularly true when the crystal has a centrosymmetric packing, as it lacks a gross dipole-moment and exhibits degenerate electronic energy states, resulting in no change in emission color under different external stimuli.[29] On the other hand, a luminogen with non-centrosymmetric crystal packing can display multi-color emission behavior in response to external stimuli, due to the presence of multiple non-degenerate metastable energy states. Here, the intriguing aspect that captivates our attention is the crystal packing mode of the regio-isomers. Both DPAMCN and DPAPCN, adopt a centrosymmetric *P21/C* space group, whereas DPAOCN crystallizes in a chiral and non-

centrosymmetric $P2_12_12_1$ space group (**Figure 7**). As previously explained, the presence of a

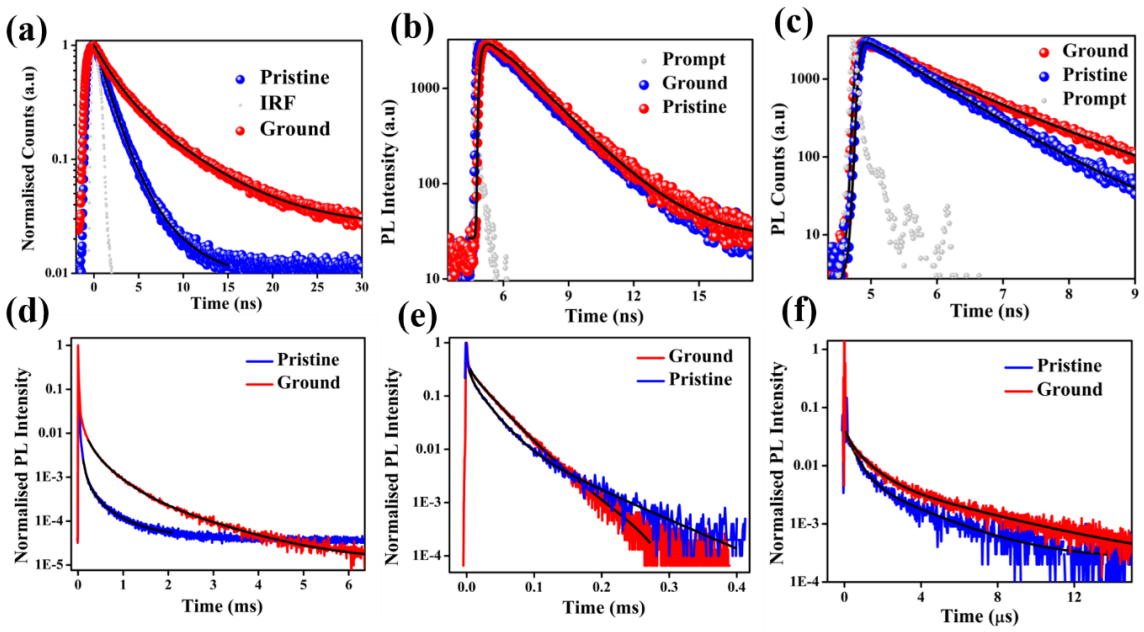

Figure 8: (a) & (d) Effect of mechanical grinding on the prompt fluorescence and delayed fluorescence lifetime of DPAOCN powder. (b) & (e) Effect of mechanical grinding on the prompt fluorescence and delayed fluorescence lifetime of DPAMCN powder. (c) & (f) Effect of mechanical grinding on the prompt fluorescence and delayed fluorescence lifetime of DPAPCN powder.

centrosymmetric packing arrangement results in the formation of degenerate energy states when subjected to external stimuli. Consequently, the green-emissive DPAMCN and red-emissive DPAPCN display a minimal shift in their emission profiles upon mechanical grinding with no apparent change in the emission color (**Figure A13 in Appendix**). Intriguingly, DPAOCN in pristine powder form, undergoes a ~ 40 nm red-shift (from ~ 550 nm to ~ 590 nm) upon mechanical grinding (with 0.2 gigapascals of pressure) with a visual emission color change from yellow (Y-form, Φ=0.24) to orange (O-form, Φ= 0.10), thus making DPAOCN as mechanically active luminogen (**Figure 7 d, e, f**). At this point, we are intrigued by the impact of mechanical grinding on the lifetimes of prompt fluorescence (PF) and delayed fluorescence (DF). Regarding para and meta isomers, there is a minimal alteration in their prompt and delayed fluorescence lifetimes following the grinding process (**Figure 8**). However, a significant change in both prompt and delayed fluorescence lifetimes is observed in the ortho isomer (DPAOCN) case. The prompt fluorescence lifetime undergoes a remarkable transformation, rising from 2.17 ns in its original state to 5.35 ns after mechanical grinding. Likewise, the delayed fluorescence lifetime experiences a substantial enhancement,

transitioning from 353 μs in its pristine state to 473 μs after grinding (**Figure 8**). Such alternation of emission lifetime is probably due to the grinding effect, which induces a significant energy change in case of mechanochromic luminescent molecules, leading to modifications in both the prompt fluorescence and the delayed fluorescence lifetime. The utmost importance of any mechanically active luminogen is its reversibility to its original color (in this case, 'Y-form'). By retaining its original color, the luminogen ensures its stability and reliability for practical applications like sensing, information storage, and visual indicator. Exposure to DCM vapor causes the compound to revert back to its original color (**Figure 7f**), resembling the pristine state (Y-form). However, extended exposure of the ground powder to DCM vapor or heating the ground sample at around 90°C results in the emergence of a different state exhibiting green emission ('G-form', emission maxima at 539 nm, Φ= 0.09) (**Figure 7 & Figure A14 in Appendix**). Thus, DPAOCN with non-centrosymmetric packing mode exhibits tri-color mechanochromic luminescence along with simultaneous TADF and RTP. The simultaneous manifestation of these properties in a single compound is exceedingly rare in the literature. It is noteworthy to mention that exposing the green emissive DCM-soaked powder to air overnight and subsequently grinding it again using a mortar and pestle results in the formation of the Y-form and O-form, respectively (**Figure 7f**). This demonstrates the reversibility of all the steps involved in the process. Another crucial factor that can dictate the mechanochromic property of a certain molecule is the amount of void space in the crystal unit cell.[30] The amount of void present in a crystal is a combined effect of short-contact non-covalent interactions and the degree of flexibility of the molecular arrangement. In order to quantitatively evaluate each type of non-covalent interaction, Hirshfeld surface analysis is performed and the specific contribution is highlighted in **Figure A15-Fig. A17 in Appendix**. At this point, it provokes us to look into the void space volume of each crystal and interestingly, the maximum void space is obtained for DPAOCN (826 $Å^3$), then comes DPAMCN (597 $Å^3$), and the minimum is obtained for DPAPCN (with only 280 $Å^3$ of void volume) (**Figure 7**). The higher void space in DPAOCN is probably due to its more sterically hindered molecular architecture which restricts the neighbouring molecule to approach closer to each other, creating a higher void volume in the unit cell (**Figure 7 & Figure A18 in Appendix**). Notably, the steric hindrance follows the trend DPAOCN>DPAMCN>DPAPCN so does the void volume. The maximum void volume in DPAOCN can provide more flexibility in the molecular scaffold and thus, upon external stimuli, twisted terminal diphenyl moieties (Θ_1= 58°, Θ_2= 63°, Θ_3= 55°, Θ4= 63°) of DPAOCN can alter the dihedral angle with the acceptor core (**Figure**

A19 in Appendix), thereby changing its emission energy and color. PXRD analysis is also carried out to look into the details of the possible phase transition of the isomers upon mechanical treatment. The simulated PXRD pattern of all the isomers aligns well with the experimentally obtained PXRD patterns (**Figure A20-A21 in Appendix**). All the luminogens exhibit sharp and highly intense diffraction peaks in pristine powder form suggesting a high degree of crystallinity in the samples. Upon grinding, intensities of some sharp diffraction peaks decreased with an appearance of broad and diffused PXRD patterns, suggesting an increase in the amorphous nature of the samples in the ground state. However, such modulation of crystallinity in DPAMCN and DPAPCN does not lead to an energetically different phase just enough to so MCL properties. In DPAOCN however, it leads to an orange emissive 'O-form', energetically different from the yellow emissive original 'Y-form'. Most importantly, upon DCM vapor treatment (in less concentration), the reversibility to the original pristine state is confirmed by the reappearance of sharp and intense diffraction peaks along with the broad halo disappearing from the PXRD pattern (**Figure A20 in Appendix**).

3.7.4 SHG properties

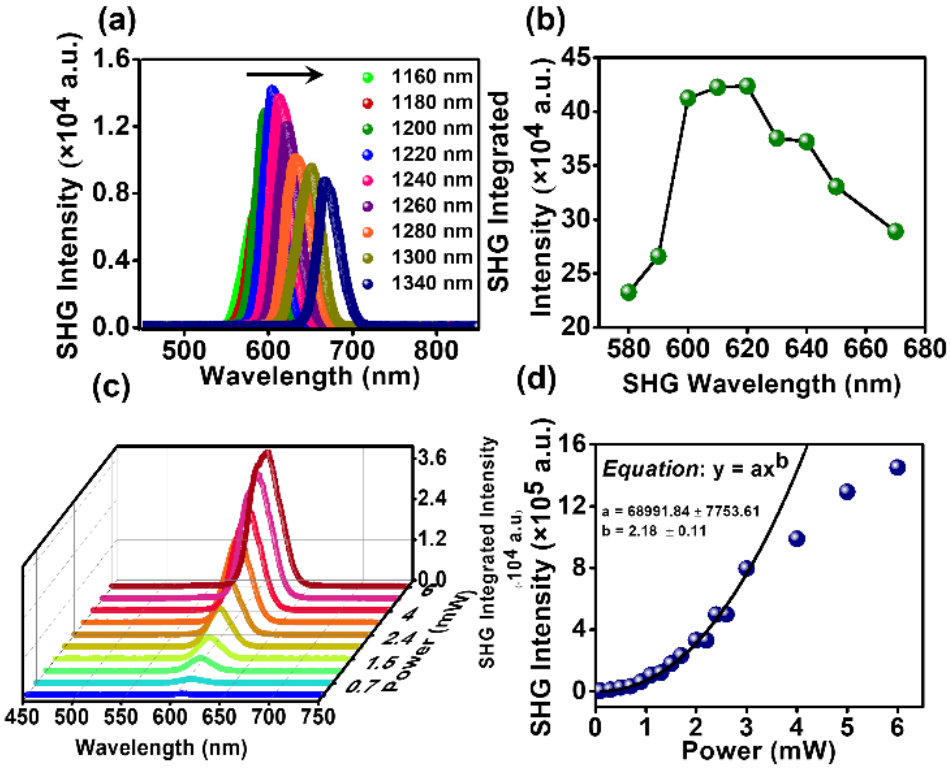

Figure 9: (a) wavelength-dependence of the SHG responses in the 1160-1340 nm region, (b) dependence of SHG integrated intensities with varying SHG wavelengths for DPAOCN

crystals, (c) Power-dependent study of the SHG responses at 610 nm for DPAOCN crystals, (d) quadratic fit of the SHG intensities with varying excitation power.

Organic non-linear optical (NLO) materials have emerged as promising alternatives to inorganic NLO systems due to their high hyperpolarizabilities, diverse topologies, ease of processing, and high stability.[31,32] Notably, the absence of inversion symmetry is the key prerequisite for a material to exhibit any second-order nonlinear process.[33,34] Nonetheless, DPAOCN stands out to be the best candidate to exhibit second harmonic generation property among the three molecules, as it exhibits non-centrosymmetric crystal packing with the $P2_12_12_1$ space group. Our research involved performing extensive measurements on our sample using second harmonic generation (SHG) at a range of wavelengths along with the second-order non-linear susceptibility ($\chi^{(2)}$) and optical stability. To conduct these experiments, we have used ultrafast pulses generated from an optical parametric amplifier (OPA) with a pulse width of approximately 50 fs.[35,36] Details of the experimental setup and procedure can be found in **section A2 in Appendix**. The non-centrosymmetric DPAOCN exhibits a significantly strong SHG response upon excitation in the 1160 – 1340 nm wavelength range. **Figure 9a** shows the SHG response obtained from DPAOCN at a constant power of 2.5 mW, whereas **Figure 9b** plots the SHG intensity vs SHG wavelength. It is evident that the maximum SHG is obtained at 610 nm, which corresponds to an excitation with 1220 nm light. Band edge resonance is the probable reason for maximum SHG response at this wavelength (**Figure A26 in Appendix**). We have also observed a weak THG response of our sample within the same excitation wavelength (**Figure A25 in Appendix**). To determine $\chi^{(2)}$ of DPAOCN, we have exploited Maxwell's equation of relative intensity (**Figure A24 in Appendix**). Here potassium dihydrogen phosphate (KDP) is used as the reference SHG material to calculate the second-order susceptibility. KDP has a $\chi^{(2)}$ value of 0.37 pm/V at 1064 nm.[37–41] The $\chi^{(2)}$ value of the DPAOCN is obtained to be around 0.19 pm/V at 1220 nm (SHG output 610 nm) at which wavelength DPAOCN shows the maximum SHG. The above results suggest that DPAOCN has a much stronger SHG response at 610 nm compared to even KDP. When considering a material for use as a potential source for nonlinear optics, it is essential to take into account both its NLO efficiency and optical stability. To assess the latter, we determined the laser-induced damage threshold (LIDT) of DPAOCN (**details in Section A2 of Appendix**). The LIDT is the excitation power level at which the SHG response deviates from the expected quadratic dependence on excitation power. To find the LIDT, we measured the SHG intensity at varying excitation power levels, specifically at the excitation wavelength of 1220 nm, which

corresponds to the maximum SHG response of DPAOCN. **Figure 9c & 9d** displays the relationship between excitation power and SHG intensity, along with its quadratic fit. It becomes evident that the quadratic nature of the power dependence is lost at around 3 mW, due to saturation effects such as local heating. We found the LIDT value of DPAOCN to be 13.27 GW/cm^2 (**details in Section A2 of Appendix**), which is comparable to other popular commercially available SHG materials such as BBO (~10 GW/cm^2) and KDP (~3 GW/cm^2). Therefore, DPAOCN proves to be both highly efficient in terms of second-order susceptibility and optically stable, making it a suitable material for practical SHG applications.

3.8 Applications:

3.8.1 Converted LEDs (c-LEDs) fabrication

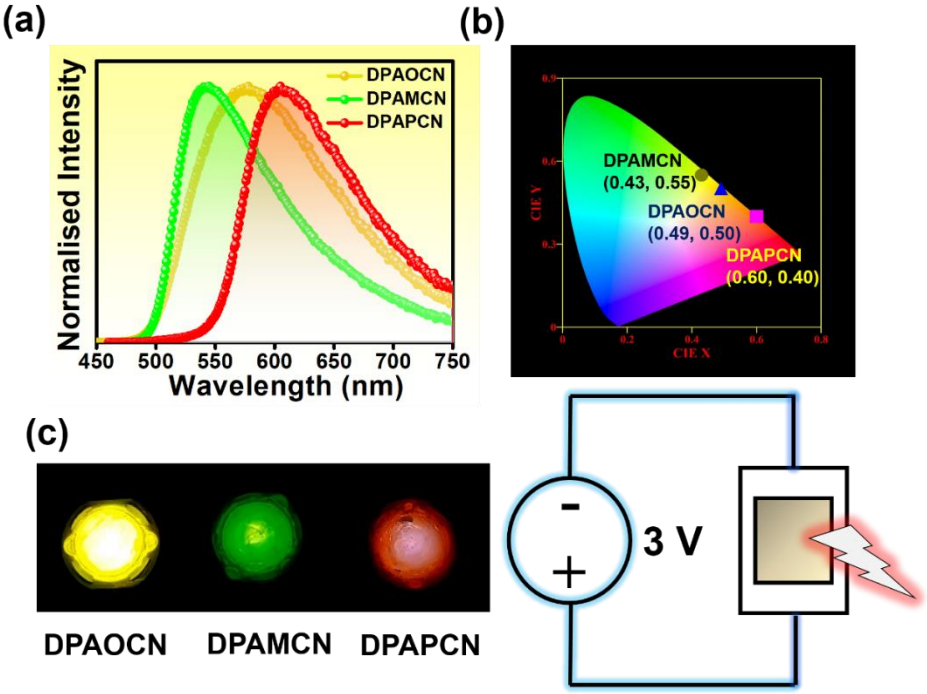

Figure 10: (a) Emission spectra of all three fabricated c-LEDs, (b) CIE-chromaticity plots (GO-CIE, CIE-1931) of the emission spectra obtained in all three isomers, (c) emission glow from all three c-LEDs in three different color regimes and the schematic of the c-LED devices fabricated.

Drawing inspiration from three distinct emission properties of the isomers, we embarked on the creation of c-LEDs. For that, the samples were blended at a 10 wt% ratio with polymethyl methacrylate (PMMA) using chloroform as the solvent. This blend was subsequently applied as a coating atop InGaN chips (**Figure A27 in Appendix**), with an elaborate fabrication

procedure outlined in **section A3 of Appendix**. Intriguingly, when a 3V bias is applied, the c-LED coated with DPAOCN emits a captivating yellow light, while those coated with DPAMCN and DPAPCN radiate green and red, respectively (**Figure 10c**). It's noteworthy that these emission colors closely mirror the photoluminescent (PL) emissions from the 10 wt% doped PMMA films, mentioned in the earlier section (**Figure 10a**). This observation points to the potential utilization of these three regio-isomers in the creation of OLEDs for three distinct color regimes—green, yellow, and red.

3.8.2 Two-photon cell imaging

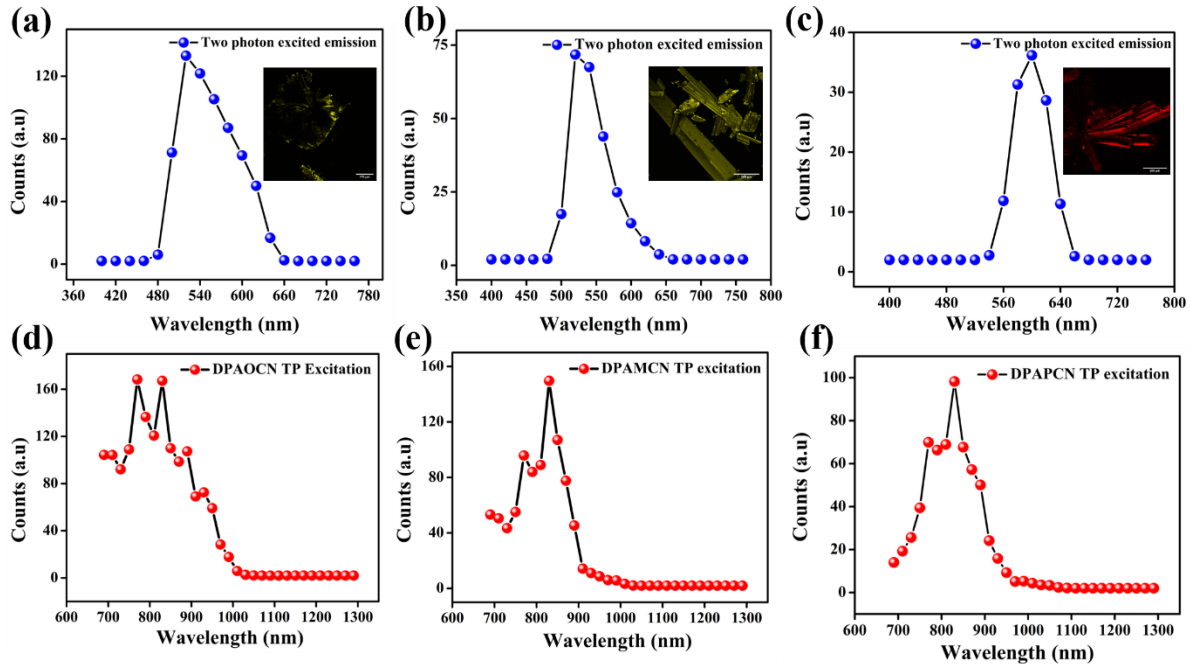

Figure 11: Two-photon excited emission spectra of (a) DPAOCN crystals, (b) DPAMCN crystals and (c) DPAPCN crystals (excitation wavelength kept at 830 nm and emission collected in 400-780 nm region, in the inset, two-photon confocal microscopy images (at 10X objective) of two-photon illuminated emission from DPAOCN, DPAMCN and DPAPCN crystals (excitation 840 nm). Two-photon excitation spectra of (d) DPAOCN crystals, (e) DPAMCN crystals, and (f) DPAPCN crystals. The wavelength range window for data collection is 690 nm- 1290 nm in all cases. The emission window is as follows: 580 nm-625 nm for DPAOCN, 522 nm-598 nm for DPAMCN, and 590 nm- 660 nm for DPAPCN. For both excitation and emission spectra, 20 nm step size has been used.

Due to the greater optical penetration, excellent spatial resolution, and minimal optical scattering, two-photon-excited organic luminogens have attracted significant attention in comparison to typical one-photon-excited fluorophores.[42–45] Such "two-photon absorption"

active materials are particularly useful for cell imaging since they inflict the target cell with the least amount of photo damage. Large π- conjugated organic chromophores with enforced co-planarity and donor-acceptor groups at the center or at the end of the molecular scaffolds tend to exhibit strong two–photon absorption behavior.[46] This is due to higher transition dipole moment values between the ground, intermediated, and final states leading to higher

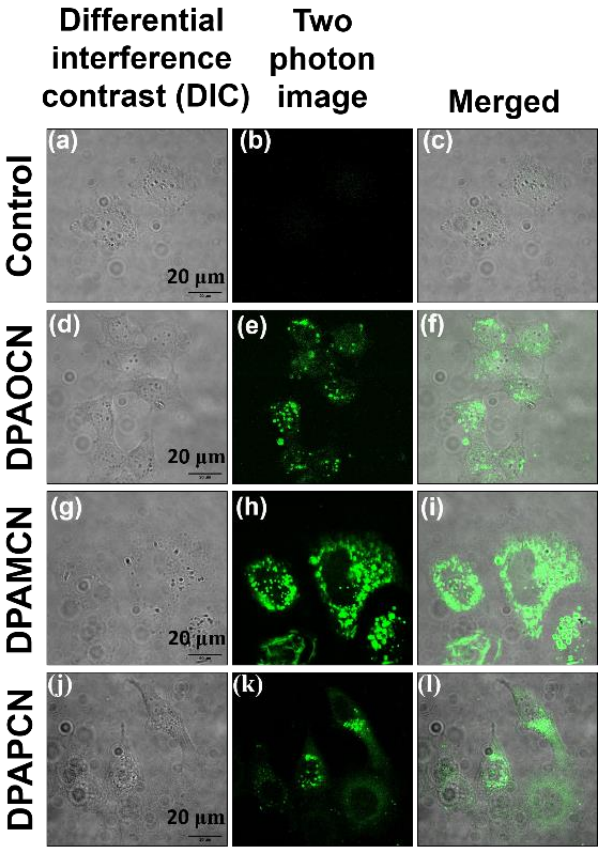

Figure 12: Two-photon microscopy image (excitation wavelength = 800 nm, collection window is from 530 nm to 620 nm for DPAOCN, 510 nm to 580 nm for DPAMCN, and 550 to 630 for DPAPCN) of MCF-7 cells: top row- without the treatment of dye or the control and the rests -with the treatment of 10 µM dye. (a, d, g, j) differential interference contrast (DIC) images, (b) cells without dye treatment, the two-photon image of cells treated with dye (e- DPAOCN, h- DPAMCN and k- DPAPCN) and (c, f, i, l) DIC image merged with dye treated confocal images.

two-photon absorption cross-section values. Our molecules' strong charge transfer behavior prompted us to investigate their two-photon absorption behavior and here, it is discovered that all three luminogens are two-photon active in both the liquid and solid crystalline states (**Figure A28 in Appendix**). **Figure 11** shows the two-photon excitation spectra and two-photon excited

emission spectra of the three luminogens in their crystalline state. We conduct a two-photon cell imaging experiment as a result of these exciting features. It is clear from the two-photon image that our luminogens can effectively illuminate cells, majorly the cytoplasmic part (**Figure 12**). Additionally, the MTT viability assay of MCF7 cells is used to investigate the cytotoxic behavior of our luminogens. No significant cell death (more than 50%) is observed in samples incubated with drug concentrations up to 15 µM (**Figure A29 in Appendix**), indicating the molecules do not exhibit toxic behavior to the cells up to that concentration.

3.8.3 Multi-color writing and erasing

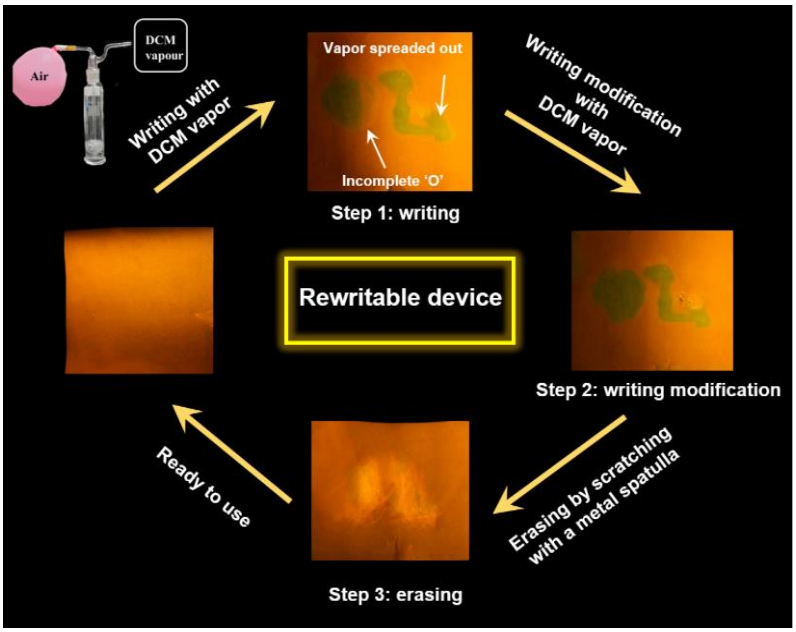

Figure 13: Demonstration of rewritable data recording based on multi-stimuli responsive behavior of DPAOCN. On the right, the demonstration of DCM vapor creation has been shown. Emission photos have been collected using 365 nm UV irradiation.

The reversible tri-color emission characteristics of DPAOCN hold promise for a variety of potential applications, such as rewritable media[47-48] To demonstrate this, a Whatman filter paper is dipped into a stock solution of DCM, kept there for 30 minutes, and then dried for another 30 minutes in vacuum. An orange background was found to be created after the drying process. After that, the word ‘OL’ (abbreviation of organic light) was written on it using DCM vapor. Initially, we intentionally spread out DCM vapor on the letters 'L' and 'O' was left incomplete to showcase the device's writing improvement potential. Thereafter, the writing was further improved with DCM vapor. The word ‘OL’ is now complete. To remove the word, a metal spatula was used to scratch it away, leaving only the orange background visible (**Figure**

13). Consequently, this smart stimuli-responsive material enables a convenient cycle of writing and erasing.

3.9 Conclusions

Overall, the trifecta of TADF, SHG, and mechanochromic luminescence (MCL) among three donor-acceptor based regio-isomers has been successfully studied in this research article. Through extensive experimentation, we have established that TADF properties can be thoroughly tuned from the ortho to the para isomer. Herein, the ortho-isomer, DPAOCN, exhibits the slowest rate of reverse intersystem crossing (RISC) (~ 10^2-10^4 s^{-1}), whereas, the para-isomer, DPAPCN, dazzles with the highest TADF efficiency with the RISC rate of near ~ 106 s^{-1}. These differences in TADF efficiency mainly stem from the variation in energy splitting (ΔE_{ST}) values and the extent of spin-orbit coupling (SOC) between the lowest singlet and triplet states. Moreover, the crystal space groups of all three isomers are different, as the ortho-isomer adopts a non-centrosymmetric and chiral $P2_12_12_1$ space group, whilst the other two crystallize in centrosymmetric $P2_1/C$ space group. Intriguingly, the non-centrosymmetric crystal packing of the ortho-isomer opened up two different avenues of photonics research. It exhibits excellent mechanochromic luminescence behavior with green, yellow, and orange emissions along with outstanding SHG characteristics with $\chi^{(2)}$ value of 0.19 pm/V at 1220 nm and LIDT value of 13.27 GW/cm^2. To the best of our knowledge, it is the first ever reported organic luminogen to exhibit simultaneous TADF, SHG, and mechanochromic luminescence properties. Further, the electroluminescence potential of all three isomers has been explored by converted LED (cLEDs) devices fabrication. Also, the isomers have demonstrated two-photon absorption activity in both solution and crystal states. This unique characteristic has been successfully exploited in two-photon confocal cell imaging, without significant cell death observed at concentrations up to 15 µM of the dye.

3.10 Appendix

Section A1: Detailed synthesis and characterization data:

Synthesis of (a) DPAOCN, (b) DPAMCN, and (c) DPAPCN:

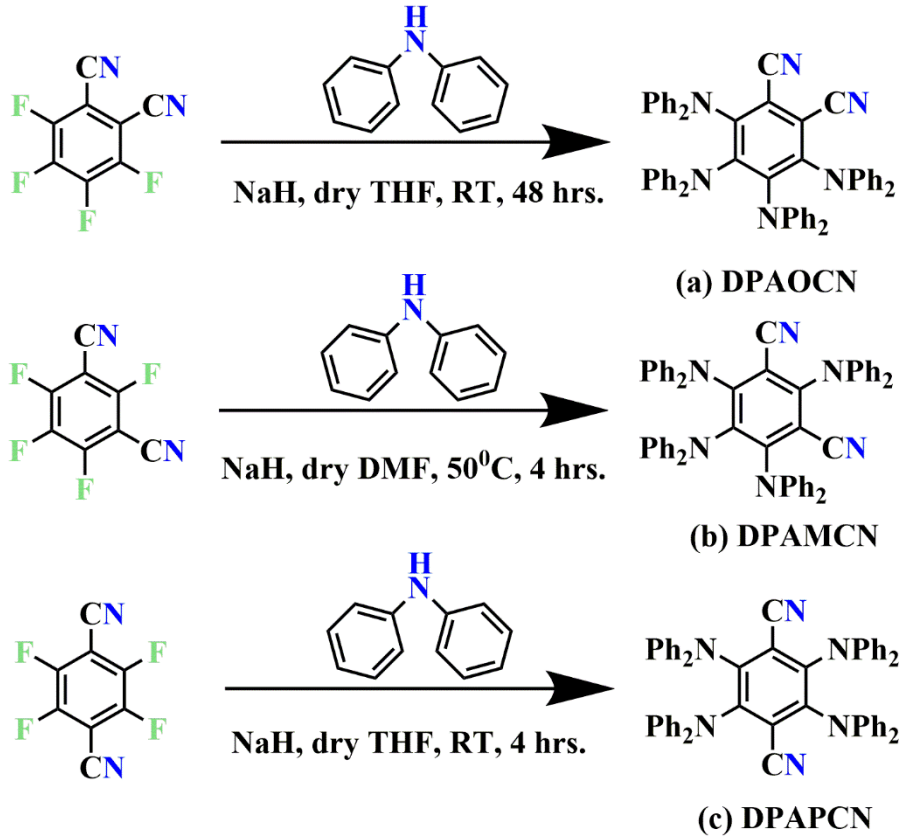

Scheme S1: synthesis scheme of (a) DPAOCN, (b) DPAMCN, and (c) DPAPCN.

Synthesis of (a) DPAOCN: In a Schlenk RB flask equipped with a magnetic bead, diphenylamine (0.845 gm, 5 mmol) is taken and dissolved in 5 ml of anhydrous THF with argon flow. Vacuum-dried NaH (60% in oil, 300 mg, 7.5 mmol) is added slowly to the mixture and stirred at RT for 30 minutes. After that, tetrafluorophthalonitrile (0.2 gm, 1 mmol) is added to the reaction mixture, and the reaction is allowed to stir for another 48 hours at room temperature under argon (scheme S1). After 48 hours, the excess NaH is quenched by dropwise addition of distilled water. The mixture was then concentrated under a vacuum and washed several times with water and DCM. Finally, the crude product is purified by SiO_2 column chromatography with a hexane/DCM solvent system. Yield: ~ 80%.

Synthesis of (b) DPAMCN: In a Schlenk RB flask equipped with a magnetic bead, diphenylamine (1.01 gm, 6 mmol) is taken and dissolved in 5 ml of anhydrous DMF with argon flow. Vacuum-dried NaH (60% in oil, 320 mg, 8 mmol) is added slowly to the mixture and stirred at 50°C for one hour. After 1 hour, tetrafluoroisophthalonitrile (0.2 gm, 1 mmol) is added to the reaction mixture, and the reaction is allowed to stir for another 4 hours at 50°C under argon (scheme S1). The completion of the reaction is confirmed by TLC. Excess NaH, is then quenched with a dropwise addition of distilled water. The mixture was then washed several times with water and ethyl acetate. Finally, the crude product is purified by SiO_2 flash column chromatography with a hexane/DCM solvent system. Yield: ~ 55%.

Synthesis of (c) DPAPCN: In a Schlenk RB flask equipped with a magnetic bead, diphenylamine (0.845 gm, 5 mmol) is taken and dissolved in 5 ml of anhydrous THF with argon flow. Vacuum-dried NaH (60% in oil, 300 mg, 7.5 mmol) is added slowly to the mixture and stirred at RT for 30 minutes. After that, tetrafluoroterephthalonitrile (0.2 gm, 1 mmol) is added to the reaction mixture, and the reaction is allowed to stir for another 4 hours at room temperature under argon (scheme S1). After 48 hours, the excess NaH is quenched by dropwise addition of distilled water. The mixture was then concentrated under a vacuum and washed several times with water and DCM. Finally, the crude product is purified by SiO_2 column chromatography with a hexane/DCM solvent system. Yield: ~ 50%.

^{1}H NMR data of (a) DPAOCN:

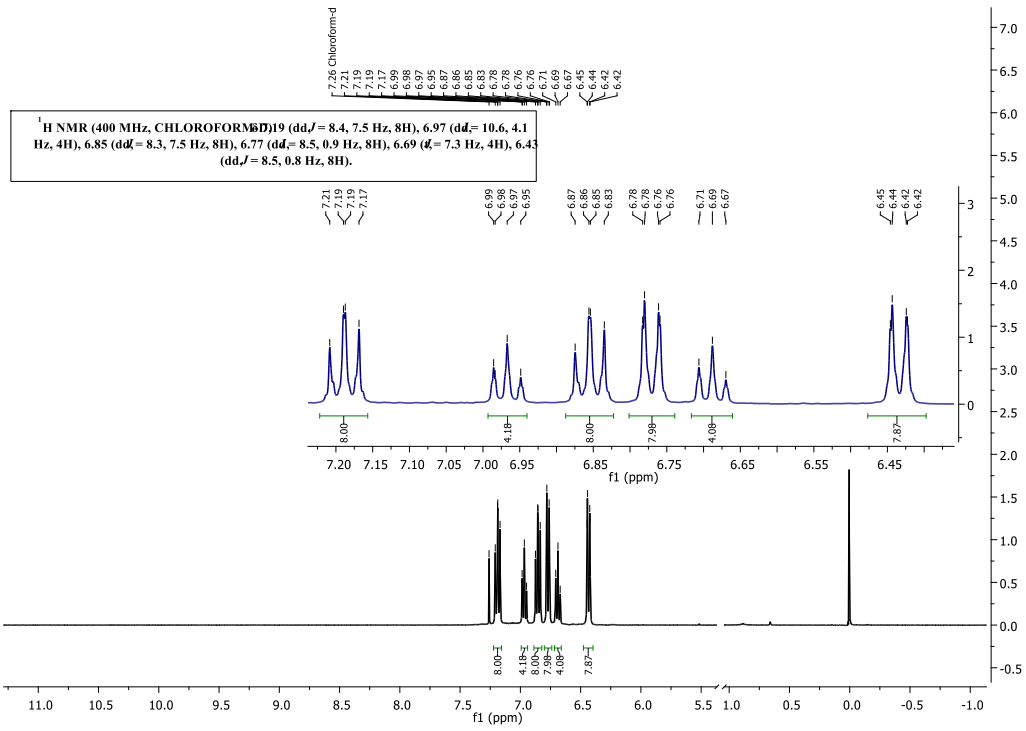

^{1}H NMR data of (b) DPAMCN:

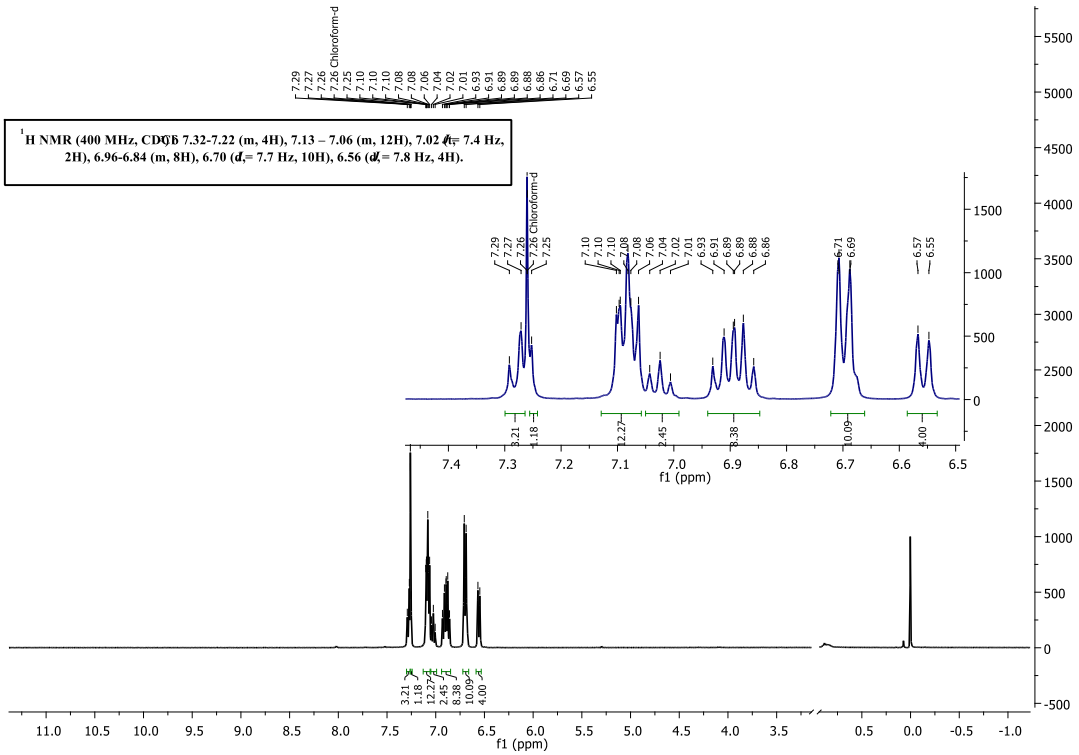

^{1}H NMR data of (c) DPAPCN:

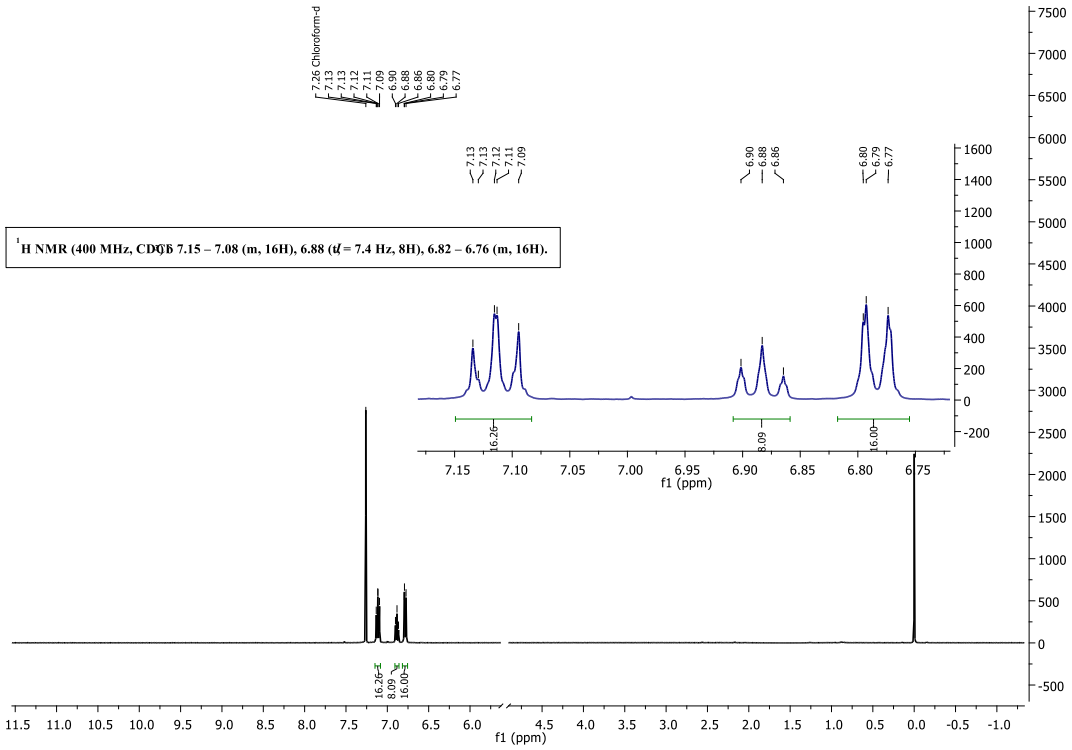

^{13}C NMR data of (a) DPAOCN:

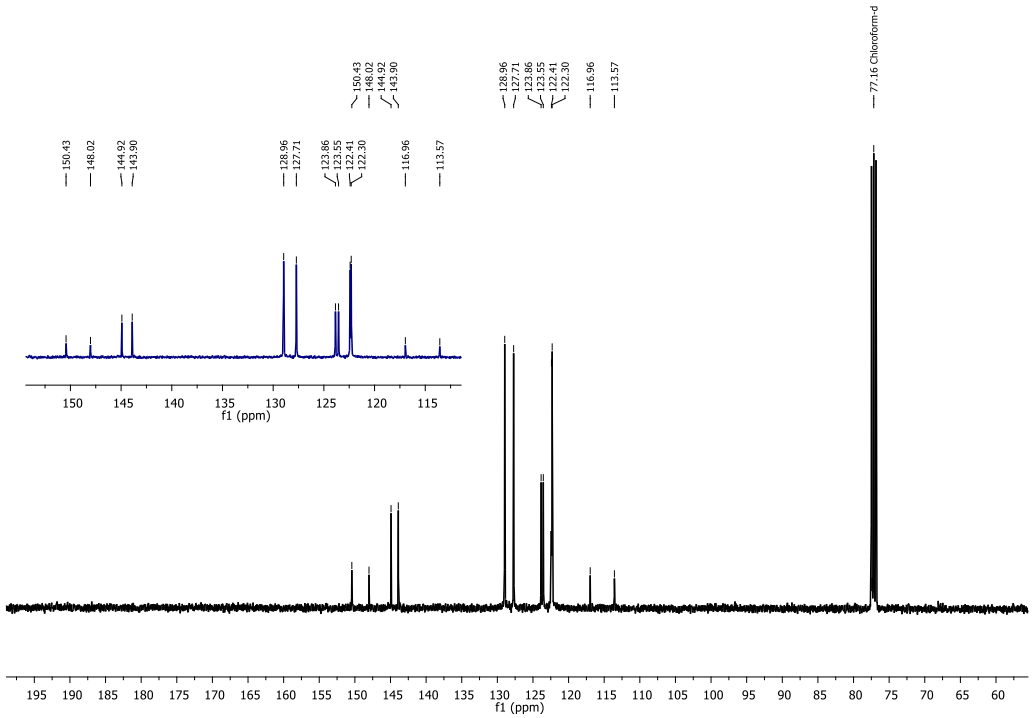

^{13}C NMR data of (b) DPAMCN:

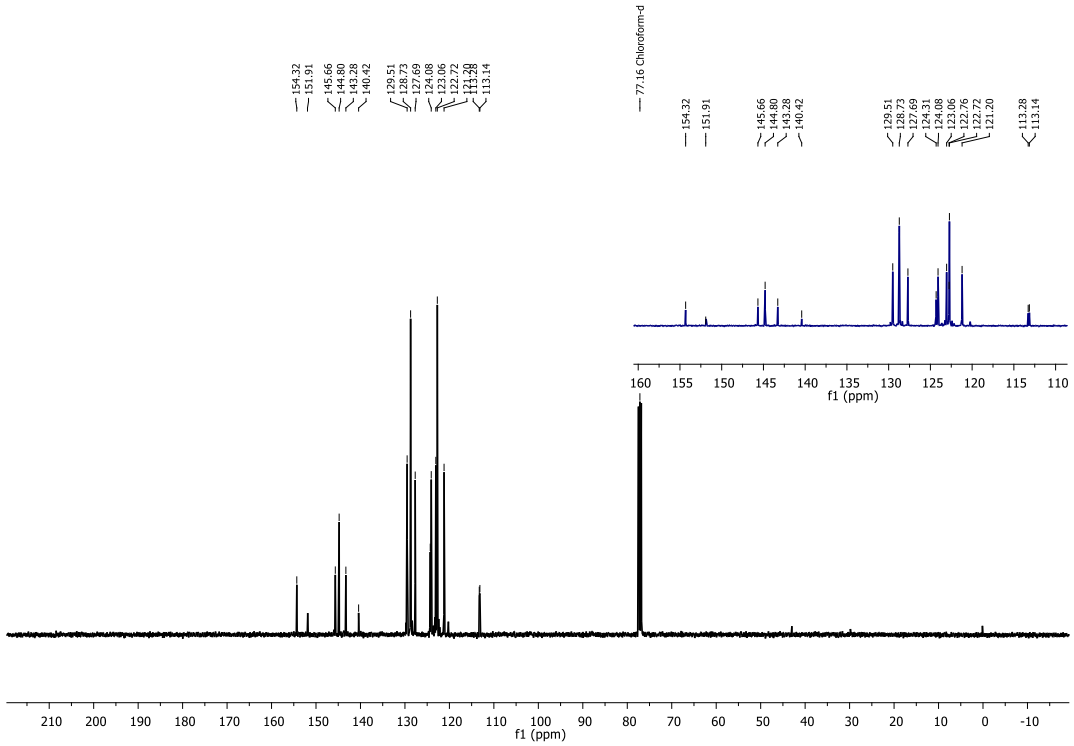

^{13}C NMR data of (c) DPAPCN:

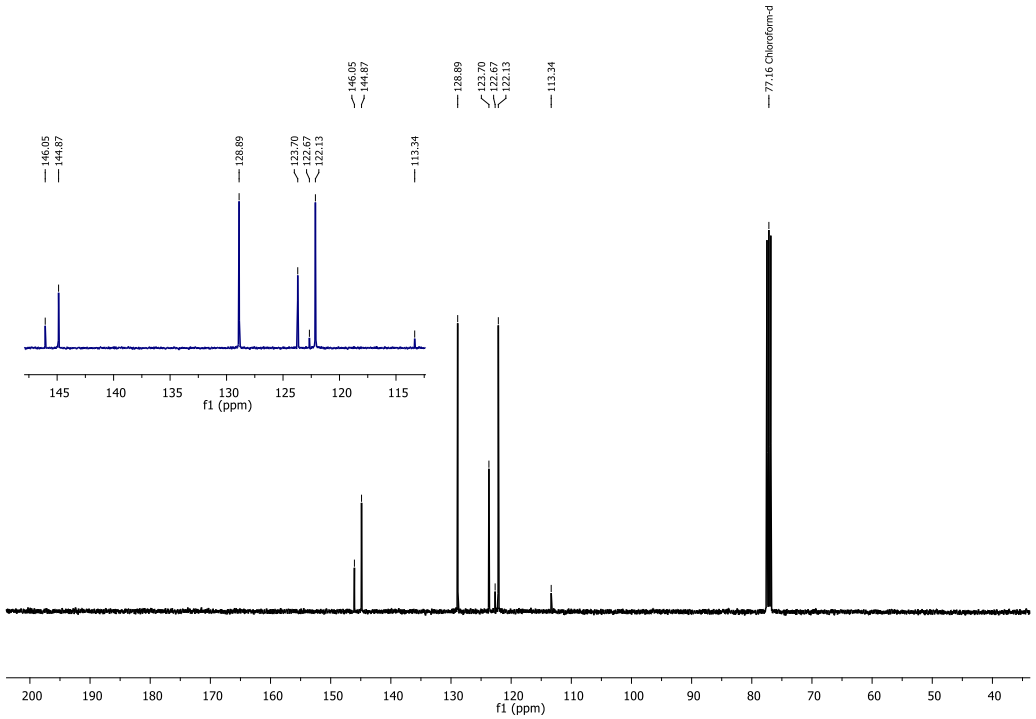

HRMS data of (a) DPAOCN:

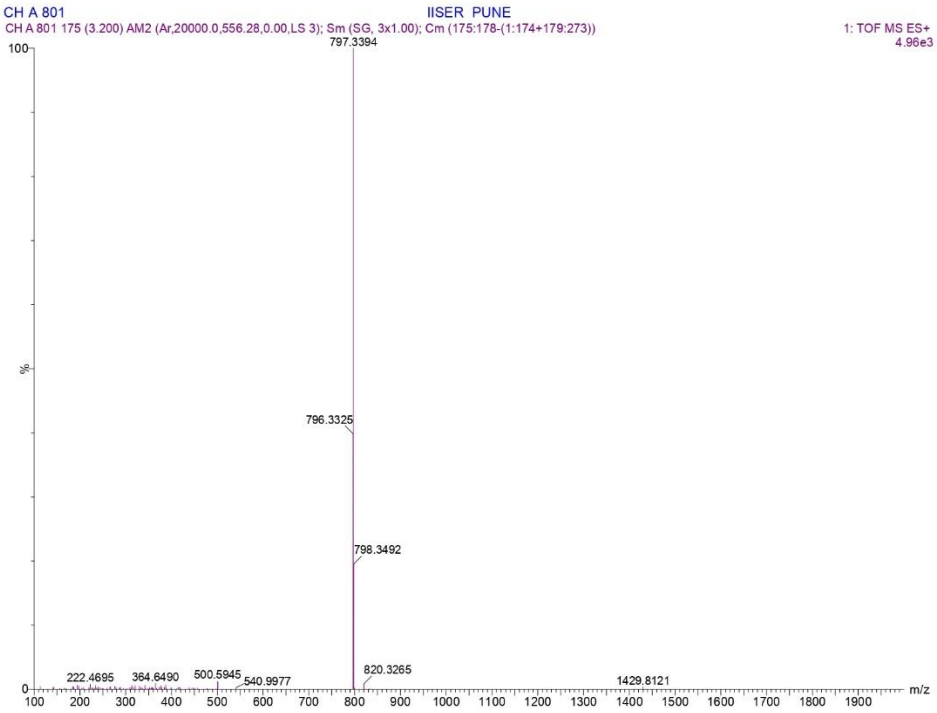

HRMS data of (b) DPAMCN:

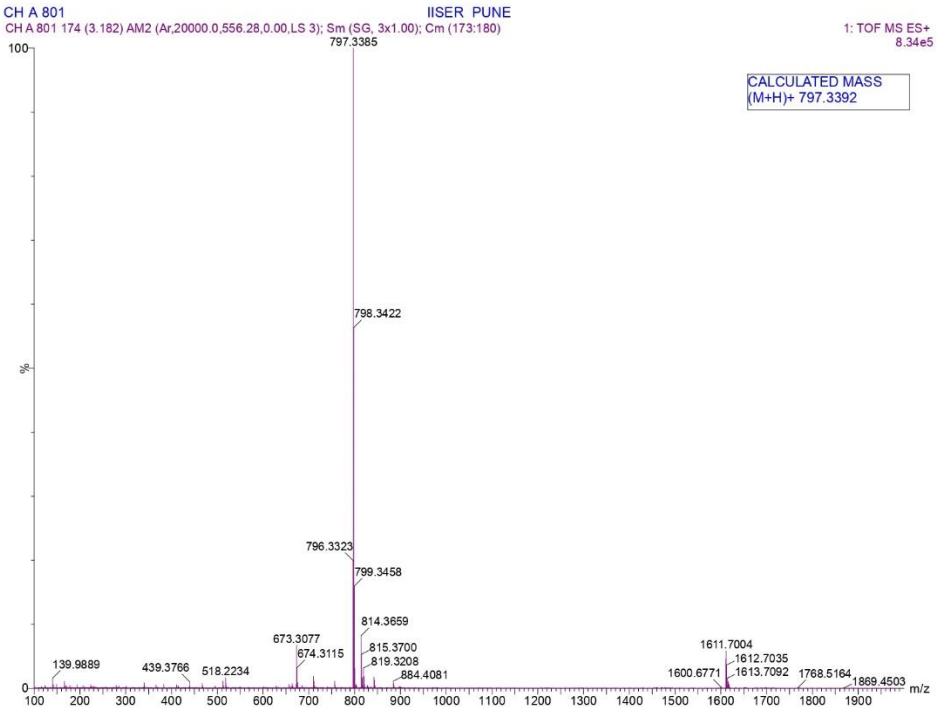

HRMS data of (c) DPAPCN:

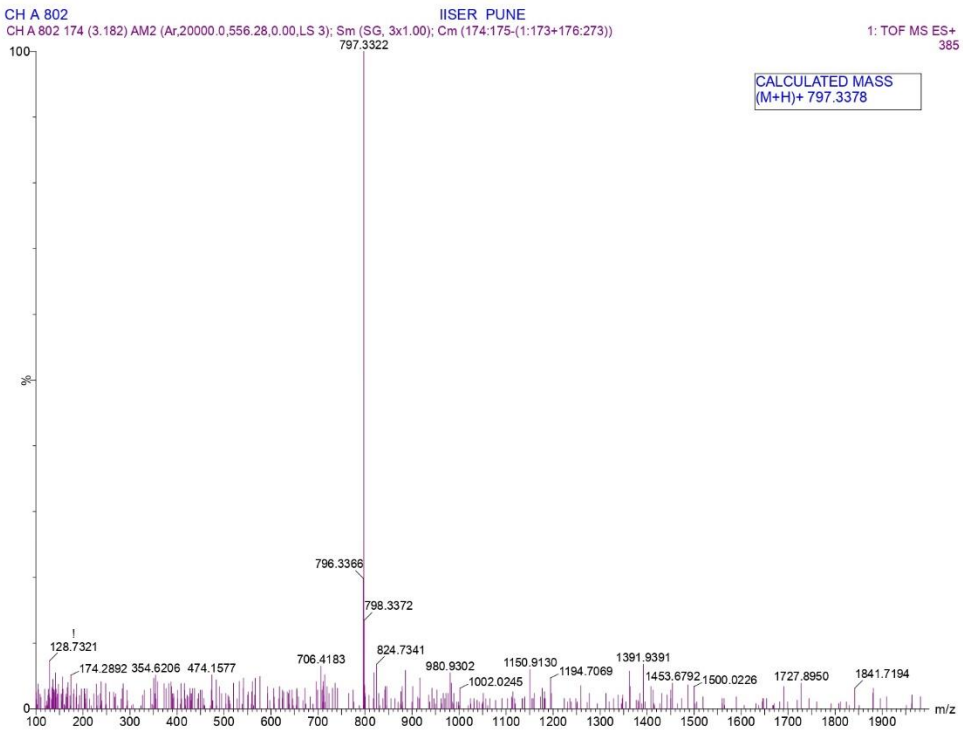

Crystallographic data

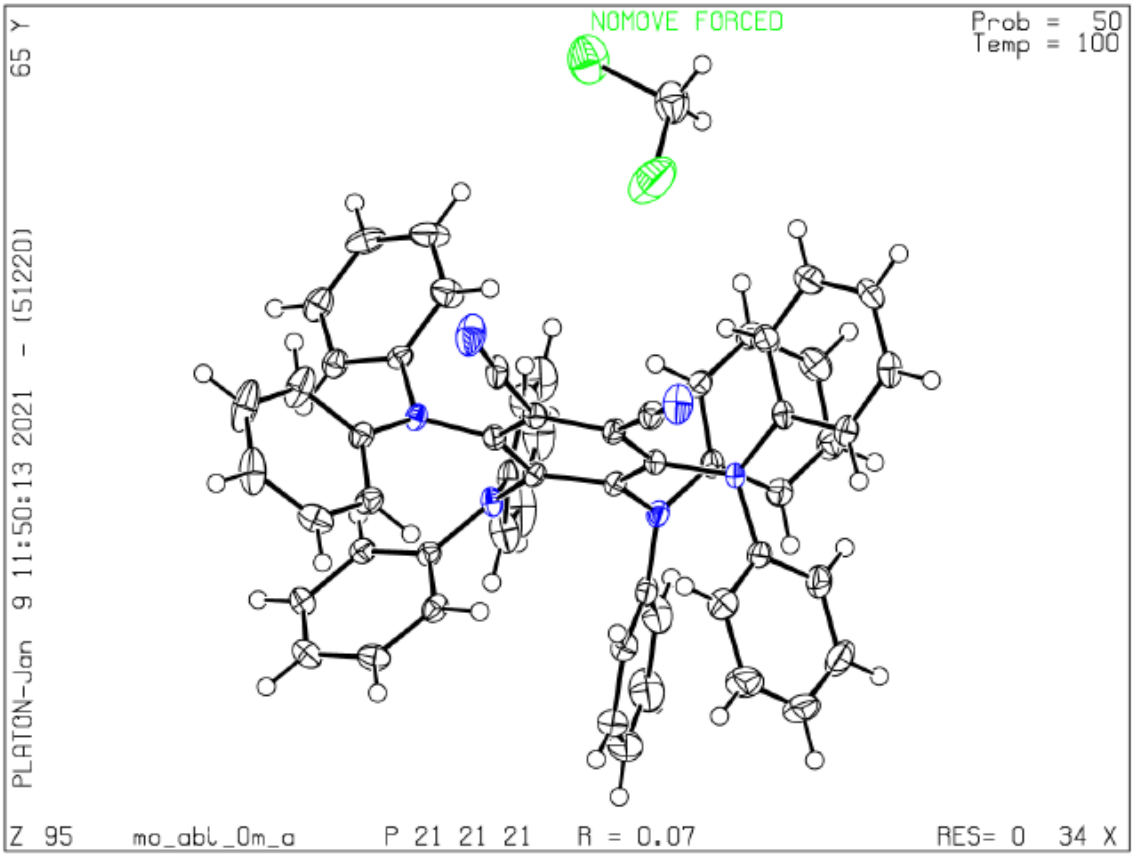

Table 1: Crystal data and structure refinement for DPAOCN.

Identification code	DPAOCN
CCDC No.	2287184
Empirical formula	$C_{57}H_{42}Cl_2N_6$
Formula weight	881.87
Temperature/K	100(2)
Crystal system	orthorhombic
Space group	$P2_12_12_1$
a/Å	9.771(3)
b/Å	21.156(7)
c/Å	22.933(8)
α/°	90
β/°	90

γ/°	90
Volume/Å^3	4741(3)
Z	4
ρcalc (g/cm^3)	1.235
μ/mm^{-1}	0.182
F(000)	1840.0
Radiation	MoKα (λ = 0.71073)
2Θ range for data collection/°	3.85 to 58.53
Index ranges	$-11 \leq h \leq 13$, $-28 \leq k \leq 28$, $-31 \leq l \leq 30$
Reflections collected	87524
Independent reflections	12600 [R_{int} = 0.1422, R_{sigma} = 0.1198]
Data/restraints/parameters	12600/0/586
Goodness-of-fit on F^2	1.039
Final R indexes [I>=2σ (I)]	R_1 = 0.0670, wR_2 = 0.1568
Final R indexes [all data]	R_1 = 0.1403, wR_2 = 0.1857
Largest diff. peak/hole / e Å^{-3}	0.68/-0.56
Flack parameter	0.15(3)

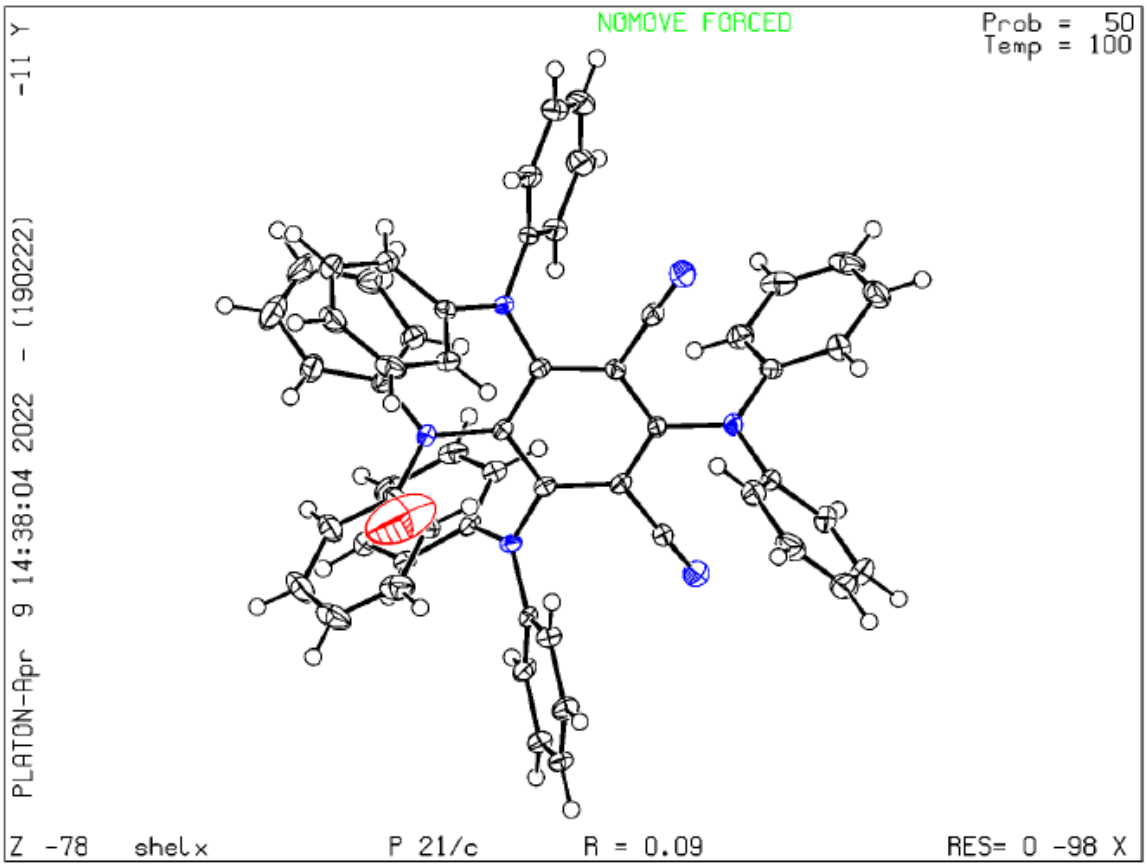

Table 2: Crystal data and structure refinement for DPAMCN.

Identification code	DPAMCN
CCDC No.	2271434
Empirical formula	$C_{56}H_{40}N_6O$
Formula weight	812.94
Temperature/K	100(2)
Crystal system	monoclinic
Space group	$P2_1/C$
a/Å	13.956(3)
b/Å	13.033(3)
c/Å	23.580(5)
α/°	90
β/°	93.210(6)
γ/°	90
Volume/Å^3	4282.1(15)
Z	4

ρcalc (g/cm^3)	1.261
μ/mm-1	0.077
F(000)	1704.0
Radiation	MoKα (λ = 0.71073)
2Θ range for data collection/°	4.28 to 56.728
Index ranges	-18 ≤ h ≤ 15, -17 ≤ k ≤ 16, -31 ≤ l ≤ 31
Reflections collected	98411
Independent reflections	10719 [R_{int} = 0.2496, R_{sigma} = 0.1347]
Data/restraints/parameters	10719/0/569
Goodness-of-fit on F^2	1.060
Final R indexes [I>=2σ (I)]	R_1 = 0.0882, wR_2 = 0.1764
Final R indexes [all data]	R_1 = 0.1629, wR_2 = 0.2104
Largest diff. peak/hole / e Å^{-3}	0.57/-0.72

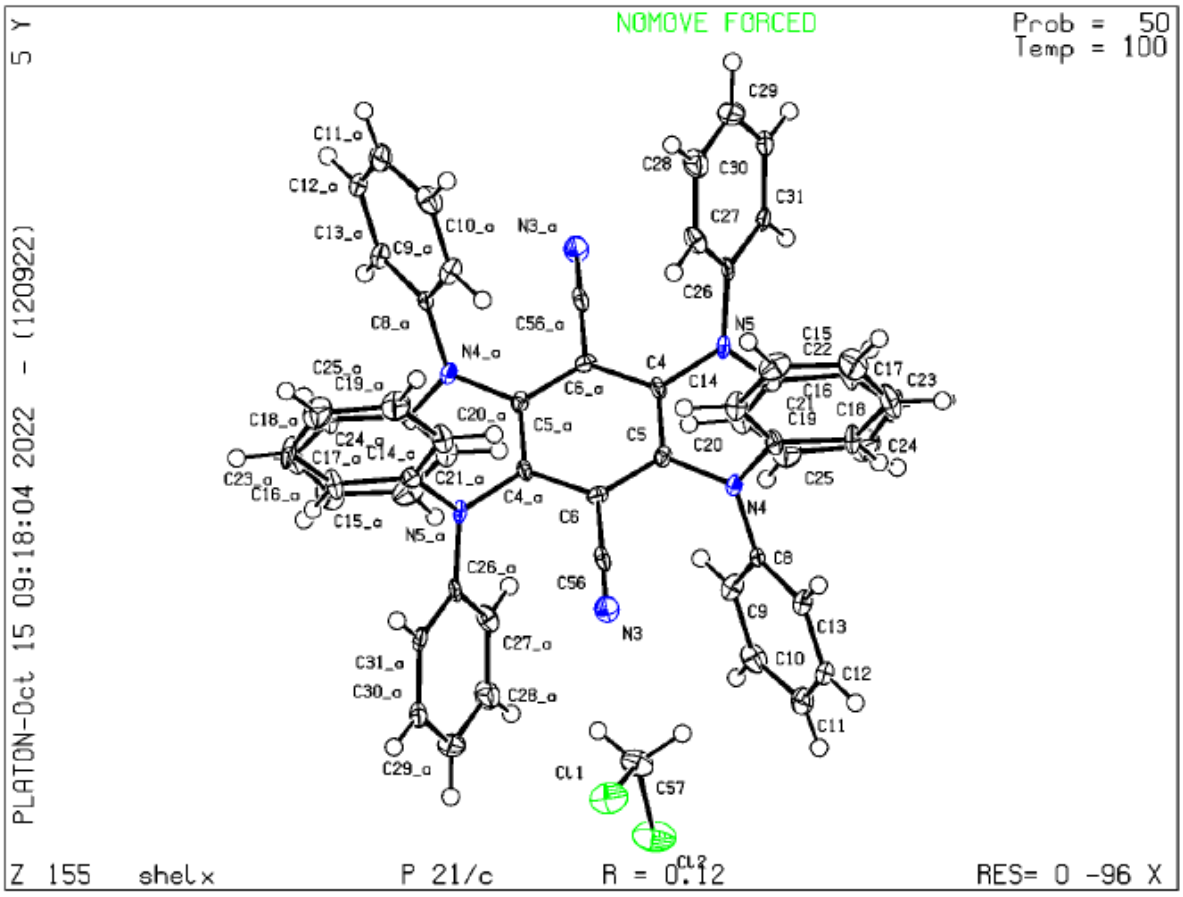

Table 3: Crystal data and structure refinement for DPAPCN.

Identification code	DPAPCN

CCDC No.	2287185
Empirical formula	$C_{58}H_{44}Cl_4N_6$
Formula weight	966.79
Temperature/K	100(2)
Crystal system	monoclinic
Space group	$P2_1/C$
a/Å	12.415(2)
b/Å	11.6613(19)
c/Å	17.594(3)
α/°	90
β/°	109.655(5)
γ/°	90
Volume/Å^3	2398.9(7)
Z	2
ρcalc (g/cm^3)	1.339
μ/mm^{-1}	0.294
F(000)	1209.0
Radiation	MoKα (λ = 0.71073)
2Θ range for data collection/°	4.272 to 48.998
Index ranges	$-14 \leq h \leq 14$, $-13 \leq k \leq 13$, $-20 \leq l \leq 19$
Reflections collected	33520
Independent reflections	3995 [R_{int} = 0.0645, R_{sigma} = 0.0373]
Data/restraints/parameters	3995/0/308
Goodness-of-fit on F^2	1.339
Final R indexes [I>=2σ (I)]	R_1 = 0.1161, wR_2 = 0.3582
Final R indexes [all data]	R_1 = 0.1258, wR_2 = 0.3634
Largest diff. peak/hole / e Å^{-3}	1.21/-0.60

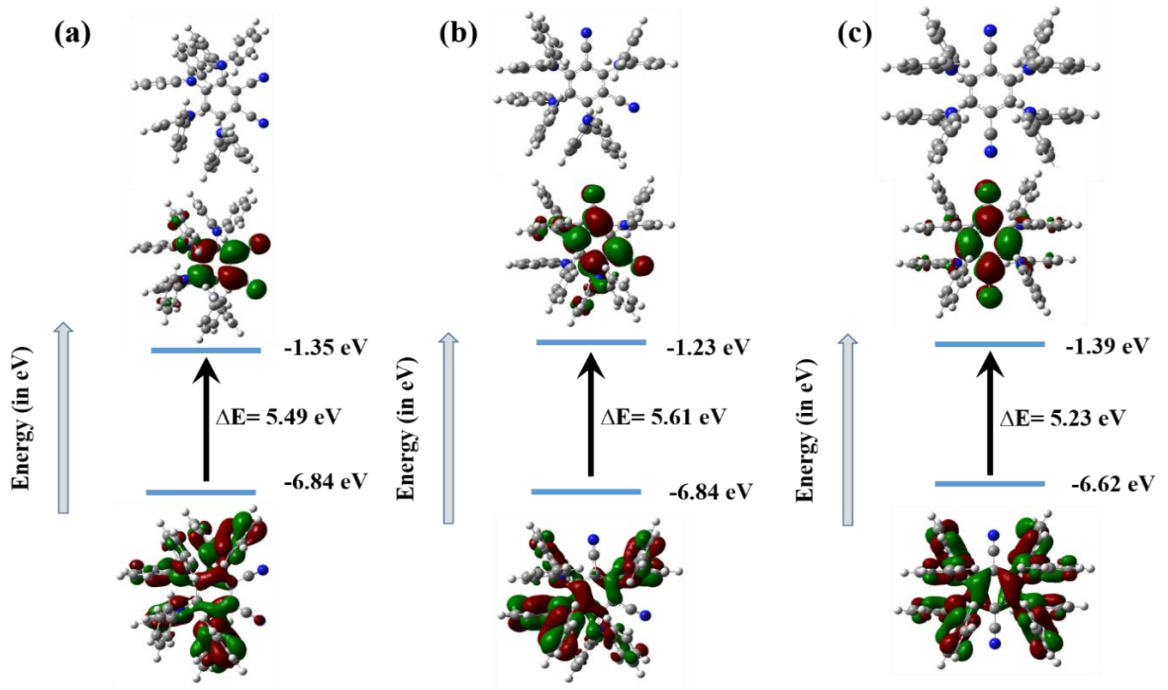

Figure A1: Ground state frequency analyzed optimized structure**s,** HOMO, and LUMO orbitals of (a) DPAOCN, (b) DPAMCN, and (c) DPAPCN along with their energy gaps.

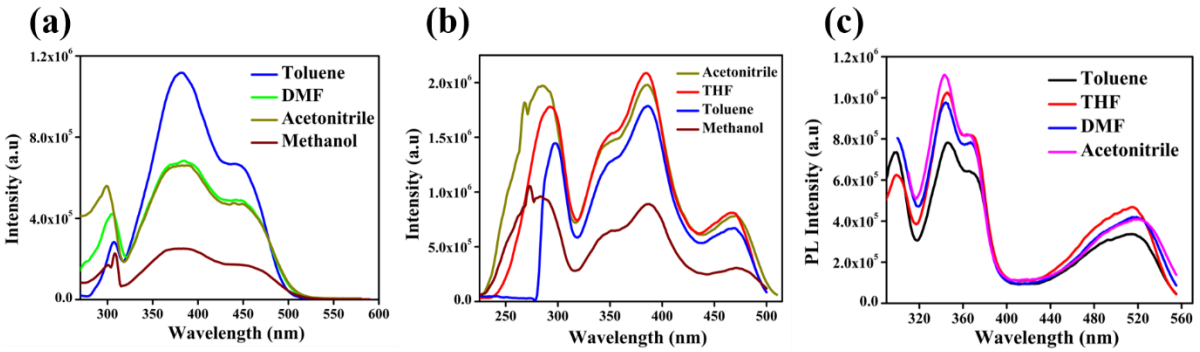

Figure A2: Excitation spectra of (a) DPAOCN, (b) DPAMCN, and (c) DPAPCN in different solvents (10 µm concentration).

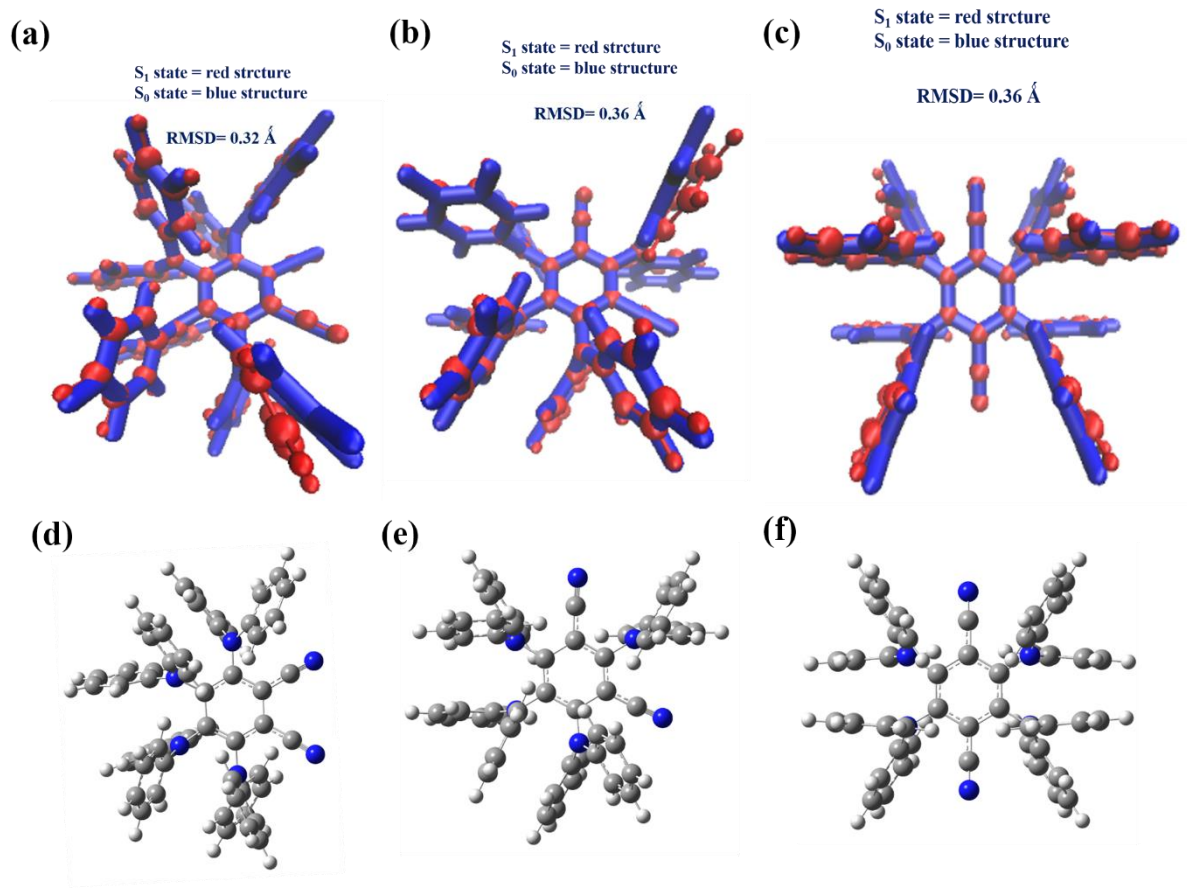

Figure A3: Root mean square deviation (RMSD) between the ground state (S_0 state) and excited state (S_1 state) of (a) DPAOCN, (b) DPAMCN, and (c) DPAPCN; calculated and plotted using VMD software, here blue structures in all three cases denote the S_0 state and red structures denote the S_1 state. Optimized S_1 state molecular geometries of (d) DPAOCN, (e) DPAMCN, and (f) DPAPCN. For S_1 state optimization, TD-SCF method, and B3LYP/6-31G (d, p) level of theory have been used in all three cases prior to ground state optimization at B3LYP/6-31G (d, p).

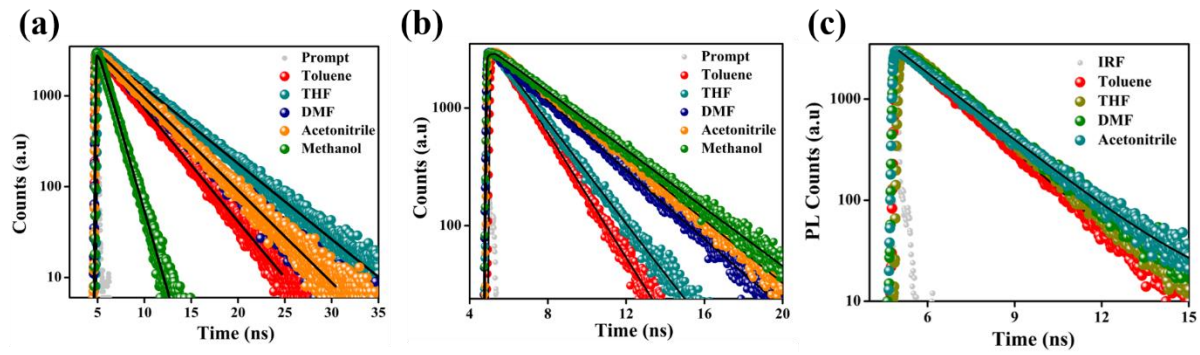

Figure A4: Time-resolved fluorescence decay profiles of (a) DPAOCN, (b) DPAMCN, and (c) DPAPCN in solvents of varying polarity (concentration 10 µm).

Solvent system	Decay type	Components
Toluene	Mono-exponential	3.57 ns
THF	Mono-exponential	5.35 ns
DMF	Mono-exponential	4.35 ns
Acetonitrile	Mono-exponential	4.34 ns
Methanol	Mono-exponential	1.25 ns

Table A1: Time-resolved fluorescence decay type and components in different solvents of DPAOCN (concentration 10 µm).

Solvent system	Decay type	Components
Toluene	Mono-exponential	1.69 ns
THF	Mono-exponential	2.06 ns
DMF	Mono-exponential	3.03 ns
Acetonitrile	Mono-exponential	3.31 ns
Methanol	Mono-exponential	3.61 ns

Table A2: Time-resolved fluorescence decay type and components in different solvents of DPAMCN (concentration 10 µm).

Solvent system	Decay type	Components
Toluene	Mono-exponential	1.73 ns
THF	Mono-exponential	1.83 ns
DMF	Mono-exponential	1.97 ns

Acetonitrile	Mono-exponential	2.01 ns

Table A3: Time-resolved fluorescence decay type and components in different solvents of DPAPCN (concentration 10 µm).

Sample	λ_{em}	τ_1	α_1	τ_2	α_2
DPAOCN	530 nm	3.5 ns	64.1±0.7 %	**6±0 ps**	**37.2±0.8 %**
DPAOCN	550 nm	3.5 ns	93±0.6 %	**6.5±0 ps**	**7±1.1 %**
DPAOCN	560 nm	3.5 ns	98.5±1.1 %	**9±0 ps**	**1.4±0.9 %**
DPAMCN	500 nm	1.6 ns	64.8±0.4 %	**3.6±0.1 ps**	**35.1±0.7 %**
DPAMCN	517 nm	1.6 ns	84.2±0.3 %	**2.4±0.1 ps**	**15.7±0.6 %**
DPAMCN	540 nm	1.6 ns	100%	-	-
DPAPCN	550 nm	1.7 ns	62.4±0.9 %	**7.3±0.4 ps**	**37.5±1.54 %**
DPAPCN	560 nm	1.7 ns	74±1.8 %	**8±1.1 ps**	**26±2.45 %**
DPAPCN	570 nm	1.7 ns	75.6±1.5 %	**7.6±0.9 ps**	**24±2.3 %**

Table A4: Fluorescence up-conversion decay transients and their respective wavelength-based contributions for all three isomers in toluene. Shorter decay components and their respective contributions have been highlighted in bold.

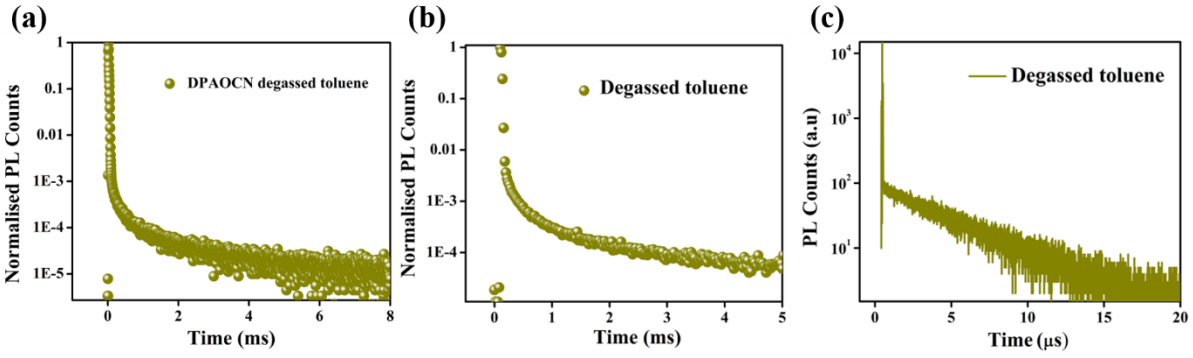

Figure A5: Delayed fluorescence lifetimes of (a) DPAOCN, (b) DPAMCN, (c) DPAPCN in degassed toluene (for 30 µm of luminogen concentration).

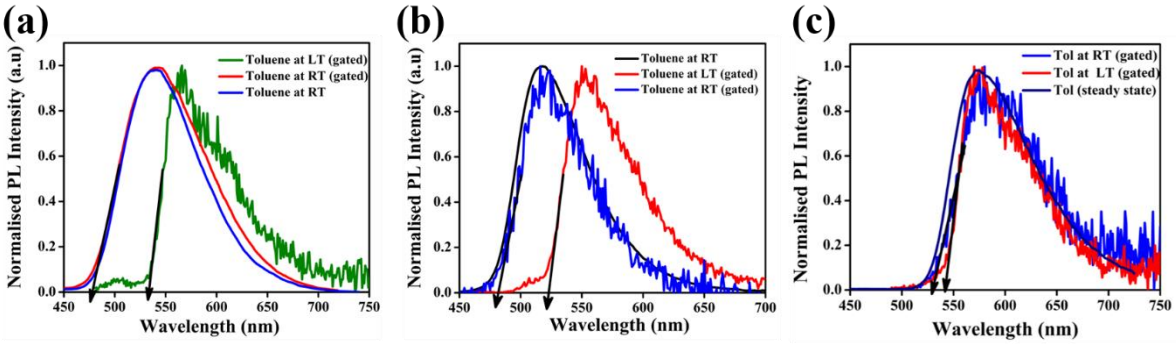

Figure A6: Steady-state and time-gated emission spectra of (a) DPAOCN, (b) DPAMCN, (c) DPAPCN at room temperature (298 K) and 77 K in degassed toluene. At RT, for DPAOCN & DPAMCN, 50 μs delay time and 2 ms sample windows have been used. For DPAPCN, 5 μs delay time and 1 ms sample windows have been used. At 77 K(low-temperature), for DPAOCN & DPAMCN, 0.25 ms delay time and 10 ms sample windows have been used. For DPAPCN, due to its relatively lower lifetime, 0.1 ms delay time and 10 ms sample windows have been used.

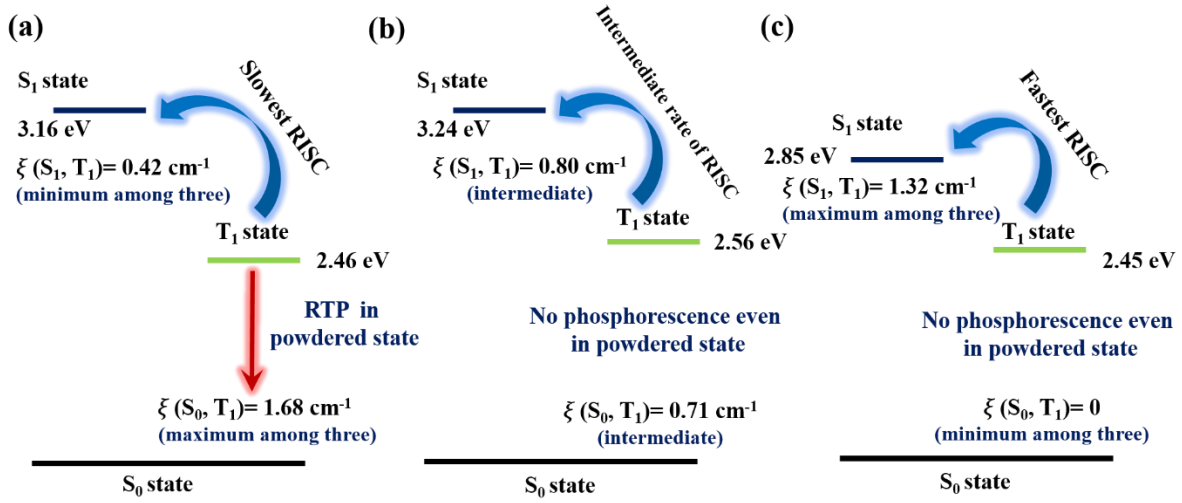

Figure A7: Energy diagram of (a) DPAOCN, (b) DPAMCN, and (c) DPAPCN obtained from TD-DFT (50-50) calculation using TD-SCF method at CAM-B3LYP/6-311++G (d, p) level of theory.

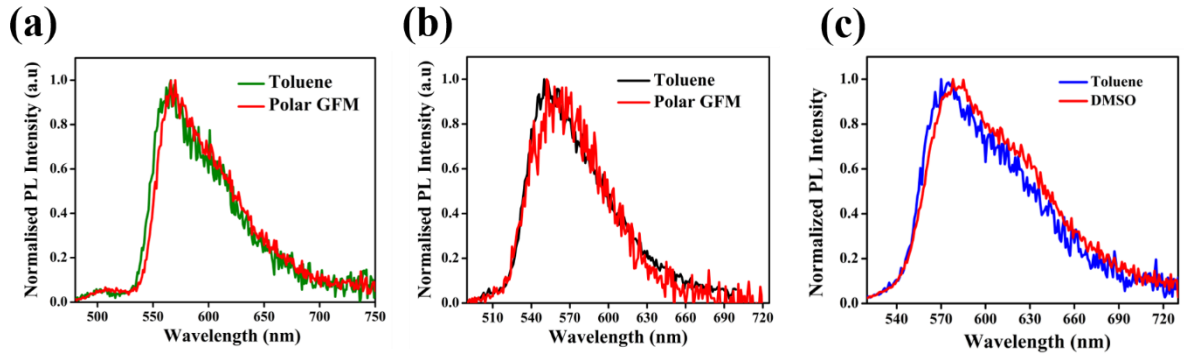

Figure A8: Time-gated emission spectra at 77K of (a) DPAOCN, (b) DPAMCN, and (c) DPAPCN in toluene and polar glass-freezing alcoholic mixtures (GFM) (for DPAOCN and DPAMCN). For DPAPCN, DMSO has been used due to the isomer's poor solubility in GFM. Concentration= 30 µm. For DPAOCN & DPAMCN, 0.25 ms delay time and 10 ms sample windows have been used. For DPAPCN, due to its relatively lower lifetime, 0.1 ms delay time and 10 ms sample windows have been used.

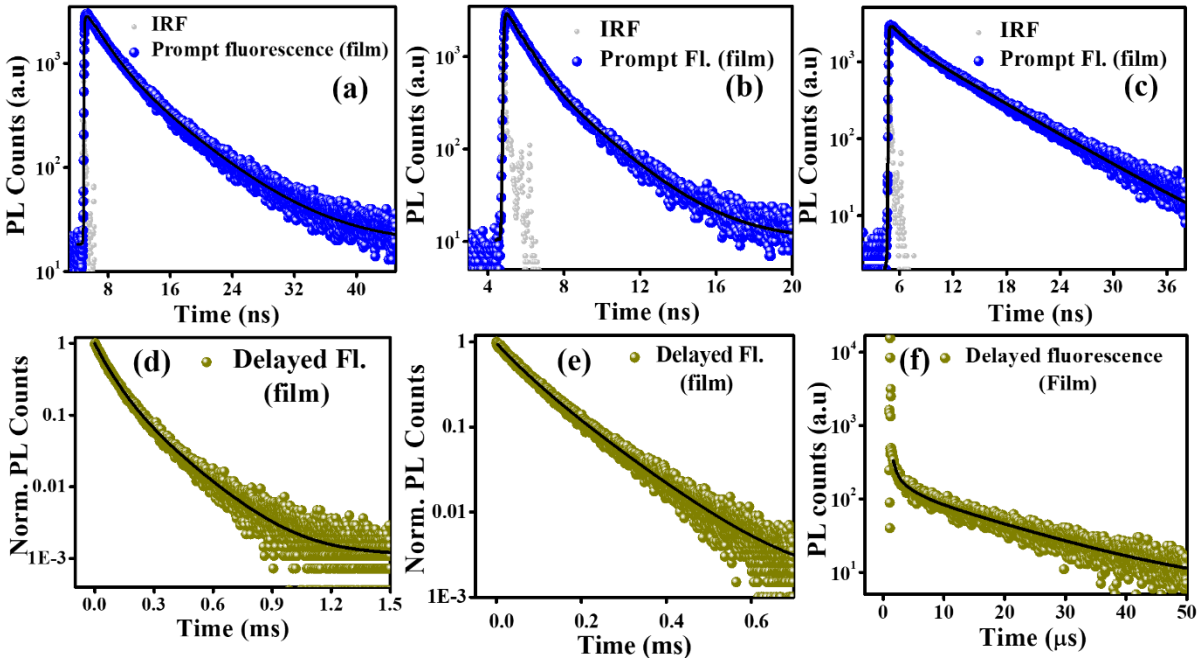

Figure A9: (a) & (d) prompt fluorescence and delayed fluorescence lifetime of 10wt % DPAOCN doped PMMA film. (b) & (e) prompt fluorescence and delayed fluorescence lifetime of 10wt % DPAMCN doped PMMA film. (c) & (f) prompt fluorescence and delayed fluorescence lifetime of 10wt % DPAPCN doped PMMA film. Averaged prompt fluorescence lifetime (τ_{PF}) of DPAOCN, DPAMCN, and DPAPCN are found to be 4.39 ns, 1.19 ns, and 1.79 ns, respectively.

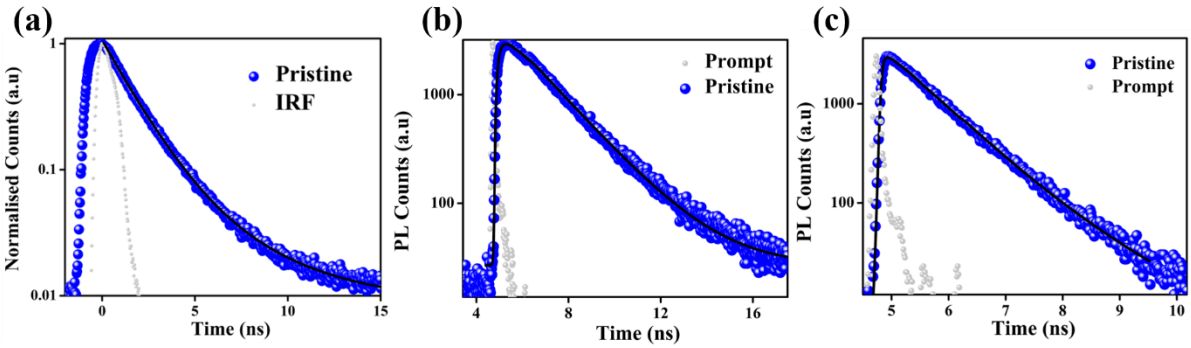

Figure A10: Prompt fluorescence emission lifetime of (a) DPAOCN powder, (b) DPAMCN powder, and (c) DPAPCN powder. Averaged prompt fluorescence lifetime (τ_{PF}) of DPAOCN, DPAMCN, and DPAPCN powder are found to be 2.1 ns, 1.1 ns, and 0.8 ns, respectively.

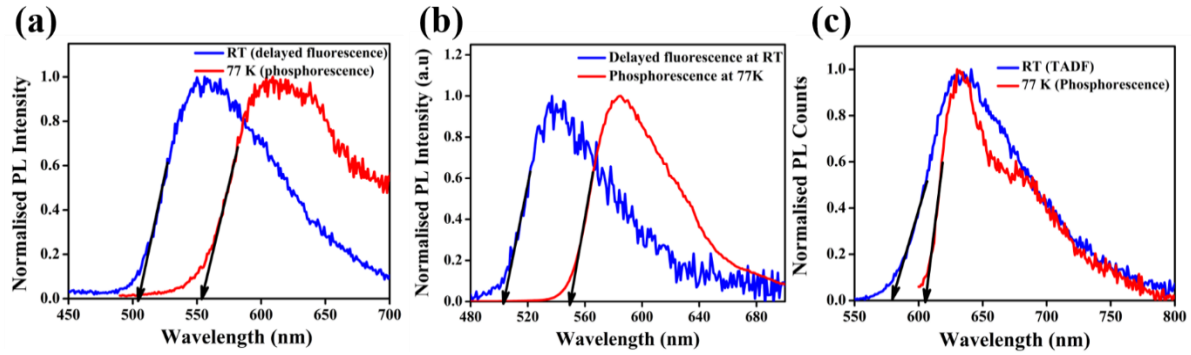

Figure A11: Time-gated spectra of (a) DPAOCN, (b) DPAMCN, and (c) DPAPCN powder at RT and at 77 K (50 µs delay for RT spectra and 0.25 ms delay for 77 K spectra in case of DPAOCN and DPAMCN to remove residual TADF photon counts. For DPAPCN, due to its relatively lower lifetime, RT spectra were collected using a 10 µs delay, and 77 K spectra were collected using a 0.1 ms delay. Sample windows for all room-temperature spectra measurements have been kept at 2 ms and for all low-temperature spectra measurements have been kept at 10 ms.

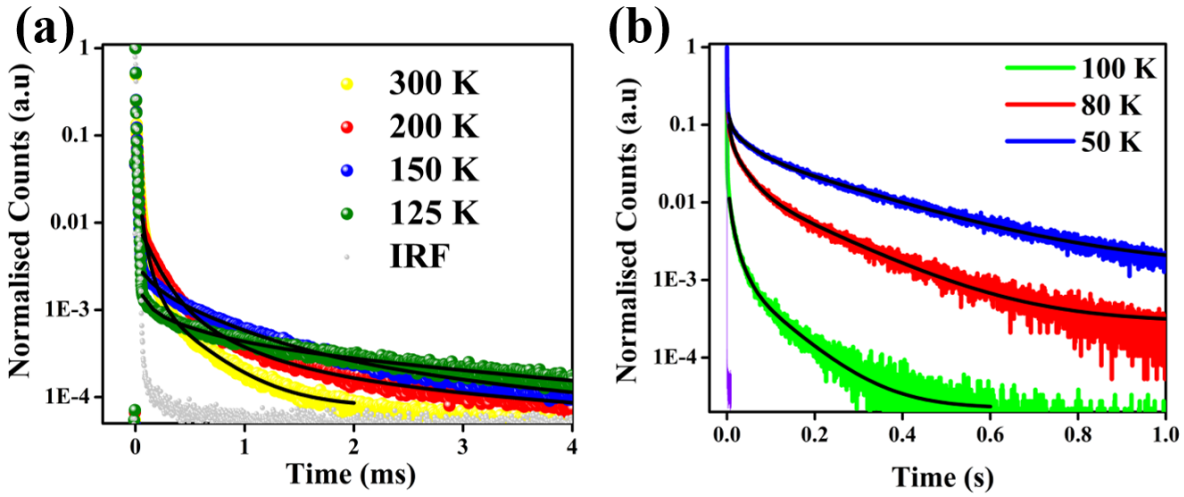

Figure A12: Temperature-dependent PL decay of DPAOCN powder (collection wavelength at 600 nm) in (a) a shorter time window and (b) a longer time window (excitation wavelength= 375 nm).

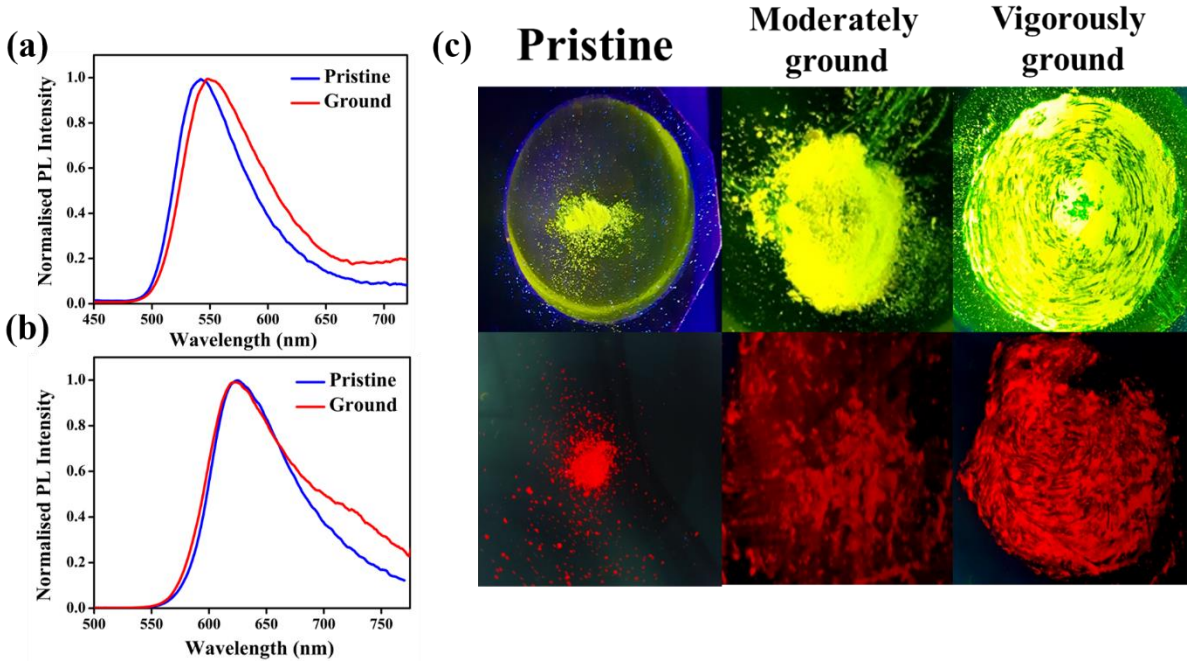

Figure A13: (a) & (b) Grinding effect on DPAMCN and DPAPCN pristine powder respectively (ex. 380 nm). (c) Photographic images (irradiated using 365 nm UV lamp) of grinding effect on DPAMCN (top) and DPAPCN (bottom) powder.

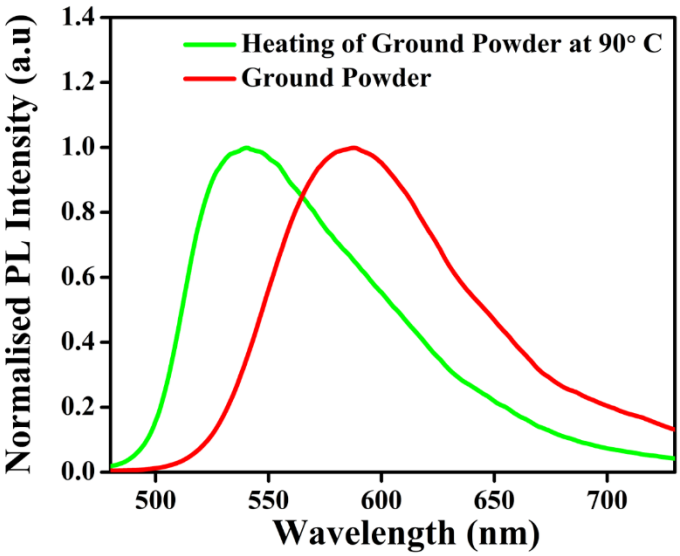

Figure A14: Heating effect on the DPAOCN ground powder (O-form) to yield G-form.

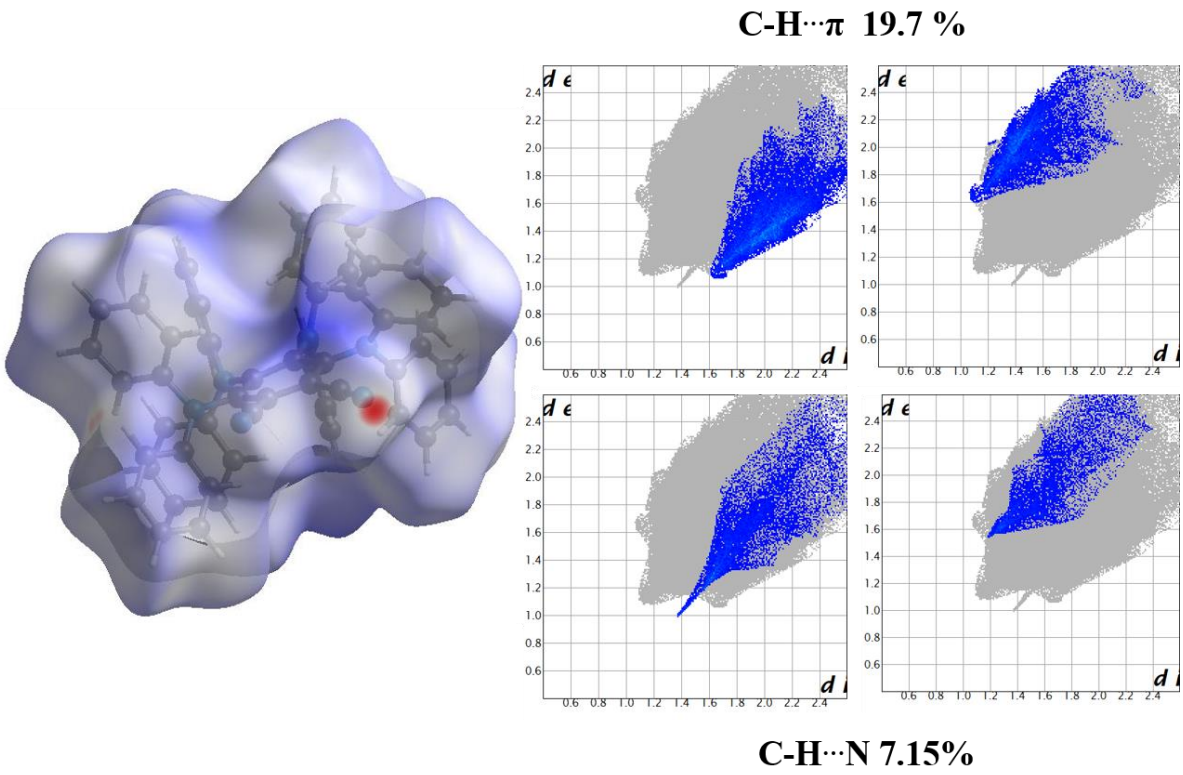

Figure A15: Hirshfeld surface analysis[49-51] of DPAOCN crystal and fingerprint plot giving quantitative description regarding several non-covalent interactions using crystal explorer 3.1 software[52] with iso-value 0.5. The d_e & d_i values of each fingerprint plot are within the range of 0.4-2.6.

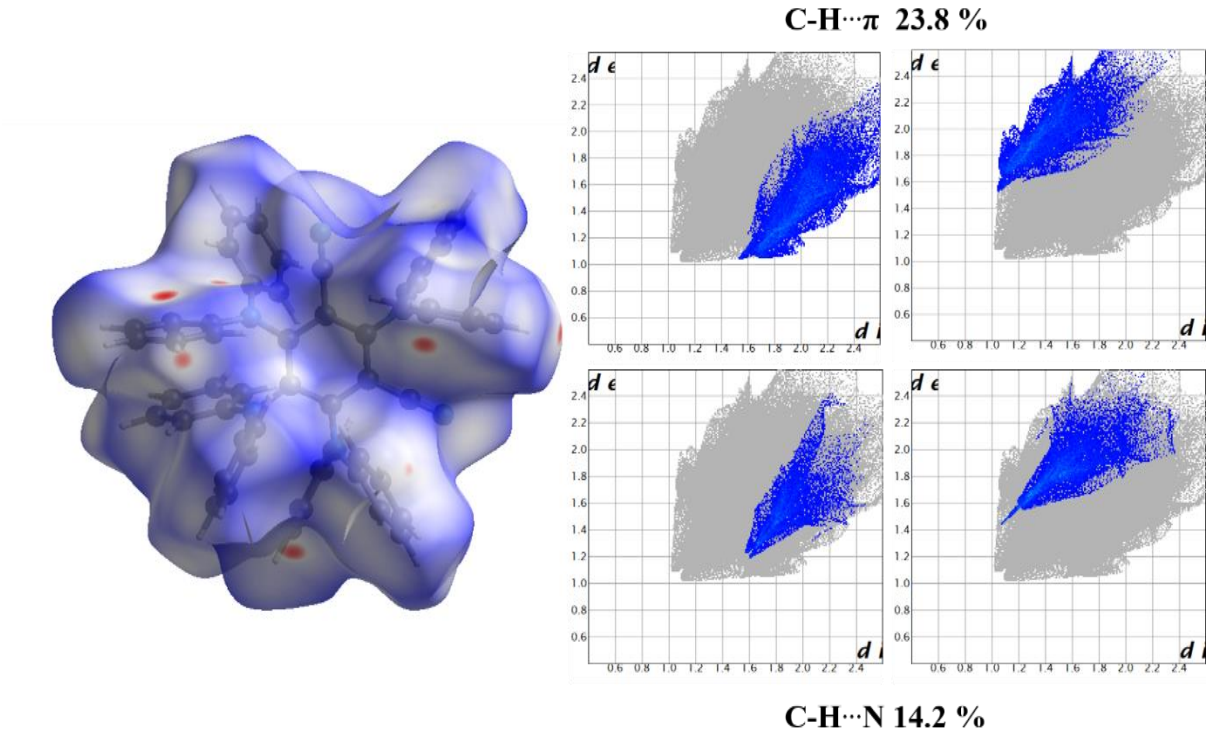

Figure A16: Hirshfeld surface analysis of DPAMCN crystal and fingerprint plot giving quantitative description regarding several non-covalent interactions. The d_e & d_i values of each fingerprint plot are within the range of 0.4-2.6.

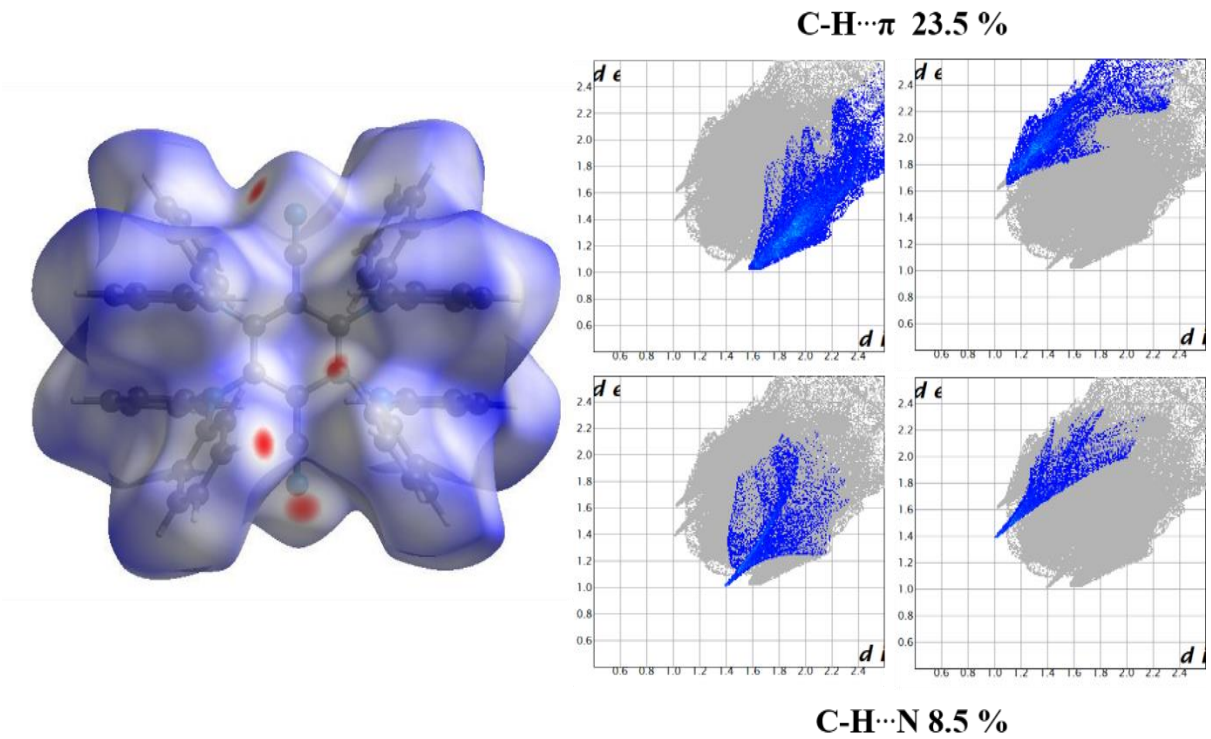

Figure A17: Hirshfeld surface analysis of DPAPCN crystal and fingerprint plot giving quantitative description regarding several non-covalent interactions. The d_e & d_i values of each fingerprint plot are within the range of 0.4-2.6.

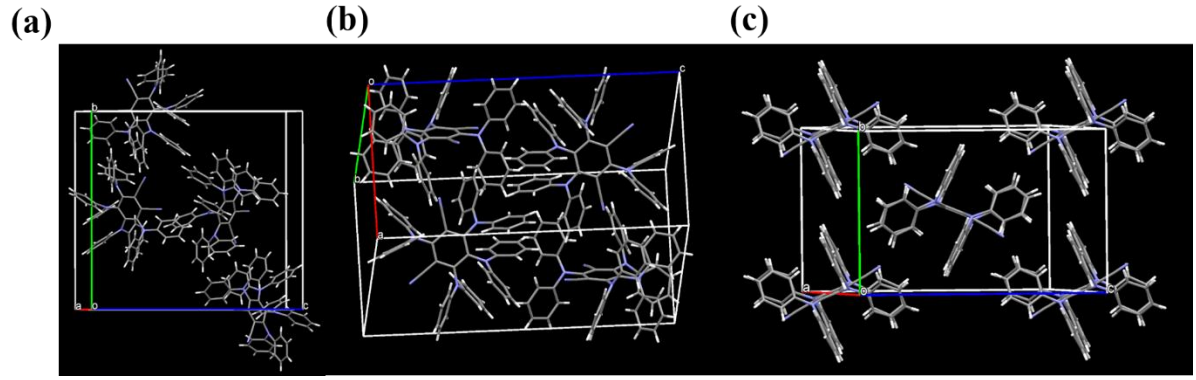

Figure A18: Crystal unit cell packing of all three luminogens (a) DPAOCN (Z= 4, cell volume= 4740 Å^3), (b) DPAMCN (Z= 4, cell volume= 4282 Å^3), (c) DPAPCN (Z= 2, cell volume= 2398 Å^3).

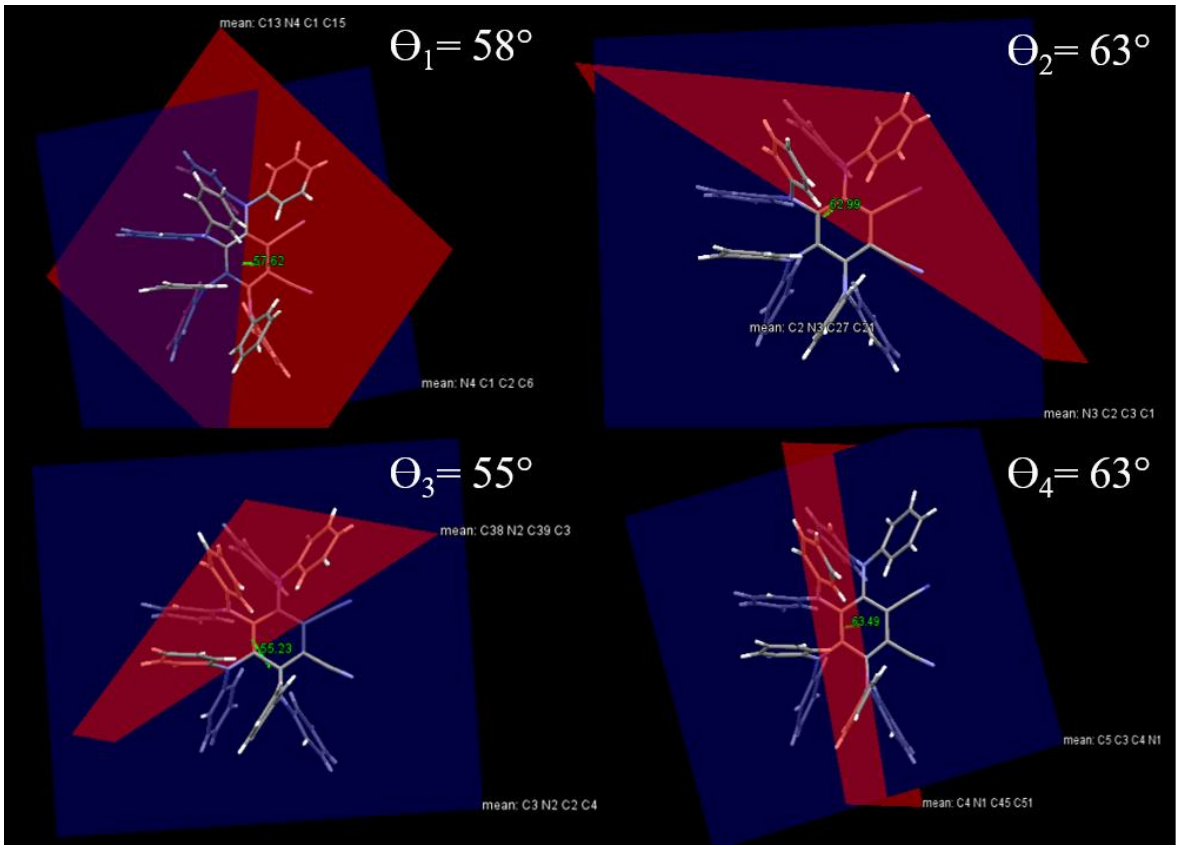

Figure A19: Dihedral angles of each peripheral diphenylamine moiety with the central phthalonitrile core of DPAOCN.

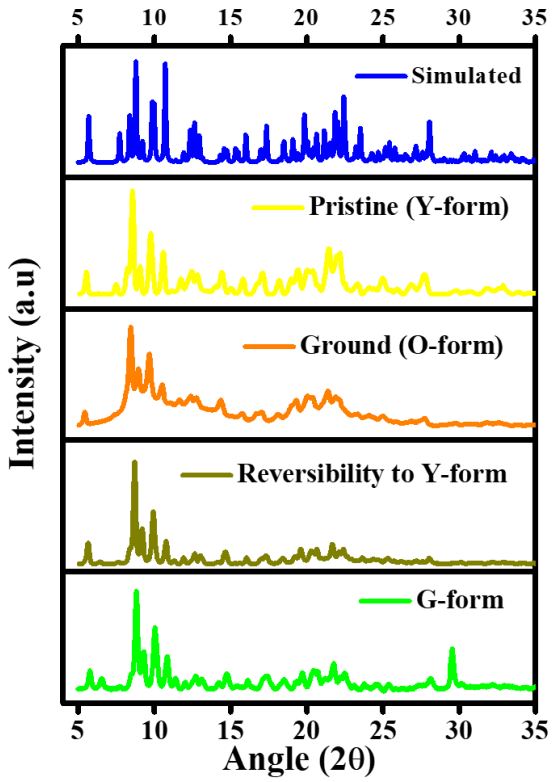

Figure A20: Simulated and experimental PXRD patterns of all forms of DPAOCN. Y-form = pristine form, O-form = ground form (obtained after mechanical grinding), reversibility to Y-form = exposing less DCM vapor on O-form or the ground powder, G-form= after prolonged exposure of DCM vapor on O-form or after heating the ground powder (O-form) at ~ 90°C.

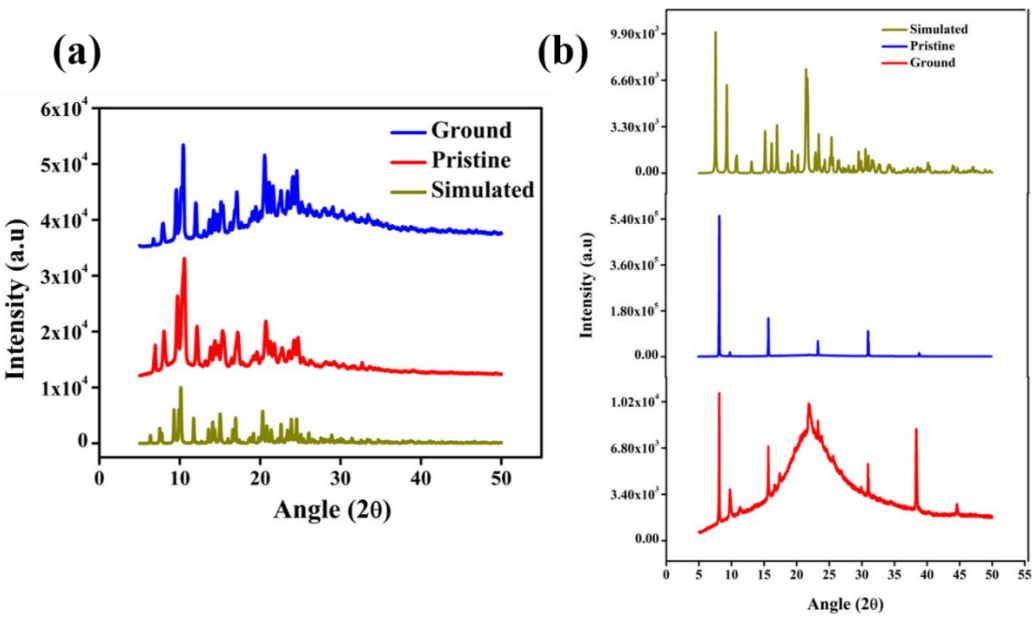

Figure A21: Simulated and experimental PXRD patterns of (a) DPAMCN, (b) DPAPCN powder under external stimuli.

Note A1: Large change in prompt and delayed emission lifetimes of DPAOCN:

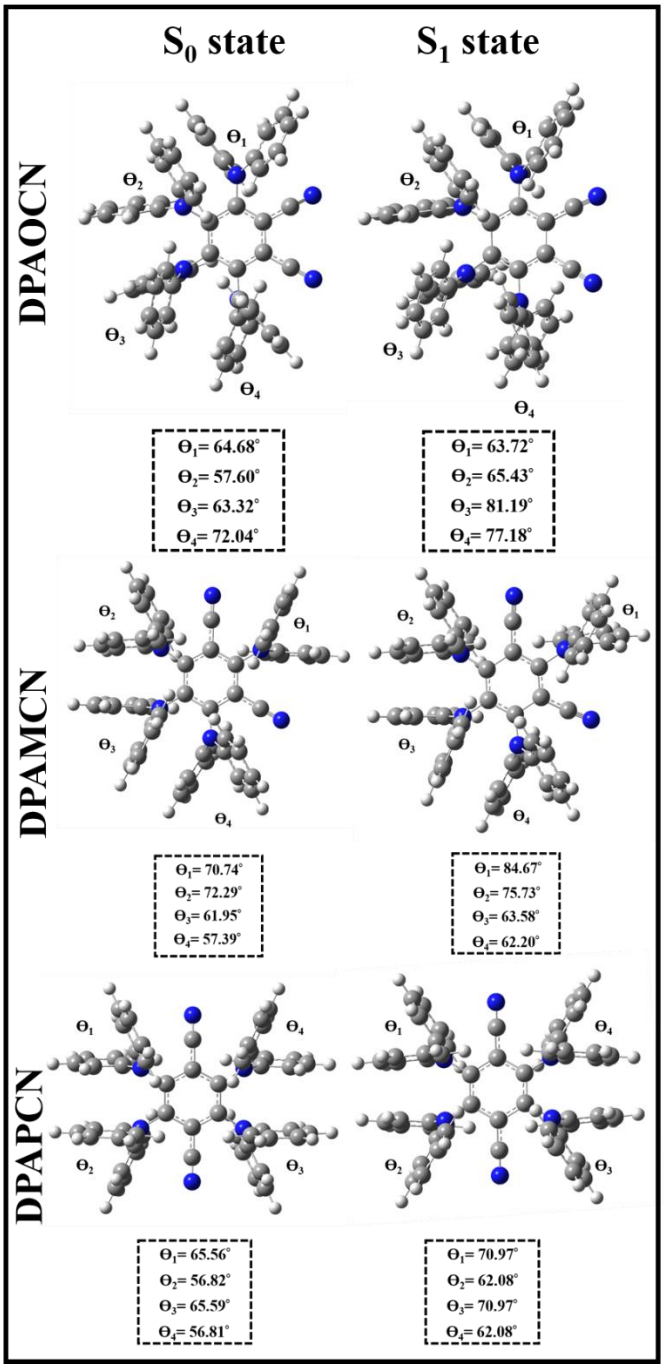

Figure A22: Optimized ground state (S_0 state) and excited state (S_1 state) structures of all three isomers in the gas phase at B3LYP/ 6-31G (d,p) level of theory.

Large changes in prompt and delayed fluorescence lifetime are attributed to large energy changes upon mechanical grinding in the case of mechano-active DPAOCN. Herein, we would like to draw the readers' attention to an intriguing aspect. Our theoretical outcomes from TDDFT calculation unambiguously indicate that the ICT excitation/emission processes of all

three isomers should be accompanied by variations of intramolecular D–A twisting (Figure A22). In powder form and especially in a system with large steric hindrance like DPAOCN, such structural relaxation would be strongly suppressed by constraints from the dense and rigid molecular packings that make the D and A units remain in the initial less twisted arrangements even in the excited state. However, upon grinding a large energy change is highly anticipated because the disordered amorphous states are generally less dense and possess a relatively large free volume which is accompanied by a large void volume of the DPAOCN molecule, in that case, the specific diphenyl amine donor units can more freely rotate to afford near orthogonal excited D–A structures with energetically different and more stabilized ICT excited state. Consequently, the PL spectra underwent conspicuous redshifts along with significant lifetime changes through the crystalline to amorphous transformation. On the contrary, such energy changes are less feasible in the other two isomers due to relatively lower steric hindrance and void volume and moreover, due to its centro-symmetric packing.

Note A2: Role of DCM adsorption and amount of DCM adsorbed by O-form (ground orange emissive powder) upon DCM vapour treatment:

Herein, adsorbed DCM is playing a crucial role in the modulation of crystallinity, as well as reversibility of the tri-color stimuli-responsiveness. Polar DCM molecules by creating a dipole-dipole interaction alter the donor-acceptor dihedral angle of the molecule, thus changing the emission color of the system. We performed a control experiment to support this statement- the ground powder (O-form) was fumed with vapor of non-polar solvent like- hexane, and this time no color change was observed (Figure A23, below), supporting our claim of solvent-sample dipole-dipole interaction. It is worth noting that upon DCM vapour treatment a blue shift of the ground O-form is taking place, suggesting a lowering of the D-A dihedral angle of the luminogen by solvent dipole interaction. Moreover, analysis of the PXRD patterns of all the DCM-treated samples shows that the vapor treatment does not significantly change the crystalline phase as the position of the PXRD peaks remains nearly unchanged, the only change being the modulation of crystallinity of the samples. In order to quantify the amount of DCM adsorbed by the O-form (ground orange emissive powder) to revert back to Y-form and further forming the G-form, we conducted a TGA experiment using three samples: (a) ground powder (O-form), (b) a small amount of sample treated with DCM vapor (forming the Y-form), and (c) a large amount of sample treated with DCM vapor (forming the G-form). Samples b and c exhibited a decrease in weight between 40-120°C (Figure A23, below), which is attributed to the adsorption of DCM vapor. It was further determined that sample b adsorbed approximately

2% of DCM vapor, while sample c adsorbed up to 6%, indicating varying levels of DCM adsorption.

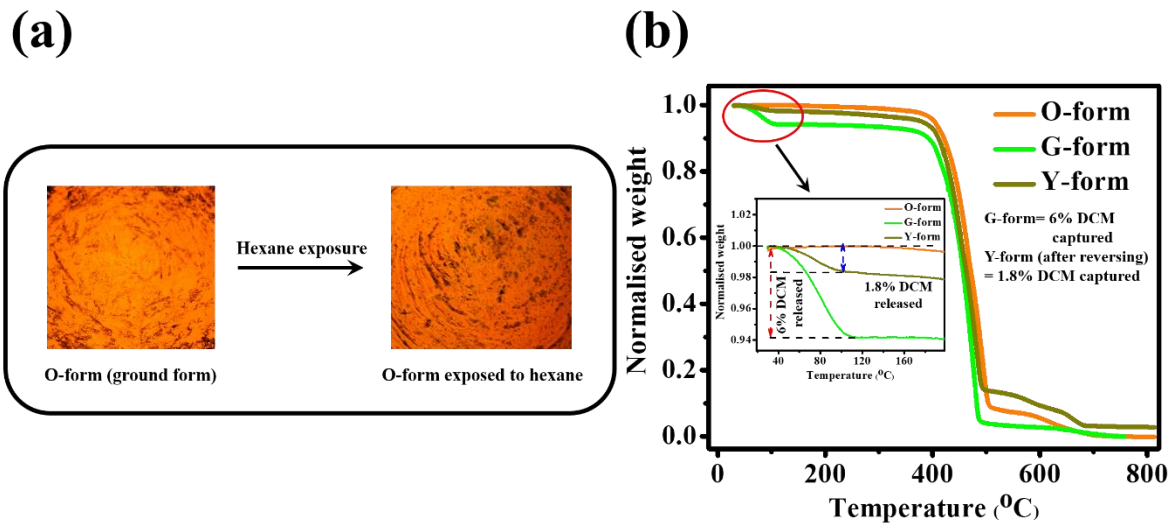

Figure A23: (a) No emission color change upon hexane fuming of the ground powder (O-form), (b) TGA data of ground powder (O-form), a small amount of sample treated with DCM vapor (forming the Y-form), and a large amount of sample treated with DCM vapor (forming the G-form).

Section A2:

Experimental Setup for Second-Harmonic Generation:

For conducting SHG experiments, we have used ultrafast (~50 fs) pulses of different wavelengths from an optical parametric amplifier (OPA) as the excitation source. The OPA (TOPAS-C, Light Conversion) is pumped by a regenerative amplifier (Spitfire Pro XP, Spectra-Physics) with a pulse width of 45 fs (FWHM), 1 KHz repetition rate, and 800 nm center wavelength. Further, the amplifier was seeded with a mode-locked Ti: Sapphire oscillator (Tsunami, Spectra-Physics) of 80 MHz repetition rate and 800 nm central wavelength. The pump beam from the OPA passes through a neutral density (N. D.) filter for power-dependent measurements followed by an 850 nm of long-pass filter for the purity of the pump beam. The filtered output was then focused using a plano-convex lens of 200 mm focal length. To avoid damage, we kept the sample away from the focus where the spot size of the beam is 400 μm. The output SHG signal was then collimated using a 25 mm plano-convex lens and filtered using a 750 nm short-pass filter to remove any residual pump beam. The collimated

output was then detected using a miniature spectrometer (USB4000, Ocean Optics) coupled to an optical fiber.

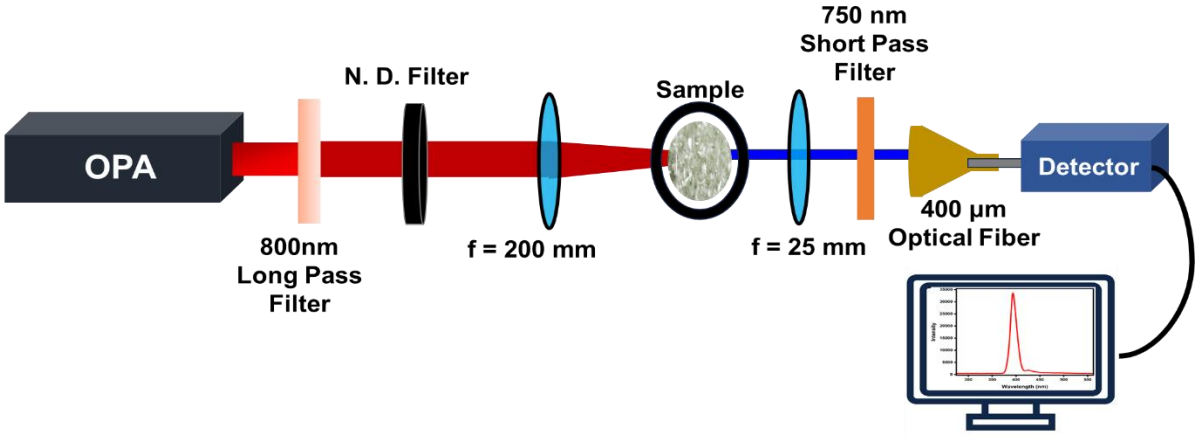

Scheme S2: experimental set-up for second harmonic generation.

Calculation of second-order nonlinear susceptibility ($\chi^{(2)}$):

To calculate the second-order nonlinear conversion efficiency of the DPAOCN crystals, we have relied on modified Maxwell's nonlinear equation of relative intensity given by equation (1):[53]

$$\chi_S{}^{(2)} = \chi_R{}^{(2)} \sqrt{\frac{I_S(2\omega)}{I_R(2\omega)}} \qquad \text{---------- (1)}$$

Where $\chi_S{}^{(2)}$ and $\chi_R{}^{(2)}$ are the second-order NLO susceptibilities of the sample and reference and $I_S(2\omega)$ and $I_R(2\omega)$ are the relative SHG intensities of the sample and reference, respectively. We have used potassium dihydrogen phosphate (KDP) as the reference for determining second-order susceptibility from the SHG data. Our sample shows $\chi_S{}^{(2)}$ = 0.038 pm/V at 1064 nm. Next, we determined the $\chi^{(2)}$ at 1220 nm of the sample from the SHG data of the sample and KDP at an excitation wavelength of 1220 nm by using the equation (2):

$$\chi_{\omega_1}{}^{(2)} = \chi_{\omega_2}{}^{(2)} \left(\frac{2\omega_2}{2\omega_1}\right) \sqrt{\frac{I(2\omega_1)}{I(2\omega_2)}} \qquad \text{---------- (2)}$$

where $\chi_{\omega_1}{}^{(2)}$ and $\chi_{\omega_2}{}^{(2)}$ are the second-order susceptibilities at fundamental pump frequencies ω_1 and ω_2 and the $I(2\omega_1)$and $I(2\omega_2)$ are their respective intensities. We have calculated $\chi^{(2)}$ =

0.19 pm/V of DPAOCN at 1220 nm. As a result, our sample showed comparable SHG with that of the commercially available materials.[54-55]

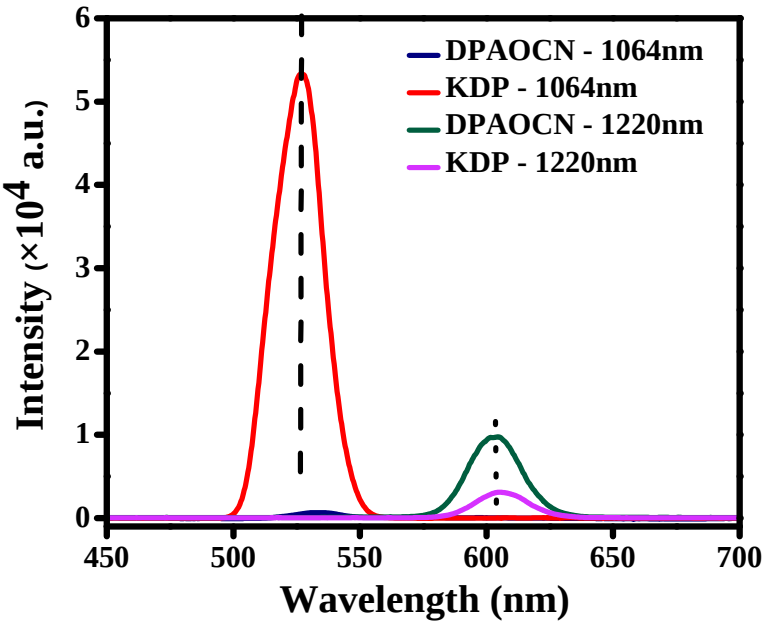

Figure A24: $\chi^{(2)}$ value determination of DPAOCN crystals using KDP as reference.

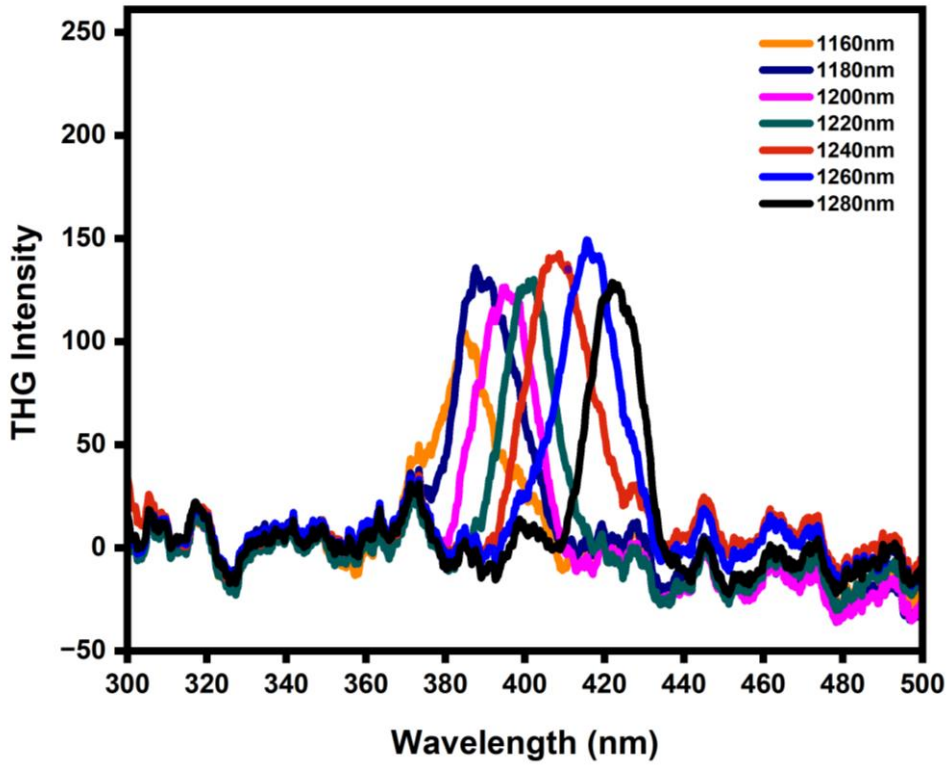

Figure A25: Wavelength dependence of very weak third harmonic signal of DPAOCN crystals.

Calculation of Laser-Induced Damage Threshold (LIDT):

The laser-induced damage threshold (LIDT) is a measure of the optical stability of a nonlinear material used in NLO procedures. The sample's LIDT is determined by the pump strength at which the SHG response deviates from quadratic behavior. In our sample, the LIDT is the intensity corresponding to 3 mW.

$$Peak\ Intensity = \frac{Energy\ \ per\ pulse}{Pulse\ width \times Effective\ Spot\ Area}$$

$$Where,\quad Energy\ per\ pulse = \frac{Average\ Power}{Repetition\ Rate}$$

$$LIDT = \quad Peak\ Intensity = \frac{Average\ Power}{Repetition\ Rate \times Pulse\ Width \times Effective\ Spot\ Area}$$

$$LIDT = \quad Peak\ Intensity = \frac{3 \times 10^{-3}\ W}{1000\ Hz \times 45 \times 10^{-15}\ s \times \pi \times (400 \times 10^{-6} m)^2}$$

$$\text{LIDT} = \quad \text{Peak Intensity} = 13.27\ \text{GW/cm}^2$$

Using the aforementioned equation, we determined the LIDT for our sample, which is 13.27 GW/cm^2 with the necessary laser information.

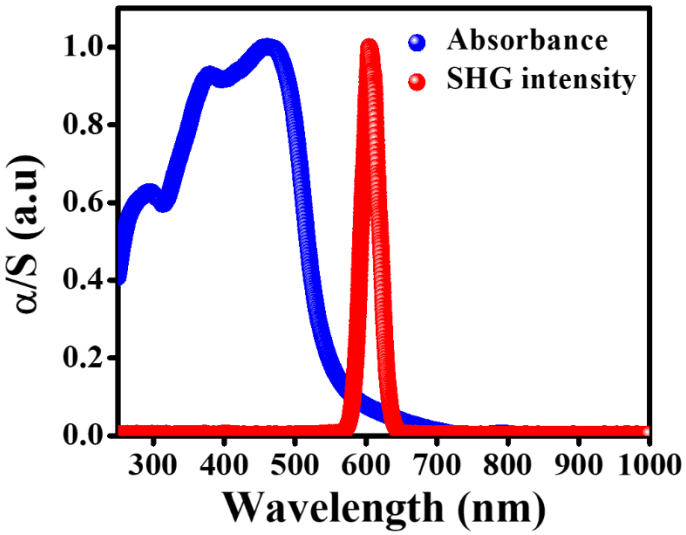

Figure A26: Absorbance spectra of the DPAOCN crystals along with the maximum SHG signal at 610 nm. The absorbance spectrum is obtained by converting the diffuse reflectance spectrum using the Kubelka-Munk transformation, $\alpha/S = (1-R)^2/2R$.

Section A3:

Fabrication of converted LEDs and related measurements:

Commercially available InGaN chips (power = 3W, λ_{EL}= 390-395 nm, V_F = 3.1 V, I_F = 700 mA) were purchased from ASIAN ELECTRONICS, India (Figure A27). The optimal sample, at 10 wt% doped with poly (methyl methacrylate) or PMMA was mixed in chloroform and heated at 50°C with stirring for 10 minutes. After that, the mixture was coated on top of the UV chip, dried under an IR lamp source, and was used further for emission measurement.

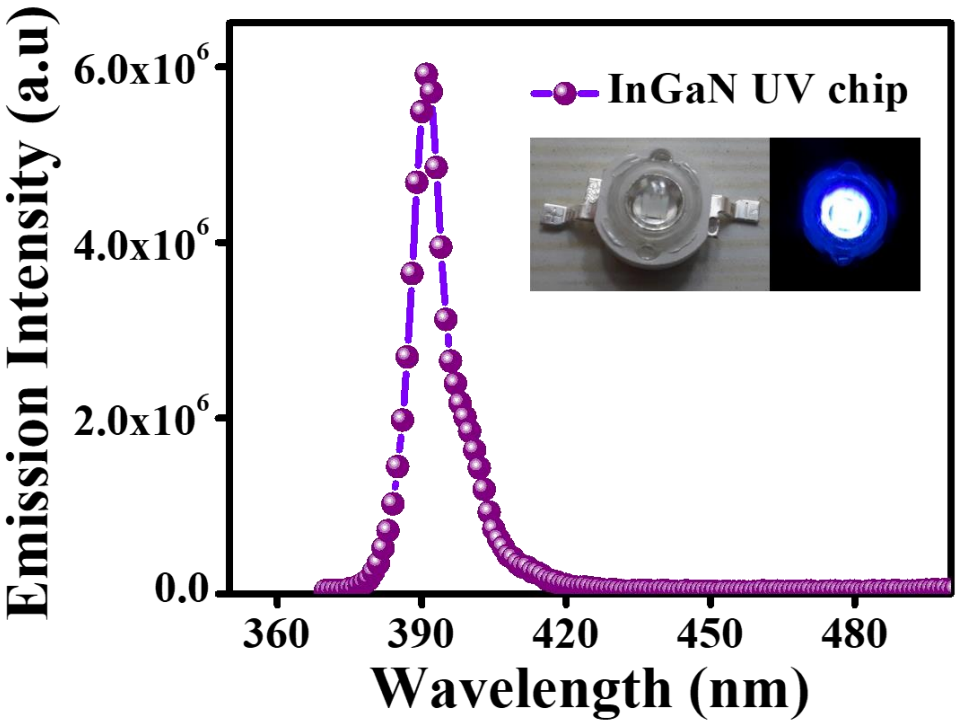

Figure A27: Electroluminescence spectra of the InGaN chip centered at 390-395 nm region. Inset shows its photo under daylight and its electroluminescence under a 3 V bias.

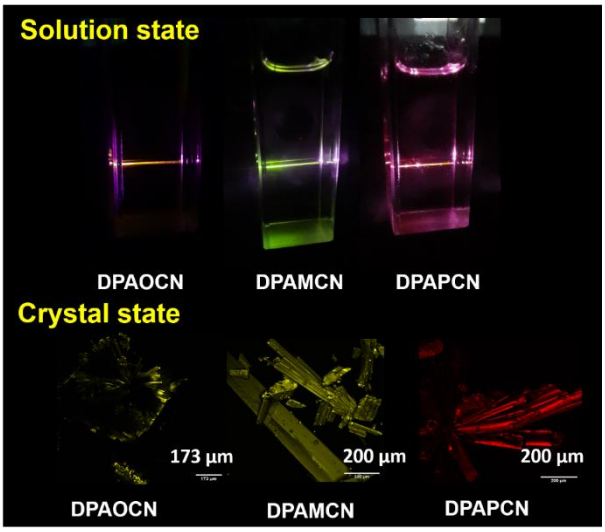

Figure A28: Two-photon absorption properties of all three regio-isomers in solution (DCM) and crystal state. For solution, an 800 nm laser source is used; crystals' confocal two-photon excited microscopic images have been collected using an 840 nm laser excitation source at 10X objective.

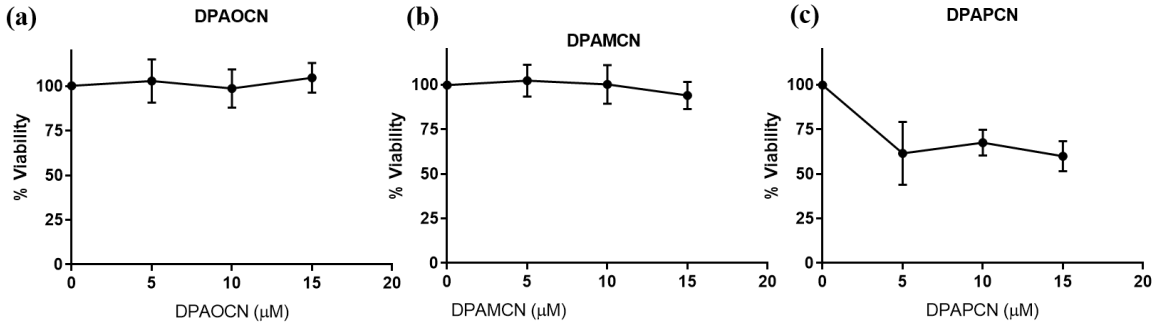

Figure A29: MTT viability assay of MCF7 in the presence of different concentrations of dye (a) DPAOCN, (b) DPAMCN, and (c) DPAPCN.

3.10 References

(1) S. Qi, S. Kim, V.-N. Nguyen, Y. Kim, G. Niu, G. Kim, S.-J. Kim, S. Park and J. Yoon, *ACS Appl. Mater. Interfaces*, 2020, **12**, 51293–51301.

(2) Y. Tao, K. Yuan, T. Chen, P. Xu, H. Li, R. Chen, C. Zheng, L. Zhang and W. Huang, *Adv. Mater.*, 2014, **26**, 7931–7958.

(3) G. Hong, X. Gan, C. Leonhardt, Z. Zhang, J. Seibert, J. M. Busch and S. Bräse, *Adv. Mater.*, , DOI:10.1002/adma.202005630.

(4) M. Y. Wong and E. Zysman-Colman, *Adv. Mater.*, 2017, **29**, 1605444.

(5) F. Fang, L. Zhu, M. Li, Y. Song, M. Sun, D. Zhao and J. Zhang, *Adv. Sci.*, 2021, **8**, 2102970.

(6) M. A. Bryden and E. Zysman-Colman, *Chem. Soc. Rev.*, 2021, **50**, 7587–7680.

(7) G. Li, F. Zhan, W. Lou, D. Wang, C. Deng, L. Cao, Y. Yang, Q. Zhang and Y. She, *J. Mater. Chem. C*, 2020, **8**, 17464–17473.

(8) H. Uoyama, K. Goushi, K. Shizu, H. Nomura and C. Adachi, *Nature*, 2012, **492**, 234–238.

(9) Z. Xie, C. Cao, Y. Zou, X. Cao, C. Zhou, J. He, C. S. Lee and C. Yang, *Adv. Funct. Mater.*, , DOI:10.1002/adfm.202112881.

(10) W. Li, B. Li, X. Cai, L. Gan, Z. Xu, W. Li, K. Liu, D. Chen and S. J. Su, *Angew. Chemie - Int. Ed.*, 2019, **58**, 11301–11305.

(11) D. G. Congrave, B. H. Drummond, P. J. Conaghan, H. Francis, S. T. E. Jones, C. P. Grey, N. C. Greenham, D. Credgington and H. Bronstein, *J. Am. Chem. Soc.*, 2019, **141**, 18390–18394.

(12) T. Hatakeyama, K. Shiren, K. Nakajima, S. Nomura, S. Nakatsuka, K. Kinoshita, J. Ni, Y. Ono and T. Ikuta, *Adv. Mater.*, 2016, **28**, 2777–2781.

(13) J.-X. Chen, W.-W. Tao, W.-C. Chen, Y.-F. Xiao, K. Wang, C. Cao, J. Yu, S. Li, F.-X. Geng, C. Adachi, C.-S. Lee and X.-H. Zhang, *Angew. Chemie Int. Ed.*, 2019, **58**, 14660–14665.

(14) Y. Song, M. Tian, R. Yu and L. He, *ACS Appl. Mater. Interfaces*, 2021, **13**, 60269–60278.

(15) M. Yu, X. Zhu, J. Zeng, H. Liu, R. Huang, Z. Zhuang, P. Shen, Z. Zhao and B. Z. Tang, *J. Mater. Chem. C*, 2021, **9**, 14808–14814.

(16) Y. Liu, J. Yang, Z. Mao, Y. Wang, J. Zhao, S. J. Su and Z. Chi, *Chem. Sci.*, 2023, **14**, 1551–1556.

(17) S. K. Pathak, G. Li, C. Zhou, Z. Wang and H. Liu, *J. Mater. Chem. C*, 2023, **11**, 6685–6694.

(18) K. K. Jha, S. Dutta and P. Munshi, *Cryst. Growth Des.*, 2018, **18**, 1126–1135.

(19) M. Jin, T. Seki and H. Ito, *J. Am. Chem. Soc.*, 2017, **139**, 7452–7455.

(20) S. Guerin, S. A. M. Tofail and D. Thompson, *NPG Asia Mater.*, 2019, **11**, 1–5.

(21) G. M. Sheldrick, A Short History of {\it SHELX}. *Acta Crystallogr. Sect. A* 2008, **64**, 112–122.

(22) G. M. Sheldrick, Crystal structure refinement with SHELXL. *Acta Crystallogr., Sect. A: Found. Adv.* 2015, **71**, 3−8.

(23) Frisch, M. J.; Trucks, G. W.; Schlegel, H. B.; Scuseria, G. E.; Robb, M. A.; Cheeseman, J. R.; Scalmani, G.; Barone, V.; Mennucci, B.; Petersson, G. A.; et al. Gaussian 09, Revision C.01; Gaussian Inc.: Wallingford, CT, 2009.

(24) A. D. Becke, Phys. Rev. A 1988, **38**, 3098–3100.

(25) C. Lee, W. Yang, R. G. Parr, Phys. Rev. B 1988, **37**, 785–789.

(26) S. V. K. Isukapalli, R. S. Lekshmi, P. K. Samanta, S. R. Vennapusa, J. Chem. Phys. 2020, **153**, 124301.

(27) X. Gao, S. Bai, D. Fazzi, T. Niehaus, M. Barbatti, W. Thiel, J. Chem. Theory Comput. 2017, **13**, 515–524.

(28) T. Moitra, P. Karak, S. Chakraborty, K. Ruud and S. Chakrabarti, *Phys. Chem. Chem. Phys.*, 2021, **23**, 59–81.

(29) B. Roy, M. C. Reddy, S. N. Panja and P. Hazra, *J. Phys. Chem. C*, 2019, **123**, 3848–3854.

(30) B. Roy, M. C. Reddy and P. Hazra, *Chem. Sci.*, 2018, **9**, 3592–3606.

(31) S. Semin, X. Li, Y. Duan and T. Rasing, *Adv. Opt. Mater.*, 2021, **9**, 2100327.

(32) A. Miniewicz, S. Bartkiewicz, E. Wojaczynska, T. Galica, R. Zalesny and R. Jakubas, *J. Mater. Chem. C*, 2019, **7**, 1255–1262.

(33) A. Dey and G. R. Desiraju, *Chem. Commun.*, 2005, 2486–2488.

(34) R. W. Boyd, H. Shin, M. Malik, C. O'Sullivan, K. W. C. Chan, H. J. Chang, D. J. Gauthier, A. Jha, J. Leach, S. Murugkar and B. Rodenburg, in *Nonlinear Optics*, Optica Publishing Group, Kauai, Hawaii, 2011, p. NWC2.

(35) S. Maqbool, Z. Thekkayil and P. Mandal, *Adv. Opt. Mater.*, 2023, **n/a**, 2202942.

(36) R. Chakraborty, P. K. Rajput, G. M. Anilkumar, S. Maqbool, R. Das, A. Rahman, P. Mandal and A. Nag, *J. Am. Chem. Soc.*, 2023, **145**, 1378–1388.

(37) N. Youngblood, R. Peng, A. Nemilentsau, T. Low and M. Li, *ACS Photonics*, 2017, **4**, 8–14.

(38) L. Yao, Z. Zeng, C. Cai, P. Xu, H. Gu, L. Gao, J. Han, X. Zhang, X. Wang, X. Wang, A. Pan, J. Wang, W. Liang, S. Liu, C. Chen and J. Tang, *J. Am. Chem. Soc.*, 2021, **143**, 16095–16104.

(39) Y. Xie, F. Liang, B. Zhang, B. Ge, H. Yu, Z. Lin, Z. Wang, H. Zhang, B. Huang and J. Wang, *ACS Omega*, 2019, **4**, 1045–1052.

(40) F. O. Saouma, C. C. Stoumpos, J. Wong, M. G. Kanatzidis and J. I. Jang, *Nat. Commun.*, 2017, **8**, 742.

(41) R. C. Eckardt, H. Masuda, Y. X. Fan and R. L. Byer, *IEEE J. Quantum Electron.*, 1990, **26**, 922–933.

(42) T. Liu, L. Xu, H. Wang, B. Chen and S. Shi, *ACS Appl. Bio Mater.*, , DOI:10.1021/acsabm.3c00298.

(43) Q. Lu, C.-J. Wu, Z. Liu, G. Niu and X. Yu, *Front. Chem.* , 2020, 8, 1205.

(44) L. Xu, J. Zhang, L. Yin, X. Long, W. Zhang and Q. Zhang, *J. Mater. Chem. C*, 2020, **8**, 6342–6349.

(45) Y. Wang, H. Wu, P. Li, S. Chen, L. O. Jones, M. A. Mosquera, L. Zhang, K. Cai, H. Chen, X.-Y. Chen, C. L. Stern, M. R. Wasielewski, M. A. Ratner, G. C. Schatz and J. F. Stoddart, *Nat. Commun.*, 2020, **11**, 4633.

(46) A. Chatterjee, J. Chatterjee, S. Sappati, T. Sheikh, R. M. Umesh, M. D. Ambhore, M. Lahiri and P. Hazra, *J. Phys. Chem. B*, 2021, **125**, 12832–12846.

(47) J. Zhao, Z. Chi, Y. Zhang, Z. Mao, Z. Yang, E. Ubba and Z. Chi, *J. Mater. Chem. C*, 2018, **6**, 6327–6353.

(48) X. Y. Shen, Y. J. Wang, E. Zhao, W. Z. Yuan, Y. Liu, P. Lu, A. Qin, Y. Ma, J. Z. Sun and B. Z. Tang, *J. Phys. Chem. C*, 2013, **117**, 7334–7347.

(49) A. D. Martin, J. Britton, T. L. Easun, A. J. Blake, W. Lewis, M. Schröder, *Cryst. Growth Des.* 2015, **15**, 1697–1706.

(50) A. D. Martin, K. J. Hartlieb, A. N. Sobolev, C. L. Raston, *Cryst. Growth Des.* 2010, **10**, 5302–5306.

(51) J. J. McKinnon, D. Jayatilaka, M. A. Spackman, *Chem. Commun.* 2007, **37**, 3814–3816.

(52) P. R. Spackman, M. J. Turner, J. J. McKinnon, S. K. Wolff, D. J. Grimwood, D. Jayatilaka, M. A. Spackman, *J. Appl. Crystallogr.* 2021, **54**, 1006–1011.

(53) A. S. Haynes, F. O. Saouma, C. O. Otieno, D. J. Clark, D. P. Shoemaker, J. I. Jang, M. G. Kanatzidis, *Chem. Mater.* 2015, **27**, 1837–1846.

(54) R. C. Eckardt, H. Masuda, Y. X. Fan, R. L. Byer, *IEEE J. Quantum Electron.* 1990, **26**, 922–933.

(55) T. Sheikh, S. Maqbool, P. Mandal, A. Nag, *Angew. Chemie Int. Ed.* 2021, **60**, 18265–18271.

Chapter-4

Navigating the ΔE_{ST} Factor by Excited State Potential Energy Surface Analysis in Aggregation Induced Delayed Fluorescence Emitters

4.1 Motivation:

Understanding the fundamental properties of luminogens with aggregation-induced delayed fluorescence (AIDF) is crucial for advancing the design and application of efficient optoelectronic materials. In this study, we focused on the AIDF behavior of three luminogens—TN, TA, and TP—aiming to uncover the mechanisms driving their unique photophysical properties. Through comprehensive theoretical analysis, we identified a substantial reduction in the singlet-triplet energy gap (ΔE_{ST}) when these luminogens transition from monomeric states to aggregated or solid states. This reduction enables thermally activated delayed fluorescence (TADF) on a microsecond time scale, a key characteristic for enhancing luminescence efficiency in solid-state applications. Moreover, these luminogens exhibit remarkable two-photon excited anti-Stokes photoluminescence emission and enhanced photocurrent generation. These phenomena are attributed to their pronounced charge transfer characteristics and extended singlet exciton lifetimes, respectively. These findings highlight the potential of TN, TA, and TP for applications in advanced photonic and optoelectronic technologies, such as organic light-emitting diodes (OLEDs) and photovoltaic devices. The insights gained from this study provide valuable guidance for designing next-generation materials with improved AIDF performance, paving the way for more efficient and versatile photonic systems.

4.2 Introduction:

Thermally activated delayed fluorescence (TADF) emitters have attracted significant interest in recent years, particularly for their applications in organic optoelectronics for OLEDs.[1] While traditional TADF emitters effectively utilize electrogenerated excitons, their performance in non-doped OLEDs is often limited by a reduced photoluminescence quantum yield (PLQY) in solid or aggregated states.[2] To overcome this challenge, the aggregation-induced emission (AIE) strategy has been introduced,[3] giving rise to a new category of TADF emitters known as aggregation-induced delayed fluorescent (AIDF) emitters.[4] These AIDF emitters demonstrate high exciton utilization and impressive photoluminescence efficiency in neat films, making them ideal for the development of highly efficient and stable non-doped OLEDs. Recent advancements, such as the molecular core-shell approach developed by Tang and co-workers, have achieved remarkable efficiency in AIDF-OLEDs, with a current efficiency of 61.4 cd A^{-1} and power efficiency of 42.8 lm W^{-1}.[5] Additionally, Chi and co-workers reported two TADF emitters featuring aggregation-induced emission based on a shamrock-shaped donor-acceptor structure, achieving a notable external quantum efficiency (EQE) of 38.7% in the sky-blue

region.[6] Yasuda and co-workers further contributed with a series of o-carborane-based emitters, showcasing high PL quantum efficiencies of up to 97% in solid-state films, along with successful non-doped OLED device fabrication.[7] While AIDF emitters have primarily been applied to non-doped OLEDs, their significant charge transfer properties and longer emission lifetimes suggest potential benefits for other areas of organic electronics, such as anti-Stokes photoluminescence (ASPL) via two-photon absorption and efficient photocurrent generation. In this report, we present three novel AIDF luminogens—TN, TA, and TP—based on triphenylamine as the donor (**Scheme 1**). These TPA-based compounds exhibit advantageous photoconductive and light-emitting properties, with enhanced conjugation improving exciton up-conversion and utilization.[8] Notably, all three emitters demonstrate two-photon activity in their aggregated and crystalline states, attributed to their large hyperpolarizability. Furthermore, they generate efficient photocurrent in the microampere (μA) range, marking them as the first AIDF emitters with this capability.

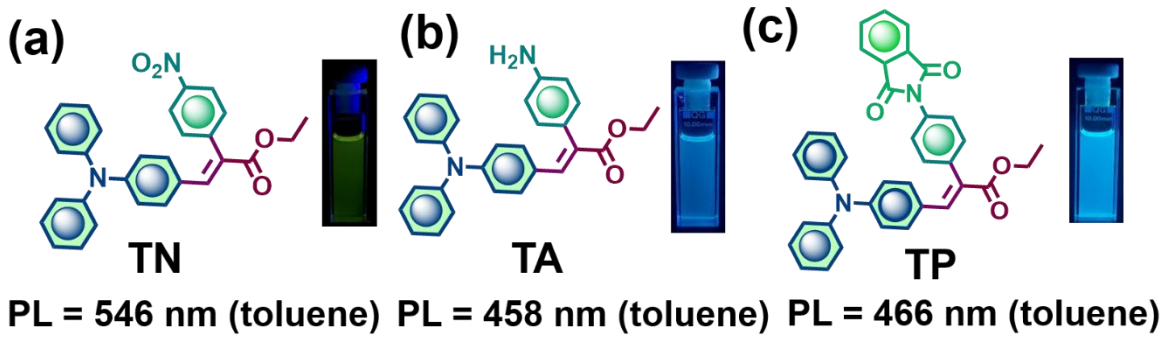

Scheme 1: Molecular structures and PL emission in toluene for all three luminogens- (a) TN, (b) TA, and (c) TP.

4.3 Brief synthesis procedure and characterization data:

The final products are synthesized through a multi-step synthetic approach. It begins with the synthesis of TPA-CHO from triphenylamine via the Vilsmeier-Haack formylation reaction (see **Section A1 of the Appendix**). This is followed by an Aldol-like condensation reaction to produce TN. The compound TA is obtained by reducing the nitro group using tetrahydroxydiboron and 4,4′-bipyridine in DMF. Finally, TP is synthesized through a condensation reaction of TA with phthalic anhydride in glacial acetic acid under reflux conditions, with further details provided in **Section A1 of the Appendix**. After a multi-step synthesis process, all three luminogens were purified by HPLC and characterized by ^{1}H NMR,

^{13}C NMR, and HRMS analysis (**Section A1 of the Appendix**). The characterization details of all the synthesized products are given below-

(a) For TPA-CHO:

^{1}H NMR (400 MHz, $CDCl_3$): δ in ppm 9.81 (s,1H), 7.76–7.62 (m, 2H), 7.34 (dd, J= 10.4, 5.4 Hz, 4H), 7.22-7.12 (m, 6H), 7.01 (t, J= 8.9 Hz, 2H)

^{13}C NMR (100 MHz, $CDCl_3$): δ in ppm 190.56, 153.45, 146.23, 131.41, 129.83, 129.29, 129.16, 126.41, 125.21, 124.24, 119.42

HRMS (ESI): calc. for $[(C_{19}H_{15}NO)H]$ $(M+H)^+$ 274.1232, measured 274.1237.

(b) For TN:

^{1}H NMR (300 MHz, DMSO-d_6): δ in ppm 8.25 (d, *J* = 8.7 Hz, 2H), 7.78 (s, 1H), 7.57 – 7.43 (m, 2H), 7.33 (dd, *J* = 8.4, 7.4 Hz, 4H), 7.21 – 7.07 (m, 2H), 7.07 – 7.01 (m, 4H), 6.97 – 6.87 (m, 2H), 6.71 – 6.62 (m, 2H), 4.17 (q, *J* = 7.0 Hz, 2H), 1.19 (t, *J* = 7.1 Hz, 3H)

^{13}C NMR (75 MHz, DMSO-d_6): δ in ppm 166.60, 149.29, 147.40, 146.41, 144.25, 140.94, 132.58, 131.62, 130.30, 127.78, 126.10, 125.10, 124.36, 119.94, 61.31, 14.62

HRMS (ESI): calc. for $[C_{29}H_{24}N_2O_4]$ $(M)^+$ 464.1736, measured 464.1737.

(c) For TA:

^{1}H NMR (300 MHz, DMSO-d_6): δ in ppm 7.53 (s, 1H), 7.32 (t, *J* = 7.7 Hz, 4H), 7.06 (dt, *J* = 25.0, 7.5 Hz, 8H), 6.81 (d, *J* = 8.0 Hz, 2H), 6.66 (d, *J* = 8.5 Hz, 2H), 6.54 (d, *J* = 7.9 Hz, 2H), 5.16 (s, 2H), 4.14 (q, *J* = 7.1 Hz, 2H), 1.20 (t, *J* = 7.1 Hz, 3H)

^{13}C NMR (75 MHz, DMSO-d_6): δ in ppm 168.19, 148.66, 148.36, 146.73, 138.17, 132.05, 130.97, 130.54, 130.20, 128.17, 125.61, 124.62, 123.23, 120.58, 114.41

HRMS (ESI): calc. for $[(C_{29}H_{26}N_2O_2)H]$ $(M+H)^+$ 435.2068, measured 435.2065.

(d) For TP:

^{1}H NMR (300 MHz, DMSO-d_6): δ in ppm 7.97 (dd, *J* = 5.5, 3.0 Hz, 2H), 7.91 (dd, *J* = 5.5, 3.1 Hz, 2H), 7.73 (s, 1H), 7.50 (d, *J* = 8.4 Hz, 2H), 7.38 – 7.28 (m, 6H), 7.21 – 7.09 (m, 2H), 7.09 – 7.03 (m, 4H), 6.99 – 6.90 (m, 2H), 6.68 – 6.59 (m, 2H), 4.20 (d, *J* = 7.1 Hz, 2H), 1.23 (d, *J* = 7.1 Hz, 3H).

^{13}C NMR (75 MHz, DMSO-d_6): δ in ppm 167.45, 148.98, 146.49, 136.38, 135.20, 132.33, 132.04, 131.73, 130.30, 129.27, 127.92, 126.02, 125.03, 123.92, 119.89, 61.14, 14.74

HRMS (ESI): calc. for $[C_{37}H_{38}N_2O_4]$ $(M)^+$ 564.2049, measured 564.2046.

4.4 Instrumentation:

Data characterization using ^{1}H NMR (at 300 MHz) and ^{13}C NMR (at 75 MHz) of all the final compounds are performed using Bruker Avance™ II NMR spectrometer with deuterated dimethylsulphoxide (DMSO-d_6) as solvent (having residual dimethylsulphoxide, 0.1%) and tetramethylsilane (TMS) as the internal standard. Chemical shift (δ) values are measured in ppm relative to DMSO resonance at δ = 2.54 ppm for ^{1}H NMR and at δ = 40.45 ppm for ^{13}C NMR. High-resolution mass spectra (HRMS) for all the compounds are recorded using ESI TOF in Water's SYNAPT G2 mass spectrometer. HPLC measurements were carried out using Water's Acquity-H Class UPLC with a UV detector (Agilent eclipse plus-C18 RRHD column). The injection volume is 0.5 µL and the flow rate is kept at 0.5 mL/min. Single-crystal diffraction analysis data were collected at 100 K with a BRUKER KAPPA APEX II CCD Duo diffractometer (operated at 1500 W power: 50 kV, 30 mA) using graphite monochromatic Mo Kα radiation (λ = 0.71073 Å). The structures were solved by direct methods and refined by least-squares against F2 utilizing the software packages SHELXL-2017,[9a,b], and WINGX.[10] More information on crystal structures can also be obtained from the Cambridge Crystallographic Data Centre under the CCDC deposition number. Steady-state solution-based absorption spectra are recorded on Shimadzu, UV-2600 UV spectrophotometer. Steady-state emission spectra and time-gated emission spectra of all the samples in solution and solid state are carried out using Fluoromax-4C spectrofluorimeter and Fluorolog-3 phosphorimeter (HORIBA), respectively. All the PLQY values mentioned in the manuscript have been obtained by a direct method (absolute quantum yield measurement) using an integrating sphere

(Horiba K-sphere). Time-resolved PL decay profiles have been recorded by Time-Correlated Single Photon Counting (TCSPC) and Multi-Channel Scanning (MCS) methods either using a diode-laser source (375 nm, for a total time window of < 50 μs) or a spectra LED source (357 nm) in HORIBA Scientific instrument. The data was fitted with the help of DAS6 Fluorescence Decay Analysis Software from HORIBA by examining $\chi 2$-values and visually inspecting residuals where the fit with $\chi 2$ = (1-1.2) value is taken as the best fit. For the two-photon absorption experiment, an 800 nm mode-locked Ti-Sapphire laser (Mai-Tai, Spectra-Physics) excitation source was focussed on the sample. Leica multiphoton microscope (Germany) was utilized for the two-photon cell imaging at 63X oil immersion objective.

4.5 Experimental section:

Density Functional Theory (DFT) calculation:

Quantum chemical calculations are performed using the Gaussian 09 program[11] using a high-performance cluster facility provided by IISER Pune. Initially, geometry optimization of all the luminogens is carried out in the solution phase (THF) using the IEFPCM method and the nature of the stationary point (minima on the PE surface) is confirmed by frequency analysis[12-13] at the B3LYP/6-31G (d,p) level. Furthermore, TD-DFT calculations are carried out for excited state geometry optimisation (S_1 state) using TD-SCF method at the B3LYP/6-31G (d, p) level of theory after obtaining a frequency-analyzed ground state optimized structure at the same level of theory. For potential energy surface construction, a relaxed scanning has been performed along the donor-acceptor dihedral angle with a difference of 2° for a total of 20 steps.

QM/MM Calculations:

The quantum mechanics/molecular mechanics (QM/MM) model was built based on the single crystal structure and was utilized to analyze the electronic properties of the active QM molecule embedded in the aggregated crystal state. The surrounding molecules were defined as a rigid MM component to simulate the effect of a solid-state environment.[14] The high layer for QM was computed using the TD-DFT method of B3LYP/6-31G (d, p) level, and the low layer for MM is described by the universal force field (UFF)[15] augmented by Coulomb interactions which are in accordance with the quantum method. The monomer was configured to a high layer for QM calculated by the TD-DFT method of B3LYP/6-31G (d, p) level.

Preparation of neat films:

To prepare neat films, 0.5 mg of each luminogen is dissolved in 1 ml of spectroscopic-grade THF solvent. The solution is then drop-cast onto a clean quartz substrate and dried under reduced pressure for at least one hour to eliminate any solvent trapped within the film layer.

Cell culture and drug treatments:

HeLa cells were a generous gift from Dr. Sorab Dalal (ACTREC, India). The cells were maintained in 35 mm dishes (VWR, USA) and grown in Dulbecco's Modified Eagle Medium (DMEM; HiMedia, India) containing 4.5g/L Glucose and supplemented with 10% heat-inactivated FBS (Thermo Scientific, USA) and 1X Pen-Strep antibiotics (Thermo Scientific, USA) and incubated at 37°C in a humidified incubator with 5% CO_2 (Eppendorf, GmbH).

For the MTT cell viability assay, 10,000 HeLa cells per well were seeded in a 96-well plate (Eppendorf, Gm) and incubated at 37°C with 5% CO_2 for 18 hours post-seeding. Cells were treated with different concentrations of the compounds TN, TA, and TP or DMSO control (5µM, 10µM, and 15µM). 24 hrs post-treatment, drug-containing media was removed, and 100 µL of DMEM containing 0.5 mg/ml MTT (HiMedia, India) was added to each well and incubated at 37ºC in the dark for four hours. Post incubation, the MTT-DMEM solution was aspirated, and the purple MTT-formazan crystals were solubilized in 100 µL of DMSO and incubated for 15 mins in the dark before recording absorbance. The absorbance was recorded at 570 nm using the EnVision Nexus Multimode plate reader (Revvity, USA).

For multiphoton imaging experiments, $0.15x10^6$ HeLa cells were seeded on coverslips (pre-washed with 95% EtOH) in a 35 mm culture dish (VWR, USA) and incubated at 37°C with 5% CO_2 for 18 hrs. Cells were then treated with 10 µM of compound (TN, TA, and TP) and incubated for 24 hrs. Post-treatment, cells are washed twice with 1X DPBS and fixed with 4% formaldehyde for 20 minutes in the dark. After fixation, cells were again washed with PBS and mounted onto slides. The cells were imaged on a multiphoton confocal microscope at an excitation wavelength of 820 nm (Leica, Germany) and observed with a 63X oil immersion objective.

Detailed procedure for photo-current generation:

Here, the photocurrent generation experiment was performed in chronoamperometry mode, where current was measured as a function of time at a fixed potential of 0.9 V. A three-electrode configuration was used for the photocurrent measurement, where the working electrode comprising the target compound was drop-casted onto a FTO substrate. The Ag/AgCl electrode

functioned as the reference, and another FTO plate was employed as the counter electrode. 0.2M sodium sulphate solution is used as electrolyte. Here the working electrode was prepared by dissolving 1 mg of the compound in 0.5 mL of chloroform, followed by dropcasting the resultant solution onto the surface of an FTO plate.

4.6 Results and Discussion:

4.6.1 Photophysical characteristics in the monomeric and aggregated state:

In all three emitters, the triphenylamine (TPA) group acts as a donor, as evidenced by the frontier molecular orbital analysis, with the HOMO located on the TPA moieties (**Figure 1**). On the other hand, the LUMO is localised predominantly in the peripheral nitro-benzene moiety, ester carbonyl group, and phthalimide moiety in the case of TN, TA, and TP, respectively (**Figure 1**).

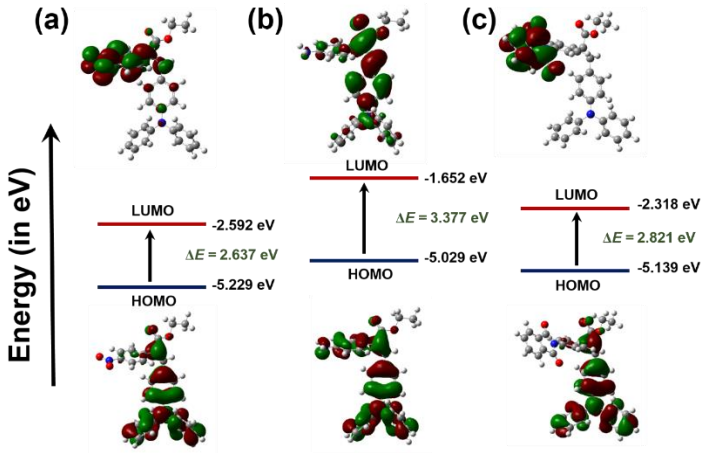

Figure 1: HOMO and LUMO molecular orbitals in the ground state optimized structures of (a) TN, (b) TA, and (c) TP.

The luminogens in toluene (30 µM) exhibit a strong absorption band in the 360-415 nm region (**Figure A1 in Appendix**), which is attributed to the S_0-S_2 transition for TN & TP and a combination of both S_0-S_2 and S_0-S_1 transitions for TA, based on the simulated absorption spectra obtained from TD-DFT calculation (**Table A4- A6 in Appendix**). Noticeably, the emission features were found to be different for all three. TN in toluene emits in the yellow region (λmax ~ 550 nm), whereas TA (λmax ~460 nm) & TP (λmax ~ 465 nm) emit in the cyan-blue region (**Figure A1 in Appendix**), probably attributed to an increased charge transfer character in TN due to its maximum conjugation length and S_1 state dipole moment (**Figure A2 in Appendix**). It is worth noting that the time-resolved photoluminescence (PL) decay of

all the luminogens in solvents like- toluene and THF only shows a short ~ns component and is devoid of any longer component in µs-ms time scale suggesting the absence of any triplet harvesting process in solution (**Figure A4-A5 in Appendix**).

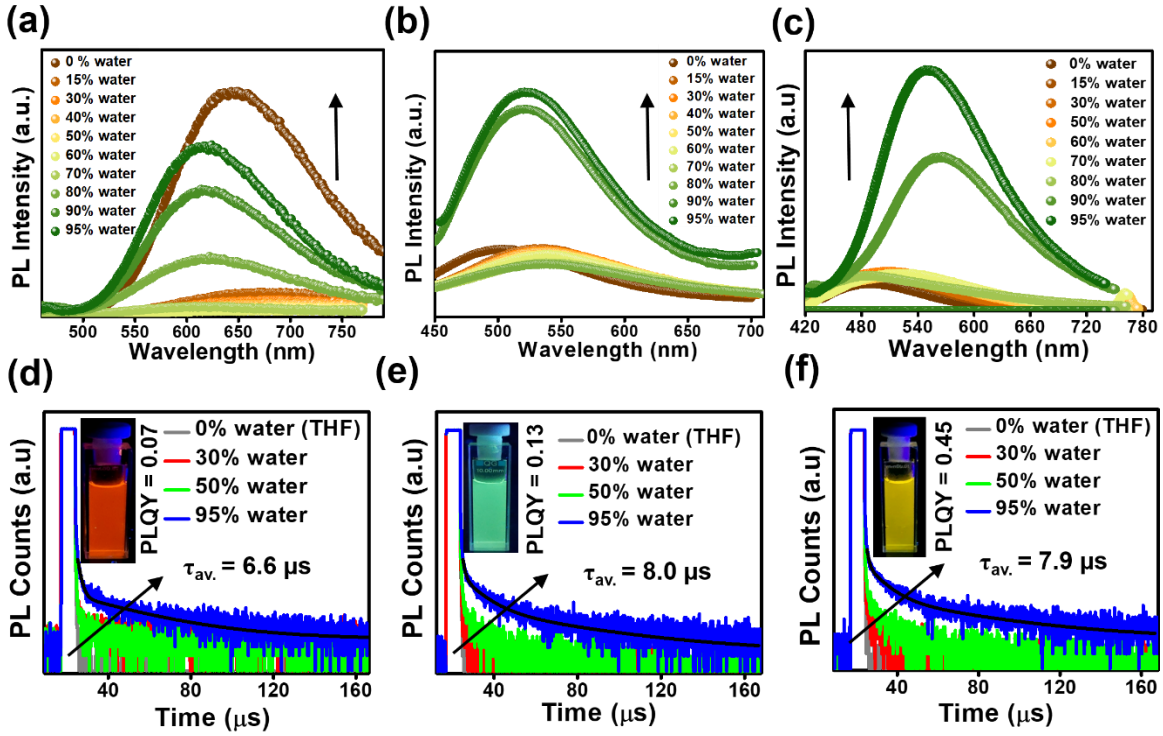

Figure 2: Emission spectra in binary THF/water mixture for (a) TN, (b) TA and, (c) TP. Variation of lifetime (ex. 355 nm) in ~µs time-scale with water content for (d) TN, (e) TA and (f) TP. Aggregate PLQY and average lifetime (at 95% water content) have been shown along with.

However, an intriguing photophysical characteristic emerges in the aggregated state. All three molecules exhibit a profound aggregation induced enhanced emission (AIEE) behavior after an initial solvatochromic emission quenching up to ~60-70% of water content in THF. Impressively, at a water concentration of 95% , the emission profiles demonstrate enhancement of intensity of approximately 16-fold for TN, 5-fold for TA, and 10-fold for TP, as illustrated in **Figure 2 a, b, c, and A6, Table A7 in Appendix**. Importantly, the molecular aggregates formed at 95% water content exhibit PL decay times in the microsecond (µs) range, with average lifetimes of 6.6 µs, 8.0 µs, and 7.9 µs for TN, TA, and TP, respectively (**Figure 2d, e, f**). Here it is important to note that this long emission lifetime component was not prominent at very low water content (<50%) when the aggregated are not formed. In this regard, it is worth mentioning that the aggregation-induced emission (AIE) characteristics of the luminogens can be linked to their crystal packing, specifically due to the suppression of

detrimental π···π stacking interactions in the aggregated state. Stronger π···π interactions can increase planarity and exciton−phonon coupling in the solid state, often leading to reduced emission. Effective π···π stacking interactions typically occur within a distance of 3.3-3.8 Å[16] beyond this range, their strength diminishes, making aggregation-caused quenching (ACQ) less likely. For the three luminogens under investigation, an analysis of their crystal structures reveals increased distances for potential π···π stacking interactions: 6.1 Å for TN, 4.7 Å for TA, and 5.1 Å for TP (**Figure 3a, d, g**). Additionally, the space-filling model demonstrates that the planar aromatic groups of neighboring molecules are positioned in a manner that prevents significant π···π overlap, further reducing the likelihood of quenching (**Figure 3b, e, h, c, f, i**).

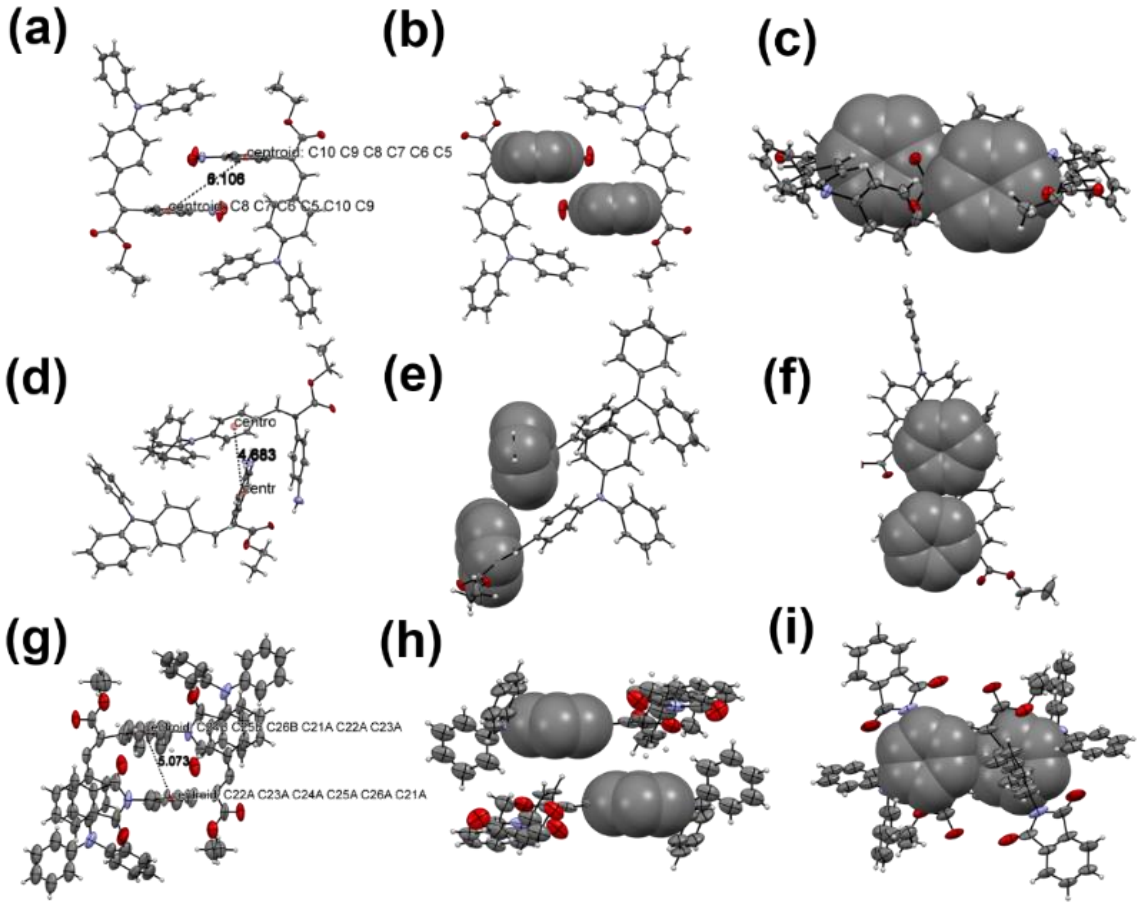

Figure 3: π···π stacking interactions distance of two neighboring molecules of (a) TN, (b) TA and (c) TP. Spacefilling model of (b) TN, (e) TA, and (h) TP from side-view. Spacefilling model of (c) TN, (f) TA, and (i) TP from top-view.

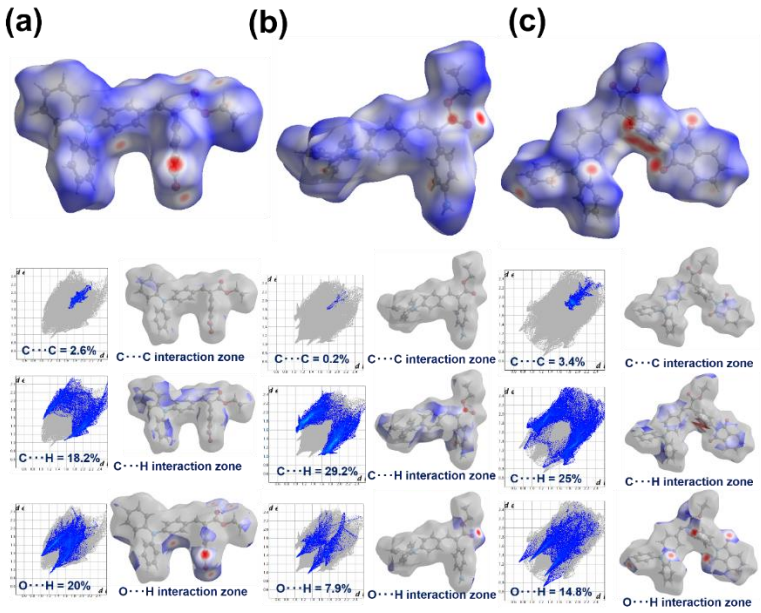

Figure 4: Normalized distance (d_{norm}) mapped over Hirshfeld surface of each luminogen ((a) TN, (b) TA, and (c) TP) along with generated fingerprint plots obtained from dnorm to decipher the percentage of each type of non-covalent interaction. The grey part in the fingerprint plot indicates total interactions.

Moreover, in all three crystals, the 2-D fingerprint plot reveals minimal π···π stacking interactions, accounting for less than 5% and characterized by weak strength (shown in blue) (**Figure 4**). This finding supports the AIE properties of the molecules. Furthermore, we evaluated the strength and impact of other short intermolecular contacts that create a constrained environment, limiting the motion of high-energy bond vibrations (with C−H stretching around 0.37 eV in aromatic compounds).[17] This restriction helps to decrease nonradiative deactivation in the aggregated or solid-state, thus enhancing the AIE effect. Notably, significant contributions from C−H···π interactions (approximately 10.3 kJ/mol)[15] and C−H···O interactions (typically between 41−104 kJ/mol)[18] were identified, with the latter exhibiting strong interactions (indicated by red patches) (**Figure 4**), which further promote the AIE characteristics.

To investigate whether this aggregation behavior persists with a further increase in the extent of aggregation, we conducted additional studies on neat films and molecular crystals. The neat films of all three luminogens exhibit different emission features with TN emitting orange-red emission (maxima at ~620 nm), TA exhibiting cyan-green emission (maxima at ~520 nm) and TP exhibiting greenish yellow emission (maxima at ~ 545 nm) (**Figure 5**). In addition to the

short ~ ps-ns component (due to prompt S_1-S_0 emission), all three neat films exhibit a much longer emission lifetime of 27.3 µs, 8.64 µs, and 7.83 µs for TN, TA, and TP, respectively (**Figure 5**) suggesting the persistent role of aggregation in the emission process.

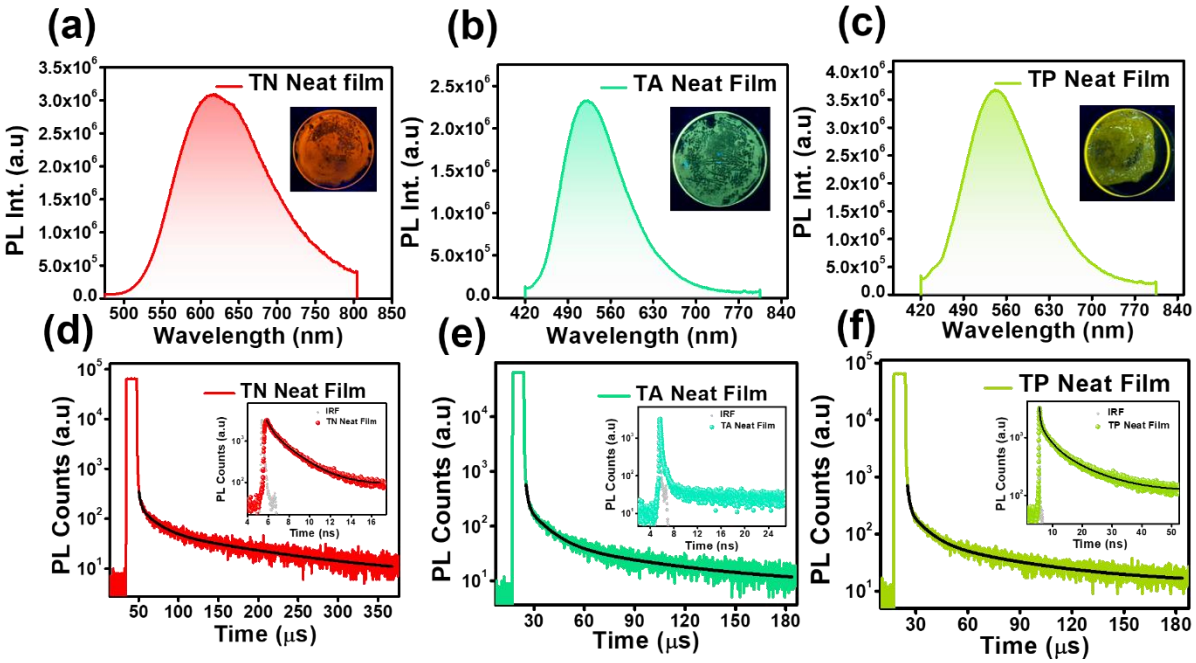

Figure 5: Steady-state emission spectra for the neat film of (a) TN, (b) TA, and (c) TP (inset shows the UV excited neat film emission) and time-resolved emission decay profiles (λex = 357 nm) for the neat film of (d) TN, (e) TA, and (f) TP in the microsecond time scale (λex = 357 nm) (inset shows the decay profiles in the nanosecond time scale, λex = 375 nm). The average delayed fluorescence lifetime (τ_{DF}) of TN, TA, and TP neat films were found to be 27.3 µs, 8.64 µs, and 7.83 µs respectively. (Note: Decays in the nanosecond time scale with τav < 50 ps fall below the detection limit of the TCSPC instrument and hence have not been fitted).

To demonstrate that residual solvent molecules do not influence the emission in the neat films or solvatochromic emission of solvents does not play any role in it, we compared the emissions of films made from solvents of different polarities, specifically THF (polarity index 4.0) and acetonitrile (polarity index 5.8). We found no significant changes in emission features among all three luminogens (**Figure A7 of Appendix**), indicating that trapped solvent molecules do not play a role in the emission process. Additionally, we recorded and compared PL excitation spectra for the solution phase (monomeric state) and neat films. The significant differences in spectral onset and width between the two phases suggest that aggregation occurs in the neat films (**Figure A8 of Appendix**), which induces exciton coupling and alters the spectral

features. Thus, the observed change in emissions from neat films results from the alteration of excited state energy levels due to aggregation, rather than from trapped solvent residue.

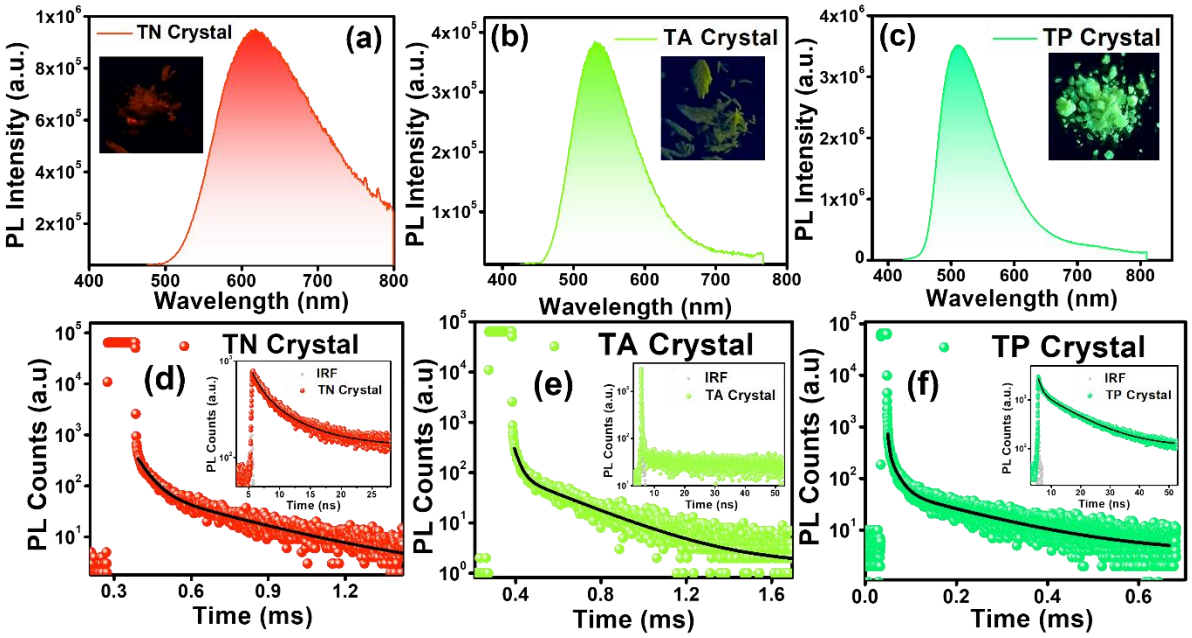

Figure 6: Steady-state emission spectra of the crystals of (a) TN, (b) TA, and (c) TP along with the UV (365 nm) excited crystal emission shown in the insets. Time-resolved emission decay profiles for the crystals of (d) TN, (e) TA, and (f) TP in the sub-millisecond time scale (λ_{ex} = 357 nm). Insets show the decay profiles in the nanosecond time scale (λ_{ex} = 375 nm). Average delayed fluorescence lifetime (τ_{DF}) of TN, TA, and TP crystals were found to be 104 µs, 86 µs, and 20 µs respectively. (Note: Decays in the nanosecond time scale with τ_{av} < 50 ps fall below the detection limit of the TCSPC instrument and hence have not been fitted).

Moreover, the molecular crystals of the respective emitters also emit in three different regions, with emission maxima at 620 nm, 525 nm, and 510 nm for TN, TA, and TP, respectively (**Figure 6**). Here also, along with a short ~ ns component, a much longer emission lifetime is observed for all three crystals with an average lifetime of 104 µs, 86 µs, and 20 µs for TN, TA, and TP, respectively (**Figure 6**). Noticeably, the longer lifetime component exhibits a marked increase with the extent of aggregation, progressing from a THF-water binary mixture with 95% water content, to neat films, and ultimately to molecular crystals. This suggests a unique role of aggregation in the kinetics of this emission process. To know, the origin of such a longer lifetime, time-gated emission measurements were carried out. A significantly superimposed gated emission spectrum with the steady state emission profile indicates a probable occurrence of thermally activated delayed fluorescence (TADF) as in both cases the emission takes place from the lowest singlet S_1 state (**Figure 7**). This was further confirmed by photophysical

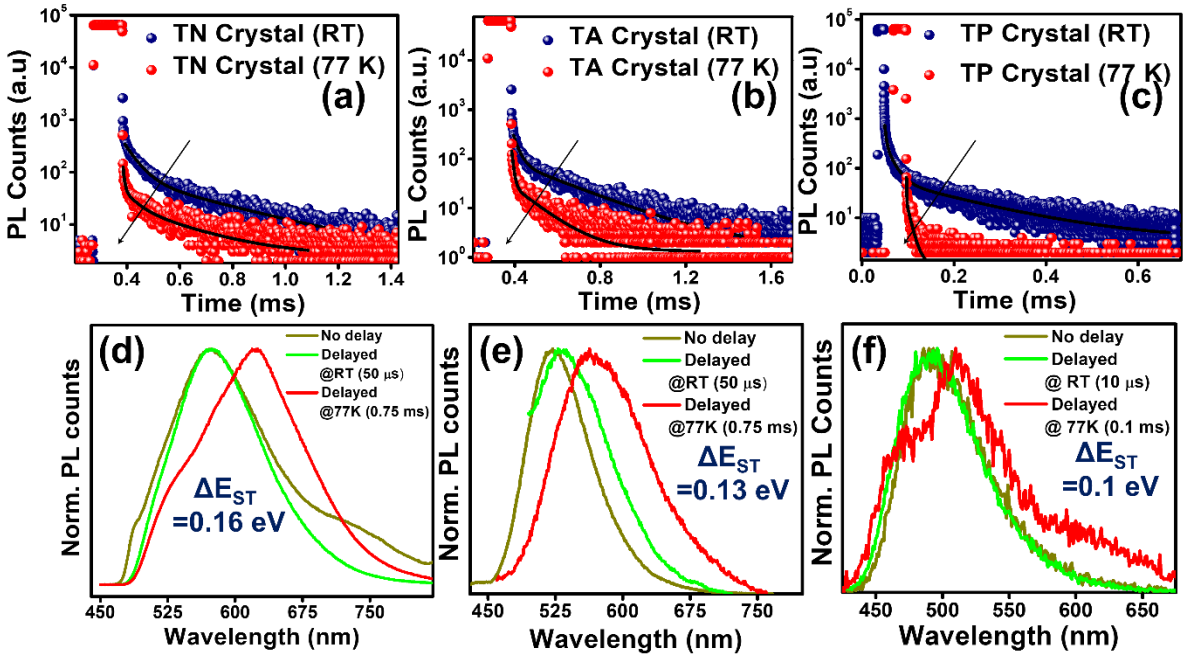

Figure 7: Time-resolved emission decay profiles (λ_{exc} = 357 nm) for the crystals of (a) TN, (b) TA, and (c) TP at RT (298 K) and 77 K. Average delayed fluorescence lifetime (τ_{DF}) of TN, TA and TP crystals at RT were found to be 104 µs, 86 µs and 20 µs respectively and at 77 K, their lifetimes were reduced to 48 µs, 31 µs and 3 µs respectively. Time-gated emission spectra for the crystals of (a) TN, (b) TA, and (c) TP at RT (298 K) and 77 K with different delays. Experimentally calculated ΔE_{ST} is obtained from the emission peak positions. Time delays of detection for all spectra are mentioned. For the collection of delayed spectra at RT, a 5 ms sample window has been employed for TN and TA and a 500 µs sample window for TP. The sample window for emission measurements at 77 K is kept at 10 ms for all three crystals.

investigation at cryogenic temperature. At 77K, the TADF emission bands were found to be weakened with a red shift of the emission maxima suggesting the presence of phosphorescence emission from the lowest triplet T_1 state (**Figure 7**). From the peak position of the respective spectra, the S_1-T_1 energy gaps (ΔE_{ST}) were estimated to be 0.16 eV, 0.13 eV, and 0.10 eV for TN, TA, and TP crystals, respectively (**Figure 7**). Such low ΔE_{ST} values are particularly advantageous for facilitating TADF, as they imply a reduced activation barrier for the reverse intersystem crossing (RISC) process.[19] Noticeably, the experimentally obtained ΔE_{ST} values are in line with the delayed fluorescence lifetimes, with TP with the least ΔE_{ST} value exhibiting the minimum TADF lifetime. Furthermore, DF lifetimes were measured at a temperature of 77 K. In all three cases, the DF lifetime was found to be reduced at 77 K compared to room temperature due to an inefficient thermal up-conversion process at lower temperatures (**Figure**

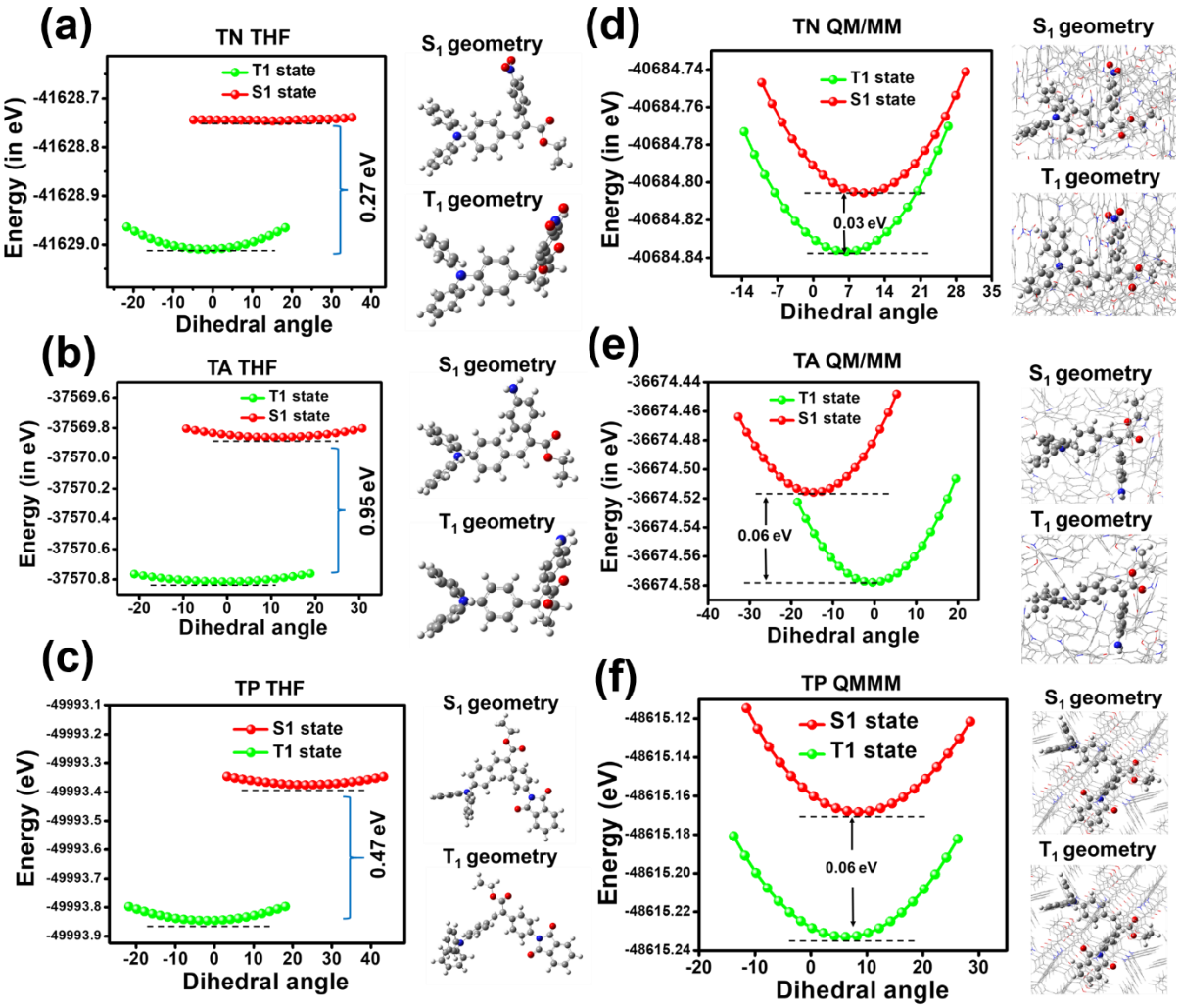

Figure 8: Potential energy scanning along the dihedral angle between donor and acceptor moieties in the solvent phase using the ICFPCM model and the crystal phase using the QM/MM model for [(a) and (d)] TN, [(b) and (e)] TA, and [(c) and (f)] TP. For the solvent-based and QM/MM calculation (high layer)- DFT calculation has been performed at B3LYP, 6-31G (d, p) level of theory, while the low-layer for QM/MM-based calculation has been treated with a classical UFF model of theory.

7). Our designed luminogens, therefore are categorized as AIDF type of molecules, as the spin-flip process only gets activated in the aggregated or solid state, not in the monomeric state. To understand the specific role of aggregation in the delayed fluorescence process, we performed a combined solvent-phase and QM/MM (quantum mechanics/molecular mechanics) based DFT calculation (**Figure A10 & A11 in Appendix**). The solvent-based (IEFPCM/THF) calculation was used to model the monomeric/solution state, while the QM/MM calculation was used to model the aggregated/solid state. In the THF-based calculation, the theoretically calculated Δ_{EST} values are found to be 0.27 eV, 0.95 eV, and 0.47 eV for TN, TA, and TP,

respectively (**Figure 8**). These high ΔE_{ST} values are not suitable for efficient reverse intersystem crossing (RISC), which may be the reason for the emitters not showing TADF emission in the solution phase. Interestingly, calculations on the aggregated state convey a different story with much lowered ΔE_{ST} values of 0.03 eV, 0.06 eV, and 0.06 eV for TN, TA, and TP, respectively (**Figure 8**). This narrow energy gap between the S_1 and T_1 states can make the reverse intersystem crossing (RISC) process much more efficient and presumably could be the reason for the activation of TADF in aggregated or solid states.

4.6.2 Photocurrent measurements:

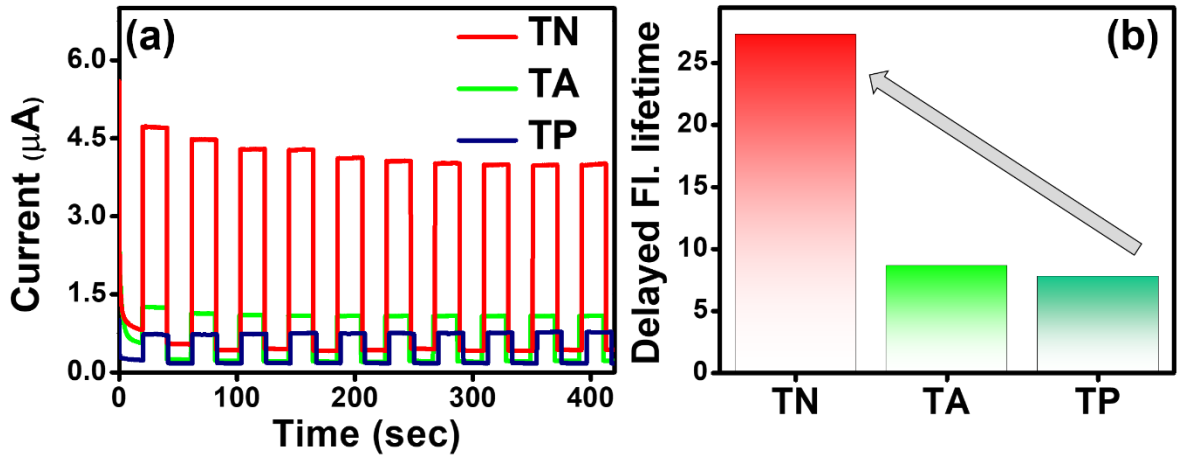

Figure 9: (a) Photocurrent generation by the luminogens upon exciting with a 365-370 nm 60 W UV LED lamp having peak irradiance of 3.5 W/cm^2. (b) Neat film DF lifetime of the luminogens.

The aggregation-induced delayed fluorescence (AIDF) properties and long-range charge transfer characteristics of these luminogens were effectively utilized for photocurrent generation. In conventional organic fluorophores, singlet excitons typically decay on a picosecond to nanosecond timescale, resulting in limited exciton diffusion lengths (L_S) constrained to just a few nanometers. Importantly, the exciton diffusion length is proportional to the square root of the singlet exciton lifetime (τ_S),[20] which restricts the efficiency of these materials as photocurrent generators. In contrast, our AIDF emitters exhibit significantly longer singlet lifetimes (in the microsecond regime), allowing for greater exciton diffusion lengths and facilitating efficient photocurrent generation. Consequently, all three luminogens produced photocurrents in the microampere range when excited with a 365-370 nm UV source (**Figure 9**). Notably, the drop-casted TN film exhibited the highest photocurrent of ~4 μA, while TP

demonstrated the lowest (**Figure 9a**). Careful analysis of the photophysical properties reveals that the delayed fluorescence lifetimes in neat films follow the trend: TN (27.3 µs) > TA (8.64 µs) > TP (7.83 µs) (**Figure 9b**). This indicates that TN, with its longest singlet exciton lifetime, achieves the greatest diffusion length, thereby maximizing its photocurrent generation capability.

4.6.3 Two-photon absorption and cell-imaging experiment:

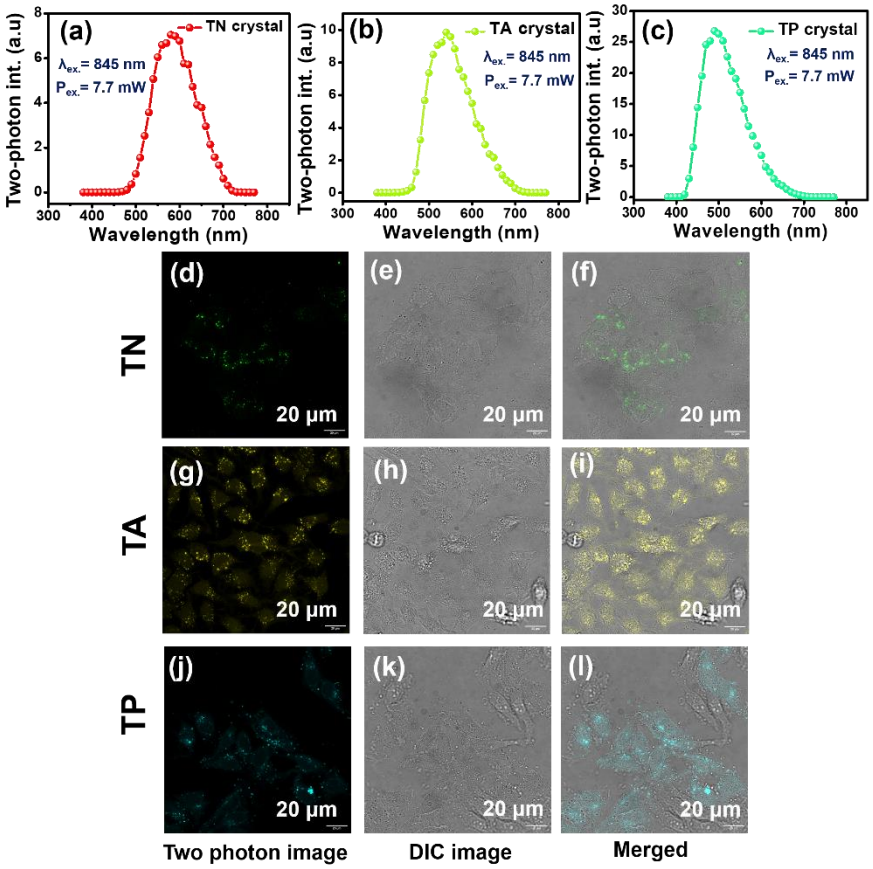

Figure 10: Two-photon excited emission spectra (ex. 845 nm, power= 7.7 mW) of (a) TN, (b) TA and (c) TP crystals. Two-photon microscopy image (excitation wavelength = 820 nm, collection window is from 600 nm to 630 nm for TN, 505 nm to 535 nm for TA, and 540 to 580 for TP) of HeLa cells: (d, g, j) dye treated two-photon imaging, (e, h and k) differential interference contrast (DIC) images, and (f, i, l) DIC image merged with dye treated confocal images.

Given their superior optical penetration, excellent spatial resolution, and minimal optical scattering, two-photon-excited organic luminogens have garnered significant interest compared to typical one-photon-excited fluorophores.[21] These two-photon active materials are especially valuable for cell imaging because they cause the least amount of damage to the target

cell.[22] Given the extensive π-conjugated structures and strong charge transfer properties of our luminogens, which contribute to significant hyperpolarizability and enable efficient two-photon absorption, we investigated their two-photon absorption behavior. Our findings indicated that all three luminogens exhibit two-photon activity in both molecular aggregates and crystalline forms (**Figure 10a, b, c & Figure A14 in Appendix**). The two-photon excited emission spectra (excited at 845 nm) for these aggregates and crystals closely resemble the single-photon excited emission spectra (excited at 420 nm) (**Figure A12 in Appendix**). The emission spectra are also found to be anti-Stokes shifted, with excitation occurring in the 690 nm to 1100 nm range (**Figures A13 & A14 in Appendix**). Furthermore, a power-dependent two-photon emission intensity plotted in the log-log scale shows a slope of approximately 2 (**Figures A13 & A14 in Appendix**), suggesting a minimal contribution from the first-order emission. Additionally, two-photon cell imaging experiments demonstrated that our luminogens effectively illuminate cells, particularly the cytoplasmic region (**Figure 10 d-l**), verified against a control experiment (**Figure A15 in Appendix**). We also assessed the cytotoxicity of our luminogens using the MTT cell viability assay on HeLa cells. The results, confirmed across three biological replicates, show no significant cell death (viability remains over 80%) with drug concentrations up to 15 µM (**Figure A16 in Appendix**), indicating that the luminogens are not toxic to cells at these levels.

4.7 Conclusion:

In summary, we report three donor-acceptor-based luminogens—TN, TA, and TP—with aggregation-induced delayed fluorescence (AIDF) properties. The combined solvent phase and QM/MM-based calculation reveal a drastic lowering of ΔE_{ST} values in the aggregated state, responsible for the observed behavior. Their strong charge-transfer nature and AIDF characteristics have been used to increase singlet exciton diffusion length for efficient photo-current generation. Additionally, their promising two-photon absorption capabilities demonstrate their potential for anti-Stokes shifted photoluminescence (ASPL) and two-photon cell imaging.

4.8 Appendix:

Section A1) Detailed synthetic procedure:

Synthetic scheme:

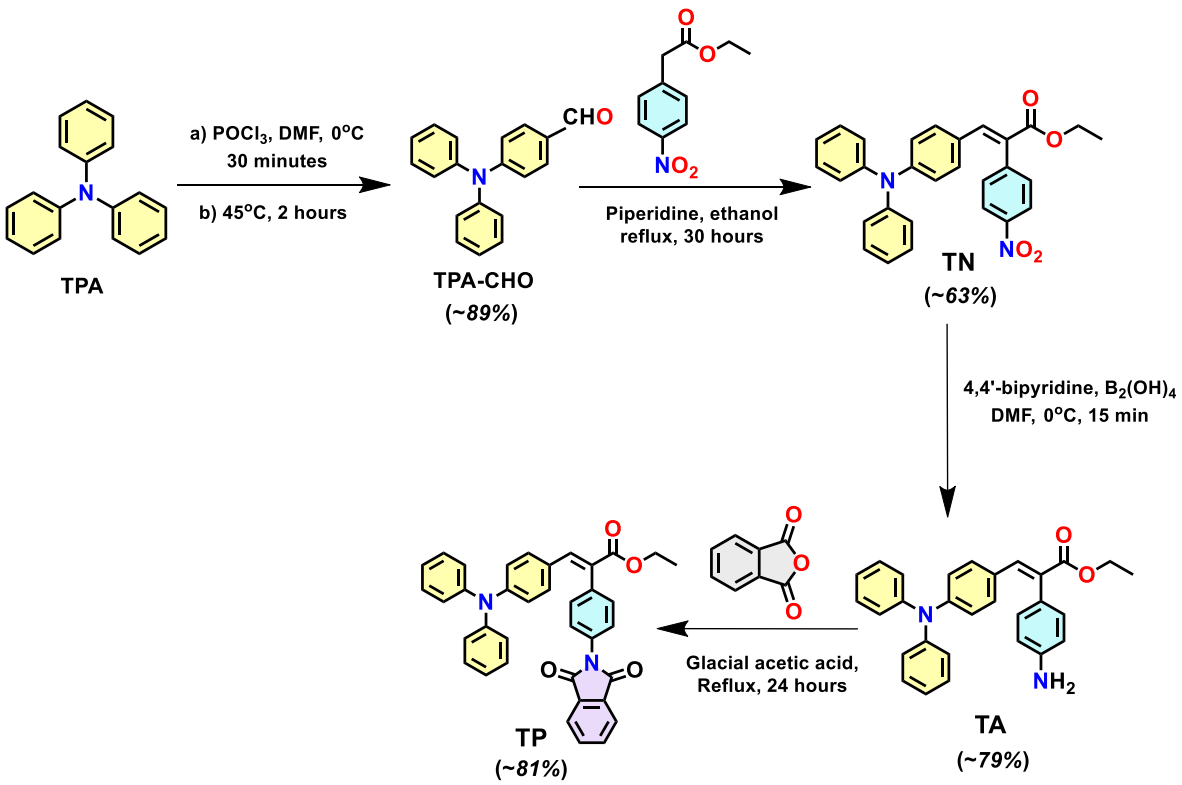

Scheme S1: Synthetic route of the designed compounds

Synthesis of TPA-CHO:

Triphenylamine (4 g, 16 mmol, 1 equiv.) was dissolved in dry DMF (17.8 mL) in a round bottom flask under a nitrogen atmosphere and the solution was cooled at 0°C with continuous stirring. Phosphoryl Chloride (7.6 mL, 82 mmol, 5.13 equiv.) was added to the solution dropwise and stirred at 0°C for 30 minutes. The reaction mixture was cooled to room temperature and kept under stirring for an hour. It was then heated to 45°C and allowed to proceed for two more hours after which the crude product was poured into ice water and neutralized with aq. NaOH (10 g/ 100 ml). The light-yellow precipitate obtained is purified by

column chromatography and characterized by ^{1}H NMR, ^{13}C NMR, and HRMS techniques (4.46 g, 89% yield).[22a]

Synthesis of TN:

To a stirred solution of TPA-CHO (3 g, 10.98 mmol) and ethyl 2-(4-nitrophenyl)acetate (2.52 g, 12.08 mmol) in ethanol (30 mL) at 25°C was added with piperidine (1.62 ml, 16.48 mmol) and stirred at 120°C for 30 hours. After the consumption of the starting material, the reaction mixture was evaporated. The product was obtained as a mixture of (E) and (Z) isomers in the ratio of 4:1. Therefore, the mixture is separated by preparative HPLC to afford the pure E-isomer TN as a yellow solid, which is characterized by ^{1}H NMR, ^{13}C NMR and HRMS techniques (3.2 g, 63 % yield).

Synthesis of TA:

To a stirred solution of TN (3.0 g, 6.46 mmol) in DMF (15 mL) at 0°C was added tetrahydroxydiboron (1.73 g, 19.39 mmol) and 4,4′-bipyridine (0.05 g, 0.32 mmol). The resulting mixture is allowed to stir at 0°C for 15 minutes. Once the starting material was completely consumed, the reaction mixture was quenched with water and extracted thrice with ethyl acetate. The organic layer is separated, washed with brine, dried, and concentrated under reduced pressure. This was further purified by flash column chromatography to yield the pure compound TA, which was further characterized by HRMS, ^{1}H, and ^{13}C NMR techniques (2.2 g, 79% yield).

Synthesis of TP:

TA (2 g, 4.6 mmol) and phthalic anhydride (750 mg, 5.06 mmol) were dissolved in 40 ml of glacial acetic acid. The mixture was refluxed under stirring for 24 hours. After the starting material was consumed, the mixture was cooled to room temperature and neutralized with a

saturated sodium bicarbonate solution. The solution was extracted with ethyl acetate, washed with water and brine and the organic layer was dried over anhydrous Na_2SO_4. The pure product TP is yielded by silica gel column chromatography and characterized by HRMS, ^{1}H, and ^{13}C NMR techniques (2.1 g, 81% yield).

Characterisation data

^{1}H NMR of TPA-CHO:

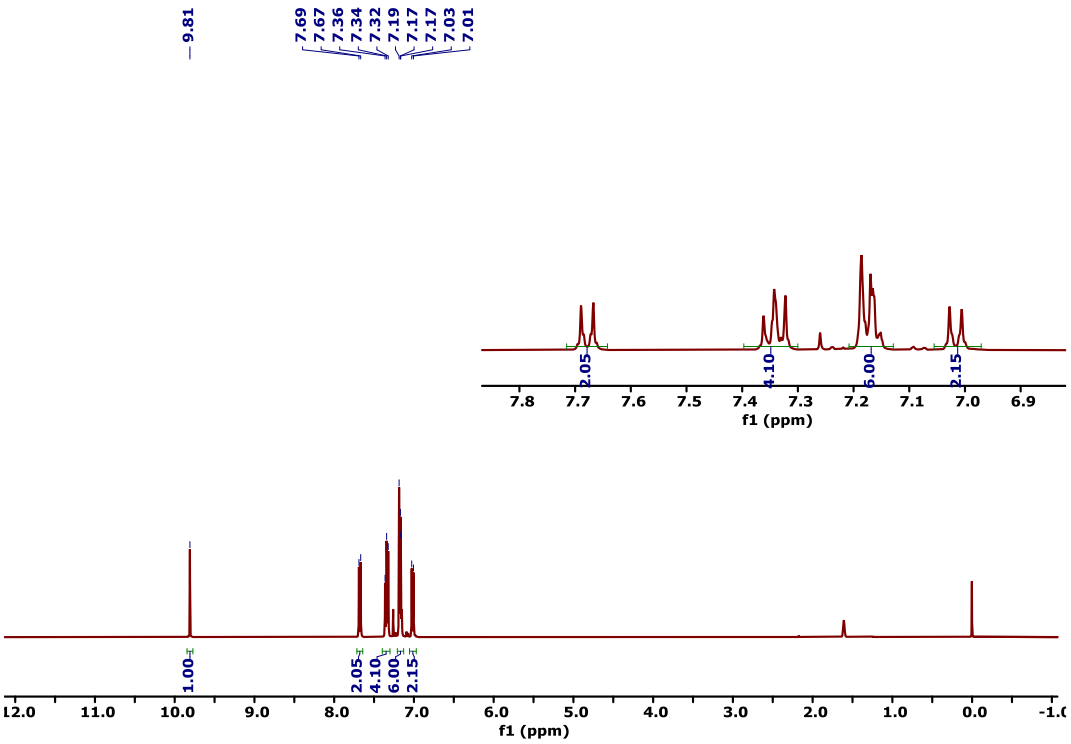

^{13}C NMR of TPA-CHO:

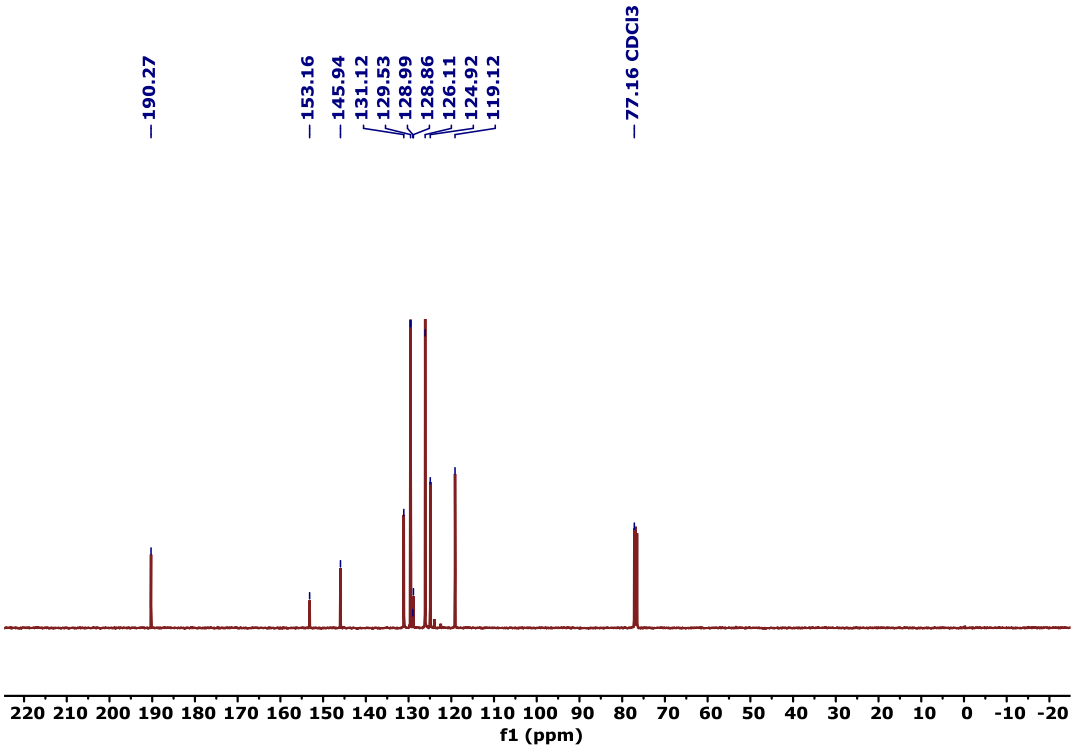

HRMS of TPA-CHO:

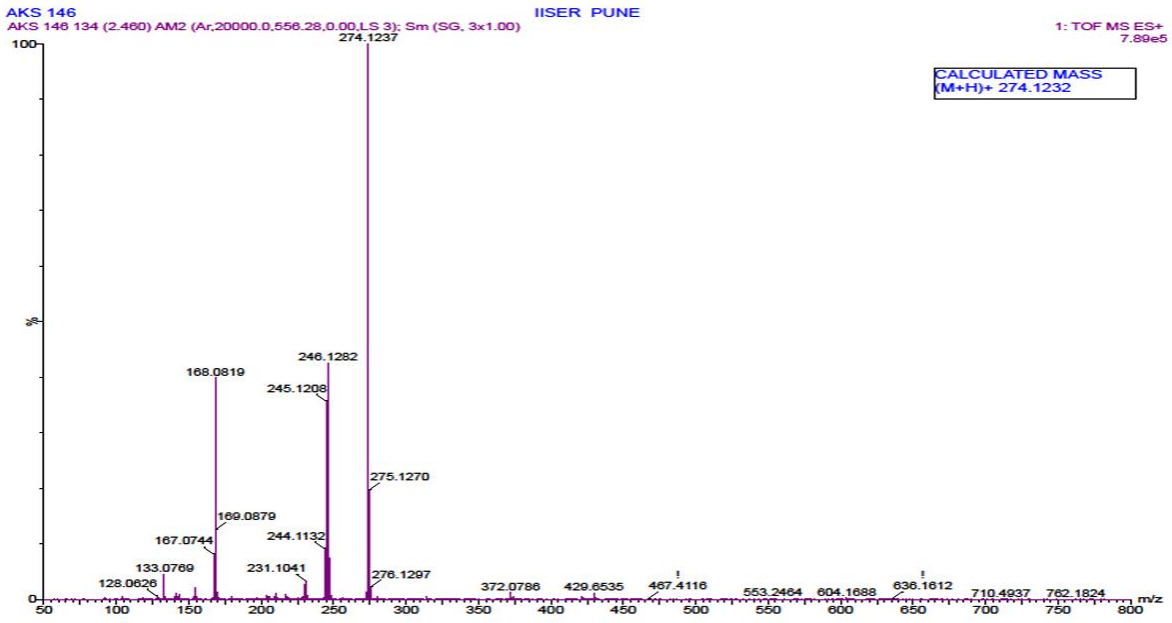

^{1}H NMR of TN:

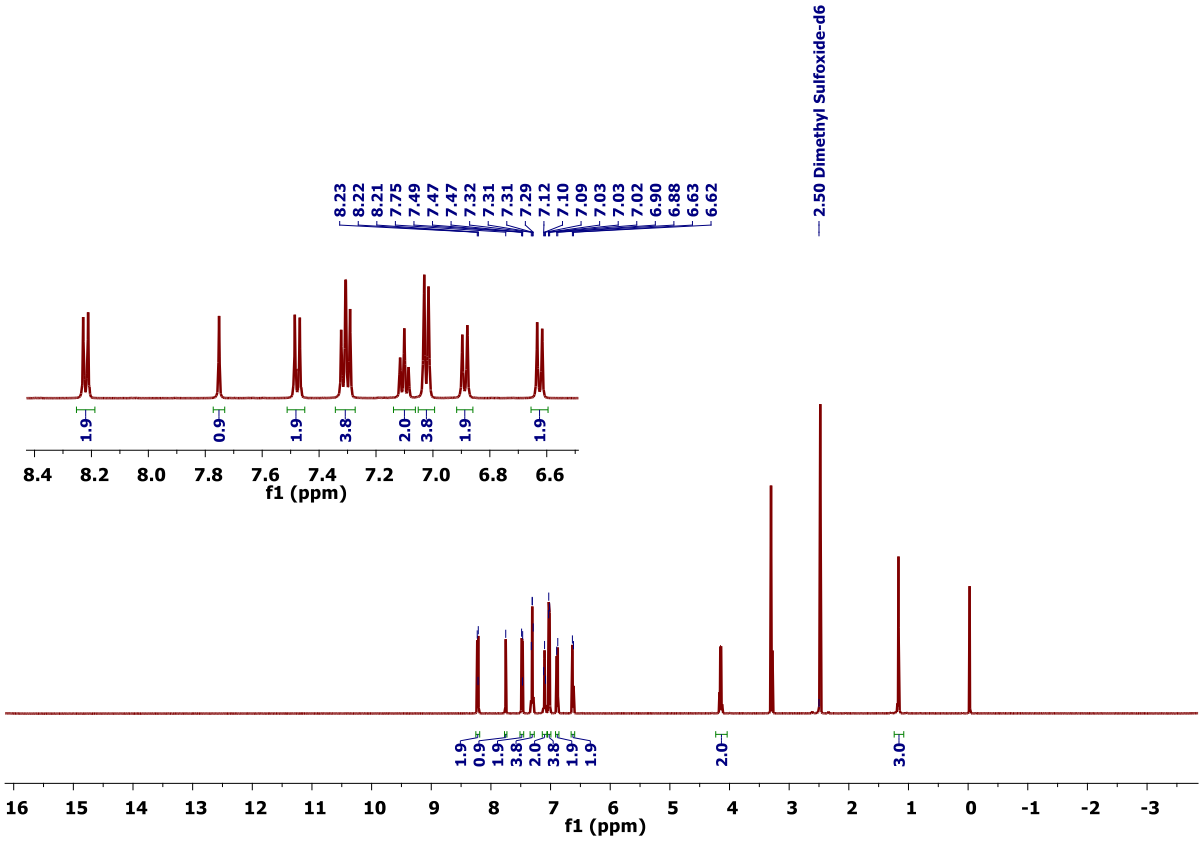

^{13}C NMR of TN:

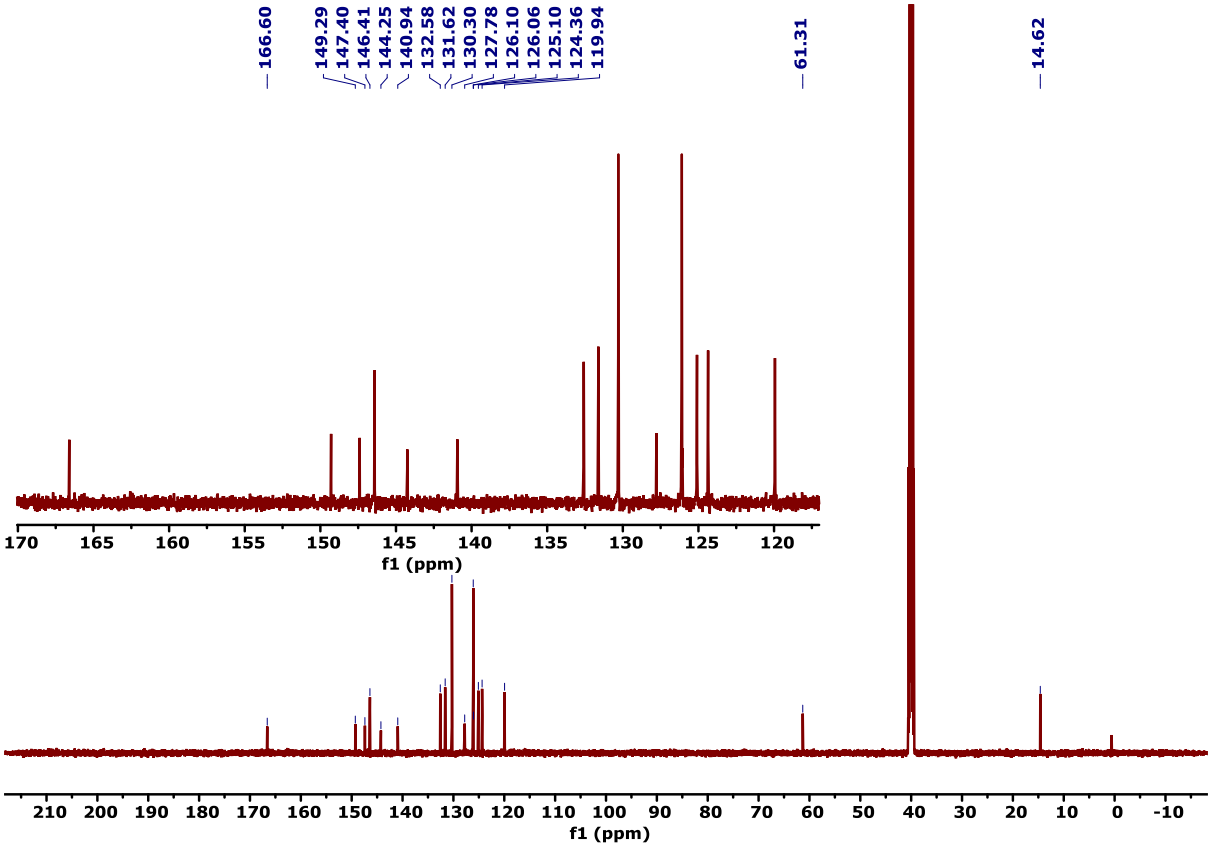

HRMS of TN:

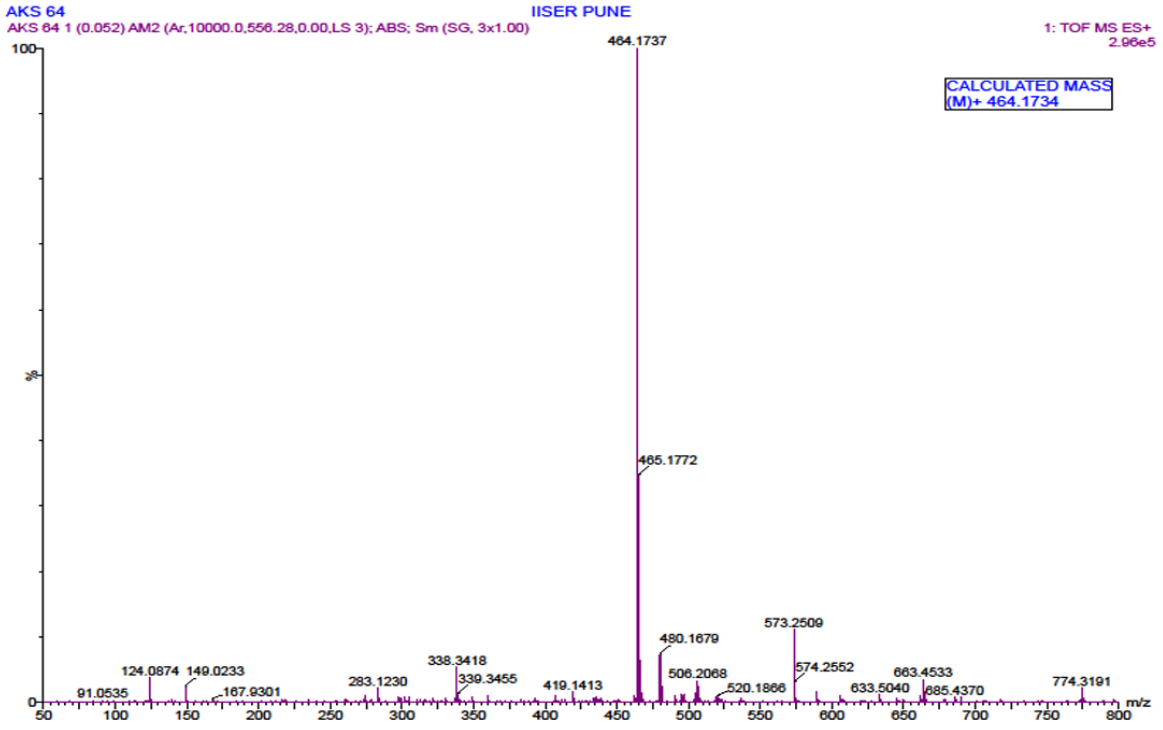

HPLC data for TN:

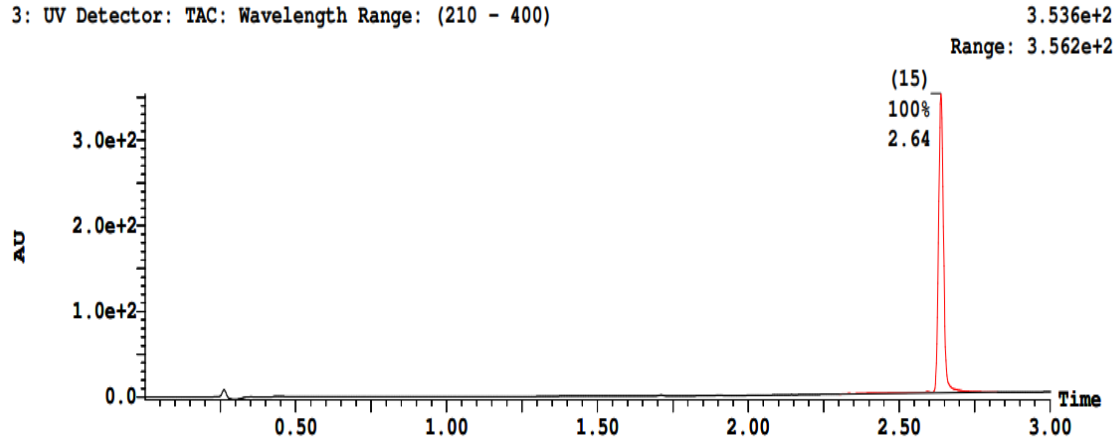

^{1}H NMR of TA:

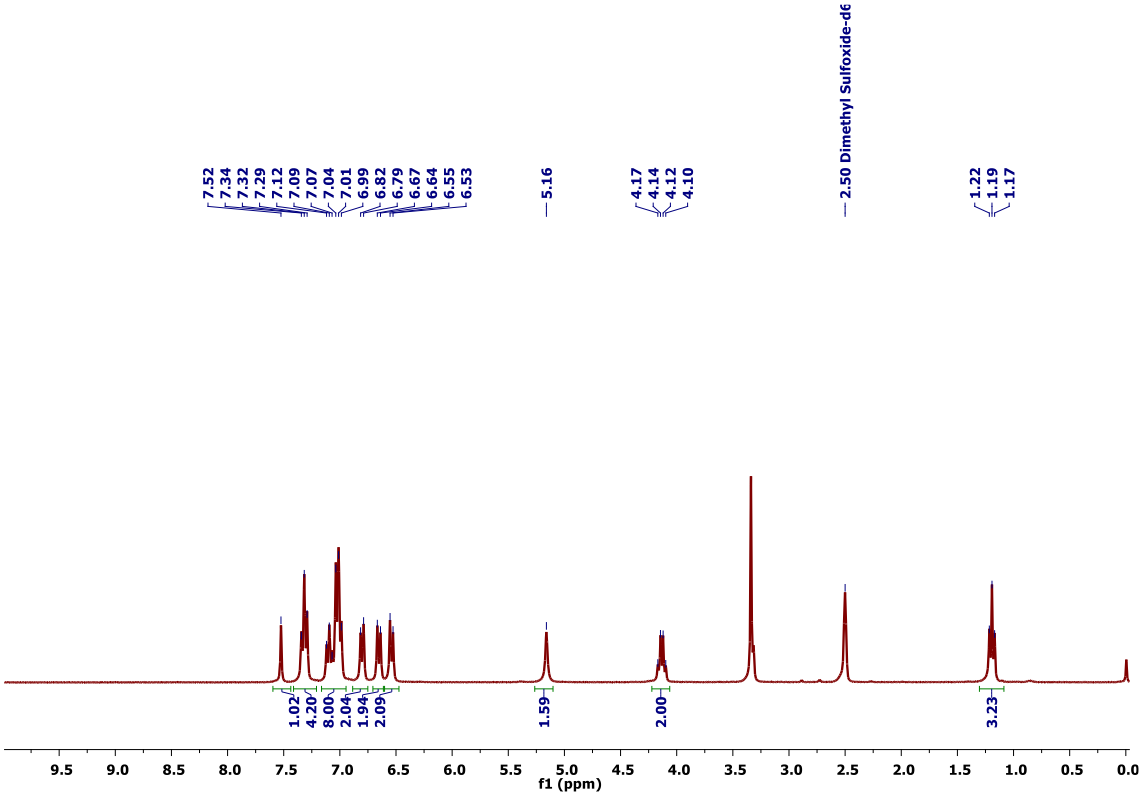

^{13}C NMR of TA:

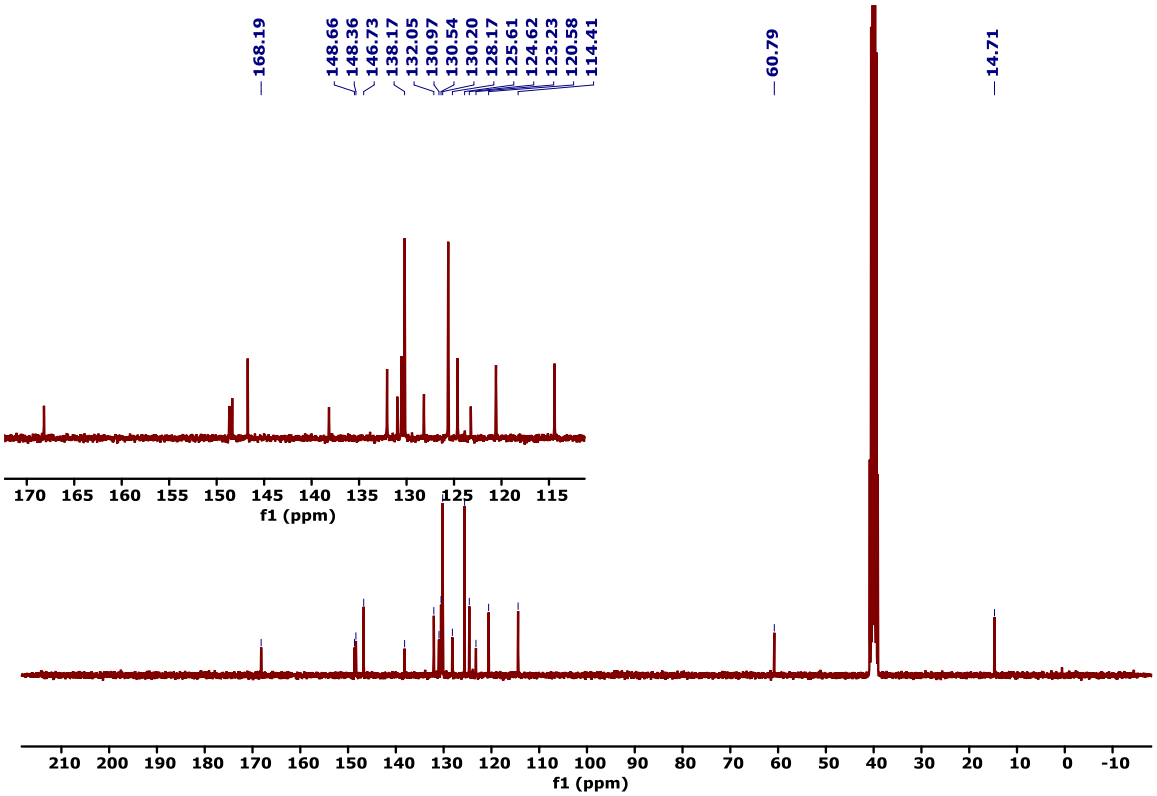

HRMS of TA:

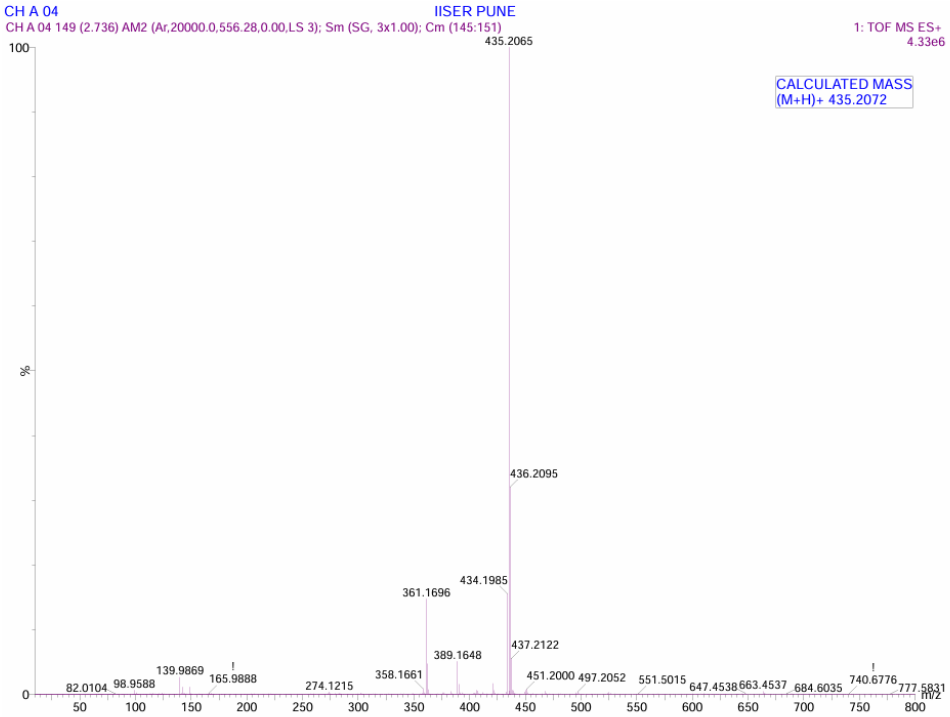

HPLC data of TA:

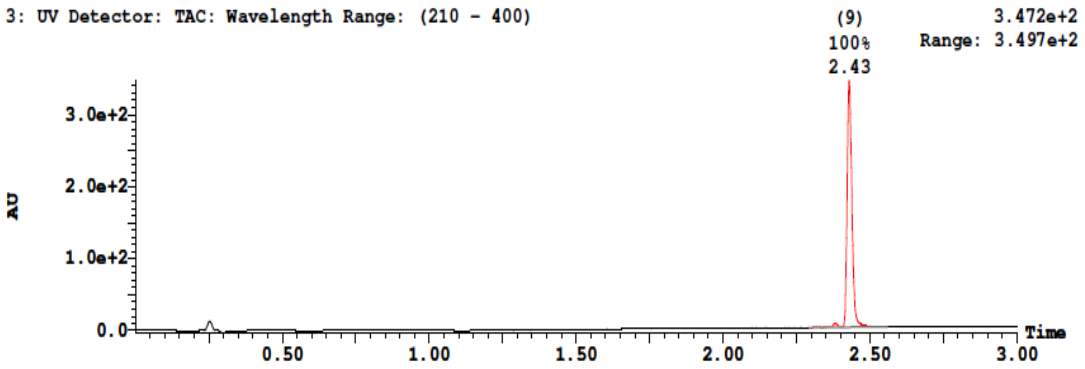
3: UV Detector: TAC: Wavelength Range: (210 - 400)
(9)
100%
2.43
3.472e+2
Range: 3.497e+2
AU
3.0e+2
2.0e+2
1.0e+2
0.0
0.50
1.00
1.50
2.00
2.50
3.00
Time

^{1}H NMR of TP:

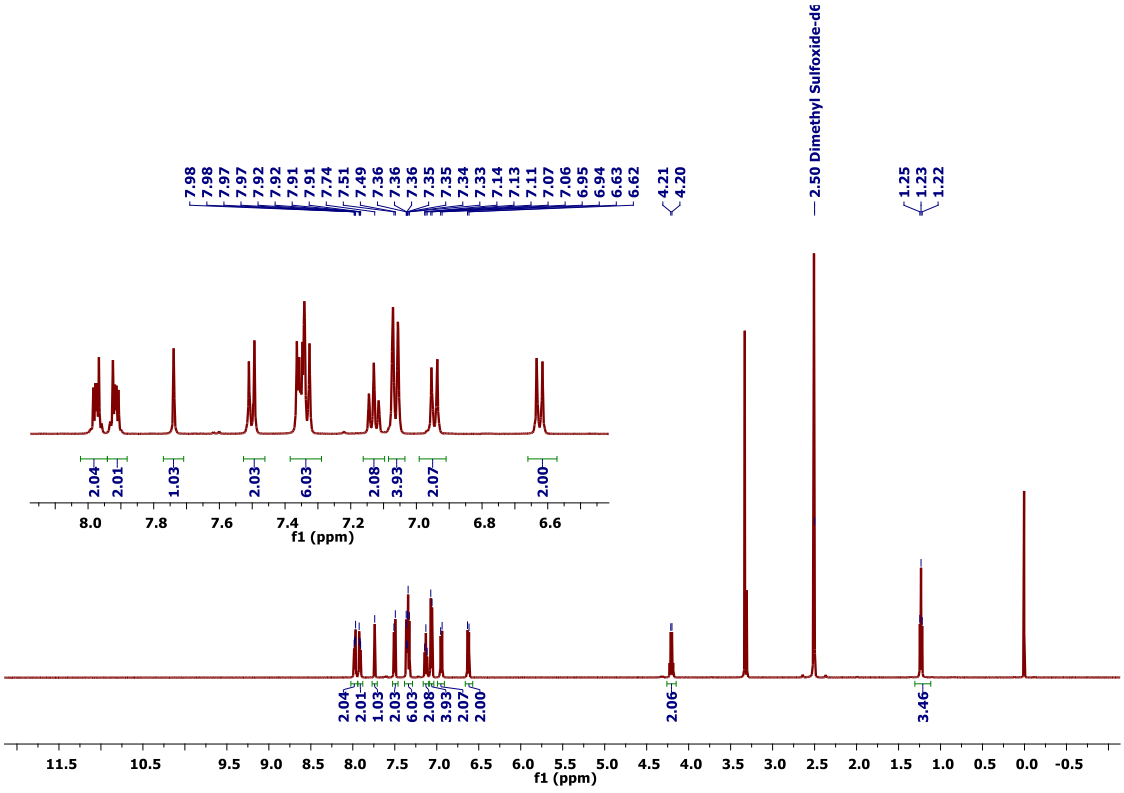
2.50 Dimethyl Sulfoxide-d6
f1 (ppm)

^{13}C NMR of TP:

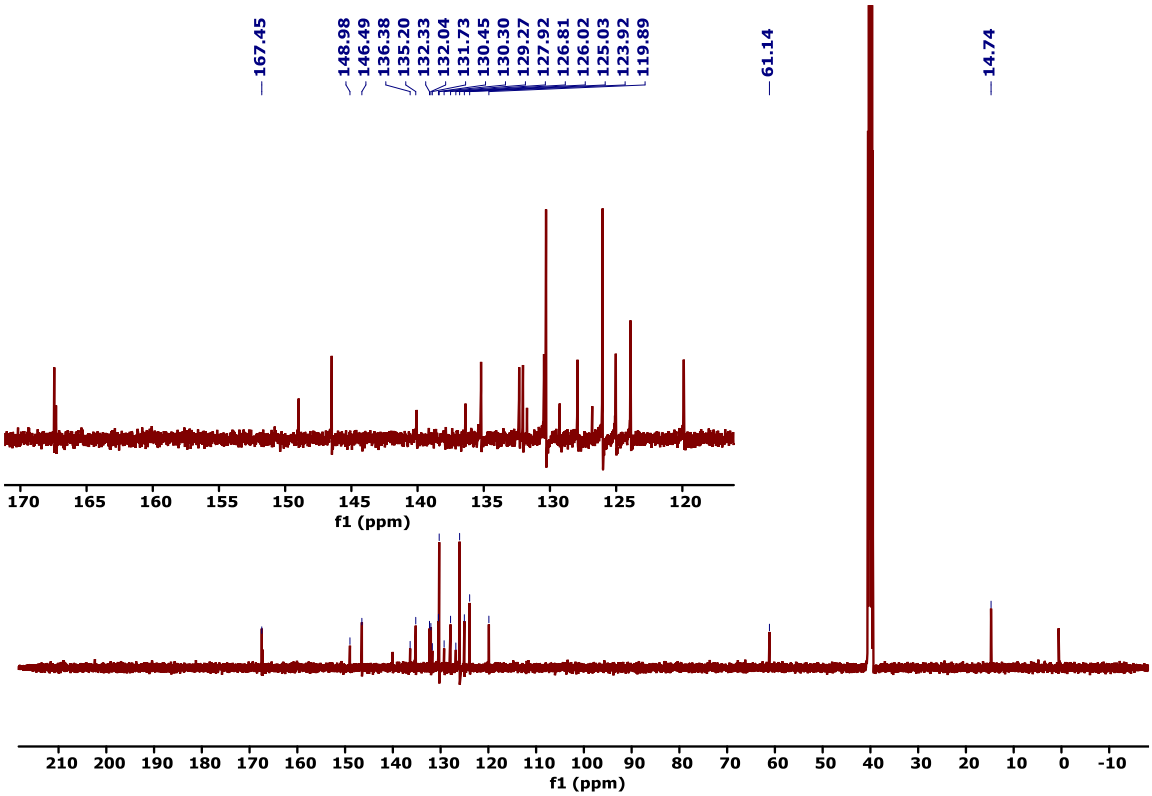

HRMS of TP:

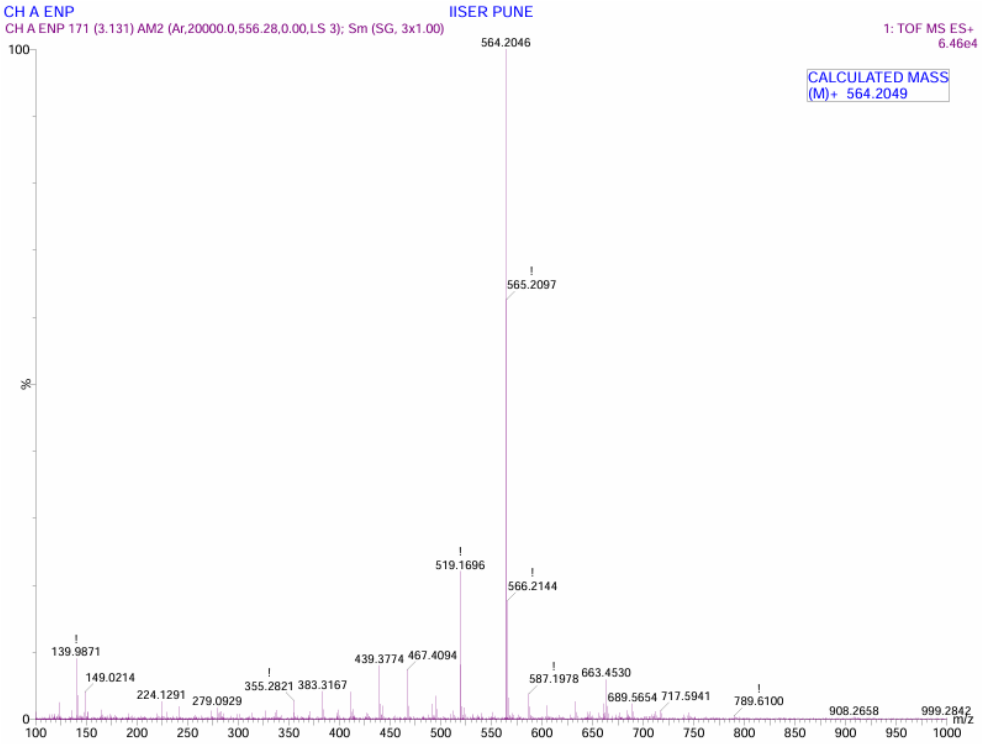

HPLC data for TP:

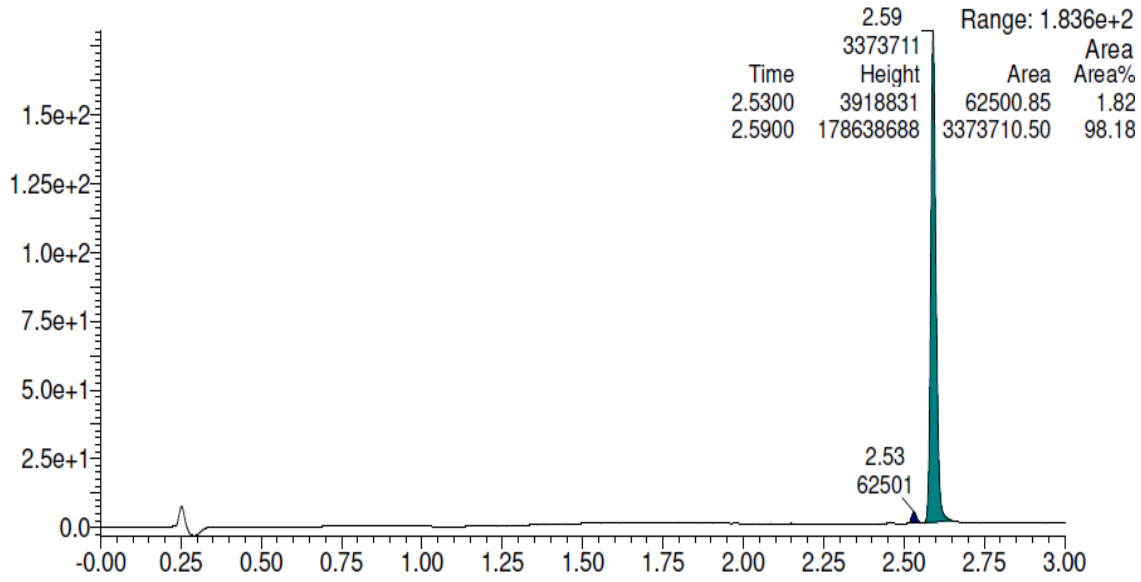

Crystallographic data

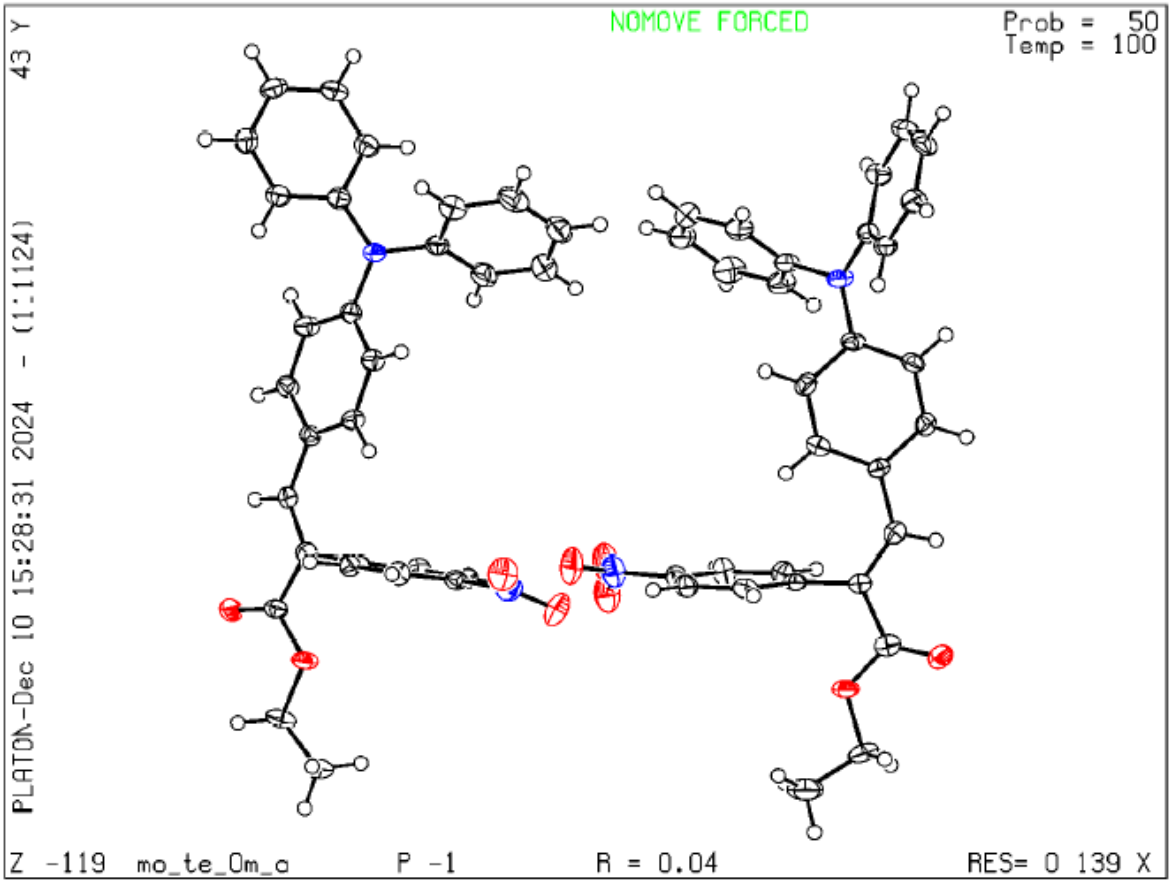

Table S1. Crystal data and structure refinement for **TN**

Identification code	TN
CCDC No.	2387501
Empirical formula	$C_{29}H_{24}N_2O_4$
Formula weight	464.50
Temperature /K	100 K
Crystal system	Triclinic
Space group	*P-1*
a/ Å	11.184(11)
b/ Å	13.742(13)
c/ Å	16.798(17)
α/°	72.17(3)
β/°	74.47(3)
γ/°	87.49(4)

Volume / Å^3	2366(4)
Z	4
ρcalc (g/cm^3)	1.304
μ/ mm^{-1}	0.088
F (0 0 0)	976
Crystal size/mm^3	0.5 × 0.03 × 0.01
Radiation	MoKα (λ = 0.71073)
2θ range for data collection/º	3.116 to 42.996
Goodness-of-fit on F^2	1.030
Final R indexes [I>=2σ (I)]	R_1 = 0.0419, wR_2 = 0.0949
Final R indexes [all data]	R_1 = 0.0660, wR_2 = 0.1102

Explanation of CheckCIF alerts for TN

Alert level A

THETM01_ALERT_3_A The value of sine(theta_max)/wavelength is less than 0.550

Calculated sin(theta_max)/wavelength = 0.5156

Explanation: This is due to the use of the OMIT command in the refinement process. Data at higher angles 2 theta = 43 were omitted because I/sigma dropped below 3 indicating that the data were no longer reliable for refinement purposes. This approach was taken to ensure the accuracy and quality of the refinement process.

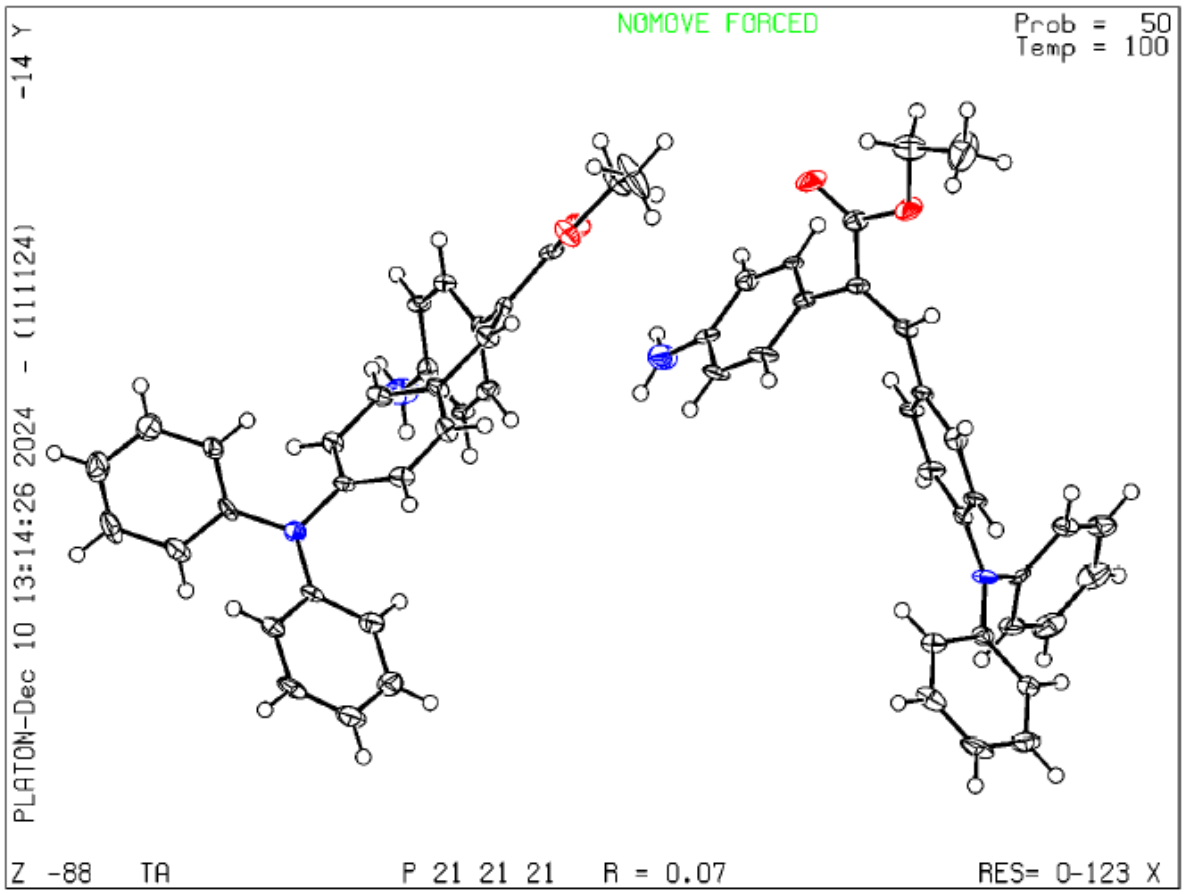

Table S2. Crystal data and structure refinement for **TA**

Identification code	TA
CCDC No.	2378737
Empirical formula	$C_{29}H_{26}N_2O_2$
Formula weight	434.52
Temperature /K	100 K
Crystal system	Orthorhombic
Space group	$P2_12_12_1$
a/ Å	11.2750(12)
b/ Å	13.8596(14)
c/ Å	29.694(3)
α/°	90
β/°	90
γ/°	90
Volume / Å³	4640.3(8)

Z	8
ρcalc (g/cm^3)	1.244
μ/ mm^{-1}	0.078
F (0 0 0)	1840.0
Crystal size/mm^3	0.4 × 0.03 × 0.02
Radiation	MoKα (λ = 0.71073)
2θ range for data collection/º	3.864 to 44.992
Goodness-of-fit on F^2	1.076
Final R indexes [I>=2σ (I)]	R_1 = 0.0661, wR_2 = 0.1381
Final R indexes [all data]	R_1 = 0.1017, wR_2 = 0.1539

Explanation of CheckCIF alerts for TA

Alert level A

THETM01_ALERT_3_A The value of sine(theta_max)/wavelength is less than 0.550 Calculated sin(theta_max)/wavelength = 0.5383

Explanation: This is due to the use of the OMIT command in the refinement process. Data at higher angles 2 theta = 45 were omitted because I/sigma dropped below 3 indicating that the data were no longer reliable for refinement purposes. This approach was taken to ensure the accuracy and quality of the refinement process.

Alert level B

RINTA01_ALERT_3_B The value of Rint is greater than 0.18 Rint given 0.244

Explanation: The high R_{int} arises from weak diffraction due to the poor quality of the crystal Efforts to obtain better crystals were unsuccessful.

PLAT340_ALERT_3_B Low Bond Precision on C-C Bonds ..... 0.01147 Ang.

Explanation: It is due to poor quality data of weakly diffracted crystals.

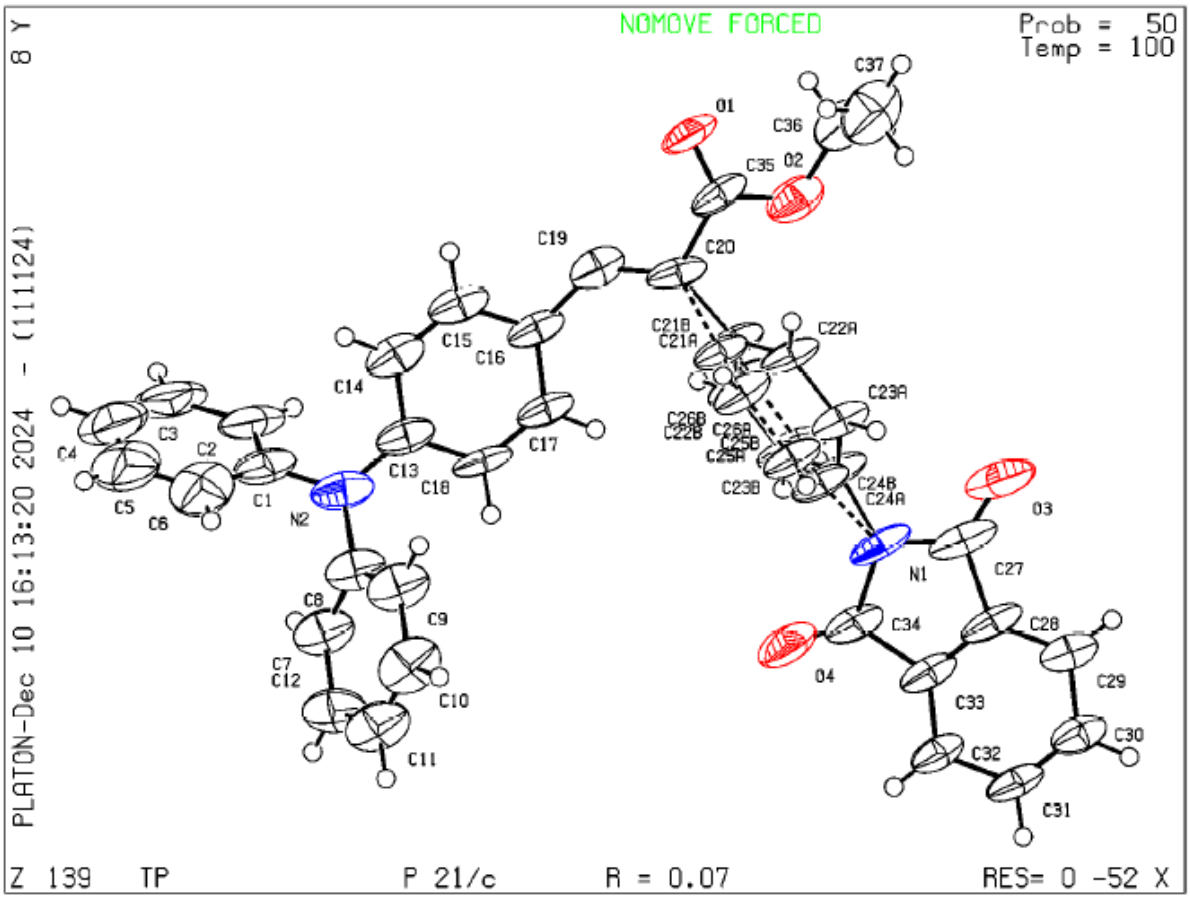

Table S3. Crystal data and structure refinement for **TP**

Identification code	TP
CCDC No.	2387502
Empirical formula	$C_{37}H_{27}N_2O_4$
Formula weight	563.60
Temperature /K	100 K
Crystal system	Monoclinic
Space group	*P2₁/c*
a/ Å	15.833(7)
b/ Å	10.282(4)
c/ Å	18.493(7)
α/°	90
β/°	103.027(11)
γ/°	90
Volume / Å³	2933(2)

Z	4
ρcalc (g/cm^3)	1.276
μ/ mm^{-1}	0.083
F (0 0 0)	1180.0
Crystal size/mm^3	0.4 × 0.2 × 0.05
Radiation	MoKα (λ = 0.71073)
2θ range for data collection/º	4.522 to 42.996
Goodness-of-fit on F^2	1.012
Final R indexes [I>=2σ (I)]	R_1 = 0.0699, wR_2 = 0.1458
Final R indexes [all data]	R_1 = 0.1638, wR_2 = 0.2053

Explanation of CheckCIF alerts for TP

Alert level A

THETM01_ALERT_3_A The value of sine(theta_max)/wavelength is less than 0.550 Calculated sin(theta_max)/wavelength = 0.5156

Explanation: This is due to the use of the OMIT command in the refinement process. Data at higher angles 2 theta = 43 were omitted because I/sigma dropped below 3 indicating that the data were no longer reliable for refinement purposes. This approach was taken to ensure the accuracy and quality of the refinement process.

Alert level B

PLAT340_ALERT_3_B Low Bond Precision on C-C Bonds ..... 0.014 Ang.

Explanation: This is due to poor quality data of weakly diffracted crystals.

Note: The crystals were all weakly diffracting and as a consequence data were cut at 2 theta (Θ) = 43º in the case of TN and TP and for TA, the data were cut at 2 theta (Θ) = 45 º. However, the data were sufficient to confirm connectivity in all cases and geometric parameters are not discussed.

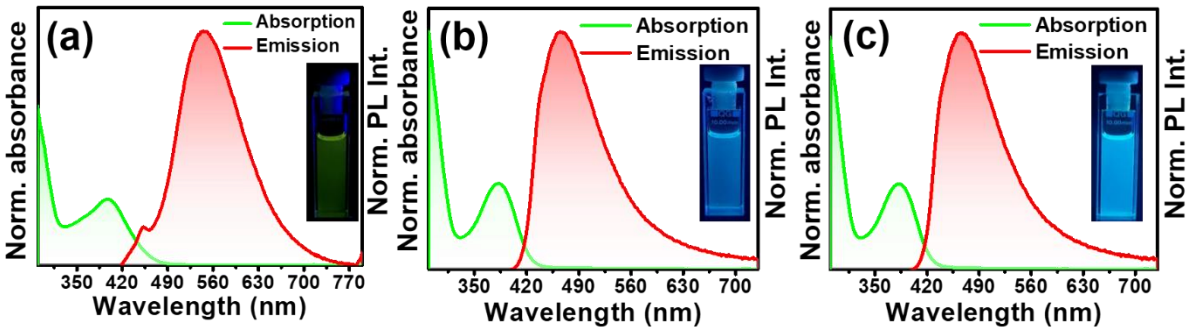

Figure A1: Absorption and emission spectra in toluene of (a) TN, (b) TA and, (c) TP. Inset: Cuvette images of the toluene solutions under UV irradiation. (Concentration: 30 μM)

Excited State	Energy (eV)	Wavelength (nm)	Orbital configuration	Oscillator strength (*f*)
1 (T_1)	2.0159	615	HOMO-1 to LUMO HOMO-1 to LUMO+1 HOMO to LUMO HOMO to LUMO+1	0.000
2 (S_1)	2.2548	550	HOMO to LUMO	0.135
6 (S_2)	3.0530	406	HOMO to LUMO+1	0.750

Table A4: Excited state parameters of TN at Franck-Condon geometry of the ground state.

Excited State	Energy (eV)	Wavelength (nm)	Orbital configuration	Oscillator strength (*f*)
1 (T_1)	2.1573	575	HOMO-2 to LUMO HOMO to LUMO	0.000
2 (S_1)	2.9259	424	HOMO-1 to LUMO HOMO to LUMO	0.702
5 (S_2)	3.3090	375	HOMO-1 to LUMO HOMO to LUMO	0.160

Table A5: Excited state parameters of TA at Franck-Condon geometry of the ground state.

Excited State	Energy (eV)	Wavelength (nm)	Orbital configuration	Oscillator strength (*f*)

1 (T_1)	2.193	565	HOMO-2 to LUMO+1 HOMO-1 to LUMO+1 HOMO to LUMO+1	0.000
2 (T_2)	2.5015	496	HOMO to LUMO	0.000
3 (S_1)	2.5090	494	HOMO to LUMO	0.000
4 (S_2)	2.9770	417	HOMO to LUMO+1	0.815

Table A6: Excited state parameters of TP at Franck-Condon geometry of the ground state.

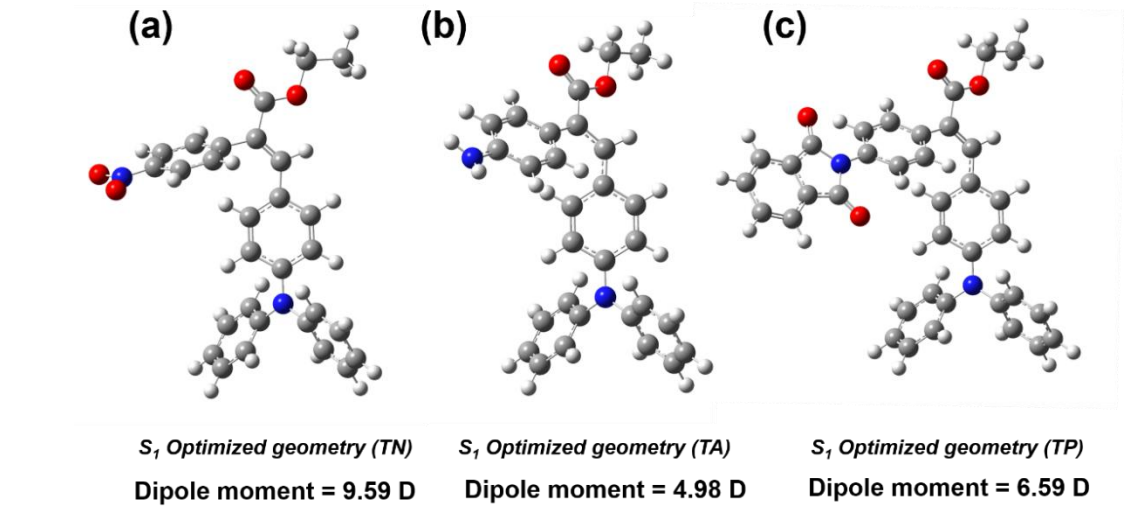

Figure A2: Optimized S_1 molecular geometries of (a) TN, (b) TA, and (c) TP. For S_1 state optimization, the TD-SCF method and B3LYP/6-31G (d, p) level of theory have been used in THF solvent using the IEFPCM solvent model. The dipole moments in the S_1 excited state are found to be 9.59 D, 4.98 D, and 6.59 D for TN, TA, and TP, respectively.

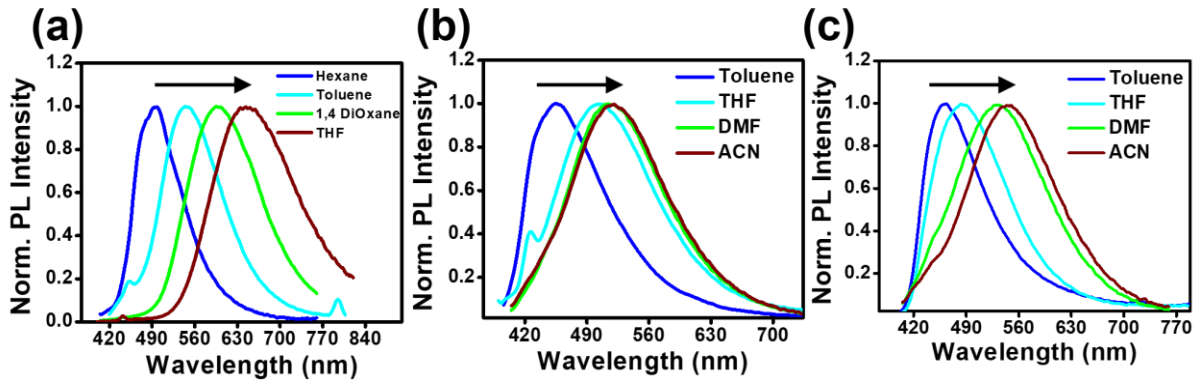

Figure A3: Solvatochromic emission studies of all three luminogens- (a) TN, (b) TA, and (c) TP in solvents of different polarities.

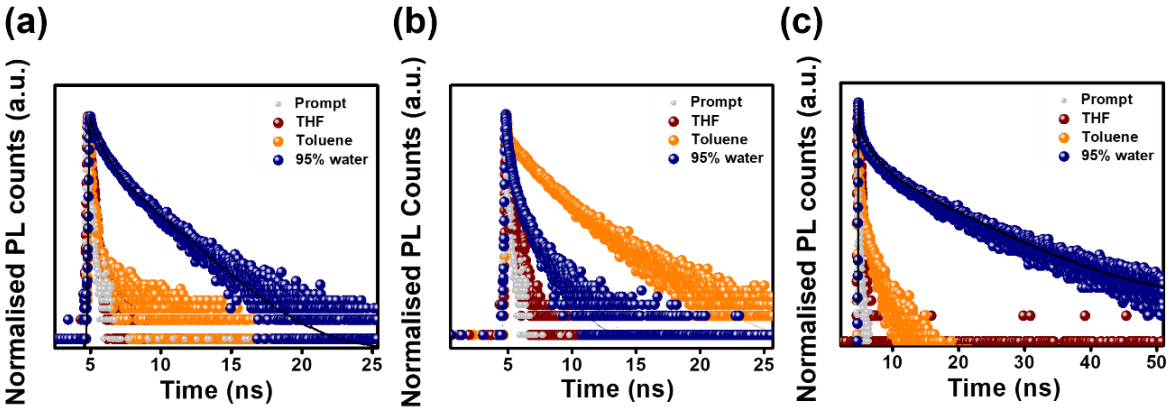

Figure A4: Time-resolved fluorescence decay profiles of (a) TN, (b) TA, and (c) TP in the nanosecond time scale (λ_{ex} = 375 nm). Solutions are made with a concentration of 20 μM. (Note: Decays with τ_{av} < 50 ps fall below the detection limit of the TCSPC instrument and hence have not been fitted).

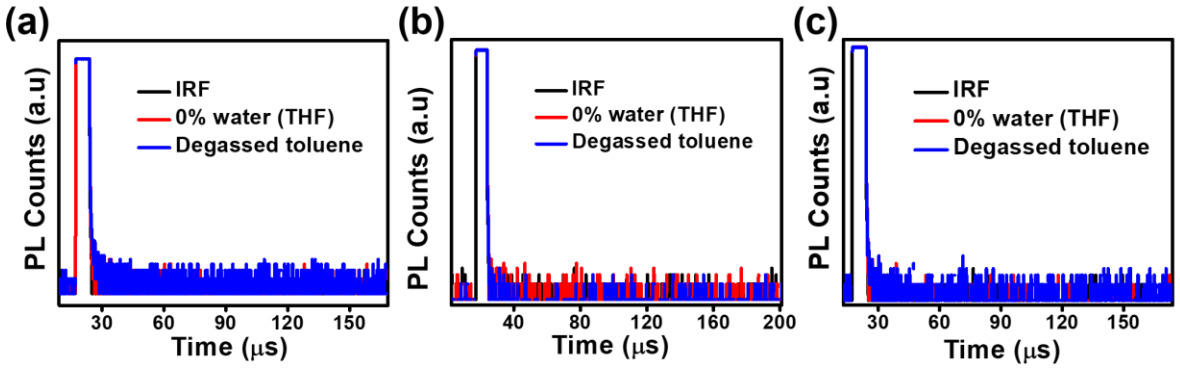

Figure A5: Time-resolved fluorescence decay profiles of (a) TN, (b) TA, and (c) TP in the micro-second time scale (λ_{ex} = 357 nm). No lifetime component in ~μs-ms region found in all three. Solutions are made with a concentration of 20 μM.

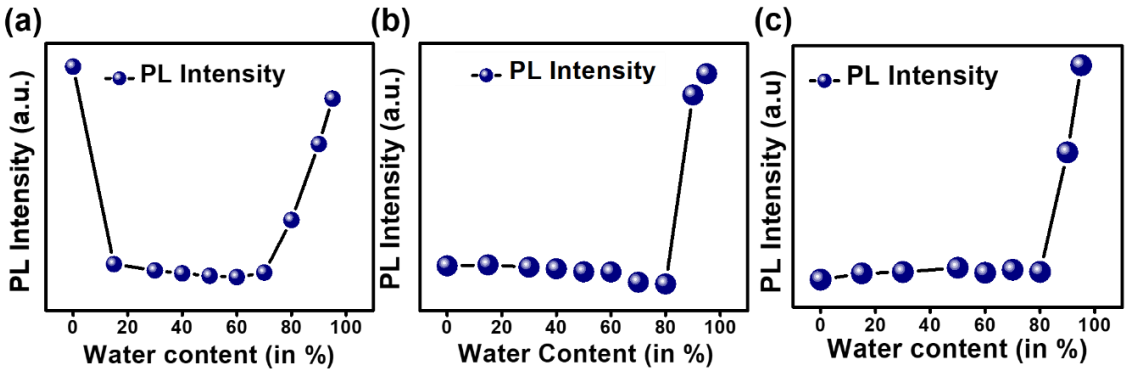

Figure A6: Photoluminescence intensity of THF-water binary solutions of (a) TN, (b) TA, and (c) TP plotted against the water content.

Water content (in %)	PLQY (TN)	PLQY (TA)	PLQY (TP)
0%	***9.9%***	***2.7%***	***4.9%***
15%	0.8%	2.8%	6%
30%	0.6%	2.7%	6.3%
50%	0.5%	2.5%	7%
60%	0.5%	2.5%	6.1%
70%	0.8%	2%	6.7%
80%	3%	2%	6.3%
90%	6%	10.1%	27.8%
95%	***7%***	***13%***	***45%***

Table A7: PLQY variation of all three luminogens in different water content.

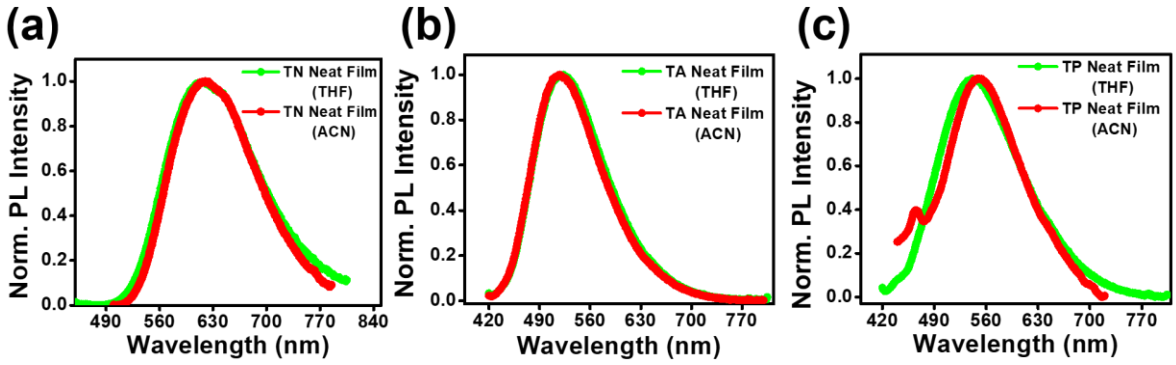

Figure A7: Steady-state emissions of neat films for (a) TN, (b) TA, and (c) TP were made from solvents of different polarities, i.e., THF and acetonitrile.

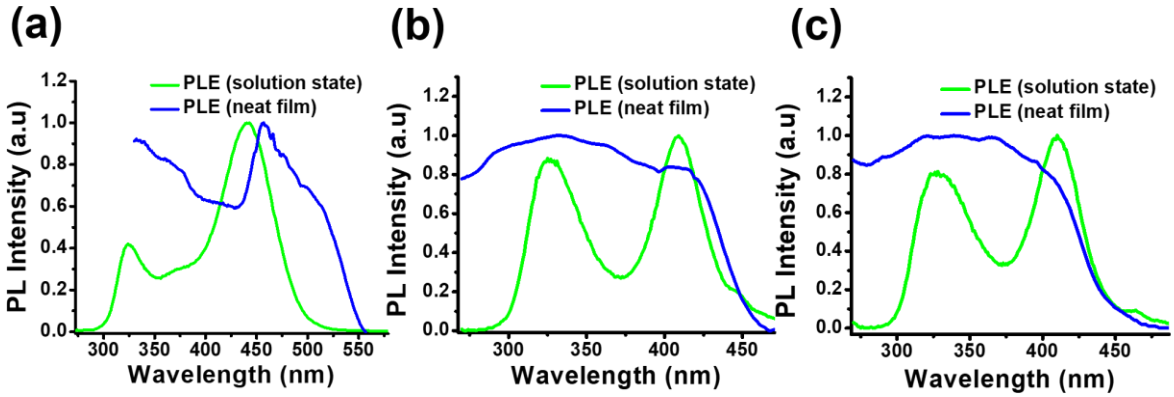

Figure A8: PL excitation spectra of solution phase (THF as solvent) and neat films of (a) TN, (b) TA, and (c) TP.

Note A1: Crystalline/amorphous nature of the neat films

A PXRD (Powder X-ray Diffraction) experiment was conducted to determine the crystalline or amorphous nature of the neat films. The PXRD patterns for both TN and TA exhibited no sharp or intense diffraction peaks, but instead displayed a broad halo, indicating that the neat films of TN and TA are amorphous (Figure A9). In contrast, the PXRD pattern for TP showed several sharp and intense diffraction peaks, suggesting that the TP neat films possess a higher level of crystallinity (Figure A9). The crystals of all three luminogens show distinct and intense

diffraction peaks in their PXRD patterns (although PXRD patterns of crystals always lead to selective diffraction from some planes due to their mostly single crystalline nature). In contrast, the films of TN and TA are amorphous, meaning they do not maintain the same arrangement as observed in the crystals. However, for TP, the diffraction peaks obtained from the neat film closely match the positions seen in the crystals, indicating that it retains a similar structural arrangement (Figure A9).

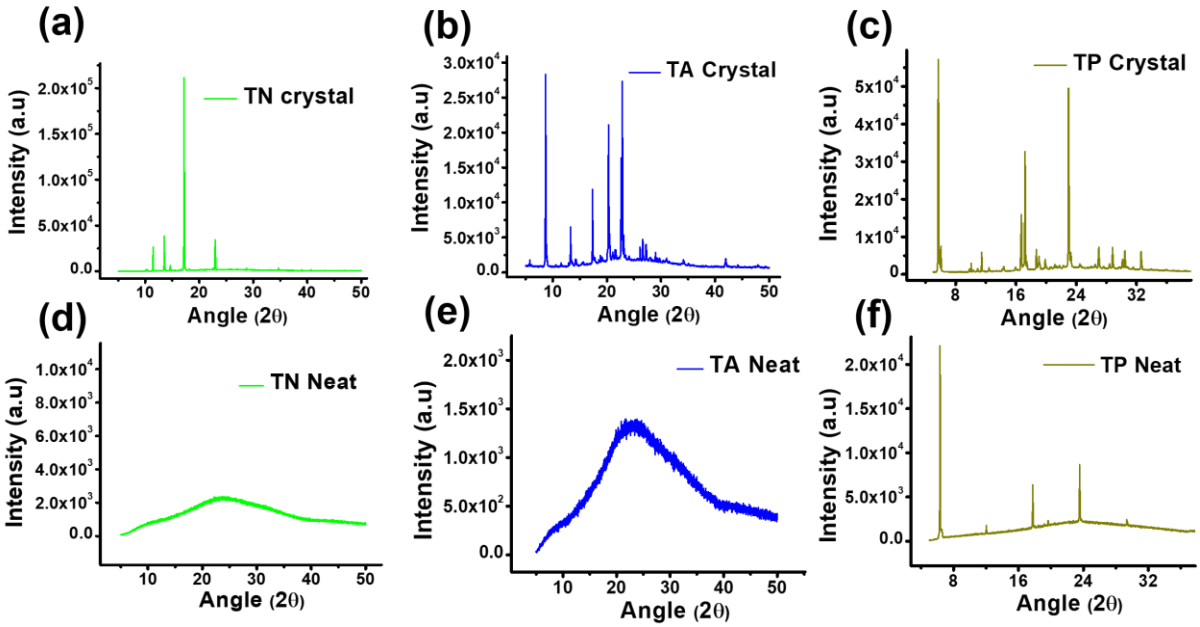

Figure A9: PXRD patterns of the crystals of (a) TN, (b) TA, and (c) TP. PXRD patterns of the neat films of (d) TN, (e) TA, and (f) TP.

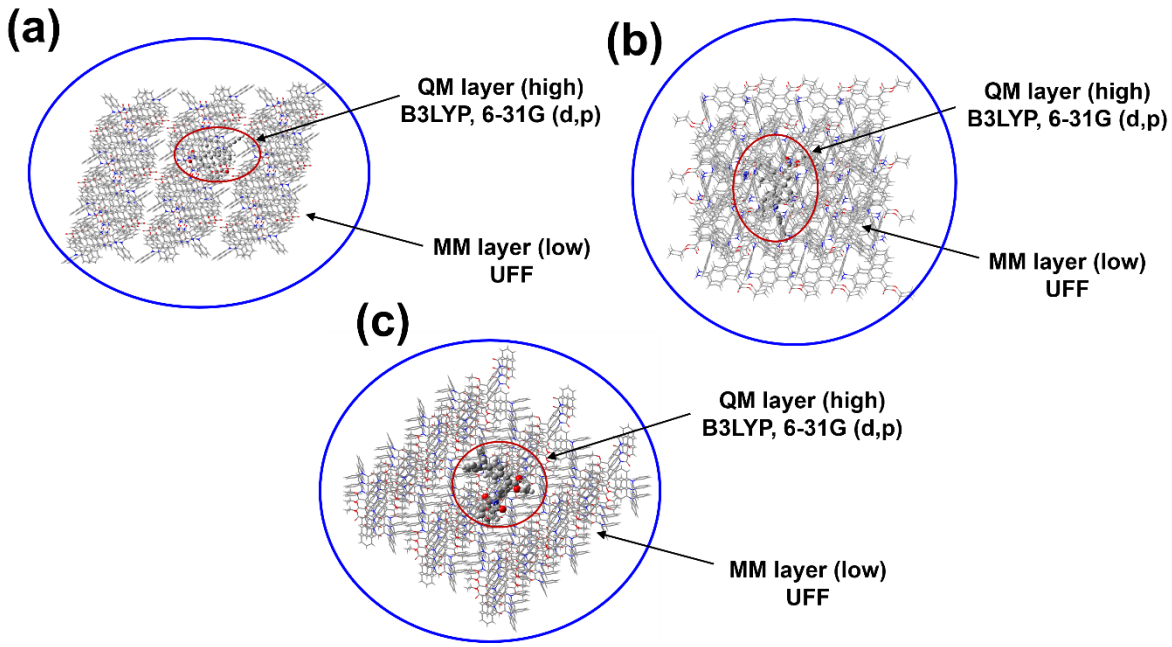

Figure A10: QM and MM layers were chosen from the crystal structure for QM/MM simulations for (a) TN, (b) TA, and (c) TP. For the QM/MM calculation, the QM layer has been treated with B3LYP, 6-31G (d, p) level of theory, while the MM layer has been treated with a classical UFF model of theory.

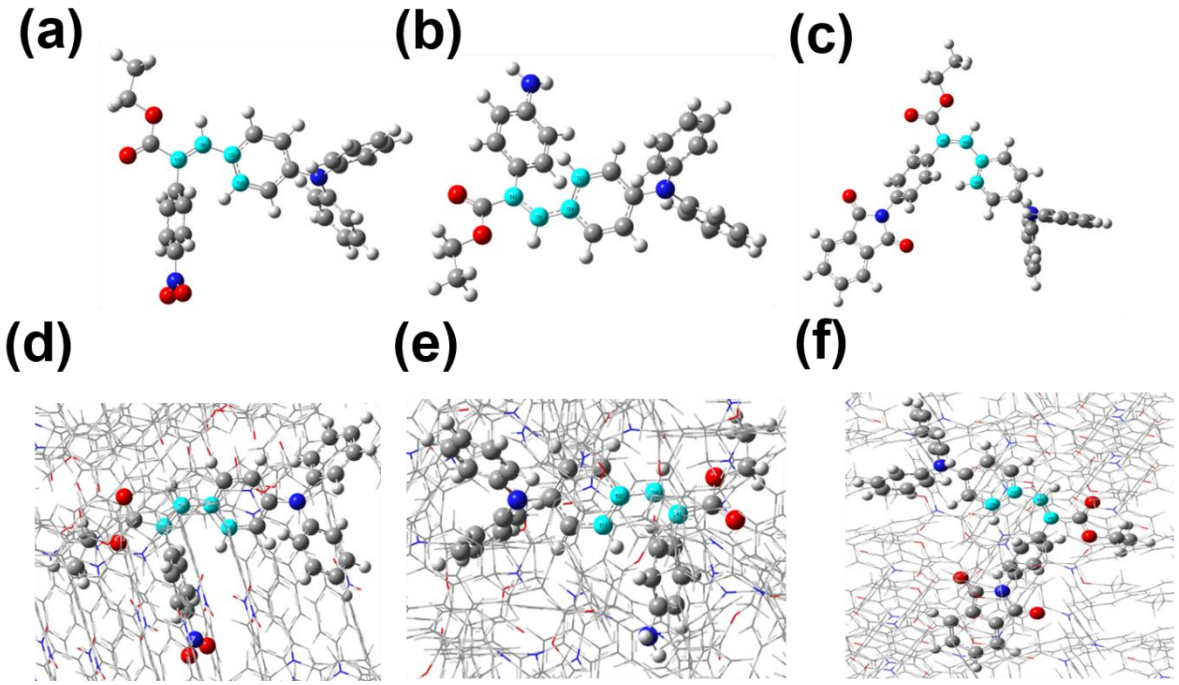

Figure A11: The dihedral angle chosen for Potential energy surface (PES) scanning along (marked in cyan color) for THF-based (a-TN, b-TA, c-TP) and QM/MM-based calculation (d-TN, e-TA, f-TP).

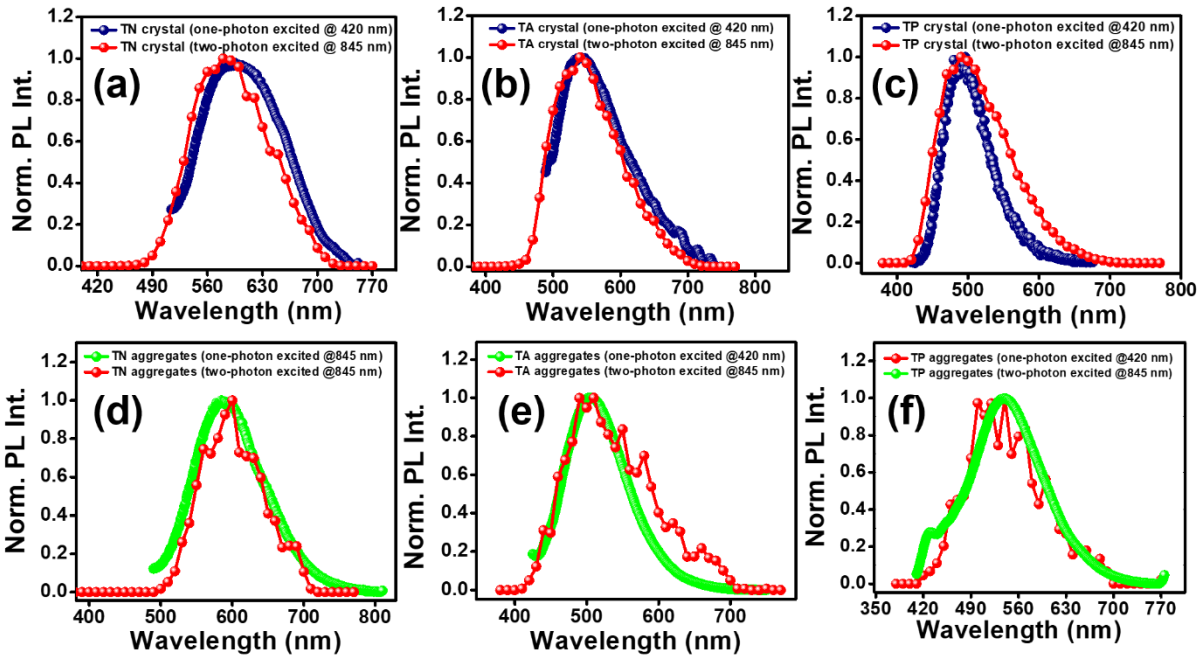

Figure A12: One-photon and two-photon excited emission spectra of the crystals of (a) TN, (b) TA, and (c) TP. One-photon and two-photon excited emission spectra of the molecular aggregates (formed at 95% water- 5% THF binary mixtures) of (d) TN, (e) TA, and (f) TP.

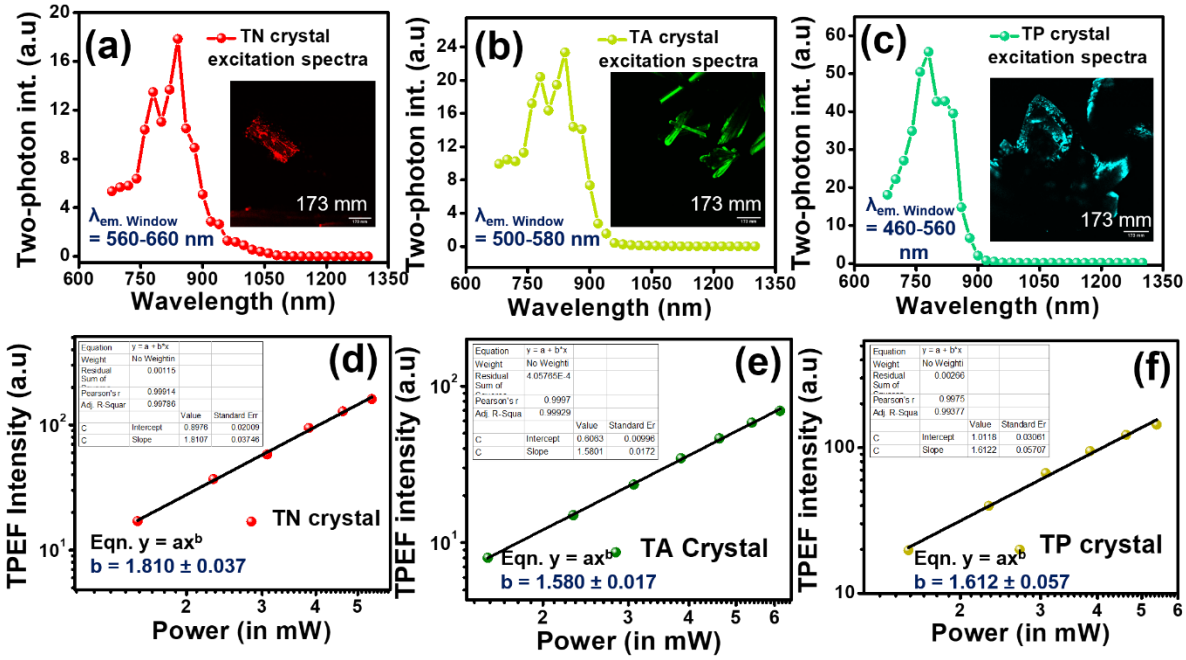

Figure A13: Two-photon excitation spectra for (a) TN (emission range= 560-660 nm), (b) TA (emission range 500-580 nm) and, (c) TP (emission range= 460-560 nm). Excitation power dependent (exc. 845 nm) two-photon excited emission intensity (plotted in log-log scale) for (d) TN, (e) TA and (f) TP.

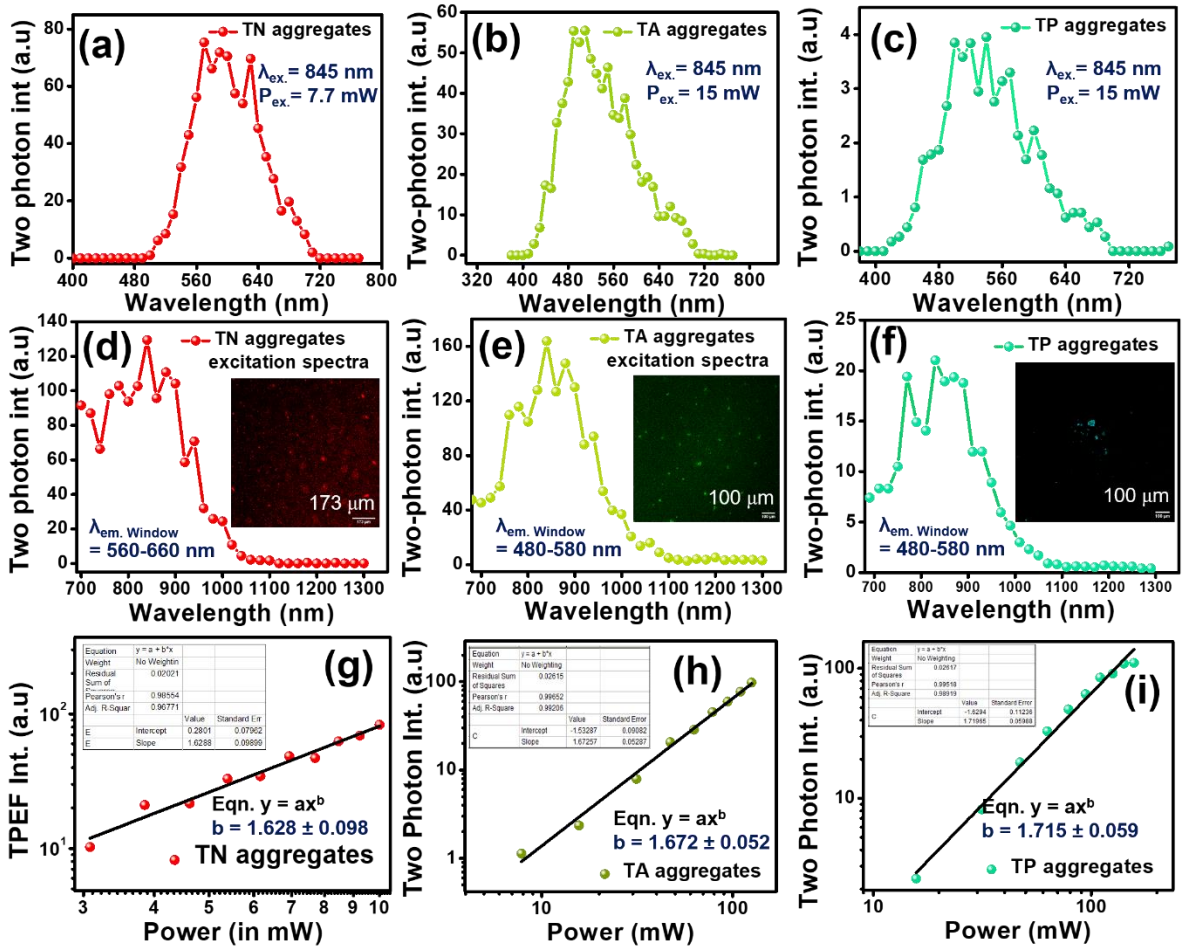

Figure A14: Two-photon excited emission spectra (ex. 845 nm, power= 7.7 mW for TN and 15 mW for TA & TP) of (a) TN, (b) TA, and (c) TP aggregates (formed at 95% water- 5% THF binary mixtures). Two-photon excitation spectra for (d) TN (emission range= 560-660 nm), (e) TA (emission range 480-580 nm), and, (f) TP (emission range= 480-580 nm). Excitation power dependent (ex. 845 nm) two-photon excited emission intensity (plotted in log-log scale) for (g) TN, (h) TA, and (i) TP aggregates.

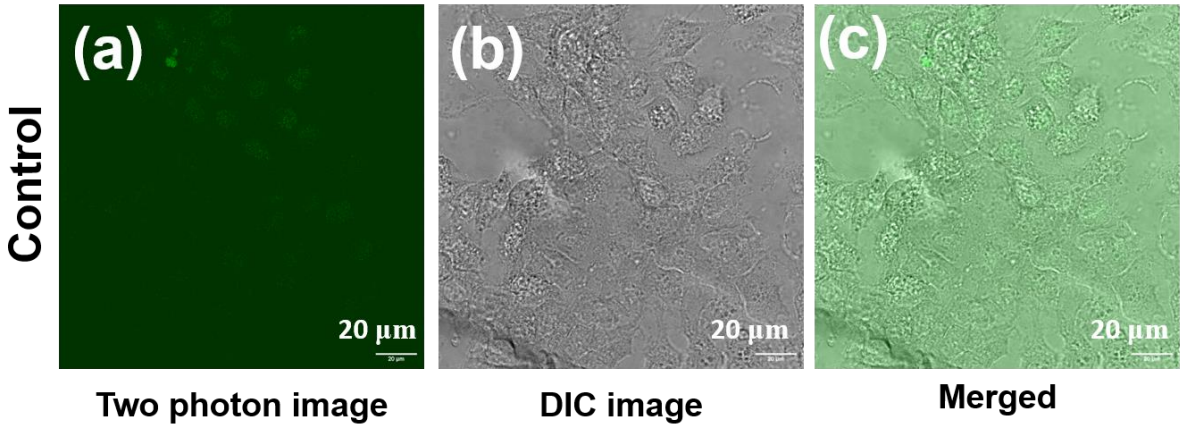

Figure A15: Control experiment for two-photon microscopy imaging of HeLa cells. (a) cells without dye treatment, (b) Differential interference contrast (DIC) image, (c) Merged image of DIC image and cells without dye treatment.

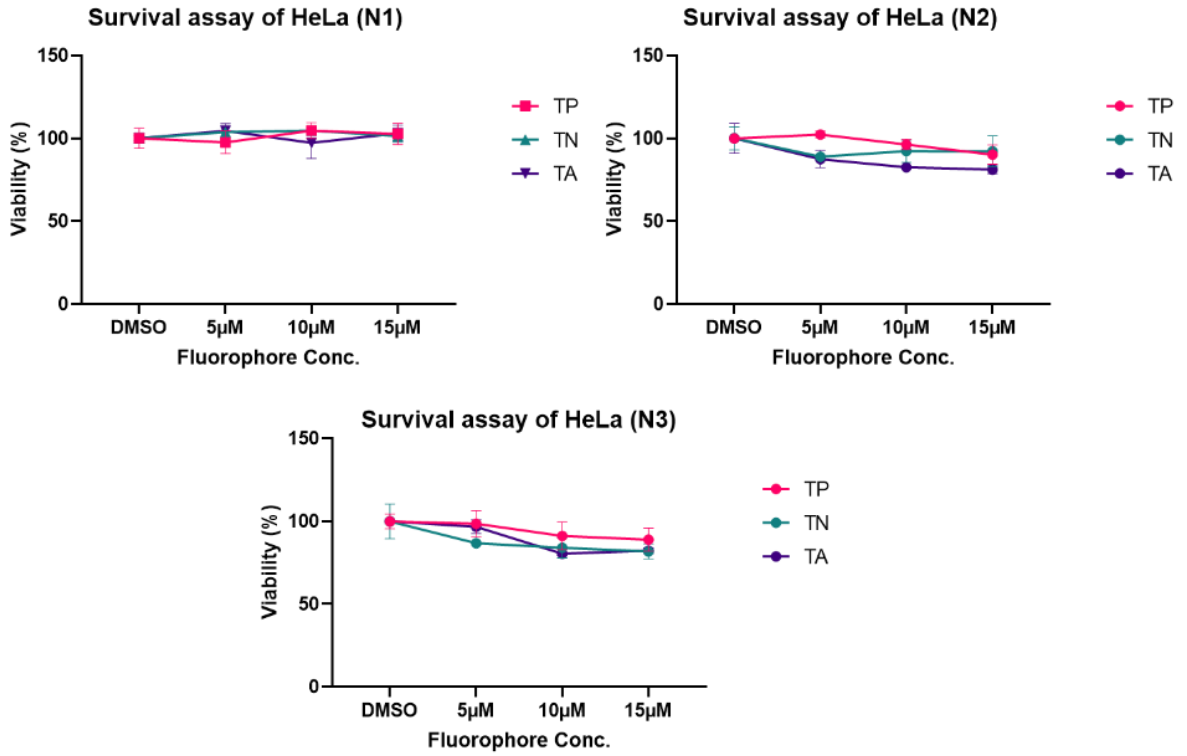

Figure A16: MTT viability assay of HeLa in the presence of different concentrations of dye (TN, TA, and TP) across three biological replicates**.**

4.9 References:

(1) (a) H. Uoyama, K. Goushi, K. Shizu, H. Nomura and C. Adachi, *Nature*, 2012, **492**, 234-238, b) Y. Tao, K. Yuan, T. Chen, P. Xu, H. Li, R. Chen, C. Zheng, L. Zhang and W. Huang, *Adv. Mater*., 2014, **26**, 7931-7958, c) G. Hong, X. Gan, C. Leonhardt, Z. Zhang, J. Seibert, J. M. Busch and S. Bräse, *Adv. Mater.* 2021, **33**, 2005630, d) T.-L. Wu, M.-J. Huang, C.-C. Lin, P.-Y. Huang, T.-Y. Chou, R.-W. Chen-Cheng, H.-W. Lin, R.-S. Liu and C.-H. Cheng. *Nature Photonics*, 2018, **12**, 235-240, e) K. Bergmann, R. Hojo and Z. M. Hudson, *J. Phys. Chem. Lett.*, 2023, **14**, 310-317, f) X.-K. Chen, D. Kim and J.-L. Brédas, *Acc. Chem. Res.*, 2018, **51**, 2215-2224, g) P. Data, P. Pander, M. Okazaki, Y. Takeda, S. Minakata and A. P. Monkman. *Angew. Chem. Int. Ed.*, 2016, **55**, 5739-5744, h) X.-K. Chen, Y. Tsuchiya, Y. Ishikawa, C. Zhong, C. Adachi and J. -L. Brédas, *Adv. Mater.*, 2017, **27**, 1702767.

(2) a) J. Xu, X. Zhu, J. Guo, J. Fan, J. Zeng, S. Chen, Z. Zhao and B. Z. Tang, *ACS Materials Lett*. 2019, **1**, 613−619, b) J. Liu, J. Fan, K. Zhang, Y. Zhang, C.-K. Wang and L. Lin, *Chinese Phys. B.* 2020, **29**, 088504, c) D. Barman and P. K. Iyer, *J. Phys. Chem. C*, 2023, **127**, 2694−2704.

(3) a) J. Luo, Z. Xie, J. W. Y. Lam, L. Cheng, H. Chen, C. Qiu, H. S. Kwok, X. Zhan, Y. Liu, D. Zhuc and B. Z. Tang, *Chem. Commun*., 2001, 1740–1741, b) S. G. R., M. Pandey and A. S. J. Chakravarthy, *Mater. Chem. Front*., 2021, **5**, 1541 1584, c) J. Mei, Y. Hong , J. W. Y. Lam , A. Qin , Y. Tang and B. Z. Tang, *Adv. Mater*. 2014, **26**, 5429–5479, d) P.-A. Yin, Q. Wan, Y. Niu, Q. Peng, Z. Wang, Y. Li, A. Qin, Z. Shuai and B. Z. Tang, *Adv. Electron. Mater*. 2020, **6**, 2000255, e) H. Wang, Q. Gong, G. Wang, J. Dang and F. Liu, *J. Chem. Theory Comput*. 2019, **15**, 5440−5447, f) R. C. -Otero, Q. Li and L. Blancafort. *Chem. Asian J.* 2019, **14**, 700–714.

(4) a) Y. Matsui, Y. Yokoyama, T. Ogaki, K. Ishiharaguchi, A. Niwa, E. Ohta, M. Saigo, K. Miyata, K. Onda, H. Naito and H. Ikeda, *J. Mater. Chem. C*, 2022, **10**, 4607–4613, b) J. Fan, L. Lin and C. -K. Wang, *J. Mater. Chem. C*, 2017, **5**, 8390-8399, c) N. Aizawa, C. -J. Tsou, I. S. Park and T. Yasuda, *Polymer Journal*, 2017, **49**, 197-202, d) B. Zhang, Y. Kong, H. Liu, B. Chen, B. Zhao, Y. Luo, L. Chen, Y. Zhang, D. Han, B. Z. Tang and L. Niu, *Chem. Sci*., 2021, **12**, 13283.

(5) D. Liu, M. Zhang, W. Tian, Y. Sun, Z. Zhao and B. Z. Tang, *Aggregate*, 2022, **3**, e164.

(6) G. Li, J. Pu, Z. Yang, H. Deng, Y. Liu, Z. Mao, J. Zhao, S. -J. Su and Z. Chi. *Aggregate*, 2023, **4**, e382.

(7) R. Furue, T. Nishimoto, I. S. Park, J. Lee and T. Yasuda, *Angew. Chem. Int. Ed*. 2016, **55**, 7171–7175.

(8) S.-L. Lai, Q.-X. Tong, M.-Y. Chan, T.-W. Ng, M.-F. Lo, S.-T. Lee and C.-S. Lee, *J. Mater. Chem*., 2011, **21**, 1206–1211.

(9) (a) Sheldrick, G. M. Acta Crystallogr., Sect. A: Found. Crystallogr. 2008, **64**, 112. (b) Sheldrick, G. M. SHELXL-97, Program for Crystal Structure Solution and Refinement; University of Göttingen: Göttingen, Germany, 1997.

(10) Farrugia, L. J. J. Appl. Crystallogr. 1999, **32**, 837.

(11) Frisch, M. J.; Trucks, G. W.; Schlegel, H. B.; Scuseria, G. E.; Robb, M. A.; Cheeseman, J. R.; Scalmani, G.; Barone, V.; Mennucci, B.; Petersson, G. A.; et al. Gaussian 09, Revision C.01; Gaussian Inc.: Wallingford, CT, 2009.

(12) A. D. Becke, *Phys. Rev. A* 1988, **38**, 3098–3100.

(13) C. Lee, W. Yang, R. G. Parr, *Phys. Rev. B* 1988, **37**, 785–789.

(14) T. Vreven, K. Morokuma, O. Farkas, H. B. Schlegel, M. J. Frisch, *J. Comput. Chem*. 2003, **24**, 760-769.

(15) H. Lin, D. G. Truhlar, *Theor. Chem. Acc*. 2007, **117**, 185-199.

(16) Janiak, C. A Critical Account on π−π Stacking in Metal Complexes with Aromatic Nitrogen-Containing Ligands. J. Chem. Soc. Dalt. Trans. 2000, **21**, 3885−3896.

(17) Gong, Y.; Chen, G.; Peng, Q.; Yuan, W. Z.; Xie, Y.; Li, S.; Zhang, Y.; Tang, B. Z. Achieving Persistent Room Temperature Phosphorescence and Remarkable Mechanochromism from Pure Organic Luminogens. Adv. Mater. 2015, **27**, 6195−6201.

(18) Xie, Z.; Yang, B.; Li, F.; Cheng, G.; Liu, L.; Yang, G.; Xu, H.; Ye, L.; Hanif, M.; Liu, S.; et al. Cross Dipole Stacking in the Crystal of Distyrylbenzene Derivative: The Approach toward High Solid-State Luminescence Efficiency. J. Am. Chem. Soc. 2005, **127**, 14152−14153.

(19) T. J. Penfold, F. B. Dias and A. P. Monkman, *Chem. Commun*., 2018, **54**, 3926-3935.

(20) C. Deibel, Photocurrent Generation in Organic Solar Cells, *Semiconductors and Semimetals*, 2011, **85**, 297-330.

(21) a) Q. Lu, C.-J. Wu, Z. Liu, G. Niu and X. Yu, *Front. Chem*., 2020, **8**, 617463, b) Y. Wang, H. Wu, P. Li, S. Chen, L. O. Jones, M. A. Mosquera, L. Zhang, K. Cai, H. Chen, X.-Y. Chen, C. L. Stern, M. R. Wasielewski, M. A. Ratner, G. C. Schatz and J. F. Stoddart, *Nat. Commun*., 2020, **11**, 4633, c) L. Xu, J. Zhang, L. Yin, X. Long, W. Zhanga and Q. Zhang, *J. Mater. Chem. C*, 2020, **8**, 6342—6349, d) T. Liu, L. Xu, H. Wang, B. Chen and S. Shi, *ACS Appl. Bio Mater*., 2023, **6**, 2849−2859.

(22) a) A. Chatterjee, J. Chatterjee, S. Sappati, T. Sheikh, R. M. Umesh, M. D. Ambhore, M. Lahiri and P. Hazra, *J. Phys. Chem. B*, 2021, **125**, 12832−12846, b) A. Chatterjee, J. Chatterjee, S. Sappati, R. Tanwar, M. D. Ambhore, H. Arfin, R. M. Umesh, M. Lahiri, P. Mandal and P. Hazra, *Chem. Sci*.,2023, **14**, 13832–13841.

Chapter-5

Donor Unit Engineering and Structural Dynamics for Enhanced TADF Performance in Organic Molecular Aggregates

5.1 Motivation

Thermally activated delayed fluorescent (TADF) emitters have emerged as a promising class of materials for organic light-emitting diodes (OLEDs), representing the third generation of OLED materials. Their ability to harvest triplet excitons through reverse intersystem crossing (RISC) has enabled significant advancements in device efficiency. However, the widespread application of conventional TADF emitters in solid-state lighting is hindered by their inherent near-planar molecular structures, which often lead to enhanced electron-vibration coupling (EVC) and aggregation-caused quenching (ACQ) effects. These limitations significantly compromise their emission efficiencies in solid-state environments. A potential solution to these challenges lies in the synergistic integration of TADF with the principles of aggregation-induced emission (AIE). Unlike conventional systems, AIE-active materials exhibit enhanced emission in the aggregated state, effectively counteracting ACQ effects. The incorporation of AIE properties into TADF emitters offers a novel strategy to mitigate EVC and optimize emission performance in the solid state. This chapter focuses on exploring this innovative approach, investigating the design and performance of such materials with increased TADF efficiency in a solid/aggregated state. Furthermore, the study highlights the critical role of excited-state structural reorganization in dictating these properties, providing deeper insights into the photophysical processes governing these materials. By addressing these challenges, this research aims to open new avenues for the development of high-efficiency solid-state photonic devices, contributing to the advancement of next-generation OLED technologies.

5.2 Introduction

Lighting accounts for approximately 20% of global electricity consumption, with much of this demand being met by inefficient incandescent and fluorescent bulbs. The advent of solid-state lighting (SSL) technologies, particularly organic light-emitting diodes (OLEDs), has ushered in a new era of energy-efficient and environmentally friendly lighting solutions.[1-6] OLEDs are self-illuminating, consume less power, are resistant to vibrations, and offer versatile design possibilities, including flexible substrates. Despite these advantages, early OLEDs based on fluorescent molecules were hindered by significant limitations such as inefficient charge injection and low internal quantum efficiency (IQE).[7-8] The IQE of these devices was restricted to around 25%, as only singlet excitons contributed to light emission while triplet excitons decayed non-radiatively. Efforts to overcome these limitations led to the development of triplet-triplet annihilation (TTA) strategies, which marginally improved IQE to 62.5%.[9-11] However, the intrinsic shortcomings of fluorescent OLEDs necessitated alternative

approaches. Phosphorescent OLEDs (PHOLEDs), employing organometallic compounds, emerged as a significant advancement, achieving up to 100% IQE by harvesting both singlet and triplet excitons.[12-13] Nevertheless, PHOLEDs are not without challenges, including high costs and efficiency roll-off at high brightness levels. Recently, thermally activated delayed fluorescence (TADF) materials have garnered attention as a promising solution to these issues.[14-18] Metal-free TADF materials utilize a small energy gap (ΔE_{ST}) between singlet and triplet states to efficiently harvest triplet excitons via reverse intersystem crossing (RISC).[19-23] This mechanism enables delayed fluorescence, addressing many limitations of earlier OLED technologies. However, the planar molecular structures of conventional TADF emitters often result in enhanced electron-vibration coupling (EVC) upon aggregation, which limits their applicability in solid-state lighting applications, such as non-doped OLEDs and organic solid-state lasing (OSSLs).[24] The aggregation-induced emission (AIE) strategy[25-30] has emerged as a leading method to improve TADF efficiency in solid or aggregated states. Scientists worldwide have proposed various design strategies to combine AIE with TADF emitters. Notable advancements include the work of Prof. Ikeda and co-workers, who in 2022 synthesized two novel TADF emitters—2Cz2SB and 2Mi2SB—featuring N-heterocycle and aryl sulfonyl groups with enhanced TADF efficiency in aggregated states. TR-IR analysis of SO-stretching vibrations revealed that the magnitude of geometrical changes in the solid state of 2Cz2SB is suppressed, demonstrating that this substance displays AIE behavior.[31] Moreover, Yoon and co-workers designed three red-emissive TADF emitters with aggregation-induced emission (AIE) behavior-PXZ-NI, PTZ-NI, and Lyso-PXZ-NI. All these emitters were utilized in efficient luminescence lifetime imaging (LLIM), where Lyso-PXZ-NI was specifically able to be used as a lyso-tracker.[32] Building on this foundation, our group recently reported three triphenylamine-based solid-state TADF emitters (TN, TA, and TP) and demonstrated how delayed fluorescence is activated in aggregated states due to a substantial reduction in ΔE_{ST}. A detailed potential energy surface (PES) analysis highlighted the importance of structural factors in solid-state TADF efficiency.[33] However, the conventional focus on ΔE_{ST} alone is insufficient; a more comprehensive investigation into other factors influencing TADF efficiency is needed.

In this study, we explore the critical role of excited-state structural reorganization along with the spin-orbit mixing and energy barrier factors in enhancing delayed fluorescence in solid or aggregated states. We designed and synthesized a novel series of TADF emitters incorporating phenoxazine, carbazole, tert-butyl carbazole, and benzocarbazole as donor units anchored to a

1,3-dicyano benzene acceptor core (**Scheme 1**). Among these, the phenoxazine-based emitter exhibited remarkable TADF efficiency with yellow-orange emission, a rapid RISC rate of approximately in the order of ~10^5-10^6 s^{-1}, and an exceptionally small ΔE (<100 meV). In contrast, carbazole-based emitters displayed cyan-green emission, longer TADF lifetimes, and slower RISC rates due to reduced donor strength. All luminogens demonstrated enhanced delayed fluorescence, with dramatically enhanced quantum yields in aggregated forms or neat films. Computational analyses revealed that the enhanced delayed fluorescence in aggregated/solid-state stemmed from excited-state structural reorganization along with S_1-T_1 energy barrier and spin-orbit coupling mixing between these singlet and triplet excited states. Furthermore, solution-processed OLED devices incorporating these emitters achieved external quantum efficiencies (EQE) exceeding 20%. These findings provide significant insights into optimizing high-efficiency TADF emitters in solid-state for next-generation optoelectronic devices, paving the way for more efficient, sustainable, and versatile lighting technologies.

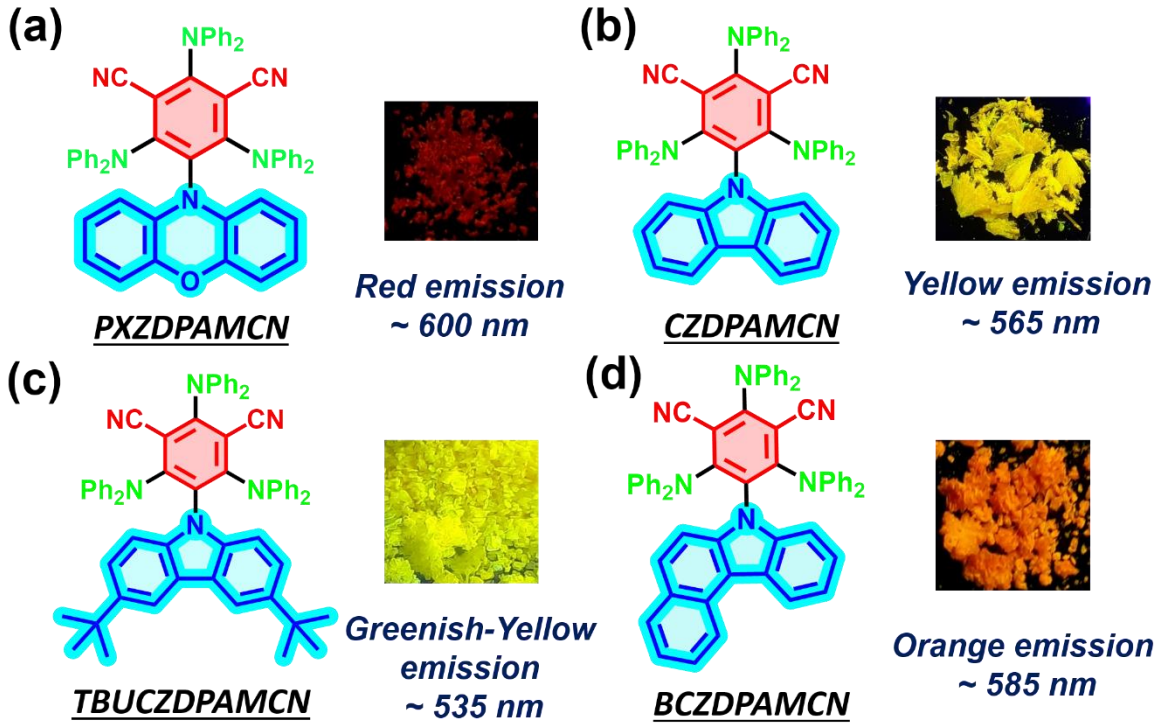

Scheme 1: Molecular structures of all four luminogens- a) PXZDPAMCN, b) CZDPAMCN, c) TBUCZDPAMCN, d) BCZDPAMCN and their UV irradiated crystals.

5.3 Brief synthesis procedure and characterization data

All final products were synthesized using a two-step synthetic procedure. First, 3DPAFMCN (**Scheme S1 in the Appendix**) was synthesized through a nucleophilic substitution reaction in

dry THF, using NaH as a base and stirring at room temperature. 3DPAFMCN serves as the common precursor for the four final products: PXZDPAMCN, CZDPAMCN, TBUCZDPAMCN, and BCZDPAMCN. These products were synthesized by reacting 3DPAFMCN with phenoxazine, carbazole, tert-butyl carbazole, and benzocarbazole, respectively (**detailed procedure in section A1 of Appendix**). All the final products have been purified by SiO_2-column chromatography using DCM-hexane as the solvent system. The products have been characterized by ^{1}H NMR, ^{13}C NMR, HRMS and single-crystal X-ray diffraction. The purity of each compound has been further confirmed by HPLC. The characterization data has been stated below-

(a) For PXZDPAMCN:

^{1}H NMR (400 MHz, $CDCl_3$): δ 7.33 (dd, *J* = 8.5, 7.5 Hz, 4H), 7.15 (dd, *J* = 8.5, 1.0 Hz, 4H), 7.08 (dd, *J* = 11.6, 4.2 Hz, 3H), 6.99 (t, *J* = 7.9 Hz, 7H), 6.85 (t, *J* = 7.4 Hz, 4H), 6.71 (d, *J* = 7.7 Hz, 8H), 6.42 (dd, *J* = 5.8, 3.6 Hz, 4H), 6.18 – 6.09 (m, 2H), 6.03 (dd, *J* = 6.0, 3.4 Hz, 2H).
^{13}C NMR (101 MHz, $CDCl_3$): δ 155.01, 154.78, 145.82, 145.22, 143.00, 129.54, 129.20, 128.42, 124.88, 124.61, 123.57, 123.40, 122.22, 121.58, 115.22, 113.47, 113.03, 106.51.
HRMS (ESI): calc. for [($C_{56}H_{38}N_6O$) H] $(M+H)^+$ 811.3185, found 811.3138.

(b) For CZDPAMCN:

^{1}H NMR (400 MHz, $CDCl_3$): δ 7.53 (d, *J* = 7.3 Hz, 2H), 7.36 (dd, *J* = 8.4, 7.5 Hz, 4H), 7.19 (dd, *J* = 8.5, 1.0 Hz, 4H), 7.10 (dd, *J* = 10.6, 4.2 Hz, 2H), 7.07 – 7.02 (m, 2H), 6.96 (dd, *J* = 11.1, 3.7 Hz, 2H), 6.92 (d, *J* = 8.1 Hz, 2H), 6.76 (t, *J* = 7.9 Hz, 8H), 6.61 (t, *J* = 7.4 Hz, 4H), 6.46 (d, *J* = 7.6 Hz, 8H).
^{13}C NMR (101 MHz, $CDCl_3$): δ 155.27, 155.10, 145.80, 144.85, 138.63, 129.59, 128.74, 127.04, 124.64, 124.11, 123.57, 123.54, 122.45, 122.16, 119.67, 113.40, 109.87, 107.46.
HRMS (ESI): calc. for [($C_{56}H_{38}N_6$) H] $(M+H)^+$ 795.3236, found 795.3243.

(c) For TBUCZDPAMCN:

^{1}H NMR (400 MHz, $CDCl_3$): δ 7.49 (s, 2H), 7.35 (t, *J* = 7.9 Hz, 4H), 7.19 (d, *J* = 7.5 Hz, 4H), 7.13 – 7.04 (m, 4H), 6.75 (t, *J* = 7.9 Hz, 10H), 6.59 (t, *J* = 7.4 Hz, 4H), 6.46 (d, *J* = 7.5 Hz, 8H), 1.34 (s, 18H).

^{13}C NMR (101 MHz, $CDCl_3$): δ 155.27, 155.09, 145.80, 145.03, 143.01, 137.04, 129.55, 128.66, 124.53, 124.00, 123.55, 123.45, 122.64, 122.03, 115.67, 108.97, 34.67, 32.17.

(d) For BCZDPAMCN:

^{1}H NMR (400 MHz, $CDCl_3$): δ 8.40 (d, *J* = 8.3 Hz, 1H), 8.09 – 7.99 (m, 1H), 7.83 (d, *J* = 8.0 Hz, 1H), 7.58 (t, *J* = 7.2 Hz, 1H), 7.52 (d, *J* = 8.8 Hz, 1H), 7.39 (dd, *J* = 14.8, 6.7 Hz, 5H), 7.22 (d, *J* = 7.7 Hz, 4H), 7.11 (ddd, *J* = 8.8, 7.3, 3.5 Hz, 5H), 7.06 – 7.01 (m, 1H), 6.71 (t, *J* = 7.8 Hz, 8H), 6.52 (t, *J* = 7.3 Hz, 4H), 6.44 (d, *J* = 7.8 Hz, 8H).

^{13}C NMR (101 MHz, $CDCl_3$): δ 155.47, 155.27, 145.79, 144.74, 137.79, 136.86, 129.62, 128.97, 128.73, 126.51, 125.98, 124.76, 124.16, 123.61, 123.37, 122.94, 122.44, 121.59, 120.69, 116.24, 113.38, 111.69, 110.35, 107.41.

5.4 Instrumentation

The characterization of all synthesized compounds was performed using ^{1}H NMR (400 MHz) and ^{13}C NMR (100 MHz) with JEOL ECS-400 and Bruker Ascend™ 400 spectrometers. Deuterated chloroform ($CDCl_3$) served as the solvent (containing residual chloroform), and tetramethylsilane (TMS) was used as the internal standard. The chemical shift values (δ) were reported in ppm, referenced to $CDCl_3$ (δ = 7.26 ppm for ^{1}H NMR and δ = 77.16 ppm for ^{13}C NMR). High-resolution mass spectra (HRMS) were obtained using an ESI TOF system on a Waters SYNAPT G2 mass spectrometer. Single-crystal diffraction data were collected at 100 K using a BRUKER KAPPA APEX II CCD Duo diffractometer (operating at 50 kV, 30 mA, 1500 W) with graphite-monochromated Mo-Kα radiation (λ = 0.71073 Å). Structural analysis was conducted using direct methods and refined via least squares against F2 using the SHELXL-97[34-35] software suite. Details of crystal structures are available in the Cambridge Crystallographic Data Centre (CCDC) under the respective deposition numbers. UV-vis absorption spectra were recorded using a Shimadzu UV-2600 spectrophotometer, while steady-state and time-gated emission spectra for solution and solid-state samples were measured using a Fluoromax-4C spectrofluorometer and a Fluorolog-3 phosphorimeter (HORIBA), respectively. All photoluminescence quantum yield (PLQY) values reported in this chapter were determined through absolute quantum yield measurements using a Horiba K-sphere integrating sphere. Time-resolved photoluminescence (PL) decay profiles were obtained employing Time-Correlated Single Photon Counting (TCSPC) and Multi-Channel Scanning (MCS) techniques. Measurements utilized either a 375 nm diode laser source for time windows shorter than 50 μs or a 357 nm spectra LED source, both on a HORIBA Scientific instrument. Data analysis was conducted using DAS6 Fluorescence Decay Analysis Software (HORIBA), with the quality of fit assessed through χ^2-values and visual inspection of residuals.

5.5 Experimental section

Fabrication of Emitter-Doped PMMA Films:

PMMA was dissolved in spectroscopic-grade chloroform at 50°C with stirring for 10 minutes, followed by sonication for 5 minutes. Emitters were added to the PMMA solution, and 0.2 ml of the mixture was spin-coated onto quartz plates at 2000 rpm for 30 seconds. The coated plates were dried under a high vacuum for 20 minutes before photophysical measurements.

Density Functional Theory (DFT) Calculations:

Quantum chemical computations were performed using Gaussian 09 software[36] on a high-performance cluster at IISER Pune. Initial geometry optimizations of luminogens were conducted in the gas phase, followed by frequency analyses[37-38] at the B3LYP/6-31 G(d,p) level to confirm minima on the potential energy surface. Time-dependent DFT (TD-DFT) calculations were performed to examine HOMO-LUMO distributions and singlet/triplet state energies.

Spin-orbit coupling matrix element calculation:

SOC values between excited singlet and triplet states were calculated using the zeroth-order regular approximation (ZORA). In this approximation, the SOC operator, $\widehat{H}_{SOC,}$ is described as[39]

$$\widehat{H}_{SOC} = \frac{c^2}{(2c^2 - v)^2}\sigma \cdot (\nabla v \times p)$$

Where c, v, σ, and p signify the speed of light, Kohn-Sham potential, Pauli spin-matrix vector, and linear momentum operator respectively. Perturbations were applied to scalar relativistic orbitals post-SCF and TD-DFT calculations. B3LYP functional was employed, and the computations were conducted using the PYSOC program.[40]

QM/MM Calculations:

The quantum mechanics/molecular mechanics (QM/MM) model was constructed based on the single-crystal structure to investigate the electronic properties of the QM molecule in the aggregated crystal state. The surrounding molecules were treated as a rigid MM component to mimic the solid-state environment. The QM region was analyzed using the TD-DFT method at

the B3LYP/6-31G(d,p) level, while the MM region[41] was described using the universal force field (UFF),[42] supplemented by Coulomb interactions consistent with the quantum calculations. Additionally, the monomer was set as the QM high layer and computed using TD-DFT with the B3LYP/6-31G(d,p) level.

Preparation of Neat Films:

Neat films were prepared by dissolving 0.5 mg of each luminogen in 1 ml of spectroscopic-grade THF. The resulting solution was drop-cast onto a clean quartz substrate and subsequently dried under reduced pressure for a minimum of one hour to ensure the removal of residual solvent from the film layer.

5.6 Results and Discussion

5.6.1 Design strategy and frontier molecular orbital analysis:

All four emitters discussed in this chapter are designed to exhibit aggregation-induced emission (AIE) by restricting intermolecular rotations and vibrations in the solid or aggregated state compared to their behavior in solution. A 1,3-dicyanobenzene core serves as the acceptor, with three of its positions on the benzene ring substituted with flexible diphenylamine moieties (**Scheme 1**). Noticeably, the flexibility of these diphenylamine units allows for significant rotation and vibration in solution, which becomes restricted upon aggregation, resulting in AIE characteristics. The remaining position on the benzene core is modified with donor groups of varying strengths—phenoxazine, carbazole, tert-butyl carbazole, and benzocarbazole—yielding the final products PXZDPAMCN, CZDPAMCN, TBUCZDPAMCN, and BCZDPAMCN, respectively.

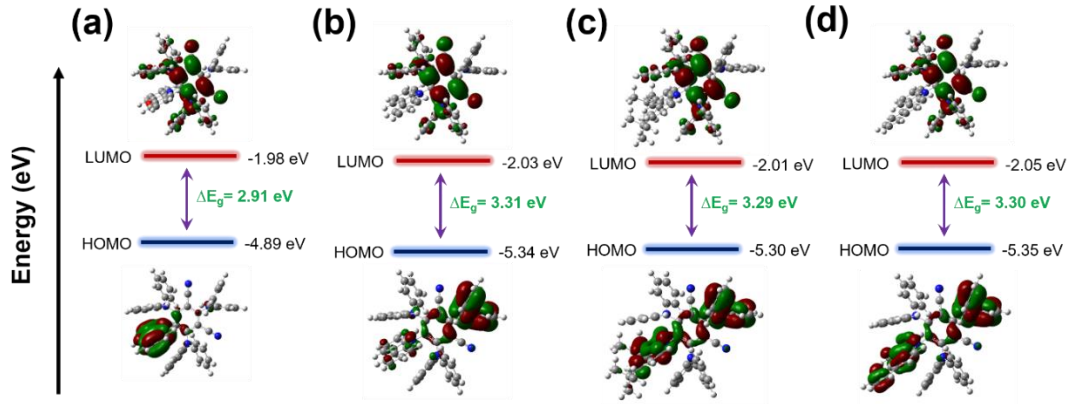

Figure 1: HOMO and LUMO molecular orbitals along with the energy gaps in (a) PXZDPAMCN, (b) CZDPAMCN, (c) TBUCZDPAMCN, (d) BCZDPAMCN.

From the frontier molecular orbital analysis (**Figure 1**), it is evident that in PXZDPAMCN, the highest occupied molecular orbital (HOMO) is exclusively localized on the phenoxazine moiety, whereas in the other cases, the HOMO electron density is predominantly distributed over the diphenylamine moiety situated between the two cyano groups. Additionally, phenoxazine exhibits the strongest donor strength, as evidenced by the highest HOMO energy level observed in PXZDPAMCN compared to the other three compounds. In all four emitters, the lowest unoccupied molecular orbital (LUMO) is predominantly localized on the 1,3-dicyanobenzene core, resulting in relatively consistent LUMO energy levels across the series (**Figure 1**). Consequently, PXZDPAMCN exhibits the smallest HOMO-LUMO energy gap, which could potentially contribute to altered emission properties compared to the other compounds.

5.6.2 Photophysics in solution state and doped films:

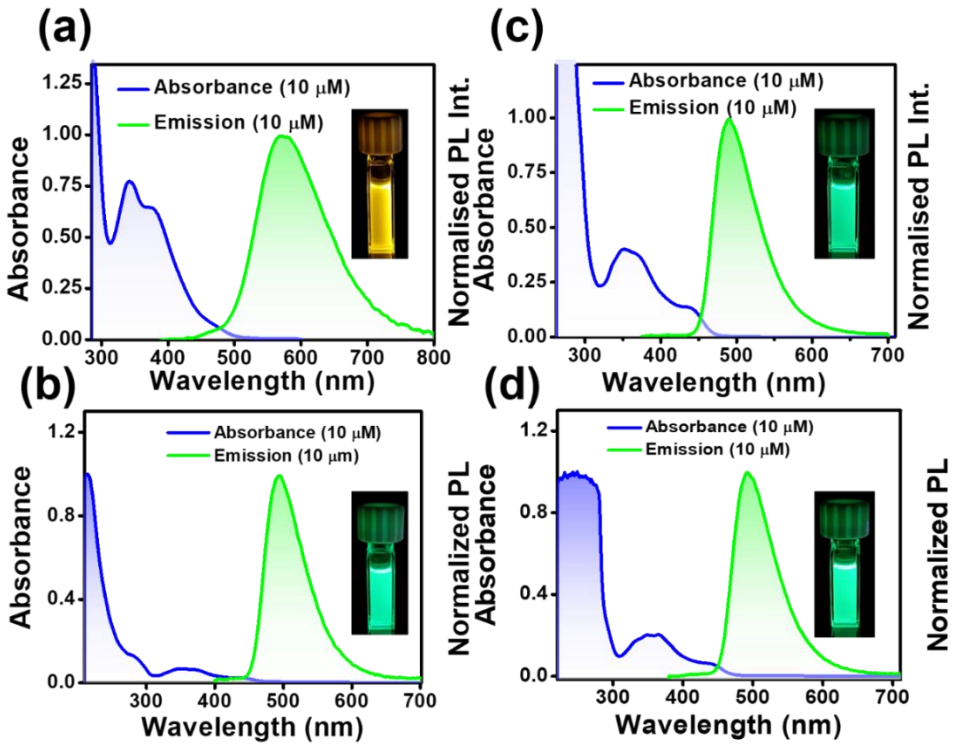

Figure 2: Absorption and emission spectra in toluene (10 μM) along with the emission shown in cuvette.

In toluene, all the emitters demonstrate two absorption bands: a high-energy (HE) locally excited band and a low-energy (LE) charge transfer (CT) band, which is characteristic of the

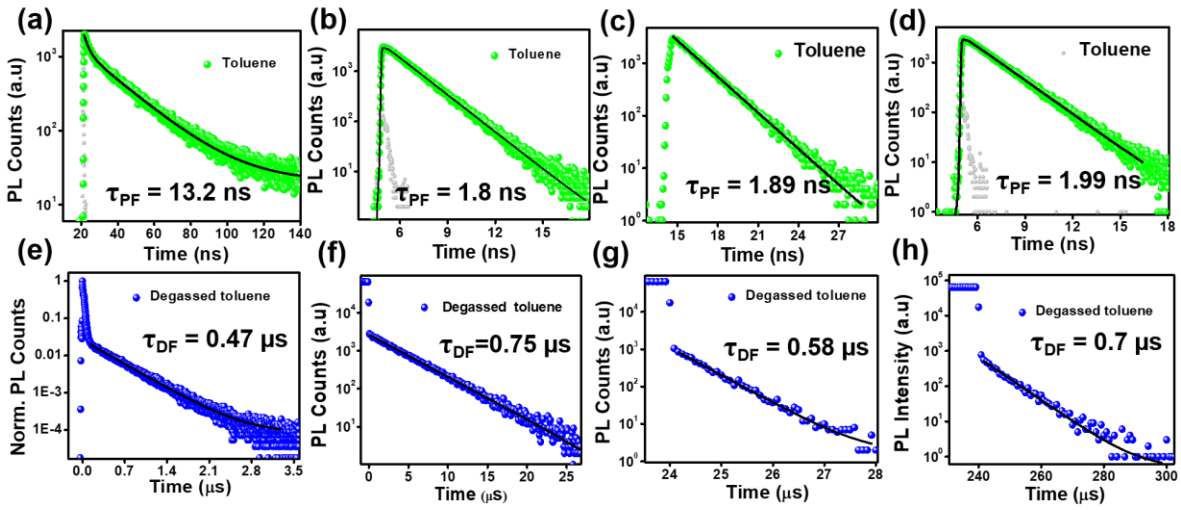

Figure 3: Prompt fluorescence (PF) and delayed fluorescence (DF) lifetimes in degassed toluene (10 µM) of (a) PXZDPAMCN, (b) CZDPAMCN, (c) TBUCZDPAMCN and (d) BCZDPAMCN.

donor-acceptor (D-A) nature of the emitters. In all cases, the HE band is observed in the 310-400 nm range, while the LE band appears above 400 nm. Notably, with the exception of PXZDPAMCN, the low-energy CT band is located around 440 nm. This is due to the similar donor strengths of the other emitters, resulting in comparable levels of charge transfer. In contrast, for PXZDPAMCN, the CT band is more stabilized and is found at approximately 470 nm (**Figure 2**). This stabilization is attributed to the more effective charge transfer resulting from phenoxazine's greater donating strength, as mentioned earlier. This trend extends to the emission properties of the emitters. All emitters, except PXZDPAMCN, emit cyan-green light (~500 nm) in toluene, whereas PXZDPAMCN exhibits a red-shifted yellow emission (~575 nm) (**Figure 2**), reflecting the enhanced CT character of its S_1 state. The higher CT nature of the excited state in PXZDPAMCN results in a forbidden emission with a lower radiative decay rate. This is consistent with the prompt fluorescence (PF) lifetimes where PXZDPAMCN shows a significantly longer lifetime (τ_{av} = 13.2 ns) compared to the other emitters (τ_{av} = 2 ns) (**Figure 3**). Computational analyses across gas, solvent (THF as a model), and crystal phases further corroborate these findings, revealing that PXZDPAMCN has the lowest emission transition dipole moments (TDM), contributing to its delayed emission and extended PF lifetime (**Table 1**).

Table 1: Transition dipole moment (TDM) of all four emitters across different phases-

Molecule	Gas phase (in debye)	Solvent phase (THF) (in debye)	Crystal phase (in debye)
PXZDPAMCN	0.368 D	0.596 D	0.277 D
CZDPAMCN	0.524 D	1.97 D	1.17 D
TBUCZDPAMCN	0.492 D	2.09 D	1.07 D
BCZDPAMCN	0.980 D	1.95 D	1.10 D

All four emitters, alongside the short ~ns component, exhibit a long sub-µs component in degassed toluene (**Figure 3**), indicating a forbidden spin-flip mechanism in the emission process. To determine the origin of these long-lived emissions, we performed time-gated emission spectra measurements. Remarkably, in all cases, the steady-state and time-gated (5 µs delayed) emission spectra show perfect overlap (**Figure 4**). This suggests that the delayed emission originates from the S_1 state, indicating the presence of thermally activated delayed fluorescence (TADF). A degassing experiment with toluene using N_2 and O_2 was conducted to quantify the delayed fluorescence quantum yield (**Figure 4**). It is important to note that in the presence of molecular oxygen, the emission is quenched due to effective triplet-triplet energy transfer that suppresses the triplet excitons, allowing only the prompt fluorescence emission to persist. From the toluene degassing experiment and absolute PLQY measurements, the results indicate that the maximum contribution of delayed fluorescence (DF), which is about three times that of the prompt fluorescence (PF), is observed in PXZDPAMCN, featuring a reverse intersystem crossing (RISC) rate of approximately 7.1×10^6 s^{-1}, the highest among the four emitters studied (**Table A3 in Appendix**). To examine whether the same trend exists in real OLED applications, we conducted photophysical characterizations on emitter-doped films with PMMA as the host. PMMA is

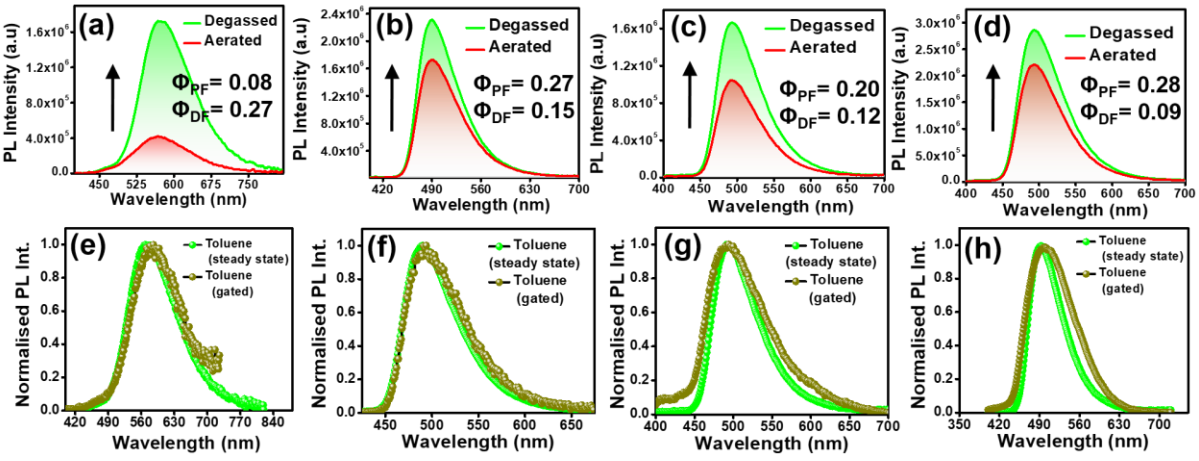

Figure 4: Emission spectra in degassed (N_2) and aerated (O_2) conditions in toluene of (a)

PXZDPAMCN, (b) CZDPAMCN, (c) TBUCZDPAMCN and (d) BCZDPAMCN. Steady-state and time-gated emission spectra of (e) PXZDPAMCN, (f) CZDPAMCN, (g) TBUCZDPAMCN, and (h) BCZDPAMCN. For time-gating 5 µs delay and 1 ms sample-window is applied.

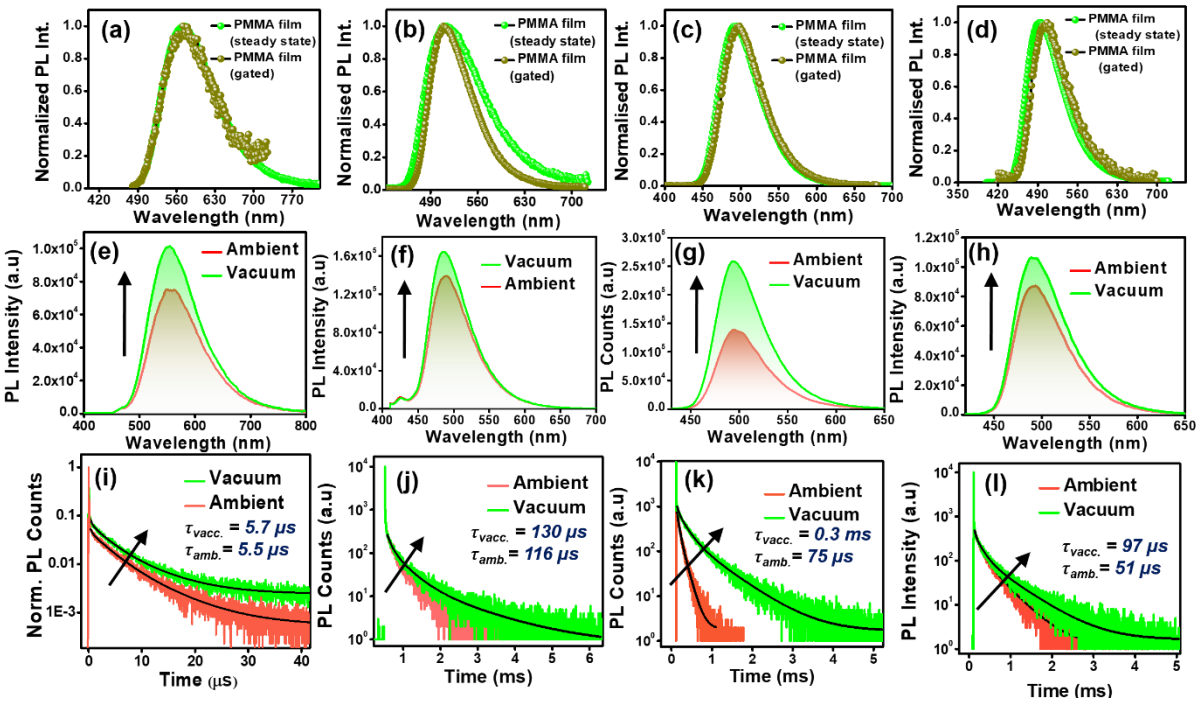

Figure 5: Steady-state and time-gated emission spectra (10 µs delay, 1 ms window) in 1wt% emitter doped PMMA films of (a) PXZDPAMCN, (b) CZDPAMCN, (c) TBUCZDPAMCN, and (d) BCZDPAMCN. Steady-state emission spectra in ambient and vacuum conditions in 1wt% emitter doped PMMA films of (e) PXZDPAMCN, (f) CZDPAMCN, (g) TBUCZDPAMCN, and (h) BCZDPAMCN. Variation of delayed fluorescence lifetime in 1wt% emitter doped PMMA films of (i) PXZDPAMCN, (j) CZDPAMCN, (k) TBUCZDPAMCN, and (l) BCZDPAMCN.

notable for providing a high triplet energy of approximately 3.1 eV, which prevents back-energy transfer from the emitter to the host. It also creates a rigid matrix environment that reduces non-radiative deactivation pathways, thereby improving the emission efficiency of flexible D-A-based TADF emitters. In the case of 1 wt% emitter-doped PMMA films, the steady-state and time-gated emission spectra are perfectly overlapped, indicating that TADF emission is involved. Among the emitters studied, PXZDPAMCN shows the shortest delayed fluorescence (DF) lifetime of 5.5 µs under ambient conditions, compared to 116 µs for CZDPAMC, 75 µs for TBUCZDPAMCN, and 51 µs for BCZDPAMCN (**Figure 5**). PXZDPAMCN also exhibits a maximum reverse intersystem crossing (RISC) rate of

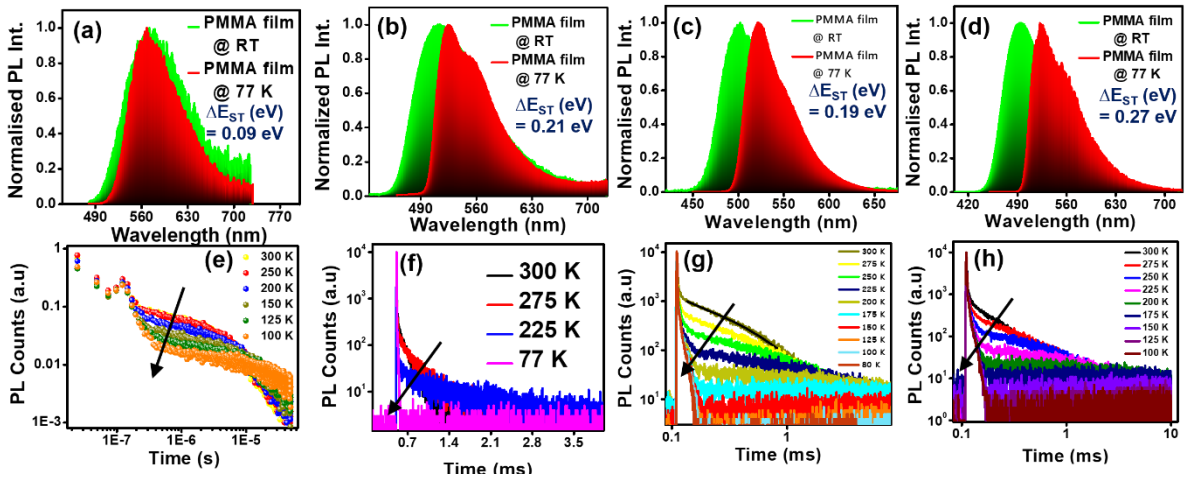

Figure 6: Time-gated emission spectra (10 μs delay, 1 ms window for RT & 5 ms delay, 100 ms window for 77 K) in 1wt% emitter doped PMMA films of (a) PXZDPAMCN, (b) CZDPAMCN, (c) TBUCZDPAMCN, and (d) BCZDPAMCN. Temperature-dependent TRPL decay profiles in 1wt% emitter doped PMMA films of (e) PXZDPAMCN, (f) CZDPAMCN, (g) TBUCZDPAMCN, and (h) BCZDPAMCN.

approximately 2×10^5 s^{-1} (**Table A3 in Appendix**). Interestingly, the same S_1-radiative decay rate is observed, with PXZDPAMCN demonstrating the longest photoluminescence (PL) lifetime of 7.71 ns due to the maximum charge transfer character of the S_1 state (**Figure A3 in Appendix**). The doped films demonstrate an increased emission intensity and a delayed fluorescence lifetime under vacuum conditions, indicating the involvement of sensitive triplet excitons in the emission process (**Figure 5**). It is important to note that thermally activated delayed fluorescence (TADF) typically requires a higher temperature to become active. At cryogenic temperatures, TADF emission is less likely to occur, and instead, the emission is observed as triplet (phosphorescent) emission. A temperature-dependent time-resolved photoluminescence (TRPL) experiment shows a decrease in delayed fluorescence lifetime as the temperature decreases in all four cases (**Figure 6**), supporting the conclusion that the emission mechanism is indeed a thermally activated delayed fluorescence or TADF process. Additionally, the time-gated emission spectra confirm this observation; at 77 K, all the emission spectra exhibit a redshift accompanied by weakened or diminished TADF emission. From the emission spectra recorded at both room temperature (RT) and 77 K, the singlet-triplet energy gap (ΔE_{ST}) can be experimentally estimated. Notably, the red shift in PXZDPAMCN is the smallest, with an ΔE_{ST} value of only 0.09 eV, which may explain the efficient reverse intersystem crossing (RISC) observed in this case. In contrast, the estimated ΔE_{ST} values in the other compounds are relatively higher, at 0.21 eV, 0.19 eV, and 0.27 eV for

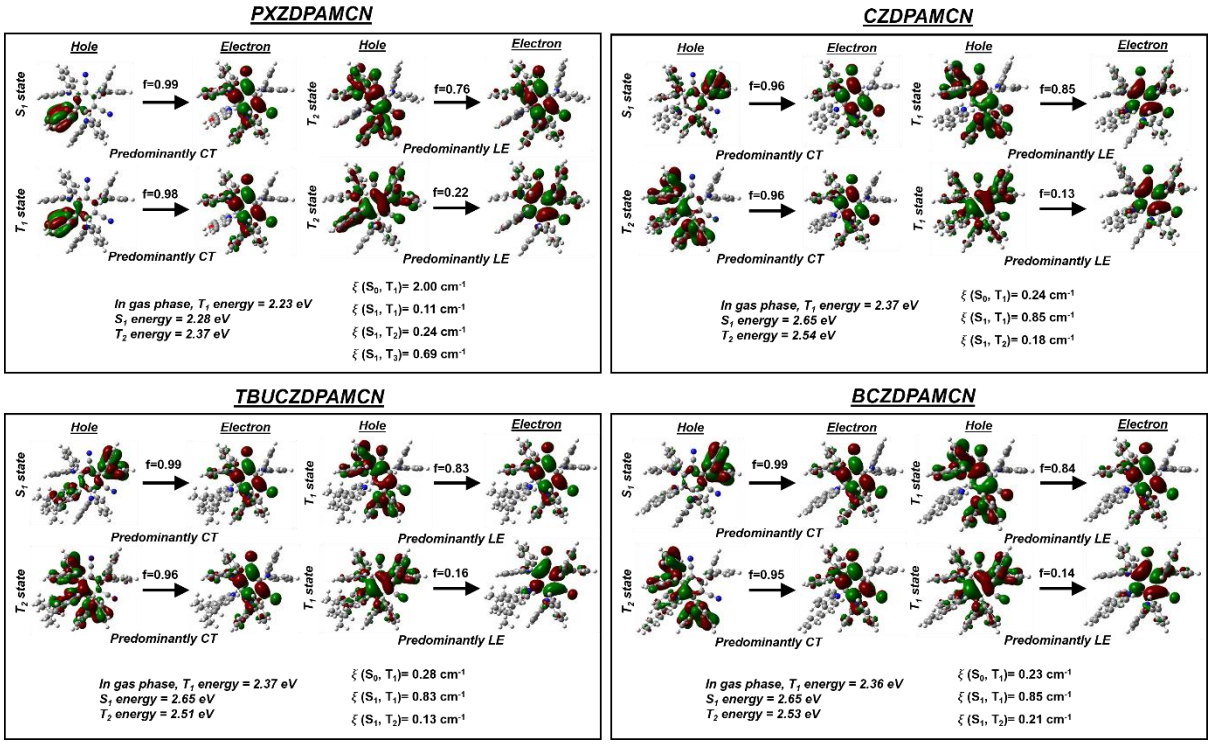

Figure 7: Natural transition orbital (NTO) analysis, energies, and spin-orbit coupling calculations of S_1, T_1 & T_2 states of all four emitters.

CZDPAMN, TBUCZDPAMCN, and BCZDPAMCN, respectively (**Figure 6**). Noticeably, the triplet emission band of PXZDPAMCN is noticeably broad and unstructured, while the triplet emission bands of the other three compounds exhibit a more structured form with vibrational progression (**Figure 6**). This suggests that the lowest T_1 state of PXZDPAMCN is predominantly of charge-transfer (CT) nature, whereas the T_1 states of the other compounds are likely to be locally excited (LE) in nature. This conclusion was supported by a gas phase time-dependent density functional theory (TD-DFT) calculation performed at the B3LYP/6-31G (d, p) level of theory. The single-point TD-DFT calculations at the ground-state optimised geometry in the gas phase closely align with the experimental results; for PXZDPAMCN, the theoretically obtained ΔE_{ST} was found to be 0.05 eV, compared to the experimentally measured value of 0.09 eV. For the other three compounds, the calculated ΔE_{ST} values were approximately 0.27 eV, which are also in close agreement with the experimental values mentioned earlier (**Figure 7**). Consequently, all additional necessary calculations were conducted at this level of theory. We conducted a natural transition orbital (NTO) analysis to predict the characteristics of the excited states, which is crucial for understanding the efficiency of thermally activated delayed fluorescence (TADF) in relation to spin-orbit mixing and

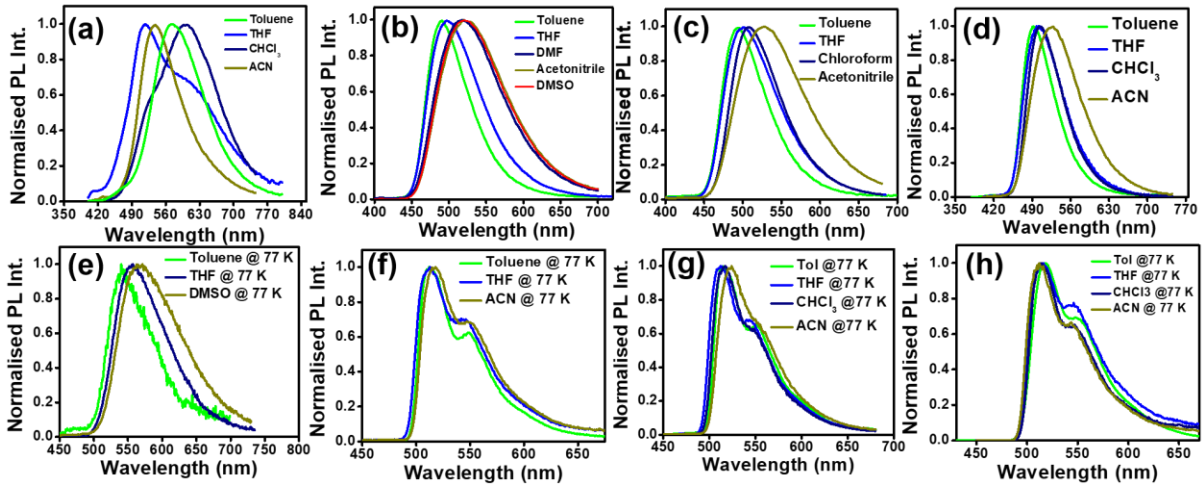

Figure 8: Polarity-dependent emission studies in different solvents at RT of (a) PXZDPAMCN, (b) CZDPAMCN, (c) TBUCZDPAMCN, and (d) BCZDPAMCN. Polarity-dependent phosphorescence emission studies in different solvents at RT of (e) PXZDPAMCN, (f) CZDPAMCN, (g) TBUCZDPAMCN, and (h) BCZDPAMCN. Phosphorescence emission was obtained using 5 ms of delay time with a sample window of 100 ms.

reverse intersystem crossing (RISC) rates. In all three cases analyzed, the NTO analysis shows that the S_1 state is predominantly charge transfer (CT), with the contributing hole-electron pairs demonstrating complete spatial separation (**Figure 7**). This finding is further supported by solvatochromic emission studies in solution, which consider solvents with a wide range of polarity differences. In all four cases, these typical donor-acceptor (D-A) based emitters exhibit a significant solvatochromic shift (**Figure 8**) in response to changes in polarity, reinforcing the predominant CT nature of the S_1 state. In contrast, the NTO analysis of the lowest triplet state, T_1, suggests a different behavior. In the case of PXZDPAMCN, the hole-electron pair in the T_1 state exhibits significant spatial separation, indicating a predominantly CT nature. However, for all other cases, the hole-electron pairs show overlapping regions, suggesting a predominantly local (LE) nature (**Figure 7**). This is further confirmed by polarity-dependent phosphorescence emission spectra measurements. In PXZDPAMCN, the phosphorescence emission undergoes a considerable red shift with increasing polarity. Conversely, in the other three cases, the phosphorescence emission is structured with distinct vibrational progressions, similar to what we observed in the 1 wt% PMMA film (**Figure 8**). In these instances, the triplet emission remains relatively unchanged with increasing solvent polarity from non-polar toluene to highly polar acetonitrile/DMSO solvent, indicating a predominant locally excited (LE)

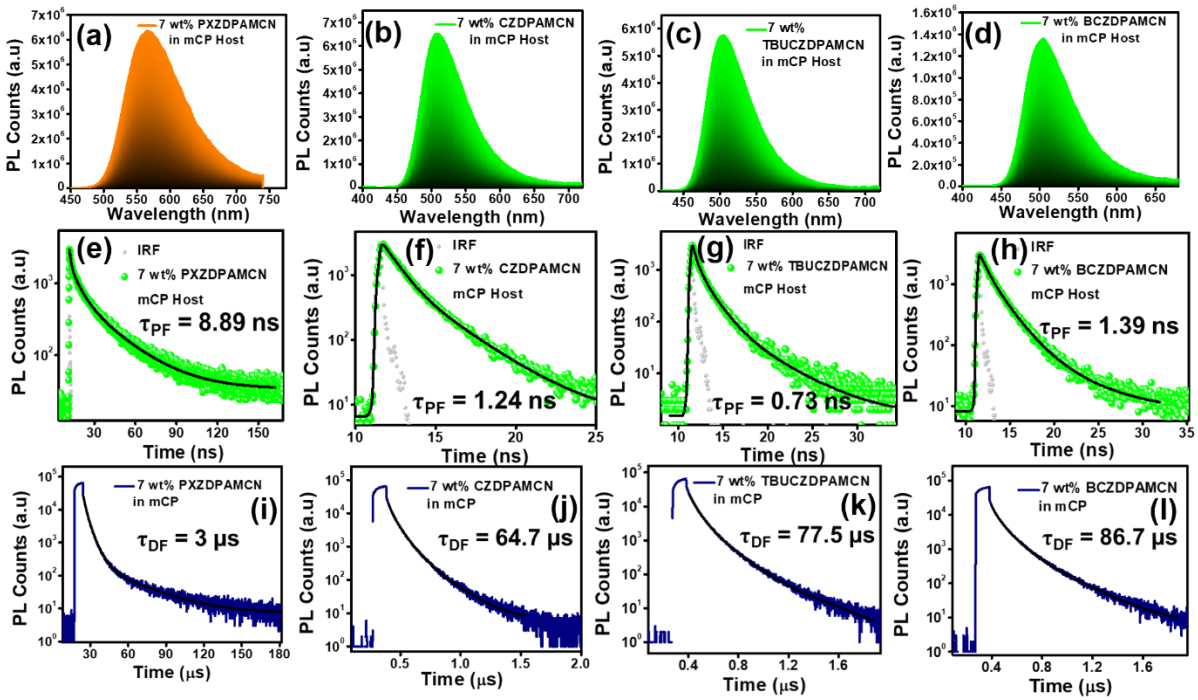

Figure 9: Steady state emission spectra in 7 wt% emitter doped mCP films of (a) PXZDPAMCN, (b) CZDPAMCN, (c) TBUCZDPAMCN, and (d) BCZDPAMCN. Prompt fluorescence lifetime in 7 wt% emitter doped mCP films of (e) PXZDPAMCN, (f) CZDPAMCN, (g) TBUCZDPAMCN, and (h) BCZDPAMCN. Delayed fluorescence lifetime in 7 wt% emitter doped mCP films of (i) PXZDPAMCN, (j) CZDPAMCN, (k) TBUCZDPAMCN, and (l) BCZDPAMCN.

nature of the T_1 state (**Figure 8**). The differences between the S_1 and T_1 states are particularly significant when considering the spin-orbit mixing of these two states, which is essential for facilitating the RISC process. The calculated spin-orbit coupling matrix element (SOCME) values between the two states are relatively high for organic emitters, measuring 0.85 cm^{-1} for CZDPAMCN, 0.83 cm^{-1} for TBUCZDPAMCN, and 0.85 cm^{-1} for BCZDPAMCN (**Figure 7**). In contrast, for PXZDPAMCN, the SOCME value is notably lower at 0.11 cm^{-1} due to the predominant charge transfer (CT) nature of both the S_1 and T_1 states (**Figure 7**). This lower SOCME value reduces the spin-orbit mixing of these two states, resulting in a significantly decreased reverse intersystem crossing (RISC) rate, despite a minimal energy gap of only 0.09 eV between S_1 and T_1. Interestingly, both in solution and in doped films, PXZDPAMCN exhibits the highest RISC rates (**Table A3 in Appendix**), indicating that another important factor influences the RISC rate in this compound. A detailed analysis of the natural transition orbitals (NTO) for other excited triplet states reveals that the hole-electron pairs in the T_2 state

of PXZDPAMCN have a very high overlap, suggesting that it is predominantly of localized

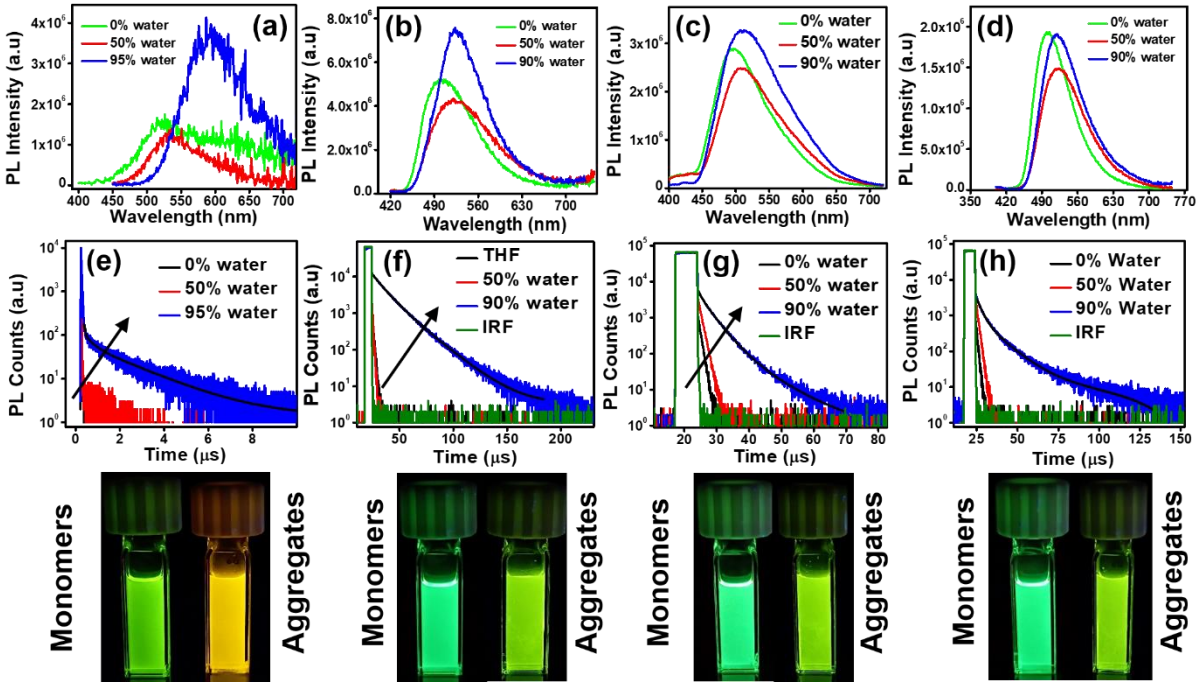

Figure 10: Variation of time-gated emission intensity with different water content in THF-water binary mixtures of (a) PXZDPAMCN, (b) CZDPAMCN, (c) TBUCZDPAMCN, and (d) BCZDPAMCN. Variation of delayed fluorescence lifetime with different water content in THF-water binary mixtures of (e) PXZDPAMCN, (f) CZDPAMCN, (g) TBUCZDPAMCN, and (h) BCZDPAMCN.

electronic (LE) character (**Figure 7**). This T_2 state is energetically very close to the lowest triplet T_1 state, with a small energy gap of just 0.14 eV (**Figure 7**). Notably, these energetically proximate T_1 (CT) and T_2 (LE) states can undergo strong vibronic coupling, which can enhance the RISC rate in these types of emitters.[43] In contrast, this factor is less significant in other emitters, as the lowest triplet (T_1) states in these systems predominantly exhibit a locally excited (LE) character. Consequently, there is strong spin-orbit coupling between the singlet (S_1) and triplet (T_1) states. Additionally, the T_2 states in these systems are primarily of a charge-transfer (CT) nature, resulting in minimal spin-orbit coupling (< 0.25 cm^{-1}). Therefore, except for PXZDPAMCN, the thermally activated delayed fluorescence (TADF) mechanism in these emitters is more likely to proceed via the S_1(CT)-T_1(LE) pathway rather than involving higher triplet states. Additionally, we utilized a molecular host, mCP (1,3-Bis(N-carbazolyl) benzene),[44] which has a high triplet energy of 2.91 eV and is commonly used as a low-polarity host in OLED fabrication. We conducted photophysical characterization for all the emitters. The photoluminescence (PL) and delayed fluorescence (DF) lifetimes, as well as the

photoluminescence quantum yield (PLQY), showed consistent trends (**Figure 9**), indicating that these features can be effectively translated into real OLED applications.

5.6.3 TADF efficiency in monomers vs aggregates:

The flexible molecular architecture of donor-acceptor-based luminogens is inherently fascinating as it enables diverse photophysical properties primarily due to the significant suppression of intermolecular vibrations and rotations in the aggregated state, coupled with the emergence of strong excitonic coupling. Given the three flexible diphenyl amine groups in each of our designed luminogens, it prompted us to investigate the TADF properties in their molecular aggregates as well. Similarly, like toluene, all the luminogens exhibit a sub-μs

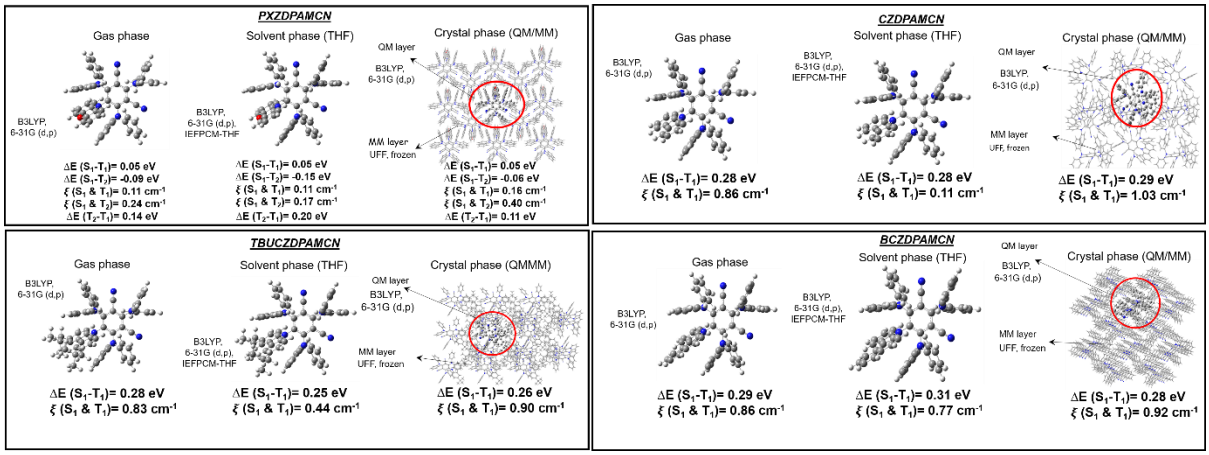

Figure 11: Optimized geometries across the gas phase, solvent phase (THF), and aggregated phase (obtained from QM/MM calculation) along with the relevant singlet-triplet energy gaps and their spin-orbit coupling matrix element (SOCME) values.

delayed fluorescence component in a more polar solvent-THF. However, the quantified delayed fluorescence contributions in THF were found to be negligibly small (< 0.05) (**Figure 10, Table A1 in Appendix**). Interestingly, the emission features in the molecular aggregates are found to be remarkably different. The delayed fluorescence lifetimes in all four cases are found to be increased significantly in the molecular aggregates formed in binary mixtures of THF-water at ~95% of water content. This was further verified by a time-gated emission measurement, where the molecular aggregates show enhanced emission suggesting a more efficient delayed fluorescence in molecular aggregates (**Figure 10**). In all four cases, the delayed fluorescence quantum yields are quantified to be Φ_{DF}=0.46, Φ_{DF}=0.24, Φ_{DF}=0.27, Φ_{DF}=0.15 for PXZDPAMCN, CZDPAMCN, TBUCZDPAMCN, and BCZDPAMCN, respectively (**Table A2 in Appendix**). It is to be noted that even in molecular aggregates,

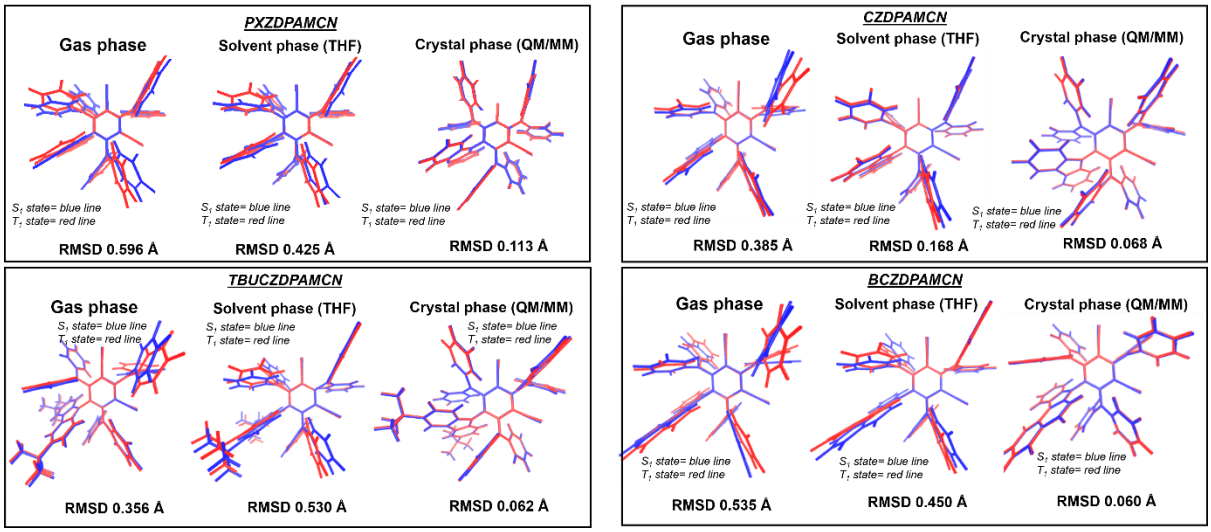

Figure 12: Root mean square deviation (RMSD) values between the optimized S_1 & T_1 geometries across the gas phase, solvent phase (THF), and aggregated phase (obtained from QM/MM calculation).

PXZDPAMCN is found to be the most efficient delayed fluorescence emitter. To explain the observed more efficient delayed fluorescence in molecular aggregates, detailed TD-DFT calculations are carried out across three different phases, i.e. gas phase, solvent phase (using THF as a model) to model the monomeric phase, and quantum mechanics/molecular mechanics (QM/MM) calculations to model the aggregated state. Notably, in QM/MM calculations, one molecule is treated quantum mechanically, whereas the surrounding molecules are treated classically. Herein, the quantum mechanical treatment in all three phases has been performed at B3LYP/6-31G (d, p) level of theory with the IEFPCM solvent model has been utilized for solvent treatment. For classical treatment of the surrounding molecules in QM/MM calculations, a universal force field (UFF) has been utilized (**Figure 11**). The RISC rates that dictate the efficiency of TADF are greatly driven by two main factors, i.e. the S_1 & T_1 energy gaps or ΔE_{ST} and the extent of spin-orbit coupling (SOCME) between these two states. Interestingly, in all four cases, the calculated ΔE_{ST} between the lowest S_1 & T_1 states show no notable changes across these three different phases (**Figure 11**), which necessitates a more detailed and careful look into the other parameters. As mentioned previously, in PXZDPAMCN, due to the predominant CT nature of the T_1 state, a strong vibronic coupling between the T_1(CT) and T_2(LE) states is one of the most important keys in dictating the TADF properties. In polar solvents such as THF, the T_1(CT) state experiences substantial stabilization, while the T_2 state, with its predominantly locally excited (LE) character, remains energetically almost unaffected. This stabilization increases the T_1(CT)-T_2(LE) energy gap in polar solvents,

resulting in negligible delayed fluorescence efficiency observed in THF. In contrast, in the aggregated state, the molecular environment is predominantly hydrophobic due to the aromatic rings of the emitters. This hydrophobic environment suppresses the stabilization of the T_1(CT) state, leading to a significantly reduced T_1(CT)-T_2(LE) energy gap, enhanced vibronic coupling, and consequently stronger delayed fluorescence. Computational calculations across three different phases corroborate these findings. In THF, the T_1-T_2 energy gap is calculated to be 0.20 eV, whereas in the aggregated phase, this gap decreases to 0.10 eV. Additionally, in the aggregated phase, the S_1(CT)-T_2(LE) energy gap decreases by approximately 0.09 eV, and the spin-orbit coupling between these states increases from 0.17 cm^{-1} to 0.40 cm^{-1} (**Figure 11**). These findings are one of the most important reasons for explaining the enhanced delayed fluorescence in the aggregated state of PXZDPAMCN. In contrast, the TADF mechanism in other emitters differs due to the predominantly locally excited (LE) character of the T_1 state and the predominantly charge-transfer (CT) character of the T_2 state. For these emitters, the S_1-T_2 and T_1-T_2 energy gaps are less significant because the spin-orbit coupling between S_1 and T_2 is inherently weak. As a result, the T_1 state primarily governs the TADF efficiency. Notably, while the S_1-T_1 energy gap (ΔE_{ST}) remains almost constant across different phases, a detailed comparison reveals a significant increase in the spin-orbit coupling (SOC) between S_1 and T_1 in the aggregated state compared to THF. For instance, in CZDPAMCN, the $\xi(S_1\text{-}T_1)$ value increases from 0.11 cm^{-1} to 1.03 cm^{-1}; in TBUCZDPAMCN, it rises from 0.44 cm^{-1} to 0.90 cm^{-1}; and in BCZDPAMCN, it increases from 0.77 cm^{-1} to 0.92 cm^{-1} (**Figure 11**). These enhancements in SOC in the aggregated state play a crucial role in dictating the TADF performance of these emitters. At this juncture, it is crucial to recognize that TADF operates as an endothermic transition, where an exciton jumps from the excited triplet state (T_1) to the excited singlet state (S_1) through reverse intersystem crossing (RISC). The efficiency of this process hinges critically on the geometrical alignment of the S_1 and T_1 states—a substantial mismatch can impose a prohibitive barrier to the RISC process, stifling the TADF process despite an exceptionally small ΔE_{ST}.[45] A detailed examination of the structural differences between the S_1 and T_1 states reveals an intriguing trend across all four luminogens. In both the gas phase and THF, there is a significant structural disparity between the S_1 and T_1 geometries, quantified by large root mean square deviations (RMSDs). This pronounced difference is further confirmed by the overlaid structures of the two states, which visibly highlight the geometrical mismatch (**Figure 12**). Such substantial structural differences are known to introduce a high energy barrier for the lowest triplet to singlet thermal upconversion or reverse

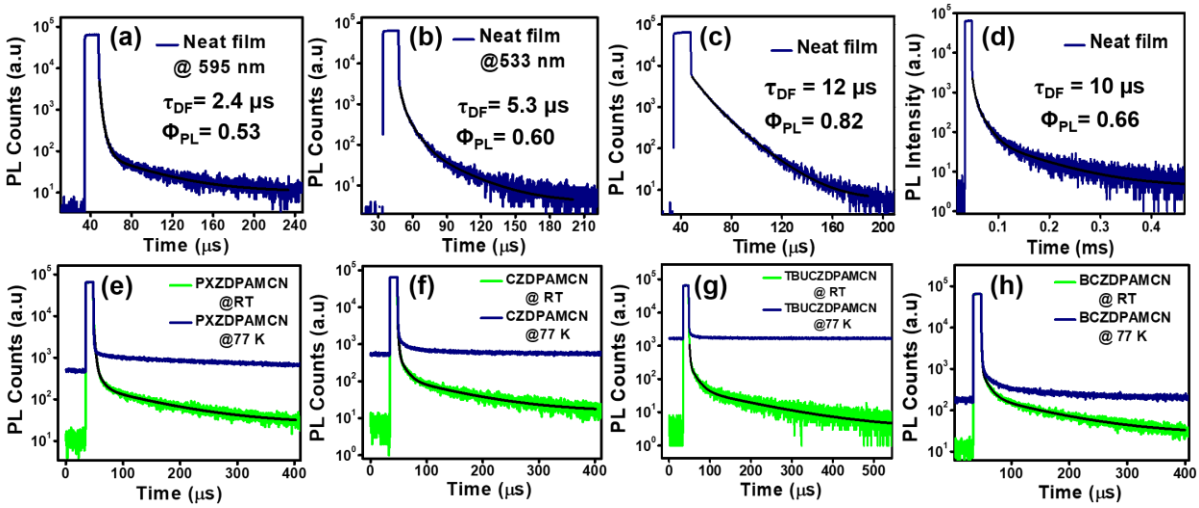

Figure 13: Delayed fluorescence lifetime in neat films along with their PLQY of (a) PXZDPAMCN, (b) CZDPAMCN, (c) TBUCZDPAMCN, and (d) BCZDPAMCN. Delayed fluorescence lifetime variation at RT and 77 K for (e) PXZDPAMCN, (f) CZDPAMCN, (g) TBUCZDPAMCN, and (h) BCZDPAMCN.

intersystem crossing (RISC), thereby reducing the efficiency of delayed fluorescence in monomeric states. In contrast, the structural differences between the S_1 and T_1 states in the aggregated phase, as determined through QM/MM calculations, are found to be negligibly small. This is evident from the nearly identical overlaid geometries of S_1 and T_1 in the aggregated state (**Figure 12**). The reduced structural disparity minimizes the energy barrier between these states, facilitating a much more efficient RISC process and, consequently, significantly enhancing delayed fluorescence in the aggregated phase. Whether these trends remain consistent with the further extent of aggregation, photophysical characterization in neat films has been carried out. All four luminogens in neat films exhibit a slightly increased delayed fluorescence lifetime, with maintaining a high PLQY of Φ=0.53, Φ=0.60, Φ=0.82 and Φ=0.66 for PXZDPAMCN, CZDPAMCN, TBUCZDPAMCN and BCZDPAMCN, respectively (**Figure 13**). All four neat films exhibit a decreased DF lifetime with a long phosphorescence tail at 77 K. These results suggest the trends to be consistent with a higher extent of aggregation (**Figure 13**).

5.6.4 Mechanochromic luminescence (MCL) properties:

Donor-acceptor luminogens exhibiting mechanochromic luminescence (MCL) properties have garnered significant attention as promising candidates for diverse applications, including optical storage, mechanical sensing, security devices, and advanced optoelectronics. We

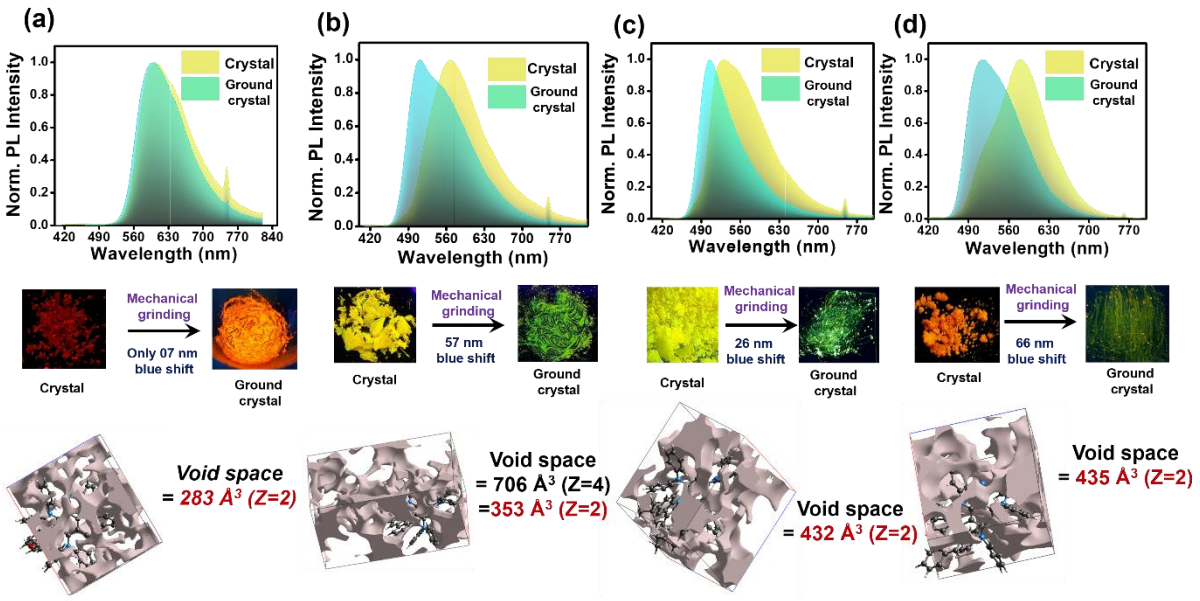

Figure 14: Steady-state emission spectra upon mechanical grinding with their emission photo and void volumes of molecular crystals of (a) PXZDPAMCN, (b) CZDPAMCN, (c) TBUCZDPAMCN, and (d) BCZDPAMCN.

postulated that the integration of MCL with thermally activated delayed fluorescence (TADF) functionalities could provide a robust strategy for designing multifunctional organic materials. The synergistic effects of these properties could enable sophisticated sensing mechanisms, where emission colors and intensities are modulated by external stimuli such as pressure or temperature changes. These materials show considerable promise for use in stress, pressure, and thermal indicators in high-tech sectors like aerospace and submarine technologies. The molecular architectures of the studied luminogens incorporate highly flexible diphenylamine moieties, whose flexibility allows alterations in the donor-acceptor (D-A) dihedral angles under mechanical pressure, ultimately resulting in MCL. The crystals of the four luminogens—PXZDPAMCN, CZDPAMCN, TBUCZDPAMCN, and BCZDPAMCN—exhibit emissions ranging from greenish-yellow to red, with emission maxima observed at ~605 nm, ~565 nm, ~530 nm, and ~580 nm, respectively. Upon applying mechanical pressure, all emitters except PXZDPAMCN display significant blue shifts in their emission spectra, with shifts of ~57 nm, ~26 nm, and ~66 nm recorded for CZDPAMCN, TBUCZDPAMCN, and BCZDPAMCN, respectively (**Figure 14**). These blue shifts result in ground crystals emitting green light, enabling a distinct emission switch characteristic of mechano-active behavior. In contrast, PXZDPAMCN exhibits only a negligible blue shift (~9 nm) upon grinding, rendering it mechano-inactive.

To elucidate the unique mechanochromic behavior, natural transition orbital (NTO) analysis was conducted to examine the contributing canonical orbitals in the S_1 excited state of each emitter. In all cases except PXZDPAMCN, the hole orbitals were predominantly localized on the diphenylamine moieties between the two cyano groups, attributed to the diphenylamine's strong electron-donating capacity relative to carbazole-based donors (**Figure 7**). However, in PXZDPAMCN, the hole orbital is mainly situated on the phenoxazine moiety due to its even greater donating strength (**Figure 7**). The rigidity of the phenoxazine moiety, caused by its bridged oxygen structure, limits its ability to alter its dihedral angle with the acceptor, unlike the flexible diphenylamine moiety with rotatable phenyl groups. This structural rigidity underpins PXZDPAMCN's mechano-inactivity, while the flexibility of the other emitters facilitates their mechano-active behavior. Another critical factor influencing MCL properties is the crystal void volume within the unit cell. A higher void volume enhances the flexibility of the D-A emitters to adjust their dihedral angles, promoting mechanochromic luminescence. Calculated void volumes for the four emitters are 283 Å^3, 353 Å^3, 432 Å^3, and 435 Å^3 for PXZDPAMCN, CZDPAMCN, TBUCZDPAMCN, and BCZDPAMCN, respectively (with Z=2) (**Figure 14**). The significantly lower void volume in PXZDPAMCN explains its mechano-inactivity compared to the other emitters. Additionally, all three mechano-active emitters (CZDPAMCN, TBUCZDPAMCN, and BCZDPAMCN) exhibit long delayed fluorescence components in the microsecond range within their ground crystals, accompanied by altered delayed fluorescence lifetimes (**Figure A5 in Appendix**). This confirms that these emitters are MCL-TADF materials, making them highly suitable for cutting-edge optoelectronic applications.

5.7 Applications:

5.7.1 Solution processable device fabrication:

The high photoluminescence quantum yields (PLQYs) of all four luminogens in molecular hosts, such as mCP, position them as excellent candidates for high-performance TADF-based organic light-emitting diodes (OLEDs). To assess their electroluminescent (EL) properties, three solution-processed OLEDs were fabricated with doped emitting layers (EMLs) structured as follows: ITO/PEDOT:PSS (40 nm)/PVK (30 nm)/CZDPAMCN or tBu-CZDPAMCN:mCP or PXZDPAMCN:CBP (30 nm)/PPT (10 nm)/TPBi (40 nm)/LiF (2 nm)/Al (100 nm). In this design, the EML for CZDPAMCN and TBUCZDPAMCN employed mCP as the host matrix,

with an emitter doping concentration of 7 wt%. For PXZDPAMCN, CBP was chosen as the host under the same doping conditions to optimize performance.

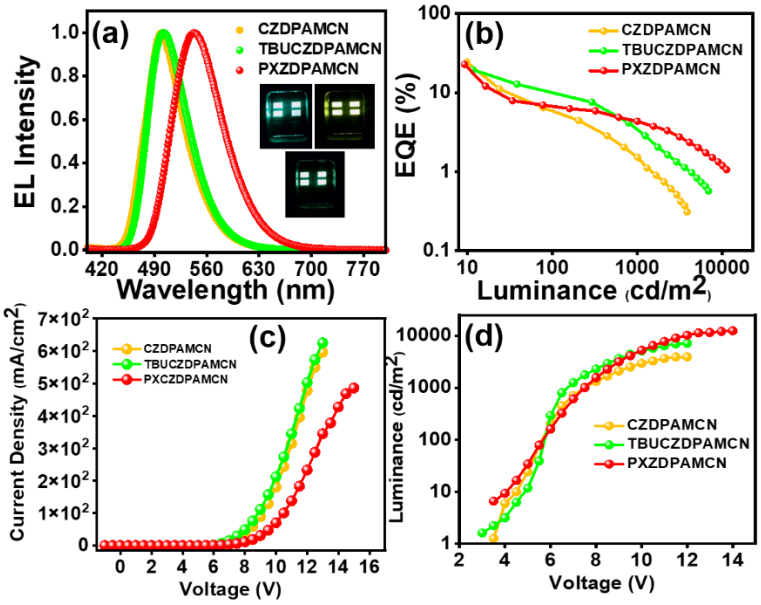

Figure 15: (a) Electroluminescence spectra of the fabricated solution-processable devices Inset shows the device photo and electroluminescence (top left-CZDPAMCN, top right-PXZDPAMCN & bottom-TBUCZDPAMCN). (b) Variation of the total EQE with luminance. (c) Variation of the current density of the fabricated devices with applied voltage and (d) Luminance-voltage curve for all three fabricated devices.

The device architecture incorporates PEDOT:PSS (40 nm) as the hole injection layer, PVK (30 nm) as the hole transport layer, PPT as the hole blocking layer, TPBi as the electron transport layer, LiF as the electron injection layer, Al as the cathode, and ITO as the transparent anode. BCZDPAMCN was excluded from OLED fabrication due to its slightly lower PLQY in molecular hosts and its emission maxima being comparable to those of CZDPAMCN and TBUCZDPAMCN. The EL spectra of all three emitters closely resemble their respective PL spectra. Among the devices, the OLED with PXZDPAMCN exhibited the broadest full-width at half-maximum (FWHM) emission, attributed to the greater charge transfer character of its S_1 excited state. The maximum external quantum efficiencies (EQE_{max}) of the OLEDs were measured to be 22.8%, 24.4%, and 19.5% for PXZDPAMCN, CZDPAMCN, and TBUCZDPAMCN, respectively (**Figure 15**). These EQEs are higher than those of widely reported emitters, such as 4CzIPN (EQEmax = 19.3 ± 1.5%) and the series of emitters reported by Yasuda and colleagues (maximum EQEmax = 18.2%). All three devices exhibited low turn-on voltages (Von) in the range of 3.0–3.5 V. The luminances were moderate to high, with

PXZDPAMCN achieving the highest maximum luminance at 11,485 cd/m². Additionally, efficiency roll-off at a high luminance of 4000 cd/m² was analyzed. PXZDPAMCN demonstrated the lowest efficiency roll-off (~89%), compared to CZDPAMCN (~98%) and TBUCZDPAMCN (~94%) (**Figure 15**). This superior performance of PXZDPAMCN is attributed to its fastest rate of reverse intersystem crossing (RISC) and shortest delayed fluorescence lifetime. These factors help mitigate biexcitonic quenching effects such as triplet-triplet annihilation (TTA) and singlet-triplet annihilation (STA), as supported by previous studies.[46-47]

5.7.2 Manifestation of yellow narrow-band singlet emission sensitized by cyan-green TADF emitters:

The emission FWHMs of the D-A based TADF emitters discussed in the last section are found to be a little higher. Notably, using these broad-band TADF emitters, and by utilizing their triplet-harvesting efficiencies, a narrow-band all singlet emission can be obtained that provides improved efficiencies in the fabricated devices. This process is usually termed Hyperfluorescence (HF) and a more detailed discussion has been done in the introduction section. While most HF emitters developed to date have focused on blue or green emission, there has been limited exploration of HF systems in the yellow emission region. In this work, we utilized two highly efficient cyan-green emitters, CZDPAMCN and TBUCZDPAMCN, to

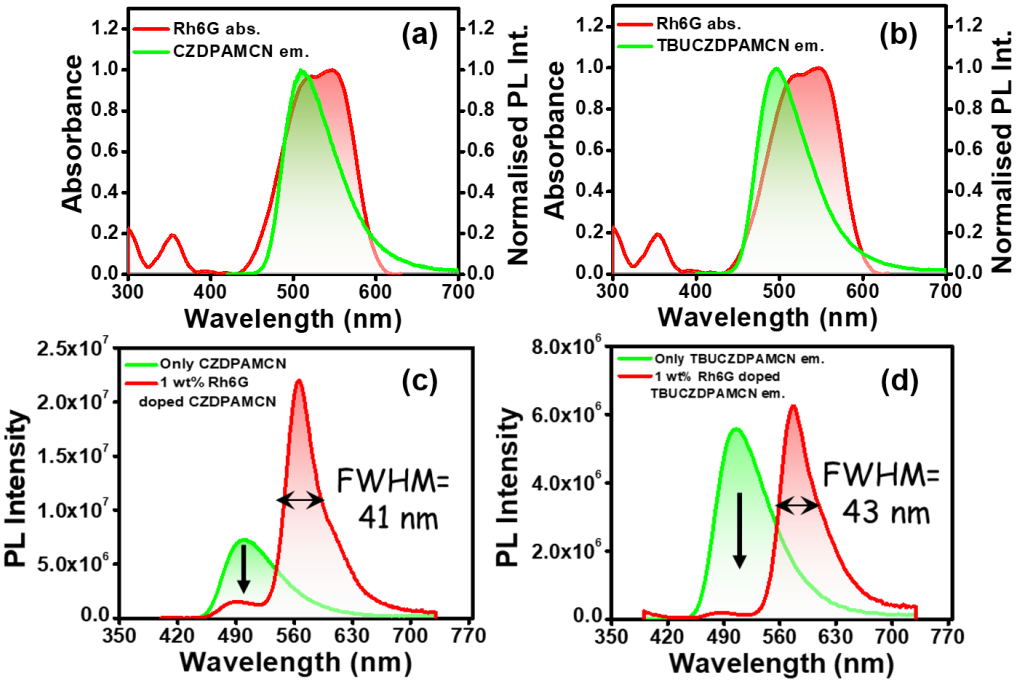

Figure 16: Overlap of emission spectra of the donor (TADF emitter) and absorption spectra of the acceptor (Fluorescent emitter) for (a) CZDPAMCN–Rh6G and (b) TBUCZDPAMCN–

Rh6G system. Effect of 1wt% Rh6G doping on the emission spectra for (c) CZDPAMCN–Rh6G and (d) TBUCZDPAMCN–Rh6G system.

achieve yellow emission via energy transfer to Rh6G, a well-known dye. The emission spectra of the TADF sensitizers overlap effectively with the absorption spectra of Rh6G in a PMMA host matrix, making the system ideal for Förster resonance energy transfer (FRET) (**Figure 16**). The calculated overlap integrals for the donor-acceptor pairs CZDPAMCN–Rh6G and TBUCZDPAMCN–Rh6G are 6.964×10^{15} $M^{-1}cm^{-1}nm^4$ and 5.994×10^{15} $M^{-1}cm^{-1}nm^4$, respectively. To fabricate the yellow HF systems, we doped the PMMA host with 10 wt% of the TADF assistant dopants (CZDPAMCN or TBUCZDPAMCN) and 1 wt% of Rh6G, serving as the terminal narrow-band fluorescent emitter. The FWHM of the emissions from CZDPAMCN and TBUCZDPAMCN alone in the PMMA host exceeds 60 nm. However, upon doping with 1 wt% Rh6G, the TADF emission is quenched, and the overall emission becomes dominated by Rh6G emission (**Figure 16**) upon excitation of the TADF dopants at 375 nm, where Rh6G exhibits minimal absorption. To confirm whether this emission quenching is mediated by the FRET process, time-resolved photoluminescence (TRPL) studies were conducted. Excitation

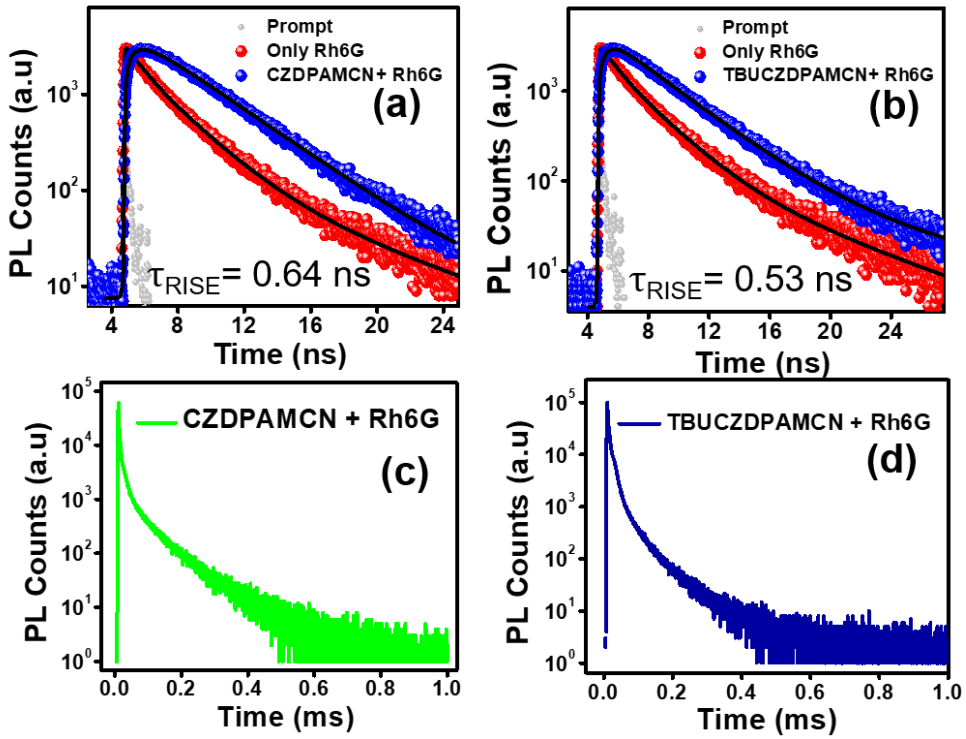

Figure 17: Rise component or growth component visible against a control upon collecting the TCSPC decay at 575 nm (Rh6G emission) upon exciting the TADF assistant dopant at 375 nm

for (a) CZDPAMCN–Rh6G and (b) TBUCZDPAMCN–Rh6G system. Decay transients in ~sub-ms timescale proving upon collecting the TCSPC decay at 575 nm (Rh6G emission) upon exciting the TADF assistant dopant at 375 nm for (a) CZDPAMCN–Rh6G and (b) TBUCZDPAMCN–Rh6G system.

at 375 nm and monitoring of the PL decay at the TADF dopant emission maxima (500 nm for both emitters) revealed reduced prompt fluorescence (PF) and delayed fluorescence (DF) lifetimes (**Figure A6 in Appendix**), indicating an additional energy transfer pathway. Further, TRPL decay profiles collected at the Rh6G emission maximum (575 nm) showed a growth component followed by decay, with lifetimes of 0.64 ns for the CZDPAMCN–Rh6G system and 0.53 ns for the TBUCZDPAMCN–Rh6G system (**Figure 17**). This growth component was attributed to the FRET process, with calculated FRET rates of $1.56 \times 10^9\ s^{-1}$ and $1.89 \times 10^9\ s^{-1}$, respectively. From FRET calculations, the Förster radii (R_0) and donor-acceptor average distances (R_{DA}) were determined. The R_0 values for CZDPAMCN and TBUCZDPAMCN were 8.0 nm and 8.2 nm, respectively, both larger than the corresponding R_{DA} values of 6.7 nm and 7.1 nm. These findings confirm the high efficiency of the FRET process necessary for HF. While the efficiency of the FRET process was established, the extent of triplet harvesting from the TADF emitter to the fluorescent emitter required further verification. To address this, TRPL decay profiles were collected at the Rh6G emission maximum (575 nm) under excitation of the TADF assistant dopants at 375 nm. Control experiments without TADF dopants showed no decay transients in the microsecond time scale, as expected for Rh6G, a traditional fluorescent emitter. In contrast, in the presence of TADF dopants, a long decay transient in the microsecond range was observed (**Figure 17**), confirming efficient triplet harvesting via FRET. This finding substantiates the effectiveness of the HF systems developed in this study.

5.8 Conclusions:

This study provides a comprehensive exploration of the factors influencing the enhanced TADF efficiencies of molecular aggregates, highlighting the critical roles of energy gaps, spin-orbit mixing, and excited state structural reorganization. Through the design and synthesis of a new series of TADF emitters, we demonstrate that the choice of donor unit—specifically phenoxazine, carbazole, and related derivatives—significantly affects the reverse intersystem crossing (RISC) rates, TADF lifetimes, and emission properties. Notably, the phenoxazine-based compound exhibits the highest TADF efficiency and rapid RISC rates in the order of

~10^6 cm^{-1}, while carbazole-based emitters reveal slower rates (in the order of ~10^3-10^4 cm^{-1}) and longer TADF lifetimes, with distinct emission colors. Moreover, the incorporation of carbazole-based emitters with mechanochromic luminescence (MCL) properties without compromising TADF performance suggests the potential for multifunctional luminogens. The successful fabrication of OLED devices with external quantum efficiencies exceeding 20% underscores the practical applicability of these materials in advanced optoelectronic technologies. This work contributes essential insights into the design of high-performance TADF emitters and sets the stage for the development of efficient, solution-processable materials for next-generation organic electronics, offering a pathway toward more efficient light-emitting and sensing technologies.

5.9 Appendix:

Section A1) Detailed synthetic procedures:

Synthesis scheme:

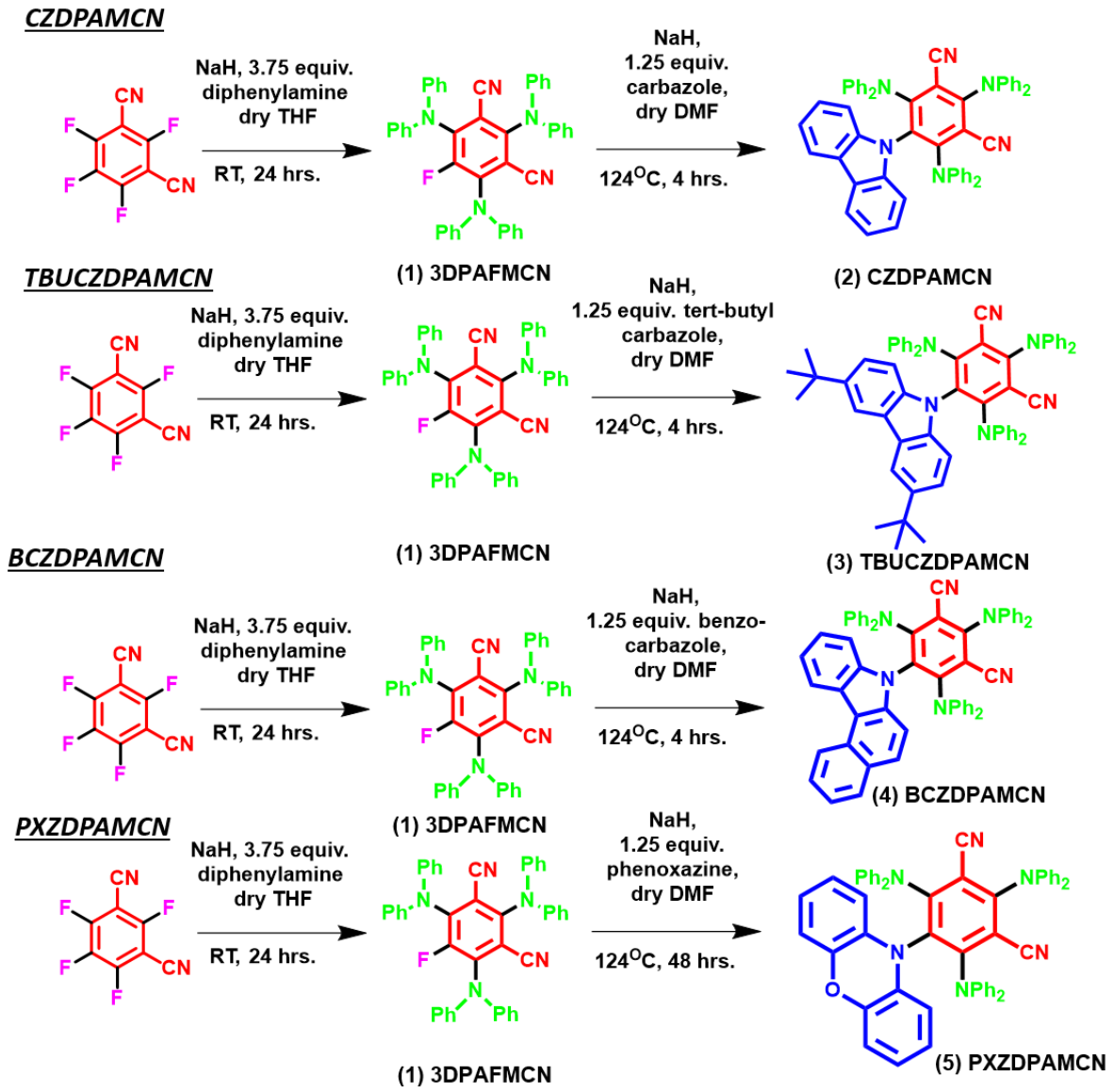

Scheme S1: synthetic routes of the designed compounds.

Synthesis of (1) 3DPAFMCN:

In a Schlenk RB flask equipped with a magnetic stir bar, 630 mg (3.75 mmol) of diphenylamine is dissolved in 20 ml of anhydrous tetrahydrofuran (THF) under an argon atmosphere. Slowly, 240 mg (6 mmol) of vacuum-dried sodium hydride (60% in oil) is added to the mixture, which is then stirred at room temperature for 30 minutes. After this period, 0.2 mg (1 mmol) of tetrafluoroisophthalonitrile is added to the reaction mixture, and stirring is continued for another 24 hours at room temperature under argon (**scheme S1**). The completion of the reaction

is confirmed by thin-layer chromatography (TLC). Excess sodium hydride is quenched by the dropwise addition of distilled water. The mixture is then washed several times with water and ethyl acetate. Finally, the crude product is purified using silica gel flash column chromatography with a hexane/dichloromethane (DCM) solvent system, yielding approximately 80%.

^{1}H NMR (400 MHz, $CDCl_3$): δ 7.36 – 7.23 (m, 12H), 7.16 (t, *J* = 7.3 Hz, 2H), 7.12 – 6.98 (m, 16H).

^{13}C NMR (101 MHz, $CDCl_3$): δ 153.82, 151.95, 151.92, 151.24, 145.64, 145.42, 143.23, 143.12, 129.57, 129.50, 124.72, 124.14, 122.83, 122.86, 117.90, 112.76, 112.73, 109.06, 109.03.

^{19}F NMR (377 MHz, $CDCl_3$): δ -121.27.

HRMS (ESI): calc. for [($C_{44}H_{30}N_5F$) H] $(M+H)^+$ 648.2568, found 648.2556.

Synthesis of (2) CZDPAMCN:

In a Schlenk round-bottom flask equipped with a magnetic stir bar, 65 mg (0.386 mmol, 1.25 equivalents) of carbazole is dissolved in 20 ml of anhydrous DMF under an argon atmosphere. Slowly, 14 mg (0.580 mmol, 1.88 equivalents) of vacuum-dried sodium hydride (60% in oil) is added to the mixture, which is then stirred at room temperature for 30 minutes. After this time, 0.2 g (0.308 mmol, 1 equivalent) of 3DPAFMCN is introduced to the reaction mixture, and stirring is continued for another 4 hours at 124°C under argon (see **Scheme S1**). The completion of the reaction is confirmed by thin-layer chromatography (TLC). Excess sodium hydride is quenched by adding distilled water dropwise. The mixture is then washed several times with water and ethyl acetate. Finally, the crude product is purified using silica gel flash column chromatography with a hexane/dichloromethane (DCM) solvent system, resulting in a 70% yield.

Synthesis of (3) TBUCZDPAMCN:

In a Schlenk round-bottom flask equipped with a magnetic stir bar, 108 mg (0.386 mmol, 1.25 equivalents) of tert-butyl carbazole is dissolved in 20 ml of anhydrous DMF under an argon atmosphere. Slowly, 14 mg (0.580 mmol, 1.88 equivalents) of vacuum-dried sodium hydride (60% in oil) is added to the mixture, which is stirred at room temperature for 30 minutes. After this time, 0.2 g (0.308 mmol, 1 equivalent) of 3DPAFMCN is introduced into the reaction

mixture, and stirring continues for an additional 4 hours at 124°C under argon (see **Scheme S1**). The completion of the reaction is confirmed by thin-layer chromatography (TLC). Excess sodium hydride is quenched by adding distilled water dropwise. The mixture is then washed several times with water and ethyl acetate. Finally, the crude product is purified using silica gel flash column chromatography with a hexane/dichloromethane (DCM) solvent system, resulting in a yield of 75%.

Synthesis of (4) BCZDPAMCN:

In a Schlenk round-bottom flask equipped with a magnetic stir bar, 84 mg (0.386 mmol, 1.25 equivalents) of benzo-carbazole is dissolved in 20 ml of anhydrous DMF under an argon atmosphere. Slowly, 14 mg (0.580 mmol, 1.88 equivalents) of vacuum-dried sodium hydride (60% in oil) is added to the mixture, which is stirred at room temperature for 30 minutes. After this time, 0.2 g (0.308 mmol, 1 equivalent) of 3DPAFMCN is introduced into the reaction mixture, and stirring continues for an additional 4 hours at 124°C under argon (see **Scheme S1**). The completion of the reaction is confirmed by thin-layer chromatography (TLC). Excess sodium hydride is quenched by adding distilled water dropwise. The mixture is then washed several times with water and ethyl acetate. Finally, the crude product is purified using silica gel flash column chromatography with a hexane/dichloromethane (DCM) solvent system, resulting in a yield of 60%.

Synthesis of (5) PXZDPAMCN:

In a Schlenk round-bottom flask equipped with a magnetic stir bar, 71 mg (0.386 mmol, 1.25 equivalents) of phenoxazine is dissolved in 20 ml of anhydrous DMF under an argon atmosphere. Slowly, 14 mg (0.580 mmol, 1.88 equivalents) of vacuum-dried sodium hydride (60% in oil) is added to the mixture, which is stirred at room temperature for 30 minutes. After this time, 0.2 g (0.308 mmol, 1 equivalent) of 3DPAFMCN is introduced into the reaction mixture, and stirring continues for an additional 48 hours at 124°C under argon (see **Scheme S1**). The completion of the reaction is confirmed by thin-layer chromatography (TLC). Excess sodium hydride is quenched by adding distilled water dropwise. The mixture is then washed several times with water and ethyl acetate. Finally, the crude product is purified using silica gel flash column chromatography with a hexane/dichloromethane (DCM) solvent system, resulting in a yield of 30%.

Characterization data

^{1}H NMR of (1) 3DPAFMCN:

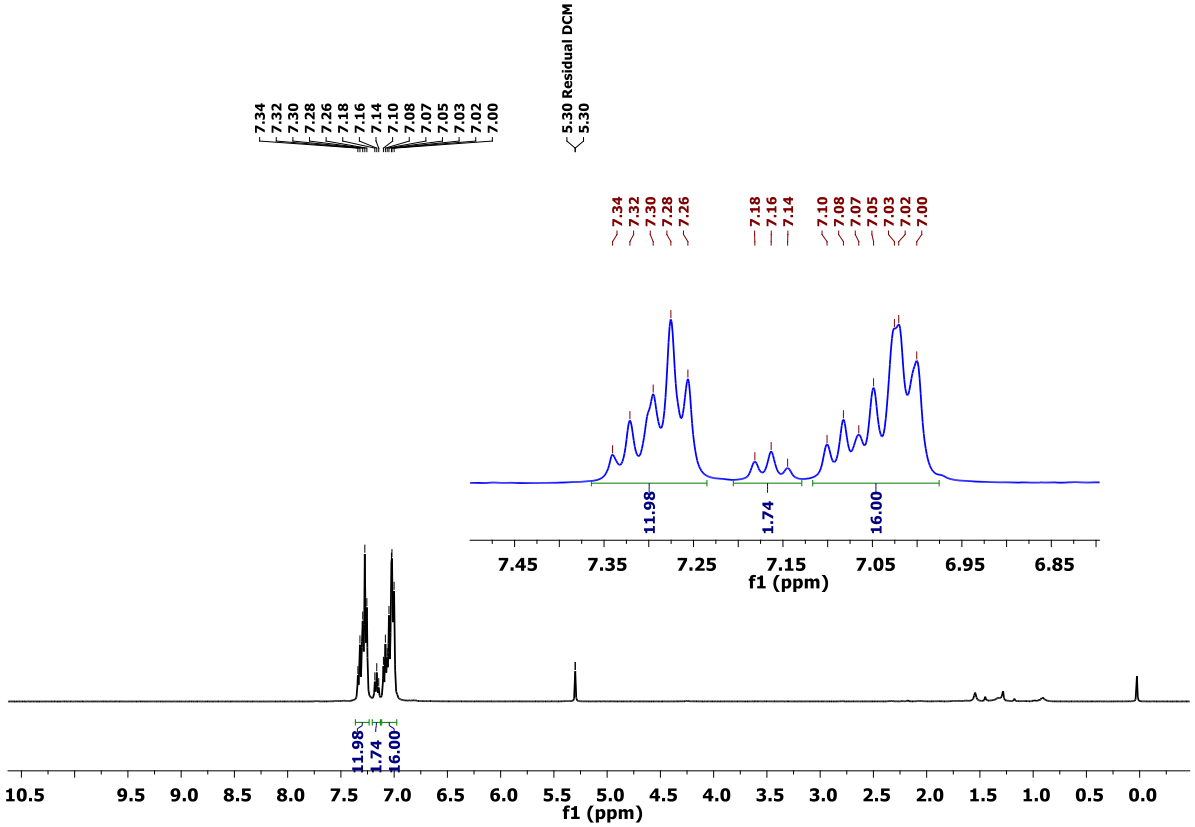

^{13}C NMR of (1) 3DPAFMCN:

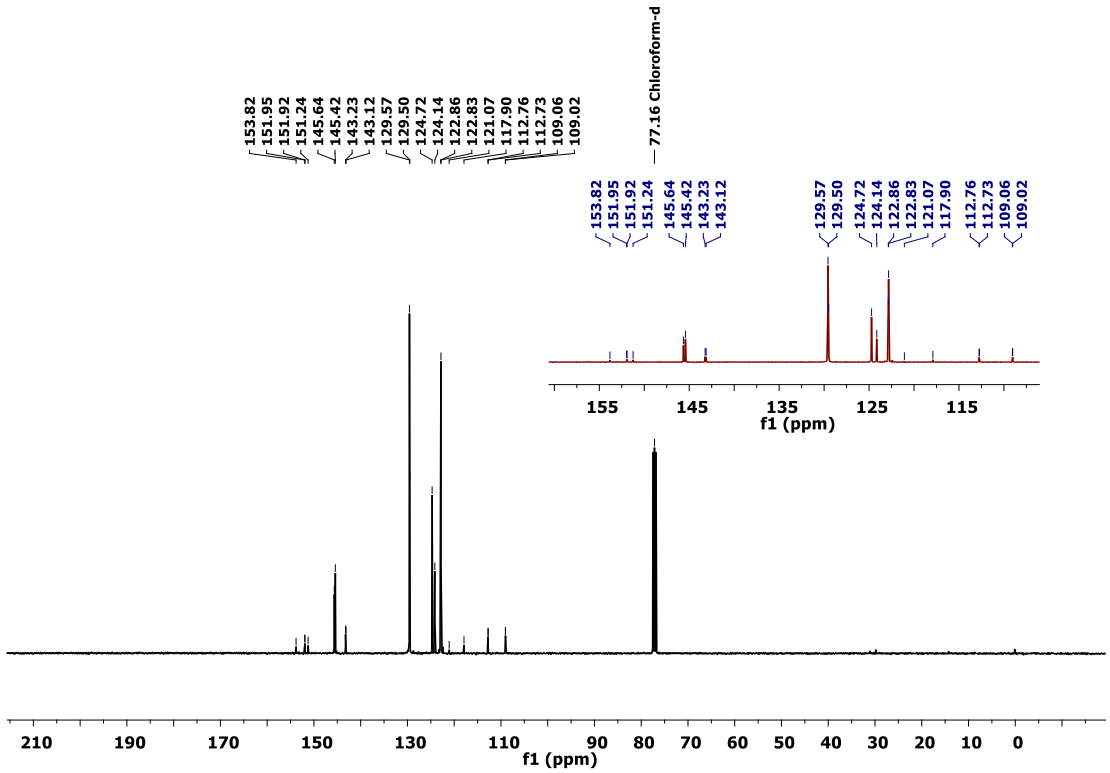

^{19}F NMR of (1) 3DPAFMCN:

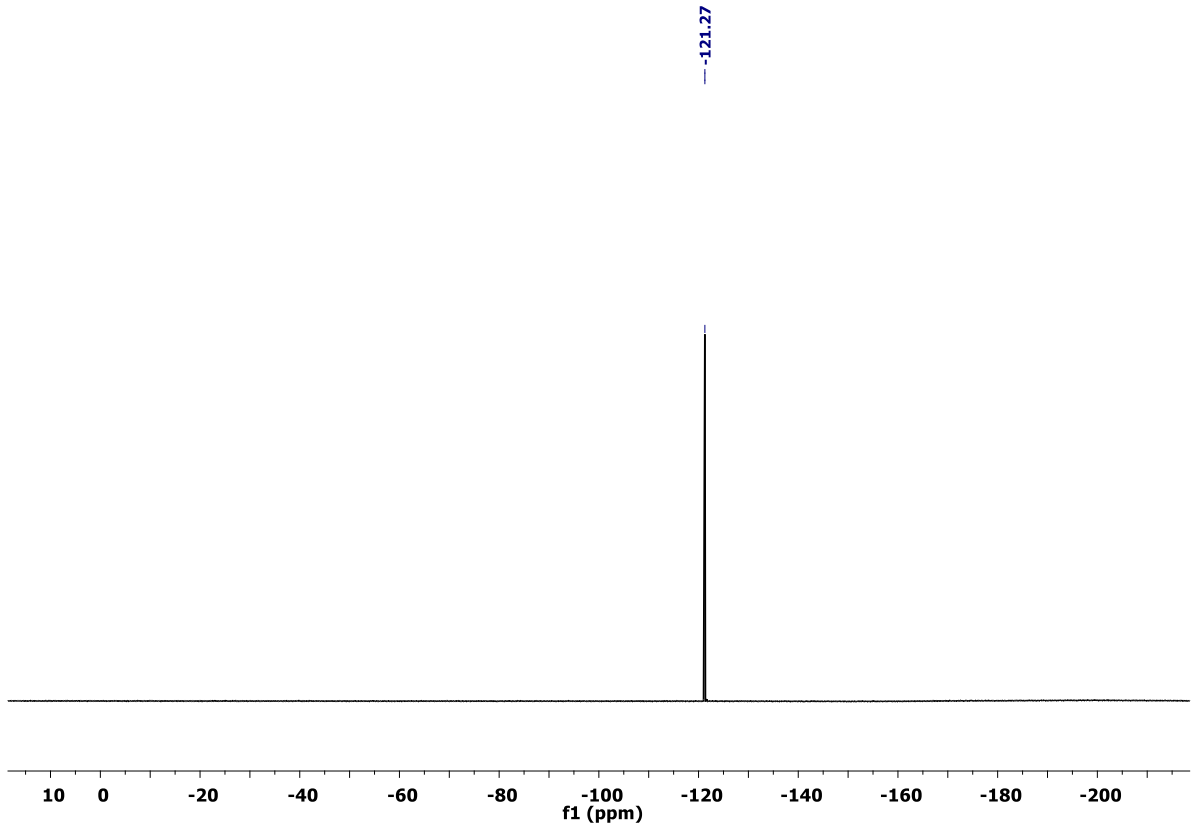

HRMS of (1) 3DPAFMCN:

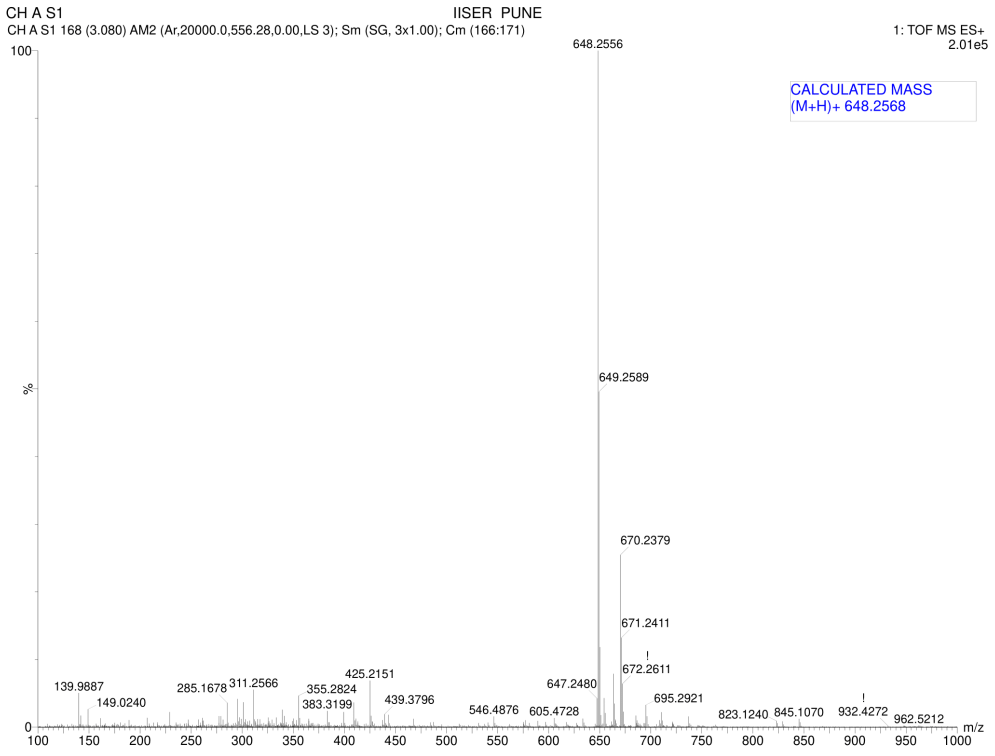

^{1}H NMR of (2) CZDPAMCN:

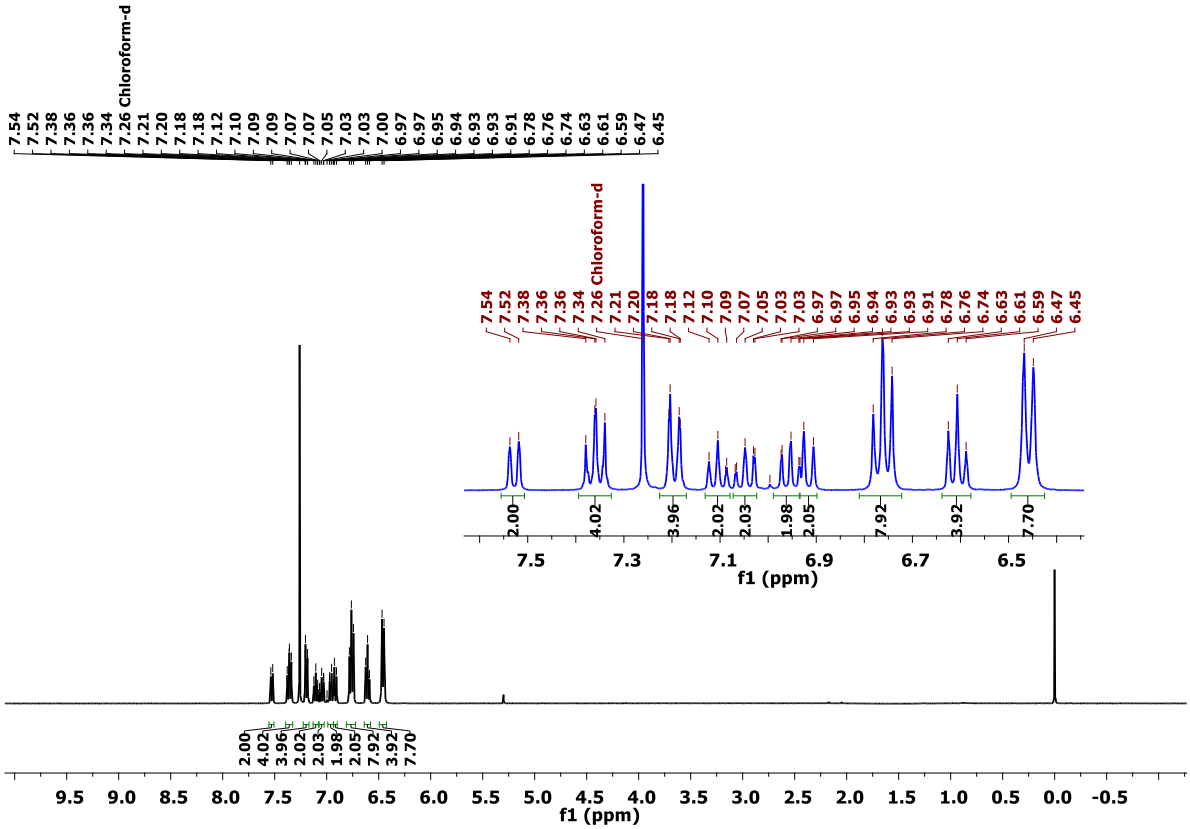

^{13}C NMR of (2) CZDPAMCN:

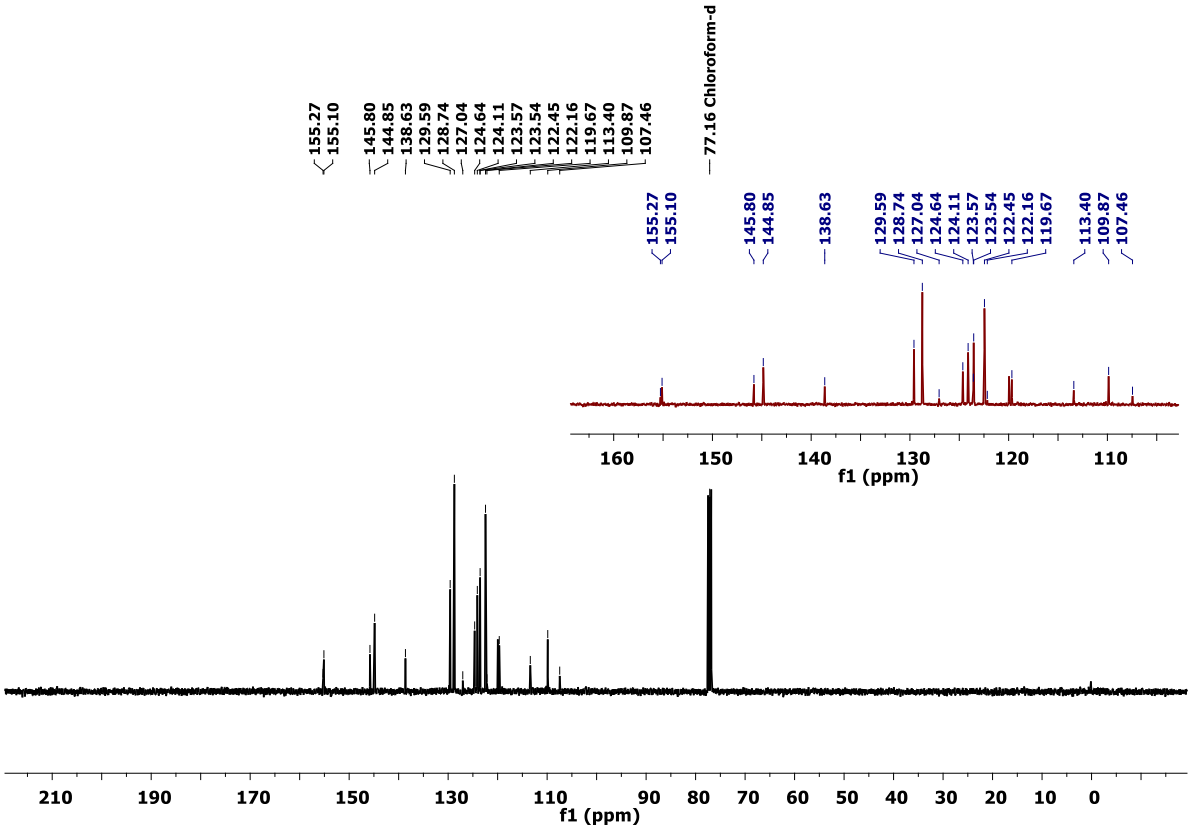

HRMS of (2) CZDPAMCN:

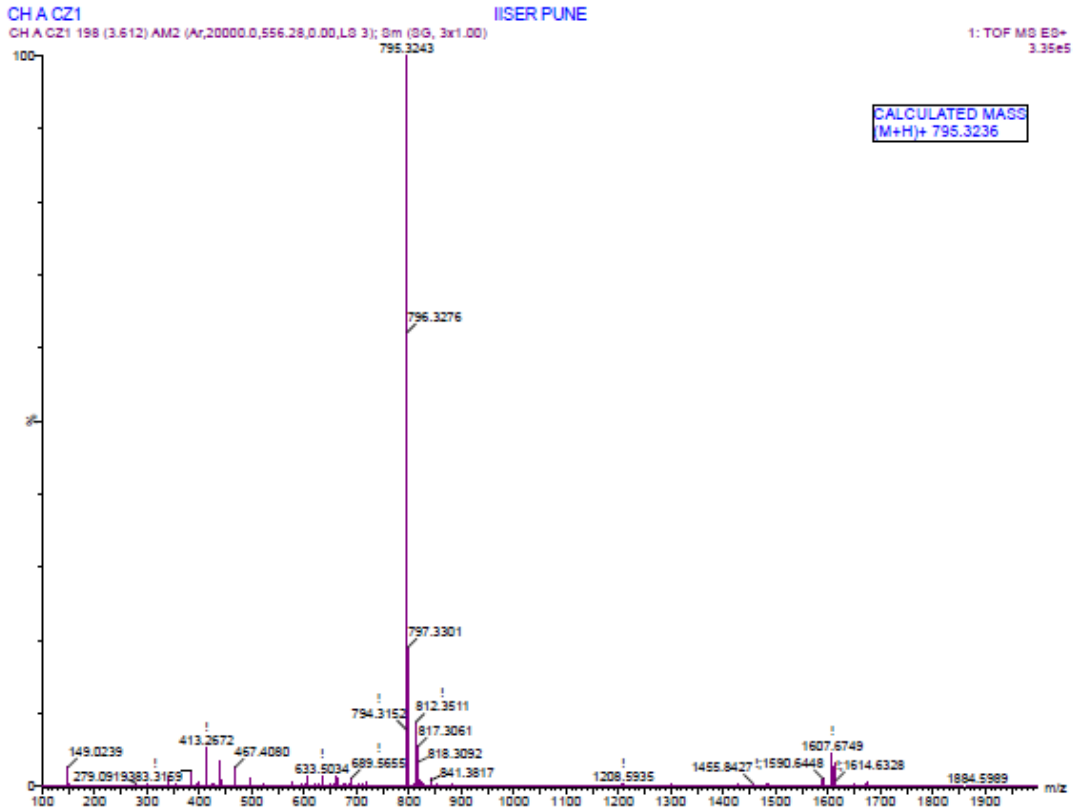

HPLC purity of (2) CZDPAMCN:

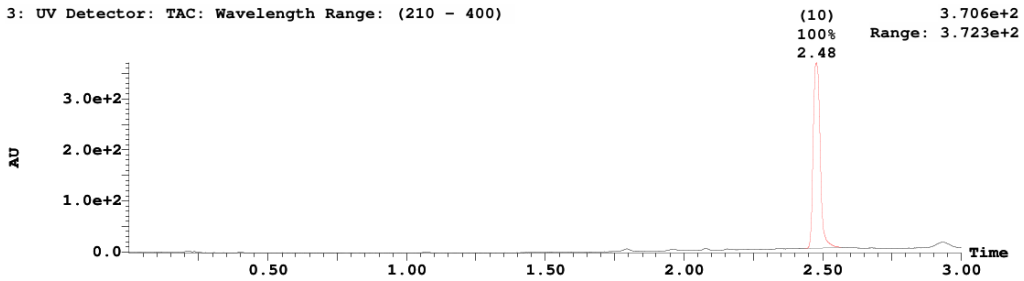

[1]H NMR of (3) TBUCZDPAMCN:

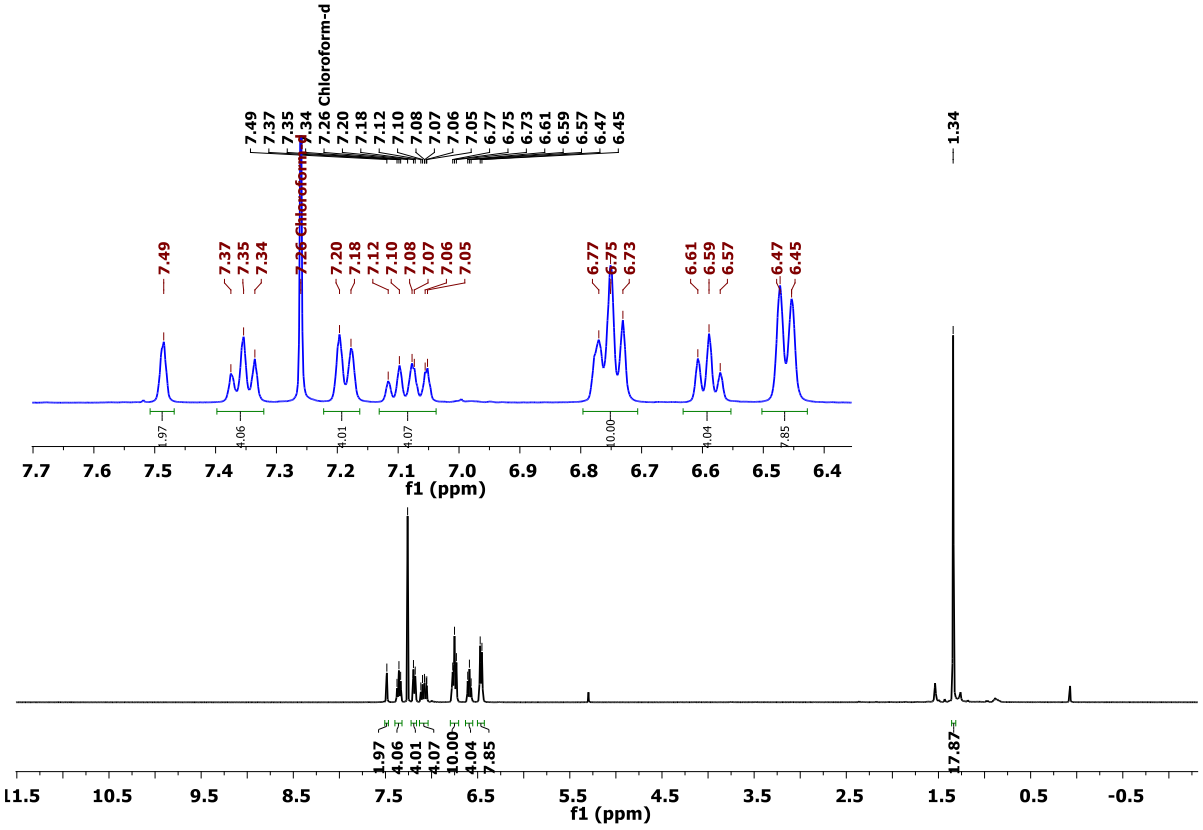

[13]C NMR of (3) TBUCZDPAMCN:

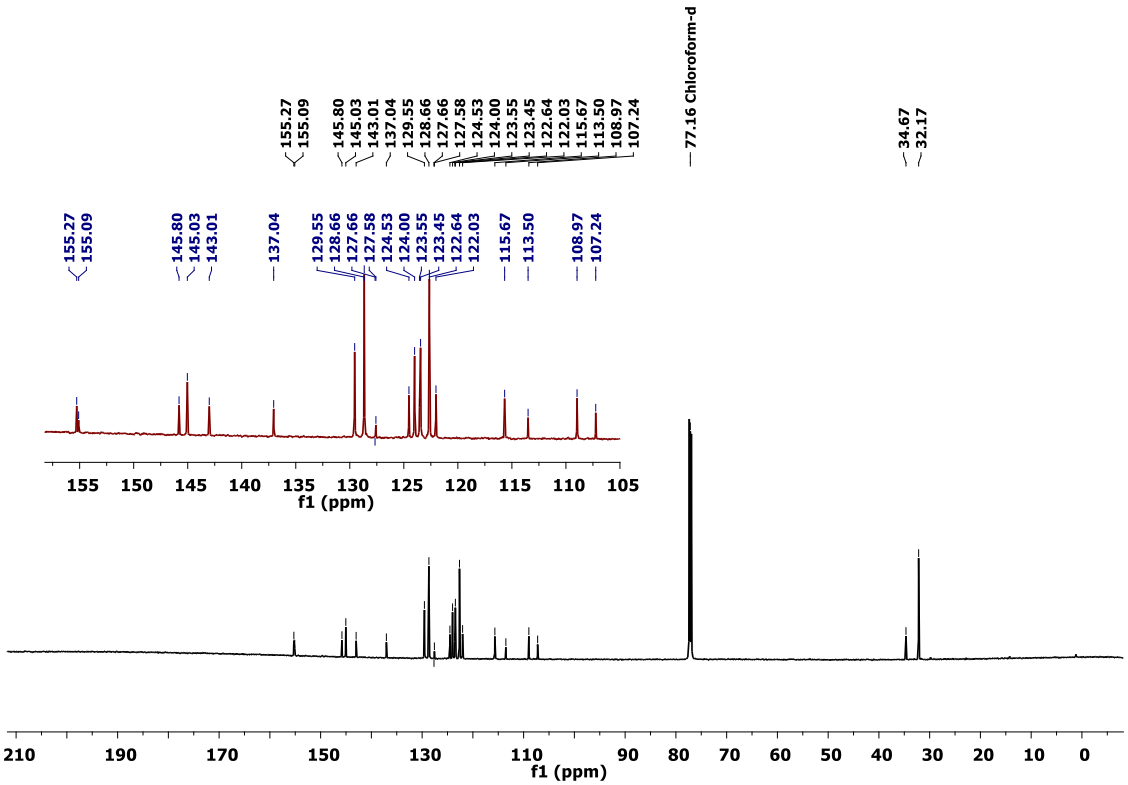

HRMS of (3) TBUCZDPAMCN:

HPLC purity of (3) TBUCZDPAMCN:

^{1}H NMR of (4) BCZDPAMCN:

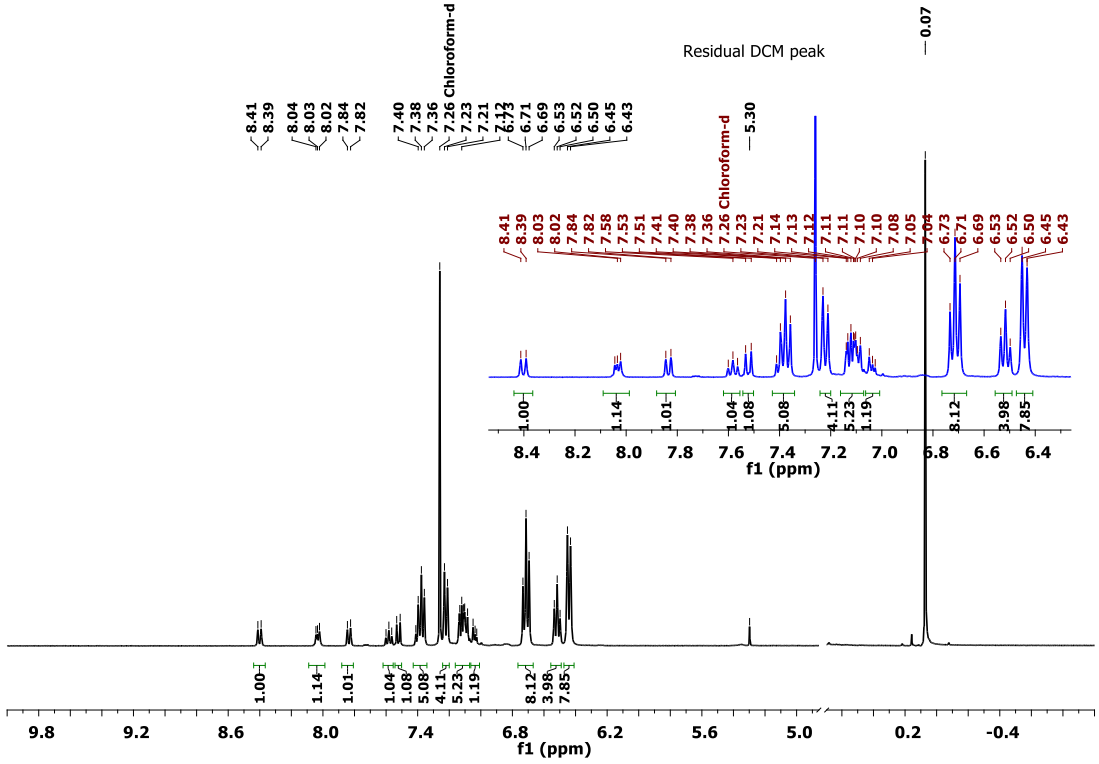

^{13}C NMR of (4) BCZDPAMCN:

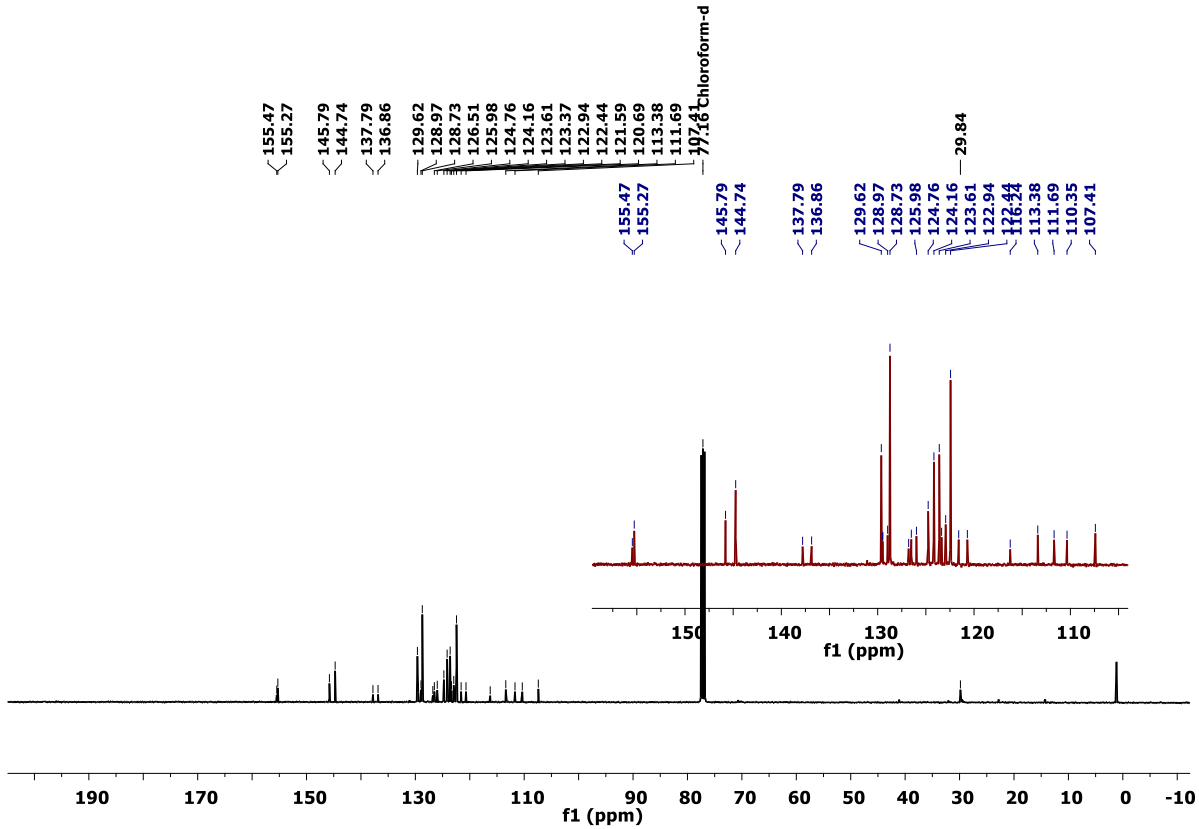

HRMS of (4) BCZDPAMCN:

HPLC purity of (3) BCZDPAMCN:

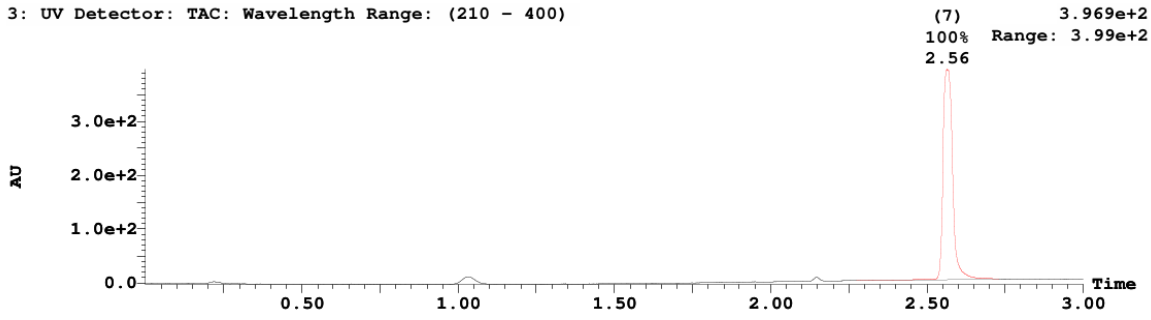

^{1}H NMR of (5) PXZDPAMCN:

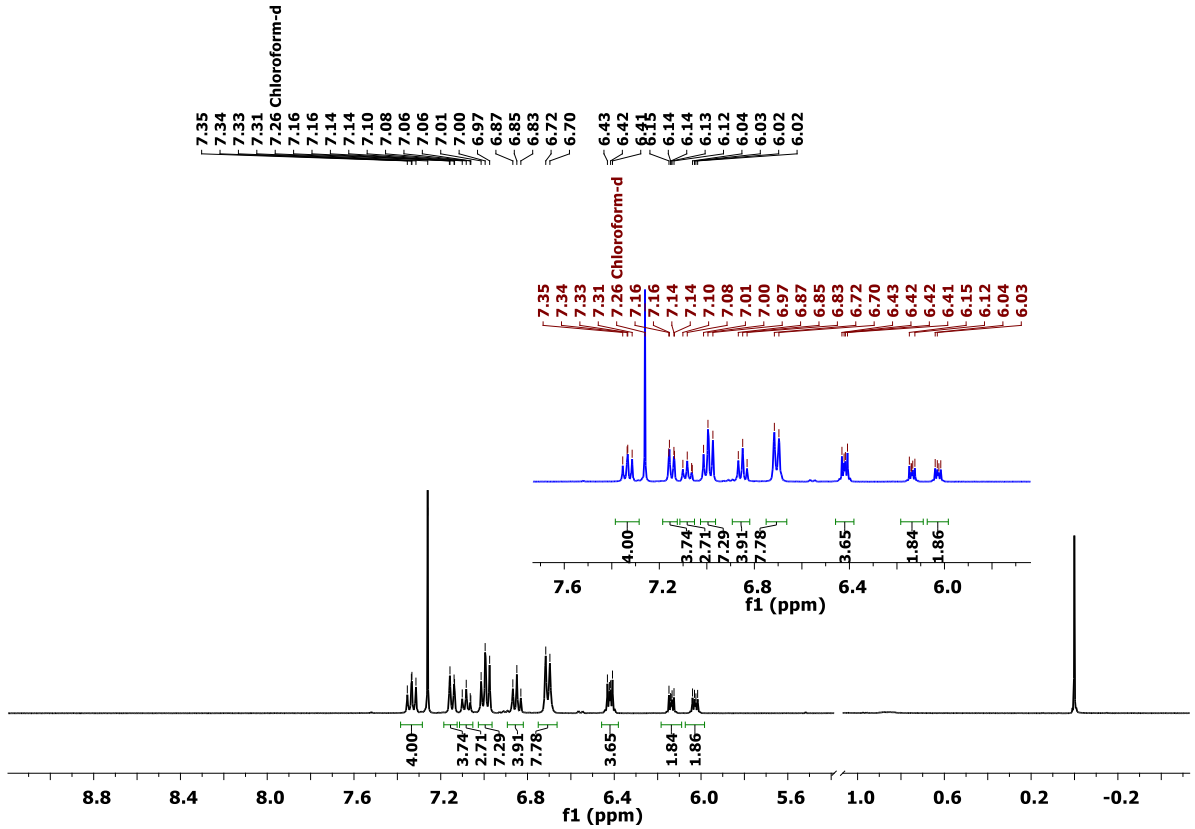

^{13}C NMR of (5) PXZDPAMCN:

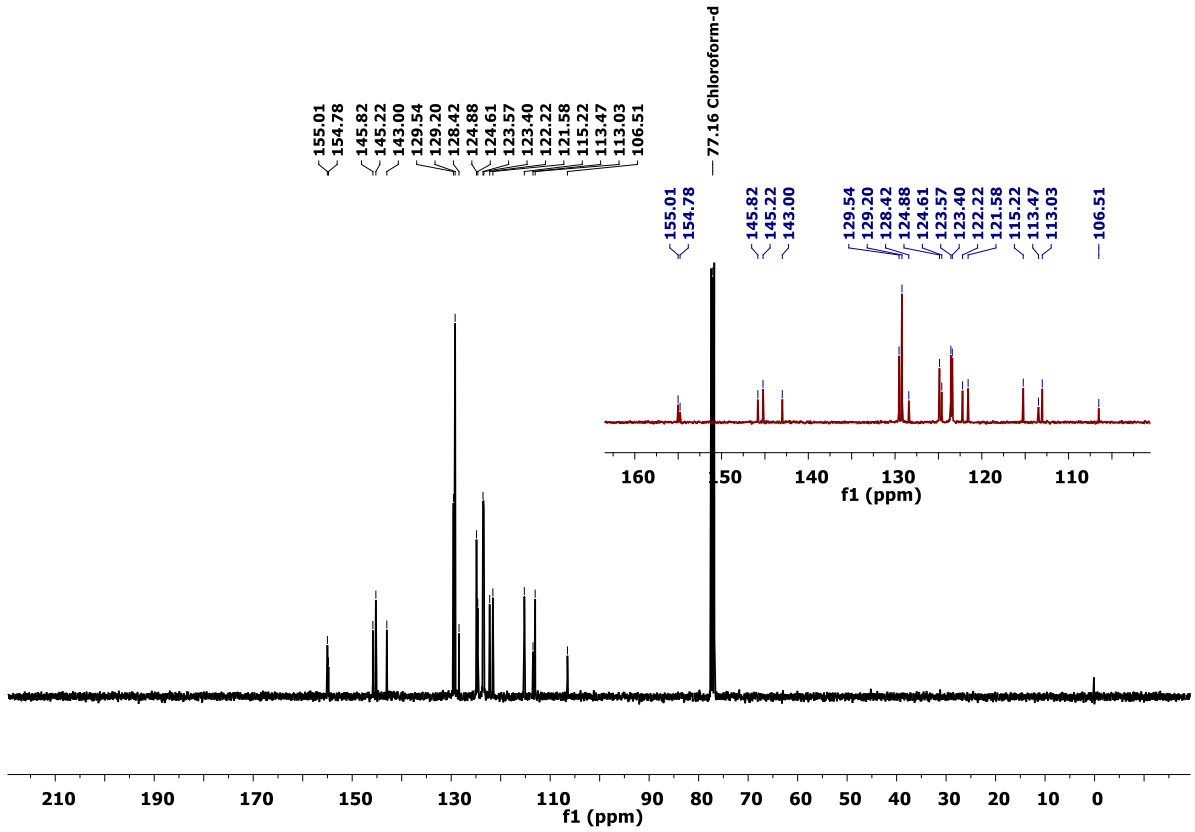

HRMS of (5) PXZDPAMCN:

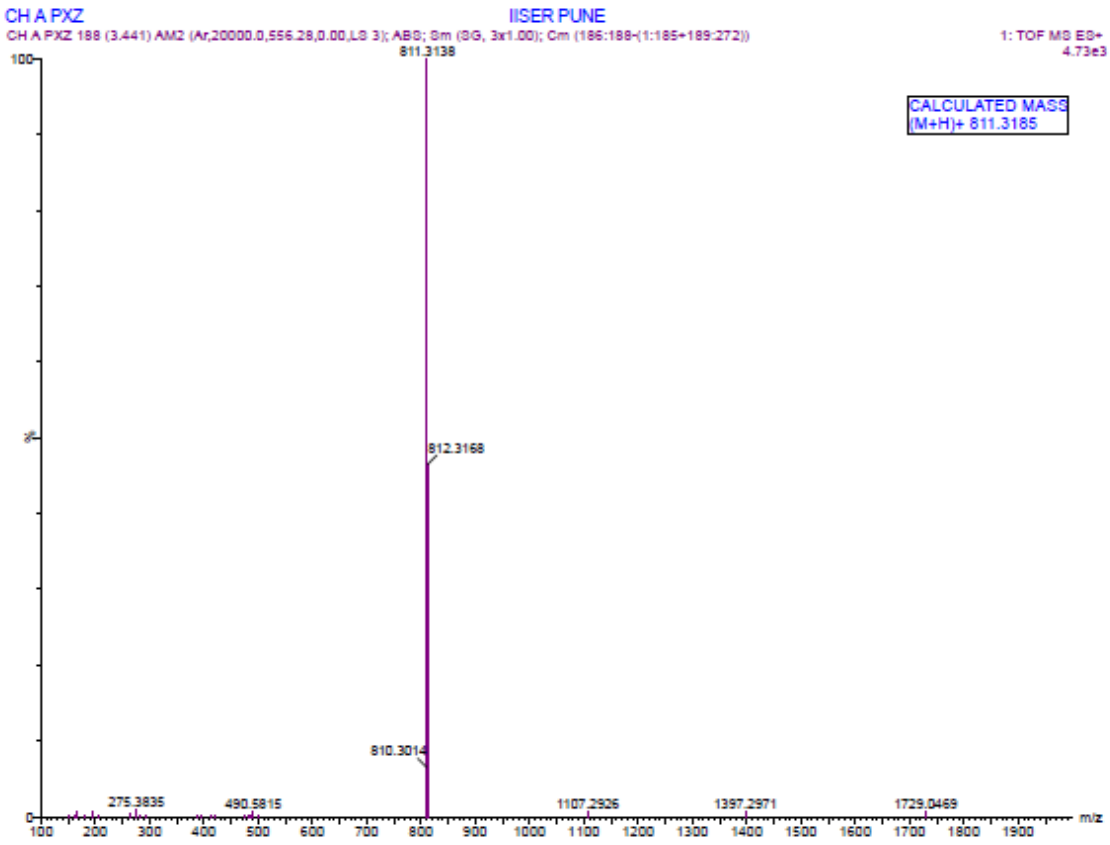

HPLC purity of (5) PXZDPAMCN:

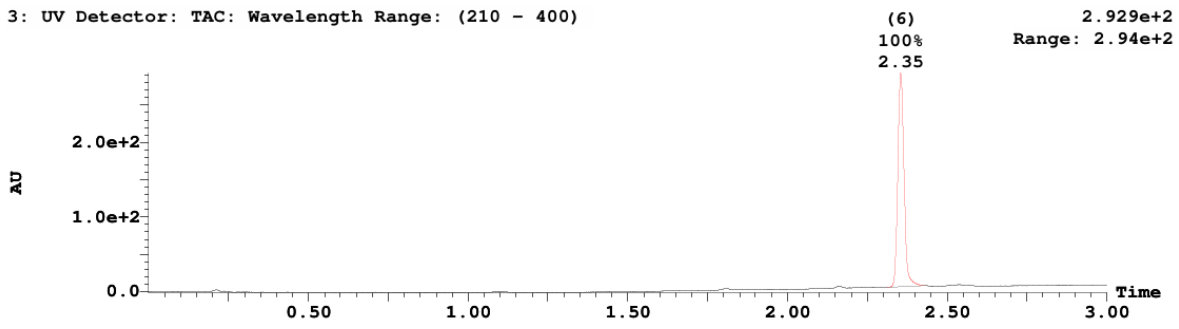

Crystallographic data

Crystallographic data for PXZDPAMCN:

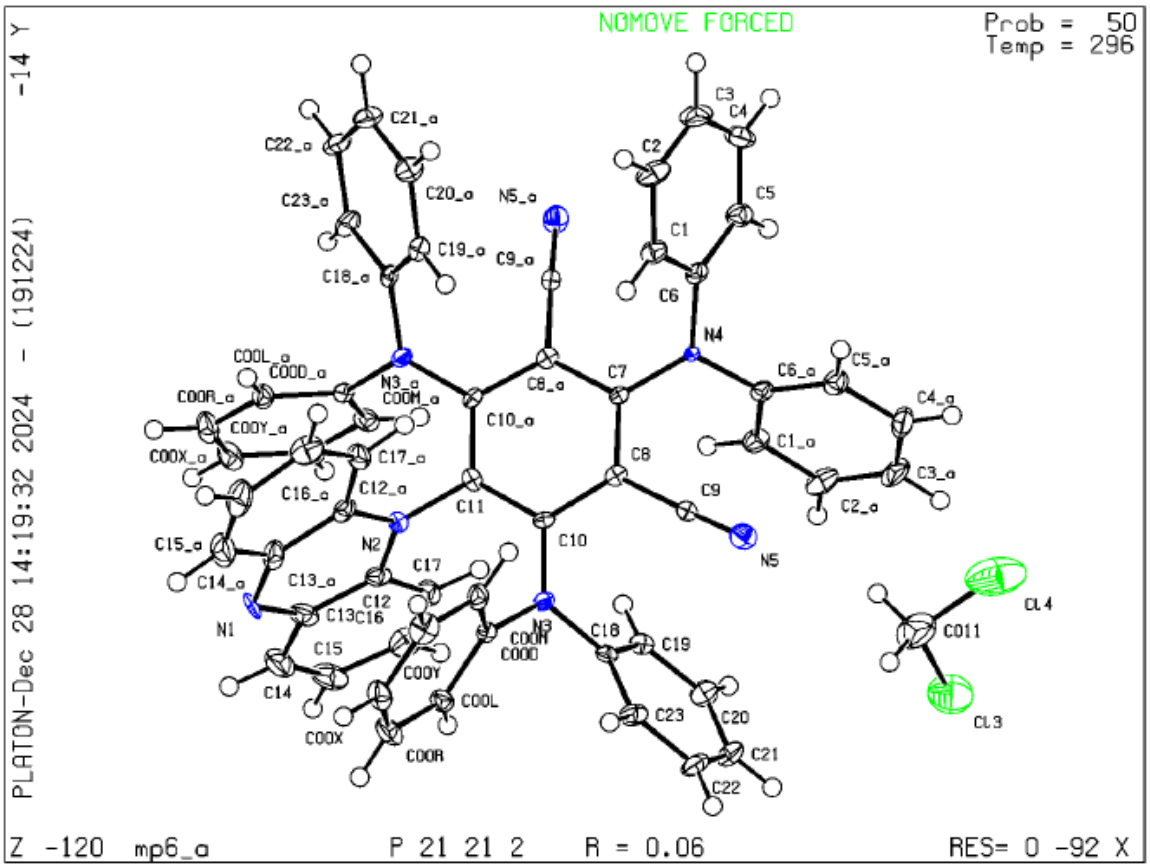

Bond precision: C-C = 0.0060 A Wavelength=0.71073

Cell: a=16.038(2) b=11.2742(13) c=13.1959(15)
alpha=90 beta=90 gamma=90

Temperature: 296 K

	Calculated	Reported
Volume	2386.0(5)	2386.0(5)
Space group	P 21 21 2	P 21 21 2
Hall group	P 2 2ab	P 2 2ab
Moiety formula	C56 H38 N7, 2(C H2 Cl2)	?
Sum formula	C58 H42 Cl4 N7	C56 H38 Cl N6 O
Mr	978.79	846.37
Dx,g cm-3	1.362	1.178
Z	2	2
Mu (mm-1)	0.297	0.125
F000	1014.0	882.0
F000'	1015.49	
h,k,lmax	21,15,17	21,15,17
Nref	5988[3366]	5958
Tmin,Tmax		
Tmin'		

Correction method= Not given

Data completeness= 1.77/0.99 Theta(max)= 28.388

R(reflections)= 0.0588(3835) wR2(reflections)= 0.1409(5958)

S = 1.017 Npar= 315

Crystallographic data for CZDPAMCN:

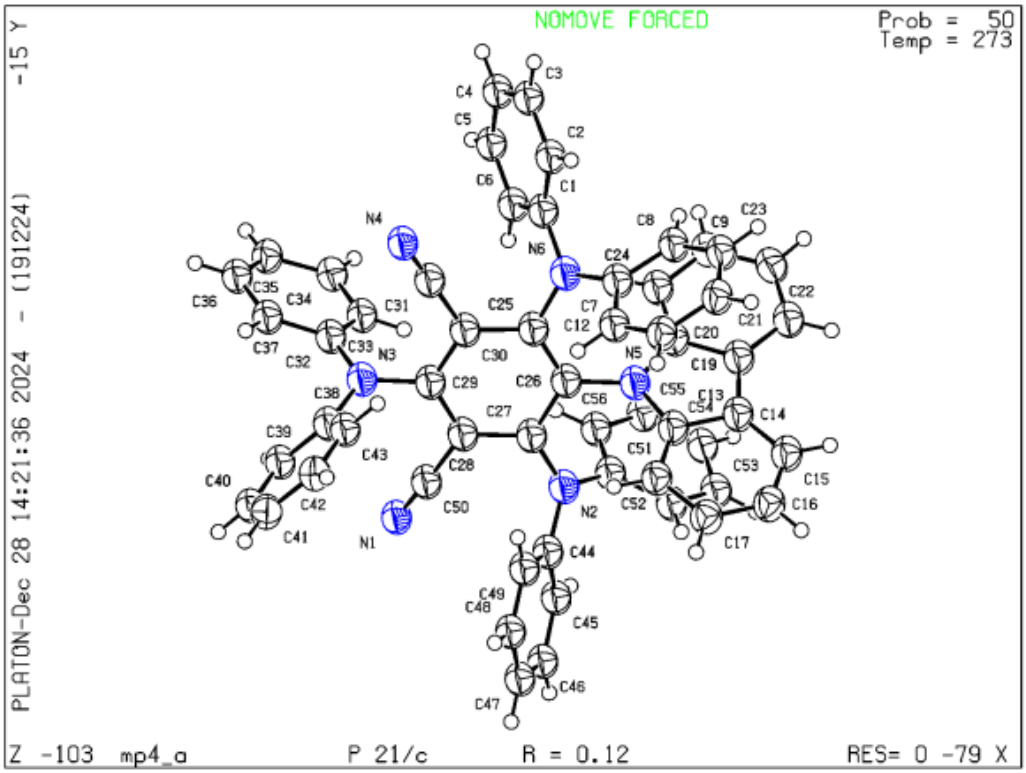

Bond precision:	C-C = 0.0158 A	Wavelength=0.71073	
Cell:	a=13.574(13)	b=13.051(12)	c=23.97(2)
	alpha=90	beta=90	gamma=90
Temperature:	273 K		

	Calculated	Reported
Volume	4246(7)	4246(7)
Space group	P 21/c	P 21/c
Hall group	-P 2ybc	-P 2ybc
Moiety formula	C56 H38 N6	?
Sum formula	C56 H38 N6	C56 H38 Cl N6
Mr	794.92	830.37
Dx,g cm-3	1.244	1.299
Z	4	4
Mu (mm-1)	0.074	0.138
F000	1664.0	1732.0
F000'	1664.57	
h,k,lmax	13,13,24	13,13,24
Nref	4881	4574
Tmin,Tmax		
Tmin'		

Correction method= Not given

Data completeness= 0.937 Theta(max)= 21.489

R(reflections)= 0.1172(1877) wR2(reflections)= 0.3952(4574)

S = 1.041 Npar= 559

Crystallographic data for TBUCZDPAMCN:

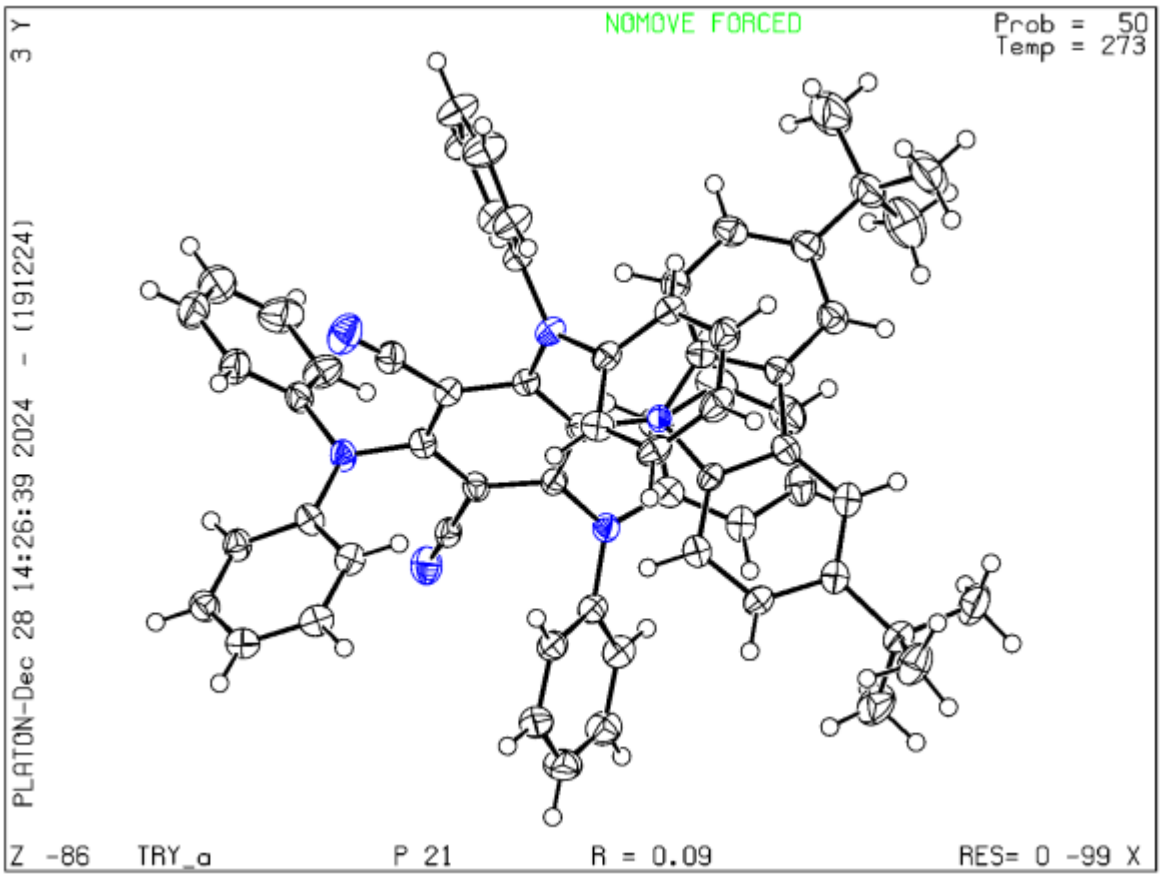

Bond precision: C-C = 0.0104 A Wavelength=0.71073

Cell: a=13.221(2) b=12.898(2) c=14.959(3)
alpha=90 beta=97.316(5) gamma=90

Temperature: 273 K

	Calculated	Reported
Volume	2530.1(7)	2530.2(7)
Space group	P 21	P 21
Hall group	P 2yb	P 2yb
Moiety formula	C64 H54 N6	?
Sum formula	C64 H54 N6	C H N O
Mr	907.13	43.03
Dx,g cm-3	1.191	2.090
Z	2	74
Mu (mm-1)	0.070	0.188
F000	960.0	1628.0
F000'	960.32	
h,k,lmax	17,17,19	17,17,19
Nref	12617[6582]	12283
Tmin,Tmax		
Tmin'		

Correction method= Not given

Data completeness= 1.87/0.97 Theta(max)= 28.327

R(reflections)= 0.0922(6947) wR2(reflections)= 0.2932(12283)

S = 1.006 Npar= 637

Crystallographic data for BCZDPAMCN:

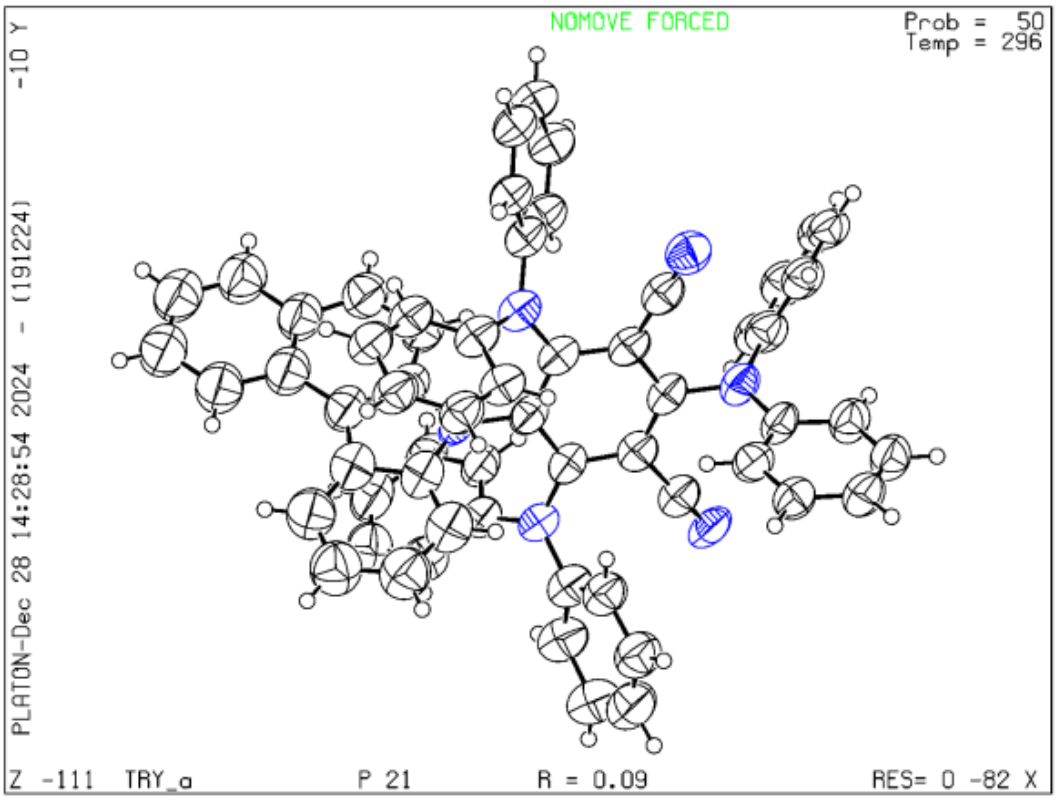

Bond precision: C-C = 0.0227 A Wavelength=0.71073

Cell: a=13.330(7) b=12.746(6) c=13.658(7)
alpha=90 beta=91.971(14) gamma=90

Temperature: 296 K

	Calculated	Reported
Volume	2319(2)	2319(2)
Space group	P 21	P 21
Hall group	P 2yb	P 2yb
Moiety formula	C60 H40 N6	?
Sum formula	C60 H40 N6	C H N
Mr	844.98	27.03
Dx,g cm-3	1.210	1.316
Z	2	68
Mu (mm-1)	0.072	0.093
F000	884.0	952.0
F000'	884.30	
h,k,lmax	13,13,14	13,13,14
Nref	5308[2806]	5298
Tmin,Tmax		
Tmin'		

Correction method= Not given

Data completeness= 1.89/1.00 Theta(max)= 21.500

R(reflections)= 0.0936(2938) wR2(reflections)= 0.2497(5298)

S = 1.081 Npar= 597

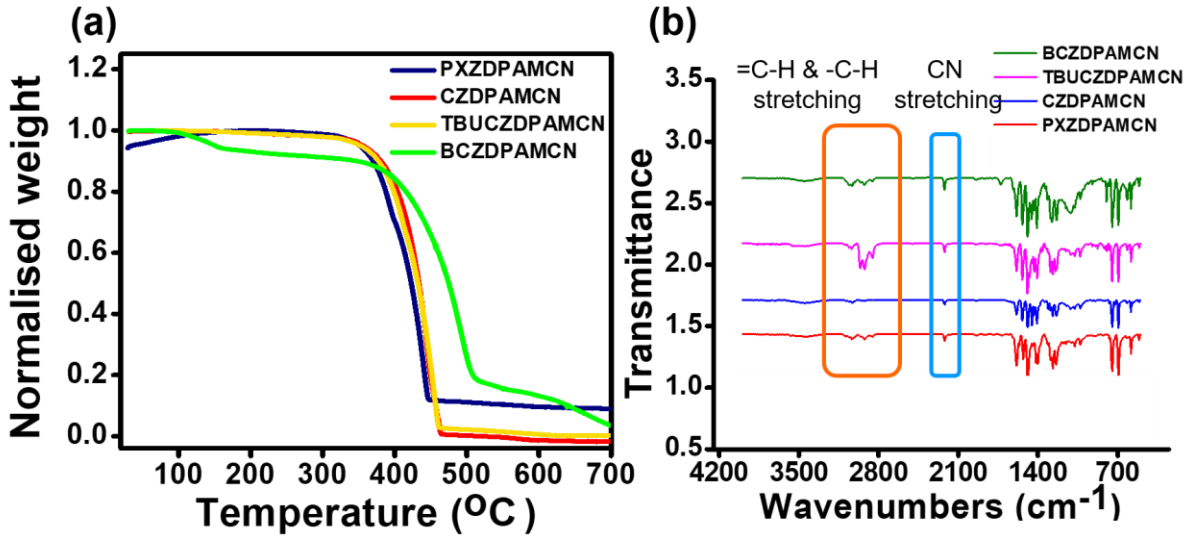

Figure A1: (a) TGA data of all four luminogens, (b) FT-IR data of all four luminogens.

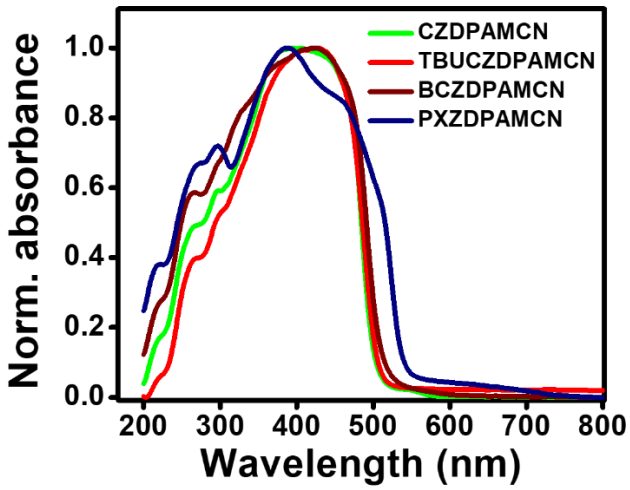

Figure A2: UV-VIS-DRS data of all four luminogens in their pristine powder form.

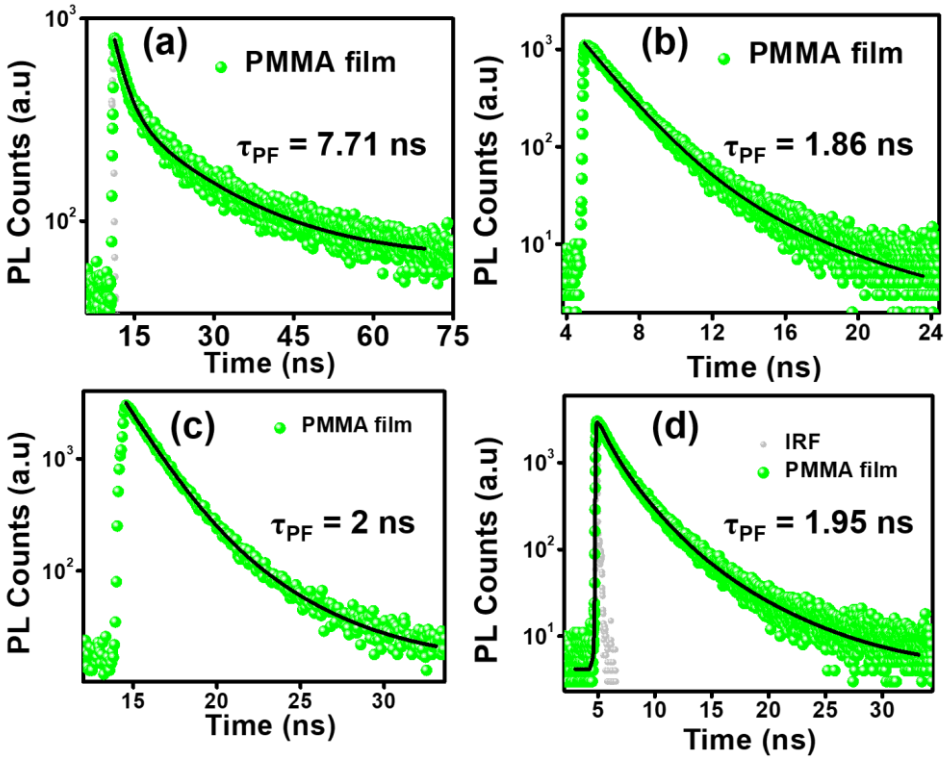

Figure A3: Prompt fluorescence (PF) lifetime of all four luminogens in 1wt% doped PMMA films (excitation wavelength=375 nm).

Table A1: Total PLQY and relative PF & DF contributions of all four luminogens in THF (10 µM conc.)

Compounds	Total PLQY	PF contribution	DF contribution
PXZDPAMCN	0.13	0.12	0.01
CZDPAMCN	0.41	0.40	0.01
TBUCZDPAMCN	0.46	0.44	0.02
BCZDPAMCN	0.51	0.49	0.02

Table A2: Total PLQY and relative PF & DF contributions of all four luminogens in their aggregates form obtained at 95% water content in THF-water binary mixtures (10 µM conc.).

Compounds	Total PLQY	PF contribution	DF contribution
PXZDPAMCN	0.68	0.22	0.46
CZDPAMCN	0.70	0.46	0.24
TBUCZDPAMCN	0.64	0.37	0.27
BCZDPAMCN	0.50	0.35	0.15

Table A3: Photophysical data of all four emitters in different states. All the quantum yields have been measured using an integrated sphere. ϕ_{PF} and ϕ_{DF} signify fractional quantum yield of prompt and delayed fluorescence, respectively.

Compound	ϕ_{PF} (sol./ film)	ϕ_{DF} (sol./ film)	k_r[a] (S_1-S_0) (s^{-1}) (sol./ film)	k_{ISC}[b] (S_1-T_1) (s^{-1}) (sol./ film)	k_{RISC}[c] (T_1-S_1) (s^{-1}) (sol./ film)
PXZDPAMCN	0.08/ 0.79	0.27/ 0.19	6.0×10^6 s^{-1}/ 1.0×10^8 s^{-1}	7.0×10^7 s^{-1}/ 2.7×10^7 s^{-1}	7.1×10^6 s^{-1}/ 2.0×10^5 s^{-1}
CZDPAMCN	0.27/ 0.69	0.15/ 0.12	1.5×10^8 s^{-1}/ 3.7×10^8 s^{-1}	4.0×10^8 s^{-1}/ 1.7×10^8 s^{-1}/	9.4×10^5 s^{-1}/ 4.2×10^3 s^{-1}/
TBUCZDPAMCN	0.20/ 0.49	0.12/ 0.42	1.0×10^8 s^{-1}/ 2.4×10^8 s^{-1}/	4.2×10^8 s^{-1}/ 2.5×10^8 s^{-1}/	1.3×10^6 s^{-1}/ 5.6×10^8 s^{-1}
BCZDPAMCN	0.28/ 0.53	0.09/ 0.11	1.4×10^8 s^{-1}/ 2.7×10^8 s^{-1}	3.6×10^8 s^{-1}/ 2.4×10^8 s^{-1}	5.8×10^5 s^{-1}/ 4.5×10^3 s^{-1}

[a] k_r (S_1-S_0) = $\phi_{PF}/\tau_{PF,}$ [b] k_{ISC} (S_1-T_1)= $(1-\phi_{PF})/\tau_{PF}$, [c] k_{RISC} (T_1-S_1)= ϕ_{DF} / ($k_{ISC}.\tau_{PF}.\tau_{DF}.\phi_{PF}$).

Note A1: Expansion on VMD and RMSD Calculations:

VMD (Visual Molecular Dynamics) is a molecular visualization and analysis software widely used for studying biomolecular systems and performing computational chemistry simulations. It offers extensive tools for trajectory analysis, including Root Mean Square Deviation (RMSD) calculations, which are essential for assessing the structural similarity between molecular geometries over time. In this work, RMSD was calculated using the built-in RMSD trajectory tool in VMD to quantify the structural deviations between two molecular geometries. The RMSD value is computed using the equation:

$$\mathrm{RMSD} = \sqrt{\frac{1}{N}\sum_{i=1}^{N}\left(\mathbf{r}_i^{\mathrm{ref}} - \mathbf{r}_i^{\mathrm{target}}\right)^2}$$

where N is the number of atoms considered, and $\mathbf{r}_i^{\text{ref}}$ and $\mathbf{r}_i^{\text{target}}$ are the atomic coordinates of the reference and target structures, respectively.

Implementation in VMD:

- The RMSD Trajectory Tool in VMD was utilized to compare the molecular conformations obtained from simulations.
- The structures were first aligned using the backbone atoms (or a specific selection of atoms), ensuring that rotational and translational differences did not affect the RMSD values.
- The trajectory was loaded into VMD, and RMSD was computed over time to evaluate conformational stability.
- Tcl scripting in VMD was also employed to automate the RMSD calculations for multiple geometries, ensuring a consistent and reproducible analysis.

Note A2: Expansion on IRF (instrument response function) in TRPL decay analysis:

The Instrument Response Function (IRF) represents the temporal resolution of the detection system in a TRPL experiment. It accounts for the broadening and distortions introduced by the finite response time of the laser pulse, detector, and electronics. Correcting for IRF is crucial for obtaining accurate decay lifetimes, especially when studying fast decay components in the sub-nanosecond range.

1. Measurement and Characterization of IRF

- The IRF is typically measured by detecting the scattered laser pulse from a non-emissive sample (e.g., a dilute colloidal solution or a scattering medium like silica powder).
- The full width at half maximum (FWHM) of the IRF determines the system's temporal resolution, which must be considered when extracting decay lifetimes.
- In streak camera measurements, the IRF width is influenced by the temporal resolution of the streak tube and optical system.
- In Time-Correlated Single Photon Counting (TCSPC), the IRF shape is affected by the timing jitter of the detector and electronics.

2. Deconvolution of IRF in TRPL Analysis

Since the observed TRPL decay is a convolution of the actual decay function and the IRF, a numerical deconvolution method (such as the reconvolution fitting approach) is used to retrieve the intrinsic lifetime. This is performed using software tools like FluoFit, OriginPro, or custom Python/Matlab scripts that fit the decay to an exponential function convolved with the measured IRF.

The observed signal I(t) is expressed as:

$$I(t) = \int_0^t IRF(t') \cdot e^{-t'/\tau} dt'$$

Where τ is the true photoluminescence lifetime.

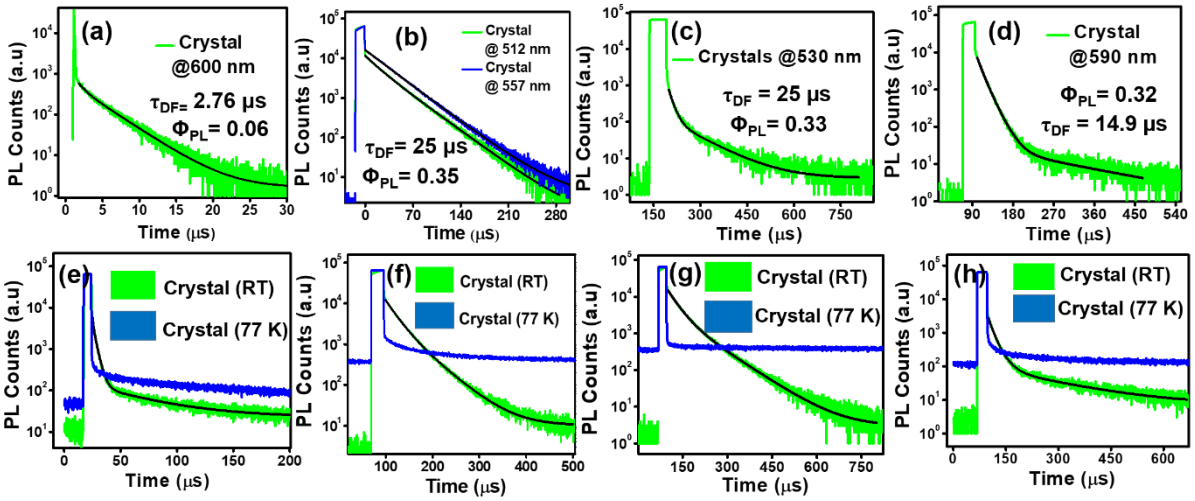

Figure A4: Delayed fluorescence lifetime in molecular crystals along with their PLQY of (a) PXZDPAMCN, (b) CZDPAMCN, (c) TBUCZDPAMCN, and (d) BCZDPAMCN. Delayed fluorescence lifetime variation at RT and 77 K for (e) PXZDPAMCN, (f) CZDPAMCN, (g) TBUCZDPAMCN, and (h) BCZDPAMCN.

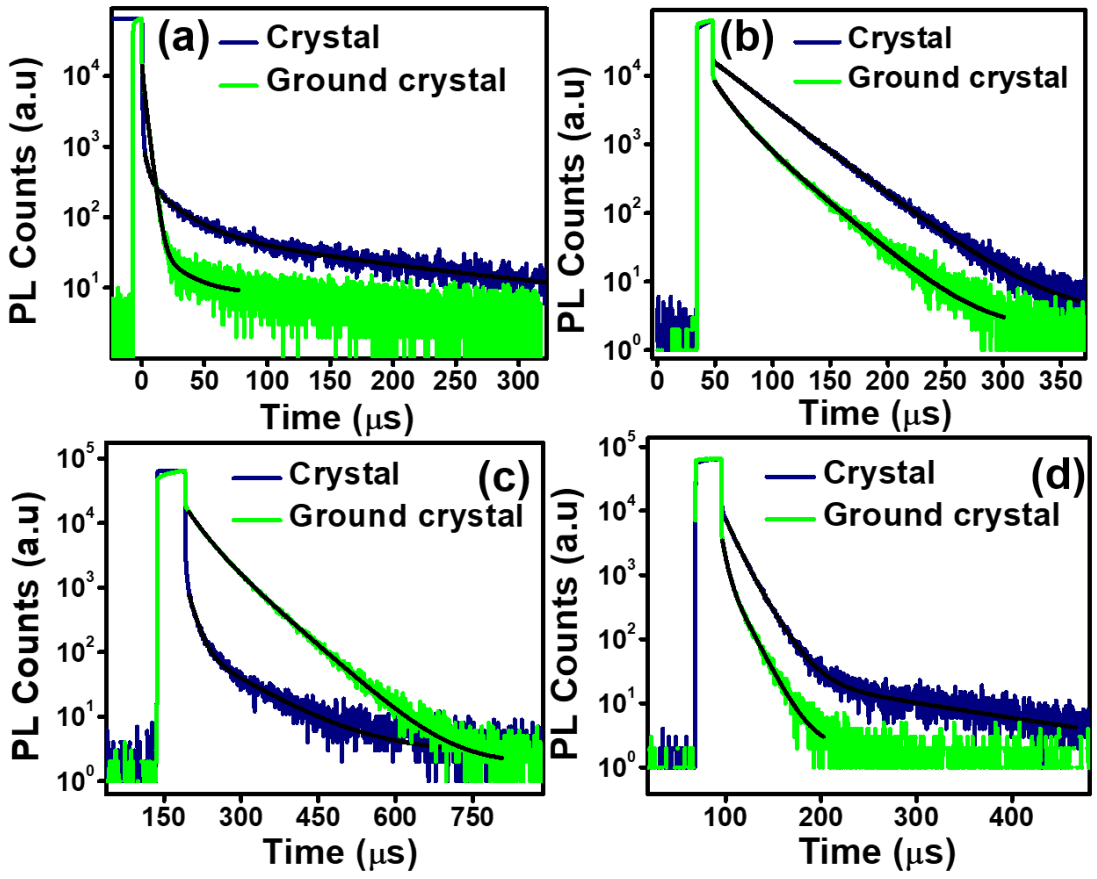

Figure A5: Variation of delayed fluorescence lifetime upon mechanical grinding of the molecular crystals for (a) PXZDPAMCN, (b) CZDPAMCN, (c) TBUCZDPAMCN, and (d) BCZDPAMCN.

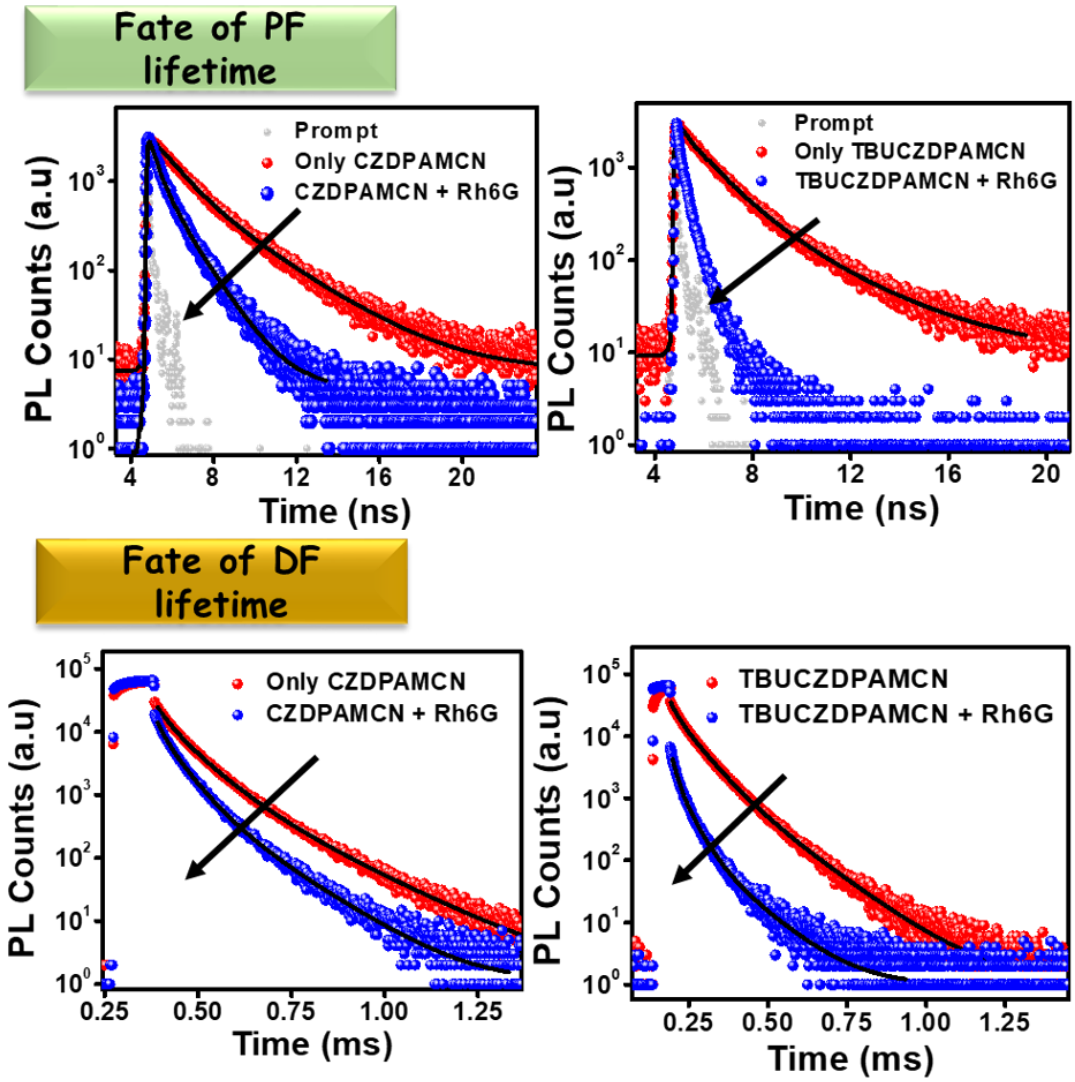

Figure A6: Fate of prompt fluorescence and delayed fluorescence of the TADF assistant dopant upon doping with 1wt% of Rh6G in PMMA host.

5.10 References:

(1) Xia, S. C.; Kwong, R. C.; Adamovich, V. I.; Weaver, M. S.; Brown, J. J. OLED Device Operational Lifetime: Insights and Challenges. *2007 IEEE International Reliability Physics Symposium Proceedings. 45th Annual*, April 15−19, 2007; IEEE: pp 253−257.

(2) Köhler, A.; Bässler, H. Electronic Processes in Organic Semiconductors: An Introduction; John Wiley & Sons, 2015.

(3) J. H. Burroughes, D. D. C. Bradley, A. R. Brown, R. N. Marks, K. Mackay, R. H. Friend, P. L. Burns and A. B. Holmes, *Nature*, 1990, **347**, 539.

(4) R. H. Friend, R. W. Gymer, A. B. Holmes, J. H. Burroughes, R. N. Marks, C. Taliani, D. D. C. Bradley, D. A. Dos Santos, J. L. Bredas, M. Logdlund and W. R. Salaneck, *Nature*, 1999, **397**, 121–128.

(5) C.W. Tang and S. A. VanSlyke, *Appl. Phys. Lett.*, 1987, **51**, 913–915.

(6) A. Misra, P. Kumar, M. N. Kamalasanan and S. Chandra, *Semicond. Sci. Technol.*, 2006, **21**, R35–R47.

(7) A. R. Brown, K. Pichler, N. C. Greenham, D. D. C. Bradley, R. H. Friend and A. B. Holmes, *Chem. Phys. Lett.*, 1993, **210**, 61 —66.

(8) M. A. Baldo, D. F. O'Brien, M. E. Thompson and S. R. Forrest, *Phys. Rev. B: Condens. Matter Mater. Phys.*, 1999, **60**, 14422–14428.

(9) J.-H. Kim, F. Deng, F. N. Castellano and J. Kim, *Chem. Mater.*, 2012, **24**, 2250–2252.

(10) A. Monguzzi, R. Tubino, S. Hoseinkhani, M. Campione and F. Meinardi, *Phys. Chem. Chem. Phys.*, 2012, **14**, 4322.

(11) R. S. Khnayzer, J. Blumhoff, J. A. Harrington, A. Haefele, F. Deng and F. N. Castellano, *Chem. Commun.*, 2012, **48**, 209–211.

(12) Y. G. Ma, H. Y. Zhang, J. C. Shen and C. M. Che, *Synth. Met.*, 1998, **94**, 245–248.

(13) M. A. Baldo, D. F. O'Brien, Y. You, A. Shoustikov, S. Sibley, M. E. Thompson and S. R. Forrest, *Nature*, 1998, **395**, 151–154.

(14) A. Endo, K. Sato, K. Yoshimura, T. Kai, A. Kawada, H. Miyazaki and C. Adachi, *Appl. Phys. Lett.*, 2011, **98**, 083302.

(15) Q. S. Zhang, B. Li, S. P. Huang, H. Nomura, H. Tanaka and C. Adachi, *Nat. Photonics*, 2014, **8**, 326–332.

(16) S. Hirata, Y. Sakai, K. Masui, H. Tanaka, S. Y. Lee, H. Nomura, N. Nakamura, M. Yasumatsu, H. Nakanotani, Q. S. Zhang, K. Shizu, H. Miyazaki and C. Adachi, *Nat. Mater.*, 2015, **14**, 330–336.

(17) H. Uoyama, K. Goushi, K. Shizu, H. Nomura and C. Adachi, *Nature*, 2012, **492**, 234–238.

(18) K. Suzuki, S. Kubo, K. Shizu, T. Fukushima, A. Wakamiya, Y. Murata, C. Adachi and H. Kaji, *Angew. Chem., Int. Ed.*, 2015, **54**, 15231–15235.

(19) Y. Tao, K. Yuan, T. Chen, P. Xu, H. Li, R. Chen, C. Zheng, L. Zhang and W. Huang, *Adv. Mater.*, 2014, **26**, 7931–7958.

(20) Y. Im, M. Kim, Y. J. Cho, J.-A. Seo, K. S. Yook and J. Y. Lee, *Chem. Mater.*, 2017, **29**, 1946–1963.

(21) M. Y. Wong and E. Zysman-Colman, *Adv. Mater.*, 2017, **29**, 1605444.

(22) B. Wex and B. R. Kaafarani, *J. Mater. Chem. C*, 2017, **5**, 8622–8653.

(23) P. K. Samanta, D. Kim, V. Coropceanu and J.-L. Bredas, *J. Am. Chem. Soc.*, 2017, **139**, 4042–4051.

(24) S. Li, J. Chen, Y. Wei, J. De, H. Geng, Q. Liao, R. Chen and H. Fu, *Angew. Chem., Int. Ed.*, 2022, **61**, e202209211.

(25) J. D. Luo, Z. L. Xie, J. W. Y. Lam, L. Cheng, H. Y. Chen, C. F. Qiu, H. S. Kwok, X. W. Zhan, Y. Q. Liu, D. B. Zhu and B. Z. Tang, *Chem. Commun.*, 2001, 1740–1741.

(26) J. Mei, N. L. C. Leung, R. T. K. Kwok, J. W. Y. Lam and B. Z. Tang, *Chem. Rev.*, 2015, **115**, 11718–11940.

(27) M. Kang, Z. Zhang, N. Song, M. Li, P. Sun, X. Chen, D. Wang and B. Z. Tang, *Aggregate*, 2020, **1**, 80–106.

(28) D. Wang, H. Su, R. T. K. Kwok, X. Hu, H. Zou, Q. Luo, M. M. S. Lee, W. Xu, J. W. Y. Lam and B. Z. Tang, *Chem. Sci.*, 2018, **9**, 3685–3693.

(29) Q. Hu, M. Gao, G. Feng and B. Liu, *Angew. Chem., Int. Ed.*, 2014, **53**, 14225–14229.

(30) M. Chen, X. Hu, J. Liu, B. Li, N. L. C. Leung, L. Viglianti, T. S. Cheung, H. H. Y. Sung, R. T. K. Kwok, I. D. Williams, A. Qin, J. W. Y. Lam and B. Z. Tang, *Chem. Sci.*, 2018, **9**, 7829– 7834.

(31) M. Yasunori, Y. Yudai, O. Takuya, I. Kenta, N. Akitsugu, O. Eisuke, S. Masaki, M. Kiyoshi, O. Ken, N. Hiroyoshi and I. Hiroshi, *J. Mater. Chem. C*, 2022, **10**, 4607-4613.

(32) S. Qi, S. Kim, V. N. Nguyen, Y. Kim, G. Niu, G. Kim, S. J. Kim, S. Park and J. Yoon, *ACS Appl. Mater. Interfaces*, 2020, **12**, 51293–51301.

(33) A. Chatterjee, S. Narayanan, S. Thorat, A. J. Malik, M. D. Ambhore, A. Narayanan, A. K. Sihag, S.B. Sukumaran, M. Lahiri and P. Hazra, *Chem. Commun.*, 2025, Advance Article.

(34) G. M. Sheldrick, A Short History of {\it SHELX}. *Acta Crystallogr. Sect. A* 2008, **64**, 112–122.

(35) G. M. Sheldrick, Crystal structure refinement with SHELXL. *Acta Crystallogr., Sect. A: Found. Adv.* 2015, **71**, 3−8.

(36) Frisch, M. J.; Trucks, G. W.; Schlegel, H. B.; Scuseria, G. E.; Robb, M. A.; Cheeseman, J. R.; Scalmani, G.; Barone, V.; Mennucci, B.; Petersson, G. A.; et al. Gaussian 09, Revision C.01; Gaussian Inc.: Wallingford, CT, 2009.

(37) A. D. Becke, Phys. Rev. A 1988, **38**, 3098–3100.

(38) C. Lee, W. Yang, R. G. Parr, Phys. Rev. B 1988, **37**, 785–789.

(39) S. V. K. Isukapalli, R. S. Lekshmi, P. K. Samanta, S. R. Vennapusa, J. Chem. Phys. 2020, **153**, 124301.

(40) X. Gao, S. Bai, D. Fazzi, T. Niehaus, M. Barbatti, W. Thiel, J. Chem. Theory Comput. 2017, **13**, 515–524.

(41) T. Vreven, K. Morokuma, O. Farkas, H. B. Schlegel, M. J. Frisch, *J. Comput. Chem*. 2003, **24**, 760-769.

(42) H. Lin, D. G. Truhlar, *Theor. Chem. Acc*. 2007, **117**, 185-199.

(43) J. Gibson, A. P. Monkman and T. J. Penfold, *ChemPhysChem*, 2016, **17**, 2956.

(44) R. J. Holmes, S. R. Forrest, Y. J. Tung, R. C. Kwong, J. J. Brown, S. Garon and M. E. Thompson, *Appl. Phys. Lett.*, 2003, **82**, 2422.

(45) M. Saigo, K. Miyata, S. i. Tanaka, H. Nakanotani, C. Adachi and K. Onda, *J. Phys. Chem. Lett.*, 2019, **10**, 2475–2480.

(46) C. Gao, W. W.-H. Wong, Z. Qin, S.-C. Lo, E. B. Namdas, H. Dong and W. Hu, *Adv. Mater*., 2021, **33**, 2100704.

(47) C. Murawski, K. Leo and M. C. Gather, Efficiency Roll-Off in Organic Light-Emitting Diodes, *Adv. Mater.*, 2013, **25**, 6801–6827.

Thesis Summary and Future Outlook

This thesis focuses on the design, development, and optimization of multifunctional organic luminogens to overcome significant challenges in optoelectronic and sensory applications. It addresses the issue of aggregation-caused quenching (ACQ) in organic emitters, a major obstacle to efficient solid-state luminescence, by leveraging advanced mechanisms such as thermally activated delayed fluorescence (TADF), room-temperature phosphorescence (RTP), and aggregation-induced emission (AIE). Through systematic molecular design and structural modifications, the study provides a framework for developing efficient, versatile, and high-performing luminogens. A comprehensive introduction is presented to the principles of light emission in organic materials, focusing on the interplay between molecular aggregation and photophysical pathways. The thesis explores the importance of triplet harvesting mechanisms, particularly TADF, and their role in enhancing solid-state luminescence for applications like organic light-emitting diodes (OLEDs). It also highlights alternative strategies, including RTP and hyperfluorescence, to achieve efficient exciton utilization. The research develops novel AIE-active luminogens through molecular modifications that transform ACQ-dominated systems into highly functional materials. By engineering the acceptor core and linker groups, these luminogens are designed to exhibit multifunctional properties such as AIE, RTP, and mechanochromism. These findings underscore the transformative potential of structural engineering in optimizing luminescent behavior. A detailed investigation is conducted into the role of regioisomeric donor-acceptor systems in tuning TADF, mechanochromism, and second harmonic generation (SHG) properties. The study reveals how molecular geometry significantly impacts photophysical behavior, with notable differences in TADF efficiency, spin-orbit coupling, and reverse intersystem crossing rates. These insights contribute to the understanding of how subtle changes in molecular structure can lead to substantial improvements in functionality. The thesis also examines the factors governing aggregation-induced delayed fluorescence (AIDF), focusing on the role of energy gap reductions (ΔE_{ST}) and charge-transfer characteristics. These emitters demonstrate enhanced luminescence efficiency and potential for advanced applications, including two-photon cell imaging and anti-Stokes shifted photoluminescence. Finally, the role of donor unit engineering in optimizing TADF performance is explored in depth. Luminogens based on phenoxazine, carbazole, and their derivatives are synthesized to investigate the effects of donor units on RISC rates, emission lifetimes, and efficiency. These materials are shown to achieve remarkable TADF efficiencies and external quantum efficiencies in OLED devices, demonstrating their practical

applicability in optoelectronics. Overall, this thesis makes significant contributions to the understanding and application of organic luminogens by addressing ACQ and achieving efficient triplet harvesting. It provides valuable insights into molecular design principles, photophysical mechanisms, and functional optimization. The findings lay the groundwork for developing solution-processable, multifunctional materials for next-generation technologies in optoelectronics, bioimaging, and sensory devices.

The findings of this thesis provide a robust foundation for advancing multifunctional

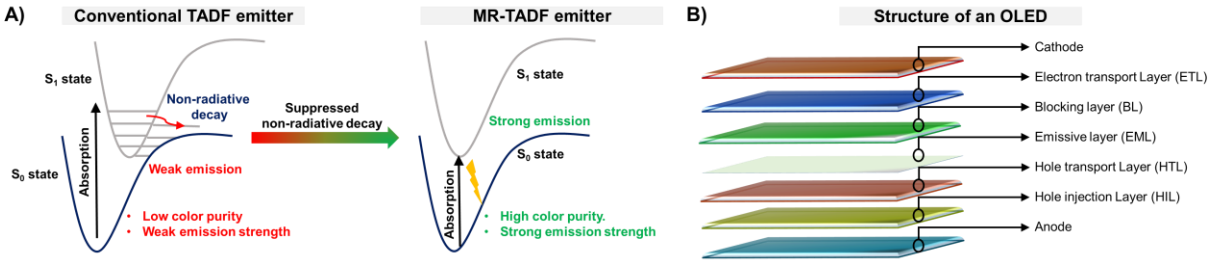

Figure 1: (A) Potential energy surface of conventional TADF emitters vs MRTADF emitters, showing the advantages of MR-TADF emitters. (B) different layers of an OLED device.

luminogens, particularly in addressing challenges associated with triplet harvesting efficiency and solid-state luminescence. However, a significant area for further exploration lies in enhancing optical color purity, an essential criterion for practical applications in lighting and display technologies. Conventional triplet harvesting methods, such as thermally activated delayed fluorescence (TADF) and room-temperature phosphorescence (RTP), often produce a mixture of wavelengths, leading to compromised color fidelity. While color filters can partially address this issue, they incur substantial energy losses, making them less viable for efficient real-world applications. To overcome these limitations, multiple resonance TADF (MR-TADF) emitters have emerged as promising alternatives due to their intrinsic narrow-band emission and reduced Stokes shifts. Nevertheless, the planar structures typical of MR-TADF emitters often enhance electron-vibration coupling (EVC) during aggregation, resulting in emission quenching. Future research should focus on functional group engineering to introduce twists in the molecular geometry of MR-TADF emitters.[1-2] This approach can mitigate aggregation-induced quenching, enabling narrow-band emission and enhanced efficiencies in solid-state environments. Building on these insights, the proposed research aims to design and synthesize two distinct sets of TADF emitters: (1) twisted MR-TADF emitters for efficient narrow-band emission and (2) twisted conventional TADF emitters for broad-band emission. Comparative studies on their photophysical properties, particularly reverse intersystem crossing (kRISC) rates, can deepen our understanding of their performance and applicability.

Two rapidly advancing research areas are identified for exploration:

1. Organic Solid-State Lasing (OSSLs): Twisted MR-TADF emitters are inherently suited for OSSLs[2] due to their high emission transition dipole moments (μ_{S1-S0}) and minimal Stokes shifts, which facilitate efficient population inversion between singlet and ground states via rapid reverse intersystem crossing (RISC). These properties are critical for achieving efficient lasing with reduced thresholds and amplified optical gain. Developing a structure-property relationship for these emitters can pave the way for breakthroughs in solid-state lasing technologies.

2. Solid-State Anti-Stokes Shifted Photoluminescence (ASPL): The potential of MR-TADF emitters for hot-band absorption (HBA)-based ASPL emission[3] remains largely untapped, particularly in the solid state. Given their minimal structural reorganization in the excited state, MR-TADF emitters exhibit high Franck-Condon factors, making them ideal candidates for ASPL. Expanding research in this area could unlock new avenues for solid-state photonics.

Additionally, the longer lifetimes of TADF emitters, typically in the microsecond regime, present opportunities for luminescence lifetime imaging microscopy (LLIM). This capability can effectively eliminate short-lived cellular autofluorescence signals, significantly enhancing the precision and accuracy of cellular imaging. In conclusion, the future work outlined here highlights critical areas for expanding the utility of TADF and MR-TADF emitters. By addressing current limitations in optical color purity, solid-state lasing, and ASPL, this research holds the potential to drive significant advancements in solid-state photonics, bioimaging, and next-generation lighting technologies.

References: [1] Hatakeyama et al., *Adv. Mater.*, Vol. 28, No. 14, 2777–2781, (2016). [2] Li et al., *Angew. Chem. Int. Ed.*, Vol. 61, No. 39, e202209211, (2022). [3] Kohata et al., *Angew. Chem. Int. Ed.*, Vol. 62, No. 44, e202312326, (2023).

Rights and Permissions

1. Chapter 1 is partially adapted from **a)** Samanta, P. K.; Kim, D.; Coropceanu, V.; Brédas, J.-L. Up-Conversion Intersystem Crossing Rates in Organic Emitters for Thermally Activated Delayed Fluorescence: Impact of the Nature of Singlet vs Triplet Excited States. *J. Am. Chem. Soc.* **2017**, *139* (11), **b)** Chen, X.-K.; Kim, D.; Brédas, J.-L. Thermally Activated Delayed Fluorescence (TADF) Path toward Efficient Electroluminescence in Purely Organic Materials: Molecular Level Insight. *Acc. Chem. Res.* **2018**, *51* (9), 2215–2224, **c)** Mei, J.; Leung, N. L. C.; Kwok, R. T. K.; Lam, J. W. Y.; Tang, B. Z. Aggregation-Induced Emission: Together We Shine, United We Soar! *Chem. Rev.* **2015**, *115* (21), 11718–11940, **d)** Mei, J.; Hong, Y.; Lam, J. W. Y.; Qin, A.; Tang, Y.; Tang, B. Z. Aggregation-Induced Emission: The Whole Is More Brilliant than the Parts. *Adv. Mater.* **2014**, *26* (31), 5429–5479, **e)** Uoyama, H.; Goushi, K.; Shizu, K.; Nomura, H.; Adachi, C. Highly Efficient Organic Light-Emitting Diodes from Delayed Fluorescence. *Nature* **2012**, *492* (7428), 234–238, **f)** Forni, A.; Lucenti, E.; Botta, C.; Cariati, E. Metal Free Room Temperature Phosphorescence from Molecular Self-Interactions in the Solid State. *J. Mater. Chem. C* **2018**, *6* (17), 4603–4626.

a) Copyright 2017: American Chemical Society

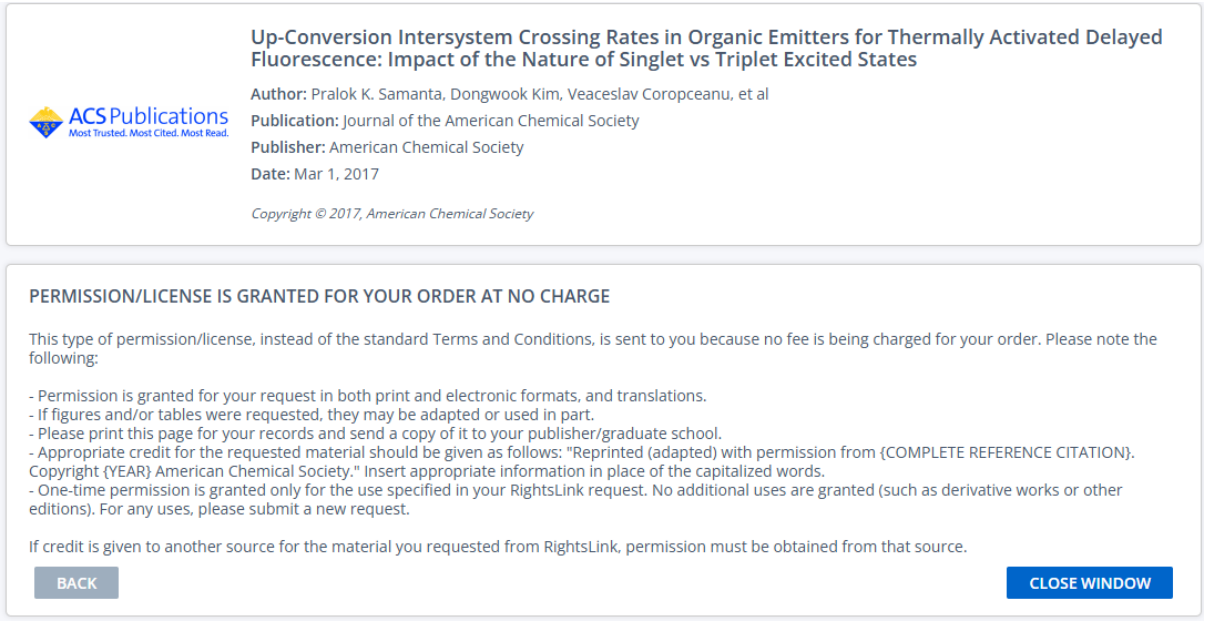

b) Copyright 2018: American Chemical Society

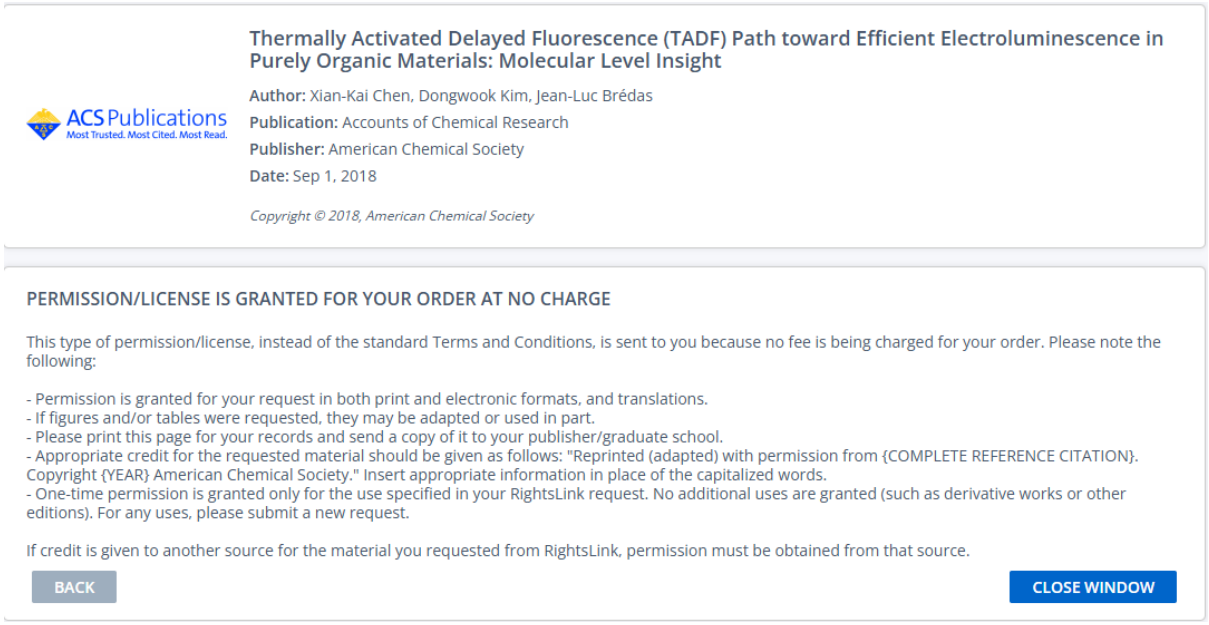

Thermally Activated Delayed Fluorescence (TADF) Path toward Efficient Electroluminescence in Purely Organic Materials: Molecular Level Insight

Author: Xian-Kai Chen, Dongwook Kim, Jean-Luc Brédas
Publication: Accounts of Chemical Research
Publisher: American Chemical Society
Date: Sep 1, 2018

Copyright © 2018, American Chemical Society

PERMISSION/LICENSE IS GRANTED FOR YOUR ORDER AT NO CHARGE

This type of permission/license, instead of the standard Terms and Conditions, is sent to you because no fee is being charged for your order. Please note the following:

- Permission is granted for your request in both print and electronic formats, and translations.
- If figures and/or tables were requested, they may be adapted or used in part.
- Please print this page for your records and send a copy of it to your publisher/graduate school.
- Appropriate credit for the requested material should be given as follows: "Reprinted (adapted) with permission from {COMPLETE REFERENCE CITATION}. Copyright {YEAR} American Chemical Society." Insert appropriate information in place of the capitalized words.
- One-time permission is granted only for the use specified in your RightsLink request. No additional uses are granted (such as derivative works or other editions). For any uses, please submit a new request.

If credit is given to another source for the material you requested from RightsLink, permission must be obtained from that source.

BACK CLOSE WINDOW

c) Copyright 2015: American Chemical Society

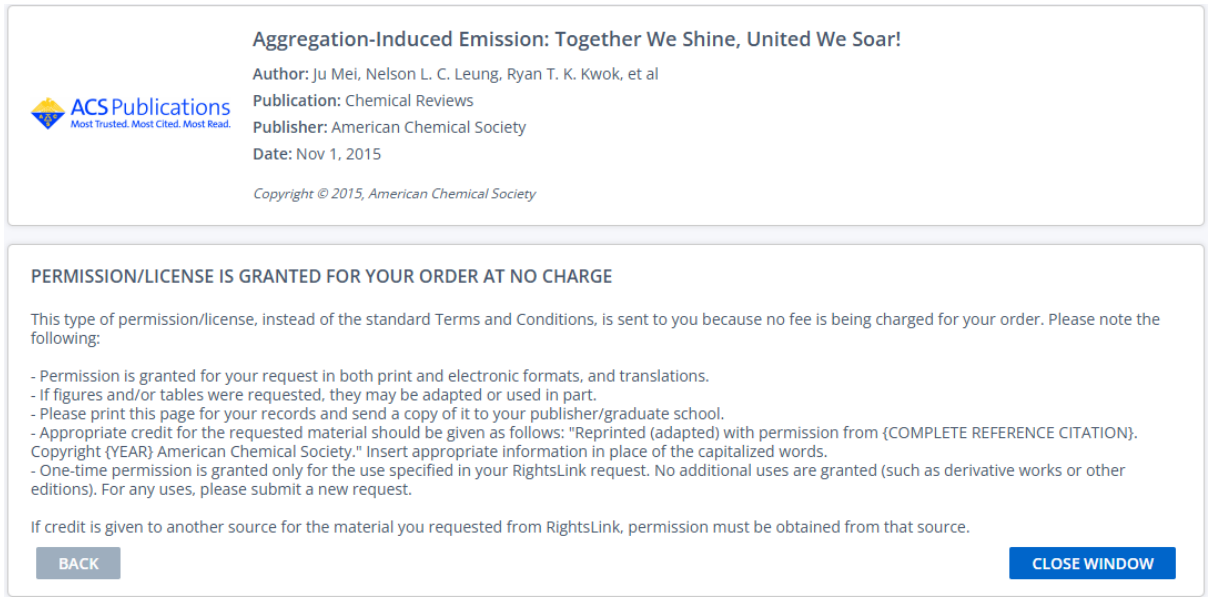

Aggregation-Induced Emission: Together We Shine, United We Soar!

Author: Ju Mei, Nelson L. C. Leung, Ryan T. K. Kwok, et al
Publication: Chemical Reviews
Publisher: American Chemical Society
Date: Nov 1, 2015

Copyright © 2015, American Chemical Society

PERMISSION/LICENSE IS GRANTED FOR YOUR ORDER AT NO CHARGE

This type of permission/license, instead of the standard Terms and Conditions, is sent to you because no fee is being charged for your order. Please note the following:

- Permission is granted for your request in both print and electronic formats, and translations.
- If figures and/or tables were requested, they may be adapted or used in part.
- Please print this page for your records and send a copy of it to your publisher/graduate school.
- Appropriate credit for the requested material should be given as follows: "Reprinted (adapted) with permission from {COMPLETE REFERENCE CITATION}. Copyright {YEAR} American Chemical Society." Insert appropriate information in place of the capitalized words.
- One-time permission is granted only for the use specified in your RightsLink request. No additional uses are granted (such as derivative works or other editions). For any uses, please submit a new request.

If credit is given to another source for the material you requested from RightsLink, permission must be obtained from that source.

BACK CLOSE WINDOW

d) Copyright 2014: John Wiley & Sons

Advanced materials

Article: Aggregation-induced emission: the whole is more brilliant than the parts.

GENERAL INFORMATION

Request ID	600194304	**Request Date**	07 Jan 2025
Request Status	Accepted	**Price**	0.00 USD

> ALL DETAILS

COMMENTS

e) Copyright 2012: Nature

CCC RightsLink

SPRINGER NATURE

Highly efficient organic light-emitting diodes from delayed fluorescence

Author: Hiroki Uoyama et al
Publication: Nature
Publisher: Springer Nature
Date: Dec 12, 2012

Copyright © 2012, Springer Nature Limited

Order Completed

Thank you for your order.

This Agreement between Abhijit Chatterjee ("You") and Springer Nature ("Springer Nature") consists of your order details and the terms and conditions provided by Springer Nature and Copyright Clearance Center.

License number	Reference confirmation email for license number
License date	Jan, 07 2025

Licensed Content

Licensed Content Publisher	Springer Nature
Licensed Content Publication	Nature
Licensed Content Title	Highly efficient organic light-emitting diodes from delayed fluorescence
Licensed Content Author	Hiroki Uoyama et al
Licensed Content Date	Dec 12, 2012

Order Details

Type of Use	Thesis/Dissertation
Requestor Type	academic/university or research institute
Format	print and electronic
Portion	figures/tables/illustrations
Number of figures/tables/illustrations	2
Would you like a high resolution image with your order?	no
Will you be translating?	no
Circulation/distribution	50000 or greater
Author of this Springer Nature content	no

About Your Work

Title of new work	Molecular Design Strategies for Enhancing Triplet Harvesting Efficiency in Organic Emitters and Aggregates via Thermally Activated Delayed Fluorescence (TADF) and Room Temperature Phosphorescence (RTP)
Institution name	Indian Institute of Science Education and Research, Pune
Expected presentation date	Jun 2025

Additional Data

Portions	Figures 1,5
The Requesting Person / Organization to Appear on the License	Abhijit Chatterjee

https://s100.copyright.com/AppDispatchServlet

07/01/2025, 19:26 RightsLink® by Copyright Clearance Center

Requestor Location

Mr. Abhijit Chatterjee
IISER Pune

Requestor Location

Pune, 411008
India

Billing Information

Billing Type	Invoice
Billing address	Abhijit Chatterjee IISER Pune Pune, India 411008

Tax Details

Total: 0.00 USD

CLOSE WINDOW

f) Copyright 2018: Royal Society of Chemistry

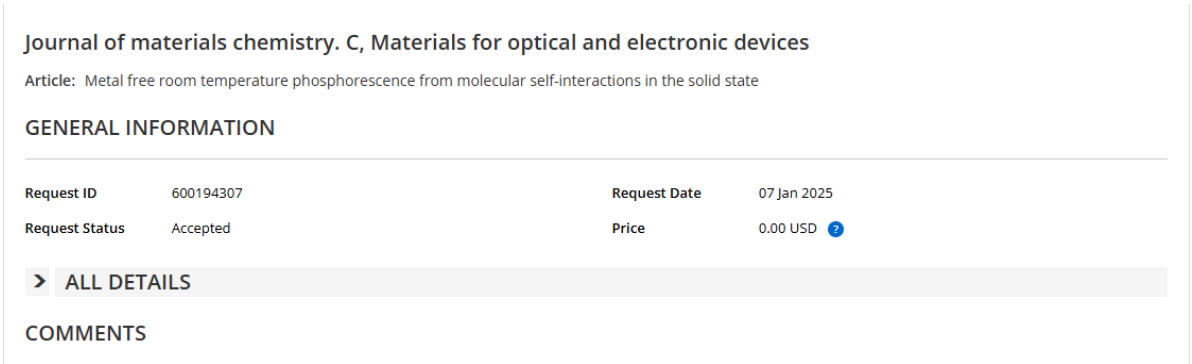

Journal of materials chemistry. C, Materials for optical and electronic devices

Article: Metal free room temperature phosphorescence from molecular self-interactions in the solid state

GENERAL INFORMATION

Request ID	600194307	Request Date	07 Jan 2025
Request Status	Accepted	Price	0.00 USD

ALL DETAILS

COMMENTS

ORDER REVIEW

1. Journal of materials chemistry. C, Materials for optical and electronic devices

0.00 USD

Article: Metal free room temperature phosphorescence from molecular self-interactions in the solid state

ISSN	2050-7526	Publisher	Royal Society of Chemistry
Type of Use	Republish in a thesis/dissertation	Portion	Chart/graph/table/figure

LICENSED CONTENT

Publication Title	Journal of materials chemistry. C, Materials for optical and electronic devices	Rightsholder	Royal Society of Chemistry
		Publication Type	Journal
		Start Page	4603
Article Title	Metal free room temperature phosphorescence from molecular self-interactions in the solid state	End Page	4626
		Issue	17
		Volume	6
Author / Editor	Royal Society of Chemistry (Great Britain)		
Date	01/01/2012		
Language	English		
Country	United Kingdom of Great Britain and Northern Ireland		

REQUEST DETAILS

ps://marketplace.copyright.com/rs-ui-web/mp/checkout/review-details

Portion Type	Chart/graph/table/figure	Distribution	Worldwide
Number of Charts / Graphs / Tables / Figures Requested	1	Translation	Original language of publication
Format (select all that apply)	Print, Electronic	Copies for the Disabled?	No
		Minor Editing Privileges?	No
Who Will Republish the Content?	Publisher, not-for-profit	Incidental Promotional Use?	No
		Currency	USD
Duration of Use	Life of current edition		
Lifetime Unit Quantity	Up to 499		
Rights Requested	Main product		

NEW WORK DETAILS

Title	Molecular Design Strategies for Enhancing Triplet Harvesting Efficiency in Organic Emitters and Aggregates via Thermally Activated Delayed Fluorescence (TADF) and Room Temperature Phosphorescence (RTP)	Institution Name	Indian Institute of Science Education and Research, Pune
		Expected Presentation Date	2025-05-31
Instructor Name	Abhijit Chatterjee		

ADDITIONAL DETAILS

Order Reference Number	N/A	The Requesting Person / Organization to Appear on the License	Mr. Abhijit Chatterjee, Indian Institute of Science Education and Research, Pune

REQUESTED CONTENT DETAILS

Title, Description or Numeric Reference of the Portion(s)	Figure 7	Title of the Article / Chapter the Portion Is From	Metal free room temperature phosphorescence from molecular self-interactions in the solid state
Editor of Portion(s)	Forni, Alessandra; Lucenti, Elena; Botta, Chiara; Carlati, Elena	Author of Portion(s)	Forni, Alessandra; Lucenti, Elena; Botta, Chiara; Carlati, Elena
Volume / Edition	6		
Page or Page Range of Portion	4603-4626	Issue, if Republishing an Article From a Serial	17
		Publication Date of Portion	2018-01-01

Total Items: 1

Total Due: 0.00 USD

2. Chapter 2 is adapted from Chatterjee, A.; Chatterjee, J.; Sappati, S.; Sheikh, T.; Umesh, R.M.; Ambhore, M. D.; Lahiri, M.; Hazra, P. Emergence of aggregationinduced emission (AIE), room-temperature phosphorescence (RTP),and multistimuli response from a single organic luminogen bydirected structural modification. *J. Phys. Chem. B* **2021**, *125*, 12832−12846.

Copyright 2021: American Chemical Society

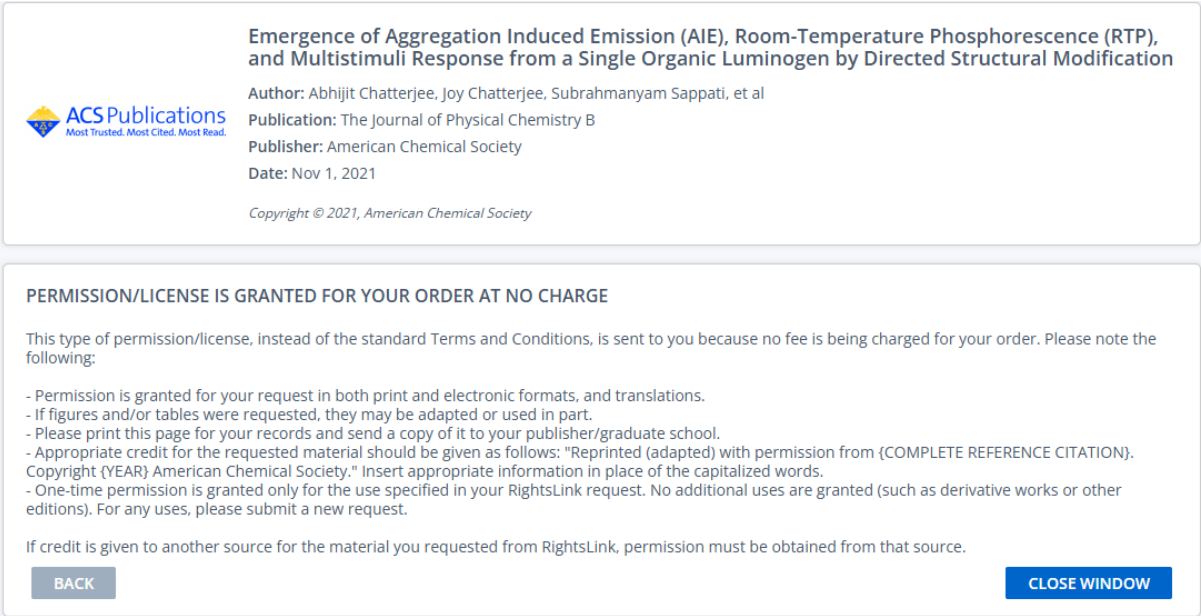

ACS Publications
Most Trusted. Most Cited. Most Read.

Emergence of Aggregation Induced Emission (AIE), Room-Temperature Phosphorescence (RTP), and Multistimuli Response from a Single Organic Luminogen by Directed Structural Modification

Author: Abhijit Chatterjee, Joy Chatterjee, Subrahmanyam Sappati, et al
Publication: The Journal of Physical Chemistry B
Publisher: American Chemical Society
Date: Nov 1, 2021

Copyright © 2021, American Chemical Society

PERMISSION/LICENSE IS GRANTED FOR YOUR ORDER AT NO CHARGE

This type of permission/license, instead of the standard Terms and Conditions, is sent to you because no fee is being charged for your order. Please note the following:

- Permission is granted for your request in both print and electronic formats, and translations.
- If figures and/or tables were requested, they may be adapted or used in part.
- Please print this page for your records and send a copy of it to your publisher/graduate school.
- Appropriate credit for the requested material should be given as follows: "Reprinted (adapted) with permission from {COMPLETE REFERENCE CITATION}. Copyright {YEAR} American Chemical Society." Insert appropriate information in place of the capitalized words.
- One-time permission is granted only for the use specified in your RightsLink request. No additional uses are granted (such as derivative works or other editions). For any uses, please submit a new request.

If credit is given to another source for the material you requested from RightsLink, permission must be obtained from that source.

BACK CLOSE WINDOW

The dissertation author is the main author of this article.

3. Chapter 3 is adapted from Chatterjee, A.; Chatterjee, J.; Sappati, S.; Tanwar, R.; Ambhore, M. D.; Arfin, H.; Umesh, R. M.; Lahiri, M.; Mandal, P.; Hazra, P. Engineering TADF, Mechanochromism, and Second Harmonic up-Conversion Properties in Regioisomeric Substitution Space. *Chem. Sci.* **2023**, *14* (47), 13832–13841.

Copyright 2023: Royal Society of Chemistry

The dissertation author is the main author of this article.

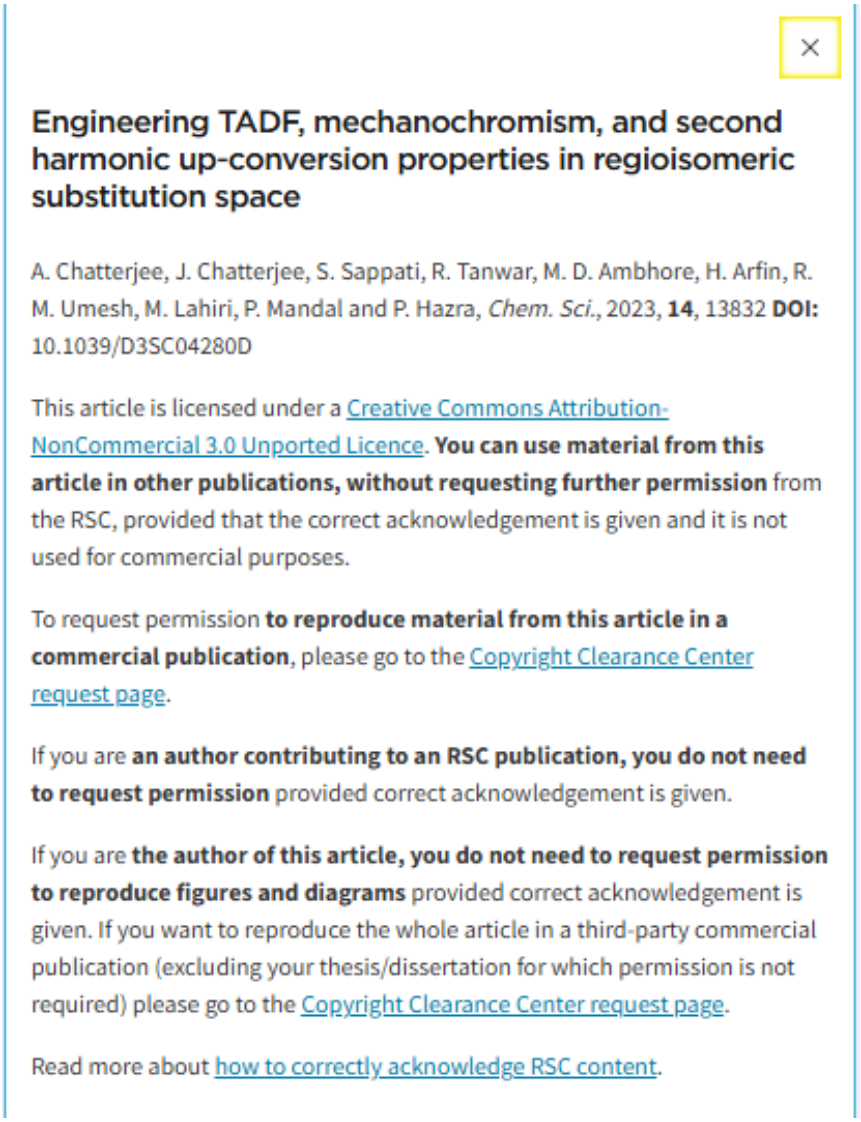

Engineering TADF, mechanochromism, and second harmonic up-conversion properties in regioisomeric substitution space

A. Chatterjee, J. Chatterjee, S. Sappati, R. Tanwar, M. D. Ambhore, H. Arfin, R. M. Umesh, M. Lahiri, P. Mandal and P. Hazra, *Chem. Sci.*, 2023, **14**, 13832 **DOI:** 10.1039/D3SC04280D

4. Chapter 4 is adapted from Chatterjee, A.; Narayanan, S.; Thorat, S.; Malik, A. J.; Ambhore, M. D.; Narayanan, A.; Sihag, A. K.; Santhosh Babu, S.; Lahiri, M.; Hazra, P. Multifunctional Luminogens with Synergy of Aggregation-Induced Delayed Fluorescence, Two-Photon Absorption and Photocurrent Generation. *Chem. Commun.* **2025**.

Multifunctional luminogens with synergy of aggregation-induced delayed fluorescence, two-photon absorption and photocurrent generation

A. Chatterjee, S. Narayanan, S. Thorat, A. J. Malik, M. D. Ambhore, A. Narayanan, A. K. Sihag, S. Santhosh Babu, M. Lahiri and P. Hazra, *Chem. Commun.*, 2025, Advance Article , **DOI:** 10.1039/D4CC05113K

The dissertation author is the main author of this article.

-The End-